Departamento de Física Teórica y del Cosmos
Universidad de Granada

Cosmic Lighthouses at High Redshift: Intervening material in sight-lines towards GRBs and QSOs

Rubén Sánchez Ramírez

Thesis submitted for the degree of

Doctor of Philosophy

May, 2016

Supervisors: Dr. Antonio de Ugarte Postigo and Prof. Alberto J. Castro Tirado

Instituto de Astrofísica de Andalucía
Consejo Superior de Investigaciones Científicas

Editor: Universidad de Granada. Tesis doctorales
Autor: Rubén Sánchez Ramírez
ISBN: 978-84-9125-969-5
URI: http://hdl.handle.net/10481/44012

Para todos aquellos que caminaron a mi lado,
aún sin yo mismo entender hacia dónde me dirigía ...

Resumen

Pese al gran avance que durante las últimas décadas ha habido en nuestro entendimiento del Universo, debido en gran medida al avance tecnólogico de la instrumentación e infraestructuras astronómicas, todavía quedan innumerables cuestiones tanto teóricas como observacionales pendientes de respuesta. En este sentido, la reciente construcción de telescopios de 8-10 m, junto al desarrollo de los dispositivos CCD, nos han permitido observar el Universo de manera mucho más profunda o, lo que es lo mismo, observarlo cuando era muy joven.

En lo referente a la cosmología observacional, en las últimas décadas se han podido hacer cartografiados del cielo en los que se detectan galaxias muy lejanas, muy jóvenes o en proceso de formación. Gracias a ello, nuestra visión del Universo a gran escala y a grandes distancias ha mejorado significativamente, aunque todavía no hemos hecho más que arañar su superficie. Debido a las limitaciones instrumentales, los cartografiados celestes que permiten la detección de la emisión de luz de galaxias lejanas y el tratamiento estadístico de los datos no son suficientes para establecer las características del Universo cuando tenía menos de 10^9 años, ya que la luz que nos alcanza desde sitios tan remotos en el Cosmos se limita a las fuentes más luminosas que existieron, lo que nos dice muy poco acerca de lo que era "normal" en dicho periodo.

El nacimiento de la espectroscopía de absorción significó una revolución para la cosmología observacional. Esta técnica aprovecha fuentes muy luminosas para su uso como "linternas" que alumbran el medio entre la fuente y la Tierra. Las propiedades de dicho medio las podemos inferir no por detectar su luz, sino a través de sus sombras. Dichas linternas fueron originalmente estrellas jóvenes y masivas, que nos permitieron estudiar nuestra propia Galaxia. Sin embargo, si lo que buscamos es salir de nuestro entorno más cercano, necesitamos en este caso no sólo linternas, sino potentes "faros" situados a grandes distancias.

Afortunadamente, nuestro Universo dista mucho de ser un lugar tranquilo y en él tienen lugar fenómenos, tanto permanentes como transitorios, lo suficientemente energéticos

como para generar fuentes de radiación electromagnéticas lo suficientemente luminosas que actúen de "faros cósmicos" incluso en el límite del Universo actualmente observable. Los dos tipos de objetos que tradicionalmente se han venido usando como fuentes retroiluminadoras son los *quásares* o QSOs, que son fuentes permanentes, y los estallidos de rayos gamma (GRBs), que pese a ser mucho más luminosos son eventos transitorios y por tanto sólo observables durante un breve periodo de tiempo.

Los GRBs son los fenómenos más violentos que se conocen en el Universo, y son en sí mismos fuentes con suficiente interés científico como para dedicar a ellos una parte de esta Tesis. Desde su descubrimiento casual durante la Guerra Fría, la naturaleza de estos breves pero intensos estallidos de emisión gamma ha interesado a los astrónomos dado que poco podía saberse de ellos con la instrumentación y los conocimientos de que entonces se disponía. No obstante, desde finales de los 80 comenzaron a sucederse una serie de trepidantes y apasionantes descubrimientos que establecieron el carácter cosmológico de estas explosiones y el descubrimiento de contrapartidas electromagnéticas asociadas a dichas fulguraciones que duraban desde unos días a meses dependiendo de la longitud de onda de la radiación.

Actualmente se dispone de archivos observacionales y desarrollo teórico suficientes como para establecer la naturaleza de los GRBs. Dicho trabajo ha servido incluso para estudios cosmólogicos, como la construcción del diagrama de Hubble a alto redshift. Sin embargo, todavía siguen abiertas muchas cuestiones, tanto en la explicación de eventos atípicos, como en los detalles de los modelos que en general los explican.

En esta tesis se ha abordado, en una primera parte, el estudio multi-frecuencia de un evento que ejemplifica las limitaciones actuales en el conocimiento de la física de los *afterglows* asociados a GRBs. GRB 110715A se detectó el 15 de julio de 2011 (el nombre de los GRBs se forma a partir de la fecha del evento) y su evolución fue seguida desde múltiples observatorios, tanto espaciales como terrestres y en longitudes de onda desde radio hasta rayos gamma. Además de su extenso seguimiento, este GRB tiene la particularidad de ser el primer *afterglow* observado con las antenas del recientemente inaugurado observatorio ALMA.

El análisis y modelado de los datos obtenidos para este evento nos ha revelado detalles tanto de los procesos físicos que tienen lugar en la emisión del *afterglow*, como de la galaxia que albergó un evento de semejante violencia. En nuestro trabajo se muestra que las observaciones son consistentes con el modelo de bola de fuego, comúnmente aceptado. En él un jet ultra-relativista, producido durante la formación de un agujero negro en el núcleo de una estrella super-masiva, produce emisión sincrotrón al chocar con el medio circundante. Sin embargo, no ha sido posible ajustar los parámetros de dicho modelo

para obtener un ajuste estadísticamente válido, indicando que es necesaria la inclusión de más procesos físicos y/o la modificación de los existentes para explicar observaciones con este nivel tan alto de cobertura espectral y temporal. Por otro lado, hemos podido inferir detalles de la galaxia anfitriona mediante espectroscopía de absorción usando el brillo del *afterglow* como faro cósmico. Los detalles estudiados son imposibles de extraer mediante la observación directa de la galaxia, ya que es sólo detectable al límite de la capacidad de los mayores telescopios de los que actualmente disponemos. Nuestras observaciones en absorción, nos indican que se trata de una galaxia enana con un fondo de radiación ionizante más bajo de lo que normalmente se observa en otras galaxias en las que ha sucedido un GRB.

En la segunda parte de esta tesis se estudian tres GRBs, cuyo nexo de unión es que se produjeron a un redshift $z>5$. Por tanto, estos eventos han supuesto una oportunidad única para el estudio del medio interestelar e intergaláctico hasta los límites del Universo observable, y abordar cuestiones fundamentales como la evolución química o el proceso de reionización del Universo.

GRB 140304A ocurrió en una galaxia a $z\sim5.3$. A partir del espectro óptico se detectó una gran absorción de hidrógeno, asociado a lo que se conoce como sistemas DLA, siendo este caso el tercero más lejano actualmente conocido en las líneas de visión hacia GRBs. La detección de líneas metálicas en dicho sistema ha permitido estimar la metalicidad de manera suficientemente robusta como para descartar un contenido en metales atípicamente bajo, lo que marcaría la observación de la esperada evolución del contenido de metales hacia un ambiente pobre, en los cuales se espera encontrar estrellas de la llamada Población III, que fueron las primeras formadas tras el periodo de recombinación.

El descubrimiento de GRB 130606A y su subDLA a $z\sim5.9$ permitió establecer de nuevo una metalicidad consistente con los valores encontrados a distancias menores, aunque hay que tener en cuenta que también se observa un contenido en metales en subDLAs mayor que en DLAs. A longitudes de onda menores que la de la absorción de hidrógeno por parte de la galaxia anfitriona del GRB, se observa la fuerte absorción del medio intergaláctico debido al efecto Gunn-Peterson, ya que en esa época el medio intergaláctico terminaba de reionizarse. Gracias a ello se ha podido constatar que las medidas de la profundidad óptica son consistentes con las obtenidas mediante las líneas de visión a QSOs, las cuales son mucho más imprecisas que las obtenidas en este trabajo.

Por último, la observación de GRB 140515A a $z\sim6.3$ ha significado la primera oportunidad para medir la fracción de hidrógeno neutro en el medio intergaláctico cuando la absorción G-P satura. Ello ha sido posible dada la baja columna de densidad de hidrógeno neutro de la galaxia anfitriona, lo que se traduce en la observación directa de un perfil de

absorción debido fundamentalmente al medio intergaláctico. Esta medida también ha permitido por primera vez obtener una medida de la fracción de hidrógeno neutro del medio intergaláctico a un redshift crítico para constreñir los modelos actuales de reionización del Universo.

Por tanto, en esta parte de la tesis hemos probado la utilidad de los GRBs como sondas cosmológicas a muy alto redshift, aprovechando su luminosidad y la facilidad de modelado de su emisión. También se ha mostrado la necesidad de continuar observando estos eventos para poder incrementar nuestro conocimiento acerca de las primeras etapas del Universo, ya que este método es mucho más prometedor que el uso de los QSOs porque estas fuentes decrecen en número a dichas distancias y los GRBs pueden incluso tener como progenitores estrellas de población III.

En la última parte de esta tesis se ha utilizado una muestra de 100 QSOs, además de datos de la literatura, para abordar un problema cosmológico clásico, como es la evolución del hidrógeno neutro a lo largo del tiempo cósmico. En 1986 se llevó a cabo el primer *survey* de DLAs. Estos sistemas, detectados en absorción en la línea de visión hacia QSOs (y GRBs, como se ha vista en la parte 2), contienen la mayor parte del hidrógeno neutro del Universo. La importancia de ello radica en que a partir de estas nubes se desencadenan los procesos de formación estelar, y por tanto están íntimamente ligados a la evolución de las galaxias. Desde principios de los 90 se obtuvieron más observaciones y se analizaron conjuntamente para inferir propiedades medias a escalas cosmológicas. La validez de dichos resultados descansa en el hecho de que en líneas de visión hacia QSOs, los DLAs se detectan como sistemas intervinientes, es decir, su frecuencia no está sesgada como en el caso de los DLA en las galaxias anfitrionas de GRBs. En esta tesis se ha analizado una muestra conjunta de DLAs visualmente identificados en los espectros, y se ha hecho un análisis detallado desarrollando nuevas técnicas y detectando y cuantificando fuentes de errores sistemáticos y estadísticos. Por primera vez se ha proporcionado una evidencia estadística robusta y justificada de una pequeña evolución de la cantidad de hidrógeno neutro desde z=0 a z∼5 en un factor ∼4.

Abstract

Despite the great progress of our understanding of the Universe in recent decades, largely due to technological advances in instrumentation and astronomical infrastructure, there are still countless observational and theoretical issues that are pending response. In this regard, the recent construction of 8-10 m telescopes, together with the development of CCD devices have allowed us to observe the Universe in a much deeper way, or what is the same, observe it when it was very young.

Regarding observational cosmology, in recent decades they have been surveys of the sky where very distant, very young, or even still forming galaxies are detected. As a result, our view of the Universe on a large scale and over long distances has significantly improved, although we have still not done more than scratch the surface. Due to instrumental limitations, surveys that detect the emission of light from distant galaxies are not sufficient to establish the characteristics of the Universe when it was less than 1 Gyr, since the light that reaches us from such remote places in the Cosmos is limited to the brightest sources that existed at the time, which tells us very little about what was “ normal ”in that period.

The birth of absorption spectroscopy meant a revolution for observational cosmology. This technique takes advantage of very luminous sources for use as “flashlights” that illuminate the environment between the source and Earth. We infer the properties of this environment not through its light, but through its “shadows”. These flashlights were originally young, massive stars, which allowed us to study our own Galaxy. However, if what we seek is out of our immediate environment, we need in this case not only flashlights, but powerful “beacons” located at great distances.

Fortunately, our Universe is far from being a quiet place and we can find phenomena, both permanent and transient, energetic enough to generate the necessary amount of electromagnetic radiation as to act as “cosmic beacons” even on the edge of the observable Universe. The two types of objects that have traditionally been used as illuminating sources are *quasars* or QSOs, which are permanent sources, and gamma-ray bursts

(GRBs), which despite being much brighter are transient and thus only observable for a short time events.

GRBs are the most violent phenomena known in the Universe, and are themselves sources with sufficient scientific interest to devote to them a part of this Thesis. Since their accidental discovery during the Cold War, the nature of these brief but intense bursts of gamma emission has interested astronomers. However, little could be learned about them with the instrumentation and knowledge available at the time. Since the late 80s a series of thrilling and exciting discoveries helped to establish the cosmological nature of these explosions, based on the discovery of the electromagnetic counterparts associated with these bursts, which lasted from a few days to months, depending on the wavelength of the observed radiation.

Currently available observational records and the development of theoretical models are helping to understand the nature of GRBs. This work has served even for cosmological studies, such as the construction of the Hubble diagram at high redshift. However, many questions still remain open, both in explaining atypical events, and in determining the details of the models.

In its first part, this Thesis has addressed a multi-frequency study an event that exemplifies the current limitations in the knowledge of the physics of the afterglows associated with GRBs. GRB 110715A was detected on July 15, 2011 (the name of the GRBs is formed from the date of the event) and its evolution was followed-up from multiple observatories, both space and ground-based, and at wavelengths ranging from radio to gamma-rays. In addition to his extensive monitoring, this GRB has the particularity of being the first afterglow observed with the antennas of the recently innaugurated ALMA observatory.

Analysis and modeling of the data obtained for this event has revealed details of both the physical processes taking place in the generation of the afterglow, and the galaxy that hosted an event of such violence. In our work we show that the observations are consistent with the commonly accepted fireball model. In this model, an ultra-relativistic jet, produced during the formation of a black hole in the core of a super-massive star, produces synchrotron emission when colliding with the surrounding environment. However, it has not been possible to adjust the parameters of the model to obtain a statistically valid fit, indicating that the inclusion of more physical processes and/or modification of the existing ones is necessary to explain observations with this high level of spectral and temporal coverage. On the other hand, we could infer details of the host galaxy by absorption spectroscopy using the brightness of afterglow as a cosmic lighthouse. These details are impossible to extract by directly observing the galaxy in emission, as it is only barely detectable with the largest telescopes currently available. Our observations in absorption, indicate that it is a dwarf galaxy with an environment of lower than normal ionisation field, as compared to other GRB host galaxies.

In the second part of this thesis three GRBs are studied, whose link is that they all occurred at a redshift $z>5$. These events have provided a unique opportunity to study the interstellar and intergalactic medium to the limits of the observable Universe, and to address key issues such as the chemical evolution or the process of reionisation of the Universe.

GRB 140304A occurred in a galaxy at $z\sim5.3$. From the optical spectrum, a strong absorption of hydrogen associated with what is known as DLA systems was detected, this case being the third farthest of the currently known in the lines of sight to GRB. Detection of metal lines in the system has allowed to estimate the metallicity robustly enough to rule out a low metallicity environment, marking the observation of the expected evolution of metal content to a poor environment in which it is expected find stars of the so-called Population III, which were first formed after the period of recombination.

The discovery of GRB 130606A and its associated subDLA at $z\sim5.9$ allowed to re-establish a metallicity consistent with the values found at lower distances, although it should be noted that a greater metal content is also typically observed in subDLAs than in DLAs. At wavelengths below that of the hydrogen absorption by the host galaxy of the GRB, we detect a strong absorption of the intergalactic medium due to the Gunn-Peterson effect, since at the time the intergalactic medium has finished reionising. As a result we show that the optical depth measurements are consistent with those obtained by the sightlines to QSOs, which are much weaker than those obtained in this work.

Finally, the observation of GRB 140515A at $z\sim6.3$ has provided the first opportunity to measure the fraction of neutral hydrogen in the intergalactic medium when G-P absorption saturates. This has been possible due to the low column density of neutral hydrogen in the host galaxy, resulting in the direct observation of an absorption profile mainly due to the intergalactic medium. This has also allowed for the first time to obtain a measure of the fraction of neutral hydrogen in the intergalactic medium at a critical redshift to constrain the current models of reionisation of the Universe.

Therefore, in this part of the thesis we tested the usefulness of GRBs as cosmological probes to very high redshift, taking advantage of their brightness and the ease of modeling their continuum. We have also shown the need to continue observing these events in order to increase our knowledge about the early stages of the Universe, as this method is much more promising than the use of QSOs because these sources decrease in number at large distances, whereas GRBs may even be present as population III stars.

In the last part of this Thesis we have used a sample of 100 QSOs, together with literature data, to address a classic cosmological problem, as is the evolution of neutral hydrogen over cosmic time. In 1986 the first survey of DLAs was conducted. These systems detected in absorption in the line of sight to QSOs (and GRBs, as seen in Part 2) contain most of the neutral hydrogen in the Universe. The importance of this is that from these clouds the star formation processes are triggered, and are therefore closely linked to the evolution of galaxies. Since the early 90's observations were obtained and analysed together to infer the average properties at cosmological scales. The validity of these results lies in the fact that in the lines of sight to QSO, the DLAs are detected as intervening systems, i.e., their frequency is not biased as in the case of the DLA in GRB host galaxies. In this Thesis we analysed a joint sample of visually identified DLAs in QSO spectra, and made a detailed analysis developing new techniques and determining and quantifying sources of systematic and statistical errors. This has been used to provide, for the first time, a robust statistical evidence of a small amount of evolution of hydrogen from neutral z=0 to z∼5 of a factor ∼4.

Contents

List of Figures

List of Tables

THESIS INTRODUCTION

Chapter 1

The Large Scale Structure of the Universe

> *"In this age of specialization men who thoroughly know one field are often incompetent to discuss another. The great problems of the relations between one and another aspect of human activity have for this reason been discussed less and less in public. When we look at the past great debates on these subjects we feel jealous of those times, for we should have liked the excitement of such argument."*
>
> — Richard P. Feynman, *Caltech YMCA lunch forum, 1956*

Mankind has always looked up and admired the night sky. Civilisations have calibrated their calendars according to the sky and the stars. And they have always tried to understand what is out there, where do the stars come from, and what is our place in this Universe. When, in 1609, Galileo first aimed a telescope at the sky, we started a voyage to the deep and distant Universe, which has redefined the evolution of our World. Thanks to the most modern astronomical instrumentation, we are now in position to take the ultimate step and look back into the most remote and ancient Universe.

1.1 The Observable Universe

The Universe we observe from Earth can be defined as a mathematical *ball*, i.e., the space inside an sphere, centered on the observer, that contains galaxies formed by barionic (ordinary) matter, dark matter, and dark energy which can be part of larger structures (groups, clusters, filaments, etc., see Figure 1.1 for an artist visualization). This means that all we see from Earth is different from what we could observe from another planet in another galaxy, so one of the challenges for the understanding on the Cosmos' history is the extrapolation from our point of view to a more global conception on the beginning and evolution of the Universe.

Figure 1.1: Artist's logarithmic scale conception of the observable Universe with the Solar System at the center, inner and outer planets, Kuiper belt, Oort cloud, Alpha Centauri, Perseus Arm, Milky Way galaxy, Andromeda galaxy, nearby galaxies, Cosmic Web, Cosmic microwave radiation and Big Bang's invisible plasma on the edge. *Credit*: Pablo Carlos Budassi.

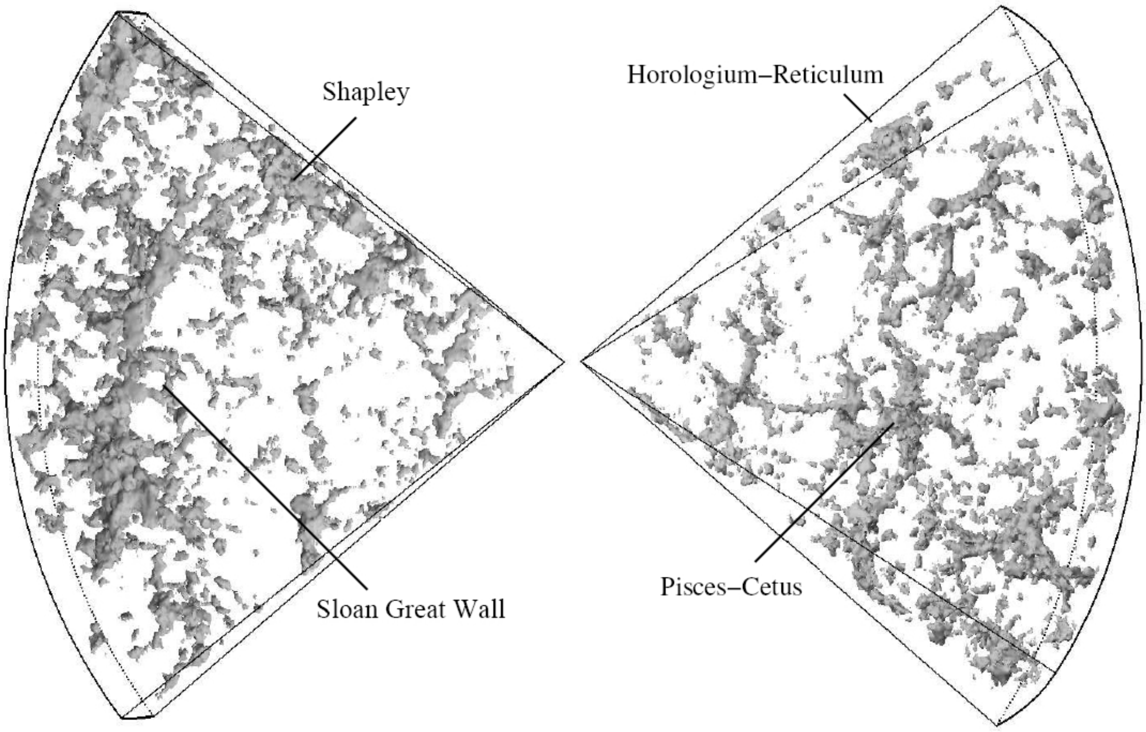

Figure 1.2: Three-dimensional DTFE reconstruction of the inner parts of the 2dF Galaxy Redshift Survey. The figure reveals an impressive view on the cosmic structures in the nearby Universe. Several superclusters stand out, such as the Sloan Great Wall, once known as the largest structure in the Universe until discovery of the Huge-LQG in January 2013. This picture was featured on 7 November 2007 on Astronomy Picture of the Day (APOD) `http://apod.nasa.gov/apod/ap071107.html`.

The surface of last scattering is the collection of points in space at the exact distance that photons from the time of photon decoupling just reach us today. These are the photons we detect today as cosmic microwave background radiation (CMBR). However, with future technology, it may be possible to observe the still older relic neutrino background, or even more distant events via gravitational waves (which also should move at the speed of light).

The best estimate of the age of the Universe is 13.799 ± 0.021 billion years (Planck *et al.*, 2014). It is estimated that the diameter of the observable Universe is about 28.5 gigaparsecs, placing its edge at about 46.5 billion light-years away.

The organization of structure of the Universe appears to follow as a hierarchical model with organization up to the scale of superclusters and filaments. It begins at the stellar level. Stars are organized into galaxies, which in turn form galaxy groups, galaxy clusters, superclusters, sheets, walls and filaments, which are separated by immense voids, creating a vast foam-like structure sometimes called the "cosmic web" (e.g. Kirshner, 2002). This network is clearly visible in the 2dF Galaxy Redshift Survey. In the Figure 1.2, a three-dimensional reconstruction of the inner parts of the survey is shown, revealing an impressive view of the cosmic structures in the nearby Universe. Several superclusters stand out, such as the Sloan Great Wall. In November 2013 astronomers discovered the Hercules–Corona Borealis Great Wall (Horváth *et al.*, 2014), an even bigger structure twice as large as the former. It was defined by mapping of gamma-ray bursts.

The End of Greatness is an observational scale discovered at roughly 100 Mpc (roughly 300 million lightyears) where the lumpiness seen in the large-scale structure of the Universe is homogenised and isotropised in accordance with the Cosmological Principle (e.g. Kirshner, 2002). The superclusters and filaments seen in smaller surveys are randomized to the extent that the smooth distribution of the Universe is visually apparent. It was not until the redshift surveys of the 1990s were completed that this scale could accurately be observed.

The more accurate are our knowledge of the Universe, the better they constrain physical models that allow us to understand how the Nature works. From an observational point of view, it is essential to apply valid and consistent techniques and strategies in order to achieve statistically significant results and validate theoretical models and/or discern between them.

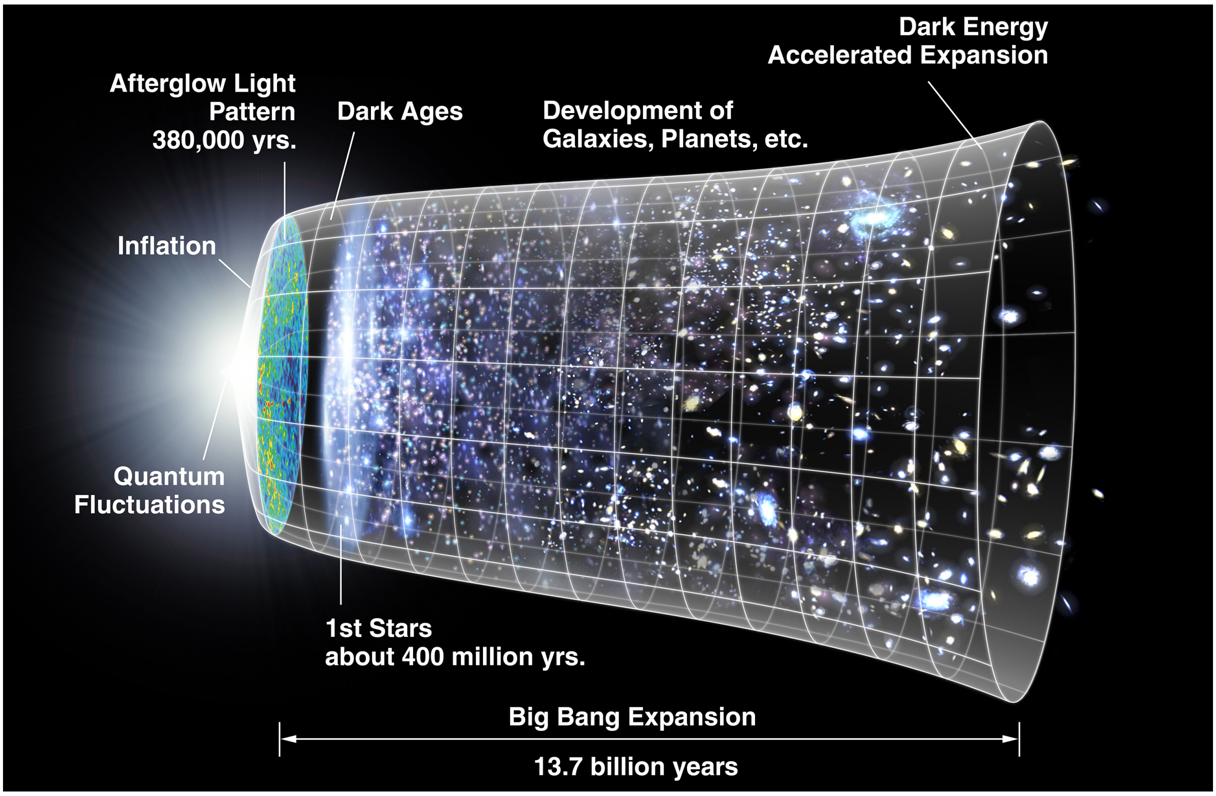

Figure 1.3: Diagram of evolution of the (observable part) of the Universe from the Big Bang (left) - to the present (right). *Credit*: NASA/WMAP Science Team.

1.2 Chronology of the Universe

All ideas concerning the very early Universe (cosmogony) are still very speculative. No experiments have yet probed energies of sufficient magnitude to provide any empiric insight into the behavior of matter at the energy levels that prevailed during these periods. Below we present a brief summary based on current ideas:

Planck epoch (From 0 to 10^{-43} seconds after the Big Bang): This is the time when one unique fundamental force ruled the Universe. Little is understood about physics at this energy regimes, so still several hypothesis propose different scenarios.

Grand unification epoch (From 10^{-43} to 10^{-36} seconds after the Big Bang): As the Universe expanded and cooled, it crossed transition temperatures at which forces separated from each other. The grand unification epoch began when gravitation separated from the other forces of nature, which are collectively known as gauge forces. The non-gravitational physics in this epoch would be described by a so-called grand unified theory (GUT). The grand unification epoch ended when the GUT forces further separate into the strong and electroweak forces.

Electroweak epoch (From 10^{-36} to 10^{-32} seconds after the Big Bang): The electroweak epoch began when the temperature of the Universe was low enough (1028 K) to separate the strong force from the electroweak force (the name for the unified forces of electromagnetism and the weak interaction). In inflationary cosmology, the electroweak epoch began when the inflationary epoch ended.

Inflationary epoch (Unknown duration, ending at $\sim 10^{-32}$ seconds after the Big Bang): Cosmic inflation was an era of accelerating expansion produced by a hypothesised field called the inflaton, which would have properties similar to the Higgs field and dark energy. While decelerating expansion would magnify deviations from homogeneity, making the Universe more chaotic, accelerating expansion would make the Universe more homogeneous. Inflation ended when the inflaton field decayed into ordinary particles in a process called "reheating", at which point ordinary Big Bang expansion began. Still there are no clear observational evidence of the validity of this theory.

Baryo-genesis: There is currently insufficient observational evidence to explain why the Universe contains far more baryons than antibaryons. After cosmic inflation ended, the Universe was filled with a quark–gluon plasma. From this point onwards the physics of the early Universe is better understood, and less speculative.

Electroweak symmetry breaking and the quark epoch (From 10^{-12} to 10^{-6} seconds after t At this time the Higgs field spontaneously acquired a vacuum expectation value, which broke electroweak gauge symmetry. There were two consequences: The weak force and electromagnetic force, and their respective bosons (the W and Z bosons and photon) manifest differently in the present Universe, with different ranges. On the other hand, via the Higgs mechanism, all elementary particles interacting with the Higgs field became massive, having been massless at higher energy levels.

Hadron epoch (From 10^{-6} to 1 seconds after the Big Bang): The quark–gluon plasma that composed the Universe cooled until hadrons, including baryons such as protons and neutrons, could form. At approximately 1 second after the Big Bang, neutrinos decoupled and began travelling freely through space (this is analogue to the cosmic microwave background that was emitted much later).

Photon epoch (From 10 seconds to $380,000$ years after the Big Bang): After most leptons and anti-leptons are annihilated at the end of the lepton epoch the energy of the Universe is dominated by photons.

Nucleosynthetic epoch (From 3 to 20 minutes after the Big Bang): Protons (hydrogen ions) and neutrons began to combine into atomic nuclei in the process of nuclear fusion. Free neutrons combined with protons to form deuterium. Deuterium rapidly fused into helium-4.

Dark ages (From 150 to 800 million years after the Big Bang): Hydrogen and helium neutral atoms began to form as the Universe cooled down. In the mean time, most of the photons in the Universe were interacting with electrons and protons in the photon–baryon fluid, i.e., the Universe was opaque. At the end of recombination, most of the protons in the Universe were bound up in neutral atoms. Therefore, the photons' mean free path became effectively infinite and the photons could then travel freely: the Universe became transparent, but at this point the only radiation emitted was the 21 cm spin line of neutral hydrogen. This cosmic event is usually referred to as decoupling, and its photons were known as the cosmic microwave background (CMB). Around the same time, existing pressure waves within the electron-baryon plasma – known as baryon acoustic oscillations (BAOs) – became embedded in the distribution of matter as it condensed, giving rise to a very slight preference in distribution of large scale objects.

Reionisation epoch (From 150 million to 1 billion years after the Big Bang: After the first stars and quasars formed from gravitational collapse, the intense UV radiation they emitted reionised the surrounding material. From this point on, most of the Universe was composed of plasma.

Formation of large scale structures : At this stage, gravitational attraction lead to the formation of groups, clusters and super-clusters of galaxies.

1.3 Observing the large-scale Universe

Different methods and techniques have been used to attempt the study of the Universe at its largest scales. In this section we present some of the observational methods that have been used over the last decades to obtain a glimpse of the furthermost regions of our Cosmos: The study of the emission of the brightest galaxies, the observation of quasi-stellar objects, and the investigation of the distant Universe through the observation of of the most luminous transient objects.

1.3.1 Large-scale surveys in emission

Recent advances of astronomical instrumentation, such as the high sensitive CCD detectors and the new generation of 8-10 m class telescopes, has improved the data quality and opened a new window to investigate our Universe.

One of the most popular ways to study the Cosmic large structure, from local to very high redshifts, are the emission surveys. They consist in the mapping of certain zones of the sky, used as valid statistical approximation of the global properties. Under this assumption, the most straightforward source of bias in the results is the limit that the main hypothesis imposes, as the surveyed regions must be large enough to properly account for the anisotropies of the Universe. The other important sources of bias are purely instrumental. All these surveys are flux limited due to the sensitivity of telescopes and detectors. Therefore, nothing can be said from these maps beyond the tip of the iceberg, so we have to take into account and try to solve the limitations of this technique.

There are two ways to map the celestial sphere:

1. **Photometric surveys**: Multi-band photometry can be considered as very low resolution spectroscopy, which can be used to derive the redshift and other physical properties of each object (Baum, 1962). This is usually done by fitting galaxy SEDs of various morphological types to the magnitudes observed in several filters. Some examples of this kind of surveys are Hubble Deep Field (HDF) North (Williams

et al., 1996) and South (Williams et al., 2000). The main advantage of this technique is that they can be very deep (up to $I \sim 28$ AB), a limit that still cannot be reached by spectroscopy. On the other hand, photometric surveys have the disadvantages of the poor spectral resolution, which translates in unavoidable degeneracies in the color-z space and difficulties to detect emission lines. Finally, it is also difficult to achieve a good compromise between resolution (the narrower and more numerous filters, the better) and SNR (the broader is the filter, the better).

2. **Spectroscopic surveys**: The analysis of the source's spectrum provides direct information on the redshift and other physical properties. Although this is the ideal method for galactic surveys, it presents several limitation, such as the observational threshold ($I \sim 24$ AB), limitations in the positioning of the fibers (which reduce the completeness factor as some sources cannot be observed in crowded fields), and the need of spectroscopic surveys to rely in existing photometric databases for target selection and identification purposes. Examples of this kind of survey can be zCOSMOS (using VLT/VIMOS; Zucca *et al.*, 2009) and Autofib (Ellis *et al.*, 1996).

1.3.1.1 Surveys of high-redshift galaxies

In order to study the highest redshift Universe, we need to obtain the deepest possible images. Consequently, at the farthest distances we are only able to obtain limited information on the most luminous sources, which will not be representative of the actual galaxy population at these redshifts. Therefore, we have to handle with care these data-sets when interpreting their results. Currently, the most distant source detected is GN-z11 from the CANDELS survey (Oesch *et al.*, 2016), with a combined photometric and spectroscopic redshift of $z = 11.09^{+0.08}_{-0.12}$.

The main techniques currently used to detect galaxies at very high redshift are based on the observation of:

Lyman Break Galaxies (LBGs): In order to select candidates from imaging surveys, the most important technique used is the "drop-out" or Lyman-break technique: it is based on the assumption that a galaxy spectrum will be significantly absorbed by H I in both its ISM and the intervening IGM at wavelengths shorter than Lyα. Therefore, high redshift colors will be red and there will be a drop out in the bluer bands affected by the break (see Figure 1.4 and, e.g., Steidel *et al.*, 1996; Warren *et al.*, 1987). By means of this technique, Bouwens *et al.* (2011) discovered a $z \approx 10$ galaxy in the HUDF survey (Beckwith *et al.*, 2006). LBG surveys are also conducted using deep ground based imaging, covering larger areas than HST is able to. For

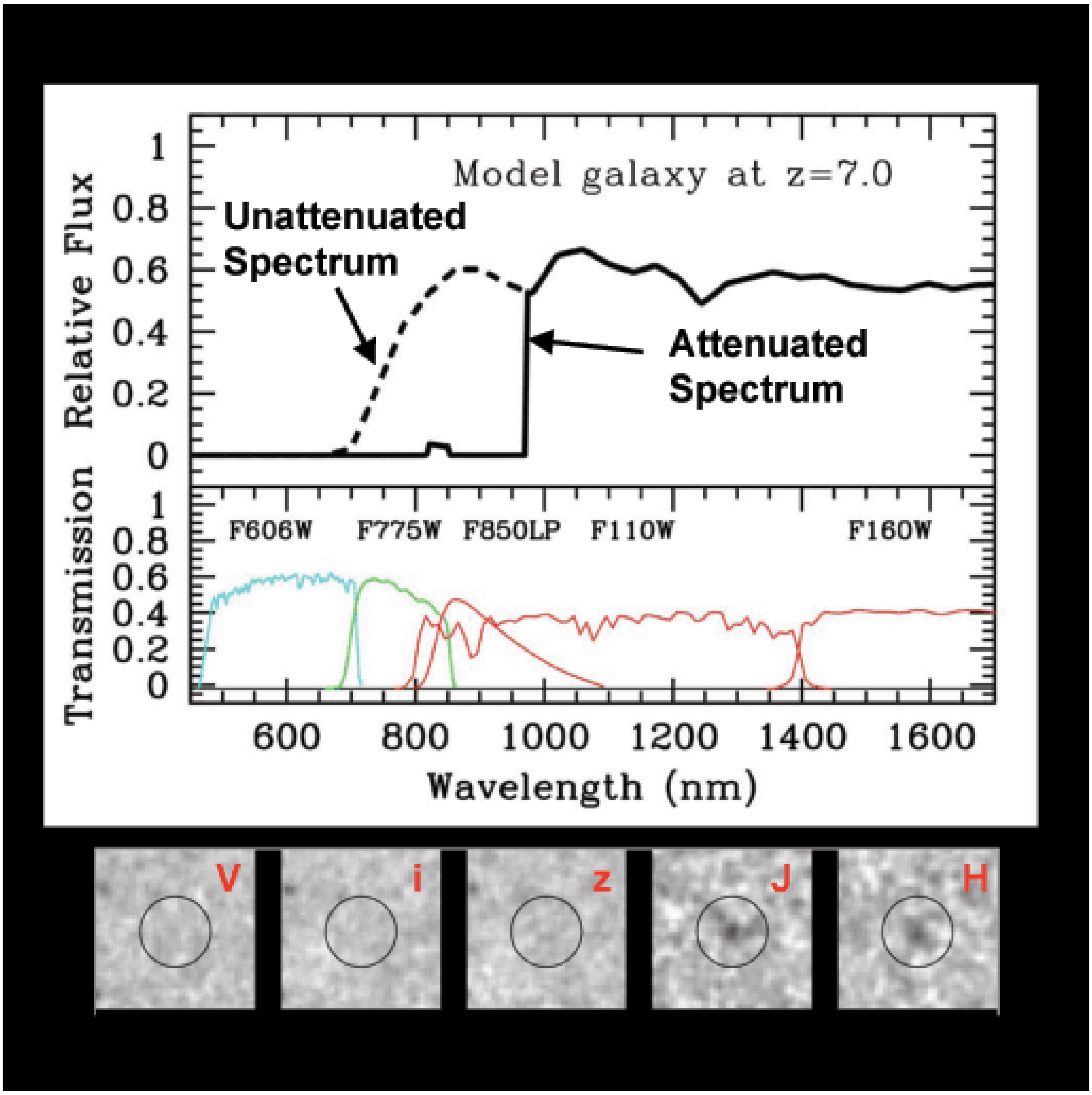

Figure 1.4: Lyman-break technique. One possible spectrum of a star-forming galaxy at a redshift of 7 is shown in the top panel. The presence of neutral hydrogen creates an abrupt drop off in flux blueward of 970 nm. The sensitivities of several of the more useful filters on HST are shown in the middle panel ("V", "i", "z", "J", and "H" bands, which have central wavelengths of 591 nm, 776 nm, 944 nm, 1119 nm, and 1604 nm, respectively). The bottom panel shows images of the redshift 7 source from the top panel, as seen through these filters. This source clearly shows up in the two longest wavelength filters "J" and "H," but completely disappears in the three bluest wavelength filters "V," "i," and "z." The presence of such a distinct break is a clear indication that we have found a galaxy at very high redshift which emitted its light at very early times. *Credit*: Rychard Bouwens.

example, Bowler *et al.* (2012) surveyed 1 deg^2, reaching a continuum level of 25 mag (AB system), and selected a sample of ∼10 highly luminous galaxies at z>6.5. Confirming LGBs spectroscopically is challenging for 8-10m class telescopes and HST. Photometric redshifts can give false high redshift sources due to confussion either by the 4000 Å break or red galactic objects (e.g. L and T dwarfs). However, at high redshift, the detection of continuum in the spectrum is usually not possible, and one has to search for emission lines arising from background noise. Often, atmospheric OH features make the detection of emission features even more difficult as they are orders of magnitude brighter and will easily outshine the galaxy emission if they are at similar wavelengths.

Lyα **emitters (LAEs):** The strongest emission line from young star-forming galaxies is Lyα. Blind searches for this emission line are usually conducted with narrow filters in a few clean (of atmospheric emission lines) wavelength windows, as z=4.5,5.7,6.5,7.0,7.3 (e.g. Iye *et al.*, 2006; Taniguchi *et al.*, 2010). A combination of both LBG and LAE techniques led to the detection of the most distant confirmed galaxy up the discovery of GN-z11 at z=8.68 (Zitrin *et al.*, 2015).

Gravitational lensing: If a high-redshift galaxy is located behind a massive cluster of galaxies, its flux can be magnified by a factor of a few-few tens due to gravitational lensing. There were some LBGs and LAEs surveys making use of this advantage. The cluster lensing and supernova survey with Hubble (CLASH Postman *et al.*, 2012) was an HST multicycle treasure program that deeply surveyed 25 massive clusters at $0.15 < z < 0.9$. Among other interesting results, the analysis of these data conducted to the detection of a likely very distant source at $z_P = 10.7^{+0.6}_{-0.4}$ (Coe *et al.*, 2013).

Sub-millimeter galaxies: In star forming galaxies, dust absorbs the huge UV radiation from OB stars and re-emits it in FIR and sub-millimeter wavelengths. Due to the shorter wavelength range sampled near this emission peak as redshift increases, the apparent flux at this band from z∼1 to 10 is comparable. Consequently, this technique is highly efficient to study high-redshift galaxies (e.g. Blain *et al.*, 2000), although, by definition, it will not detect the first galaxies that formed in metal free environments.

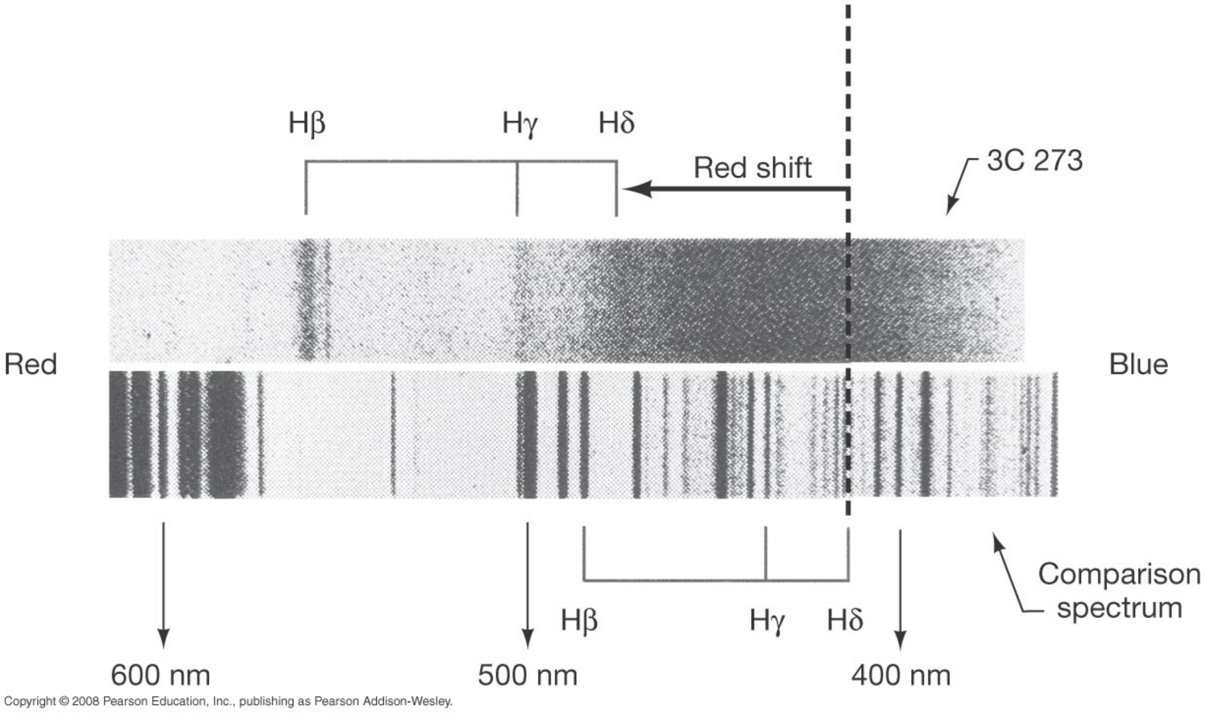

Figure 1.5: Spectrum of 3C 273.

1.4 Quasi-stellar objects – QSOs

A quasi stellar radio source (contracted to quasar) is a very powerful, luminous, and distant active galactic nucleus. It is an extremely compact region powered by accretion of material onto a super-massive rotating black hole at the center of a massive galaxy. The suggestion that the BH were involved appeared soon after their discovery (Zel'dovich & Novikov, 1964). It turned out that many quasars were not necessarily strong radio sources, so the term quasi-stellar object (QSO) started to be used frequently, as only about 10% of QSOs are radio loud.

The firsts radio surveys (such as 3C or 3rd Cambridge survey) had poor angular resolution, so many sources were unable to be associated with a particular optical source. Hazard *et al.* (1963) used the lunar occultation of 3C 273 to pin down its location, by means of the diffraction pattern produced when the source disappeared behind the moon's limb. Schmidt (1963) was then able to locate the optical counterpart and, in the position indicated by the radio observation, found two sources: a blue star and "a faint wisp or jet". The blue star, however, was not an ordinary star. Its spectrum showed strong broad emission lines that were identified with the Hydrogen Balmer series at a redshift $z = 0.16$. This discovery prompted Greenstein (1963) to look at the spectrum of another radio source (3C 48) and they found for this case $z = 0.3675$.

The key observational features of a quasar are:

- High luminosity
- Compact angular size
- Continuum emission from the core, ranging from radio to X-rays
- Emission lines
- Sporadic variability of the continuum and spectral line emission

The first key feature that was noticed was the emission line spectrum, which initially puzzled astronomers. The lines are very strong and broad in emission (something only seen in the hottest stars), featuring Hydrogen, Helium, Carbon, and Magnesium, amongst others. As well as broad lines there can be narrow, forbidden lines (the strongest are [O II], [O III], and [N II]).

The second key observation was regarding the optical emission of quasars are its very blue nature. The hottest main sequence stars have U–$B \simeq$ -0.5 mag, while typical AGN have U–$B \simeq$ -1 mag. This proved to be a relatively efficient way to search for quasars. A major example of this type of survey is the Palomar-Green (PG) catalogue (Green *et al.*, 1986), which was the source for the Palomar Bright Quasar Sample (BQS; Schmidt & Green, 1983).

The only model that has been successful in explaining how such amount of energy can be produced in a small region was the accretion of matter onto a black hole. Based on this idea, the basic inferred structure of a quasar would be:

- Central supermassive black hole, with masses reaching up to $10^9 M_\odot$
- Accretion disk surrounding the black hole, which is believed to be the source of the strong continuum.
- Broad line region (BLR). A region extending a few hundred light days from the black hole.
- Narrow line region (NLR). This region is farther and may be associated with the host galaxy.
- Finally, the other key feature, particularly in radio-loud quasars, is a jet.

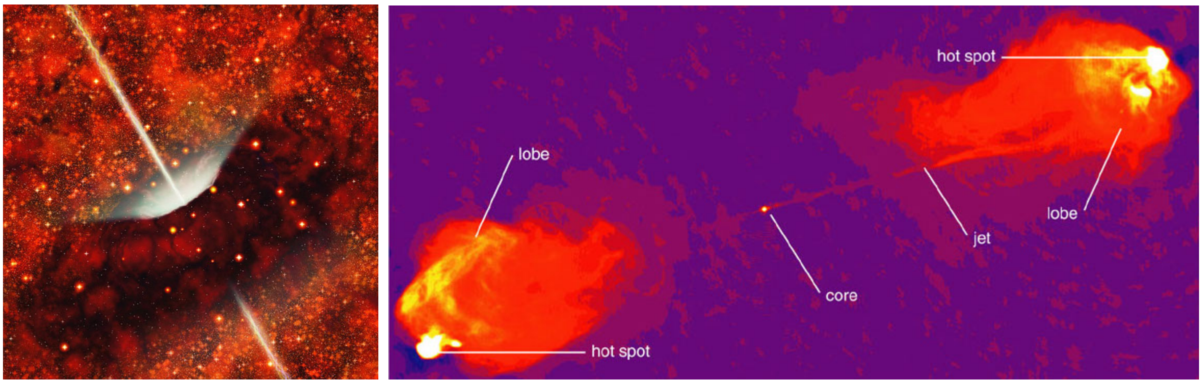

Figure 1.6: Artistic representation and radio image of a quasar. *Credit*: Pearson Education, publishing as Addison Wesley.

This basic structure of a quasar (or, more generally, of an active galactic nuclei – AGN) has formed the foundation for viewing angle unification schemes. Their essence is that they explain the observed properties of different types of AGN through the variation of the line of sight angle to the system.

Because quasars are so distant and luminous, it has been difficult to study the host galaxies which contain them. Many quasar host galaxies are interacting or merging systems, as well as normal elliptical or spirals. It has been found that radio loud quasars tend to be found in elliptical and interacting galaxies, and radio quiet seem to be present in both elliptical and spiral galaxies (e.g., Wolf & Sheinis, 2008).

Nowadays, the most luminous quasar known ($4.2 \times 10^{13} L_\odot$) is SDSS J0100+2802 (Wu *et al.*, 2015), with a redshift of 6.30. The most distant QSOs is ULAS J1120+0641 (Mortlock *et al.*, 2011), at z=7.085.

In this Thesis we will use QSOs as back illuminating sources to study intervening absorbers (see Chapter **??** for an introduction on the methods for doing this).

1.5 Luminous transient sources

Some of the most luminous objects in the Universe are of transient nature, where a large quantity of energy is rapidly released to power the emission of an enormous amount of photons during a brief period of time. Some examples of such objects can be:

X-ray Binaries are binary systems wich can be very luminous in X-rays. It is thought that the high energy radiation is produced by matter falling from one component (typically a MS star) onto a compact object, which can be a white dwarf, an neutron

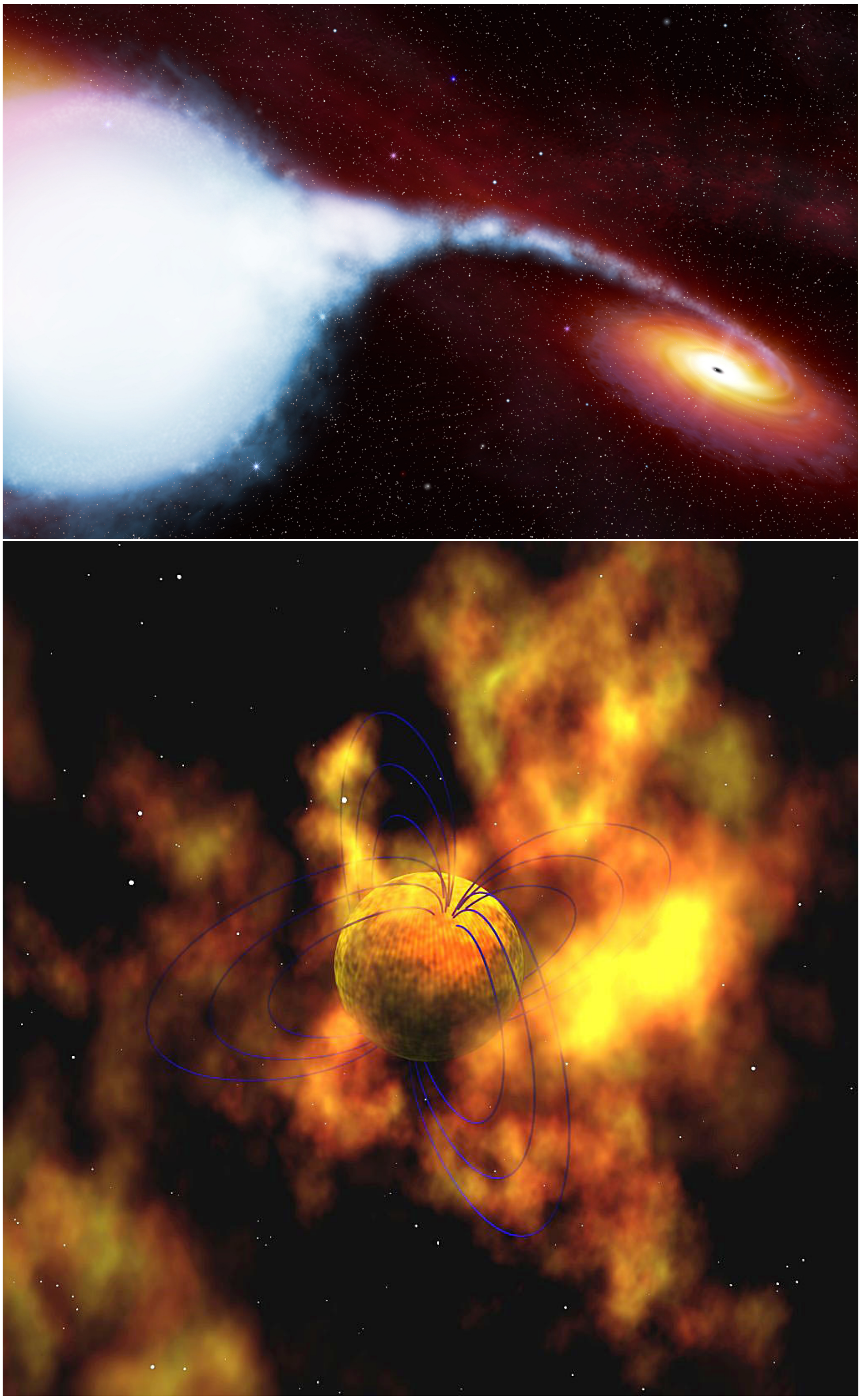

Figure 1.7: *Top:* An artist's illustration of material being gravitationally stripped off a blue supergiant variable star designated HDE 226868 onto a black hole known as Cygnus X-1 *Credit*: David A. Hardy. *Bottom:* Astronomers think soft gamma-ray repeaters are magnetars – neutron stars with a super-strong magnetic field (blue arcs in this artist's concept). *Credit*: NASA/GSFC Conceptual Image Lab

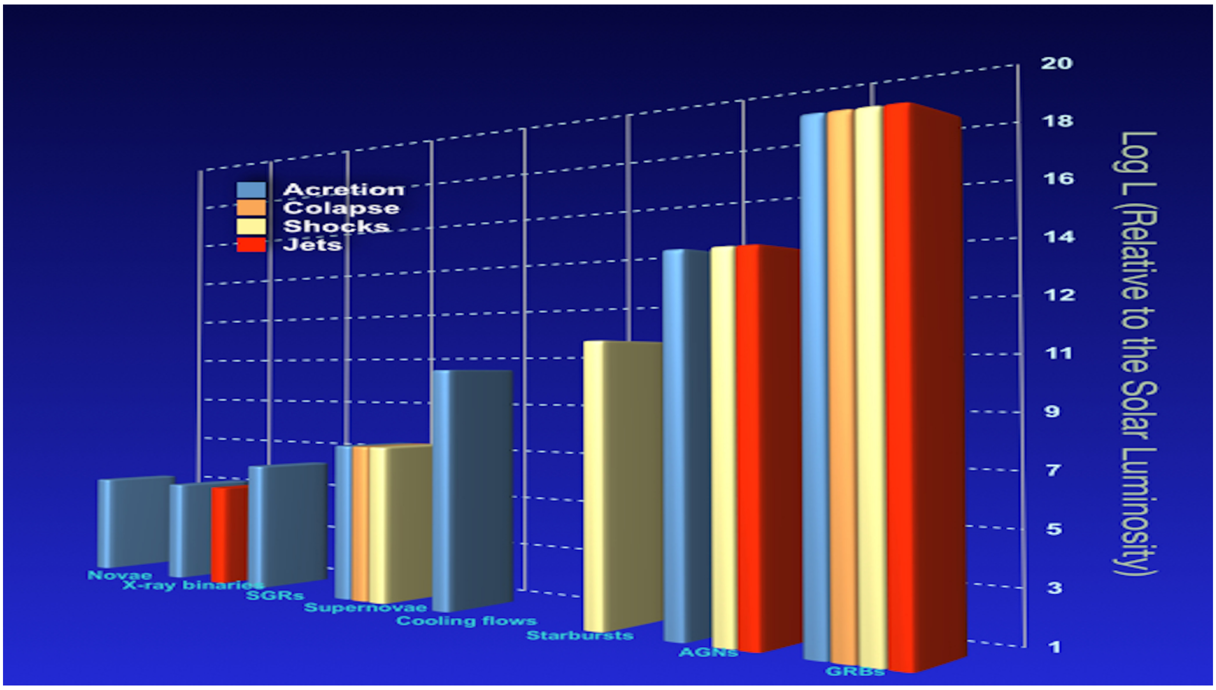

Figure 1.8: Comparison of the luminosities of the most luminous sources in the Universe, as well as the physical mechanisms that explain their emission. *Credit*: Javier Gorosabel

star or a black hole (Salpeter, 1964). There are hundreds of these sources in our galaxy, with $L_X \sim 10^{34}$ - 10^{38} erg s^{-1}, and they can also be detected in other galaxies.

Soft gamma repeaters (SGRs) are astronomical objects which emit dramatic but very brief bursts (typically a fraction of a second) of gamma-rays and X-rays at irregular intervals. SGR 0525-66 (PSR B0525-66) is was the first SGR ever detected, located in the Large Magellanic Cloud (Cline *et al.*, 1982, nowadays the only known located outside our galaxy). These phenomena has been interpreted as due to magnetars (Duncan & Thompson, 1992), a type of neutron star with extremely powerful magnetic fields. Kouveliotou *et al.* (1998) firmly established this association.

Supernovae (SNe) are stellar explosions that radiate as much energy as the Sun or any ordinary star is expected to emit over its entire life span, before fading from view over several weeks or months. The extremely luminous burst of radiation expels much of the star's material at a velocity of up to 30,000 km s^{-1}, driving a shock wave into the surrounding interstellar medium. This shock wave sweeps up an expanding shell of gas and dust called a supernova remnant. Their luminosity can be up to 10^{10} $L_{\odot}$. Supernovae can be triggered either by the sudden re-ignition of nuclear fusion in a degenerate star, or by the gravitational collapse of the core of a massive star.

- **Gamma-ray bursts (GRBs)** are the most luminous objects that we have ever detected in our Universe. In a few tens of seconds a GRB can become, in visible light, one million times brighter than the galaxy that contains it. After this, its luminosity decays rapidly and can become undetectable in just a few hours or days. In gamma-rays their emission is even more dramatic, becoming for a few seconds brighter than the rest of the Universe combined. GRBs can be 10 000 more luminous than the most luminous QSOs and a million times more luminous than the brightest SNe. Within this Thesis we will pay special attention to the study of these objects (see Chapter **??** for an introduction on GRBs) and their use (in parallel to QSOs) to illuminate the most remote corners of the Universe (see the next Chapter).

Chapter 2

The Universe in absorption

> *"Eventually, we reach the utmost limits of our telescopes. There, we measure shadows and search among ghostly errors of measurement for landmarks that are scarcely more substantial."*
>
> — Edwin P. Hubble, *The Realm of the Nebulae, 1936*

Traditionally, the study of the remote Universe has been performed through the observation of luminous objects, easily detectable with our telescopes. However, those objects represent the most extreme environments and phenomena, which are not necessarily representative of the Universe. In this chapter we show how the light emitted from those extraordinarily luminous sources in the remote Universe can be also used to study dark, cold, and calm regions that happen to lie in their sightlines, through spectroscopic studies in absorption.

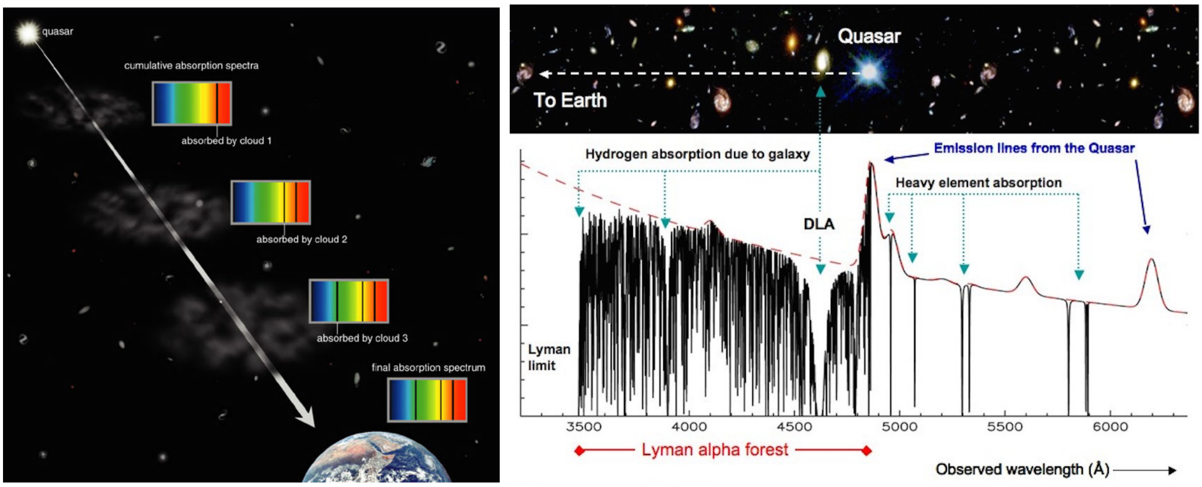

Figure 2.1: Process that forms absorption lines along the emission of the QSO. *Credit*: John Webb (left) and Pearson Education, publishing as Addison Wesley (right).

2.1 Absorption systems

An absorption system is the set of lines at the same redshift that come from the same absorber and that are imprinted on the spectrum of a back-illuminating source. Lines come from atom and/or molecule transitions, depending on the chemical composition of the absorption system. These systems can be often decomposed in several velocity components/subsystems, that can are the result of the dynamics of the cloud and/or different clouds that are distant enough to be resolved. Figure 2.1 shows the process that forms an absorption spectrum.

In Chapter 1 we presented the most luminous sources in the Universe, from which QSOs and GRBs are the best candidates for being used as cosmic lighthouses. Each of these beacons have their own particularities, advantages, and problems for their application in the study of their host galaxies and intervening systems.

On one hand, quasars shine in a roughly constant way. This means that the surrounding medium is highly ionized and near the equilibrium in a Strömgrem sphere that can extend outside the host galaxy. This fact has to be taken into account in host and IGM/CGM studies, but it greatly simplifies their observations and the construction of unbiased samples to investigate statistically the physical properties of the large-scale Universe.

On the other hand, GRBs shine from star-forming galaxies, tracing the material from the dying star along its birthplace and the rest of the galaxy to the Earth. In spite the immense energy release of this kind of explosions, their short duration implies that their environment is not altered significantly. Consequently, we expect that only fine-structure

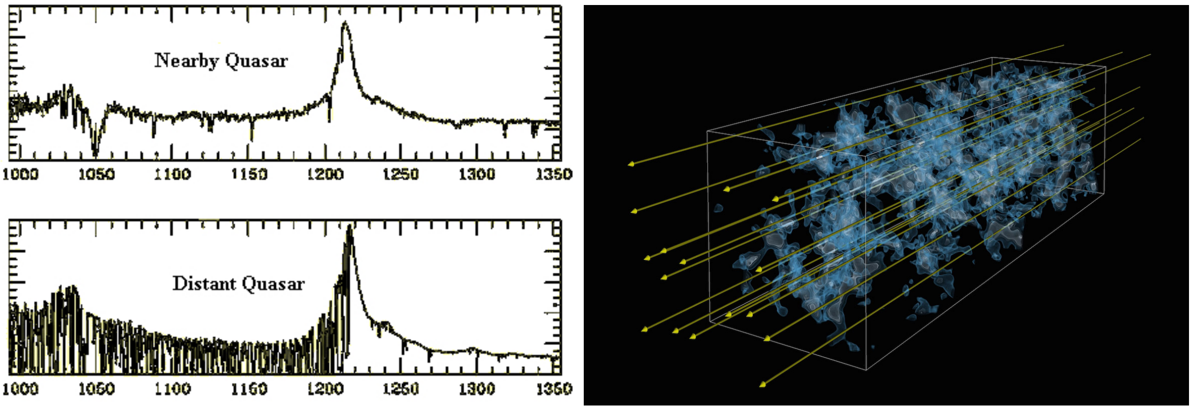

Figure 2.2: *Left*: The Lyman Alpha Forest is shown in the spectrum of the quasar on the bottom. The nearer quasar's light is not absorbed by many intervening gas clouds, so its spectrum doesn't have as many absorption features as the more distant quasar. Based on the image from Bill Keel's slide set. *Right*: Artist's impression illustrating the technique of Lyman-alpha tomography: as light from distant background galaxies (yellow arrows) travel through the Universe towards Earth, they are imprinted by the absorption signatures from hydrogen gas tracing in the foreground cosmic web. By observing a number of background galaxies in a small patch of the sky, astronomers were able to create a 3D map of the cosmic web using a technique similar to medical computer tomography (CT) scans. *Credit*: Khee-Gan Lee (MPIA) and Casey Stark (UC Berkeley).

levels are excited during the afterglow emission and that the abundances measured in spectra are representative of the real conditions of the probed clouds. However, precisely because of their short duration, it is extremely difficult to observe them unless telescopes are prepared to point to them very rapidly (within minutes to hours).

The first absorption lines detected in QSO spectra were towards the line of sight of 3C 191 (Burbidge *et al.*, 1966; Stockton & Lynds, 1966). This discovery opened the door to the extragalactic absorption studies, in which lines do not depend neither on the physical conditions nor on the distance, so the measurement of absorption lines are much more significant than emission lines.

Attending to the origin of the absorption lines, quasars absorbers (and analogously for GRBs) can be classified as:

Associated absorption lines (AALs): Systems with $z_{\mathrm{abs}}{\sim}z_{\mathrm{em}}$. They are associated to the host galaxy and/or the CGM, and are classified in two types: broad absorption lines (BALs; e.g. Weymann *et al.*, 1979), with broadening of ~10,000km s^{-1}, and narrow absorption lines (NALs; e.g. D'Odorico *et al.*, 2004), that have lower dispersions.

Intervening absorbers: Systems with $z_{\mathrm{abs}}{<<}z_{\mathrm{em}}$. They are due to gas distributed

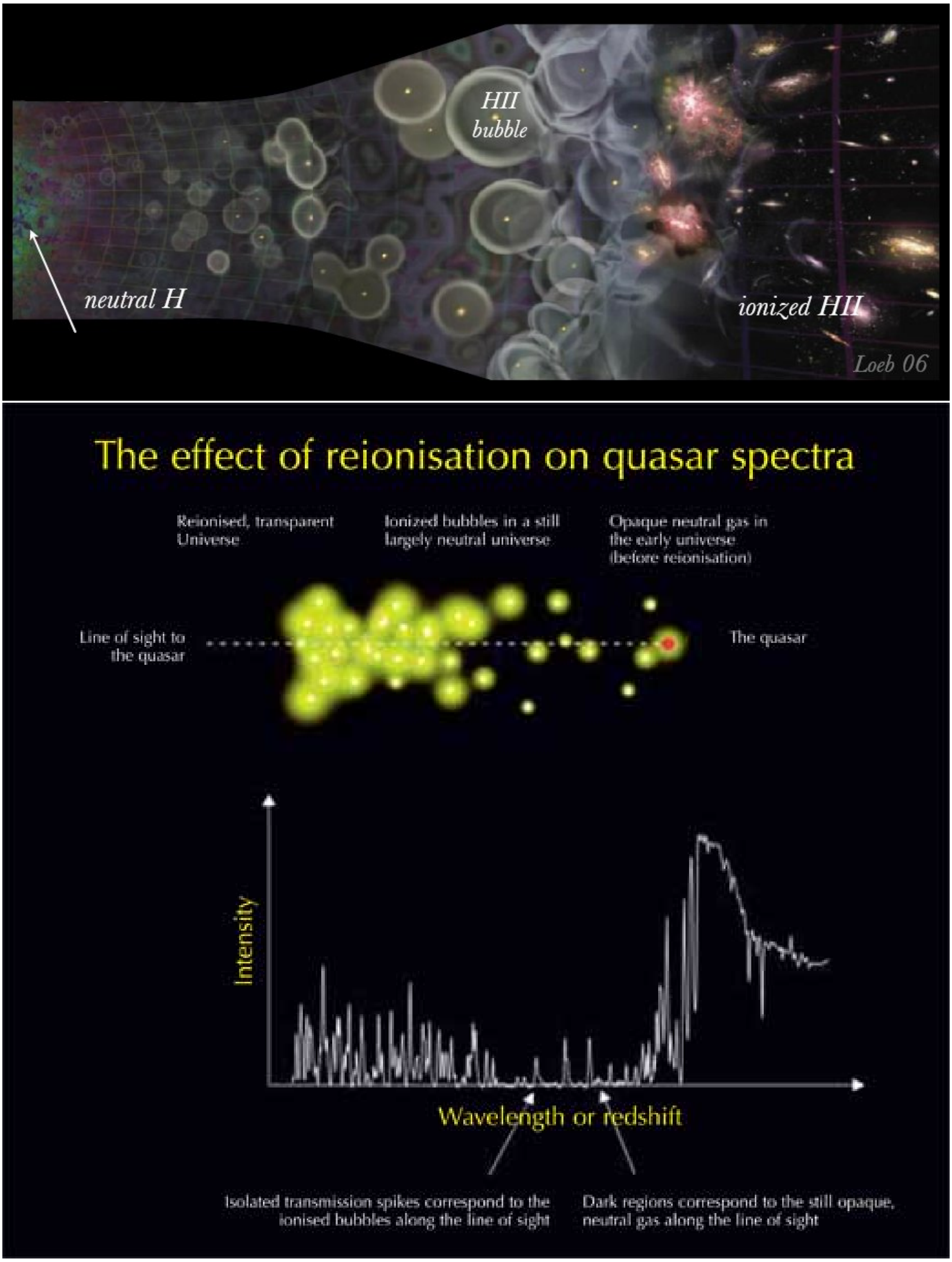

Figure 2.3: Schematic view of the translation of the IGM state into the QSO spectrum.

along the line of sight to the quasar that is unrelated with it. In order to discard possible systems in the same group or cluster, it is a common practice considering as intervening absorber those with v >5,000km s^{-1}respect to the QSO emission redshift. Their classification is based on the column density of the H I absorption:

- Lyman forest (log N(H I)<17.0): Lynds (1971) first suggested that the numerous absorption features present in a QSO spectrum (see Fig. 2.1) correspond to the Lyα transition (H Iλ1215) coming from absorption systems between the back-source and the Earth. This interpretation was definitely accepted with the work by Sargent *et al.* (1980). The sum of all these low density absorptionis in the spectrum is the so called Lyα-forest. Theoretical simulations pointed out that the forest is formed by overdensities of H I confined by the dark matter along extended filaments (Cen *et al.*, 1994), as represented in Fig 2.2.
- Lyman limit systems (LLSs; log N(H I)>17.0): These absorbers are defined as those that are dense enough so that most of the photons with $h\nu$ >13.6 eV at λ <912 Åare captured by the absorber. Technically, these systems have an optical depth $\tau_{912} > 1$. Accordingly quasar spectra will show a discontinuity in their flux at

  $$\lambda = (1 + z_{abs}) \times 912\mathring{A} \tag{2.1}$$

  that can hide completely the emission under the noise level. As the absorption cross-section depends on the frequency as

  $$\sigma = 6.3 \times 10^{-18}(E_{\gamma}/13.6eV)^{-3}cm^{2} \tag{2.2}$$

  the transparency of the medium to a ionising photon will increase when its energy becomes higher. It is thought that these systems are clouds in the outlayers of proto-galaxies (Prochaska, 1999).
- Damped Lyman α systems (DLAs; log N(H I)>20.3): These systems are defined to be dense enough to be neutral hydrogen reservoirs for star formation processes (Wolfe *et al.*, 1986).
- The Gunn-Peterson effect: Gunn & Peterson (1965) predicted a feature in the spectra of quasars due to the higher presence of neutral hydrogen in the intergalactic medium at z∼6. Further investigations were performed (e.g. Jenkins & Ostriker, 1991; Levshakov & Kegel, 1998; Songaila *et al.*, 1999) until the discovery of the trough towards SDSS J103027.10+052455.0 at z=6.28 (Becker *et al.*, 2001).

As long GRB progenitors are very massive stars, their lives are consequently very short, and are good tracers of the star-forming regions in which they are born, and from which they don't have time to exit before they die. The lines of sight from the GRB to the Earth first probe the GRB surrounding medium, and then probably the star-forming region, the disk, and finally the halo of the host galaxy. When the light is outside of the host galaxy, it traces the intervening IGM and eventually other galaxies. All these systems leave their imprint on the spectrum of the afterglow.

Therefore, GRB afterglows are useful tools to study the properties of galaxies that form GRBs. Comparing them to samples of star-forming galaxies, both in emission and absorption, we are able to assess questions ranging from specific issues on GRB progenitors and environments to general cosmology.

2.2 Damped Lyman α systems

Damped Lyman alpha absorbers comprise the neutral gas reservoir for star formation at high redshifts (Nagamine *et al.*, 2004a,b). Stars are likely to descend from cold neutral clouds, which are the predecessors of molecular clouds and the birth sites of stars (Wolfire *et al.*, 2003). Therefore, the study of DLAs provides critical information on the formation and evolution of galaxies.

Unsurprisingly, the most prominent feature seen in afterglow spectra is the Lyα line of neutral Hydrogen (H Iλ1216). In the GRB case, it is possible to perform more accurate measurements than in QSO sigh-lines due to the clean red damping wing consequence of the nearness of the absorbing cloud to the GRB progenitor.

As QSO-DLAs are intervening systems, we expect to find differences between QSO-DLA and GRB-DLA samples due to selection effects (see Fig. 2.5). The detection rate of absorbers in intervening QSO-DLA surveys depend on the product of the number of these systems at a given redshift and their cross section. Accounting for the cross section, it is expected that QSO-DLAs trace predominantly gas from the outer regions of the ISM. In contrast, GRB-DLA sight-lines are expected to start from the core of H II regions created by massive stars, and then probe from the inner to the outer regions of the ISM.

Despite the fact that the current GRB-DLA sample is significantly smaller than the QSO-DLA one, there is a clear overlap of both QSO and GRB DLA distributions around $\log N(\mathrm{H\,I}){=}21.5$, showing GRB sight-lines a much larger number of dense systems compared with the QSO-DLA sample (see also Noterdaeme *et al.*, 2015).

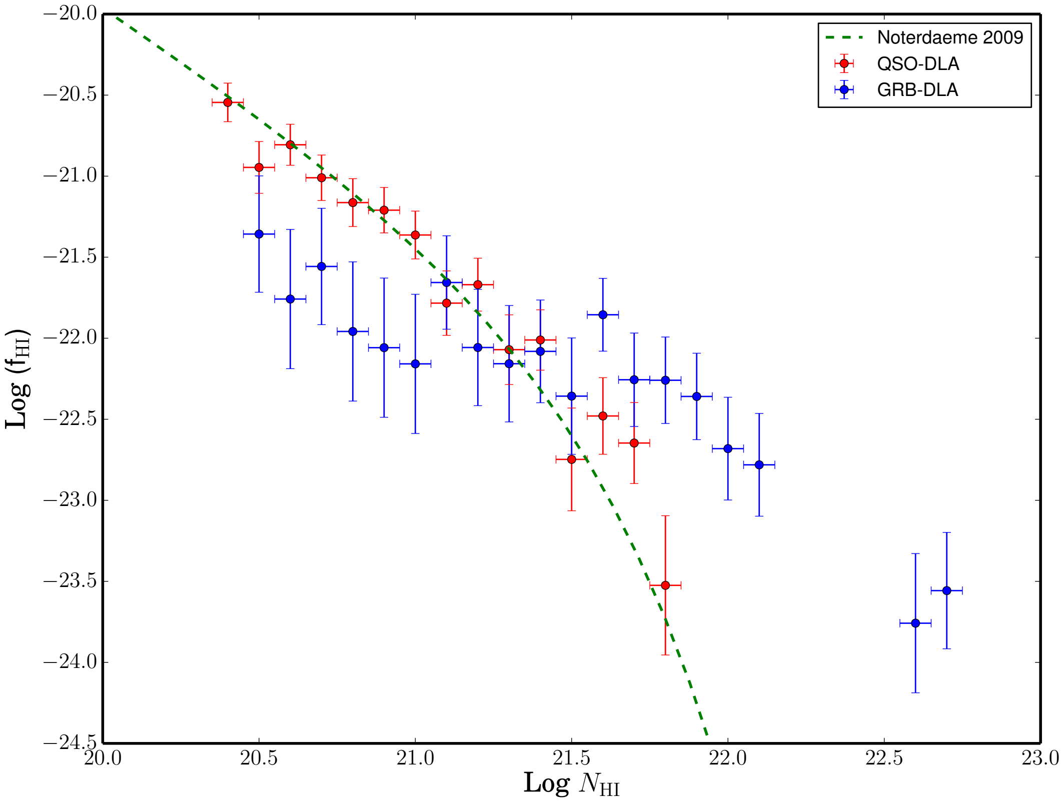

Figure 2.4: Column density distribution for our two DLA samples (QSO in red and GRB in blue). Vertical error bars are derived assuming Poissonian distribution (95% confidence level) and is over-plotted in green (dashed line) the model by Noterdaeme *et al.* (2009). Adapted from Cucchiara *et al.* (2015).

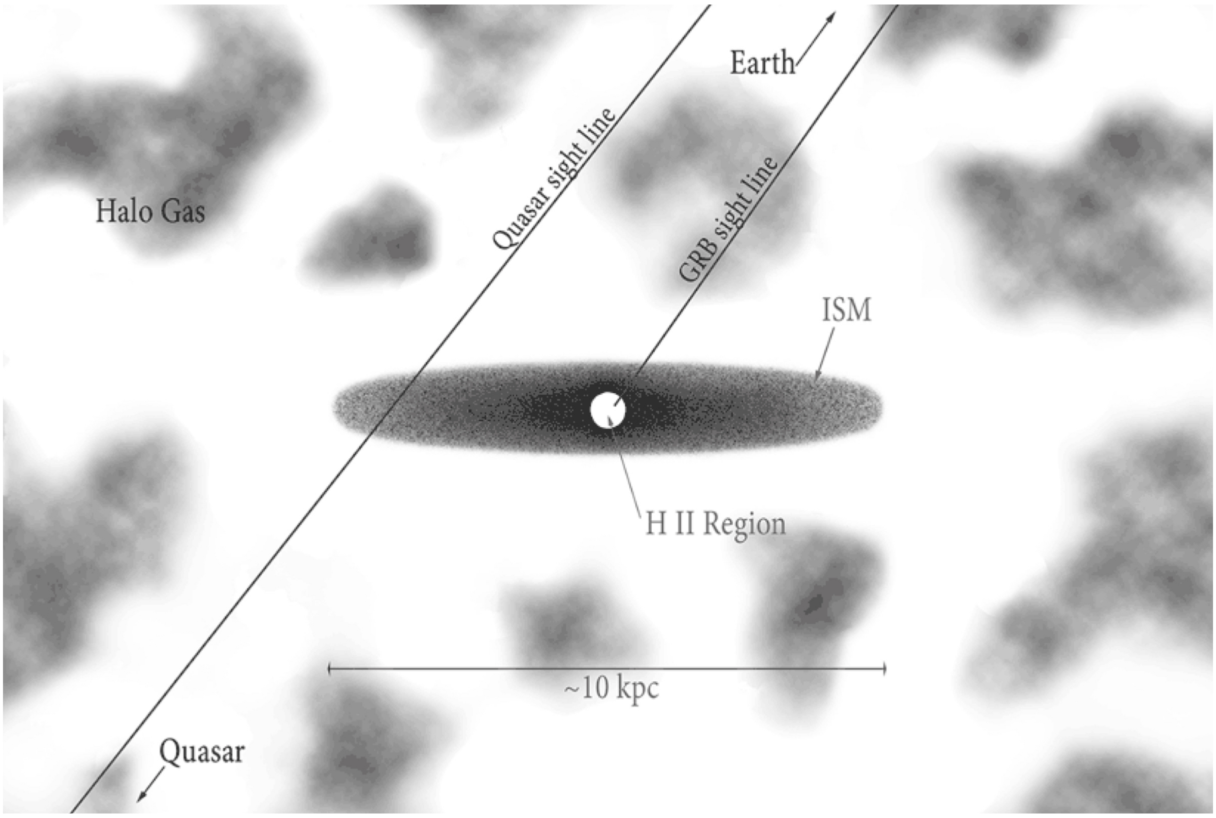

Figure 2.5: Cartoon illustrating the likely differences between QSO-DLA and GRB-DLA sight lines. Adapted from Prochaska *et al.* (2008a).

2.3 Metal abundances

The relative abundances of elements in the ISM are related with the different nucleosynthetic processes in stars and during the collapse of massive stars. The so-called α-elements (Ne, Mg, Si, S, Ar, Ca and Ti) are produced by α-capture (He) during silicon fusion taking place in massive stars before the SN explosion. Iron-peak elements like V, Cr, Mn, Fe, Co and Ni are produced mostly in SN Ia which come from less massive stars. GRB-DLAs show generally a higher α/Fe ratio than QSO-DLAs (Prochaska *et al.*, 2007), which can be due either to a nucleosynthetic origin or by dust depletion differences. The first possibility seems likely as GRBs are expected to occur in actively star forming galaxies, and the timescales to enrich the ISM significantly with Fe produced in SN Ia, might be too short for galaxies at high redshifts.

2.4 Metallicity

A central aspect of the history of the Universe is the formation and evolution of galaxies, and their gradual build-up of metallicity (Pei & Fall, 1995). The metallicity of the intervening gas towards a GRB can be measured by computing the ratio of the metal lines column density over $N(\text{H I})$. By comparing systems from low to very high redshifts, GRB-DLAs allow us to probe instantaneous star-formation galaxies able to produce GRBs.

The data collected to date show that GRBs explode generally in sub-solar metallicity environments, but generally already metal-enriched. However, it remains unclear whether there is an evolution or not of the metallicity as a function of redshift (e.g., Cucchiara *et al.*, 2015; Fynbo *et al.*, 2006; Prochaska *et al.*, 2007; Savaglio *et al.*, 2006; Schady *et al.*, 2011; Thöne *et al.*, 2013). For QSO-DLAs, however, a little anti-correlation with redshift is more evident (Rafelski *et al.*, 2012, 2014). GRB-DLAs are clearly more metal enriched. As GRBs are expected to occur in denser parts of the host galaxy, the mass-metallicity relation would give a straightforward explanation (e.g., Arabsalmani *et al.*, 2015; Fynbo *et al.*, 2008; Møller *et al.*, 2013).

On the other side, QSO-subDLAs (Péroux *et al.*, 2003) show higher metallicities than QSO-DLAs (Péroux *et al.*, 2007; Quiret *et al.*, 2016). This clearly indicates that we can not suppose that $N(\text{H I})$ correlates with the path length through the galaxy, and this fact could be due to subDLAs probing more massive galaxies or dust effects.

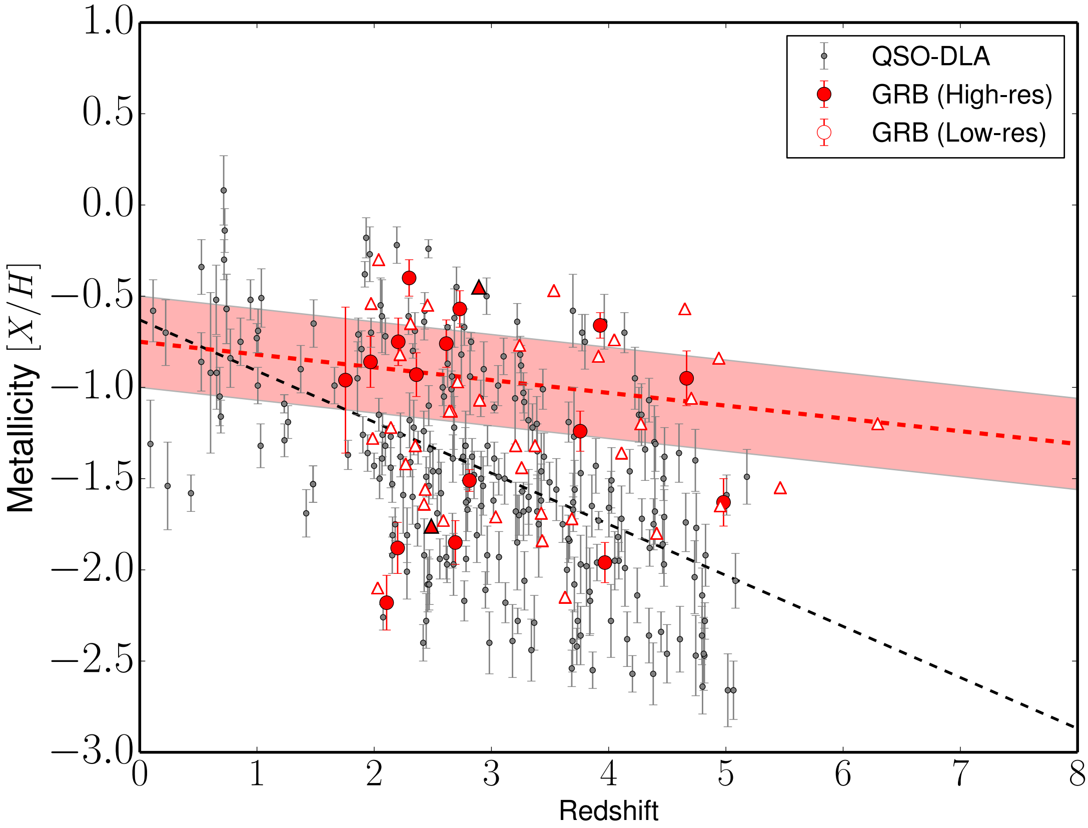

Figure 2.6: Metallicity evolution with redshift for the GRB (red) and the QSO (grey) samples. Lower limits are indicated by upward triangles, while filled/open symbols indicate if these values come from high/low resolving power instruments. A linear regression fit of the GRB-DLA data using the Schmitt survival analysis method is performed, which keeps into account the censoring within the dataset (red dashed line). The shaded area represents the 1σ error in the fitting parameters obtained using 500 bootstrap iterations. A linear fit of the QSO-DLAs metallicity is marked by the dashed black line (see text for details). Adapted from Cucchiara *et al.* (2015).

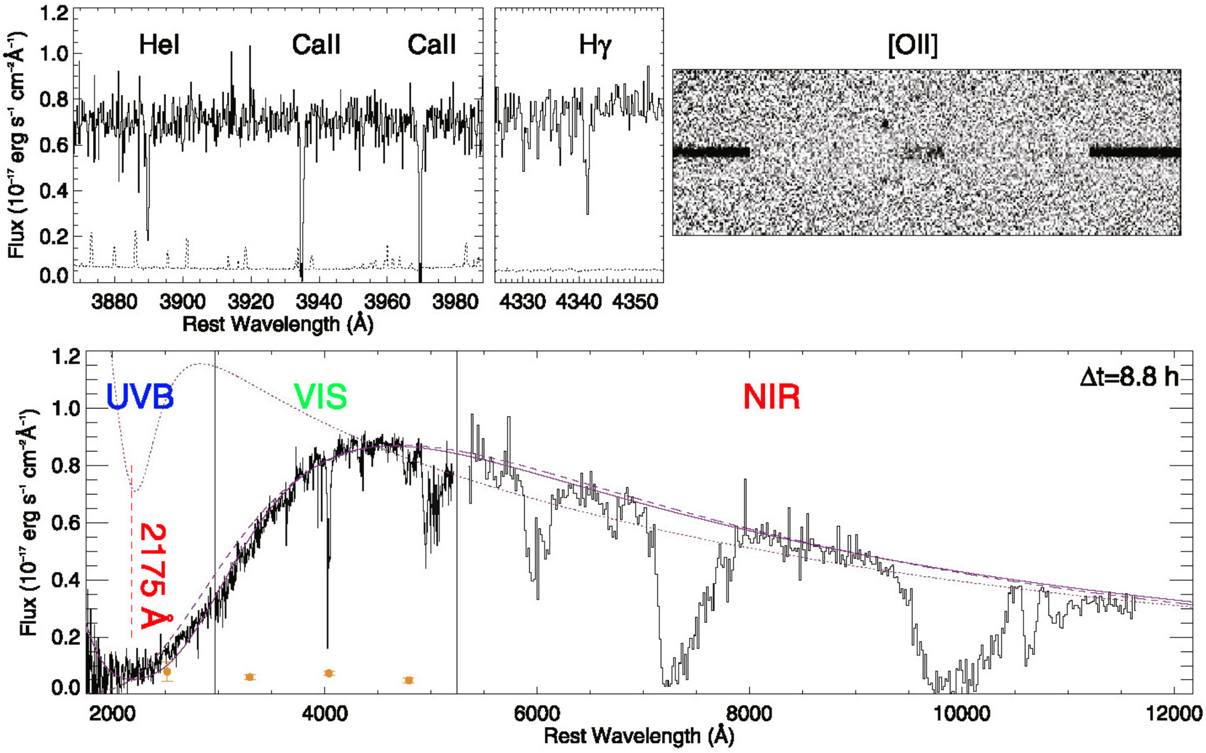

Figure 2.7: Spectroscopy of GRB 140506A and its unusual sightline. *Bottom panel*: An X-shooter spectrum taken 8.8 hr after the burst covering the range from about 2000 to 12000 Å in the rest frame of the $z = 0.889$ GRB is plotted in black and late time host photometry is overplotted in orange. *Top left*: The spectrum also shows very unusual absorption lines including absorption from excited helium as well as hydrogen Balmer lines, never seen before in any afterglow spectra. *Top right*: [O II] emission lines from the underlying host galaxy visible under the light of the afterglow. Adapted from Perley *et al.* (2016b).

2.4.1 Extinction

When we look in different directions of the sky, we see dark patches in the distribution of stars. These are not gaps where there are no stars, but instead are due to obscuration by interstellar dust clouds, such as the Horse-head nebula. This dust does not come only from thick clouds, but also spreads diffusely throughout interstellar space.

Dust extinction is the absorption and scattering of light along the line of sight of some source. The degree of reddening can be determined by measuring the colour index $(B - V)$ of the object and comparing by its intrinsic $(B - V)_0$

$$E(B - V) = (B - V) - (B - V)_0 \tag{2.3}$$

The greater the extinction, the larger the reddening. Each line of sight has its own extinction law and is usually expressed by the variation of the extinction with wavelength (i.e., A_λ/A_V or $E(\lambda - V)/E(B - V)$). Interstellar extinction is commonly obtained by comparing spectra of reddened and unreddened stars of the same spectral type. (Cardelli *et al.*, 1989) showed that Galactic sight-lines could be characterised by a single parameter R_V, although Fitzpatrick & Massa (2007) dispute this. This R_V parameter is defined by

$$R_V = \frac{A_V}{E(B - V)} \tag{2.4}$$

which average for the MW is 3.1, and it varies from sight-line to sight-line.

Sometimes dust extinction causes certain features that can be recognised. These include the 2175Å bump, the diffuse interstellar bands, or the 3.1 μm water ice and 10-18 μm silicate features. The mentioned 2175Å bump is present at all R_V values of the Galaxy, and theories attribute it to carbon.

At high redshifts evidence for dust exists from the DLA observations (Pettini *et al.*, 1994) and from the detection of dust thermal emission from QSOs, but still is not clear what is the mechanism of dust production, as it cannot be the same as at low redshift.

The advantages of GRB afterglows for the study of the extinction are

- Afterglows are very bright, allowing its detection even when affected by substantial extinction
- Afterglows have simple continua, consisting of power-law segments
- Afterglows cover a wide range of frequencies, from radio to X-rays

Early studies on dark bursts suggested that these events are fairly common and the majority of these are due to dust extinction (Kann *et al.*, 2006).

Swift has allowed larger and more complete studies, showing that the fraction of dark bursts are ~40%, and half of them are very obscured (e.g. Covino *et al.*, 2013). Detailed studies on extinction curves are presented in Covino *et al.* (2013); Japelj *et al.* (2015); Schady *et al.* (2010, 2012); Starling *et al.* (2007); Zafar *et al.* (2011). They found that best fits are similar to the curves towards the Small Magellanic Cloud (SMC), but the 2175Åextinction bump is detected in a handful of afterglows.

Some sightlines show evidence for extinction laws with no local analogue. The most exotic and mysterious case is the extinction pattern found towards GRB 140506A (Fynbo *et al.*, 2014). This afterglow shows several peculiarities:

- Absorption lines from excited Hydrogen and Helium

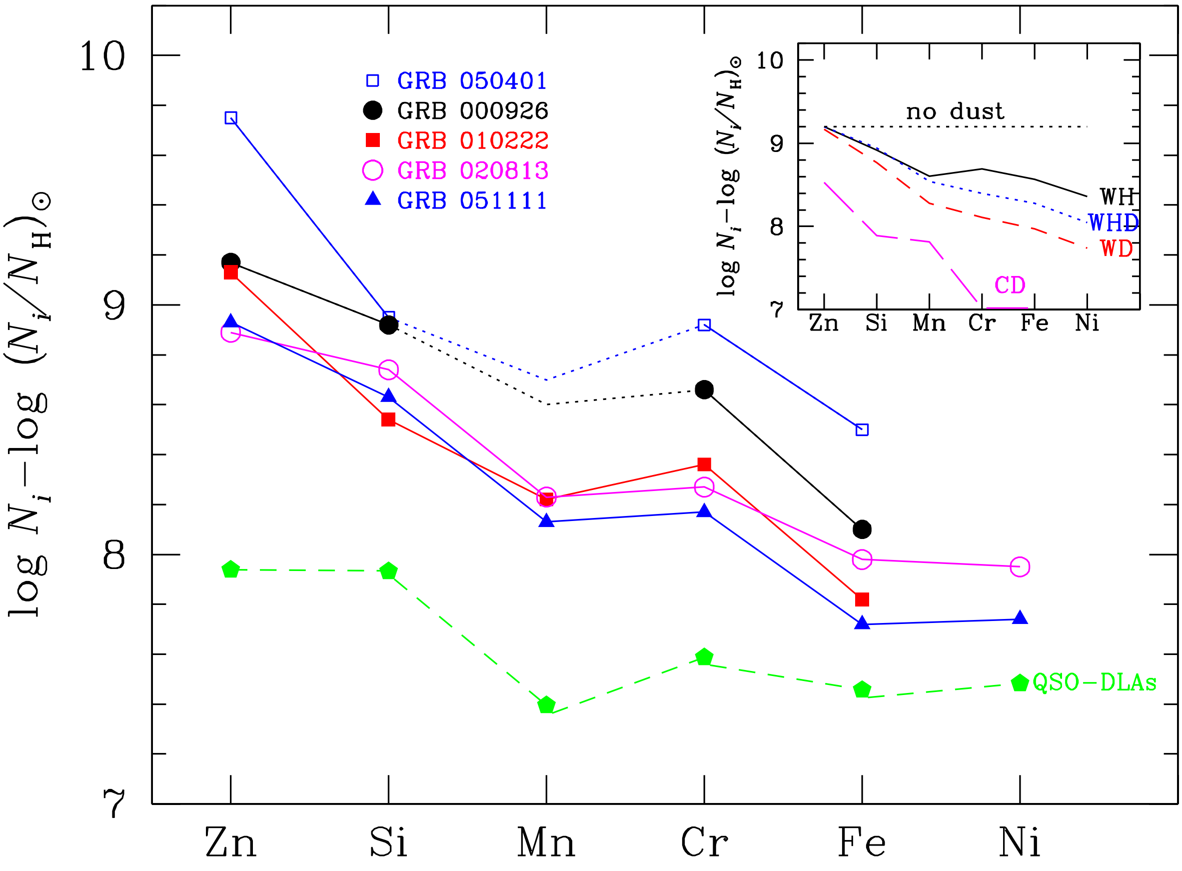

Figure 2.8: Depletion pattern in five GRB-DLAs with four or more heavy elements measured (errors are $\lesssim$0.2 dex). The dashed line at the bottom is the mean depletion pattern measured in 20 QSO-DLAs for which all six elements are detected. Metal column densities and dust depletion in GRB-DLAs are much higher than in QSO-DLAs. In the inset, the dust depletion patterns (rescaled to an arbitrary value) of the Galactic ISM are plotted for comparison; from top to bottom: warm halo, warm halo + disc, warm disc, cool disc clouds. Adapted from Savaglio (2006).

- Molecular absorption from CH^+
- Very strong dust absorption bluewards 4000Åin rest frame.

2.4.2 Dust depletion

Refractory elements, such as Fe, Ni, and Cr, can be heavily depleted into dust grains (it depends on element properties such as ionization potential and condensation temperature; Savage & Sembach, 1996), and so missing from the gas-phase abundances. To estimate the level of depletion we usually compute the relative abundance of heavily depleted species towards those undergoing little depletion (e.g., De Cia *et al.*, 2013; Vladilo *et al.*, 2006). The most suitable element to compute metallicities is Zinc, as it gets very weakly depleted. However, at $z \gtrsim 3$ Zn lines are far in the red and frequently contaminated by atmospheric features. In those cases, it is better to use Sulphur, but as it is a weak line the S II lines are not always detected. Using different metal lines and methods we can obtain the iron dust-phase column density, the dust-to-gas ratio, and the flux attenuation. The depletion patterns can also be compared with Galactic patterns to estimate the origin and the evolution of the dust-to-metal ratio (e.g., De Cia *et al.*, 2013).

2.5 Molecules

As GRB-DLAs probe the gas associated with star-forming regions, it is expected that H_2 signatures can also be easily detected on the afterglow spectra. However, it was proved to be difficult. Firstly, because molecular Hydrogen rotational and vibrational transitions are blended with the Lyα forest, so high-resolution and high-SNR are required to estimate the column density. This means that there is a systematic bias in the H_2 detections towards bright afterglows. Another issue is that $N[H_2]$ correlates with metallicity and dust depletion, so we also expect a bias towards these systems. As bright and very dusty afterglows are not common, there are only four detections of H_2 to date (D'Elia *et al.*, 2014; Friis *et al.*, 2015; Krühler *et al.*, 2013) and one of CH^+ (Fynbo *et al.*, 2014). In general, the fraction of H_2 over H I found along GRB lines of sight seems to be quite low.

2.6 Distance of the absorbing clouds to the progenitor

One of the main problems in spectroscopy is to distinguish between distances and movement of the material, as we measure projected velocities in the line of sight. Therefore, additional information is needed in order to clarify the picture.

The GRB afterglow radiation is intense enough to have an important impact on the surrounding environment at the time of explosion. UV radiation ionises the neutral gas and destroys molecules and dust up to tens of parsecs away (e.g., Draine & Hao, 2002; Perna & Lazzati, 2002). However, neutral species such as Mg I and Ca I have been detected in afterglow spectra, pointing to that these absorption systems are rather located farther than tens of parsecs away.

The first evidence that GRBs have measurable effects on their surroundings are the detection of fine-structure and metastable transitions of existing species (O I, Si II, Fe II,

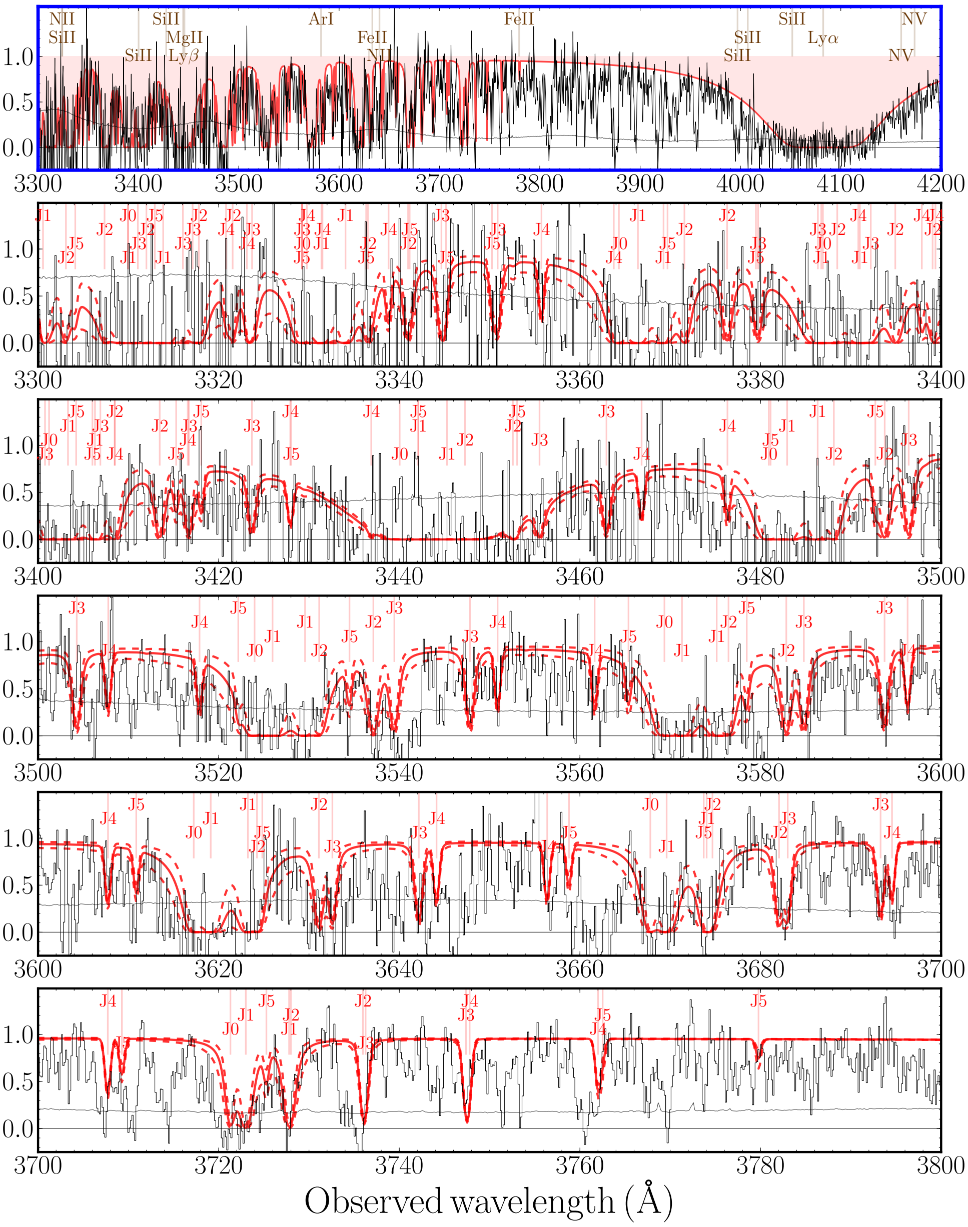

Figure 2.9: GRB spectrum between 3300 and 4200 Å illustrating the presence of H_2 absorption. The uppermost, blue-framed panel shows an overview, while the lower 5 panels show zoom-ins of 100 Åeach below 3800 Å, where most of the Lyman-Werner absorption bands are located. Light-grey lines are the normalized spectrum, while dark-grey lines indicate the error spectrum. The solid red line denote the synthetic H_2 model, with individual transitions up to J = 5 transitions marked with red labels. The dashed lines show synthetic H_2 models corresponding to the 1σ errors on the measured molecular content. In the lower panels, J0, J1, and so forth denote transitions from the J = 0, J = 1 rotational level of the vibrational ground state of the Lyman-Werner bands of H_2. Adapted from Krühler *et al.* (2013).

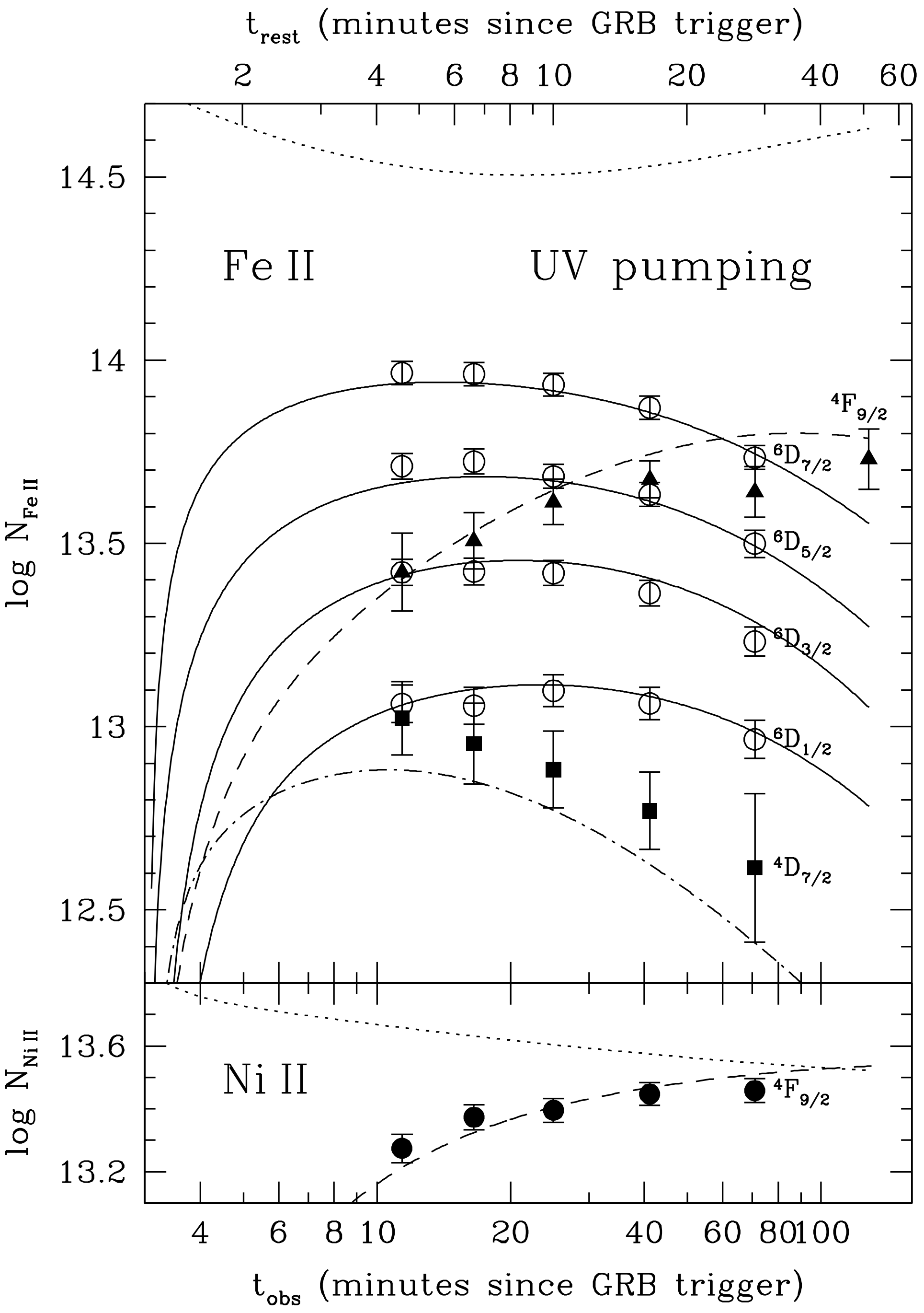

Figure 2.10: The top panel shows the observed total column densities with the UV pumping model over-plotted: solid lines for the fine-structure levels, dashed line for $^4F_{9/2}$, and dashed-dotted for $^4D_{7/2}$. The bottom panel displays the observed total column densities for Ni II $^4F_{9/2}$ (filled circles), and the best-fit Ni II model. In this Ni II fit, all parameters except for Ni II column density were fixed to the best-fit values obtained from the Fe II fit. The model prediction for the evolution of the Ni II ground state column density is indicated by the dotted line. All Fe II and Ni II column densities are very well described by the UV pumping model. Adapted from Vreeswijk *et al.* (2007).

Ni II) (Vreeswijk *et al.*, 2003). Silva *et al.* (1998) modelled the population of fine structure levels, and find out that three mechanism seem plausible to populate these levels:

1. Direct excitation from the Cosmic microwave background.
2. Collisional and direct excitation by IR radiation.
3. Indirect excitation by UV photons and subsequent fluorescence.

From the ratio between fine-structure and ground-state transitions it is possible to roughly estimate the distance between the GRB and the absorbing cloud if the radiation field produced by the afterglow is known. Furthermore, if variations of the fine-structure lines can be observed, it is possible to accurately establish the distance. This was achieved for the first time by Vreeswijk *et al.* (2007). They obtained series of high-resolution spectra using VLT/UVES which showed clear variations of Fe II* and Ni II*. By modelling the evolution of these transitions they found a strong evidence for the UV pumping being the responsible mechanism for the excitation.

Currently, it has been possible to use this type of analysis on ∼10 GRBs. The method has served to show that the excited gas is at least at ∼100 pc from the progenitor, being the surrounding medium ionised up to ∼20 pc. Many attempts to find the close signatures have been performed, but there are no robust identifications to date (Castro-Tirado *et al.*, 2010; Fox *et al.*, 2008).

2.6.1 Comparison between emission and absorption properties

A systematic study of the properties obtained by afterglow spectroscopy and direct observations of the host galaxies can provide important information on the link between the properties of the ISM and star formation through cosmic time. The first attempts on this direction have been performed by (Chen, 2012; Vergani *et al.*, 2011).

Chapter 3

Gamma-ray bursts

> *“Today, every inhabitant of this planet must contemplate the day when this planet may no longer be habitable. Every man, woman and child lives under a nuclear sword of Damocles, hanging by the slenderest of threads, capable of being cut at any moment by accident or miscalculation or by madness.”*
>
> — J.F. Kennedy, *UN General Assembly, 1961*

In the early 1960s, the Cold War between the East and West Blocks had rapidly escalated and the development of nuclear weapons had gotten to an unacceptable level. In an attempt to control this situation, the Limited Nuclear Test Ban Treaty was signed between USA, UK, and URSS in 1963 to forbid the further test of nuclear weapons. In order to verify the compliance with the ban, NASA launched a series of satellites called *Vela*[1]. They were equipped with γ-ray detectors to observe the radiation produced during the detonation. Up to 6 pairs of satellites were launched since the treatment was signed, and their detectors were triggered on many occasions. However, these flashes were not originated on the Earth...

---

[1] Vela comes from the Spanish word “velar”, wich means “to guard”

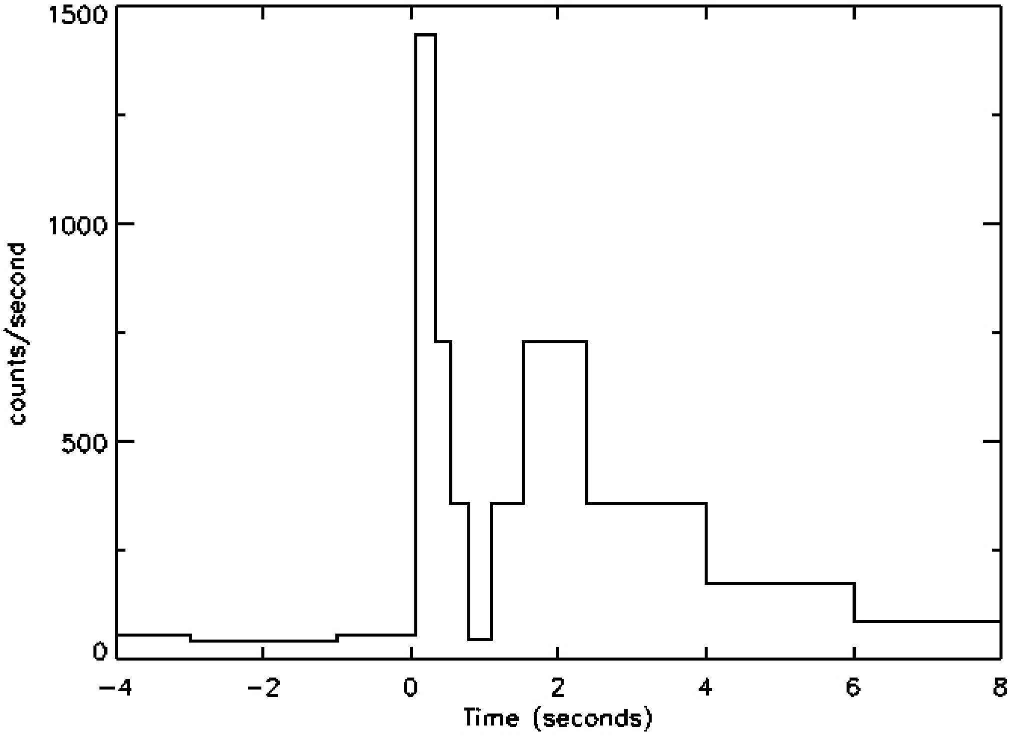

Figure 3.1: Light curve of the first GRB ever detected. Adapted from (Strong & Klebesadel, 1976).

3.1 An historical perspective

3.1.1 The discovery

In the years that followed, Ray Klebesadel and his team at Los Alamos National Laboratory (New Mexico, U.S.A.) searched the top secret *Vela* data for emissions not necessarily related to nuclear weapon tests. On the data of the *Vela 4A* and *Vela 4B* satellites, they saw a simultaneous γ-ray flash on the 2nd July 1967 at 14:19 UT (a double-peaked signal shown in Fig. 3.1), which did not resemble a nuclear test and did not seem to come from the vicinity of the Earth. Several of such mysterious events were detected during the following years. Due to the restrictions of such an experiment the results were not announced until 1973, when 16 bursts detected by the *Vela* 5 and 6 satellites were published in Klebesadel *et al.* (1973), claiming the discovery of a new type of astronomical event, the Gamma-ray Bursts (GRBs).

In the following two decades, many different models were developed trying to explain the nature of these bursts. The proposed models ranged from neutron stars colliding with comets to enigmatic events that occurred at cosmological distances (see, e.g., Nemiroff, 1994). The key parameter to discern between such an amount of possibilities is the distance. However, the poor localization of the bursts that high-energy detectors offered were insufficient to detect counterparts at other wavelengths.

3.1.2 The great debate

Fishman (1981) proposed what would come to be BATSE, the Burst And Transient Source Experiment. It was an all sky camera installed on the *Compton Gamma-Ray Observatory (CGRO)* that got launched on 1991. In the mean time, the majority of the GRB community thought that these events were Galactic, most likely due to neutron stars. The claimed detections of cyclotron lines (Fenimore *et al.*, 1988; Mazets *et al.*, 1981; Murakami *et al.*, 1988) supported this scenario. To confirm this hypothesis, BATSE should show a similar distribution on the sky than neutron stars, with a larger density along the plane of the Milky Way.

Surprisingly, the first observations by BATSE pointed to a uniform distribution of GRBs on the sky, as well as the definitive analysis (Meegan *et al.*, 1992). This fact was shocking for most of the community, but it was not considered as definitive due to other results that still suggested the neutron star origin. Imitating the classical debate between Herbert Curtis and Harlow Shapley in 1920, Robert Nemiroff organized a similar event 75 years later. This time, on the one side was was Don Lamb defending the local theory, and on the other side was Bohdan Paczyński supporting the cosmological origin (Lamb, 1995; Paczynski, 1995). Like in the original debate there was not a clear winner, but the final answer would not have to wait long.

3.1.3 Unveiling the mysteries

3.1.3.1 The distance scale problem

HETE was the first mission expected to solve the fundamental mysteries of GRBs. However, due to a failure during the uncoupling manoeuvre after the launch in 1996, it was lost when it had already reached the orbit. A second unit (*HETE-2*) was finally operative in 2000.

In the mean time, *BeppoSAX*, an Italian-Dutch satellite was launched ten years later

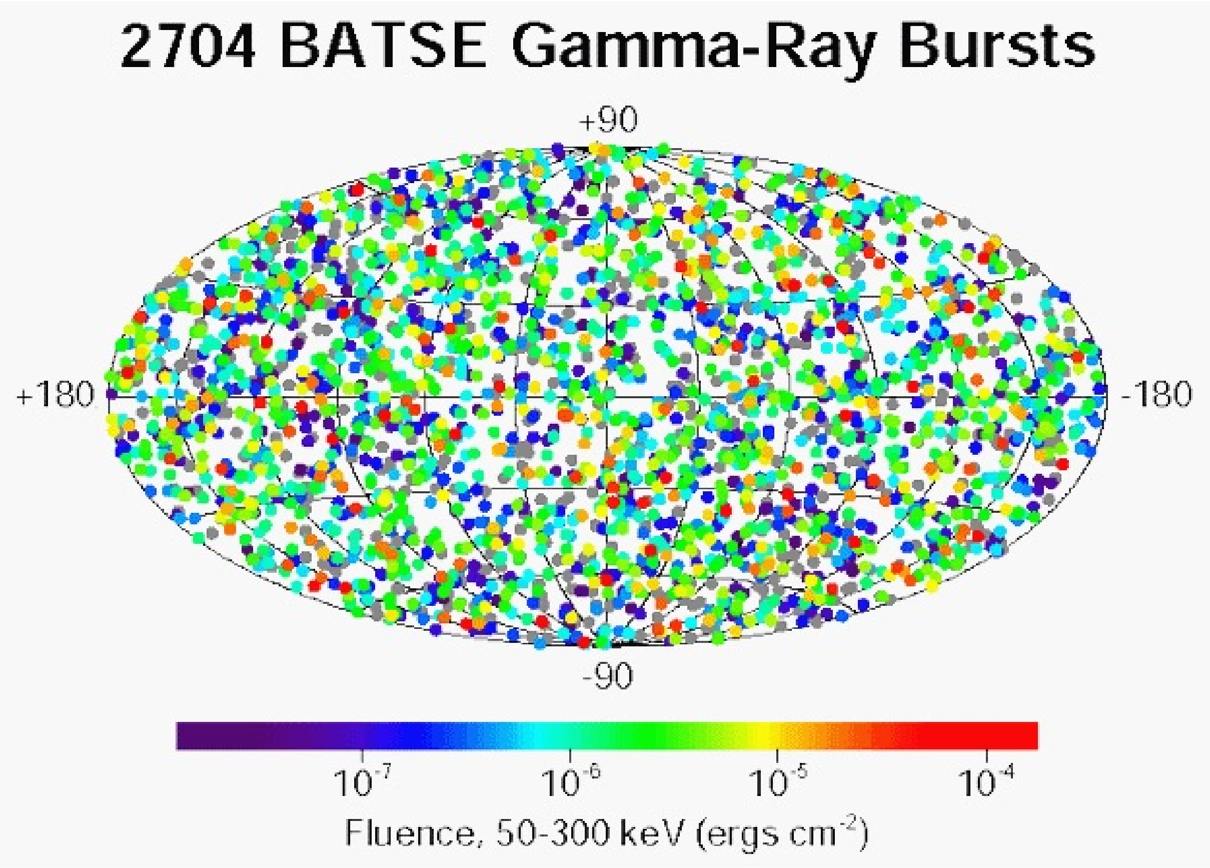

Figure 3.2: Isotropic distribution of the GRBs detected by BATSE.

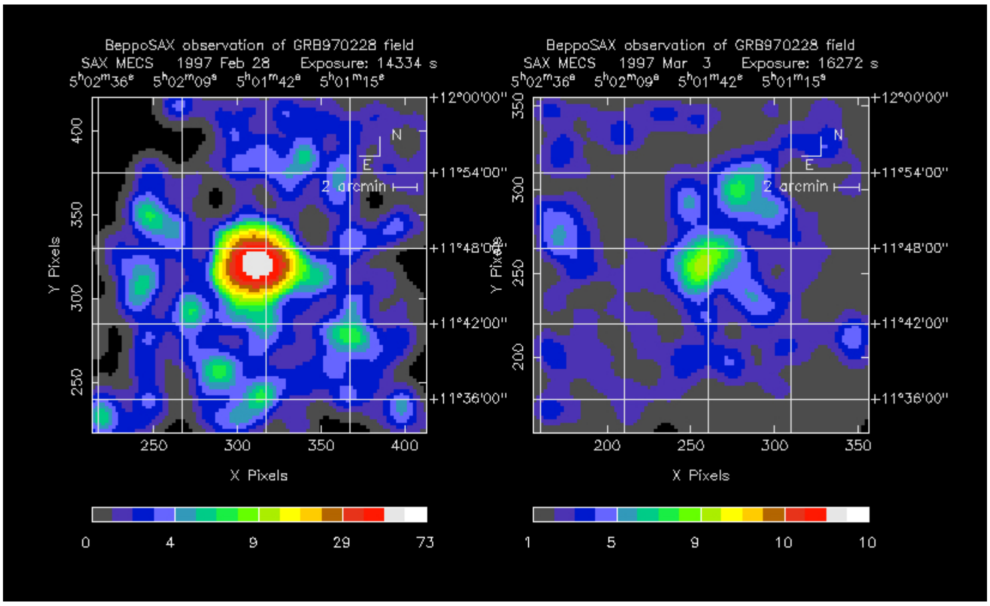

Figure 3.3: X-ray counterpart of GRB 970228 detected by *BeppoSAX*.

than expected, on 1996. Although its primary science was not GRBs, it was the satellite that finally went down in history for disentangling the mystery of γ-ray bursts. The main advance of this mission was that it carried an X-ray detector together with a γ-ray monitor. The X-ray counterparts were discovered for the first time with *GRANAT* for GRB 920723, so they knew that localizing these lower energy counterparts it would be possible to accurately determine the position of the burst in a short time interval, opening the door to ground-based observatories follow-ups in other wavelengths.

On the 20th July 1996 the first burst was detected by both instruments on-board, 3 months after the launch. The lack of experience in the data analysis delayed the communication of the result for more than a month (Piro *et al.*, 1996).

Several months later, once *BeppoSAX* team was prepared to react in a reasonable amount of time, GRB 970111 occurred and was observed by the satellite. This time, the position was circulated within 24 hours after the trigger. In Calar Alto, Spain, this burst was observed by Alberto Castro-Tirado and his PhD student Javier Gorosabel with the 2.2m telescope. Unfortunately, no optical counterpart was detected down to a limiting magnitude of ∼22.6 (Castro-Tirado *et al.*, 1997). There was no success also trying to identify a radio transient.

The next (and successful) attempt was performed in the following month. GRB 970228 was finally pinpointed by van Paradijs *et al.* (1997). The optical transient faded away and an underlying object appeared. It was proposed to be the host galaxy that would be sheltering the burst at a cosmological distance. However, to prove this hypothesis, it was

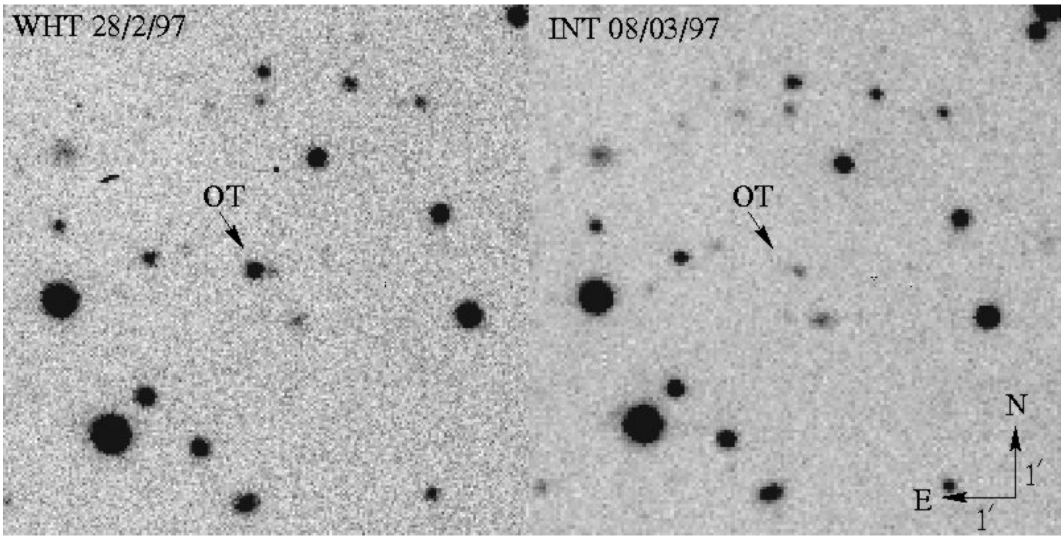

Figure 3.4: First GRB optical counterpart detected. Adapted from van Paradijs *et al.* (1997).

mandatory to obtain a spectrum of the source.

This goal was achieved with GRB 970508, initially not an interesting burst, but which was, apart from the first radio counterpart ever detected (Frail *et al.*, 1997), the first event for which an optical telescope (10 m Keck) took optical spectra (Metzger *et al.*, 1997a). Finally, a redshift of 0.835 was determined from absorption lines, solving 30 years of mystery (Metzger *et al.*, 1997b).

3.1.3.2 The problem of energetics

Once the distance scale of GRBs was determined another problem came along. The rapid variability observed in BATSE light curves indicated that the emitting region could not be larger than ∼1000 km, while the total isotropic energies released in a few seconds were of the order of 10^{52} erg. This amount of energy in such an small volume would be optically thick to pair creation and emit a thermal spectrum, which was not observed. Several effects from relativity could help to explain the problem, such as beaming, time dilation and length contraction. These ideas led to the development of the relativistic fireball model (Cavallo & Rees, 1978; Mészáros & Rees, 1993; Rees & Mészáros, 1992). Figure 3.6[1] describes a relativistic outflow from a central engine (without making any hypothesis on it). Internal shocks would explain the prompt emission while the external shock interacting with the ISM would be the origin of the afterglow.

---

[1] Adapted from `http://www.theregister.co.uk/2013/11/21/scientists_spot_bigger_ever_gamma_ray_burst_from_birth_of_black_hole/`

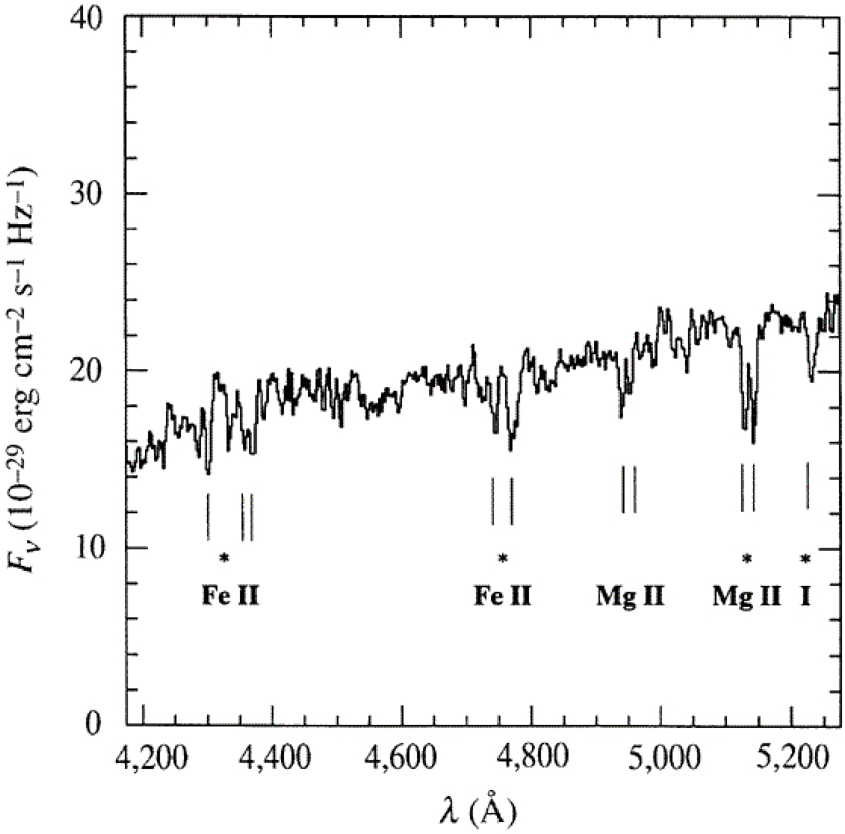

Figure 3.5: Iron and Magnesium lines in absorption at $z = 0.835$. Adapted from Metzger *et al.* (1997b).

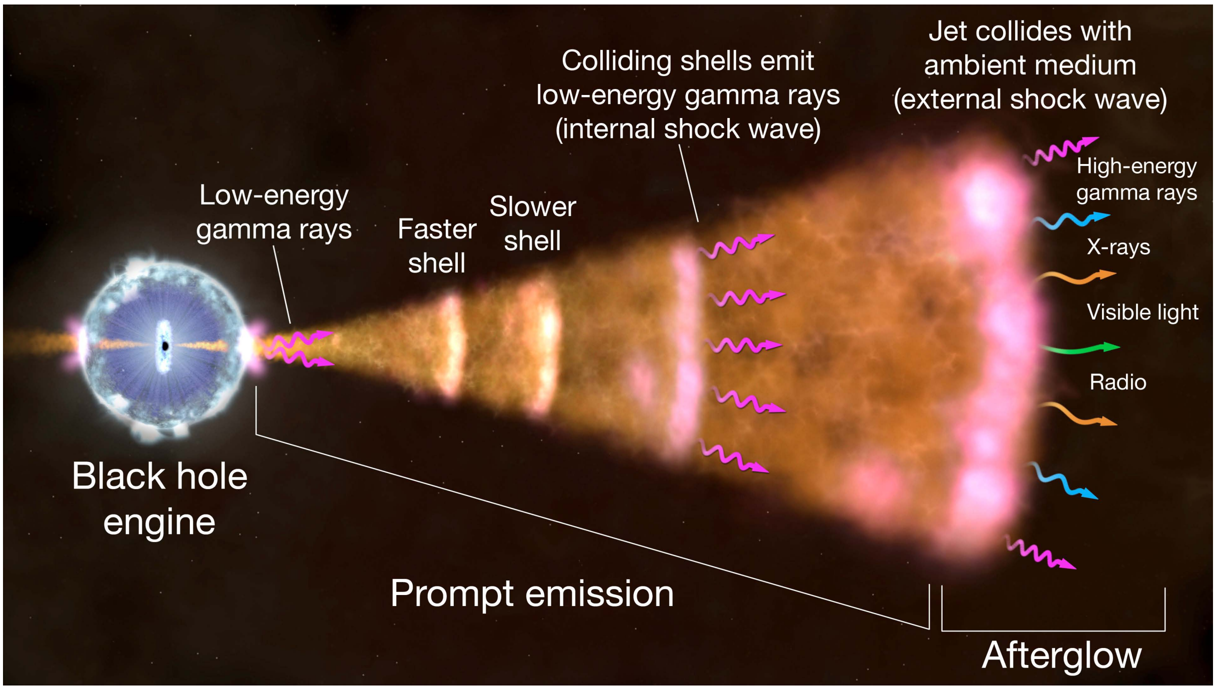

Figure 3.6: Schematic description of the GRB and the afterglow according to the fireball model. Credits: NASA's Goddard Space Flight Center

Jet-like scenarios are not required, but were introduced as a likely physical context (Mészáros & Rees, 1992a; Rees & Mészáros, 1992; Rhoads, 1997). They started to be an essential ingredient since high-redshift events implying energies $E \gtrsim 10^{53}$ erg, beyond what reasonable models could explain. (Rhoads, 1997, 1999) showed that a collimated emission would decrease by 2 or 3 orders of magnitude the released energies. Observations of a collimated emission are expected to show a *jet break* in the light curve when the Lorentz factor (Γ_0) of the outflow decrease bellow $1/\theta_0$, being θ_0 the opening angle of the jet. This behavior was first suggested by Castro-Tirado *et al.* (1999), and observed many times later.

The fireball model is based on an initial explosion of $E \sim 10^{52}$ erg. While the central engine is active, outflows of different bulk velocities are produced. Due to the relativistic and supersonic motion, the ejected matter form shells. Given their differential velocities, they collide producing *internal shocks*, resulting in the prompt γ-ray emission. When the ejected shells sweep up a significant amount of surrounding material, an external shock is formed by accelerated electrons which produce a synchrotron emission, detectable in all wavelengths, that we know as the *afterglow*.

3.1.4 The search for GRB progenitors

Kouveliotou *et al.* (1993) presented a histogram based on 222 BATSE bursts which pointed to a bimodality in the distribution (see Figure 3.7). It was interpreted as an indication of the existence of 2 GRB populations. GRBs with $T_{90} < 2$ s are called *short GRBs* (sGRBs), and have on average harder photons than longer burst, called *long GRBs* (lGRBs).

3.1.4.1 Long GRBs

Modeling the evolving SEDs of the afterglows, one can infer not only the physics of the jet, but also the structure of surrounding medium (e.g., Chevalier & Li, 1999; Sari *et al.*, 1998; Wijers & Galama, 1999). Li & Chevalier (1999) showed that a density profile $n \sim r^{-2}$ is a better representation for some burst than a constant ambient density. This result pointed to Wolf-Rayet stars as a potential progenitor for some events, such as GRB 980425.

Galama *et al.* (1998) detected a transient event on an arm of a spiral galaxy lying in the error box of GRB 980425. Its behavior was atypical in comparison with previously observed bursts. Instead of showing a fast decreasing of its brightness, it suddenly increased to decay slowly afterwards. Due to the similarity with what we expect from a supernova, GRB 980425 was identified also as SN 1998bw. It was also a peculiar event compared with the previous SN observations. Further studies showed that the explosion

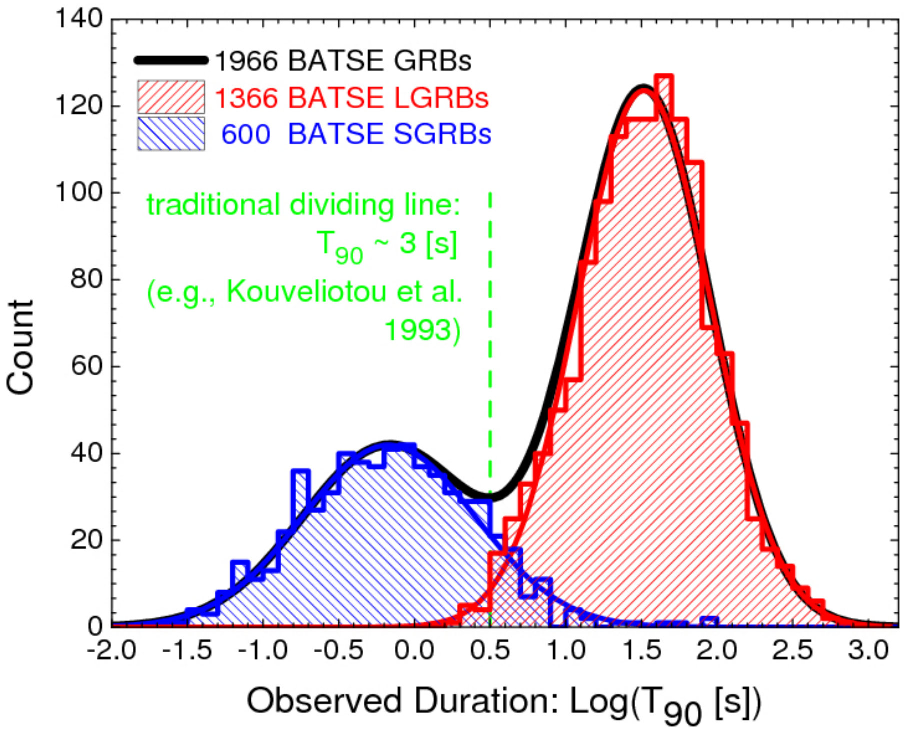

Figure 3.7: Bimodal distribution in the duration of GRBs. Adapted from (Shahmoradi, 2013)

had a huge amount of radio emission (Kulkarni *et al.*, 1998), and a energy 10 times greater than a typical supernova (hypernova, Iwamoto *et al.*, 1998). This meant a strong case for the association of certain class of burst with the violent death of massive stars, in which the formation of a black hole is unavoidable.

In spite the chances of having a SN event unrelated with a GRB in the error box are extremely low, the peculiarities of GRB 980425/SN 1998bw raised the question whether this behavior is usual in GRB events. Castro-Tirado & Gorosabel (1999) first detected the expected “bumps” in other light curves, which were later modeled by Bloom *et al.* (1999).

Finally, the definitive proof for the GRB-SN relation came with GRB 030329. Its spectroscopic follow-up showed the evolution from the afterglow power law to the supernova spectrum (Hjorth *et al.*, 2003; Stanek *et al.*, 2003).

3.1.4.2 Short GRBs

In spite the great and passionate discoveries made in the 90s for lGRBs, no afterglow was detected for a short burst during this time. This events had to wait until 2005, when

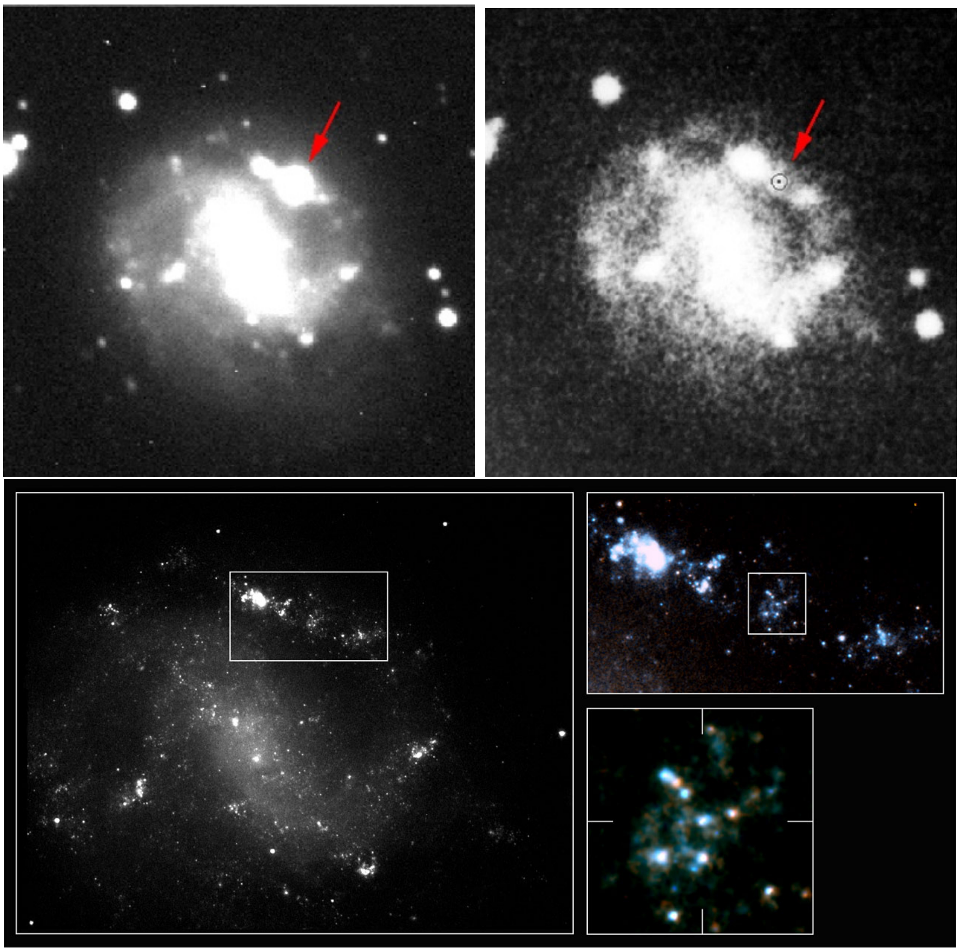

Figure 3.8: Discovery of SN 1998bw associated with GRB 980425. The upper panels show the images of the host galaxy of GRB 980425, before (right) and shortly after (left) the occurrence of SN 1998bw (Galama *et al.*, 1998). The bottom panel shows a late *HST* image of the host galaxy and SN 1998w. The 3-step zoom-in shows SN 1998bw 778 days after the explosion embedded in a large star-forming region of a spiral arm (Fynbo *et al.*, 2000)..

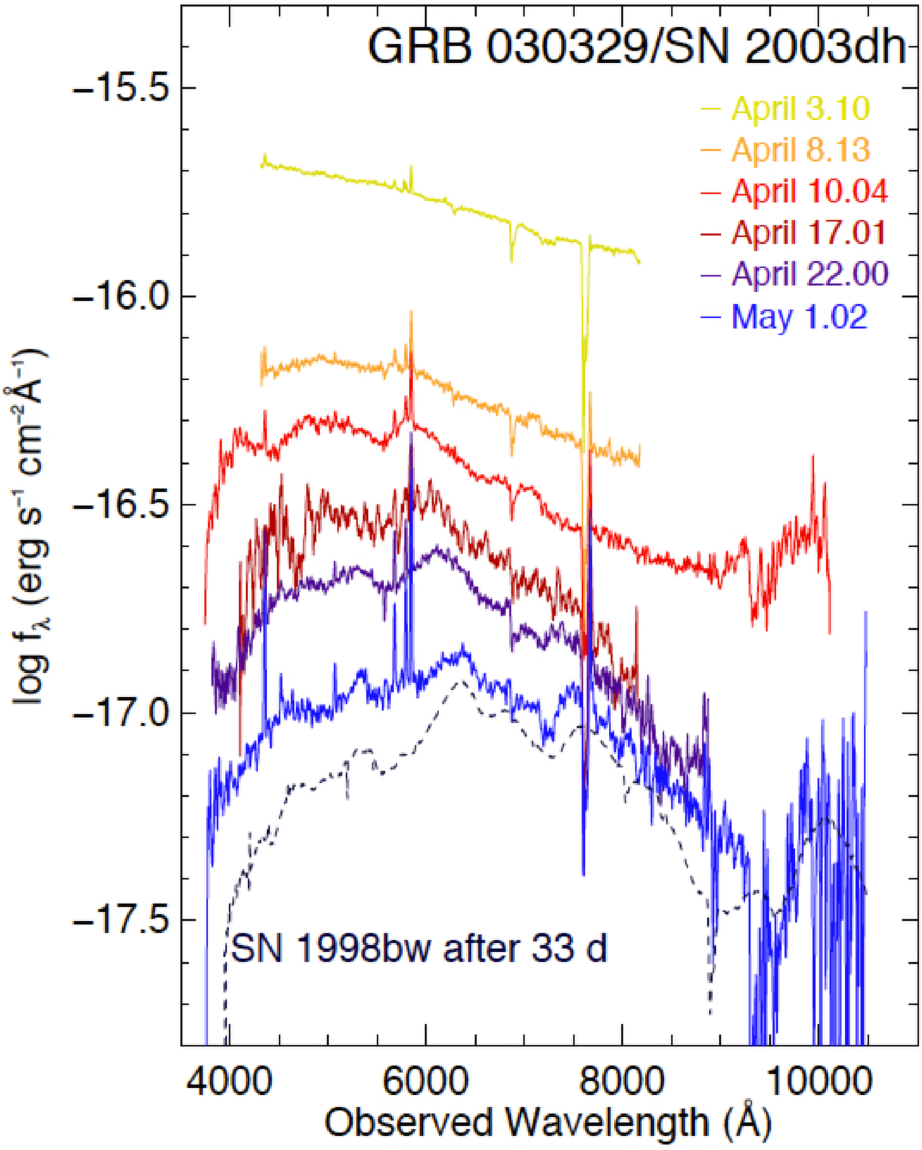

Figure 3.9: Spectral evolution of GRB 030329 from synchrotron to supernova. Adapted from Hjorth *et al.* (2003)

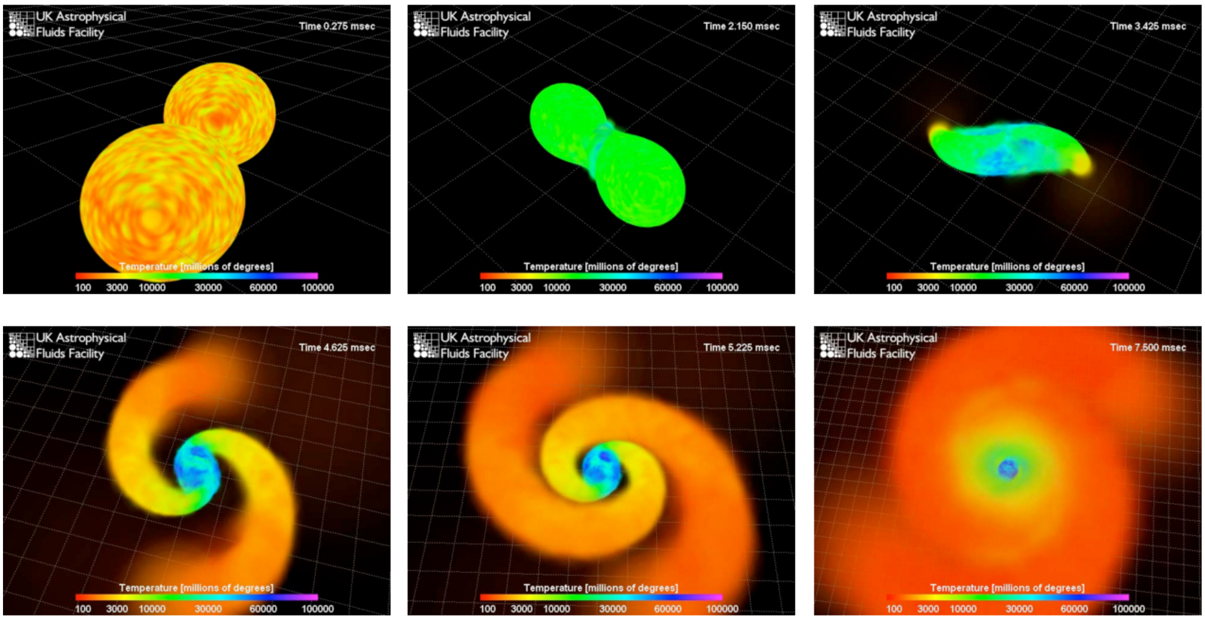

Figure 3.10: Snapshots of simulation of two neutron stars merger. Initially, they are less than 10 km apart, and moving at around v=0.2c. As the two stars spiral together, they become deformed, and finally touch. When they merge, the matter reaches T $\sim$ 1011 K. A few percent of the matter is ejected in the form of spiral arms, which cool rapidly. The whole merger process takes only a few ms. The grid in the images has a spacing of 30 km intervals. Credit: simulation by Stephan Rosswog, visualization by Richard West, http://www.ukaff.ac.uk/movies/nsmerger/

HETE-2 and *Swift* were able to precisely localize the X-ray counterparts of these hard and short flashes. The first detections of sGRB afterglows were achieved by Berger *et al.* (2005); Gehrels *et al.* (2005); Hjorth *et al.* (2005). The first observations pointed towards lower luminosities and distances and no associated supernovae. They did not seem to be originated by the death of massive stars.

Short GRBs are believed to be due to the merger of two compact objects, such a binary system containing very compact objects (neutron stars and/or black holes; e.g., Mészáros & Rees, 1992b; Narayan *et al.*, 1992). Merging of compact objects are expected to be powerful sources of gravitational waves, which have been recently discovered (Abbott *et al.*, 2016a,b).

3.2 Observational characteristics

3.2.1 Observational properties of the prompt emission

GRBs occur at a rate of a few per day on random positions of the sky. Based on the observations, there are two main phases in the GRB emission: The first one corresponds to the very early times, in which the γ-ray emission is detected (prompt phase), and the other is the afterglow phase, which is a long-lasting emission that gradually decreases.

3.2.1.1 Light curves

Prompt emission duration range from 10^{-3} s up to 10^{3} s with typical peak energies between $\sim$ 1 keV and $\sim$ 10 GeV (Mészáros, 2006). A sample of BATSE light curves are shown in Fig. 3.11. The shape of the temporal evolution is unique for each burst, and it covers from smooth behaviors to highly variable curves with multiple peaks. The observed variability is high, having been measured down to scales of 10 ms.

3.2.1.2 Spectra

GRB spectra of the prompt phase are well fitted by the empirical Band function (Band *et al.*, 1993)

$$\Phi(E) = \begin{cases} AE^{\alpha} e^{-(2+\alpha)E/E_{peak}} & E \leq \frac{\alpha-\beta}{2+\alpha} E_{peak} \\ BE^{\beta} & \text{otherwise} \end{cases} \tag{3.1}$$

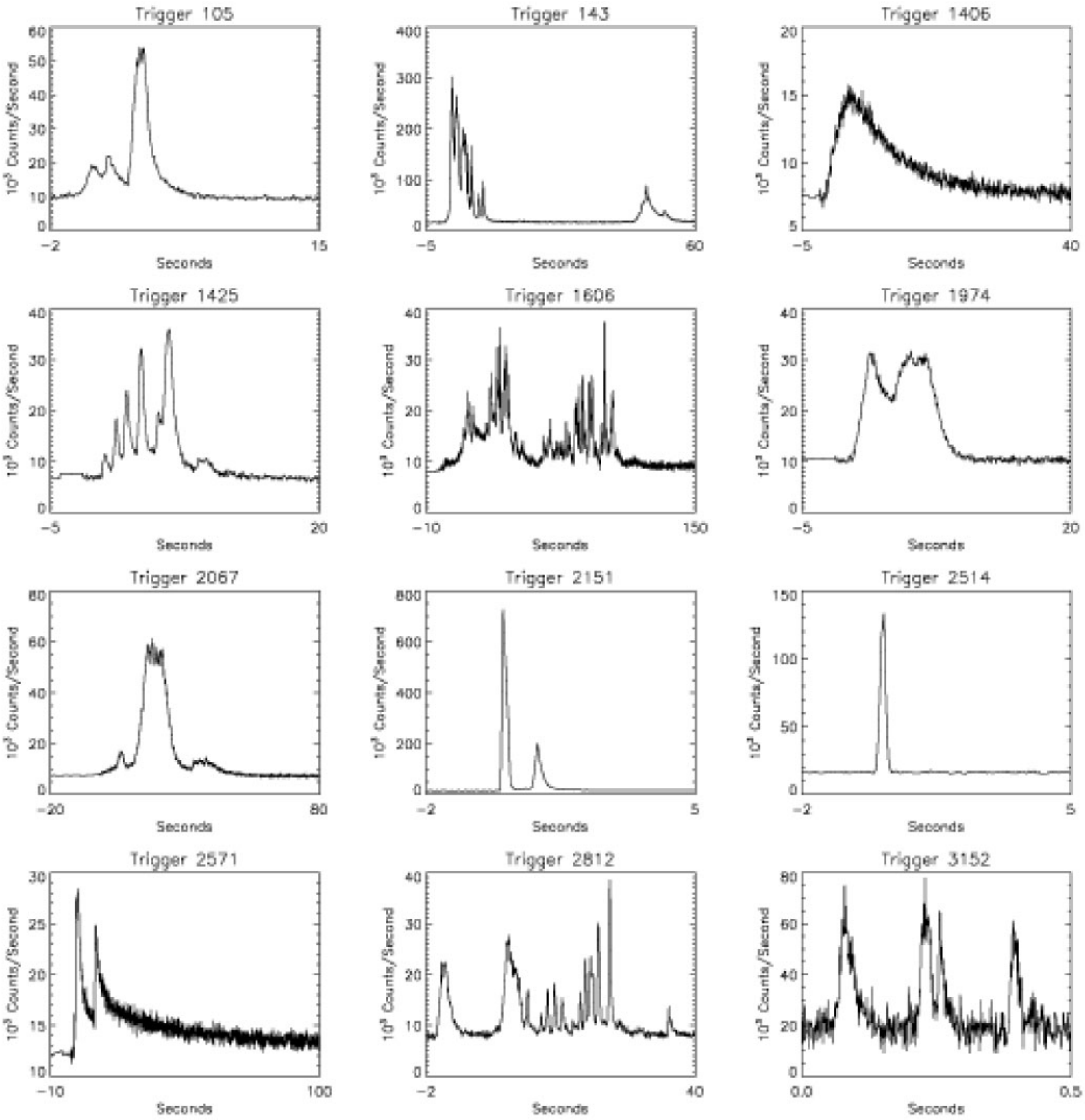

Figure 3.11: Diversity of γ-ray light curves from BATSE. Adapted from Fishman & Meegan (1995).

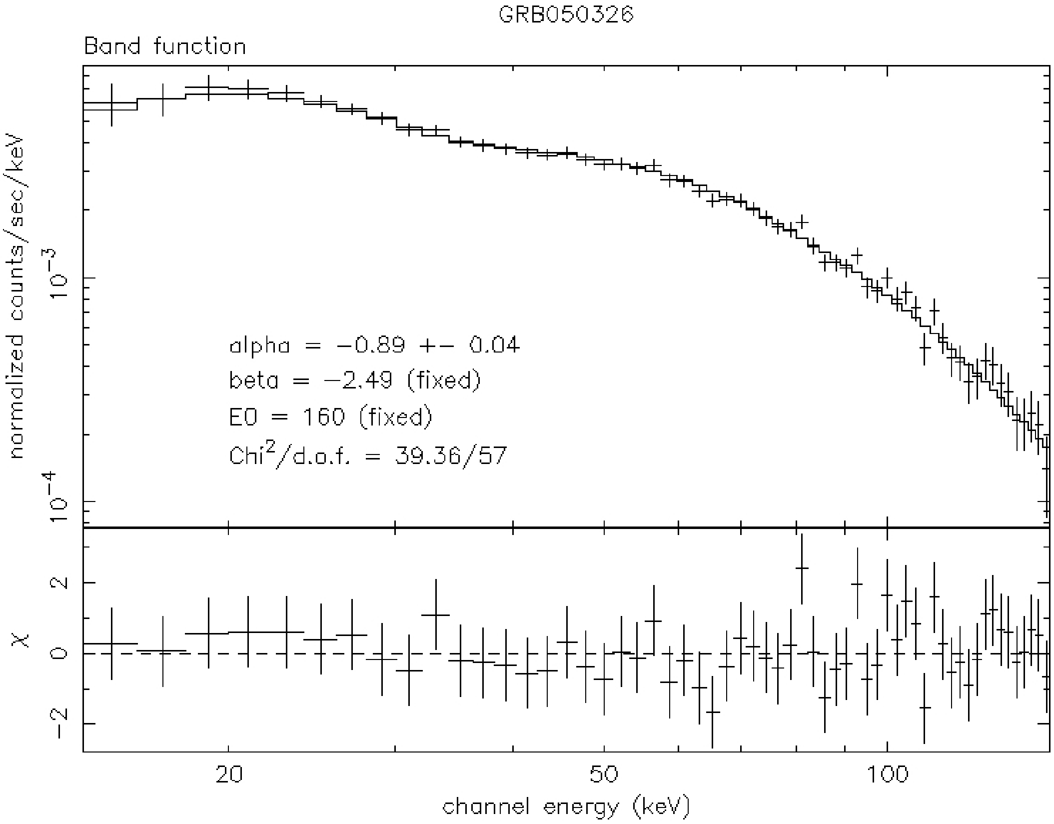

Figure 3.12: *Left:* Effective areas for Swift-BAT/XRT/UVOT and Fermi-GBM/LAT. Adapted from Stamatikos (2009). *Right:* The BAT spectrum of GRB 050326. Adapted from `http://swift.gsfc.nasa.gov/analysis/bat_digest.html`.

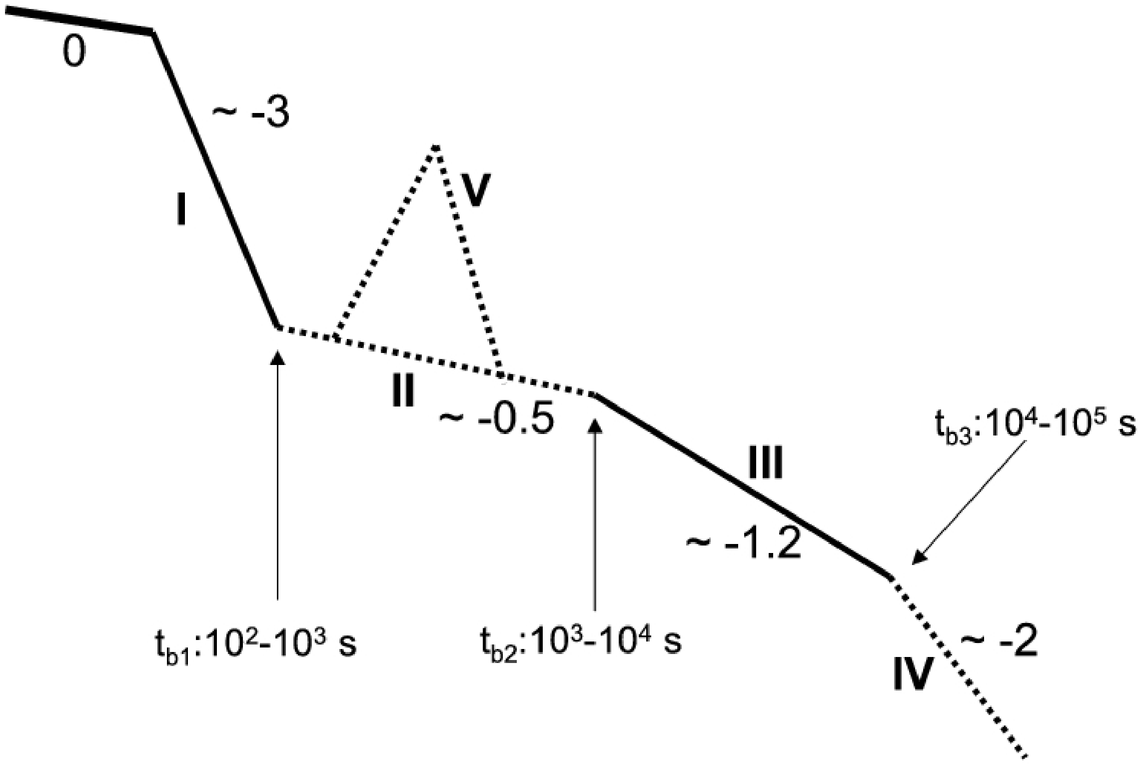

Figure 3.13: Canonical shape of GRB X-ray afterglow light curves. Adapted from Zhang *et al.* (2006)

with α the power-law index for photon energies below the break and β above. Mean values for long bursts are α = -0.92 ± 0.42 and β = -2.27 ± 0.01. Short bursts have α = -0.4 ± 0.5 and β = -2.25 (Ghirlanda *et al.*, 2002, 2009; Nava *et al.*, 2011a,b).

Band+exponential cut-off

3.2.2 Observational properties of the GRB afterglows

Figure 3.13 shows the canonical X-ray light curve from XRT (Zhang *et al.*, 2006). The prompt phase is indicated by 0, I is the steep decay phase, II is the shallow decay phase, III is know as the standard afterglow, and IV is the result of a jet break. V represent X-ray flares. Zones marked with solid lines (I and III) are the most common, being the other shown only in a fraction of bursts.

3.2.2.1 Polarisation

Polarimetric measurements are important because they are directly connected with the issue of magnetic fields and their geometry in GRBs, which remain an open question. Early attempts showed that the polarised flux is lower than 3% with a constant or smoothly variable level (e.g., Covino *et al.*, 2005). The first measurements made before and after the optical break (Gorosabel *et al.*, 2004) showed that there is no large variation (from 2.7% to 1.3%). The same weak variation is valid for the polarisation angle.

3.3 GRB-SN association

3.3.1 Photometric properties

The observer frame, optical LCs span more than 8 mags at a given observer frame post-explosion epoch. The peak SN brightness during its "bump" phase ranges from $R = 19.5$ for GRB 130702A to $R = 25$ for GRB 021211. For a GRB-SN event, there are 3 flux components in each measurement:

1. The afterglow
2. The SN
3. The host galaxy

The procedure to decompose each contribution is described in Fig. 3.15. Once the SN LC is obtained, it is usually compared to a template supernova, where the relative brightness (k) and width (stretch factor) are determined. Another approach is to fit a phenomenological model to the resultant SN LC, such as the Bazin function (Bazin *et al.*, 2011). Parameters to determine are the peak flux, the time it takes to rise and fade from peak, and the width of the LC, such as Δm_{15} parameter (decrement of magnitudes from the peak to 15 days later).

The bolometric LCs of 12 GRB-SNe are shown in Fig. 3.14. The average peak luminosity of the sample, excluding SN 2011kl, is $\bar{L_p} = (1.03 \pm 0.36) \times 10^{43}$ erg s^{-1}. Excluding this monster event, which is $\sim 5\sigma$ more luminous than the rest average, we get $\bar{L_p} = (1.24 \pm 0.71) \times 10^{43}$ erg s^{-1}. The average peak time is $t_p = 13.16 \pm 2.61$ days and $t_p = 12.95 \pm 2.72$ days. Similarly, $\Delta m_{15} = 0.72 \pm 0.12$ and $\Delta m_{15} = 0.79 \pm 0.13$. Therefore, the inclusion or not of SN 2011kl has little effect on the derived values. There are no statistical differences in the average bolometric properties between the different

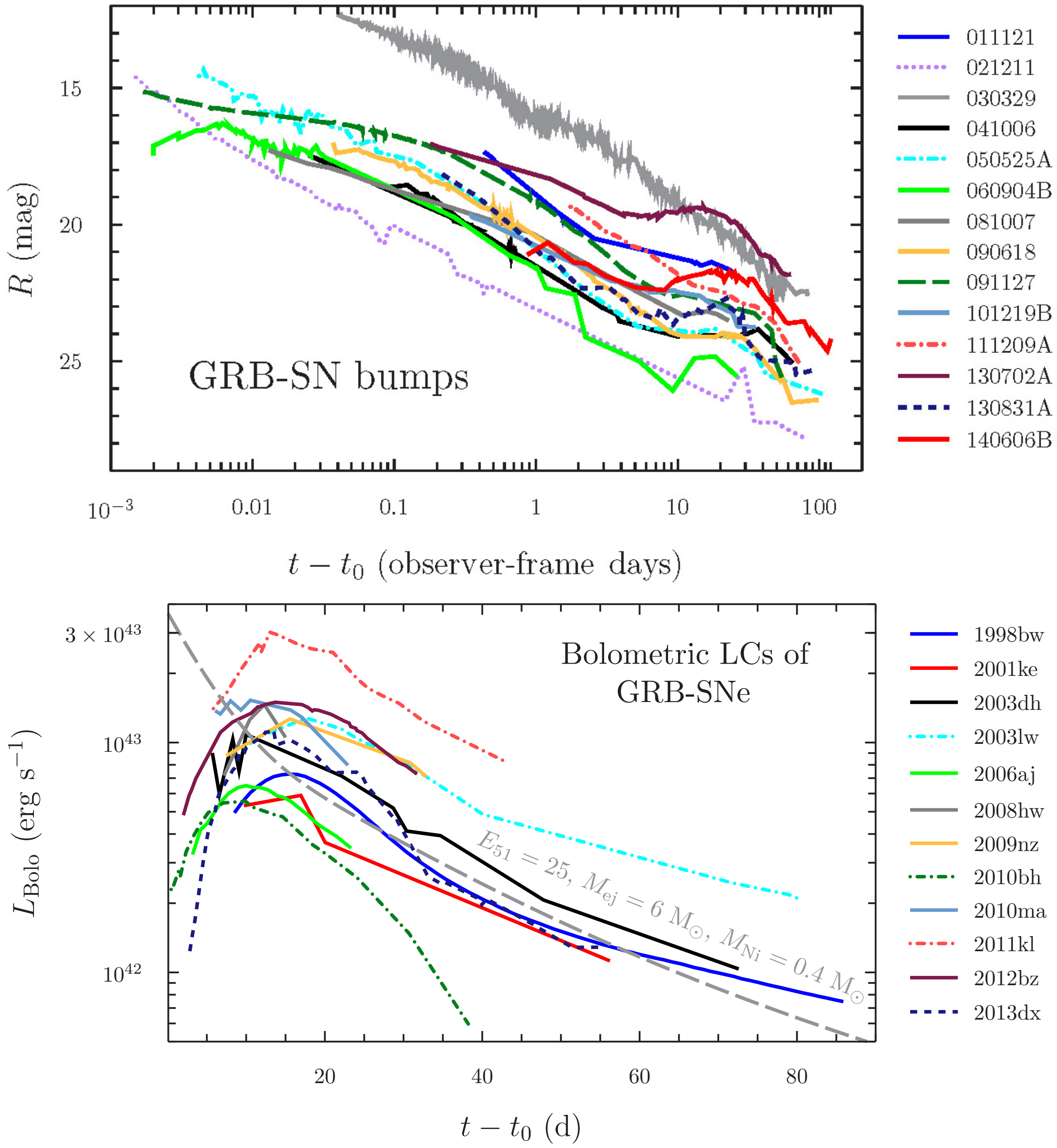

Figure 3.14: *Upper panel:* A mosaic of GRB-SNe (AG & SN). Clear SN bumps are observed for all events except SN 2003dh. *Lower panel:* Bolometric LCs of a sample of GRB-SNe. Adapted from

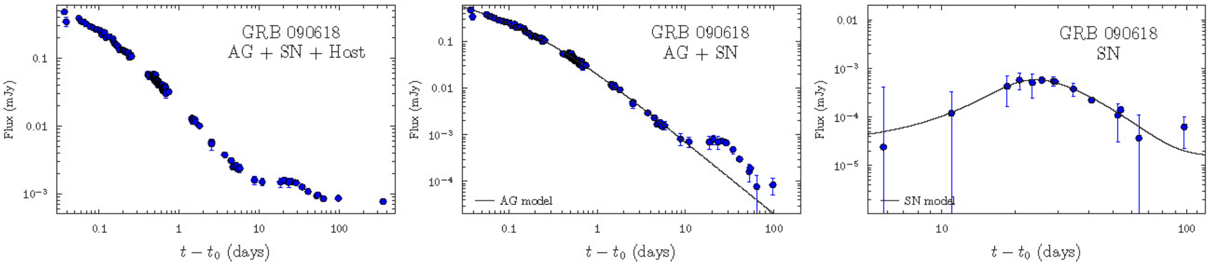

Figure 3.15: An example decomposition of the optical (R-band) LC of GRB 090618. *Left*: For a given GRB-SN event, the single-filter monochromatic flux is attributed as arising from three sources: the AG, the SN, and a constant source of flux from the host galaxy. *Middle*: Once the observations have been dereddened, the host flux is removed, either via the image-subtraction technique or mathematically subtracted away. At this point a mathematical model composed of one or more power-laws punctuated by break-times are fit to the early LC to determine the temporal behaviour of the AG. *Right*: Once the AG model has been determined, it is subtracted from the observations leaving just light from the SN. Adapted from

GRB-SNe subtypes. As found in previous studies, relativistic SNe IcBL are roughly half as energetic as GRB-SNe, and contain approximately half ejecta mass and Niquel content therein.

3.3.2 Spectroscopic properties

Optical and NIR spectra have been obtained for a dozen GRB-SNe. Those of the highest quality shows broad lines of O I, Ca II, Si II, and Fe II near maximum light. It can be detected line velocities of the order of 20,000 – 40,000 km s^{-1} (for the Fe IIλ5169 transition).

3.3.3 Phenomenological classification

Based on $E_{\gamma,\mathrm{iso}}$

- *ll*GRB-SNe: low luminosity GRB-SNe ($E_{\gamma,\mathrm{iso}} < 10^{50}$erg)
- INT-GRB-SNe: intermediate luminosity GRB-SNe ($10^{50} < E_{\gamma,\mathrm{iso}} < 10^{51}$erg)
- GRB-SNe: typical/cosmological GRB-SNe ($E_{\gamma,\mathrm{iso}} > 10^{51}$erg)

Attending the duration of the prompt emission, ultra-long-duration GRB-SNe (ULGRB-SNe) are named to those events with a γ-ray emission lasting several thousand seconds.

It is highly debated whether the γ-ray coming from *ll*GRB-SNe arises from the same mechanism than typical events or whether from a relativistic shock breakout (SBO).

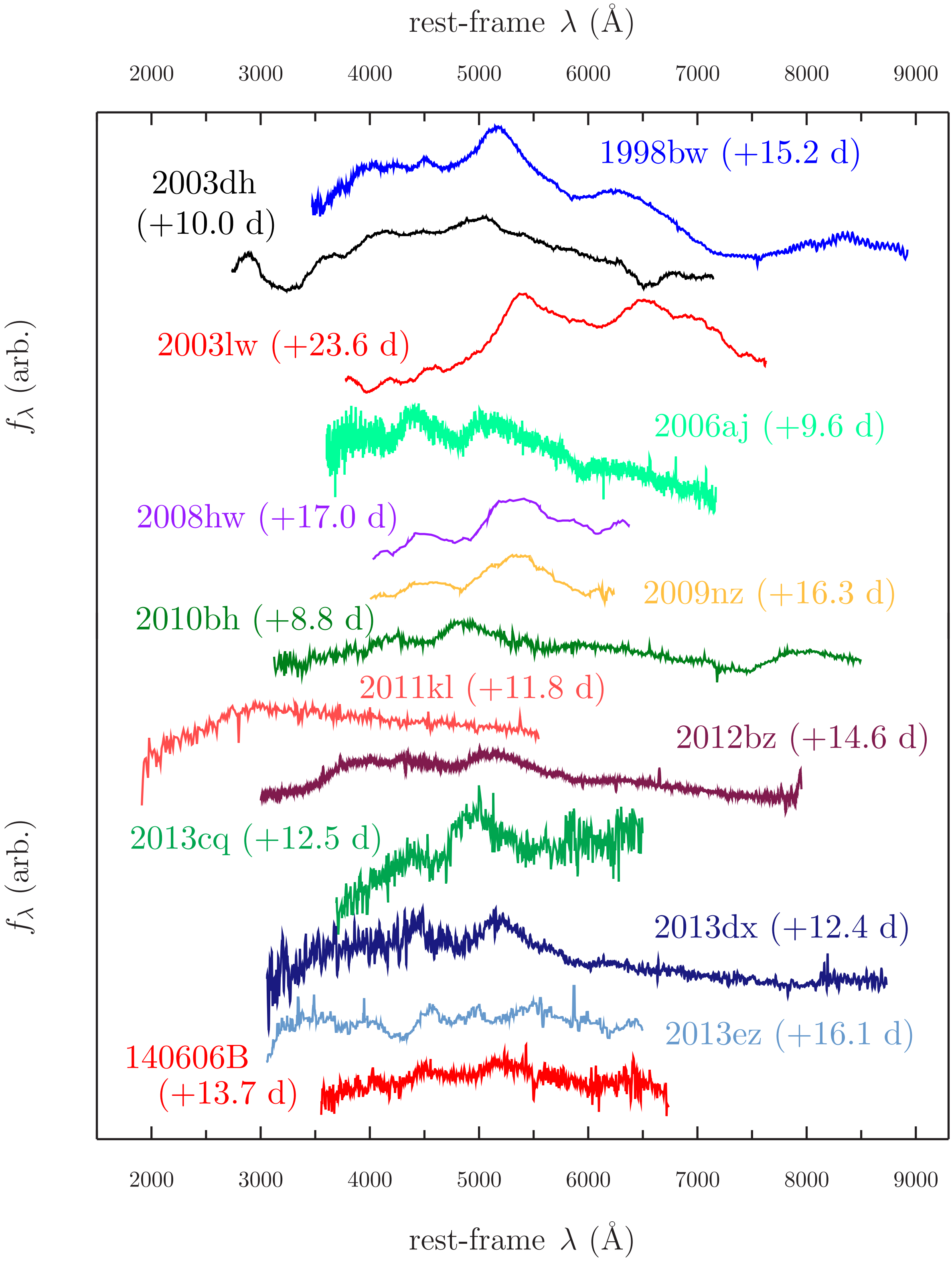

Figure 3.16: Peak/near-peak spectra of GRB-SNe. The spectra have been arbitrarily shifted in flux for comparison purposes, and to exaggerate their main features. Host emission lines have been manually removed. Adapted from

Bromberg *et al.* (2011); Kaneko *et al.* (2007) demonstrated that a key observable of llGRBs are their single-peaked, smooth, non-variable γ-ray LCs compared to the erratic LCs of jetted-GRBs. An SBO is likely present in all lGRB events, but the energy pulse is several orders of magnitude lower ($E_{\rm SBO} = 10^{44} - 10^{47}$ erg). This means that that SBO are likely not possible to detect at redshifts higher than ~0.1. In spite the SBO model successfully explains the observed characteristics of GRBs 980425, 031203, 060218, and 100316D, their SBO origins are still widely debated.

Thermal black-body components in X-ray spectra have been detected for several events, which could be attributed to thermal emission arising from a cocoon that surrounds the jet, or perhaps associated to a relativistic shock breakout. The large inferred temperatures could indicate that the radiation does not come from an SBO.

3.3.4 Short GRBs and kilonova emission

The compact coalescence scenario predicts, apart from the afterglow, emission from a SN-like transient called kilonova (KN). The KN prediction is a consequence of the decompression of the neutron star material, where a compact binary coalescence provide excellent conditions for the rapid-neutron capture process (r-process, **refs**). This process occur very quickly, and is completed in less than a second, leaving behind a broad distribution of radioactive nuclei whose decay, once the ejected matirial becomes optically thin, powers an electromagnetic transient in a process similar to that expected to causes the GRB-SNe. There have been several unfruitful searches for KN emission, getting null results up to GRB 130603B.

3.4 GRB host galaxies

3.4.1 Long GRBs

The study of lGRBs host galaxies looks forward the use of both to understand each other. By studying the population of galaxies that produces GRBs and the location of GRBs inside their hosts, we hope to identify the GRB progenitor and how it is formed (for a review see, e.g., Perley *et al.*, 2016b).

The link between lGRBs and the explosions of massive stars is well established (Hjorth & Bloom, 2012). Therefore, assuming the simplest case in which the GRB rate is independent of everything but the overall SFR, it is observationally expected that GRBs stochastically sample the star formation regions. However, as previously pointed out, there several theoretical arguments to expect that reality may be more complex.

In order to assess the question, the population of GRB hosts has to be characterised through cosmic time. Many studies simply observe the distribution of total SFR as a function of galaxy parameters in known surveys and apply empirical laws relating properties and finding the best fit model (e.g., Trenti *et al.*, 2015). Semi-analytical models have been also developed to avoid the observational dependence, but these techniques are still limited by the uncertain physics surrounding star formation and feedback.

When constructing GRB host samples, great care has to be taken to make sure that selection biases are either minimised and/or quantified. Straightforward sources of bias are dust extinction and the instrumental threshold.

3.4.1.1 Photometric properties

The GRB host population studies in the pre-*Swift* era showed that it is very faint in comparison to other star-forming galaxies and presented a lack of massive galaxies large population of of stars (Le Floc'h *et al.*, 2003). However, it must be taken into account that the number of small galaxies in the Universe is much larger and GRBs do not select galaxies on the way flux-limited surveys do. The same pre-*Swift* samples exhibited relatively blue colors. While not quantified in detail, the apparent absence of older or dusty systems suggest a trend to a metal-poor galaxy population. Systematic studies of larger samples of optically-reddened and optically-undetected burst (e.g., Perley *et al.*, 2013) confirmed that most obscured GRBs are hosts within luminous, massive, and reddened, precisely the systems found to be deficient.

Given the importance of the sample selection for minimising selection biases, several efforts were recently made, from which the most relevant are:

- **TOUGH** (Hjorth *et al.*, 2012): This sample contains 69 hosts.
- **SHOALS** (Perley *et al.*, 2016a): This sample contains 119 hosts.
- **BAT6** (Salvaterra *et al.*, 2012): This sample contains 58 hosts.

The selection criteria are quite similar, usually combining a Sun distance constraint, a foreground extinction limit, and a time requirement for the *Swift* slew. BAT6 and SHOALS also require a minimum peak flux or fluence to exclude faint burst. Finally, TOUGH and BAT6 exclude bursts near celestial poles. These techniques have increased redshift completeness from the initial ∼30% of the pre-*Swift* era to 90% or more.

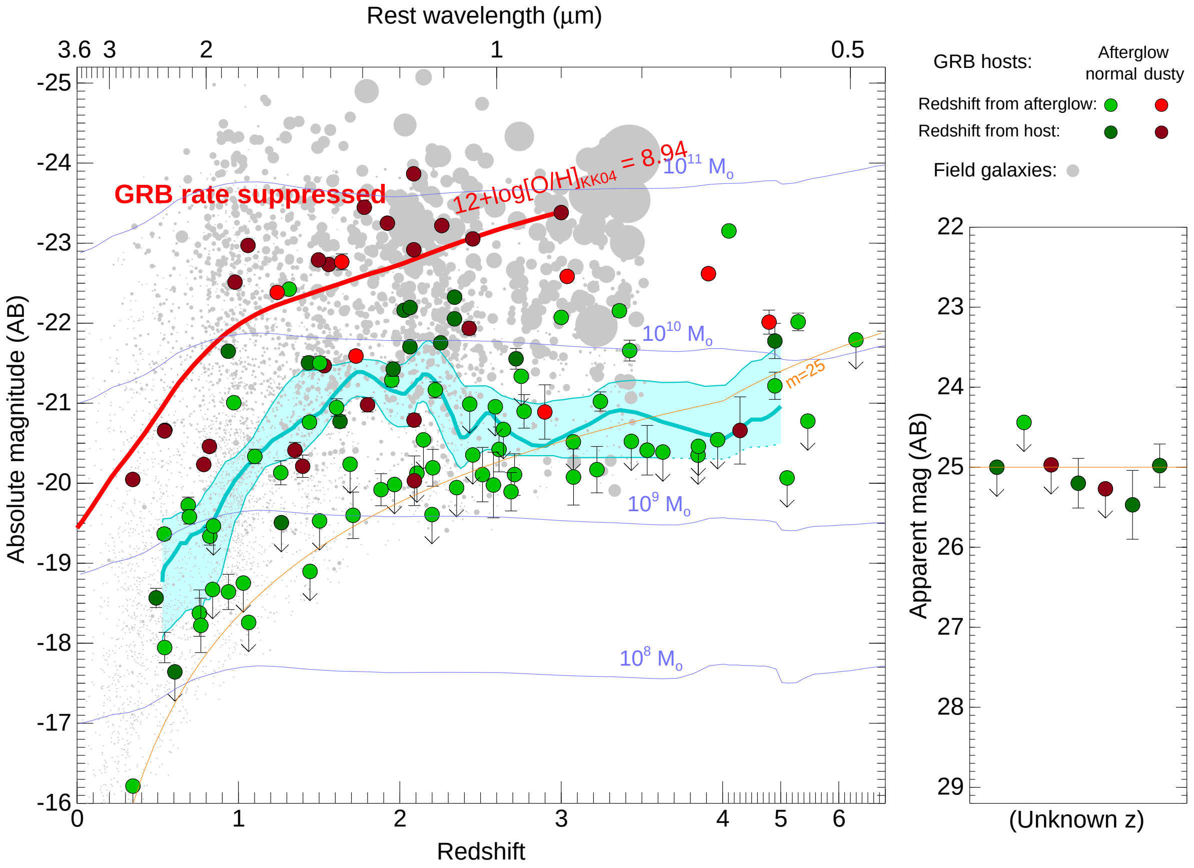

Figure 3.17: Near-infrared luminosities of GRB hosts as a function of redshift for a large and unbiased sample of 119 GRB hosts from the SHOALS sample, compared to star-forming galaxies (gray, from Kajisawa *et al.*, 2011). The horizontal blue curves indicate equivalent stellar masses. GRBs sample galaxies of all masses and redshifts, but rarely occur in the most luminous galaxies, especially at low redshift (z ¡ 1.5). The red curve shows the luminosity of a galaxy at the metallicity threshold of $12 + \log[\mathrm{O/H}] = 8.94$. Adapted from Perley *et al.* (2016b).

The K-band luminosity of low redshifts GRBs from BAT6 was analized by Vergani *et al.* (2015). They found that the deficiency of massive galaxies is still present in this unbiased sample. Furthermore, as NIR luminosity is a tracer of the galaxy stellar mass, and it is correlated with the metallicity, this can be interpreted as a metallicity bias. Recently, Perley *et al.* (2016c) found that the GRB rate increase with redshift and is uniform below a critical value of log $[O/H] = 8.94$, dropping by about an order of magnitude in more enriched galaxies. Schulze *et al.* (2015) also found that the distribution of UV luminosities in the TOUGH sample dominate the faint side at low and very high, but not at intermediate redshifts. This trend still needs to be confirmed.

Most luminous galaxies contain a huge amount of dust that scatter UV photons converting them into FIR/submm emission (dusty star-forming galaxies, DSFG; Casey *et al.*, 2014). Studies using large samples and sensitive instruments at long wavelengths indicate that DSFG hosts are not uncommon, but they represent a small percentage of the GRB host population.

3.4.1.2 Spectroscopic properties

Comparison between spectroscopic GRB and field samples of galaxies are subject to complex biases, but derived spectroscopic properties of GRB hosts are quite similar to what is inferred from photometric measurements (Krühler *et al.*, 2015). GRBs in very metal rich and very metal poor galaxies are uncommon but present, being the median metal content about 8.5. GRB hosts tend to be metal poorer than field-selected star-forming galaxies of the same mass, providing some evidence that metallicity is a dominant factor.

We have to keep in mind that galaxies do not have an homogeneous metallicity, and then measured host value can be different from progenitor's metal content. Niino (2011) found that both the existence of few high metallicity hosts as well as the systematically low metallicities of typical GRB hosts can be explained even if the progenitor is a moderately metal poor star.

Early samples suggested that strong Lyα emission could be common in GRB hosts (Fynbo *et al.*, 2003). However, larger and more uniform samples still cannot confirm this (Milvang-Jensen *et al.*, 2012).

Other authors have searched for Wolf-Rayet and other very short-lived starburst features in nearby hosts (Han *et al.*, 2010) and found some evidences pointing to a likely very young progenitor, but still far to firmly stablish it.

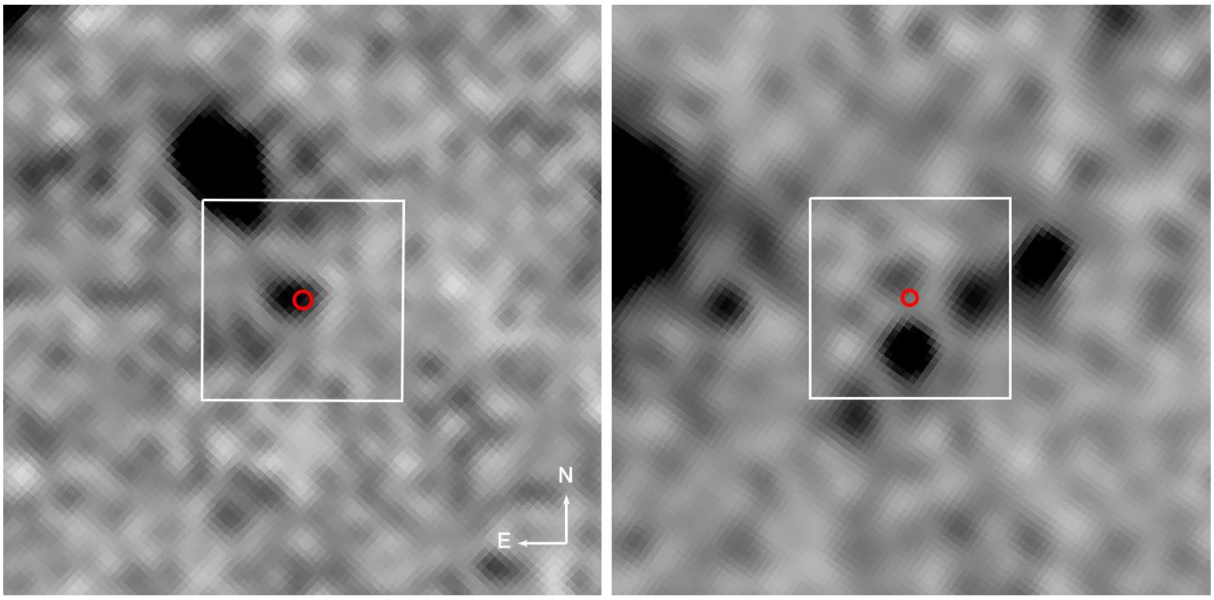

Figure 3.18: Deep HST $F140W$ filter images (lightly smoothed) of the locations of GRBs 050904 (left) and 140515A (right). Both bursts had redshifts of $z = 6.3$ and in each case the host is detected at AB magnitude ~ 28, underlying the GRB positions (indicated by red circles). These are the first GRB host galaxies found in emission at $z > 5$. The white boxes are 2 arcsec on a side. Adapted from McGuire *et al.* (2015).

3.4.1.3 GRB hosts at very high redshifts

It is more interesting when studying very high redshift GRBs use them to achieve a better understanding of the properties of star-forming galaxies at that time, as they are too faint to be easily detected with the current facilities. Addressing the problem via GRBs has the advantage that no particular form of the galaxy luminosity function is required.

Recently, HST observations have for the first time detected two $z \gtrsim 6$ GRB hosts (GRB 050904 and GRB 140515A McGuire *et al.*, 2015). The luminosity of these hosts suggests they are consistent with being faint examples of the LBG found in other deep HST surveys

3.4.2 Short GRBs

GRBs produced in this way are expected to be located in a range of normal star forming and elliptical galaxies, precisely in the outskirts which is the usual location of old merging binaries. The star formation rates, metallicities, sizes, and offsets of sGRBs are distinct from lGRB hosts, indicating that they come from different progenitors.

3.5 Cosmology with GRBs

3.5.1 Luminosity correlations of GRBs

The isotropic luminosity of a GRB is calculated by

$$L_{iso} = 4\pi d_L^2 P_{bolo} \tag{3.2}$$

where P_{bolo} is the bolometric peak flux, and d_L is the luminosity distance

$$d_L = (1+z)\frac{c}{H_0}\int\limits_0^z \frac{dz'}{E(z')} \tag{3.3}$$

where $E^2(z) = \Omega_M(1+z)^3 + \Omega_X f_X(z)$, and $f_X(z)$ is given by

$$f_X(z) = \exp\left[3\int\limits_0^z \frac{1+w(\tilde{z})}{1+\tilde{z}}d\tilde{z}\right] \tag{3.4}$$

where $w(\tilde{z})$ is the equation of state of the dark energy. Eq. 3.3 takes the form

$$d_L = (1+z)\frac{c}{H_0}\int\limits_0^z \frac{dz'}{\Omega_M(1+z')^3 + \Omega_\Lambda} \tag{3.5}$$

in a ΛCDM cosmology.

Applying the collimation correction, the total energy is

$$E_\gamma = E_{iso} \cdot F_{beam} \tag{3.6}$$

with the beaming factor $F_{beam} = 1 - \cos\theta_{jet}$ with a jet opening angle θ_{jet}. P_{bolo} and S_{bolo}, the bolometric fluence, are usually computed from the differential energy spectrum, $\Phi(E)$

$$P_{bolo} = P \times \frac{\int_{1/(1+z)}^{10^4/(1+z)} E\Phi(E)dE}{\int_{E_{min}}^{E_{max}} E\Phi(E)dE} \tag{3.7}$$

$$S_{bolo} = S \times \frac{\int_{1/(1+z)}^{10^4/(1+z)} E\Phi(E)dE}{\int_{E_{min}}^{E_{max}} E\Phi(E)dE} \tag{3.8}$$

where P and S are the observed peak and fluence, and (E_{min}, E_{max}) the detection thresholds of the observing instrument. Usually, $\Phi(E)$ is taken to be the Band function (Band *et al.*, 1993)

The most relevant correlations found to date are:

L_{iso} - τ_{lag}: It was first discovered by Norris *et al.* (2000), but recently challenged by a recent work by Bernardini *et al.* (2015). This correlation shows that the more luminous is a burst, the less time lag has it ($L_{iso} \propto \tau_{lag}^{-1.25}$)

E_{iso} - E_{peak}: Amati *et al.* (2002) found that E_{peak} and E_{iso} are correlated. This correlation can be interpreted from different theoretical frames, such as the synchrotron mechanism in relativistic shocks and emission from off-axis relativistic jets.

E_{γ} - E_{peak}: Ghirlanda *et al.* (2004a) realized that E_{peak} also correlates with E_{γ} tightly, showing also that can be a promising tool for constraining dark energy (Ghirlanda *et al.*, 2004b). It can be understood within the annular jet and photosphere models.

Several works have shown that these and other correlations must be physical, but that they can also be affected by instrumental selection effects (e.g. Shahmoradi & Nemiroff, 2011). In any case, correlations are useful to constrain dark energy and cosmological parameters (e.g., Wang *et al.*, 2015, see Fig. 3.20).

3.5.2 SFR derived from GRBs

The association of long GRBs with core-collapse supernovae (Hjorth *et al.*, 2003; Stanek *et al.*, 2003) opened a new window to measure the high-z SFR. However, one crucial problem, still to be solved, is how to calibrate the SFR with the GRB event rate.

Before *Swift*, this function was determined by fitting the observed $\log N$ - $\log P$ distribution (e.g. Guetta *et al.*, 2005). The form of this function has to be assumed (usually either a broken power-law or a power-law with exponential cut-off) and parameters degenerate, so it is challenging to obtain. A straightforward method is proposed by Lynden-Bell (1971), developed by Efron & Petrosian (1992), and used by, e.g., Wu *et al.* (2012). Results pointed that the GRB rate traces the SFR in a wide range of redshifts. However, Yu *et al.* (2015) found for the first time that the GRB rate shows an unexpectedly low-redshift excess compared to the observed SFR (see Fig. 3.22). This behavior was confirmed by Petrosian *et al.* (2015). A possible explanation for this excess could be the definition of long GRB, as T_{90} is defined in the observer frame. Moreover, some GRBs shows no SN, so they must be part of other GRB population. Finally, there may exist a subclass of low

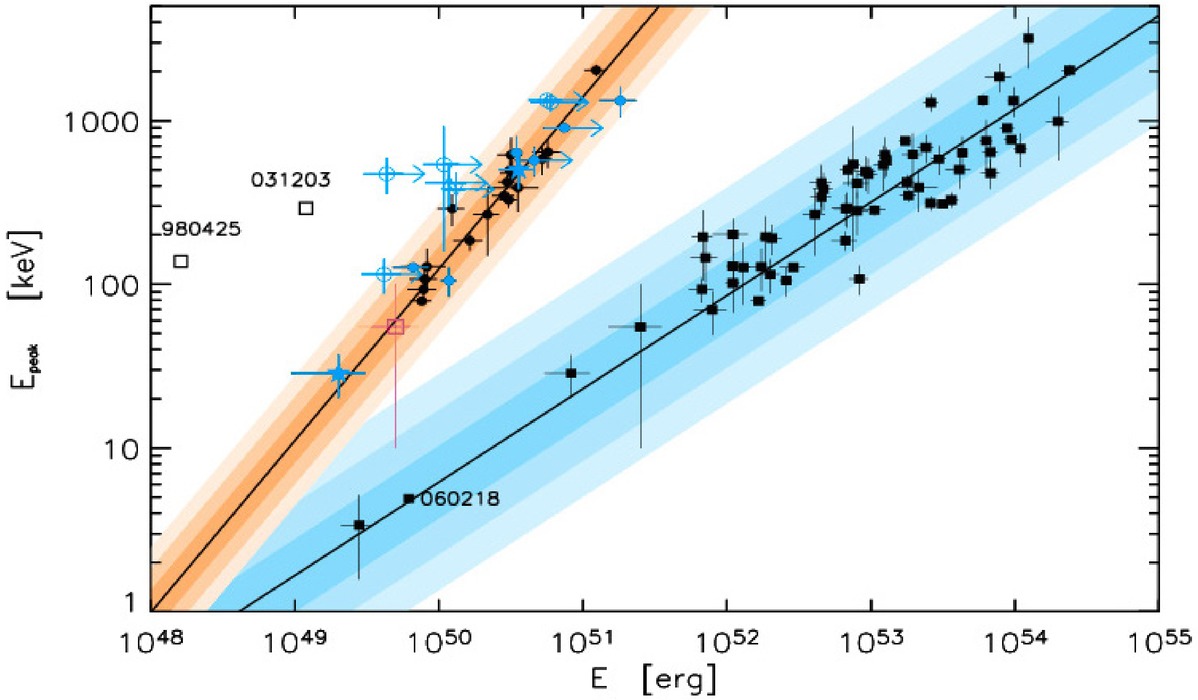

Figure 3.19: E_{peak} - E_γ and E_{peak} - E_{iso} correlations. Adapted from Ghirlanda *et al.* (2007).

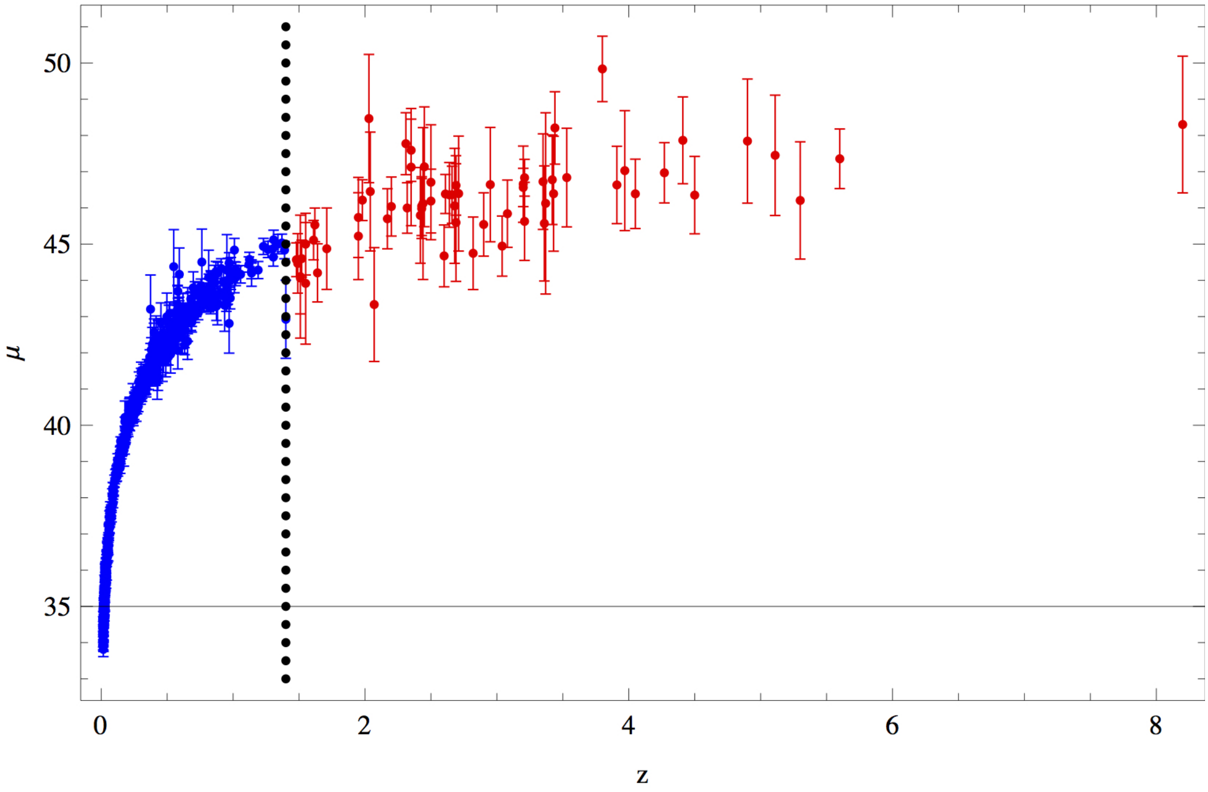

Figure 3.20: Hubble diagram of 557 SNe Ia plus 66 high-z GRBs. Adapted from Wang & Dai (2011b)

luminosity GRBs which progenitor may be different to the high luminosity bursts. Therefore, more physical criteria are required to classify GRBs and use them for cosmological purposes.

Another approach for studying SFR is proposed using only high-luminosity GRBs (e.g. Wang, 2013). The expected redshift distribution of GRBs is

$$\frac{dN}{dz} = F(z)\frac{\epsilon(z)\dot{\rho}_*}{\langle f_{beam}\rangle}\frac{dV_{com}/dz}{1+z} \tag{3.9}$$

where $F(z)$ represents the ability to obtain the redshift, $\epsilon(z)$ accounts for the fraction of stars producing GRBs, and $\dot{\rho}_*$ is the SFR density. GRBs unobservable are accounted for through $\langle f_{beam}\rangle$, and $\epsilon(z) = \epsilon_0(1+z)^\delta$, with ϵ_0 an unknown constant that includes the absolute conversion from the SFR to the GRB rate in a given GRB luminosity bin. A value of $\delta \sim 0.5 - 1.2$ was inferred by Wang (2013). For a flat Universe

$$\frac{dV_{com}}{dz} = 4\pi D_{com}^2 \frac{dD_{com}}{dz} \tag{3.10}$$

with

$$D_{com}(z) = \frac{c}{H_0}\int_0^z \frac{dz'}{\sqrt{\Omega_m(1+z')^3+\Omega_\Lambda}} \tag{3.11}$$

In Fig. 3.21 is represented the isotropic luminosity ($L_{iso} = E_{iso}(1+z)/T_{90}$) distribution as a function of redshift. The shaded area approximates the threshold of *Swift*/BAT ($F_{lim} \sim 1.2 \times 10^{-8}$ erg cm^{-2} s^{-1}. A luminosity cut of $L_{iso} > 10^{51}$ erg s^{-1} is taken for the z-range from 0 to 4, that is used as to calibrate the SFR-to-GRB conversion because SFR is well constrained at $z < 4$. The theoretical number of GRBs in the z-bin $1-4$ is

$$N_{1-4}^{th} = A\int_1^4 dz(1+z)^\delta \dot{\rho}_*(z)\frac{dV_{com}/dz}{1+z} \tag{3.12}$$

where $A = \frac{\Delta t\Delta\Omega F_0}{4\pi\langle f_{beam}\rangle}$ depends on observing time Δt, and the angular sky coverage $\Delta\Omega$. For a generic bin,

$$N_{z_1-z_2}^{th} = \langle\dot{\rho}_*\rangle_{z_1-z_2}A\int_{z_1}^{z_2} dz(1+z)^\delta\frac{dV_{com}/dz}{1+z} \tag{3.13}$$

so we can obtain the SFR as

$$\langle \dot{\rho}_* \rangle_{z_1-z_2} = \frac{N^{obs}_{z_1-z_2}}{N^{obs}_{1-4}} \frac{\int_1^4 dz(1+z)^\delta \dot{\rho}_*(z) \dfrac{dV_{com}/dz}{1+z}}{\int_{z_1}^{z_2} dz(1+z)^\delta \dfrac{dV_{com}/dz}{1+z}} \tag{3.14}$$

Current derived SFR from GRBs is shown in Fig. 3.22 as filled circles. These values are significantly larger than the ones inferred from observed galaxies. This could be due by a observational bias. However, GRB rate can be enhance at high-z by some physical reasons.

- **Metallicity evolution**: A natural origin of this excess could be due to the lower amount of metals at high-z. The most popular model for the physical explanation of LGRBs by Woosley (1993) predicts that GRBs originate from the collapse of a high mass (>30M$_\odot$), high rotating star. Low metallicities (0.1-0.3Z$_\odot$) allow progenitors to keep more of their mass to loose by stellar winds, and therefore preserve angular momentum.
- **Evolving initial mass function**: Wang & Dai (2011a) proposed that an excess in the GRB rate can be due to the evolution of the initial mass function (IMF), which determines the number of massive stars able to produce GRBs. It is suggested that this function has been evolved at high redshift to produce the transition from population III to population II stars.
- **Evolving luminosity function break**: (Virgili *et al.*, 2011) found that if the break of luminosity function evolves with redshift ($\propto L_b \times (1+z)^{\sim 0.8--1.2}$), BATSE and *Swift* data can be reconciled.

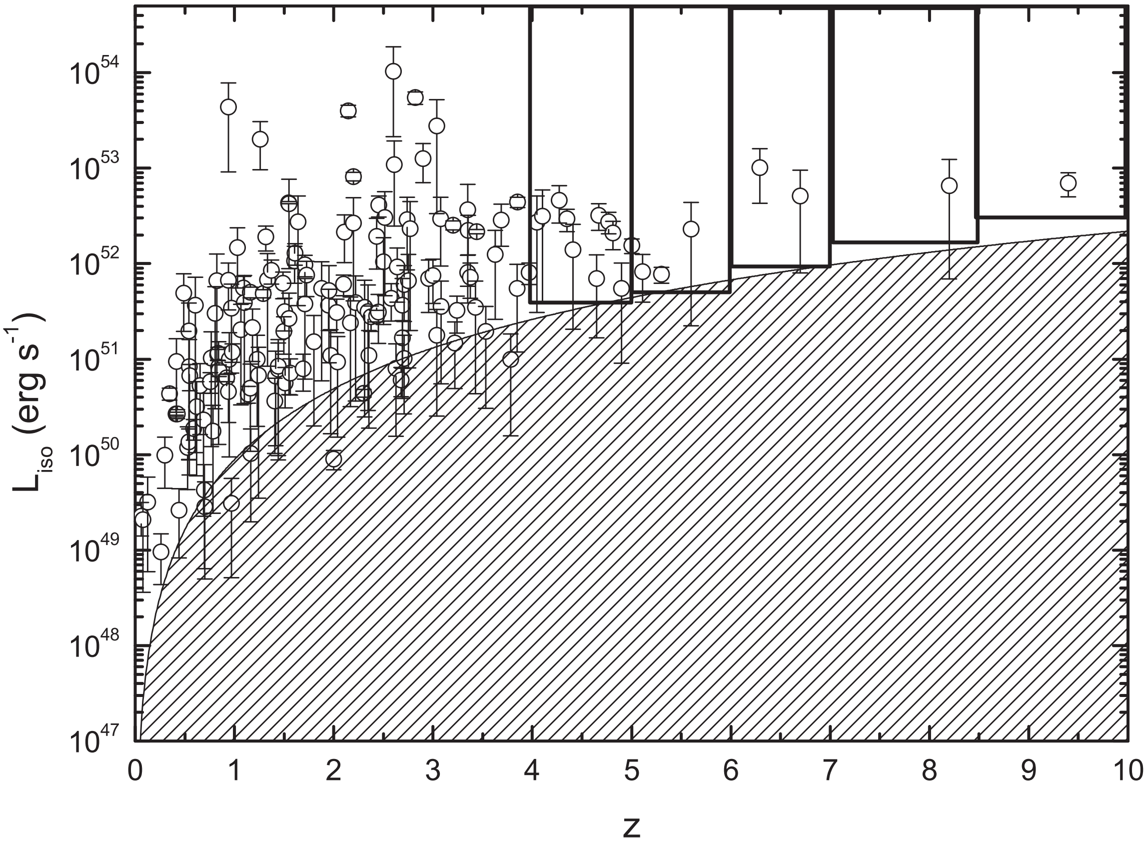

Figure 3.21: L_{iso} vs z for 157 lGRBs. The shaded area approximates the detection threshold of *Swift*. Adapted from Wang (2013).

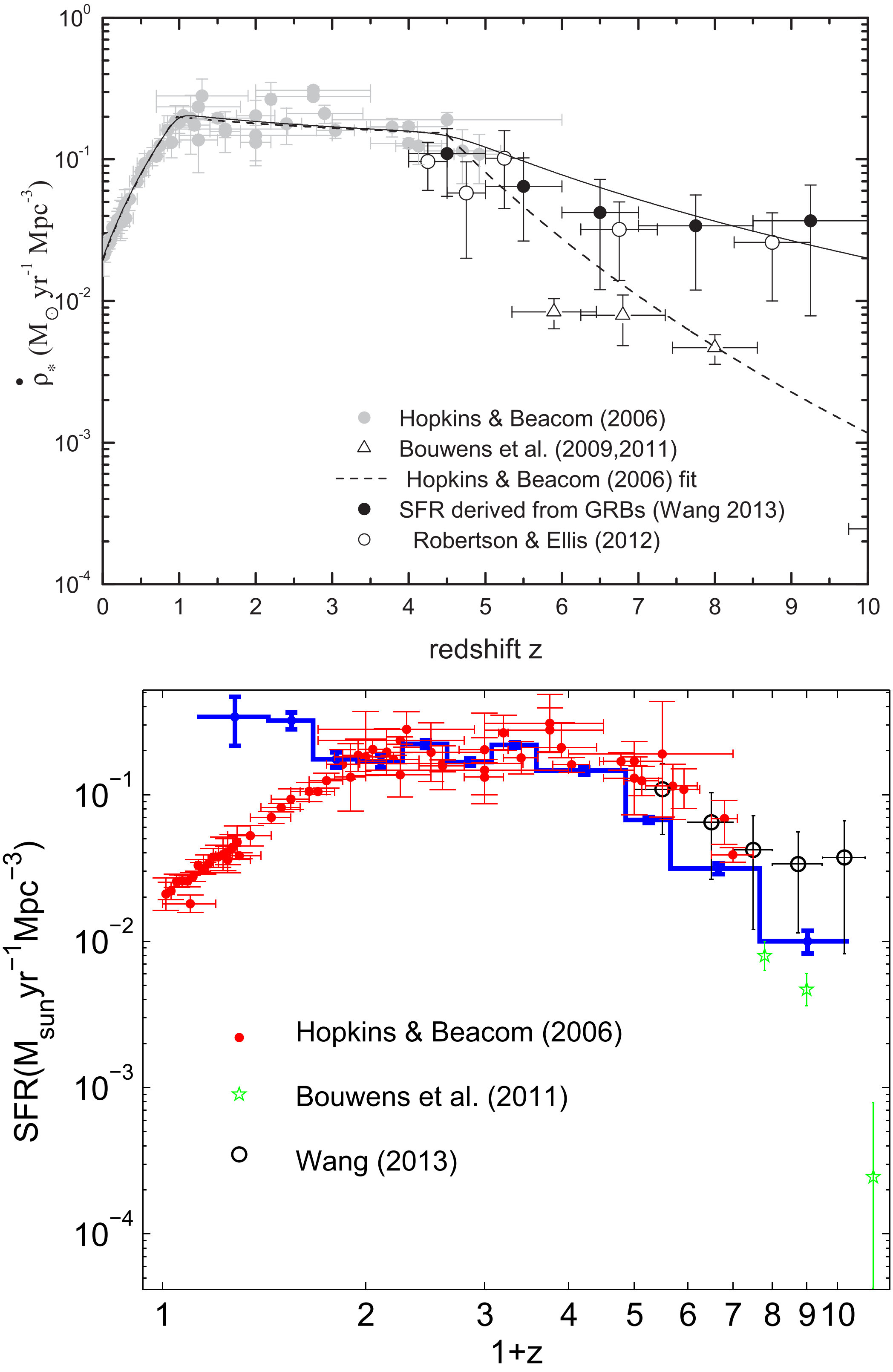

Figure 3.22: The cosmic star formation history. Adapted from Wang (2013, upper) and Yu *et al.* (2015, lower).

PART I

MULTIWAVELENGTH STUDY OF GRB AFTERGLOWS

GRB 110715A: THE FIRST GAMMA-RAY BURST OBSERVED WITH ALMA

Chapter 1

Physics of Gamma-ray bursts and their afterglows

> *"Oppenheimer, they tell me you are writing poetry. I do not see how a man can work on the frontiers of physics and write poetry at the same time. They are in opposition. In science you want to say something that nobody knew before, in words which everyone can understand. In poetry you are bound to say... something that everybody knows already in words that nobody can understand."*
>
> — P.A.M. DIRAC, *Brighter than a thousand Suns, R. Jungk, 1958*

GAMMA-RAY BURSTS (GRBs, Klebesadel *et al.*, 1973) are the most violent explosions in the Universe. They can be classified into two types based on the duration (and the hardness) of their γ-emission: short and long GRBs ($T_{90} < 2$ s with hard spectrum, and $T_{90} > 2$ s with soft spectrum, respectively; Kouveliotou *et al.*, 1993). Counterparts of these flashes are detected from X-ray to radio bands, which are known as the GRB *afterglows* and in someo cases can be observed up to several months after the burst.

Currently, the most favored model to explain the origin of GRBs is a highly magnetized relativistic jet, although more prompt polarimetric observations are needed in order to confirm this. The prompt emission likely originates from either internal shocks in the photosphere of the jet or magnetic dissipation in a magnetically dominated jet (see Zhang & Yan, 2011; Zheng *et al.*, 2012, and references therein). The afterglow emission, however, is thought to originate from external shocks caused by the jet's interaction with the interstellar medium (ISM). A reverse shock moving into the expanding jet (Mészáros & Rees, 1993; Sari *et al.*, 1998, 1999) is also expected to contribute to the multiwavelength emission. This reverse shock is supposed to be short lived, with most of the afterglow emission being generated by the forward shock.

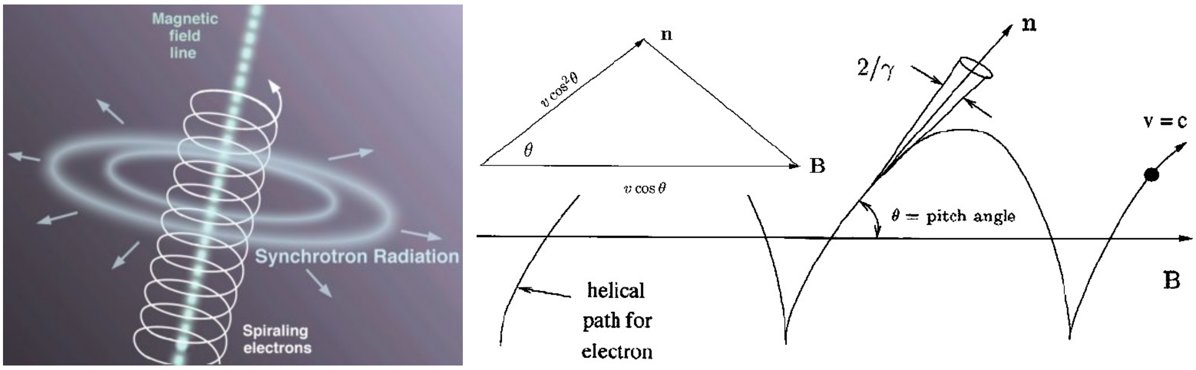

Figure 1.1: Schematic view of the synchrotron radiation by a single particle.

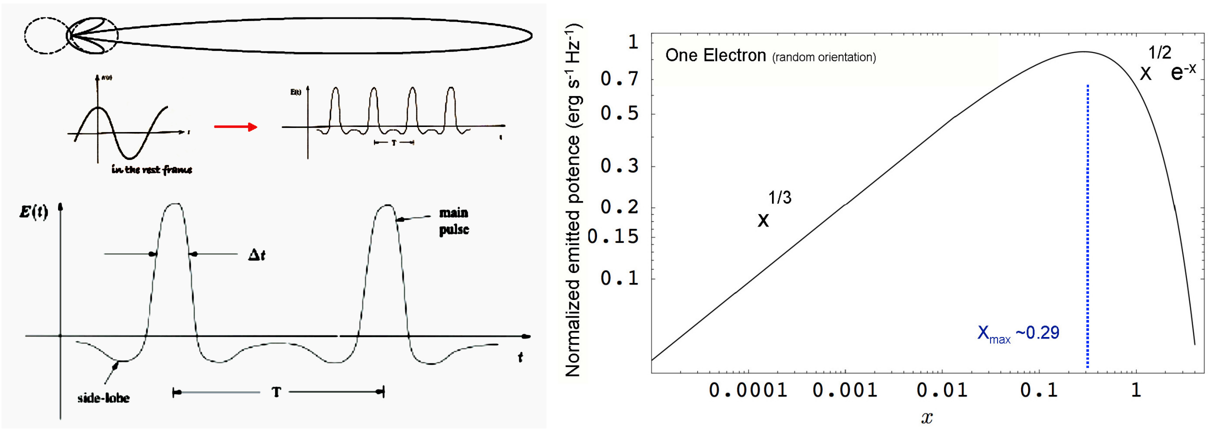

Figure 1.2: Synchrotron beaming and pulses (*left*) and spectrum (*right*) for a single particle.

1.1 Synchrotron radiation

1.1.1 Single particle

The simplest model to derive the expression of the relativistic synchrotron emission is considering a jet that has a tangled magnetic field, i.e., integration cover all viewing angles. This angle is important because the radiation from each particle is strongly beamed in the direction on which the charge is traveling, since this motion is relativistic. Beamed means that the radiation appears to be concentrated in a narrow cone, and an observer will see the emission coming from a fraction $\sim 1/\gamma$ of its orbit.

First, consider a single particle with mass m and energy

$$E = \gamma m c^2, \qquad \gamma \equiv (1-\beta^2)^{-1/2}, \qquad \beta \equiv v/c \tag{1.1}$$

moving with velocity v in a uniform magnetic field B. Equations of the motion of a particle in a magnetic field are

$$\left.\begin{array}{l}\frac{d}{dt}(\gamma m v) = \frac{q}{c}\vec{v} \\ \frac{d}{dt}(\gamma m c^2) = q\vec{v}\cdot\vec{E} = 0\end{array}\right\} \frac{v^2}{r} = \frac{q}{\gamma m c} v B \sin\alpha_p \tag{1.2}$$

The combination of a circular and uniform motions is an helical motion. Its trajectory makes an angle α_p with the direction of B (it is called "pitch angle") and r is the radius of gyration around the field lines

$$r = \frac{v}{\omega_B \sin a_p}, \qquad \omega_B = \frac{qB}{\gamma m c} \tag{1.3}$$

where ω_B is the relativistic gyro-frequency and q particle's charge.

If the orbit were circular, then the observer would detect pulses with a period $P = 2\pi/\omega_B$. However, since the particle's guiding center is moving with velocity $v\cos\alpha_p$ along the field line, and the motion has a component projected toward the observer $v^2\cos^2\alpha_p$, there is a Doppler compression of the pulse period. They are spaced apart by a period

$$T = P\sin^2\alpha_p = \frac{2\pi}{\omega_B} \tag{1.4}$$

The relativistic aberration or *beaming* follows directly from the Lorentz transform

$$\begin{array}{l} v_x \equiv \frac{dx}{dt'}\frac{dt'}{dt} = (v'_x + v)\left(1 + \frac{\beta v'_x}{c}\right)^{-1} \\ v_y \equiv \frac{dy}{dt'}\frac{dt'}{dt} = \frac{v'_y}{\gamma}\left(1 + \frac{\beta v'_y}{c}\right)^{-1} \end{array} \tag{1.5}$$

Defining as θ the angle between the direction of the emitted photon and the one of the electron, we get

$$\cos\theta = \frac{\cos\theta' + \beta}{1 + \beta\cos\theta'}, \qquad \sin\theta = \frac{\sin\theta'}{\gamma(1 + \beta\cos\theta')} \approx \frac{1}{\gamma} \approx \theta \tag{1.6}$$

since $1/\gamma << 1$. Therefore, we see the radiation confined to a very narrow beam of width $2/\gamma$.

The width of the pulse $\Delta t'$ is determined by the fraction of the gyromagnetic period P that the electron is radiating toward the observer, obtaining

$$\Delta t' = \frac{2mc}{qB\sin\alpha_p} \tag{1.7}$$

Since this pulse is subject to a Doppler compression,

$$\Delta t = \Delta t'(1-\beta) \simeq \frac{\Delta t'}{2\gamma^2} \tag{1.8}$$

we obtain

$$\Delta t = \frac{1}{\gamma^3 \omega_B \sin\alpha_p} \tag{1.9}$$

To compute the spectrum and polarisation of the synchrotron emission, we start from the expression

$$\frac{dW}{d\omega d\Omega} = \frac{q^2\omega^2}{4\pi^2 c}\left|\int \vec{n}\times(\vec{n}\times\vec{\beta}\exp[i\omega(t'-\vec{n}\cdot\vec{r}_0(t')/c]dt'\right|^2 \tag{1.10}$$

The emission can be expressed in terms of two polarisations: perpendicular and parallel to the projected direction of the magnetic field

$$\frac{dW}{d\omega d\Omega} = \frac{dW_\perp(\omega)}{d\omega d\Omega} + \frac{dW_\parallel(\omega)}{d\omega d\Omega} \tag{1.11}$$

Defining the quantities

$$\theta_\gamma^2 = 1+\gamma^2\theta^2, \qquad \eta = \omega r\theta_\gamma^3/3c\gamma^3 \tag{1.12}$$

we get

$$\begin{aligned} \frac{dW_\perp(\omega)}{d\omega d\Omega} &= \frac{q^2\omega^2}{3\pi^2 c}\left(\frac{r\theta_\gamma^2}{\gamma^2 c}\right)^2 K^2_{\frac{2}{3}}(\eta) \\ \frac{dW_\parallel(\omega)}{d\omega d\Omega} &= \frac{q^2\omega^2\theta^2}{3\pi^2 c}\left(\frac{r\theta_\gamma}{\gamma c}\right)^2 K^2_{\frac{1}{3}}(\eta) \end{aligned} \tag{1.13}$$

where K are the modified Bessel functions. Since most radiation occurs at angles $\theta \sim 0$

$$\eta \simeq \eta(\theta=0) = \frac{\omega}{2\omega_c}, \qquad \omega_c \equiv \frac{3}{2}\gamma^3\omega_B\sin\alpha_p \tag{1.14}$$

where ω_c is known as the characteristic frequency. Taking the element of solid angle to be $d\Omega = 2\pi\sin\alpha_p d\theta$, and defining

$$F(x) \equiv x\int_x^\infty K_{\frac{5}{3}}(z)dz, \qquad G(x) \equiv xK_{\frac{2}{3}}(x), \qquad x \equiv \frac{\omega}{\omega_c} \tag{1.15}$$

the total luminosity of the particle in each polarisation can be expressed as

$$\begin{aligned} P_{\perp}(\omega) &= \frac{\sqrt{3}q^3 B \sin a_p}{4\pi mc^2}[F(x)+G(x)] \\ P_{\parallel}(\omega) &= \frac{\sqrt{3}q^3 B \sin a_p}{4\pi mc^2}[F(x)-G(x)] \end{aligned} \tag{1.16}$$

The total emitted power is

$$P(\omega) = P_{\perp}(\omega) + P_{\parallel}(\omega) = \frac{\sqrt{3}q^3 B \sin a_p}{4\pi mc^2}F(x); \qquad P(\nu) = 2\pi P(\omega) \tag{1.17}$$

It can be derived, as a function of ω_c, that the peak frequency ω_m is

$$\omega_m = 0.29\omega_c \tag{1.18}$$

and eq. 1.17 get the asymptotic forms

$$\begin{aligned} &P(\omega) \propto x^{1/3} && x << 1 \\ &P(\omega) \propto x^{1/2} \exp -x && x >> 1 \end{aligned} \tag{1.19}$$

This is illustrated in Fig. 1.2.

1.1.1.1 Population of particles

From an astronomical point of view, it is much more interesting the observed spectrum from a population of particles. It will have a distribution of energies (and hence Lorentz factors) and pitch angles. The most common used distributions are an isotropic distribution of pitch angles ($p(\alpha_p) = \frac{1}{2}\sin\alpha_p$, and the power law distribution of Lorentz factors

$$N(\gamma)d\gamma = C\gamma^{-p}d\gamma, \qquad \gamma_m < \gamma < \gamma_M \tag{1.20}$$

It is also assumed that magnetic fields are tangled. Therefore

$$P_{tot}(\omega) = C\int_{\gamma_m}^{\gamma_M} P(\omega)\gamma^{-p}d\gamma \tag{1.21}$$

Solving the integral we get

$$P_{tot}(\omega) = \frac{\sqrt{3}q^3 CB \sin\alpha_p}{2\pi mc^2(p+1)}\Gamma\left(\frac{p}{4}+\frac{19}{12}\right)\Gamma\left(\frac{p}{4}-\frac{1}{12}\right)\left(\frac{mc\omega}{3qB\sin\alpha_p}\right)^{-(p-1)/2} \tag{1.22}$$

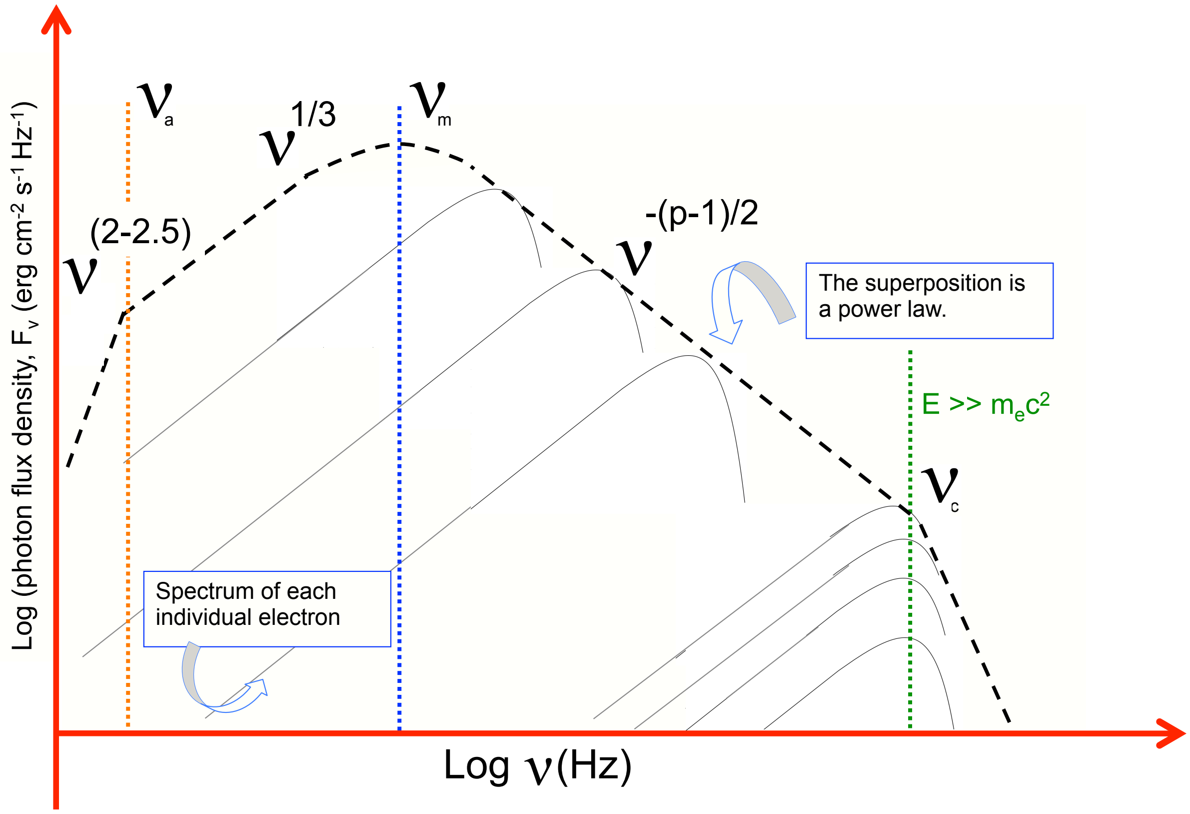

Figure 1.3: Spectrum of radiating particles with a power law distribution of energies.

In the observer frame, $P_{obs} = P_{tot}\Gamma^2$. This is a very important result, as it links an observable parameter, the power law in frequencies of the emission, to the power law slope of the particle energy distribution

$$\beta_r = (p-1)/2 \tag{1.23}$$

If the energy distribution has a cut off, the resulting emission will have a critical frequency ν_c where the power law spectrum has an exponential cutoff (analogous to the single particle spectrum). This characteristic frequency usually scales like $\nu_c \propto \gamma_m B$, where γ_m is the maximum value of the γ distribution.

1.1.2 Self-absorption

If we consider radiation from a population of particles, emitted photons will interact with the charges in the magnetic field. The absorption and stimulated emission can be studied using the Einstein coefficients

$$\begin{aligned} j_\nu &= \frac{h\nu}{4\pi} n_1 A_{21} \phi(\nu) \\ \alpha_\nu &= \frac{h\nu}{4\pi}(n_1 B_{12} - n_2 B_{21})\phi(\nu) \end{aligned} \tag{1.24}$$

As for a given photon energy there are many possible transitions

$$\alpha_\nu = \frac{h\nu}{4\pi} \sum_{E_1} \sum_{E_2} (n(E_1)B_{12} - n(E_2)B_{21})\phi_{21}(\nu) \tag{1.25}$$

This is true because we are considering a tangled magnetic field. After some operations we get

$$\alpha_\nu = \frac{c^2}{8\pi h\nu^3} \sum_{E_2} [n(E_2 - h\nu) - n(E_2)] P(\nu, E_2) \tag{1.26}$$

where

$$P(\nu, E_2) = h\nu \sum_{E_1} A_{21}\phi_{21}(\nu) = (2h\nu^3/c^2)h\nu \sum_{E_1} B_{21}\phi_{21}(\nu) \tag{1.27}$$

Therefore, changing n(E) ⇒ N(E)dE

$$N(E)dE = CE^{-p}dE, \qquad E_1 < E < E_2 \tag{1.28}$$

we finally obtain

$$\alpha_\nu = \frac{\sqrt{3}q^3}{8\pi m}\left(\frac{3q}{2\pi m^3 c^5}\right)^{p/2} C(B\sin\alpha_p)^{(p+2)/2}\Gamma\left(\frac{3p+2}{12}\right)\Gamma\left(\frac{3p+22}{12}\right)\nu^{-(p+4)/2} \tag{1.29}$$

Now, we can predict the observed spectrum

$$S_\nu = \frac{j_\nu}{\alpha_\nu} = \frac{P(\nu)}{4\pi\alpha_\nu} \tag{1.30}$$

in the optically thick and thin limits

optically thick: $F_\nu \propto I_\nu \propto S_\nu \propto B^{-1/2}\nu^{5/2}$

optically thin: $F_\nu \propto I_\nu \propto j_\nu \propto B^{(p+1)/2}\nu^{(1-p)/2}$

The turnover or *self-absorption* frequency is denoted by ν_a.

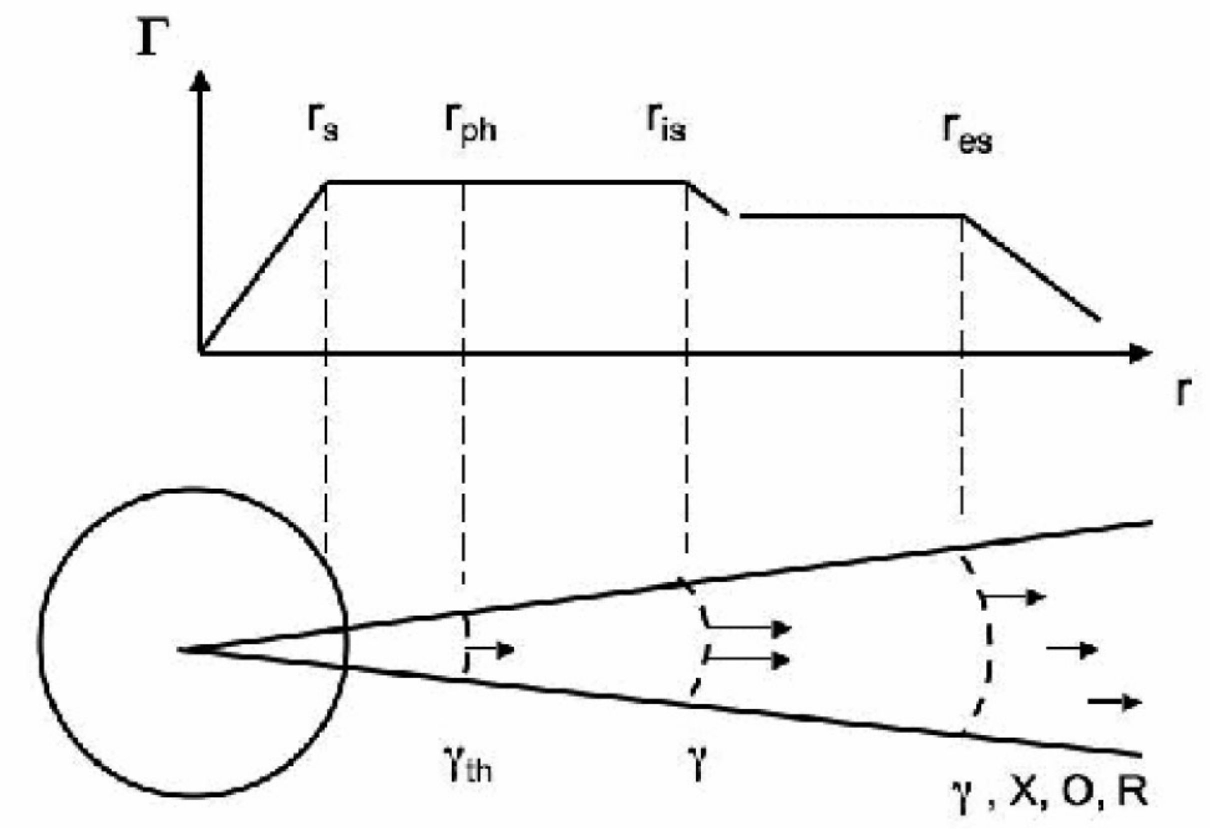

Figure 1.4: Schematic view of the evolution of the jet Lorentz factor and examples of symbolic locations of the characteristics radius.

1.2 The fireball model

As shown in the previous section, the most important parameters to characterise the synchrotron emission are p and B. Therefore, the physical model to explain the GRB emission has to include processes which output are consistent with the (directly) measured p. The value of B is generally given as a function of other dynamical parameters that better link the physical scenario and the observed spectral and time evolution.

The most popular model that roughly interpret GRB observations is the fireball model, introduced for the first time by Cavallo & Rees (1978). The mechanism to explain GRBs have to account for a huge energy liberation ($\sim 10^{54}$ erg) in short scale time intervals (from milliseconds to few hundred of seconds). Currently, we link these phenomena to the liberation of the gravitational energy into thermal energy when a black hole is formed (for a review, see, e.g., Mészáros *et al.*, 2015). As this thermal energy is produced explosively, a hot fireball with virial temperatures in the MeV range and composed by photons, electrons, positrons, nuclei, magnetic fields, as well as neutrinos and gravitational waves starts to expand. Thermal neutrinos (E $\sim 10^{53}$) and gravitational wave emission ($\nu \in$

[10^2, 10^3] Hz, E $\sim 10^{53}$ erg) escape in matter of seconds or less, as the progenitor is essentially transparent to them. On the other hand, photons, $e^{\pm}$, nucleons, and magnetic fields get trapped.

A fireball can be characterised by its initial energy E_0. In the initial stage the mean energy per baryon is $\eta = E_0/M_0c^2 >> 1$, where M_0 represents the baryon loading of the fireball. The equation of motion of a blast wave sweeping up material $m(R)$ from the surrounding medium is

$$-\frac{d\Gamma}{\Gamma^2-1} = \frac{dm + \left(\frac{\Gamma}{\Gamma^2-1}\right) dU_{adi}}{M_0 + m(R) + U} \tag{1.31}$$

where the internal energy

$$dU = dU_m + dU_{adi} + dU_{rad}; \qquad dU_m = (\Gamma - 1)dm \tag{1.32}$$

In elementary treatments of the blast wave model, it is simply assumed that a fraction ϵ_e of the forward shock power is transferred to leptons, so that

$$L'_e = \epsilon_e \frac{dE'}{dt'} \tag{1.33}$$

and some mechanism, probably the first order shock Fermi process, injects electrons with a power law distribution between electrons Lorentz factors $\gamma_m \leq \gamma \leq \gamma_M$.

The initial radius of the fireball is R_{in}. Inside, the particles have a bulk Lorentz factor $\Gamma \sim 1$ and random isotropic energies with a mean Lorentz factor $\gamma \sim \eta \sim 10^2 - 10^3$. As the initial optical depth is extremely high, radial expansion is the consequence of the high super-Eddington luminosity and the thermal energy can only be converted into bulk kinetic energy. A phase of acceleration begins and the particles are confined inside an increasingly smaller angle $(R/R_{in})^{-1}$ along the radial direction. As the expansion is adiabatic, the temperature of the fireball is $T' \propto R^{-1} \propto \Gamma^{-1}$. The bulk Lorentz factor of the expanding gas increases linearly with R until it saturates at $R_{sat} \propto \Gamma_{max} R_{in}$, with $\Gamma_{max} \sim \eta$. This highly relativistic expansion of the fireball modifies its radiation: the observed photons are blueshifted while the observed timescales are shortened. Therefore, relativistic motion provides a way to reduce the rate of pair creation, and therefore explains the observed radiation above ∼1 MeV, as the opacity of the fireball to pair creation is an efficient way to suppress these photons. Beyond R_{sat} the shell coasts a constant $\Gamma = \Gamma_{max}$.

When the fireball comoving temperature is bellow ~ 17 keV the $e^{\pm}$ pairs fall out of equilibrium and recombine. It occurs at the photospheric radius R_{ph}, $R_{ph} > R_{sat}$, defined as the radii where the optical depth equals to unity. However, this radiation is quasi-thermal, in contrast with what is observed in GRBs. Moreover, the typical time scales over which the photons escape are comparable to that during which the flow becomes optically thin (milliseconds). This is too short with respect to most GRB durations.

1.2.1 Internal shocks

As explained before, if the prompt emission would come only from the fireball photons when the high initial optical depth had decreased, it is expected both a low radiative efficiency and a quasi-thermal spectrum. However, both issues are avoided if the radiation (or at least most of it) arises in shocks (e.g. Mészáros, 2006). Internal shocks explain the conversion of kinetic energy into synchrotron and inverse Compton non-thermal spectra (Rees & Mészáros, 1992, 1994).

Let's consider the relativistic shell moving with Γ_{max} after R_{sat}. It drives a shock into the surrounding ISM, which propagates with $\Gamma_{sh} = \sqrt{2}\Gamma$. These shocks take place within the relativistic ejecta when shells with different bulk Lorentz factors merge. If we call Γ_s and Γ_f the factors for the slow and fast shells, and we assume that they are of the same order, the merged bulk Lorentz factor is

$$\Gamma_m = \sqrt{\frac{m_f\Gamma_f + m_s\Gamma_s}{m_f/\Gamma_f + m_s/\Gamma_s}} \tag{1.34}$$

and the collision time will be

$$T = \frac{\Gamma_s^2\Gamma_f^2}{(\Gamma_s^2 - \Gamma_f^2)} t_{var} \tag{1.35}$$

where t_{var} is the variability time scale in the rest frame. These shocks are collisionless because the densities are so low to take place, but the magnetic fields are able to redistribute the energy between the particles. The merge will occur at a radius $R_{is} = \Gamma^2 t_{var} c$, which has to be placed at sufficiently large distances to allow the resulting radiation to escape without adiabatic looses. The efficiency of the conversion of the kinetic energy into internal energy that will be partially radiated is

$$\epsilon = \frac{1 - (m_f + m_s)\Gamma_m}{m_f\Gamma_f + m_s\Gamma_s} \tag{1.36}$$

The interaction of two shells takes place in the form of two shocks, a forward and a reverse shock (Sari & Piran, 1995). Superimposing the pulses resulting from individual two-shells interactions, synthetic bursts can be constructed (Daigne & Mochkovitch, 1998). Playing with the initial distribution of electron Lorentz factors it is possible to reproduce most of the large variety of observed GRB light curves. The separation between the peaks corresponds to periods of time during which the inner engine is quiet (Kobayashi *et al.*, 1997). With some assumptions about the energy equipartition between the electrons, protons, and magnetic fields, the Lorentz factors of the accelerated electrons can be determined. However, it gives a spectral evolution of E_p (the peak energy) that is too step. To have a better general agreement with observations, authors assume that the equipartition depend on the strength of the shock and on the post-shock density. If GRB pulses are produced by internal shocks, their temporal and spectral properties are probably governed by the hydrodynamics of the flow rather than the geometry of the emitting shells.

1.2.2 Inverse Compton scattering

Even it is generally accepted that the photons radiated during the prompt phase are due to synchrotron, inverse Compton scattering could play an important role depending on the physical conditions within the fireball.

This effect can boost the energy of a photon by a factor of γ^2. For typical synchrotron photons in the $\sim$100 keV range the IC component will be in the GeV range. Such a high energy component has been observed in some GRBs.

1.2.3 Photospheric emission

Since few years, several works claim that there is a thermal component on top of the over non thermal spectra (see Pe'er & Ryde, 2016, and references therein). This emission was predicted by the very early cosmological GRB models, but it was later abandoned due to that the observed spectra did not show a clear evidence of a Planck spectrum.

In spite that the Band function provides good fits for most of GRB data, this model is not capable of capturing any feature coming from an hypothetical thermal emission. Furthermore, the fraction of GRBs in which a thermal component is detected correlates with their brightness, so observed bursts near the detection limits will not be possible to detect. Current models cannot robustly predict the strength of the thermal component. Finally, the main concern is the fact that the observed signal is often explained by more than one model. For example, a weak Planck component can be undistinguished from adiabatic losses, strong distortion due to sub-photospheric dissipation or strong magnetization.

Consequently, to make further progress, data should be fitted with physically-motivated models that can include a thermal component in addition to non-thermal emission. Several of such models already exists, but they are not frequently used.

1.2.4 External shocks

At the beginning of the fireball expansion the interstellar medium has no influence on the expanding shell, but it drives an external or termination shock when the jet starts to be decelerated by a swept up external matter at a radius

$$r_{es} \simeq \left(\frac{3E_0}{4\pi n_0 m_p c^2}\right)^{1/3} \Gamma^{-2/3}\, cm \tag{1.37}$$

This shock propagates with $\Gamma_{sh} = \sqrt{2}\Gamma$. As the shell radius increases, more ISM matter is accelerated via Fermi mechanism behind the shock and the shell is progressively influenced by the ISM. This influence becomes significant when the energy of the heated ISM is comparable to E_0. The afterglow emission begins when most of the bulk kinetic energy is transferred to the shocked external medium. The deceleration radius R_{dec} is defined as as the radius at which the initial part of the ejecta moving with $\Gamma_M = \eta$ sweeps up an amount of external gas to $E_0/(\eta c^2)$. Hence, the mass of the shocked material at the deceleration radius is

$$m_{dec} = \frac{M_0}{\eta} = \frac{4\pi}{3}\rho_{ext} R_{dec}^3 \tag{1.38}$$

Beyond this radius the shocked gas dominates the mass and energy of the expanding system.

Generally, two shocks form when the relativistic shell is slowed down by the ISM: a forward shock that propagates into the surrounding medium, and a reverse shock that propagates into the ejecta (Rees & Mészáros, 1992). At the very beginning as the forward shock builds up, its bolometric luminosity raises approximately as $L \propto t^2$, peaking when the radius reaches R_{dec}, and decays thereafter.

The dynamical evolution of the afterglow and its radiative properties are determined by E_0, ϵ_e, ϵ_B, n, and p. During the early phase of the external shock, the reverse shock is mildly relativistic and most of the energy conversion takes place in the forward shock (Sari & Piran, 1995).

1.2.5 Spectrum and light curves of the standard afterglow model

The standard afterglow model is based on the following approximations (Mészáros, 2002)

- Spherical outflow
- Line of sight scaling relations are assumed valid for the entire hemisphere
- Impulsive energy input E_0 and a single $\Gamma_0 = \eta$
- Highly relativistic expansion in the adiabatic regime
- Homogeneous external medium
- Time-independent shock acceleration parameters ϵ_e, ϵ_B, and p
- Only the forward shock radiation is considered

As most of electrons have their energies near $E_m = \gamma_m mc^2$, $\nu_m = \nu(\gamma_m)$. Assuming that a constant fraction of the shock ϵ_e of the shock energy e goes into electrons (Sari *et al.*, 1998) then

$$\gamma_m = \epsilon_e \frac{p-2}{p-1}\frac{m_p}{m_e}\Gamma \tag{1.39}$$

The electrons gain energy by the second-order Fermi acceleration process while they lose their energy by radiating synchrotron photons. Therefore, to compute γ_M we have to equal the acceleration rate to the radiation lose rate

$$\gamma_M = 2 \times 10^8 \frac{\sqrt{\epsilon_M}}{\epsilon_B^{1/4} n_0 \sqrt{\Gamma}} \tag{1.40}$$

where ϵ_M is a constant in the order of unity. We also define the cooling Lorentz factor γ_c as the one for which the energy lost by radiation is equal to the energy lost by adiabatic cooling

$$P(\nu_c)t = \Gamma\gamma_c mc^2, \qquad \nu_c \equiv \nu(\gamma_c) \tag{1.41}$$

so

$$\gamma_c = \frac{9 m_e (1+z)}{128 m_p \sigma_T \epsilon_B n_0 c \Gamma^3 t}, \qquad \sigma_T = \tag{1.42}$$

This means that an electron with initial Lorentz factor $\gamma_e > \gamma_c$ cools down to γ_c in a time t. The maximum emissivity appears at ν_c, and is given by

$$P(\nu, max) = \frac{\sigma_T m c^2}{3q} \Gamma B \tag{1.43}$$

The observed characteristic synchrotron frequency is given by

$$\nu = \frac{qB\gamma^2\Gamma}{2\pi m_e c(1+z)} \tag{1.44}$$

From this relation we can derive the characteristic frequencies. For example, in the adiabatic case

$$\begin{array}{ll} \nu_c = 9 \times 10^{12} \epsilon_B^{-3/2} n^{-1} E_{52}^{-1/2} t_d^{-1/2} (1+z)^{-1/2} & \mathrm{Hz} \\ \nu_m = 6 \times 10^{15} \left(\frac{p-2}{p-1}\right)^2 \epsilon_e^2 \epsilon_B^{1/2} E_{52}^{1/2} t_d^{3/2} (1+z)^{1/2} & \mathrm{Hz} \\ \nu_a = 2 \times 10^{9} \epsilon_e^{-1} \epsilon_B^{1/5} n^{3/5} E_{52}^{1/5} (1+z)^{-1} & \mathrm{Hz} \\ F_{\nu,max} = 1.1 \times 10^{5} \epsilon_B^{1/2} E_{52} n^{1/2} D_{28}^{-2} & \mu\mathrm{Jy} \end{array} \tag{1.45}$$

Two cases have to be considered:

1. $\gamma_m > \gamma_c$: All electrons cool down roughly to γ_c. This is the fast cooling case and the observed flux is given by

$$F_\nu = F_{\nu,max} \begin{cases} (\nu_a/\nu_c)^{1/3} (\nu/\nu_a)^2 & for \quad \nu < \nu_a \\ (\nu/\nu_c)^{1/3} & for \quad \nu_a \le \nu < \nu_c \\ (\nu/\nu_c)^{-1/2} & for \quad \nu_c \le \nu < \nu_m \\ (\nu_m/\nu_c)^{-1/2} (\nu/\nu_m)^{-p/2} & for \quad \nu_m \le \nu < \nu_M \end{cases} \tag{1.46}$$

   where ν_M is the frequency computed from γ_M,

$$F_{\nu,max} = N_e \frac{P_{\nu,max}}{4\pi D^2} \tag{1.47}$$

   N_e the total number of swept-up electrons in the post-shock fluid and D the distance of the source to the observer.

2. $\gamma_c > \gamma_m$: Only those electrons with $\gamma_e > \gamma_c$ can cool. This is known as the slow cooling phase, and the electrons with $\gamma_e \sim \gamma_m$ form the bulk of the population. The

flux is now given by

$$F_\nu = F_{\nu,max}\begin{cases}(\nu_a/\nu_m)^{1/3}(\nu/\nu_a)^2 & for \quad \nu<\nu_a \\ (\nu/\nu_m)^{1/3} & for \quad \nu_a\le\nu<\nu_m \\ (\nu/\nu_m)^{-(p-1)/2} & for \quad \nu_m\le\nu<\nu_c \\ (\nu_c/\nu_m)^{-(p-1)/2}(\nu/\nu_c)^{-p/2} & for \quad \nu_c\le\nu<\nu_M\end{cases} \tag{1.48}$$

In the evolution, the outflow goes for initially fast to slow cooling. Fast cooling must take place during the GRB prompt emission. If not, there would be an inefficiency problem. Moreover, if the cooling time were too long the variability would be suppressed. The transition from fast to slow cooling is expected to take place during the early stages of the external shock, in the late prompt or early afterglow phase.

The light curves at a given frequency ν can be computed by considering the time t_0 of the transition between the fast and slow cooling regimes. Since at sufficiently early times $\nu_c<\nu_m$ (fast cooling) while at later times $\nu_c>\nu_m$ (slow cooling), there is a transition when $\nu_c=\nu_m$ at a time t_0

$$t_0 = \begin{cases}210\epsilon_B^2\epsilon_e^2E_{52}n_1 & days \quad adiabatic \\ 4.6\epsilon_B^{7/5}\epsilon_e^{7/5}E_{52}^{4/5}\gamma_2^{-4/5}n_1^{3/5} & days \quad radiative\end{cases} \tag{1.49}$$

Therefore, the corresponding $\nu_0=\nu_c(t_0)=\nu_m(t_0)$ is

$$\nu_0 = \begin{cases}1.8\times10^{11}\epsilon_B^{-5/2}\epsilon_e^{-1}E_{52}^{-1}n_1^{-3/3} & \text{Hz} \quad adiabatic \\ 8.5\times10^{12}\epsilon_B^{-19/20}\epsilon_e^{-2/5}E_{52}^{-4/5}n_1^{-11/10}\gamma_2^{4/5} & \text{Hz} \quad radiative\end{cases} \tag{1.50}$$

Ignoring synchrotron self-absorption, there are two cases to consider as well:

1. $\nu>\nu_0$: This is the *high frequency* case. Areas labelled by B, C, and D of Fig. **ref** correspond to the fast cooling case, while H is now in the slow cooling case.

2. $\nu<\nu_0$: This is the *low frequency* case. Areas labelled by C, D, and H of Fig. **ref** correspond to the slow cooling case, while B still remain in the fast cooling case.

In addition, if $\epsilon_e \longrightarrow 1$ the hydrodynamic evolution changes at this stage from adiabatic to radiative, while if $\epsilon_e << 1$ the evolution stays adiabatic.

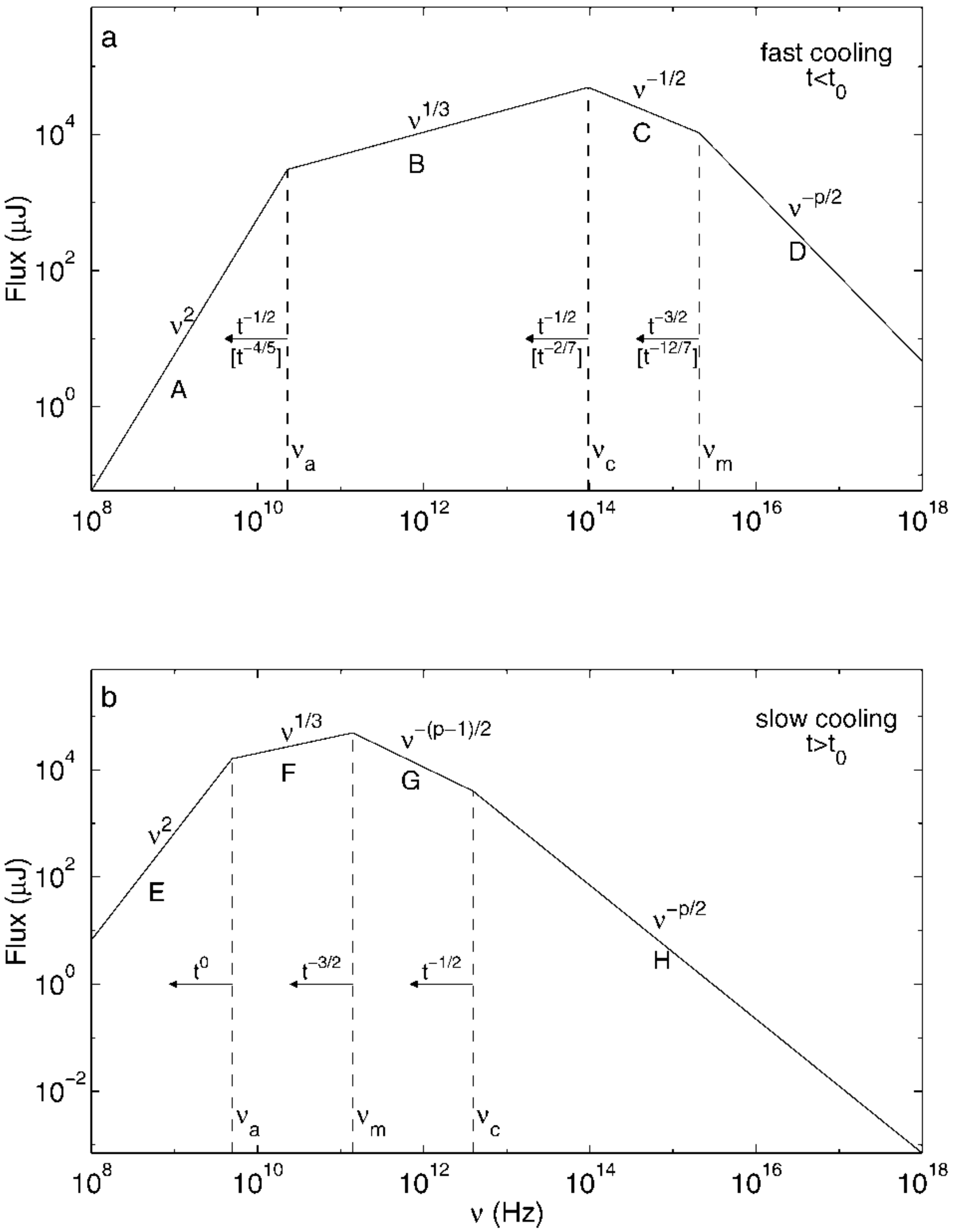

Figure 1.5: Synchrotron spectrum of a relativistic shock with a power-law electron distribution. (a) Fast cooling, which is expected at early times. The spectrum consists of four segments, identified t as A, B, C, and D. Self-absorption is important below ν_a. The frequencies, ν_m, ν_c, and ν_a, decrease with time as indicated; the scalings above the arrows correspond to an adiabatic evolution, and the scalings below, in square brackets, correspond to a fully radiative evolution. (b) Slow cooling, which is expected at late times. The evolution is always adiabatic. The four segments are identified as E, F, G, and H. Adapted from Sari *et al.* (1998).

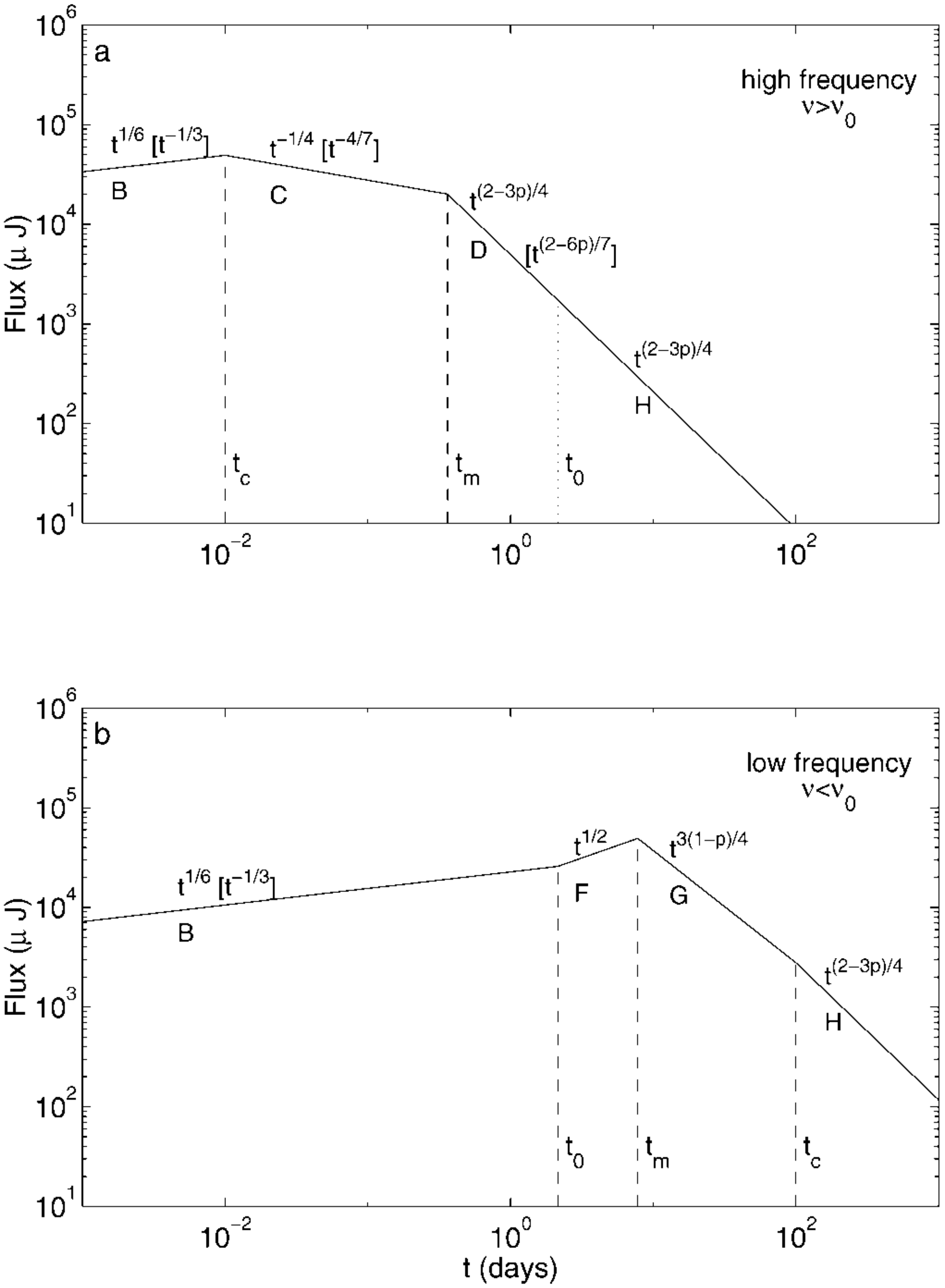

Figure 1.6: Synchrotron light curve (ignoring self-absorption). (a) High frequency case. The four segments that are separated by the critical times t_c, t_m, and t_0, correspond to the spectral segments in Fig. 1.5 with the same labels (B, C, D, and H). The observed flux varies with time as indicated; the scalings within square brackets are for radiative evolution (which is restricted to $t < t_0$), and the other scalings are for adiabatic evolution. (b) Low-frequency case. Adapted from Sari *et al.* (1998).

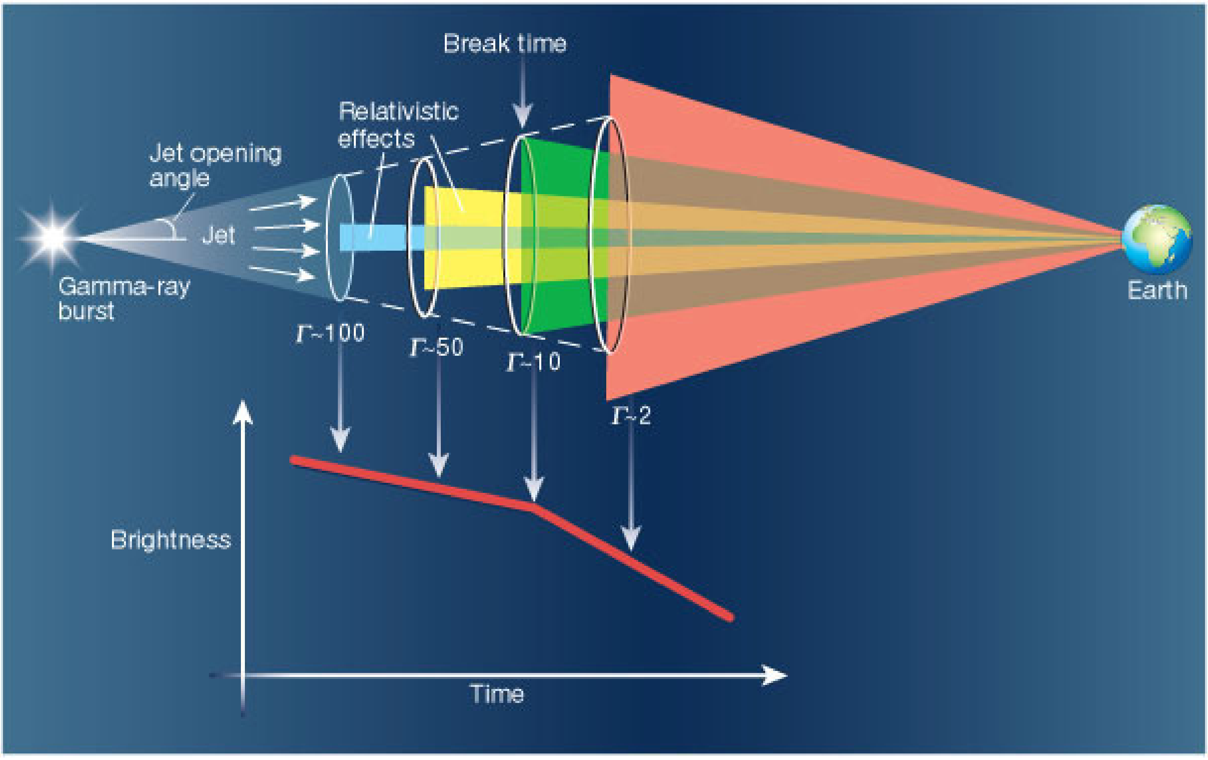

Figure 1.7: The burst launches a jet of material that moves at nearly the speed of light. Because of the effects of special relativity, an observer on Earth can initially only see a tiny fraction of that jet (light blue). As time passes and the jet runs into the surrounding material it slows down, and an observer on Earth can see more of the jet (yellow). Eventually, at the so-called break time, the entire jet becomes visible (green). Beyond this point, no new matter becomes visible and the brightness of the afterglow declines more quickly.

1.2.6 Ingredients for more realistic afterglow models

The approximations in the standard afterglow model imply simplifications which are not valid in the real conditions of most GRBs, so it is interesting consider more complex scenarios. Some possibilities are:

- The beaming of the outflow
- The impact of the reverse chock crossing the ejecta
- Inhomogeneous external mediums
- The departure from a simple energy injection

1.2.6.1 The beaming of the outflow

The extreme isotropic equivalent energies suggest that GRBs radiate into a narrow jet. A more direct evidence comes from long-term radio observations: Several months since the GRB the afterglow becomes sub-relativistic and radiates isotropically at radio wavelengths. this allows to measure the total kinetic energy of the ejecta (Frail *et al.*, 2000; Waxman *et al.*, 1998).

An additional indirect evidence is provided by the achromatic breaks seen in afterglow light-curves (see Fig. 1.7). In the uniform or 'top hat' jet the initial energy per solid angle ϵ and Γ are uniform within the half opening angle θ_j and sharply drop outside. Due to a relativistic effect, the radiation from a blob of Γ is beamed within an angle of Γ^{-1}. During the deceleration phase Γ decreases until Γ^{-1} reaches θ_j, moment at which the hydrodynamical evolution of the jet changes.

Another interesting model is the two component jet (**refs**). This model includes a narrow uniform jet of initial $\Gamma_0 > 100$ surrounded by a wider uniform jet with $\Gamma_0 \sim 10-30$. Motivation for such structure was found in the context of the cocoon in the collapsar model (Ramirez-Ruiz *et al.*, 2002) as well as in the context of a hydro-magnetically driven jet originated in the collapse of a massive star (Vlahakis *et al.*, 2003).

1.2.6.2 The impact of the reverse chock crossing the ejecta

In the standard afterglow model, the reverse shock is predicted to produce a strong optical flash and a radio flare (Mészáros & Rees, 1997; Sari & Piran, 1999; Sari *et al.*, 1999). The reverse shock heats up shell's matter, accelerates electrons and emits a single burst. After the peak of the reverse shock no new electrons are injected and the shocked material cools adiabatically. There are two limiting cases:

- If the shell density is high, the reverse shock is Newtonian and too weak to slow down the material.

- If the shell density is low, the reverse shock is relativistic and considerably decelerates the propagation.

This picture can be modified, allowing a long-lived reverse shock, if the central engine emits slowly moving material (Genet *et al.*, 2007).

1.2.6.3 Inhomogeneous external media

The shape of the spectrum will be unaffected by the choice of density profile but it will affect the evolution of spectral breaks and therefore that of light curves. For a general density profile of the circumburst medium $n(r) \propto r^{-k}$ it can be shown that $r \propto \Gamma^{-2/(3-k)}$ (see for example Chevalier & Li, 2000, Eqn. 1). For an impulsive one-time release of energy E constant and therefore

$$\Gamma \propto r^{-(3-k)/2} \tag{1.51}$$

$$t_{\oplus} \propto r/\Gamma^2 \tag{1.52}$$

where $t_{\oplus}$ is the time in the observer's frame.

Following the treatment similar to the standard fireball model, radiation is generated by the shock heated electrons which have Lorentz factor distribution $N(\gamma_e) \propto {\gamma_e}^{-p}$. The minimum Lorentz factor, γ_m, of such a distribution could be estimated by using two conservation laws:

1. Conservation of energy and
2. conservation of the total number of particles

which gives us $\gamma_m \propto \Gamma$. Similarly following standard treatment of cooling electrons the high energy cut-off of the distribution could be shown to be $\gamma_c \propto (\Gamma\ B_{co}\ t_{\oplus})^{-1}$ where B_{co} is the comoving magnetic field behind the shock wave. Corresponding break frequencies ν_m and ν_c, for the lower and higher energy cut-offs of the electron distribution, respectively would be:

$$\nu_{m\oplus} \propto \Gamma \times (\gamma_m^2\ B_{co}) \tag{1.53}$$

$$\nu_{c\oplus} \propto \Gamma \times (\gamma_c^2\ B_{co}) \tag{1.54}$$

where the co-moving break frequencies have been Doppler boosted by the multiplicative factor Γ - the bulk Lorentz factor of the shock wave.

From Eqn. 25 of Wijers & Galama (1999), spectral peak would be given by:

$$F_{\nu_m} \propto \Gamma \times (N_e P_{\nu_m}) \tag{1.55}$$

where $P_{\nu_m} \propto B_{co}$ is the power emitted by each electron and N_e is the total number of radiating electrons. For the given density profile $N_e \propto r^{3-k}$.

Temporal evolution of the spectral breaks could then be obtained:

$$\begin{aligned}
\nu_{m_\oplus} &\propto t_\oplus^{-3/2} && (1.56)\\
\nu_{c_\oplus} &\propto t_\oplus^{-\frac{4-3k}{2(4-k)}} && (1.57)\\
F_{\nu_m} &\propto t_\oplus^{-\frac{k}{2(4-k)}} && (1.58)
\end{aligned}$$

We assume that the spectral shape as given by Sari *et al.* (1998) will be unaffected by the choice of density profile. Then in the optically thin regime and for the typical afterglow parameters

$$\begin{aligned}
F_\nu &= F_{\nu_m}\left(\frac{\nu}{\nu_m}\right)^{-(p-1)/2} && \nu_m \ll \nu \ll \nu_c && (1.59)\\
F_\nu &= F_{\nu_m}\left(\frac{\nu_c}{\nu_m}\right)^{-(p-1)/2}\left(\frac{\nu}{\nu_c}\right)^{-p/2} && \nu \gg \nu_c && (1.60)
\end{aligned}$$

Substituting for the time dependence of break frequencies from Eqn. 1.58 in Eqn. 1.60, we get

$$\begin{aligned}
F_\nu(\nu, t_\oplus) &\propto \nu^{-(p-1)/2} \times t_\oplus^{-\frac{1}{4}(3p-3+\frac{2k}{4-k})} && \nu_m \ll \nu \ll \nu_c && (1.61)\\
F_\nu(\nu, t_\oplus) &\propto \nu^{-p/2} \times t_\oplus^{-(3p-2)/4} && \nu \gg \nu_c && (1.62)
\end{aligned}$$

It is to be noted that Eqn. 1.62 is independent of k and, therefore, the light curve decay in the spectral regime $\nu_m \ll \nu \ll \nu_c$, which is appropriate for the typical X-ray afterglows, does not depend on the density profile of the circus-burst medium.

1.2.6.4 The departure from a simple energy injection

More physically realistic is the situation where the ejecta has a range of bulk Lorentz factors with larger amounts of mass and energy having lower Γ. The outer shock and contact discontinuity decelerates as the fireball sweeps up external matter. This deceleration allows slower ejecta to catch up with the forward shock, replenishing and re-energizing it, and leading to additional dissipation in the reverse shock (Rees & Mészáros, 1998).

Chapter 2

GRB 110715A

Adapted from "GRB 110715A: The peculiar multiwavelength evolution of the first afterglow detected by ALMA"

— Sánchez-Ramírez et al., *MNRAS, Submitted*

In this Chapter I present the extensive follow-up campaign on GRB 110715A afterglow at 17 different wavelengths, from X-ray to radio bands, starting 81 seconds after the burst and extending up to 74 days later. We performed for the first time a GRB afterglow observation with the ALMA observatory. We find that the afterglow of GRB 110715A is particularly bright at optical and radio wavelengths. We use optical and near infrared spectroscopy to provide further information about the progenitor's environment and its host galaxy. The spectrum shows weak absorption features at a redshift $z = 0.8224$, which reveal a host galaxy environment with low ionization, column density and dynamical activity. Late deep imaging shows a very faint galaxy, consistent with the spectroscopic results. The broadband afterglow emission is modelled with synchrotron radiation using a numerical algorithm and we determine the best fit parameters using Bayesian inference in order to constrain the physical parameters of the jet and the medium in which the relativistic shock propagates. We fitted our data with a variety of models, including different density profiles and energy injections. Although the general behavior can be roughly described by these models, none of them are able to fully explain all data points simultaneously. GRB 110715A shows the complexity of reproducing extensive multi-wavelength broadband afterglow observations, as well as the need of good sampling in wavelength and time, and more complex models to accurately constrain the physics of GRB afterglows.

2.1 Observations

2.1.1 Gamma-ray emission

The *Swift* (Gehrels *et al.*, 2004) Burst Alert Telescope (BAT, Barthelmy *et al.*, 2005) triggered and located GRB 110715A on 15 July 2011 at T_0= 13:13:50 UT (Sonbas *et al.*, 2011). The gamma-ray light curve shows a double-peaked structure with a duration of T_{90}= 13.0 ± 4.0 s (90% confidence level) in the observer frame. Therefore we classify GRB 110715A as a long burst.

Analysis of the time-averaged spectrum gave the best fit as a power law with an exponential cutoff with the following parameters: $\Gamma_\gamma = 1.25 \pm 0.12$, S (15-150 keV) $=(1.18 \pm 0.02) \times 10^{-5}$ erg cm^{-2}, and $E_{\rm peak} = 120 \pm 21$ keV (90% confidence level, Sonbas *et al.*, 2011). GRB 110715A was also detected by *INTEGRAL*/SPI-ACS, Konus-*Wind* and *Suzaku*/WAM (see more details in Sonbas *et al.*, 2011).

2.1.2 X-ray afterglow observations

The X-Ray Telescope (XRT; Burrows *et al.*, 2005) onboard *Swift* began observing the field 90.9 seconds after the BAT trigger, localizing the X-ray afterglow at RA(J2000) = $15h\ 50m\ 44.00s$, Dec.(J2000) = $-46^\circ 14'\ 07''\!.5$ with an uncertainty of $1''\!.4$ (90% confidence level; Evans *et al.*, 2011).

The afterglow light curve used in this paper has been extracted from the Burst Analyzer [1] (Evans *et al.*, 2010), using the spectral slope to derive the flux densities at an energy of 2 keV. These observations are shown in Figure 2.1 and tabulated in Table A.1.

2.1.3 UV/Optical/NIR afterglow observations

GRB 110715A was followed-up in UV/Optical/NIR wavelengths with *Swift* (+UVOT) and the 2.2m MPG telescope (+GROND). Light curves are shown in Figure 2.1 and tabulated in Table A.1 as well.

This burst had a very bright optical counterpart in spite of the high Galactic extinction caused by its location close to the Galactic plane (Evans *et al.*, 2011). The GRB afterglow study was affected by the Galactic reddening, initially estimated to be $E(B-V) = 0.59$ mag according to the dust maps of Schlegel *et al.* (1998), and later $E(B-V) = 0.52$ mag

---

[1] `http://www.swift.ac.uk/burst_analyser`

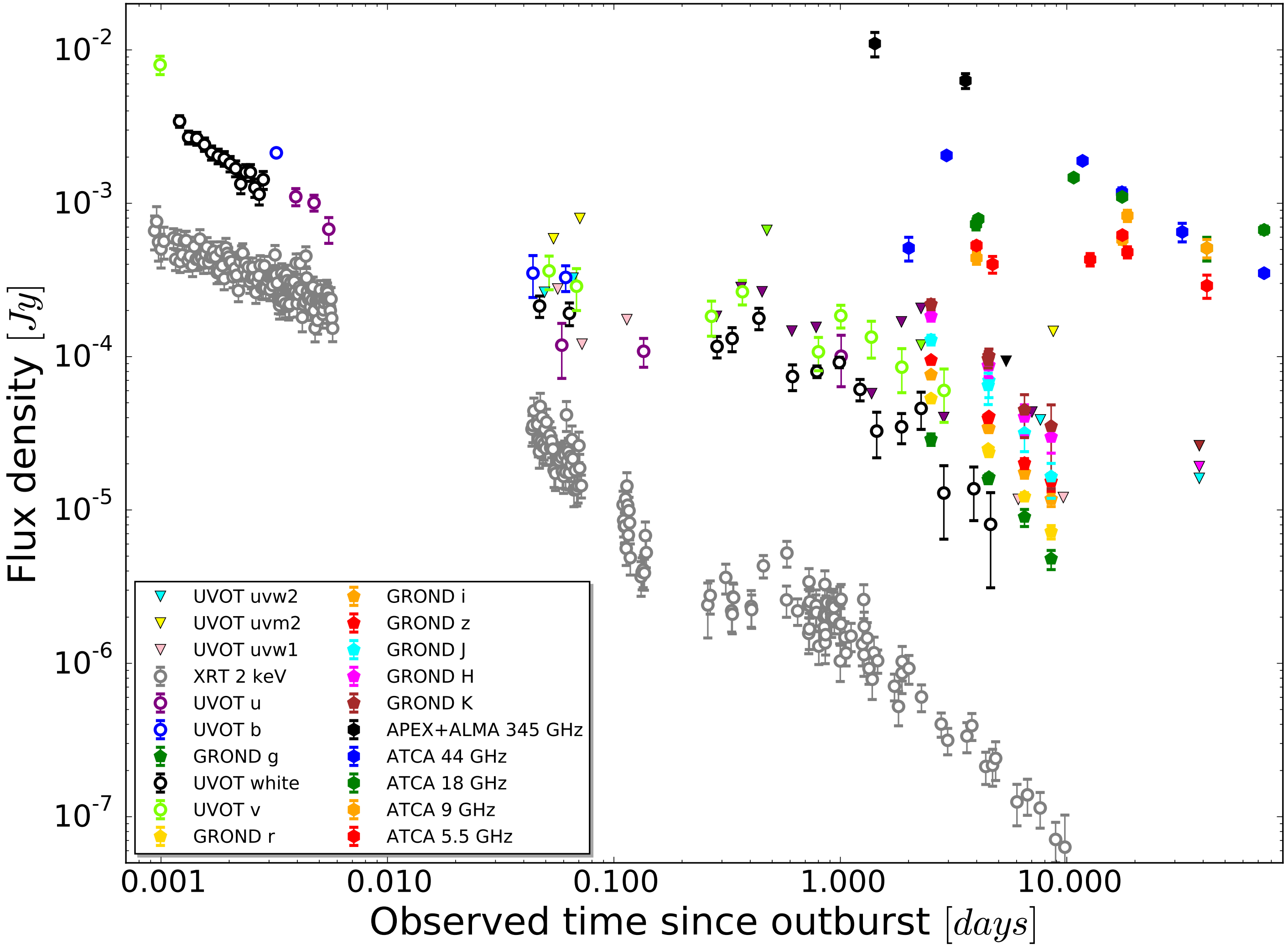

Figure 2.1: Afterglow light curve of the 17 bands observed. Upper limits are denoted by down-pointing triangles.

Table 2.1: Effective wavelengths and extinction coefficients.

Band	λ_{eff} [μm]	A$_\lambda$ $^{(a)}$
XRT 2 keV	0.620×10^{-3}	0.000
UVOT uvw2	0.193	4.099
UVOT uvm2	0.225	4.582
UVOT uvw1	0.260	3.623
UVOT u	0.351	2.587
UVOT b	0.441	2.021
GROND g'	0.459	2.018
UVOT *white*	0.483	2.566
UVOT v	0.545	1.628
GROND r'	0.622	1.393
GROND i'	0.764	1.042
FORS2 Ic	0.786	0.949
GROND z'	0.899	0.775
GROND J	1.239	0.455
GROND H	1.646	0.291
GROND K	2.170	0.187
APEX/ALMA 345 GHz	8.70×10^2	0.000
ATCA 44 GHz	6.81×10^3	0.000
ATCA 18 GHz	1.66×10^4	0.000
ATCA 9 GHz	3.33×10^4	0.000
ATCA 5.5 GHz	5.45×10^4	0.000

(a) $E(B-V) = 0.52$ mag (Schlafly & Finkbeiner, 2011) following Schlafly & Finkbeiner (2011). We adopted the latest value. Computed effective wavelengths and extinction for each band are presented in Table 2.1.

2.1.3.1 UVOT imaging

The *Swift* Ultra-Violet/Optical Telescope (UVOT; Roming *et al.*, 2005) began settled observations of the field of GRB 110715A 100s after the trigger (Breeveld *et al.*, 2011). The afterglow was detected in the *white*, u, b and v filters at RA(J2000) = 15h 50m 44.09s, Dec.(J2000) = -46°14′ 06.″5, with a 2σ uncertainty of about 0.″62. For this analysis, we have reduced both image and event mode data grouped with binning $\Delta t/t \sim 0.2$. Before the count rates were extracted from the event lists, the astrometry was refined following the methodology in Oates *et al.* (2009). The photometry was then extracted from the event lists and image files based on the FTOOLs *uvotevtlc* and *uvotmaghist*, respectively, using a source aperture centered on the optical position and a background region located in a source-free zone. We used a 3" source aperture to avoid contamination from neighbouring stars and applied aperture corrections to the photometry in order to be compatible with the UVOT calibration (Breeveld *et al.*, 2011). The analysis pipeline used software HEADAS 6.10 and UVOT calibration 20111031.

2.1.3.2 GROND imaging

We obtained follow-up observations of the optical/NIR afterglow of GRB 110715A with the seven-channel imager GROND (Gamma-ray burst optical/near-infrared detector; Greiner *et al.*, 2008) mounted on the 2.2m MPG@ESO telescope stationed in La Silla, Chile. The first observations were obtained 2.5 days after the trigger, after losing the first two nights due to weather. This first epoch suffers from very bad seeing, 1.″5 – 1.″9 depending on the band, but the optical/NIR afterglow was clearly detected (Updike *et al.*, 2011). Deeper follow-up under better conditions in three further epochs reveals a faint nearby source which exhibits a stellar PSF. The presence of this source was carefully accounted for during the data analysis. The GROND optical and NIR image reduction and photometry were performed by calling on standard IRAF tasks (Tody, 1993) using the custom GROND pipeline (Yoldaş *et al.*, 2008), similar to the procedure described in Krühler *et al.* (2008). Hereby, we used SExtractor (Bertin & Arnouts, 1996) for background modeling, and bright sources were masked out, which yields improved results in the case of this crowded field. A late epoch was obtained 38 days after the GRB which was supposed to be used for image subtraction purposes, but a positioning error led to the afterglow position being covered only in the NIR frames.

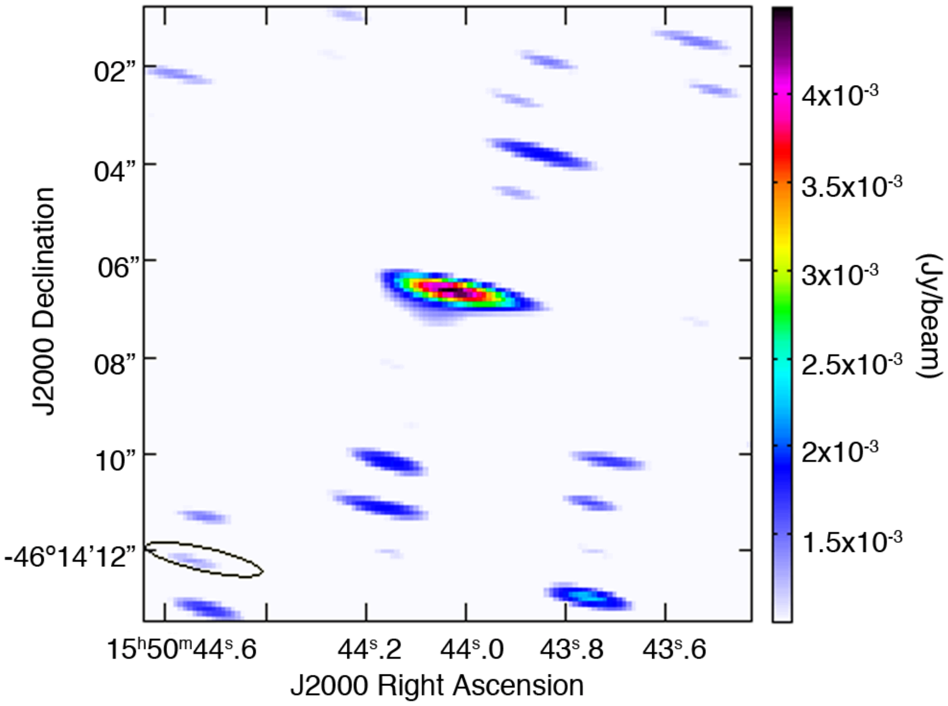

Figure 2.2: ALMA image at 345 GHz. The beam size ($0''.3 \times 0''.1$, P.A.=76 degrees) is showed in the lower left corner.

Afterglow magnitudes in the optical were measured against comparison stars calibrated to the SDSS catalogue (Aihara *et al.*, 2011), obtained from observing an SDSS field at similar airmass immediately after the fourth epoch, in photometric conditions. NIR magnitudes were measured against on-chip comparison stars taken from the 2MASS catalogue (Skrutskie *et al.*, 2006). The results of the photometry are displayed in Table A.1.

2.1.4 Submm afterglow observations

The Atacama pathfinder experiment telescope (APEX) observations began on July 16, 1.42 days after the burst and were performed in the 345 GHz band using the photometric mode of the Large Apex BOlometer CAmera (LABOCA; Siringo *et al.*, 2009) under good weather conditions. Data reduction was done using the BoA, CRUSH and miniCRUSH (Kovács, 2008) software packages. Using these observations we discovered a bright submm counterpart at 10.4 ± 2.4 mJy (de Ugarte Postigo *et al.*, 2011).

As a test of the target of opportunity programme, GRB 110715A was also observed with the Atacama Large Millimeter Array (ALMA), yielding a detection with a flux density of 4.9 ± 0.6 mJy at 345 GHz (de Ugarte Postigo *et al.*, 2012b). The ALMA observations began on July 19 at 02:50 UT (3.57 days after the burst), and they were

Table 2.2: X-shooter observations log.

Mean T-T_0 (hr)	Arm	Exp. time (s)	Slit width (")	Resolution $^{(a)}$
12.60	UVB	618.02	1.0	4350
12.60	VIS	612.04	0.9	7450
12.60	NIR	600.00	0.9 $^{(b)}$	5300

(a) Nominal values. (b) K-band blocker was not used.

carried out making use of only 7 antennas during 25 mins on source. We present the data in Figure 2.2.

In spite of being obtained during a test observation, with almost an order of magnitude fewer antennas than are available with the full observatory, this was the deepest observation carried out to date at 345 GHz of a GRB afterglow (de Ugarte Postigo *et al.*, 2012b). The ALMA observation also provides the most accurate coordinates available for this GRB. The centroid of the afterglow is located at RA(J2000) = $15h$ $50m$ $44.05s$ and Dec.(J2000) = -46°14′ 06.″5 with a synthesized beam size of 0.″3 × 0.″1 at a position angle of 76 degrees.

2.1.5 Radio afterglow observations

Following the detection of an afterglow at submm wavelengths with APEX (de Ugarte Postigo *et al.*, 2011), radio observations were obtained with the Australia Telescope Compact Array (Wilson *et al.*, 2011, ATCA) two and three days after the trigger. These observations resulted in further detections of the afterglow at 44 GHz (Hancock *et al.*, 2011). This GRB was monitored at 44, 18, 9, and 5 GHz for up to 75 days post-burst, where the flux remained at a sub-mJy level. The lower frequency observations were complicated by the presence of a second source within the field of view (MGPS J155058-461105). The data were reduced using standard procedures in MIRIAD (Sault *et al.*, 1995). An additional late-time visit was performed on 12 Aug 2013 at 5.5 GHz and 9 GHz, to understand the possible contribution of the host galaxy, which was found to be negligible at both bands. The flux evolution of the afterglow at the four ATCA frequencies is also shown in Figure 2.1 and tabulated in Table A.1, together with the rest of the observing bands.

2.1.6 Optical/nIR afterglow spectra

X-shooter (Vernet *et al.*, 2011), an optical/nIR intermediate resolution spectrograph mounted at the Very Large Telescope (VLT) Unit Telescope (UT) 2 in Paranal Obser-

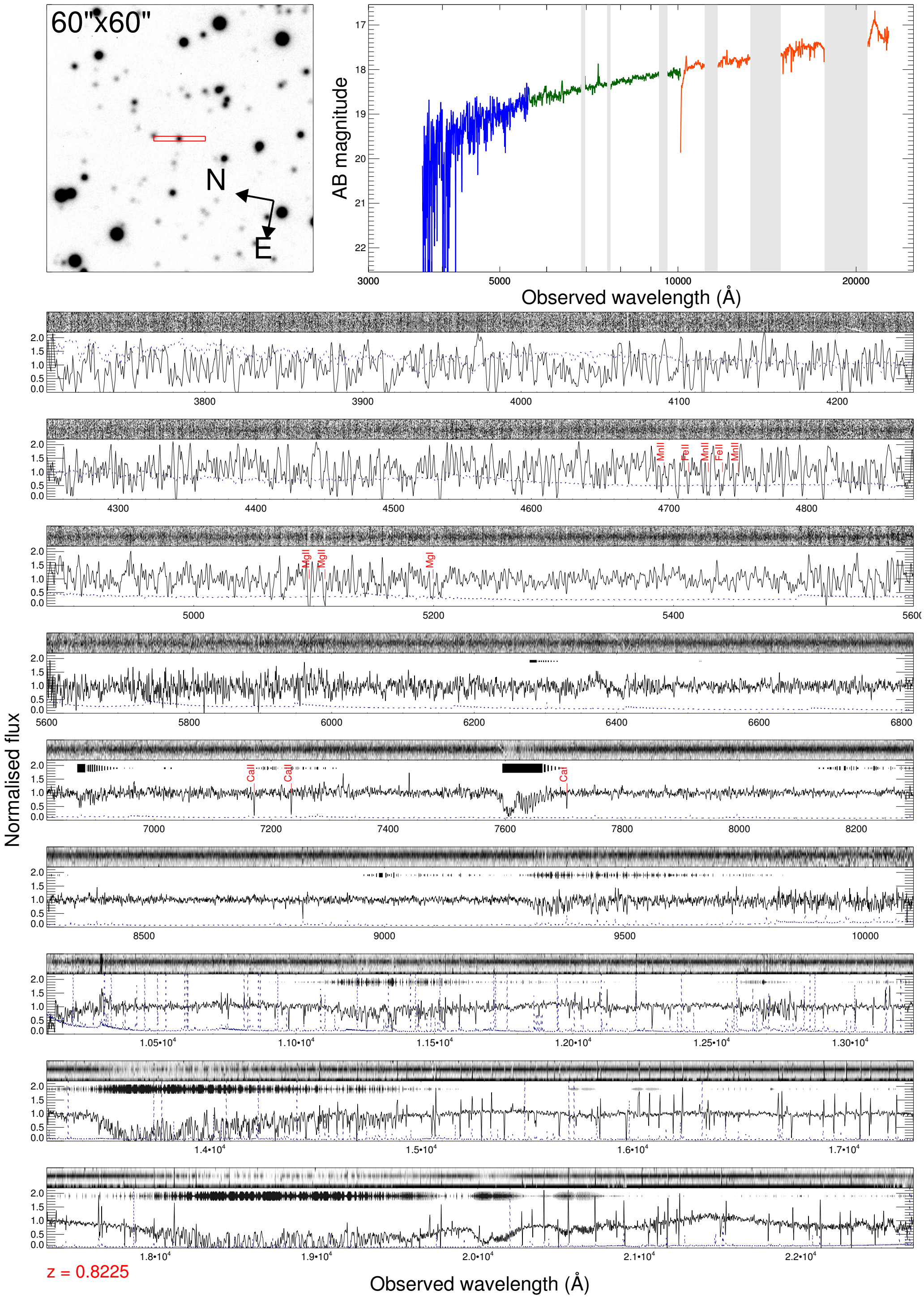

Figure 2.3: X-shooter spectra. Upper panels are the finding chart (left) and an overview of the complete flux calibrated spectra, corrected for Galactic extinction (right). In the bottom plot, we show the normalised spectra, with 3 panels per arm, starting at top with UVB and followed by VIS and NIR. Each panel includes the 2D image and 1D signal and error spectrum. Telluric absorptions are indicated by black bands above the 1D spectrum, their thickness is a measure of the absorption strength.

vatory (Chile), was used to observe the GRB afterglow starting 12.7 hrs after the *Swift* trigger. The seeing was $0\farcs9$, but observations had to be interrupted due to wind constraints (Piranomonte *et al.*, 2011). The observing log is shown in Table 2.2. We processed the spectra using version 2.0.0 of the X-shooter data reduction pipeline (Goldoni *et al.*, 2006; Modigliani *et al.*, 2010). As the observations were stopped after one exposure, the standard nodding reduction could not be performed. We thus reduced the single frames of each arm with the following steps: We performed bias subtraction, cosmic ray detection and subtraction (van Dokkum, 2001), and flat field correction on the raw frames. From these processed frames the sky emission was subtracted using the Kelson (2003) method and 1D spectra were extracted directly order by order from the sky-subtracted and flat-field divided frame using optimal extraction (Horne, 1986). The resulting spectra were merged weighting them by the errors and the final merged spectra were then averaged in IDL. The spectra were flux calibrated using observations of the standard star LTT7987 taken the same night. The complete X-shooter spectrum is shown in Fig. 2.3.

2.1.7 Host galaxy imaging

606 days after the burst, the field of GRB 110715A was revisited using GROND searching for a possible host galaxy contribution. However, the data did not reveal any underlying source. We therefore derive only detection limits.

A deeper exposure was obtained on August 2013 with FORS2 at ESO's VLT, 751 days after the burst. The observation consisted of 10 × 240 s in I_C-band, with a seeing of $0\farcs55$, and data were reduced in a similar fashion as the GROND imaging. An object is detected close to the afterglow position at a magnitude of 26.40 ± 0.36 mag.

2.2 Results and discussion

2.2.1 The afterglow of GRB 110715A in a global context

Using the UVOT and GROND data, and adding the early R_C band observations from Nelson (2011), we construct a composite light curve by shifting all data to the R_C band (no evidence for chromatic evolution is found). This light curve extends over almost four decades in time. Comparing it to the sample of long GRB afterglow light curves taken from Kann *et al.* (2006, 2010, 2011), we find that (after correcting for the significant – 1.6 magnitudes – foreground extinction) the afterglow is among the brightest ever detected (especially after ~ 0.3 days, see Fig. 2.5 left panel), comparable to those of GRB 991208

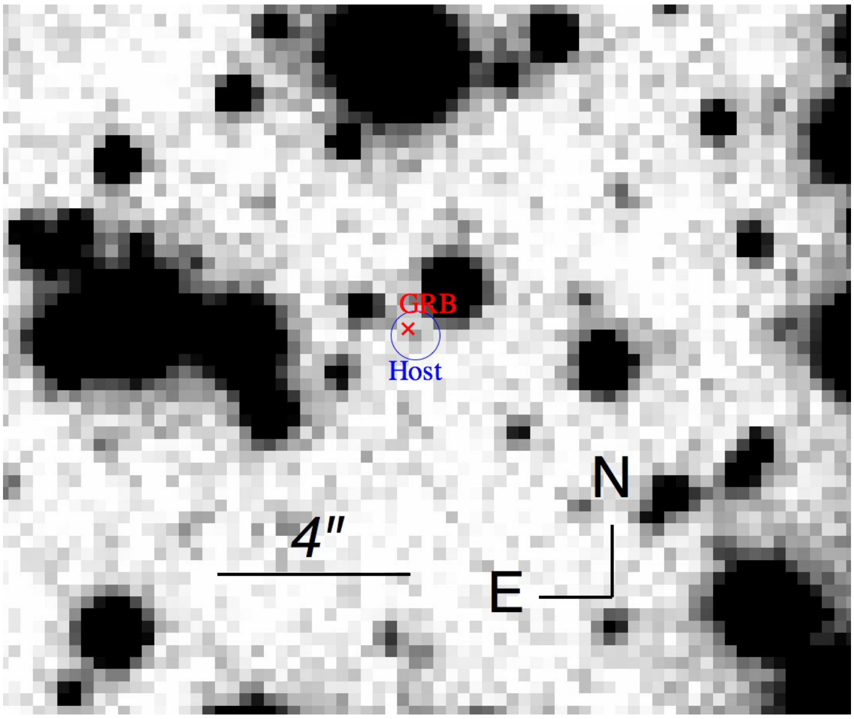

Figure 2.4: Observation of the host galaxy in the I_C-band from VLT/FORS2.

(Castro-Tirado *et al.*, 2001) and GRB 060729 (Cano *et al.*, 2011), both at lower redshift (see section 2.2.2). It becomes fainter than 20th magnitude only after about 4.5 days. Using the GROND data, we find a best fit for the Spectral Energy Distribution (SED) of the afterglow with $\beta = 0.90 \pm 0.22$, and a small (essentially zero) $A_V = 0.09 \pm 0.18$ using SMC dust. With these data and knowledge of the redshift, we use the method of Kann *et al.* (2006) to shift the afterglow, corrected for all extinction, to $z = 1$. We find a magnitude shift of $dRc = +0.38^{+0.17}_{-0.32}$. At one day after the trigger (in the $z = 1$ frame), it is $R_C = 17.97^{+0.19}_{-0.33}$, and $R_C = 13.90^{+0.23}_{-0.35}$ at 0.001 days. This places the afterglow into the tight peak found by Kann *et al.* (2010) (their figure 6), which is formed by afterglows which are likely forward-shock dominated at early times already. This does not mean that a reverse shock component is not present. According to Kann *et al.* (2010), the early afterglow can be classified as “Limit + Slow Decay” (Kann *et al.*, 2010, their table 5). In this sense, except for the rebrightenings, the afterglow is seen to be typical.

In Figure 2.6, we compare the radio and submm emission of GRB 110715A to the samples of de Ugarte Postigo *et al.* (2012b) and Chandra & Frail (2012): in submm, the afterglow peak brightness is among the brightest observed, with similar luminosity as GRB 030329, GRB 100621A or GRB 100418A, but still an order of magnitude less luminous than the highest luminosity events (GRB 980329, GRB 090313, GRB 080129 or GRB 050904). The situation in radio is similar, with GRB 110715A being amongst the brightest events.

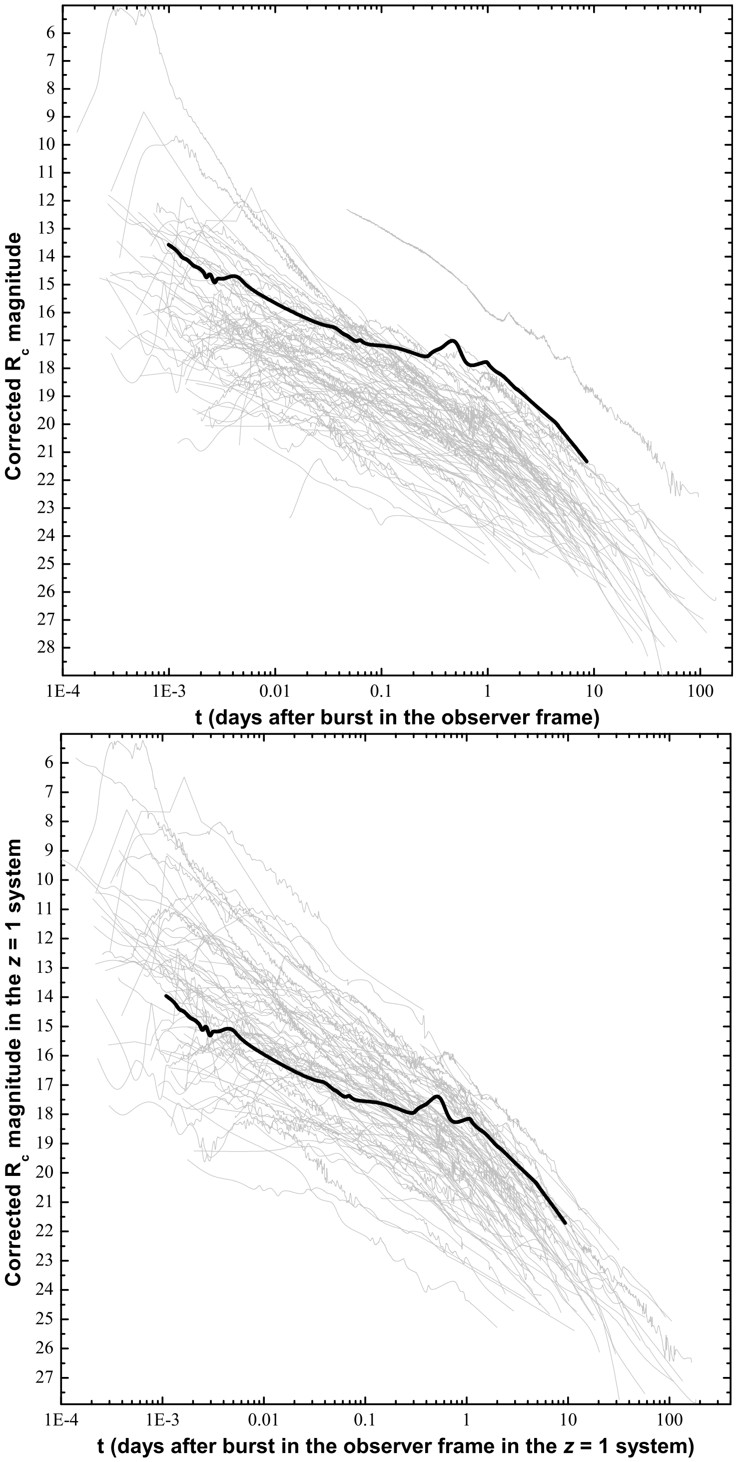

Figure 2.5: The observed R_C-band afterglow of GRB 110715A in comparison to a large sample of long GRB afterglows (left). After correction for the significant foreground extinction, it is seen to be one of the brightest afterglows ever observed. After correcting for rest-frame extinction and shifting to $z = 1$ (right), the afterglow of GRB 110715A is more common, although it remains among the more luminous detected to date at late times.

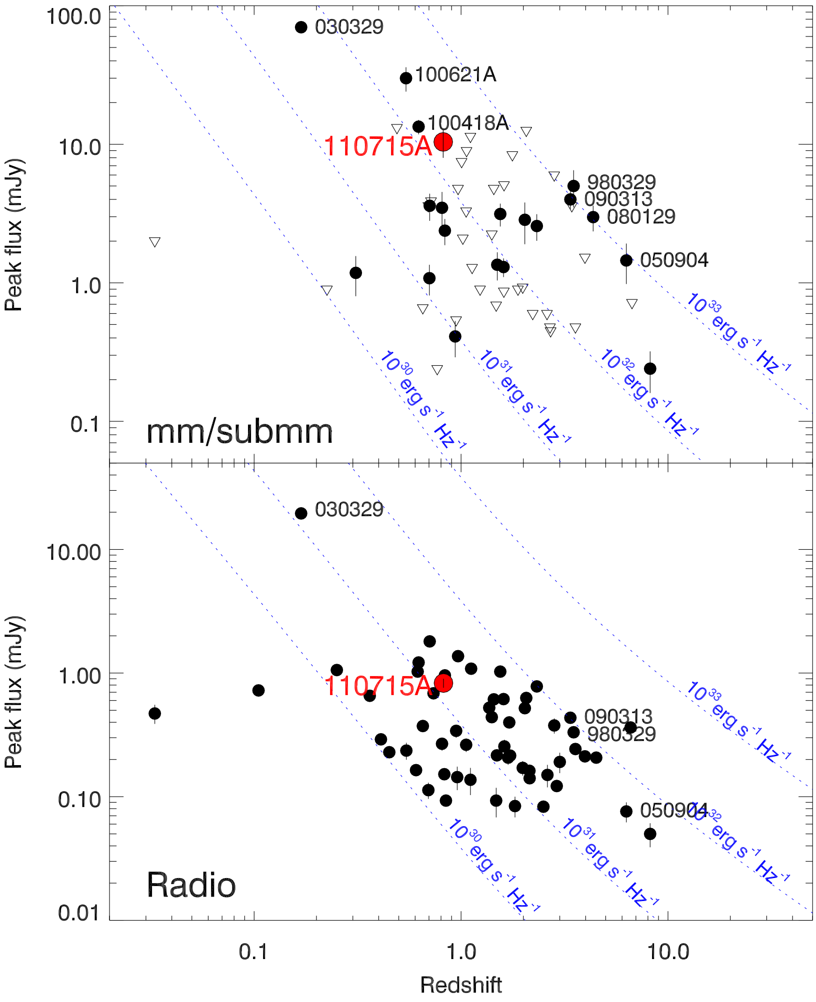

Figure 2.6: Top: mm/submm afterglow as compared with the sample of de Ugarte Postigo *et al.* (2012b). Bottom: Radio afterglow of GRB 110715A compared with the sample of Chandra & Frail (2012)

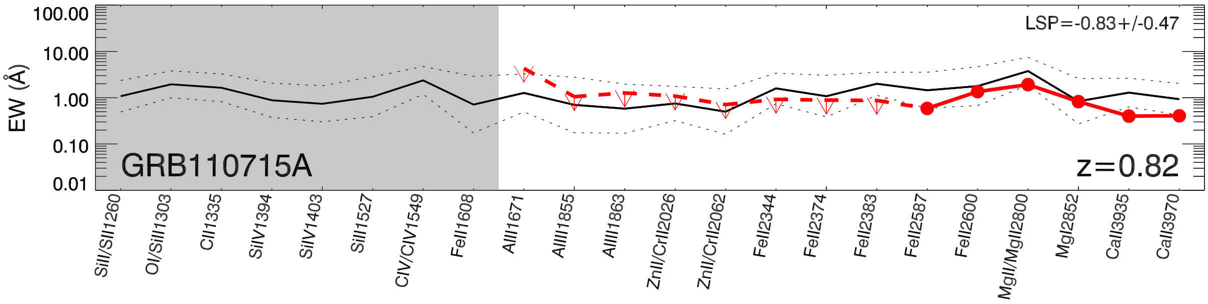

Figure 2.7: Line strength diagram of the afterglow spectrum of GRB 110715A, following the prescription of de Ugarte Postigo *et al.* (2012a).

2.2.2 Spectral absorption lines of the optical afterglow

We detect eight absorption features in the complete X-shooter spectrum that we identify as caused by Fe II, Mg II, Mg I, Ca II, and Ca I at a common redshift of 0.8224 ± 0.0001. For recent Planck cosmological parameters ($\Omega_{\rm M} = 0.315$, $\Omega_{\Lambda} = 0.685$, $H_0 = 67.3$ km s^{-1} Mpc^{-1}; Planck *et al.*, 2014), this redshift corresponds to a luminosity distance of 5357.86 Mpc.

We have measured the equivalent widths of these lines and limits for several others using the self-developed code used in Fynbo *et al.* (2009) and de Ugarte Postigo *et al.* (2012a). The results are shown in table 2.3, as well as the composite afterglow spectrum by Christensen *et al.* (2011) for comparison purposes. Using the prescriptions given by de Ugarte Postigo *et al.* (2012a), we find that the neutral element population is higher than average. Detection of Ca Iλ4227, a line rarely observed in GRB afterglows (de Ugarte Postigo *et al.*, 2012a), also supports the low ionisation hypothesis of the material in the line of sight to GRB 110715A.

Following the prescription of de Ugarte Postigo *et al.* (2012a), we obtain a line strength parameter for GRB 110715A of LSP = -0.83 ± 0.47, implying that this event is in the percentile 13.4 of line strengths, and indicating a lower than average column density of material in the line of sight (86.6% of GRBs have stronger lines). This often indicates a small host galaxy (de Ugarte Postigo *et al.*, 2012a). This is consistent with the fact that there are no velocity components in the absorption features faster than 30 km s^{-1}.

2.2.3 The host galaxy

We computed the distance between the afterglow and the host galaxy core. The centroid is offset by 0.21 ± 0.03 ″ with respect to the ALMA position, which at the redshift of GRB 110715A corresponds to 1.56 ± 0.19 kpc. This is comparable to the typical offset

Table 2.3: Features in the X-shooter spectra.

Feature	λ_{obs} [Å]	EW [Å]	EWc [Å] ^{a}
Al II λ1671	~3045	< 7.82	1.04 ± 0.02
Al III λ1855	~3380	< 1.92	0.89 ± 0.02
Al III λ1863	~3395	< 2.32	0.68 ± 0.02
Zn II λ2026+Cr II λ2026	~3692	< 1.97	0.60 ± 0.02
Cr II λ2062+Zn II λ2063	~3758	< 1.30	0.53 ± 0.02
Fe II λ2261	~4120	< 1.81	0.38 ± 0.02
Fe II λ2344	~4272	< 1.68	1.74 ± 0.02
Fe II λ2374	~4327	< 1.63	1.00 ± 0.02
Fe II λ2383	~4342	< 1.60	1.65 ± 0.02
Fe II λ2587	4714.04	1.07 ± 0.47	1.33 ± 0.02
Fe II λ2600	4737.32	2.47 ± 0.73	1.85 ± 0.03
Mg II λ2796	5096.44	1.99 ± 0.34	1.71 ± 0.02
Mg II λ2803	5109.09	1.50 ± 0.31	1.47 ± 0.02
Mg I λ2853	5198.29	1.50 ± 0.40	0.78 ± 0.01
Ca II λ3935	7171.01	0.72 ± 0.07	0.76 ± 0.02
Ca II λ3970	7234.51	0.74 ± 0.07	0.66 ± 0.02
Ca I λ4228	7705.26	0.37 ± 0.06	0.11 ± 0.02

(a) Equivalents widths measured on the composite GRB afterglow spectrum (Christensen *et al.*, 2011).

of 1.2 kpc seen for long GRBs (de Ugarte Postigo *et al.*, 2012a). The host absolute magnitude (AB) would be M = -18.2 mag at a restframe wavelength of 4200 Å, which is similar to the Johnson B-band (without needing to make assumptions on the host galaxy spectral index).

The luminosity of the host galaxy is low, even relative to other GRB hosts (which tend to occur in lower-mass and lower-luminosity galaxies than average at $z \lesssim 1.5$; e.g. Perley *et al.*, 2016a), although it is by no means extreme or exceptional. For example, relative to the UV luminosity distribution of nine galaxies at roughly similar redshift ($0.5 < z < 1.1$) in the TOUGH sample (Schulze *et al.*, 2015), this host galaxy is less luminous than six or more, depending on the unknown k-correction across the Balmer break which is not known for the TOUGH sample. We also compared this magnitude to synthetic B-band magnitudes of galaxies from the larger, multi-colour SHOALS sample (Perley *et al.*, 2016c, and work in prep.). The host of GRB is about 0.6 mag less luminous than the median B magnitude of $0.5 < z < 1.1$ galaxies in this sample, and is more luminous than only five out of these 21 galaxies. Compared to a more local galaxy population, it is slightly more luminous than the LMC ($M_B \sim -17.5$) but of course much less luminous than nearby spirals such as the Milky Way or M31 ($M_B \sim -20.5$ to -21). This faint host galaxy is consistent with the faint and unresolved absorption features seen in the afterglow spectrum. Considering also its very low ionisation environment, all evidence

Table 2.4: The lower and upper boundaries of the priors on parameters used in the analysis.

Parameter	Distribution	Lower	Upper
E_{iso} [10^{53} erg]	log-uniform	0.01	10000
Γ_0	log-uniform	10	2000
θ_0 [deg]	log-uniform	0.1	90
p	uniform	1.1	4.0
ϵ_i	log-uniform	0.0001	0.5
ϵ_e	log-uniform	0.0001	0.5
ϵ_B	log-uniform	0.0001	0.5
A_* [$5.015 \cdot 10^{11}$ cm^{-3}]	log-uniform	0.00001	100
n_0 [cm^{-3}]	log-uniform	0.0001	1000
t_{sh} [min]	log-uniform	0.00001	200
r_{sh}	uniform	1	50
t_1 [days]	log-uniform	0.0001	200
E_1/E_0	uniform	0	50
$A_{V,host}$ [mag]	uniform	0	1.0
$E(B-V)$ [mag]	Gaussian$^{(a)}$		

(a) $\mu = 0.56$, $\sigma = 0.04$

suggest that the sight-line towards GRB 110715A is probing an small dwarf host galaxy, maybe in its initial star-forming episode due to the low background ionising radiation, which keeps an unusual abundance of Ca I.

2.2.4 Modeling of the afterglow evolution

2.2.4.1 Model and fitting description

The afterglow emission was modeled with the numerical code of Jóhannesson *et al.* (2006). This software has been used successfully to model several different afterglows, including GRB 060121 (de Ugarte Postigo *et al.*, 2006), GRB 050408 (de Ugarte Postigo *et al.*, 2007), GRB 060526 (Thöne *et al.*, 2010), and GRB 050525A (Resmi *et al.*, 2012). This model assumes the emission originates in a forward shock only, with a top-hat jet configuration. The algorithm simulates that a slab of matter with mass M_0 is ejected with a Lorentz factor of Γ_0 into a cone with a half-opening angle of θ_0. The slab starts accumulating matter and slows down in the process. Energy injections (E_i) are modeled as slabs of matter moving at lower speeds than the forward shock ($\Gamma_i < \Gamma_0$) and catching up to it at later times. At the time of collision, the energy and momentum of the forward shock of the injected slab is instantaneously added to the already moving mass. The emission from any reverse shock formed in the collision is ignored. To calculate the emission, we assume that a fixed fraction of the energy of the forward shock is contained in the magnetic field and electron distribution of the forward shock. For the magnetic field, this fraction is denoted with ϵ_B. In Jóhannesson *et al.* (2006), the fraction of energy contained in the electrons was denoted with ϵ_e. This is now changed, to allow for the slope of the electron power-law distribution, p, to be less than 2. We used the formalism of Panaitescu & Kumar (2001) and denote with ϵ_i the fraction of energy contained in the electrons with the lowest energy in the distribution. The highest energy in the distribution is then limited such that the total energy of the electron distribution never exceeds a fraction ϵ_e of the forward shock energy.

To explain the data, we need a model that includes a temporary increase in flux around 0.3 days after the onset of the GRB that is observed in the light curves shown in Figure 2.1. We chose three different types of models that we expect have this behavior: a model with a constant density interstellar medium (n_0) and a single energy injection (CM), a model with a wind density external medium ($\rho = A_* r^{-2}$) and a single energy injection (WM), and a model with a wind termination shock (with fractional change in density at the shock front denoted by r_{sh}) but no energy injection (TS).

The best fit model parameters are found using Bayesian inference using the MultiNest tool (Feroz *et al.*, 2009). MultiNest is well suited for exploring the parameter space of the non-linear afterglow model and finds parameter correlation as well as all modes in the parameter space fitting the data similarly well. In addition to the afterglow model parameters, we also determine the host dust extinction in the fit, which we assume follows an SMC-like extinction curve. It is also possible to let the Galactic dust extinction vary as a nuisance parameter. This is of special interest in our case due to the large and uncertain value along the GRB line of sight through our Galaxy.

One of the main benefits of a Bayesian analysis is the introduction of prior distributions on parameters. For this analysis we have unfortunately very little prior knowledge on their values. We therefore opted for flat priors on all parameters, but Galactic reddening, and made sure the parameter limits were large enough so that the posterior is not affected by these limits unless they are physical (see Table 2.4). Examples of such physical boundaries are the requirements that the extinction of the host be positive ($A_{V,host} > 0$) and the fractional change in density at the shock front should not decrease ($r_{sh} > 1$). We also constrain the fraction of energy in the electrons (ϵ_e) and magnetic field (ϵ_B) such that the fraction of energy contained in the rest of the jet, $\epsilon = 1 - \epsilon_e - \epsilon_B$, is larger than both ϵ_e and ϵ_B. This is to make sure the jet's energy is not dominated by that of the electrons and the magnetic field. The constraint is not hard and ϵ is usually somewhere in between ϵ_e and ϵ_B if both are large like in this analysis. There is also the hard prior that $\epsilon_e > 1.1\epsilon_i$

Table 2.5: χ^2 per d.o.f. for the best fit.

Model	Evidence	χ_r^2	$\chi_{r,x}^2$ $^{(a)}$	$\chi_{r,o}^2$ $^{(b)}$	$\chi_{r,r}^2$ $^{(c)}$
CM	–1015.83	5.73	2.47	13.00	26.79
TS	–995.70	5.50	2.15	11.34	32.54
WM	–1129.24	7.30	2.76	17.48	36.38

(a) χ^2 computed only with the X-ray data.
(b) χ^2 computed only with the UV, optical and nIR data.
(c) χ^2 computed only with the submm and mm data.

Table 2.6: The Bayesian evidence and the parameter posterior mean as reported by MultiNest for the three different models of the best fit data-set.

Parameter	CM	TS	WM
$E_{\rm iso}$ [erg]	$53.63^{+0.66}_{-0.62} \times 10^{51}$	$55.10^{+0.92}_{-0.82} \times 10^{51}$	$0.38^{+0.60}_{-0.26} \times 10^{55}$
E_0 [erg]	$3.63^{+0.14}_{-0.12} \times 10^{50}$	$5.36^{+0.18}_{-0.17} \times 10^{50}$	$3.64^{+0.15}_{-0.14} \times 10^{49}$
Γ_0 1799^{+82}_{-110}	1510^{+180}_{-200}	184^{+35}_{-12}	
θ_0 [deg]	$9.44^{+0.22}_{-0.20}$	11.32 ± 0.12	$0.35^{+0.27}_{-0.13}$
p	$1.8334^{+0.0038}_{-0.0036}$	1.8148 ± 0.0041	$1.8124^{+0.0037}_{-0.0039}$
ϵ_e	$9.32^{+0.57}_{-0.41} \times 10^{-2}$	$(11.64 \pm 0.40) \times 10^{-2}$	$(8.53 \pm 0.26) \times 10^{-2}$
ϵ_i	$(8.31 \pm 0.31) \times 10^{-2}$	$(10.44 \pm 0.32) \times 10^{-2}$	$(7.62 \pm 0.19) \times 10^{-2}$
ϵ_B	$(2.72 \pm 0.28) \times 10^{-1}$	$(1.59 \pm 0.16) \times 10^{-1}$	$(4.44 \pm 0.47) \times 10^{-2}$
A_* [$5.015 \cdot 10^{11}$ cm^{-3}]		$0.01747^{+0.00078}_{-0.00074}$	$0.571^{+0.023}_{-0.022}$
n_0 [cm^{-3}]	$1.05^{+0.12}_{-0.10}$		
t_{sh} [min]		$3.13^{+0.13}_{-0.12} \times 10^1$	
r_{sh}		$8.33^{+0.56}_{-0.54}$	
t_1 [days]	$5.03^{+0.42}_{-0.44} \times 10^1$		$(6.79 \pm 0.91) \times 10^{-4}$
E_1/E_0	$1.34^{+0.59}_{-0.35}$		$49.01^{+0.43}_{-0.61}$
$E_{\rm total}$ [erg]	$1.72^{+0.42}_{-0.24} \times 10^{51}$	$10.72^{+0.36}_{-0.34} \times 10^{50}$	$3.62^{+0.14}_{-0.12} \times 10^{51}$
$A_{V,host}$ [mag]	$0.0048^{+0.0031}_{-0.0021}$	$0.0102^{+0.0063}_{-0.0046}$	$0.0099^{+0.0064}_{-0.0042}$
$E(B-V)$ [mag]	0.5249 ± 0.0030	$0.5277^{+0.0037}_{-0.0044}$	$0.5749^{+0.0035}_{-0.0043}$

so the energy in the total electron distribution is always at least 10 percent greater than that contained in the electrons with the lowest value. This constraint is actually reached in all of our models, resulting in a strong correlation between ϵ_e and ϵ_i (see Appendix **??**).

Due to several reasons, such as the high Galactic reddening, the wavelength range on which H I absorption is located, and the difficulties to compute the effective wavelength of the UVOT *white* filter due to its band width, we performed different fits in order to identify and quantify the sources of systematic uncertainties. Below we discuss the best fit results that were obtained, and refer the interested reader to the material contained in the Appendices for the result details of the complete set of Bayesian fits.

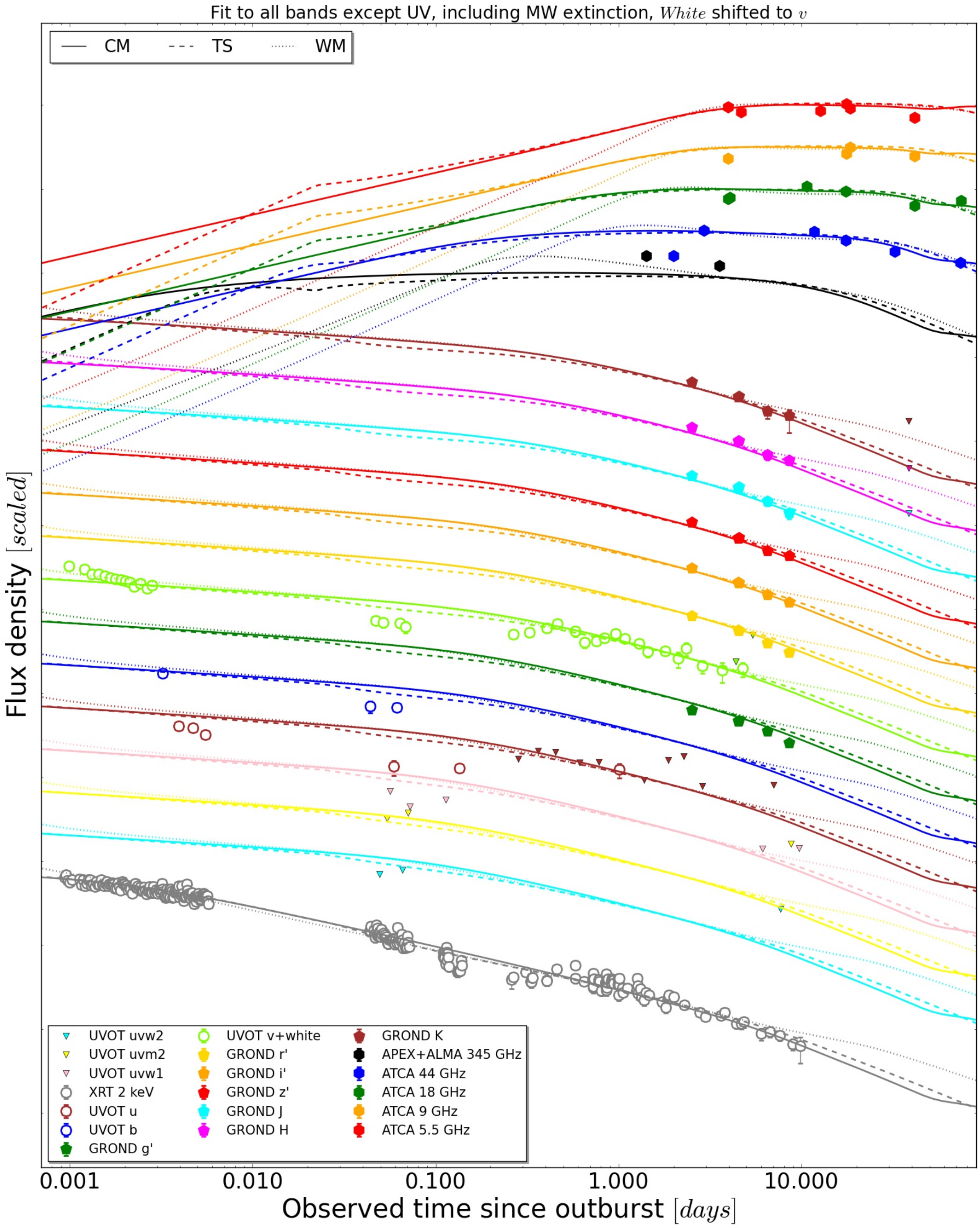

Figure 2.8: Best fits to the GRB 110715A light curves. Fluxes are independently scaled for each band for clarity.

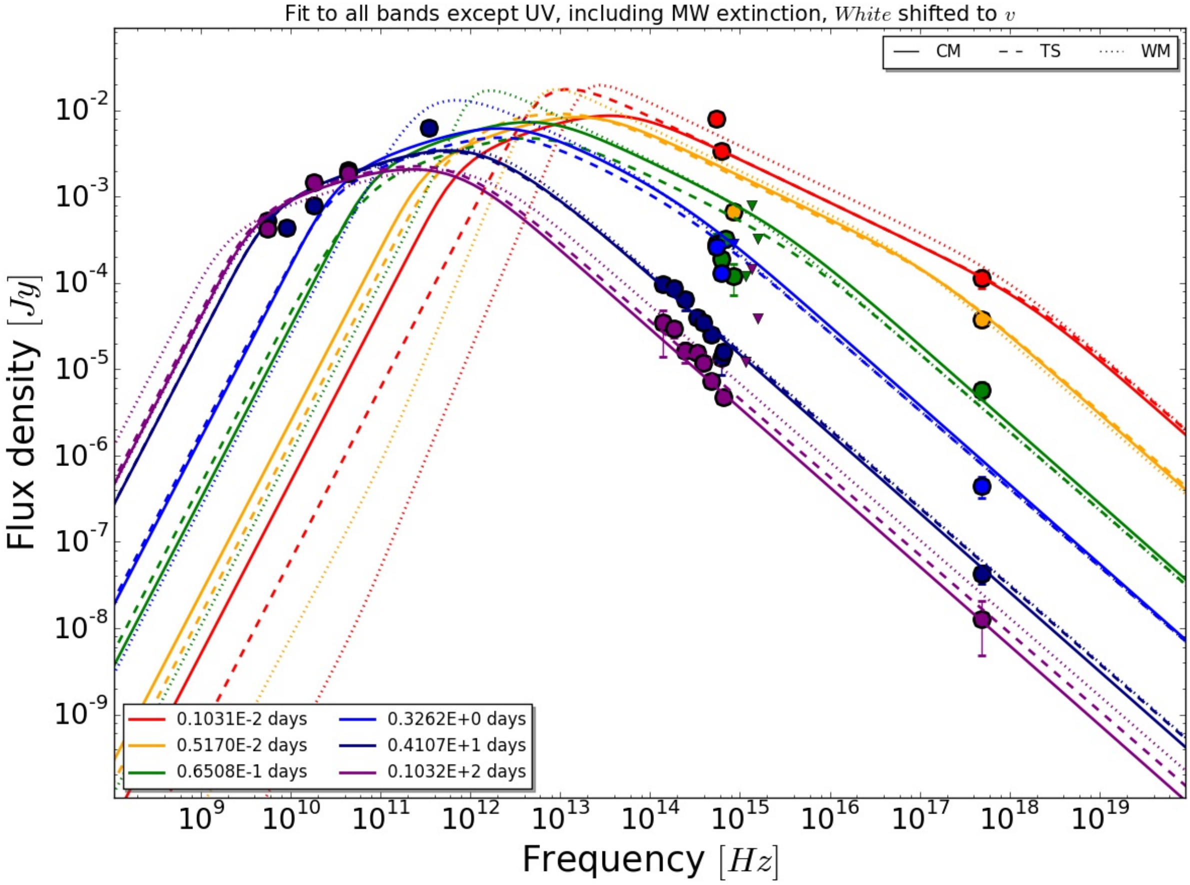

Figure 2.9: Best fits to the SED for GRB 110715A observed at several epochs.

2.2.4.2 The best fit

We found the best fit models to be those in which we excluded the UV bands, we set MW extinction as a nuisance parameter, and UVOT *white* band was shifted to V (see Appendix **??** for a detailed statistical analysis of the results for the complete grid of fits). They are shown overlaid on the data in Figures 3.1 (light curves) and 2.9 (spectral energy distributions). Bayesian evidences and χ^2s are shown in Table 2.5. This table suggests the TS fit as the most plausible model that describes the afterglow. However, none of them is either a statistically good fit or can fully explain the temporary flux increase at $\sim$0.3 days. Looking at Appendix **??**, we can also observe that there are no statistical arguments to reject most of the fits when compared with the best.

Despite the time of the wind termination shock for the best TS model being at the correct location and the magnitude of it being a factor of 2 greater than expected, the effect on the light curves is not strong enough to explain the data. Due to the spectral parameters required in the fit, the wind termination shock causes a flux decrease rather than an increase as the cooling break is just below the optical band. The slow decay in the early X-ray light curve in the model is caused by the injection break being above the X-ray frequency. This requires there to be a spectral evolution in the X-ray light curve that is not observed. In both cases the preferred location of the energy injection is at a different point than expected. For the best fit of the CM model it is much later and serves only to explain the latest radio points while for the WM model it happens very early to explain the shallower decay between 0.01 and 1 days. The best model also has a hard time explaining the rapid decline in the light curve observed by the GROND instrument. The earliest points are under-predicted while the later points are over-predicted. This is again something that all the models fail to reproduce. The CM model does a slightly better job, but the WM model is worst. The models have a similarly hard time at explaining the late time X-ray light curve as they don't decay rapidly enough.

Finally, the best model is unable to explain the early and late radio and submm data. The model has a hard time explaining the rapid rise of the 44 GHz data simultaneously with the decay of the 345 GHz data and the rather flat light curve at 5.5 GHz. The self-absorption break, ν_a, needs to pass through the 44 GHz band at around 2 days to explain the rapid size and it should have already passed the 345 GHz band at 1 day and the 5.5 GHz band at 2 days. It is impossible for the model to meet these criteria. In addition, the 44 GHz light curve starts decaying at around 10 days with a slope that is incompatible with post jet-break evolution and at the same time the 18 GHz band is compatible with being nearly constant. The CM model has similar issues as the TS model although it does slightly better at late times because the injection lifts the radio light curve to match the last points. There is, however, no other indication for the energy injection and it is unlikely to be the correct physical interpretation. The WM model does the best job with the submm and radio data, but is still far from explaining the details of the observed afterglow.

Table 2.6 shows the posterior median for the parameter values and their associated 68% statistical errors. Appendix ?? includes plots of the resulting distributions. The parameter values that give the smallest χ^2 are usually located near the peak of the posterior distributions, and their distributions are mostly symmetric, with notable exceptions in the WM model where long tails can be seen for $E_{\rm iso}$, Γ_0, and θ_0. The inferred values are mostly typical for a GRB afterglow with a few exceptions. The half opening angle θ_0 in the WM model is unreasonably low and requires an extreme confinement of the outflow. It is also the worst performer of the 3 models and we therefore consider it an unreasonable model. The value of the electron power-law index p is on the lower side and lower than expected from shock-acceleration theory (Achterberg *et al.*, 2001). It is, however, well within the range of values deduced from observations of relativistic shocks (Shen *et al.*, 2006). The fraction of energy contained in the magnetic field and the electron distribution, ϵ_B, and ϵ_e, respectively is rather large. ϵ_i is also larger than usual and constrained mostly by the equipartition requirements for the electron energy distribution rather than the position of the injection peak in the synchrotron spectrum. These large values cause the afterglow to be in the fast-cooling regime for the entire duration of the afterglow and the assumption of no radiative losses is likely invalid.

Our values for the host extinction are compatible with the value being very small as found earlier using GROND data only. The statistical error is significantly smaller because we use the entire data-set, but the exact value is model dependent.

As already discussed, the Galactic line of sight extinction is important in the GRB direction. The expected uncertainty could be large too, so similarly to the host galaxy, the Galactic $E(B-V)$ was left in some fits as a free parameter. Resulting Galactic and host galaxy solutions show a clear anti-correlation, limiting our constraints of the inferred host galaxy $A_{V,host}$. In Appendix ?? we include the two dimensional marginal plots for the $E(B-V)$ of the Galactic extinction with the rest of the parameters when it is included in the fit. As shown in Appendix 2.3, the galactic $E(B-V)$ value is model dependent, and results are somewhat bimodal, sometimes consistent with the dust maps of Schlegel *et al.* (1998), and sometimes with Schlafly & Finkbeiner (2011), the latter being the more favored. The figures also show that the upper value found for the $E(B-V)$ parameter in this analysis is basically bound by the host extinction going to 0.

We also discuss in Appendix 2.3 the hypothesis that the reverse shock (RS) contribu-

Fit Id	Evidence	χ^2_{red}	$\chi^2_{red,x}$	$\chi^2_{red,o}$	$\chi^2_{red,r}$
CM/XOR/WC	-1066.52 ± 0.19	6.52	2.45	16.49	27.98
TS/XOR/WC	-951.65 ± 0.20	6.24	2.0	16.12	30.48
WM/XOR/WC	-1181.09 ± 0.19	9.78	2.61	29.6	39.61
CM/XUOR/WN	-1677.46 ± 0.20	6.92	2.46	15.75	35.57
TS/XUOR/WN	-1503.57 ± 0.20	6.79	1.92	18.22	31.42
WM/XUOR/WN	-1753.24 ± 0.20	57.02	2.25	259.83	47.46
CM/XOR/WN	-1667.78 ± 0.20	6.79	2.45	15.86	35.35
TS/XOR/WN	-1491.05 ± 0.20	6.5	1.91	17.61	31.27
WM/XOR/WN	-1730.71 ± 0.20	54.46	2.21	261.71	47.0
CM/XOR/VC	-1039.59 ± 0.20	5.69	2.49	12.62	26.91
TS/XOR/VC	-988.59 ± 0.20	5.51	2.14	11.86	31.2
WM/XOR/VC	-1145.41 ± 0.19	7.45	2.73	18.03	37.6
CM/XOR/VN	-1015.83 ± 0.21	5.73	2.47	13.0	26.79
TS/XOR/VN	-995.70 ± 0.20	5.5	2.15	11.34	32.54
WM/XOR/VN	-1129.24 ± 0.19	7.3	2.76	17.48	36.38
CM/O/VC	-201.49 ± 0.16	175.87	8.82	37.34	2997.26
TS/O/VC	-206.60 ± 0.18	71.38	19.67	70.76	800.15
WM/O/VC	-237.56 ± 0.15	727.47	277.16	228.39	8762.93
CM/R	-267.53 ± 0.16	57.98	48.6	100.81	25.24
TS/R	-252.66 ± 0.15	195.24	135.6	457.94	23.98
WM/R	-249.27 ± 0.18	467.74	190.45	1597.79	22.54
CM/XUO/VC	-555.22 ± 0.18	164.1	1.88	13.01	3000.39
TS/XUO/VC	-466.51 ± 0.21	53.66	1.73	68.71	727.94
WM/XUO/VC	-733.27 ± 0.18	183.79	2.12	14.73	3359.54
CM/XR/	-600.80 ± 0.18	8.4	2.38	25.9	25.76
TS/XR/	-558.08 ± 0.18	8.82	1.87	29.13	28.49
WM/XR/	-671.99 ± 0.18	10.69	2.29	35.22	34.55
CM/UOR/VC	-561.73 ± 0.19	20.83	18.66	26.5	30.35
TS/UOR/VC	-541.22 ± 0.19	47.79	41.7	77.02	25.68
WM/UOR/VC	-676.66 ± 0.19	23.52	25.91	11.13	35.58
CM/XUOR/VCE	-848.73 ± 0.19	9.82	3.66	21.3	28.05
TS/XUOR/VCE	-670.00 ± 0.20	13.16	2.24	39.29	29.35
WM/XUOR/VCE	-1044.04 ± 0.19	15.01	3.05	38.75	46.29
CM/XUOR/VCL	-547.08 ± 0.18	14.02	1.65	26.9	28.55
TS/XUOR/VCL	-494.77 ± 0.19	20.93	1.86	47.0	29.91
WM/XUOR/VCL	-672.83 ± 0.18	65.64	2.99	174.44	45.23

Fit Id = (A)/(B)/(C)(D)(E)
(A) = Model used (CM/TS/WM)
(B) = Wavelength range of the observations used for the model fitting:
X = XRT 2 keV
U = UVOT UVW2, UVM2, UVW1, and U
O = Rest of the UVOT and GROND bands
R = Radio and submm bands
(C) = UVOT White band shifted to UVOT (V) or independent (W)
(D) = Treatment of the Galactic reddening:
C = Corrected
N = Set to a nuisance parameter
(E) = Time interval used for the model fitting:
E = From $t = 0.05$ days
L = From $t = 0.5$ days

tion has to be taken into account (e.g., Jelínek *et al.*, 2006; Laskar *et al.*, 2013a), as well as the possibility that a double jet model (e.g. Filgas *et al.*, 2011; Racusin *et al.*, 2008; Starling *et al.*, 2005; van der Horst *et al.*, 2014) is necessary to explain this afterglow. The conclusion is that, in spite of them possibly being present, none of the options can improve the fit starting at 0.5 days after the trigger, so other considerations must be taken into account to improve the fits we performed.

Fit Id	$E_{\mathrm{iso}}[erg]$	E_0 [erg]	Γ_0	θ_0 [deg]	p
CM/XOR/WC	$5.38^{+0.29}_{-0.27} \times 10^{52}$	$3.33^{+0.29}_{-0.23} \times 10^{50}$	1783^{+89}_{-110}	$8.83^{+0.28}_{-0.23}$	$1.8542^{+0.0040}_{-0.0041}$
TS/XOR/WC	$50.47^{+0.76}_{-0.67} \times 10^{51}$	$4.56^{+0.15}_{-0.15} \times 10^{50}$	1410^{+210}_{-220}	$10.91^{+0.12}_{-0.13}$	$1.8300^{+0.0041}_{-0.0043}$
WM/XOR/WC	$1.52^{+0.96}_{-0.70} \times 10^{55}$	$4.02^{+0.15}_{-0.14} \times 10^{49}$	$152.9^{+5.1}_{-4.4}$	$0.186^{+0.067}_{-0.041}$	$1.8510^{+0.0038}_{-0.0039}$
CM/XUOR/WN	$0.114^{+0.14}_{-0.055} \times 10^{55}$	$20.88^{+0.68}_{-0.68} \times 10^{48}$	362^{+75}_{-43}	$0.49^{+0.19}_{-0.16}$	$1.8405^{+0.0035}_{-0.0036}$
TS/XUOR/WN	$48.38^{+0.56}_{-0.50} \times 10^{51}$	$4.01^{+0.11}_{-0.10} \times 10^{50}$	1360^{+230}_{-220}	$10.46^{+0.12}_{-0.13}$	$1.8127^{+0.0041}_{-0.0039}$
WM/XUOR/WN	$0.49^{+0.16}_{-0.15} \times 10^{57}$	$2.09^{+0.32}_{-0.25} \times 10^{51}$	$67.81^{+0.55}_{-0.49}$	$0.242^{+0.052}_{-0.035}$	2.0415 ± 0.0050
CM/XOR/WN	$0.86^{+1.00}_{-0.38} \times 10^{54}$	$21.13^{+0.72}_{-0.70} \times 10^{48}$	384^{+88}_{-54}	$0.57^{+0.19}_{-0.18}$	$1.8423^{+0.0035}_{-0.0036}$
TS/XOR/WN	$48.40^{+0.54}_{-0.52} \times 10^{51}$	$4.02^{+0.11}_{-0.10} \times 10^{50}$	1350^{+230}_{-220}	$10.47^{+0.13}_{-0.12}$	$1.8137^{+0.0040}_{-0.0039}$
WM/XOR/WN	$0.49^{+0.16}_{-0.15} \times 10^{57}$	$2.08^{+0.29}_{-0.25} \times 10^{51}$	$67.90^{+0.57}_{-0.52}$	$0.244^{+0.050}_{-0.036}$	$2.0402^{+0.0049}_{-0.0050}$
CM/XOR/VC	$51.07^{+0.51}_{-0.47} \times 10^{51}$	$3.92^{+0.13}_{-0.13} \times 10^{50}$	1813^{+77}_{-100}	$10.09^{+0.17}_{-0.21}$	$1.8433^{+0.0039}_{-0.0038}$
TS/XOR/VC	$54.23^{+0.99}_{-0.88} \times 10^{51}$	$5.20^{+0.19}_{-0.17} \times 10^{50}$	1510 ± 190	$11.25^{+0.12}_{-0.13}$	$1.8273^{+0.0040}_{-0.0044}$
WM/XOR/VC	$0.38^{+0.56}_{-0.26} \times 10^{55}$	$3.66^{+0.14}_{-0.13} \times 10^{49}$	184^{+39}_{-13}	$0.36^{+0.30}_{-0.13}$	$1.8311^{+0.0040}_{-0.0037}$
CM/XOR/VN	$53.63^{+0.66}_{-0.62} \times 10^{51}$	$3.63^{+0.14}_{-0.12} \times 10^{50}$	1799^{+82}_{-110}	$9.44^{+0.22}_{-0.20}$	$1.8334^{+0.0038}_{-0.0036}$
TS/XOR/VN	$55.10^{+0.92}_{-0.82} \times 10^{51}$	$5.36^{+0.18}_{-0.17} \times 10^{50}$	1510^{+180}_{-200}	11.32 ± 0.12	1.8148 ± 0.0041
WM/XOR/VN	$0.38^{+0.60}_{-0.26} \times 10^{55}$	$3.64^{+0.15}_{-0.14} \times 10^{49}$	184^{+35}_{-12}	$0.35^{+0.27}_{-0.13}$	$1.8124^{+0.0037}_{-0.0039}$
CM/O/VC	$0.087^{+0.33}_{-0.065} \times 10^{55}$	$5.34^{+0.53}_{-0.42} \times 10^{49}$	216^{+140}_{-41}	$0.89^{+0.82}_{-0.49}$	1.702 ± 0.025
TS/O/VC	$0.211^{+0.14}_{-0.096} \times 10^{57}$	$0.36^{+0.23}_{-0.14} \times 10^{52}$	279^{+22}_{-19}	$0.521^{+0.083}_{-0.079}$	$1.567^{+0.030}_{-0.034}$
WM/O/VC	$2.13^{+0.98}_{-0.79} \times 10^{56}$	$0.401^{+0.16}_{-0.070} \times 10^{51}$	311^{+23}_{-20}	$0.170^{+0.046}_{-0.032}$	2.274 ± 0.048
CM/R	$0.165^{+0.56}_{-0.094} \times 10^{55}$	$1.69^{+0.12}_{-0.11} \times 10^{50}$	270^{+220}_{-74}	1.16 ± 0.61	$1.978^{+0.021}_{-0.020}$
TS/R	$0.0195^{+0.32}_{-0.0084} \times 10^{55}$	$1.68^{+0.38}_{-0.22} \times 10^{51}$	57^{+160}_{-28}	$11.1^{+4.2}_{-8.5}$	3.03 ± 0.10
WM/R	$1.17^{+0.15}_{-0.13} \times 10^{53}$	$1.083^{+0.12}_{-0.100} \times 10^{51}$	277^{+140}_{-94}	$11.23^{+0.61}_{-0.67}$	$3.446^{+0.072}_{-0.077}$
CM/XUO/VC	$0.90^{+0.22}_{-0.13} \times 10^{53}$	$6.99^{+0.64}_{-0.55} \times 10^{49}$	590^{+310}_{-200}	$3.20^{+0.16}_{-0.20}$	$1.7667^{+0.0047}_{-0.0044}$
TS/XUO/VC	$10.81^{+0.81}_{-0.80} \times 10^{54}$	$6.29^{+0.26}_{-0.23} \times 10^{50}$	347^{+11}_{-13}	$0.868^{+0.040}_{-0.033}$	$1.9284^{+0.0056}_{-0.0055}$
WM/XUO/VC	$0.088^{+0.11}_{-0.052} \times 10^{56}$	$0.567^{+0.11}_{-0.088} \times 10^{50}$	220^{+23}_{-15}	$0.289^{+0.18}_{-0.097}$	$1.7821^{+0.0050}_{-0.0048}$
CM/XR/	$5.68^{+0.16}_{-0.14} \times 10^{52}$	$4.40^{+0.22}_{-0.20} \times 10^{50}$	1330 ± 220	$10.09^{+0.22}_{-0.21}$	$1.7821^{+0.0054}_{-0.0059}$
TS/XR/	$4.84^{+0.13}_{-0.13} \times 10^{52}$	$4.63^{+0.20}_{-0.18} \times 10^{50}$	1250^{+250}_{-230}	$11.22^{+0.11}_{-0.12}$	$1.8425^{+0.0060}_{-0.0057}$
WM/XR/	$2.15^{+0.99}_{-0.82} \times 10^{56}$	$4.32^{+0.26}_{-0.23} \times 10^{50}$	59.8 ± 1.1	$0.162^{+0.044}_{-0.029}$	$1.7529^{+0.0071}_{-0.0067}$
CM/UOR/VC	$0.142^{+0.21}_{-0.073} \times 10^{55}$	$20.00^{+0.55}_{-0.52} \times 10^{48}$	535^{+230}_{-100}	$0.43^{+0.19}_{-0.16}$	$2.174^{+0.012}_{-0.011}$
TS/UOR/VC	$3.43^{+0.17}_{-0.17} \times 10^{53}$	$3.95^{+0.21}_{-0.20} \times 10^{50}$	1030^{+290}_{-260}	$3.894^{+0.087}_{-0.092}$	$1.8073^{+0.0075}_{-0.0071}$
WM/UOR/VC	$1.40^{+0.96}_{-0.69} \times 10^{55}$	$4.14^{+0.16}_{-0.15} \times 10^{49}$	$199.8^{+13}_{-8.3}$	$0.197^{+0.080}_{-0.046}$	2.153 ± 0.011
CM/XUOR/VCE	$6.45^{+0.29}_{-0.28} \times 10^{52}$	$3.17^{+0.17}_{-0.17} \times 10^{50}$	1680^{+130}_{-160}	$8.03^{+0.16}_{-0.14}$	1.9169 ± 0.0046
TS/XUOR/VCE	$5.78^{+0.23}_{-0.19} \times 10^{52}$	$5.42^{+0.23}_{-0.22} \times 10^{50}$	970^{+300}_{-240}	$11.13^{+0.10}_{-0.12}$	$1.9064^{+0.0051}_{-0.0052}$
WM/XUOR/VCE	$1.75^{+0.97}_{-0.73} \times 10^{55}$	$4.09^{+0.14}_{-0.14} \times 10^{49}$	$141.9^{+4.2}_{-3.3}$	$0.175^{+0.053}_{-0.035}$	$1.8991^{+0.0040}_{-0.0041}$
CM/XUOR/VCL	$0.78^{+0.59}_{-0.38} \times 10^{56}$	$2.47^{+0.15}_{-0.14} \times 10^{50}$	57.4 ± 1.1	$0.205^{+0.081}_{-0.051}$	$1.8924^{+0.0050}_{-0.0053}$
TS/XUOR/VCL	$1.33^{+0.15}_{-0.12} \times 10^{53}$	$4.69^{+0.17}_{-0.17} \times 10^{50}$	$91.5^{+4.9}_{-4.8}$	$6.80^{+0.31}_{-0.34}$	$1.9140^{+0.0049}_{-0.0052}$
WM/XUOR/VCL	$0.38^{+0.18}_{-0.15} \times 10^{57}$	$4.61^{+0.48}_{-0.39} \times 10^{52}$	$28.18^{+1.0}_{-0.77}$	$1.28^{+0.39}_{-0.24}$	$2.1936^{+0.010}_{-0.0097}$

Fit Id	ϵ_e	ϵ_i	ϵ_B	A_* $[5.015 \cdot 10^{11}\ \mathrm{cm}^{-3}]$	n_0 $[\mathrm{cm}^{-3}]$	t_{sh} [min]
CM/XOR/WC	$(1.88 \pm 0.14) \times 10^{-1}$	$(1.68 \pm 0.12) \times 10^{-1}$	$0.70^{+0.22}_{-0.14} \times 10^{-1}$		$2.77^{+0.32}_{-0.36}$	
TS/XOR/WC	$13.22^{+0.50}_{-0.43} \times 10^{-2}$	$(11.87 \pm 0.35) \times 10^{-2}$	$(2.08 \pm 0.20) \times 10^{-1}$	$0.01313^{+0.00055}_{-0.00053}$		$3.830^{+0.098}_{-0.16} \times 10^{1}$
WM/XOR/WC	$(10.67 \pm 0.29) \times 10^{-2}$	$(9.57 \pm 0.22) \times 10^{-2}$	$(3.30 \pm 0.28) \times 10^{-2}$	$0.658^{+0.024}_{-0.023}$		
CM/XUOR/WN	$49.63^{+0.49}_{-0.61} \times 10^{-2}$	$45.16^{+0.45}_{-0.54} \times 10^{-2}$	$(12.65 \pm 0.83) \times 10^{-3}$		4.36 ± 0.13	
TS/XUOR/WN	$(11.84 \pm 0.38) \times 10^{-2}$	$(10.66 \pm 0.31) \times 10^{-2}$	$(3.10 \pm 0.28) \times 10^{-1}$	0.00952 ± 0.00036		$44.52^{+0.64}_{-0.69}$
WM/XUOR/WN	$3.96^{+0.70}_{-0.35} \times 10^{-2}$	$(3.33 \pm 0.19) \times 10^{-2}$	$(0.34 \pm 0.10) \times 10^{-2}$	$0.287^{+0.039}_{-0.031}$		
CM/XOR/WN	$(49.51 \pm 0.66) \times 10^{-2}$	$45.04^{+0.49}_{-0.59} \times 10^{-2}$	$(12.53 \pm 0.82) \times 10^{-3}$		4.39 ± 0.13	
TS/XOR/WN	$(11.92 \pm 0.37) \times 10^{-2}$	$(10.74 \pm 0.30) \times 10^{-2}$	$(3.06 \pm 0.27) \times 10^{-1}$	$0.00969^{+0.00038}_{-0.00036}$		$44.60^{+0.64}_{-0.67}$
WM/XOR/WN	$3.94^{+0.64}_{-0.33} \times 10^{-2}$	$(3.33 \pm 0.19) \times 10^{-2}$	$0.334^{+0.14}_{-0.099} \times 10^{-2}$	$0.288^{+0.036}_{-0.032}$		
CM/XOR/VC	$(10.80 \pm 0.44) \times 10^{-2}$	$(9.69 \pm 0.39) \times 10^{-2}$	$2.29^{+0.26}_{-0.20} \times 10^{-1}$		$1.33^{+0.10}_{-0.14}$	
TS/XOR/VC	$(12.70 \pm 0.41) \times 10^{-2}$	$(11.41 \pm 0.33) \times 10^{-2}$	$(1.55 \pm 0.16) \times 10^{-1}$	$0.01662^{+0.00074}_{-0.00068}$		$3.157^{+0.14}_{-0.100} \times 10^{1}$
WM/XOR/VC	$(9.46 \pm 0.28) \times 10^{-2}$	$(8.46 \pm 0.21) \times 10^{-2}$	$(4.09 \pm 0.40) \times 10^{-2}$	$0.609^{+0.023}_{-0.022}$		
CM/XOR/VN	$9.32^{+0.57}_{-0.41} \times 10^{-2}$	$(8.31 \pm 0.31) \times 10^{-2}$	$(2.72 \pm 0.28) \times 10^{-1}$		$1.05^{+0.12}_{-0.10}$	
TS/XOR/VN	$(11.64 \pm 0.40) \times 10^{-2}$	$(10.44 \pm 0.32) \times 10^{-2}$	$(1.59 \pm 0.16) \times 10^{-1}$	$0.01747^{+0.00078}_{-0.00074}$		$3.13^{+0.13}_{-0.12} \times 10^{1}$
WM/XOR/VN	$(8.53 \pm 0.26) \times 10^{-2}$	$(7.62 \pm 0.19) \times 10^{-2}$	$(4.44 \pm 0.47) \times 10^{-2}$	$0.571^{+0.023}_{-0.022}$		
CM/O/VC	$0.324^{+0.13}_{-0.055} \times 10^{-1}$	$(2.49 \pm 0.29) \times 10^{-2}$	$2.08^{+0.32}_{-0.45} \times 10^{-1}$		$9.26^{+0.31}_{-0.43} \times 10^{2}$	
TS/O/VC	$0.39^{+0.18}_{-0.10} \times 10^{-1}$	$(2.72 \pm 0.55) \times 10^{-2}$	$(0.99 \pm 0.74) \times 10^{-4}$	$0.0217^{+0.011}_{-0.0076}$		$9.09^{+0.30}_{-0.40} \times 10^{1}$
WM/O/VC	$2.07^{+0.62}_{-0.41} \times 10^{-1}$	$1.79^{+0.51}_{-0.32} \times 10^{-1}$	$0.78^{+0.89}_{-0.55} \times 10^{-1}$	$0.0042^{+0.0026}_{-0.0013}$		
CM/R	$4.74^{+0.20}_{-0.25} \times 10^{-1}$	$(4.30 \pm 0.23) \times 10^{-1}$	$(1.07 \pm 0.19) \times 10^{-2}$		$5.99^{+0.60}_{-0.61}$	
TS/R	$1.59^{+0.35}_{-0.24} \times 10^{-1}$	$1.36^{+0.27}_{-0.18} \times 10^{-1}$	$0.39^{+0.29}_{-0.20} \times 10^{-1}$	$0.89^{+0.31}_{-0.19}$		$6.92^{+0.51}_{-0.49} \times 10^{4}$
WM/R	$(10.71 \pm 0.84) \times 10^{-2}$	$(9.55 \pm 0.68) \times 10^{-2}$	$0.40^{+0.20}_{-0.13} \times 10^{-1}$	$0.78^{+0.12}_{-0.11}$		
CM/XUO/VC	$1.19^{+0.29}_{-0.16} \times 10^{-1}$	$1.03^{+0.19}_{-0.13} \times 10^{-1}$	$2.48^{+0.72}_{-0.89} \times 10^{-1}$		$3.94^{+0.35}_{-0.31} \times 10^{2}$	
TS/XUO/VC	$0.047^{+0.14}_{-0.012} \times 10^{-1}$	$(3.05 \pm 0.14) \times 10^{-3}$	$(3.75 \pm 0.54) \times 10^{-1}$	$0.001110^{+0.00012}_{-0.000084}$		$46.68^{+0.14}_{-0.11}$
WM/XUO/VC	$4.60^{+0.21}_{-0.25} \times 10^{-1}$	$(4.18 \pm 0.23) \times 10^{-1}$	$(0.76 \pm 0.22) \times 10^{-2}$	$0.168^{+0.025}_{-0.021}$		
CM/XR/	$9.35^{+0.62}_{-0.49} \times 10^{-2}$	$(8.26 \pm 0.35) \times 10^{-2}$	$(1.32 \pm 0.17) \times 10^{-1}$		$1.71^{+0.16}_{-0.15}$	
TS/XR/	$(19.55 \pm 0.94) \times 10^{-2}$	$(17.57 \pm 0.77) \times 10^{-2}$	$(1.51 \pm 0.20) \times 10^{-1}$	$0.01085^{+0.00057}_{-0.00053}$		$4.39^{+0.10}_{-0.13} \times 10^{1}$
WM/XR/	$(5.05 \pm 0.25) \times 10^{-2}$	$(4.42 \pm 0.16) \times 10^{-2}$	$0.794^{+0.10}_{-0.094} \times 10^{-1}$	0.316 ± 0.015		
CM/UOR/VC	$(53.50 \pm 0.59) \times 10^{-2}$	$48.70^{+0.44}_{-0.50} \times 10^{-2}$	$(5.08 \pm 0.32) \times 10^{-3}$		12.78 ± 0.43	
TS/UOR/VC	$(4.69 \pm 0.14) \times 10^{-1}$	$(4.27 \pm 0.13) \times 10^{-1}$	$(7.08 \pm 0.96) \times 10^{-2}$	$0.462^{+0.029}_{-0.028}$		$46.84^{+0.28}_{-0.19} \times 10^{2}$
WM/UOR/VC	$(21.25 \pm 0.59) \times 10^{-2}$	$19.16^{+0.51}_{-0.49} \times 10^{-2}$	$(1.19 \pm 0.12) \times 10^{-2}$	$1.472^{+0.061}_{-0.059}$		
CM/XUOR/VCE	$(3.36 \pm 0.12) \times 10^{-1}$	$(3.04 \pm 0.11) \times 10^{-1}$	$(2.52 \pm 0.31) \times 10^{-2}$		$5.13^{+0.30}_{-0.29}$	
TS/XUOR/VCE	$(26.76 \pm 0.87) \times 10^{-2}$	$(24.20 \pm 0.76) \times 10^{-2}$	$(6.94 \pm 0.89) \times 10^{-2}$	$0.01323^{+0.00063}_{-0.00058}$		$3.40^{+0.11}_{-0.17} \times 10^{1}$
WM/XUOR/VCE	$(14.44 \pm 0.34) \times 10^{-2}$	$(13.01 \pm 0.28) \times 10^{-2}$	$(2.70 \pm 0.23) \times 10^{-2}$	0.774 ± 0.024		
CM/XUOR/VCL	$(2.25 \pm 0.10) \times 10^{-1}$	$(20.27 \pm 0.91) \times 10^{-2}$	$(1.48 \pm 0.27) \times 10^{-1}$		$1.94^{+0.25}_{-0.21}$	
TS/XUOR/VCL	$(20.95 \pm 0.78) \times 10^{-2}$	$(18.87 \pm 0.66) \times 10^{-2}$	$1.31^{+0.16}_{-0.14} \times 10^{-1}$	$0.00615^{+0.00040}_{-0.00039}$		$2.45^{+0.16}_{-0.17} \times 10^{1}$
WM/XUOR/VCL	$2.92^{+0.90}_{-0.32} \times 10^{-2}$	$(2.37 \pm 0.19) \times 10^{-2}$	$(1.05 \pm 0.31) \times 10^{-2}$	$0.122^{+0.021}_{-0.019}$		

Fit Id	r_{sh}	t_1 [days]	E_1/E_0	E_{total} [erg]	$A_{V,host}$ [mag]	$E(B-V)$ [mag]
CM/XOR/WC		$0.39^{+0.16}_{-0.14} \times 10^{-1}$	$0.940^{+0.091}_{-0.085}$	$12.65^{+0.98}_{-0.77} \times 10^{50}$	$0.0716^{+0.0042}_{-0.0037}$	
TS/XOR/WC	$16.10^{+1.0}_{-0.93}$			$9.12^{+0.30}_{-0.29} \times 10^{50}$	0.1000 ± 0.0036	
WM/XOR/WC		$(0.59 \pm 0.10) \times 10^{-3}$	$49.12^{+0.40}_{-0.55}$	$4.00^{+0.14}_{-0.13} \times 10^{51}$	$0.1645^{+0.0037}_{-0.0035}$	
CM/XUOR/WN		$(5.35 \pm 0.24) \times 10^{-2}$	$32.70^{+0.58}_{-0.60}$	$14.06^{+0.36}_{-0.36} \times 10^{50}$	$0.0132^{+0.0080}_{-0.0056}$	$0.5933^{+0.0041}_{-0.0051}$
TS/XUOR/WN	$24.8^{+1.6}_{-1.5}$			$8.02^{+0.23}_{-0.20} \times 10^{50}$	$0.0203^{+0.011}_{-0.0088}$	$0.6178^{+0.0055}_{-0.0071}$
WM/XUOR/WN		$(8.88 \pm 0.78) \times 10^{-2}$	26.3 ± 1.3	$1.13^{+0.16}_{-0.12} \times 10^{53}$	$0.786^{+0.022}_{-0.023}$	$0.459^{+0.015}_{-0.014}$
CM/XOR/WN		$(5.27 \pm 0.25) \times 10^{-2}$	$32.47^{+0.57}_{-0.60}$	$14.13^{+0.38}_{-0.37} \times 10^{50}$	$0.0132^{+0.0081}_{-0.0058}$	$0.5949^{+0.0041}_{-0.0050}$
TS/XOR/WN	24.3 ± 1.5			$8.05^{+0.23}_{-0.21} \times 10^{50}$	$0.0190^{+0.011}_{-0.0082}$	$0.6190^{+0.0054}_{-0.0073}$
WM/XOR/WN		$(9.05 \pm 0.76) \times 10^{-2}$	$26.6^{+1.5}_{-1.3}$	$1.14^{+0.15}_{-0.12} \times 10^{53}$	$0.774^{+0.022}_{-0.023}$	$0.468^{+0.015}_{-0.014}$
CM/XOR/VC		$5.18^{+0.42}_{-0.44} \times 10^{1}$	$1.20^{+0.56}_{-0.34}$	$1.71^{+0.44}_{-0.25} \times 10^{51}$	$0.0140^{+0.0036}_{-0.0035}$	
TS/XOR/VC	$10.13^{+0.69}_{-0.60}$			$10.41^{+0.39}_{-0.35} \times 10^{50}$	$0.0318^{+0.0038}_{-0.0040}$	
WM/XOR/VC		$(7.99 \pm 0.93) \times 10^{-4}$	$49.11^{+0.38}_{-0.53}$	$3.64^{+0.13}_{-0.12} \times 10^{51}$	$0.1017^{+0.0038}_{-0.0035}$	
CM/XOR/VN		$5.03^{+0.42}_{-0.44} \times 10^{1}$	$1.34^{+0.59}_{-0.35}$	$1.72^{+0.42}_{-0.24} \times 10^{51}$	$0.0048^{+0.0031}_{-0.0021}$	0.5249 ± 0.0030
TS/XOR/VN	$8.33^{+0.56}_{-0.54}$			$10.72^{+0.36}_{-0.34} \times 10^{50}$	$0.0102^{+0.0063}_{-0.0046}$	$0.5277^{+0.0037}_{-0.0044}$
WM/XOR/VN		$(6.79 \pm 0.91) \times 10^{-4}$	$49.01^{+0.43}_{-0.61}$	$3.62^{+0.14}_{-0.12} \times 10^{51}$	$0.0099^{+0.0064}_{-0.0042}$	$0.5749^{+0.0035}_{-0.0043}$
CM/O/VC		$(6.63 \pm 0.98) \times 10^{-2}$	$45.9^{+1.6}_{-2.1}$	$4.95^{+0.46}_{-0.39} \times 10^{51}$	$0.287^{+0.012}_{-0.013}$	
TS/O/VC	$43.4^{+2.6}_{-3.5}$			$0.71^{+0.46}_{-0.28} \times 10^{52}$	$0.387^{+0.011}_{-0.010}$	
WM/O/VC		$0.072^{+0.17}_{-0.071} \times 10^{2}$	$16.8^{+9.6}_{-7.6}$	$1.54^{+0.88}_{-0.64} \times 10^{52}$	$0.643^{+0.011}_{-0.012}$	
CM/R		$(0.19 \pm 0.13) \times 10^{-2}$	$3.50^{+0.27}_{-0.24}$	$15.39^{+0.97}_{-0.99} \times 10^{50}$		
TS/R	$13.7^{+6.6}_{-4.5}$			$3.37^{+0.75}_{-0.44} \times 10^{51}$		
WM/R		$4.59^{+0.17}_{-0.18} \times 10^{1}$	$9.6^{+2.4}_{-2.5}$	$2.21^{+0.64}_{-0.56} \times 10^{52}$		
CM/XUO/VC		$(13.08 \pm 0.41) \times 10^{-2}$	$12.77^{+0.32}_{-0.31}$	$1.91^{+0.15}_{-0.13} \times 10^{51}$	0.100 ± 0.011	
TS/XUO/VC	$49.60^{+0.17}_{-0.25}$			$12.58^{+0.51}_{-0.46} \times 10^{50}$	0.3672 ± 0.0074	
WM/XUO/VC		$(6.96 \pm 0.43) \times 10^{-2}$	$31.2^{+1.8}_{-1.5}$	$3.67^{+0.71}_{-0.53} \times 10^{51}$	$0.0432^{+0.0042}_{-0.0043}$	
CM/XR/		$4.96^{+0.41}_{-0.42} \times 10^{1}$	$1.65^{+0.61}_{-0.34}$	$2.35^{+0.55}_{-0.31} \times 10^{51}$		
TS/XR/	$40.6^{+3.3}_{-3.5}$			$9.25^{+0.40}_{-0.37} \times 10^{50}$		
WM/XR/		$(8.79 \pm 0.79) \times 10^{-2}$	$5.03^{+0.29}_{-0.28}$	$5.21^{+0.24}_{-0.22} \times 10^{51}$		
CM/UOR/VC		$5.40^{+0.52}_{-0.44} \times 10^{-2}$	$48.83^{+0.51}_{-0.71}$	$19.82^{+0.49}_{-0.50} \times 10^{50}$	$0.2160^{+0.0062}_{-0.0060}$	
TS/UOR/VC	$10.60^{+0.41}_{-0.39}$			$7.90^{+0.41}_{-0.40} \times 10^{50}$	$0.3961^{+0.0074}_{-0.0072}$	
WM/UOR/VC		$(4.76 \pm 0.20) \times 10^{-2}$	$49.29^{+0.31}_{-0.45}$	$4.15^{+0.15}_{-0.15} \times 10^{51}$	$0.1303^{+0.0081}_{-0.0083}$	
CM/XUOR/VCE		$0.124^{+0.21}_{-0.077} \times 10^{-2}$	$1.421^{+0.086}_{-0.082}$	$15.32^{+0.69}_{-0.63} \times 10^{50}$	$0.2073^{+0.0049}_{-0.0046}$	
TS/XUOR/VCE	$46.8^{+1.3}_{-1.6}$			$10.84^{+0.46}_{-0.43} \times 10^{50}$	0.2992 ± 0.0057	
WM/XUOR/VCE		$(6.27 \pm 0.91) \times 10^{-4}$	$49.26^{+0.33}_{-0.47}$	$4.09^{+0.13}_{-0.13} \times 10^{51}$	$0.2735^{+0.0057}_{-0.0054}$	
CM/XUOR/VCL		$(0.17 \pm 0.11) \times 10^{-2}$	0.786 ± 0.058	$8.78^{+0.53}_{-0.44} \times 10^{50}$	$0.2263^{+0.0072}_{-0.0071}$	
TS/XUOR/VCL	$48.21^{+0.79}_{-1.2}$			$9.38^{+0.34}_{-0.34} \times 10^{50}$	0.2996 ± 0.0072	
WM/XUOR/VCL		$3.84^{+0.10}_{-0.11} \times 10^{1}$	$43.3^{+2.7}_{-3.4}$	$3.98^{+0.45}_{-0.45} \times 10^{54}$	$0.5734^{+0.0071}_{-0.0074}$	

2.3 Global view of all performed fits

The results for the complete grid of fits are shown in these Appendices. This grid consists of different cuts in wavelength and time in order to get useful additional information that clarifies some details of the physical nature of the afterglow and systematic uncertainties.

To test the constraining power of each wavelength range, we split the data into three subsets: X-rays, [UV/]optical/nIR[1], and submm/mm. These were then fitted individually and also in sets of two.

We found that the optical light curves were best fit with the TS and WM model, where the early steep decay and the bump at around 0.3 days is easily explained. The TS model was slightly better, mostly due to a better fit to the early *white+v* band data. The TS model also does a better job of predicting the XRT and radio data while the WM model is orders of magnitude off. The CM model does not do as well with the optical data, a large energy injection in combination with a low value for p does a reasonable job at explaining the late light curves, but the early *white+v* band data is not explained. The CM model also fares better with predicting the XRT and radio/sub-mm data, although it is obviously not able to reproduce them completely.

The fit to the radio data is less discriminating, the WM models are better than both the TS and CM models, but only marginally. The parameters for the WM and TS models are very similar and the energy injection and wind termination shock both happen at late times to improve the fit to the late radio points. The CM model stands out from the group with the energy injection happening at early times and is therefore the worst offender at late times. The CM model, however, is best at predicting the optical and X-ray data and roughly goes through the late time optical/nIR curves and the XRT curves. The WM and TS model under-predict those same data, with the WM model being the worst offender. Early observations would helped in constraining better modeled light curves.

No attempt was made at fitting the XRT light curve only, but when we add it to the mix with either the optical/NIR or the radio/sub-mm data things change considerably. For the former set it is now the TS model that is best, trailed by the CM and then the WM model. None of the models now explain the bump in the optical light curves, but at least the TS model explains the wiggles in the XRT light curve. The early *white+v* optical data are also not explained. In this case, the TS and WM models do a fairly good job of predicting the radio/sub-mm data, but the CM model is way off. For the latter set of XRT and radio/sub-mm we get a pretty consistent picture of the three models. The TS model is best, trailed by the CM model and finally the WM model like for the

---

[1] We include in the UV UVOT filters uvw1, uvw2, uvm2, and u

entire set. The resulting parameter distributions are actually fairly close to the results of the entire dataset, indicating that the additional information from the optical data does not constrain the model much. All of the models actually predict the optical data reasonably well and the full fit gives only small visible changes. This means that the large spectral lever arm added to the very fine temporal sampling of the XRT light curves is most constraining for the model.

Our final combination is the UV/radio/sub-mm and optical/NIR data together. Here the CM model shows the best fit, which fairs similarly to the WM, and significantly better fit than TS model. None of them is able to explain the bump in optical, but the early optical and early radio/sub-mm data is well explained by the TS model. All of the models approximately predict the XRT light curve but with some offset in the temporal behaviour. There is therefore little additional constraining power in the spectral information from the XRT data, but mostly from the very detailed time behavior.

In conclusion, it seems that the fine sampling in the XRT light curve with the large spectral lever arm of the radio and sub-mm data is the most constraining data for the models. We also note that the inferred physical conditions can vary up to few orders of magnitude depending on the model and the wavelength ranges considered. Therefore, observational sampling is fundamental in order to discriminate different models and constrain its physical parameters.

Due to the high Galactic dust extinction, and hence large uncertainty, we excluded the upper limits from the UV filters of UVOT as well observations using its u-band filter. None of the models are able to accurately reproduce those data points, either when included in the fit or not.

To reduce the bias from the early UVOT *white+v* band points that can be caused by a reverse shock (RS; e.g., Jelínek *et al.*, 2006; Laskar *et al.*, 2013a), we redo the analysis with all optical points before 0.005 days turned into upper limits. The parameters of the models are mostly unchanged with this exclusions of the data. A notable exception are the values of ϵ_e, ϵ_i, and ϵ_B. ϵ_B is reduced significantly while both ϵ_e and ϵ_i increase. This affects the determined host extinction which is now determined to be twice as large. The models are still unable to reproduce the data and most of the comments still apply. The contribution of a reverse shock may help to explain the early evolution in the *white* filter and/or the early sub-mm light curve, but will not help with the rest of the data. Thus the early *white* band data is not the driving cause for the models not being able to reproduce the bump.

One possibility that has often been proposed to model complex GRB light curves is the double jet model (e.g. Filgas *et al.*, 2011; Racusin *et al.*, 2008; Starling *et al.*, 2005; van der

Horst *et al.*, 2014), the early light curve being dominated by a fast moving narrow jet while a slow moving wide jet dominates at late time. This can be considered the simplest model for a two dimensional jet. To test if this is the case here, we fit the data after 0.5 days only, turning all other points into upper limits. The TS model is still the best model in this case and it is mostly able to explain the optical and X-ray bump at 0.3 days, but all the other considerations still apply and the radio/sub-mm data is still poorly modeled. We therefore conclude that a double jet model is not appropriate for this case.

Chapter 3

Conclusions

- We present an extensive follow-up of the afterglow of GRB 110715A in 17 bands ranging from a few seconds up to 74 days after the trigger. The line of sight is affected by strong foreground Galactic extinction, which complicated the follow-up and the analysis of the data.

- GRB 110715A had a very bright afterglow at all wavelengths, although its intrinsic luminosity is not exceptional.

- Optical/nIR spectroscopy obtained with X-shooter shows weak absorption features at a redshift of $z = 0.8224$ with no resolved velocity components ($\lesssim 30$ km s^{-1}). Absorption line ratios indicate a low ionization environment, confirmed by the rare detection of Ca I.

- Deep late imaging reveals a faint host galaxy with an absolute magnitude of $\mathrm{M}_B =$ -18.2. This is consistent with the weak absorption features detected in the spectrum.

- We attempted to model the broadband data with a fireball model based on the prescription of Jóhannesson *et al.* (2006). The best model implies a forward shock evolving through a wind environment with a termination shock. In spite of describing roughly the behavior of the afterglow, none of the models is able to get a statistically acceptable fit. This shows the need for better broadband sampling and more complex models to accurately describe the physics of GRB afterglows. There are several works that explore other possibilities, such as magneto-hydrodynamic simulations (van Eerten *et al.*, 2012), which was satisfactorily used, e.g., in Guidorzi *et al.* (2014); Ryan *et al.* (2015); Zhang *et al.* (2015), or central engine activities (Zhang *et al.*, 2014). These and other effects might be considered together in future works to get a more accurate view of the GRB afterglow physics.

- Radio and sub-mm, along with X-ray observations, have been proven to be the most constraining bands for the afterglow modeling. We were limited by sensitivity for a long time in the crucial wavelength range of sub-mm, but now that ALMA is available, we have a good chance of getting high-quality data for a larger number of GRBs. This new, current and future facilities will allow us to probe the emission mechanisms in greater detail than previously possible, and will be determinant in the evolution of the GRB afterglow models.

PART II

ABSORPTION SYSTEMS IN THE LINE OF SIGHT TO GRBS:

THE TALE-END OF THE REIONIZATION EPOCH

Chapter 1

Introduction

> *"It is, indeed an incredible fact that what the human mind, at its deepest and most profound, perceives as beautiful finds its realization in external nature.... What is intelligible is also beautiful."*
>
> — Subrahmanyan Chandrasekhar, *Beauty and the Quest for Beauty in Science, 1979*

These sources are described in the next sections.

1.1 The reionisation epoch

1.1.1 High redshift galaxies as the source of reionisation

IGM was almost completely ionized up to $z{\sim}6$. This places a minimum requirement of the number of UV ionizing photons to maintain atoms ionized

$$\dot{\mathcal{N}}_{ion}(z) = 10^{51.2} s^{-1} Mpc^{-3} \left(\frac{C}{30}\right) \times \left(\frac{1+z}{6}\right)^3 \left(\frac{\Omega_b h^2}{0.02}\right)^2 \tag{1.1}$$

where $C \equiv \frac{\langle n_H^2 \rangle}{\langle n_H \rangle^2}$ is the clumping factor of the IGM (Miralda-Escudé *et al.*, 2000).

As AGN population at high redshift shows a rapid decline, it is commonly assumed that stellar sources reionised the Universe. Robertson *et al.* (2010).

There are three uncertainties sources to come from: SFR, clumping factor and UV scape fraction.

In order to determine SFR

Determination of the escape fraction remains a key challenge.

1.1.2 QSOs as probes for the study of the reionization epoch

By mid-2012 only 33 QSOs at $z_{\rm em}>6$ (Fig.), most of them discovered using wide-field surveys such as Sloan Digital Sky Survey (SDSS**ref**), the Canadian-French High-z Quasar Survey (CFHQS; Willott *et al.*, 2010), and the UK Infrared Deep Sky Survey (UKIDSS; Mortlock *et al.*, 2009).

Currently, the highest redshift quasar is at z=7.085 (Mortlock *et al.*, 2011).

The density of luminous quasars is a strong function of redshift (see Fig. , and, e.g., Boyle *et al.*, 2000). Compared to the evolution of SFR, QSO density peaks at higher redshifts and evolves much faster. In mentioned figure, we observe that quasar density at $z{\sim}6$ is consistent with the extrapolation of the QSO luminosity function from redshifts 3 to 5, indicating a value ∼40 times smaller than at $z{\sim}3$. However, highest redshift quasars are among the most luminous quasars at any redshift, with black hole masses ranging from 10^8 to 10^9 $\rm M_\odot$.

The average SEDs of luminous quasars show little evolution in the UV (rest frame) out to high redshift, as well as their metallicities (e.g., De Rosa *et al.*, 2011; Fan *et al.*, 2004). This lack of evolution demonstrate that the emission line region and the accretion disk are not related with the cosmic environment.

However, it was observed some QSOs at high redshift with *Spitzer* that show no dust emission in the FIR down to a faint limit (Jiang *et al.*, 2010). Therefore, these quasars are at a very early evolutionary stage, and they are likely first generation quasars born in dust-free environment and too young to have a detectable amount of dust.

FIR to millimeter continuum observations suggest an enormous SFR (10^2 - 10^3 $M_\odot$ YR^{-1} Wang *et al.*, 2008), also supported by very strong metal emission lines. Radio-line observations of bright sub-millimeter quasars at z~6 detected strong CO emission in their host galaxies (e.g., Wang *et al.*, 2010). They found molecular masses ~10^{10} $M_\odot$ and a deviation from the black hole - bulge mass (M-σ) relation of a factor 15 above, indicating that black holes grow much faster than their host galaxy assembling.

1.1.3 GRBs as probes for the study of the reionization epoch

GRBs can be detected at $z>10$. At such redshifts, time dilation makes that their afterglows fill fade $(1 + z)$ times slower, and consequently it is easier follow up them (e.g. Ciardi & Loeb, 2000)

Since the recombination epoch (z~1200 Komatsu *et al.*, 2011) the Universe became mostly neutral, i.e., it started the so called (*dark ages* Rees, 1998). From z~50 the first generation of dark matter halos with $\sim 10^6 M_\odot$ formed, making that barions collapsed, and then originating the first generation, or Population III (Pop-III) stars by z~20-30, and characterized mainly by a zero metallicity and masses ranging 30-100$M_\odot$ (Abel *et al.*, 2002; Yoshida *et al.*, 2006).

The main consequence of the born of these Pop-III stars is that, as they were a powerful UV emitters, they provided an important radiative feedback by ionizing the surrounding ISM and even IGM. Consequently, the death of them also produced the first ISM chemical enrichment by super/hyper-nova, as well as the first black holes and AGN. Furthermore, it also meant the beginning of the *cosmic reionization* (Dunkley *et al.*, 2009). Therefore, one of the key questions in modern cosmology is the understanding of the processes that conducted to the end of the dark ages by the first stars and galaxies (e.g. Barkana & Loeb, 2001; Bromm *et al.*, 2009). Formation of the first galaxies was delayed until more massive halos became available (Bromm & Yoshida, 2011). Since this epoch, the Universe started to change rapidly due to the input of ionizing radiation and heavy elements. This fundamental process, as well as the assembly process of the first galaxies are strongly dependent on the feedback exerted by Pop III stars, that is determined by their IMF (e.g. Glover, 2005).

1.2 The first stars

Current view is that the physical conditions in the early Universe favored an IMF for the Pop III stars biased towards top-heavy, i.e., massive stars were predominant (Abel *et al.*, 2002; Bromm & Larson, 2004; Bromm *et al.*, 2002). This is due to the less cooling efficiency in pure H/He gas, reaching temperatures of ∼200K in contrast to ∼10K in dusty molecular clouds. Another important fact is that these stars were formed typically in isolation, one per mini-halo. Recent works have refined this paradigm and confirmed the basic prediction, that is that the first stars were typically massive (few tens of solar masses) and few of them formed as a member of multiple systems with $>100\mathrm{M}_\odot$, but still the final mass of Pop III stars and their final IMF remains largely uncertain (Hosokawa *et al.*, 2011; McKee & Tan, 2008; Stacy *et al.*, 2012).

A crucial uncertainty is the physical mechanism responsible for the Pop III to II transition. Current thinking is that it was driven by chemical feedback, estimating a $Z_{crit} \sim 10^{-4}\mathrm{Z}_\odot$. The underlying physics is really complex, resulting in some models claiming that C I and fine-structure levels of O I may drive this transition (Bromm & Loeb, 2003), and others identifying dust cooling as the key agent (Schneider *et al.*, 2006).

1.2.1 Are Pop III stars GRB progenitors?

Conditions to trigger a collapsar (Woosley, 1993) event are quite stringent and often difficult to fulfill simultaneously (e.g. Belczynski *et al.*, 2007). The hardest requirement is that they must have enough angular momentum. Almost nothing is still known on this, but a first attempt has recently carried out by Stacy *et al.* (2011, 2013), showing that they could be be typically fast rotators. Thus, it is plausible that LGRBs occur in the early Universe.

In order to estimate the GRB rate at very high redshifts, Bromm & Loeb (2006) used

$$\frac{dN^{obs}_{GRB}}{dz} = \phi^{obs}_{GRB}(z)\frac{\Delta t_{obs}}{1+z}\frac{dV}{dz} \tag{1.2}$$

where $dN^{obs}_{GRB}dz$ is the number of GRBs within the interval dz, and $\phi^{obs}_{GRB}(z)$ the number of bursts per comoving volume

$$\phi^{obs}_{GRB}(z) = \eta_{GRB}\phi_*(z) \int\limits_{L_{lim(z)}}^{\infty} p(L)dL \tag{1.3}$$

where η_{GRB} is the GRB formation efficiency, $\phi_*(z)$ the cosmic SFRD, $p(L)$ the GRB luminosity function, and $L_{lim(z)}$ the minimum intrinsic luminosity required to detect a burst at a given redshift with a given instrument. Numbers for the *Swift* capabilities are not promising, but we could be lucky...

Chapter 2

GRB140304A

Adapted from "GRB 140304A"

— Jeong, Sánchez-Ramírez et al., *A&A, in preparation*

2.1 Observations

2.1.1 *Swift* observations

At 13:22:31 UT, the *Swift*/BAT triggered and located GRB 140304A. *Swift* slewed immediately to the burst. The BAT on-board calculated location is RA($J2000$) = 02h 02m 40s, Dec($J2000$) = +33d 29$'$07”with an uncertainty of 3$'$(radius, 90% containment, including systematic uncertainty). The BAT light curve showed a multi-peaked structure with a total duration of about 20 sec. The peak count rate was ∼3600 counts/sec (15-350 keV), at ∼0 sec after the trigger.

The XRT began observing the field at 13:23:46.2 UT, 75.2 seconds after the BAT trigger. Using promptly downlinked data a bright, uncatalogued X-ray source is found with an enhanced position RA($J2000$) = 02h 02m 33.90s Dec($J2000$) = +33d 28$'$27.9”with an uncertainty of 2.2”(radius, 90

UVOT took a finding chart exposure of 250 seconds with the U filter starting 137 seconds after the BAT trigger. No credible afterglow candidate has been found in the initial data products.

2.1.2 INTEGRAL/SPI-ACS observations

We additionally collected data from the SPI-ACS experiment onboard *INTEGRAL* observatory, which is sensitive to the energy range >80 keV. First results are consistent with those from *Swift*/BAT: there is a weak hard activity in the energy range >80 keV corresponding to the GRB prompt emission, but there is no credible emission in this energy range in the X-rays. However, in the source reference frame this energy range corresponds to $80 \times (1+z) \sim 500$ keV, and so it is typical for long duration GRBs.

2.1.3 Optical imaging

We performed the optical follow-up of GRB 140304A with BOOTES 4, MASTER II, and Harold L. Johnson telescopes.

2.1.4 Optical spectroscopy

We took optical spectra with OSIRIS at the 10.4m Gran Telescopio de Canarias (GTC). Observations started on Mar 04, 2014, i.e. ∼ 7.36 h after the *Swift* trigger, using the

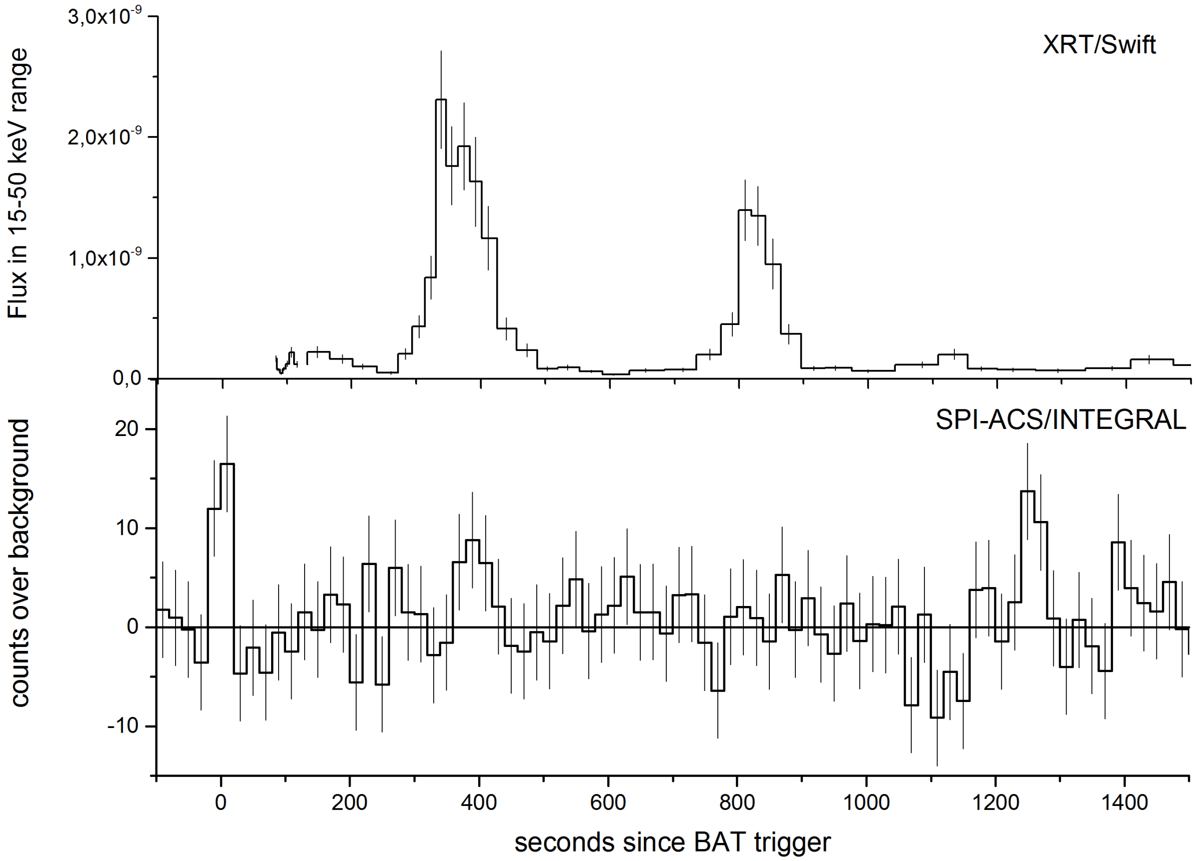

Figure 2.1: Flaring activity observed by *Swift* and *INTEGRAL*.

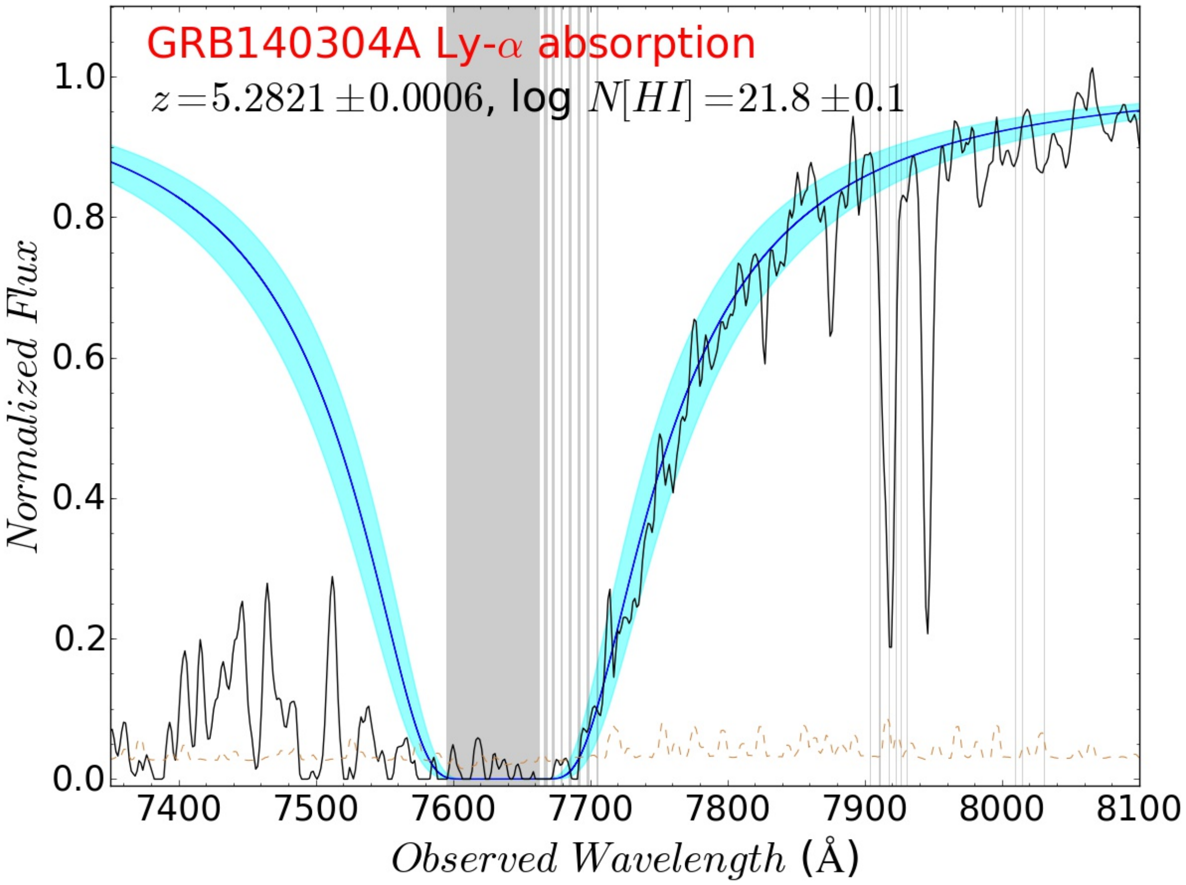

Figure 2.2: Voigt profile fit to the Lyα red damping wing absorption towards GRB 140304A. Solid cyan area represents the 68% confidence interval.

R2500I volume-phased holographic grating (VPH), and consisted in 2 × 1200 s exposures. The 1.0”slit was positioned on the location of the host galaxy in paralactic angle. The spectra were reduced and calibrated following standard procedures using custom tools based in IRAF and Python. They had been flux calibrated using observations of the spectrophotometic standard star HILT600, observed in the same night with a 2.52”slit. We renormalised the flux level in order to correct for slit losses using the photometric value obtained from the acquisition image.

2.2 Results and Discussion

2.2.1 Hydrogen abundance

Our GTC combined spectrum exhibits a clear broad Lyα absorption at $z \sim 5.283$ (Jeong *et al.*, 2014). We fitted this damped feature using the same prescription and tools as in

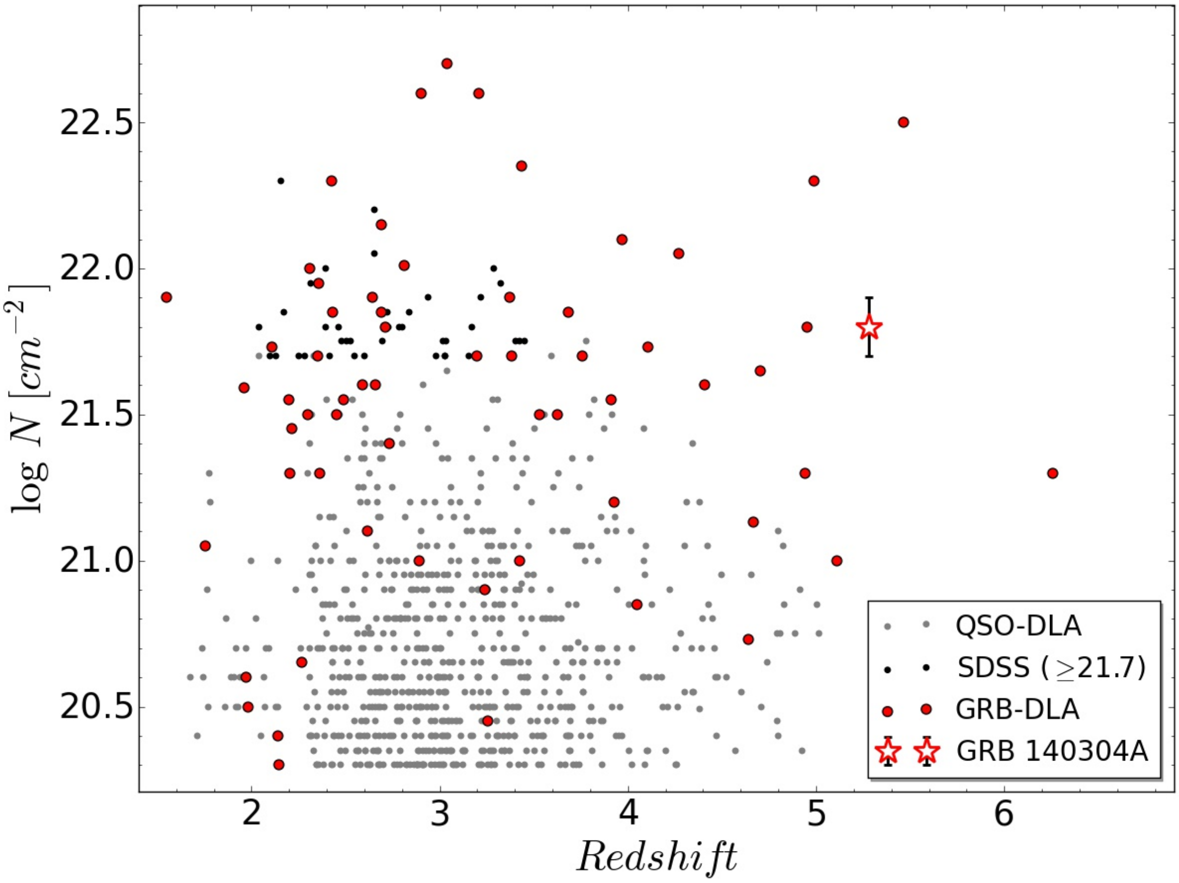

Figure 2.3: Comparison of the measured column density of the GRB 140304A DLA with the GRB-DLA compilation by Cucchiara *et al.* (2015) and the QSO-DLA one by Sánchez-Ramírez *et al.* (2016). QSO-DLA information is complemented with the $\log N(\text{H I}) \geq 21.7$ DLAs from the SDSS sample (Noterdaeme *et al.*, 2012). The error bar represents the 68% confidence interval.

Sánchez-Ramírez *et al.* (2016), obtaining log N(H I)= 21.8 ± 0.1 (see Fig. 2.2). Due to the wavelength range covered by the spectrum, higher order Lyman series could not be fitted, which reduces the chances of overestimating the Hydrogen column density (e.g. Crighton *et al.*, 2015; Sánchez-Ramírez *et al.*, 2016). However, GRB sight lines benefit from little absorption in the red damped wing. Therefore, if the continuum is well determined, the model fitting to this wing provides a robust way for the N(H I) determination.

In Fig. 2.3, we place this result into context, comparing it with the GRB-DLA compilation by Cucchiara *et al.* (2015), which extend previous works by, e.g., Schady *et al.* (2011); Thöne *et al.* (2013), and QSO-DLA (Sánchez-Ramírez *et al.*, 2016) populations. We chose the latter QSO-DLA compilation (with a combined total of 742 systems, see Part 3 of this Thesis), instead of the larger SDSS sample (over 3 400 DLA systems in the statistical sample), because the SDSS DLA catalogue is strongly affected by systematics, and contains many false positives (Noterdaeme *et al.*, 2012). The compilation by Sánchez-Ramírez *et al.* (2016) takes only visually confirmed DLAs, which reduces the effect of systematics, so its distribution is more representative of the actual DLA population. However, we include in Fig. 2.3 log N(H I)≥21.7 DLAs from the SDSS sample to remark the fact that the detection of these high column density systems is very rare towards QSO lines of sight. Indeed, the number of observed intervening DLAs had to be of a few thousand before one starts to detect log N(H I)$\gtrsim$ 22 absorbers (Noterdaeme *et al.*, 2009, 2012), values easily found towards GRB sightlines (e.g., de Ugarte Postigo *et al.*, 2012a; Fynbo *et al.*, 2009; Jakobsson *et al.*, 2006; Schady *et al.*, 2011; Thöne *et al.*, 2013). Our measurement is the third farthest DLA detected to date, and a new evidence that GRB and QSO DLA samples are drawn from different populations. GRB-DLAs are selected by the GRB γ-ray emission, which are thought to be produced in the cores of star forming regions, whereas QSO-DLAs are random lines of sight that pierce intervening systems, so most likely the probe halo clouds.

2.2.2 Metal abundances

A series of absorption lines due to different species (S, Si, O, and C) are clearly detected at the same redshift of the Lyα feature, as well as at least one intervening C IV system at $z = 4.3403 \pm 0.0001$. A plot of the GTC spectrum and line identifications is provided in Fig. 3.7. We measured the equivalent widths (EWs) of the lines fitting Gaussians profiles and computing the sum over the line model. This approximation is in our case valid due to the low resolution of the GTC/OSIRIS spectrum, as the convolution of the instrumental profile with the actual Voigt profile makes the absorption remain approximately Gaussian. Furthermore, using this method we can estimate the redshift and EW of each blended

Table 2.1: EW measurements for the systems detected on the GRB 140304A afterglow spectrum.

Feature	Wavelength	z	EW	eEW
SIIλ1254	7875.5	5.2813	0.23	0.04
SIIλ1260	7913.4	5.2829	0.42	0.01
SiIIλ1260	7919.3	5.2831	0.85	0.03
SiII*λ1265	7945.8	5.2825	1.03	0.03
SiIIλ1304	-	-	-	-
SiII*λ1309	8224.6	5.2818	0.49	0.01
CIIλ1334	8383.5	5.2820	0.86	0.02
CII*λ1336	8390.1	5.2814	0.85	0.02
SiIVλ1394	8755.0	5.2816	0.65	0.04
SiIVλ1403	8812.1	5.2819	0.50	0.05
CIVλ1548	8267.9	4.3403	0.64	0.02
CIVλ1551	8281.6	4.3403	0.50	0.02

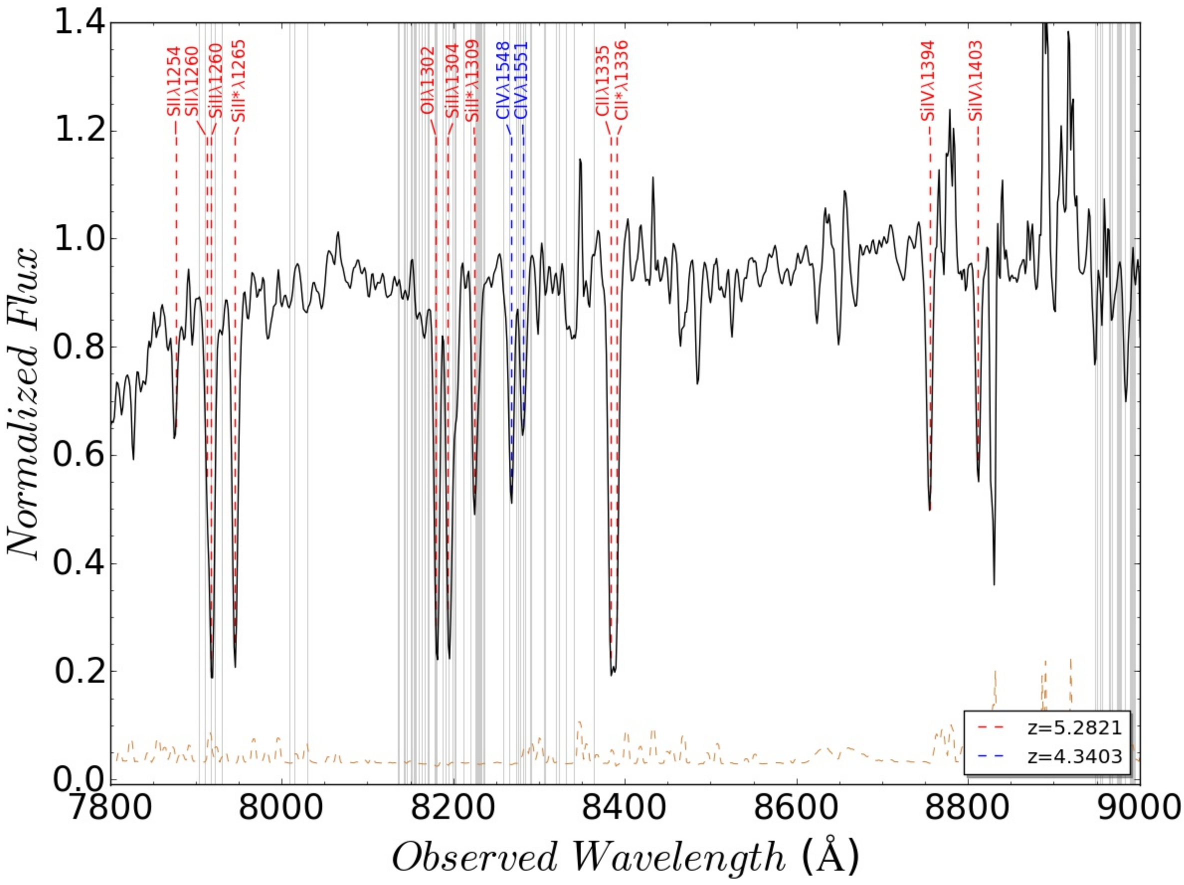

Figure 2.4: Lines detected on the GTC optical spectrum.

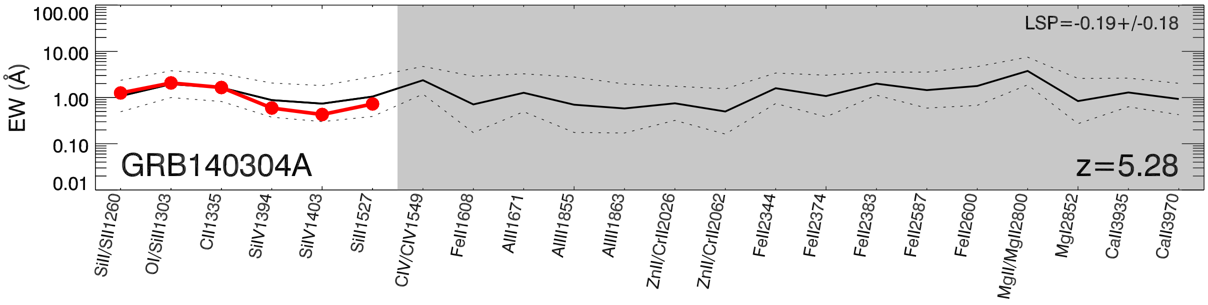

Figure 2.5: Line strength diagram of GRB 140304A, based on the prescription of de Ugarte Postigo *et al.* (2012a).the line strengths of GRB 140304A are shown in red, and compared with the sample of GRB spectra in black. The sample average strengths are shown by a black line, whereas dotted lines show the 1-sigma deviations. The shaded area corresponds to lines that were not covered by our spectrum, or strongly affected by telluric features.

Table 2.2: CoG MCMC fitting results.

Parameter	Median	95% c.i.
b_{eff}	$19.23^{+0.23}_{-0.41}$	[18.81, 20.25]
$\log N[S]$	$15.74^{+0.10}_{-0.07}$	[15.18, 16.77]
$\log N[Si^{*}]$	$17.12^{+0.01}_{-0.01}$	[17.06, 17.19]

feature. Results are presented in Table 2.1. With the redshifts obtained by the line fitting, we are able to refine the redshift up to $z = 5.2821 \pm 0.0006$. We excluded in this computation the Si IIλ1304 line, as it is blended with some unknown intervening feature and no constraint on this component can be imposed in order to perform an accurate deblending.

Using the prescription of de Ugarte Postigo *et al.* (2012a) we calculate the line strength parameter (LSP) of this spectrum, which can be used to compare the absorption features of this line of sight with those of a large sample of GRB afterglow spectra. We derive a LSP = -0.19±0.18, which implies features very similar to those of the sample, just slightly below the average, at a line strength percentile of 41 (41% of the sample has weaker features). In Fig. 2.5 we show line strength diagram in which line strengths are individually compared with the sample. There we see that the absorption lines are almost on the average of the sample, with the exception of the Si IV lines which are slightly below, probably indicating a slightly lower than average ionisation field in the host galaxy of GRB 140304A.

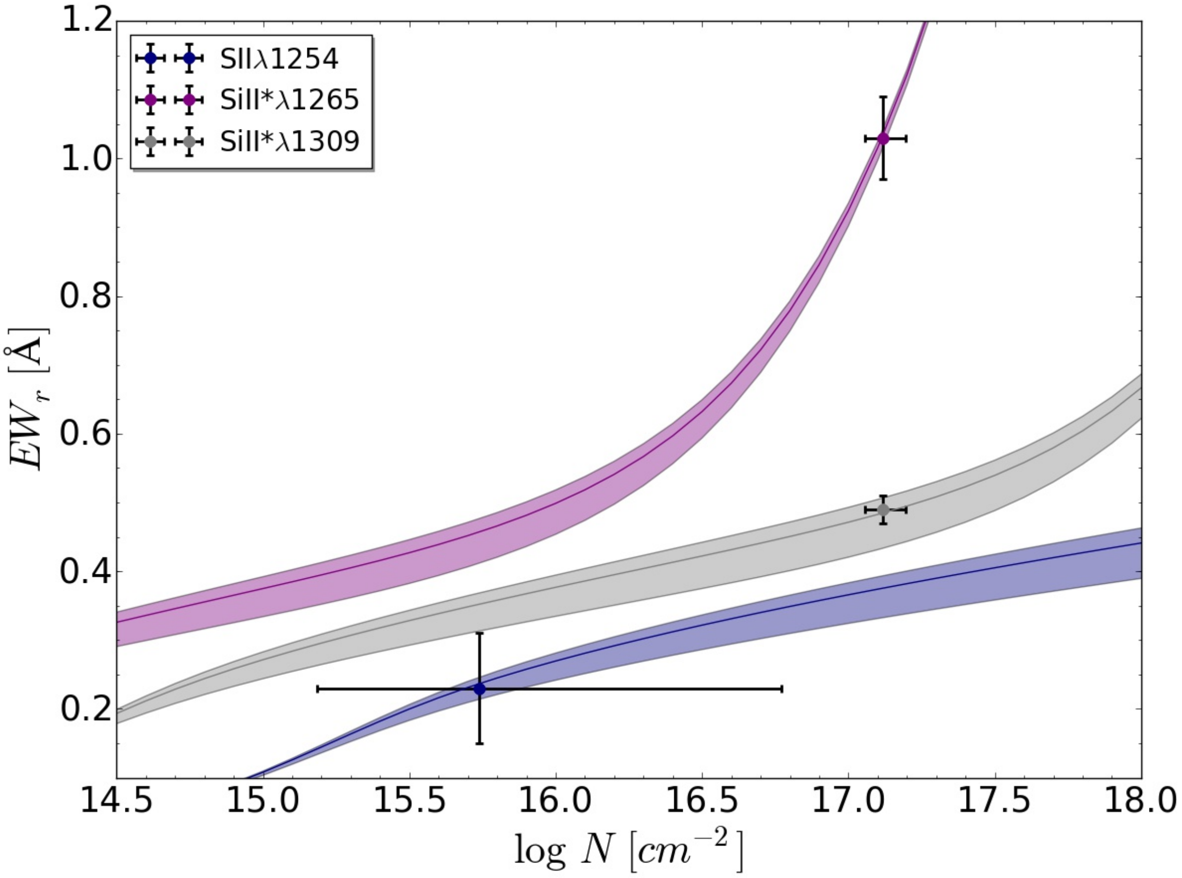

Figure 2.6: CoG analysis for the 3 features selected to estimate the metallicity of the GRB environment. Errors are represented at 95% confidence level.

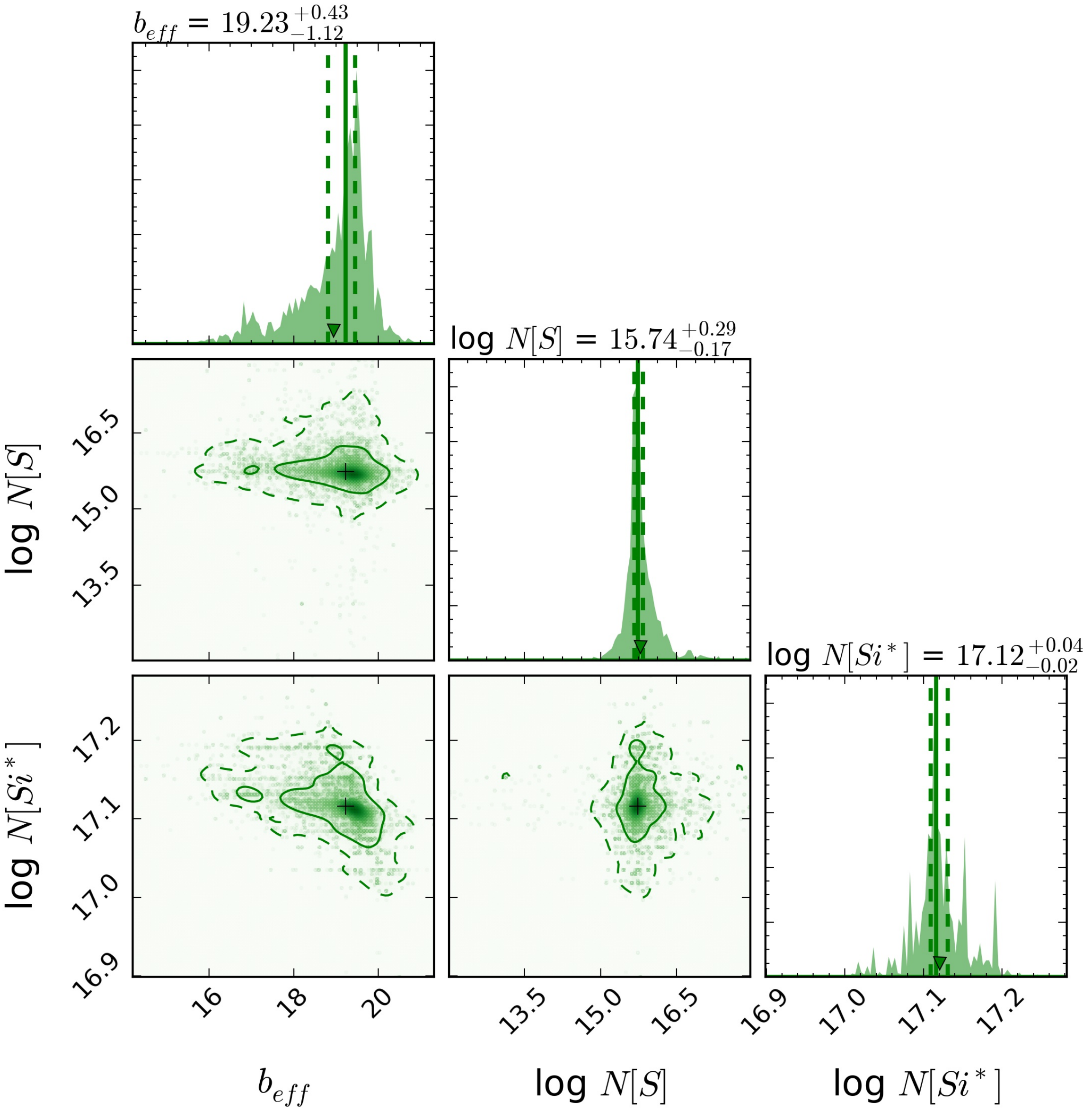

Figure 2.7: Posterior distributions of the fitted parameters. We plot the 95% confidence intervals, and dashed vertical lines limit the 68% area. Median values are marked in orange.

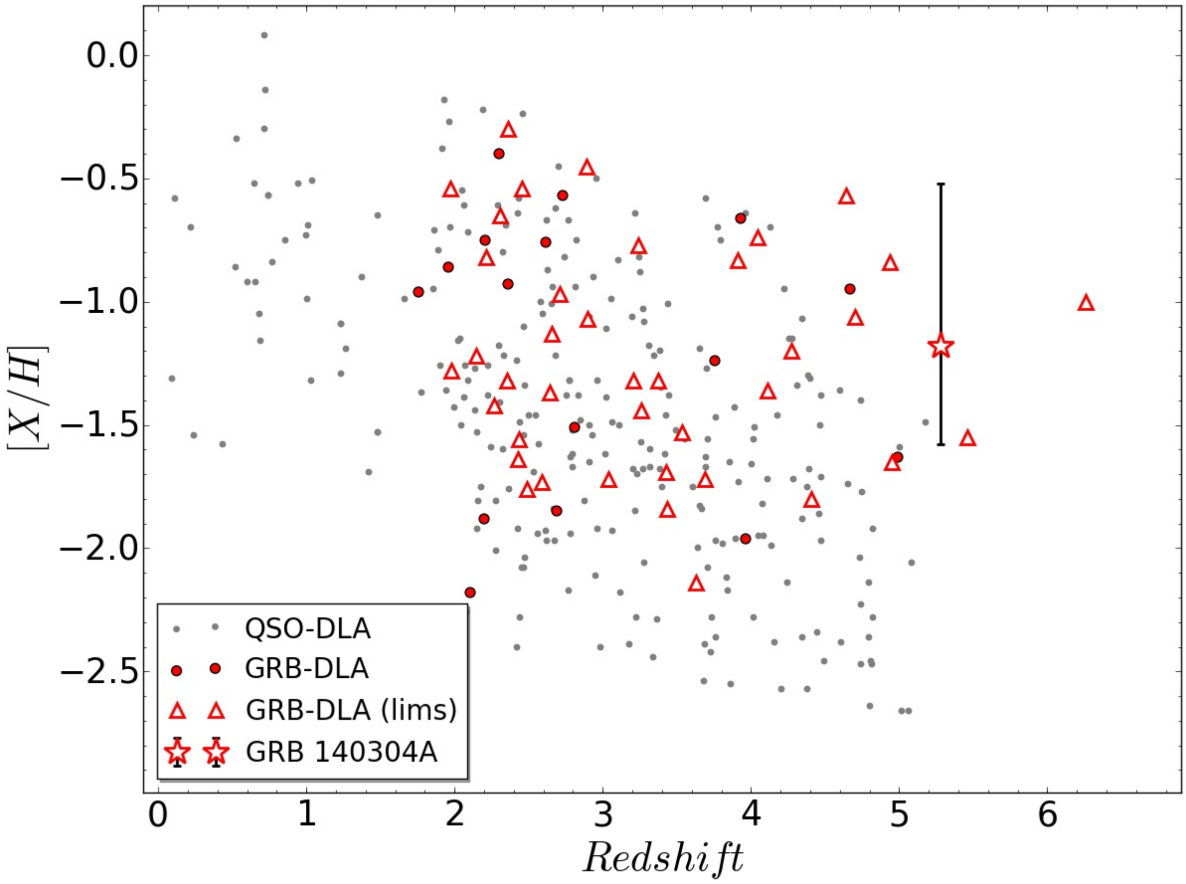

Figure 2.8: Comparison of the measured metallicity of the GRB 140304A DLA with the GRB-DLA compilation by Cucchiara *et al.* (2015); Thöne *et al.* (2013) and the QSO-DLA one by Rafelski *et al.* (2012, 2014). The error bar represents the 95% confidence interval.

2.2.3 Metallicity estimation

We estimate the metallicity of the GRB environment using a novel technique based on the Curve of Growth (CoG) analysis (**ref**). As we cannot perform direct Voigt profile fitting on low resolution spectra, and we don't have available a weak enough line (within the linear regime) to directly measure the abundance, this method uses EW measurements as alternative to constrain b and $\log N[X]$. However, Prochaska (2006) already pointed out that this kind of analysis can underestimate severely column density determinations because in strong transitions the blending of the GRB environment absorption with near weaker systems leads to EW overestimates and unphysically high fitted b values. In order to avoid this issue, we took benefit of the observed Si II* transitions. This is because, in spite of being strong transitions, the fine-structure excited population originates from the UV radiation due to the GRB afterglow, which generally results in close component features, as only the clouds that are whithin few kpc to the GRB are excited. Furthermore, we assume that the low ionisation absorption comes from the same system than Si II*. This scenario can be supported by, e.g., the results of GRB 080310 (De Cia *et al.*, 2012), but we caution that it has not necessarily be true for this line of sight. For the metallicity estimator we chose the S IIλ1254 feature, as it is the weakest unblended line available on our spectrum.

Driven by the limitations that our feature selection imposes to the fit, as we have 3 points for 3 unknown parameters (b_{eff}, $\log N[S]$, and $\log N[Si^*]$), we decided to perform a Markov Chain Monte-Carlo analysis of the CoG of each feature by using *pymc*. This Bayesian approach can take profit of the prior knowledge we have on the parameters. We opted for uninformative flat prior distributions for the column density, limiting their values from 5 to 23. However, following de Ugarte Postigo *et al.* (2012a), we assumed that b_{eff} is log-normally distributed as they found from high resolution studies. On this way, we restrict the possibility that b_{eff} takes unrealistic values along the iterations due to contamination in a given feature (Prochaska, 2006). Due to resolution and SNR limitations, the implementation of more complex models, e.g., with a few velocity components, will not improve the results. For the fitting function (the model to fit with *pymc*), we coded up a routine that, given any value of the incoming parameters (b_{eff} and N), it computes as the output the EW of a synthetic Voigt profile generated with these parameters.

The results of the fit are displayed in Table 2.2. We performed several test to check for the convergence of the procedure, that showed positive results. Moreover, in Fig. 2.7 we see that posterior distributions are well behaved, showing only little skewness in the b_{eff} distribution. In Fig. 2.6 we represent each feature and its CoG, showing errors at 95% confidence level. This plot shows clearly that Si II*λ1265 (a strong feature with an oscillator strength value $f = 1.05$) is at the beginning of the damped regime, so the column density of the excited Silicon is accurately constrained by this line. Consequently, b_{eff} fit is mainly driven by Si II*λ1309. However, the poor constraint on EW of the S IIλ1254 line, with the fact that it is mildly saturated, make that Sulphur abundance cannot be determined with a similar precision as excited Silicon. Looking at Fig. 2.7, we can observe that there is only an expected mild correlation between b_{eff} and $\log N[Si^{*}]$, but not for b_{eff} and $\log N[S]$, most likely due to the uncertainty in the EW measurement. Probably, this would explain why Si II*λ1309 is not able to be as constraining as expected to estimate b_{eff}.

Using the Sulphur abundance, which is a non-refractory element and thus will not be substantially depleted onto dust (Savage & Sembach, 1991), we obtain $[S/H] = -1.13^{+0.10}_{-0.07}$ with a probability of 95% that the value falls between $[-1.49, -0.52]$. This posterior metallicity distribution was obtained performing a Monte-Carlo simulation with the S distribution coming from the MCMC fit, and assuming normal distributions for the errors of all the other parameters but the Solar Hydrogen abundance (Asplund *et al.*, 2009). In Fig. 2.8 we place the GRB 140403A point (star) among the GRB-DLA sample compiled by Cucchiara *et al.* (2015) and the high resolution QSO-DLA sample from Rafelski *et al.* (2012, 2014). The GRB sample is clearly dominated by limits, making it difficult to derive robust conclusions. However, the Figure suggest that GRB metallicities did not substantially evolve with redshift, matching both GRB-DLA and QSO-DLA populations at low- but not at high-redshift. Our new measurement is therefore consistent with the non evolution picture of the metal content in star forming regions up to $z \sim 5$.

2.3 Conclusions

- We detect a Damped Lyman-α system at $z = 5.2821 \pm 0.1$ on the optical spectra towards GRB 140304A. This is the third farthest DLA detected to date. The Voigt profile fitting give a column density value of $\log N(\text{H I}) = 21.8 \pm 0.1$.
- There are several absorption lines at the same redshift as the Lyα absorption due to S, Si, O, and C, as well as at least one C IV intervening system.
- We measured the EW of the lines and compared them with the results from de Ugarte Postigo *et al.* (2012a), finding that the 41% of the sample has weaker features.
- We estimated the metal abundances of the S II and Si II* ions by using a novel technique based on the CoG method and the Bayesian inference, finding acceptable results.

- We obtained $[S/H] = -1.13^{+0.10}_{-0.07}$, a value consistent with the non evolution picture of the metal content in star forming regions up to $z{\sim}5$.

Chapter 3

GRB 130606A

Adapted from "GRB 130606A within a sub-DLA at redshift 5.91"

— Castro-Tirado, Sánchez-Ramírez et al., *A&A, submitted*

3.1 Introduction

The detection of individual Population III (Pop III Bromm *et al.*, 2009) stars, either extant in the Galactic halo or at the moment of their deaths, as highly energetic supernova explosions (Mackey *et al.*, 2003) or as gamma-ray bursts (Bromm *et al.*, 2002), is one of the most challenging and profound objectives in modern observational astronomy. It is widely accepted that massive Pop III stars should be viable GRB progenitors (Bromm & Loeb, 2006) and potentially observable out to very high redshifts (Ciardi & Loeb, 2000; Lamb & Reichart, 2000). Such distant GRBs can serve as ideal background sources, with their extremely bright, featureless afterglow continuum emission, to illuminate the early intergalactic medium (IGM). At the earliest times, quasars become increasingly rare and faint to effectively play this role, but GRBs offer a potential window into the ionization and metal enrichment state of the IGM at very high redshifts.

It has been recently suggested (Cooke *et al.*, 2011a,b; Fabbian *et al.*, 2009) that very metal-poor damped Lyman-alpha (DLA) systems (regions of high column density of neutral gas at high redshifts (Wolfe *et al.*, 2005) could bear the chemical signature of the first generation of stars, born a few hundred million years after the Big Bang.

Indeed, it has been suggested that metal-free regions persist to values of z $\leq$ 6, allowing Pop III stars with masses in the range 140-260 solar masses to be observed as pair-production instability supernovae (Scannapieco *et al.*, 2005), although a core-collapse (Type II) supernova instead is also plausible (Wang *et al.*, 2012). In spite of the fact that no GRB has so far been firmly associated with a Pop III collapse yet, the high z values found for several GRBs reinforces the potential of GRBs to provide bright background sources to illuminate the early intergalactic medium at a time when quasars are too rare and dim to serve this purpose.

A ∼275 s cosmic gamma-ray burst (GRB 130606A) was recorded by *Swift* and KONUS-*Wind* on 6 June 2013, 21:04:34 U.T. (T_0) (Barthelmy *et al.*, 2013; Golenetskii *et al.*, 2013), displaying a bright afterglow (the emission at other wavelengths following the gamma-rays) in X-rays, but no apparent optical transient emission (Ukwatta *et al.*, 2013) in the range of the UVOT telescope aboard *Swift*. The TELMA 0.6m diameter telescope at the BOOTES-2 station automatically responded to the alert and an optical counterpart was identified (Jelínek *et al.*, 2013), thanks to the spectral response of the detector up to 1 μm, longer than that of *Swift*/UVOT (0.17-0.65 μm).

The detection of the afterglow at BOOTES-2/TELMA prompted spectroscopic observations with the 10.4 m Gran Telescopio Canarias (GTC) starting 1.4 hr after the event, which revealed a very distant explosion at a very high redshift (z ∼ 6) (Castro-Tirado *et al.*, 2013c), a value later refined to z = 5.91 (Castro-Tirado *et al.*, 2013b), when the Universe was only ∼950 million years old.

3.2 Observations

3.2.1 X-ray observations

The *Swift* X-ray Telescope (XRT) started collecting data in window timing mode (WT) ∼60 s after the initial BAT trigger on June 6 at 21:05:35 U.T., switching to photon counting mode (PC) after ∼ 500s. The position of the source was monitored up to ∼ 3 × 10^5 s post-trigger. The data were processed using the *Swift* software v.2.6. A cleaned event file was generated using the default pipeline, which removes the effects of hot pixels and Earth brightness. From this cleaned event list, the source and background light curves and spectra were extracted from a region of 20" using xselect. In general, no pile-up was found in either the WT or the PC data. The data have been fit using a fixed Galactic column density at 2 × $10^{20}\,\mathrm{cm}^{-2}$ and a varying column density in the rest frame in the range 2-6 × $10^{22}\,\mathrm{cm}^{-2}$.

3.2.2 Optical/nIR Observations

3.2.2.1 Photometry

Early time prompt optical observations were carried out by the Watcher telescope starting on June 6, 21:06:49 U.T., i.e. ∼ 135 s after the first *Swift*/BAT trigger (T_0 = 21:04:34 UT). The BOOTES-2/TELMA observations, which resulted in the optical afterglow discovery, started on June 6, 21:17:33 U. T., i.e. ∼660 s after the first *Swift*/BAT trigger. The Watcher observations partially cover the second *Swift*/BAT peak. Additional Johnson R and V–band images were acquired with the 1.23m telescope of Calar Alto (CAHA) observatory, Spain. Late epoch optical observations were obtained with the 0.7m Abastumani Observatory, the AZT-11 (1.25m) telescope at SRI "Crimean Astrophysical Observatory", the T100 (1m) telescope at TÜBITAK National Observatory, the 1.5m OSN telescope at Observatorio de Sierra Nevada and with the 10.4m Gran Telescopio Canarias (GTC) equipped with the OSIRIS imaging spectrograph (Fig. 3.2). Optical photometry is based on isophotal corrected photometry by IRAF/PHOT31 against standard reference Landolt fields imaged at the 1.5m OSN telescope in order to provide reference stars in the field (Table 3.2).

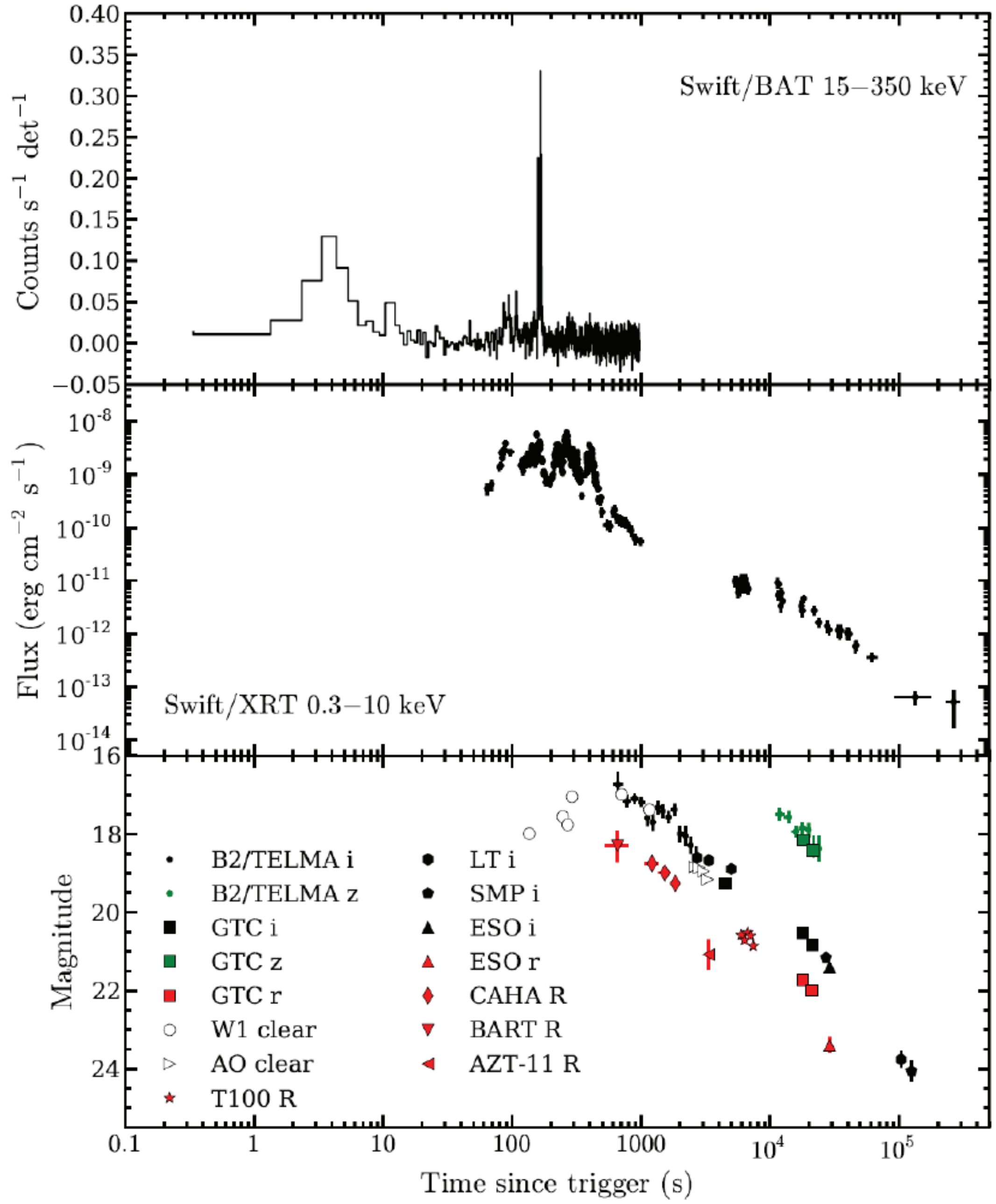

Figure 3.1: The GRB 130606A prompt gamma-ray emission and the multiwavelength afterglow evolution. The *Swift*/BAT light curve shows a double-peaked structure with the initial peak lasting ∼10 s and a brighter second peak at T_0+150 s of ∼20 s duration. The gamma-ray lightcurve is compared with the multiwavelength (X-ray, optical) GRB 130606A afterglow lightcurves. Significant temporal (and spectral) evolution is noticeable in the XRT data. The lower panel shows the rising optical afterglow lightcurve based on Watcher data, prior to the well sampled decay, based on the data gathered by BART, BOOTES-2/TELMA, 0.7m AO, T100, 1.23m CAHA, AZT-11, 1.5m OSN and 10.4m GTC (Table 3.1, complemented with other data published elsewhere; Afonso *et al.*, 2013; Butler *et al.*, 2013a,b; Virgili *et al.*, 2013a,b). 1σ error bars are plotted.

Table 3.1: Optical and near-IR observations gathered at several astronomical observatories worldwide. $VRIH$-band magnitudes are given in the Vega system whereas *clear* and Sloan-filter magnitudes are given in the AB system. Not corrected for Galactic extinction.

Start Time (JD) (a)	Magnitude	Filter	Telescope (b)
2456450.379734	17.99 ± 0.11	*clear*	0.4m Watcher
2456450.381019	17.55 ± 0.08	*clear*	0.4m Watcher
2456450.381273	17.76 ± 0.10	*clear*	0.4m Watcher
2456450.381528	17.04 ± 0.06	*clear*	0.4m Watcher
2456450.386308	16.99 ± 0.10	*clear*	0.4m Watcher
2456450.391528	17.38 ± 0.14	*clear*	0.4m Watcher
2456450.382210	>16.5	R	0.25m BART
2456450.38575	18.30 ± 0.40	R	0.25m BART
2456450.385800	16.73 ± 0.34	i'	0.6m TELMA
2456450.387112	17.16 ± 0.16	i'	0.6m TELMA
2456450.388424	17.10 ± 0.13	i'	0.6m TELMA
2456450.389742	17.18 ± 0.12	i'	0.6m TELMA
2456450.391053	17.59 ± 0.20	i'	0.6m TELMA
2456450.392371	17.70 ± 0.20	i'	0.6m TELMA
2456450.393677	17.32 ± 0.16	i'	0.6m TELMA
2456450.395124	17.42 ± 0.16	i'	0.6m TELMA
2456450.396963	17.56 ± 0.15	i'	0.6m TELMA
2456450.399062	17.38 ± 0.15	i'	0.6m TELMA
2456450.401339	17.99 ± 0.21	i'	0.6m TELMA
2456450.403521	18.04 ± 0.24	i'	0.6m TELMA
2456450.406057	18.29 ± 0.21	i'	0.6m TELMA
2456450.408959	18.61 ± 0.30	i'	0.6m TELMA
2456450.514739	17.49 ± 0.15	Z	0.6m TELMA
2456450.537466	17.56 ± 0.16	Z	0.6m TELMA
2456450.560270	17.93 ± 0.15	Z	0.6m TELMA
2456450.583792	17.84 ± 0.16	Z	0.6m TELMA
2456450.606892	17.89 ± 0.17	Z	0.6m TELMA
2456450.629280	18.32 ± 0.26	Z	0.6m TELMA
2456450.651610	18.37 ± 0.31	Z	0.6m TELMA
2456450.392159	18.75 ± 0.03	R	1.23m CAHA
2456450.395772	18.99 ± 0.04	R	1.23m CAHA
2456450.399383	19.26 ± 0.06	R	1.23m CAHA
2456450.403071	>21.5	V	1.23m CAHA
2456450.408137	18.84 ± 0.05	*clear*	0.7m AO
2456450.410694	18.86 ± 0.04	*clear*	0.7m AO
2456450.413241	18.95 ± 0.05	*clear*	0.7m AO
2456450.415799	19.16 ± 0.06	*clear*	0.7m AO
2456450.416655	21.08 ± 0.38	R	1.25m AZT-11
2456450.447046	20.58 ± 0.07	R	1.0m T100
2456450.451171	20.71 ± 0.07	R	1.0m T100
2456450.455296	20.51 ± 0.07	R	1.0m T100
2456450.459379	20.60 ± 0.08	R	1.0m T100
2456450.463463	20.86 ± 0.09	R	1.0m T100
2456450.582700	>25	g'	10.4m GTC
2456450.583935	21.73 ± 0.07	r'	10.4m GTC
2456450.120092	22.00 ± 0.07	r'	10.4m GTC
2456450.429560	19.27 ± 0.05	i'	10.4m GTC
2456450.584792	20.53 ± 0.05	i'	10.4m GTC
2456450.621551	20.83 ± 0.05	i'	10.4m GTC
2456450.585938	18.14 ± 0.08	z'	10.4m GTC
2456450.622558	18.42 ± 0.08	z'	10.4m GTC
2456451.480060	>22.1	I	1.5m OSN
2456496.462500	>21.5	H	3.5m CAHA

(a) Values measured since 21:04:34 UT June 6, epoch of the first *Swift*/BAT trigger time (Julian Date (JD) is 2556450.378171)

(b) 0.4m Watcher is at Boyden Observatory (South Africa). 0.25m BART is at Astronomical Institute at Ondrejov (Czech Republic). 0.6m TELMA is at Algarrobo Costa (Málaga, Spain). 0.7m AO is at the Abastumani Observatory (Georgia). T100 is at the TÜBITAK National Observatory (Turkey). AZT-11 is the 1.25m telecope at the SRI "Crimean Astrophysical Observatory" (Ukraine). 1.5m OSN is at Observatorio de Sierra Nevada in Granada (Spain); 3.5m CAHA is at the German-Spanish Calar Alto Observatory in Almería (Spain); GTC is the 10.4-m Gran Telescopio Canarias in Canary Islands (Spain).

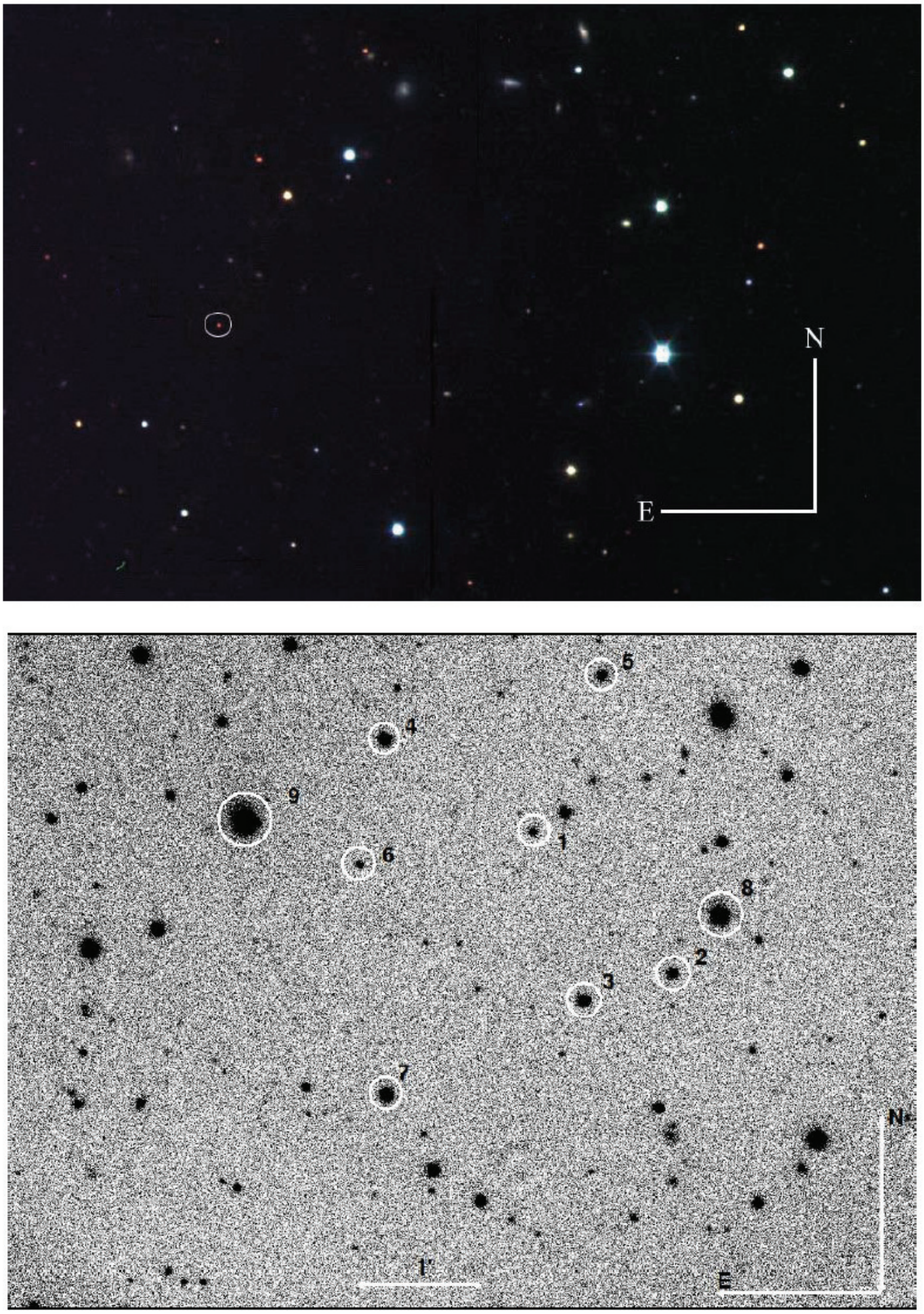

Figure 3.2: The colour composite image of the field around GRB 130606A and reference stars in the line of sight. Upper panel: The highly reddened GRB afterglow (circled) and the surrounding field, based on g' r' i' images obtained at the 10.4m GTC on June 7, 2013. The field of view is 3.8 × 2.8 arcmin^2. Lower panel: Reference stars for photometric calibration in the field around GRB 130606A (Table 3.2). The field of view (r'-band image) is 6.8 × 5.0 arcmin^2.

Table 3.2: Reference stars in the field of GRB 130606A.

N	R.A.(J2000)	Dec(J2000)	R-band mag	I-band mag	H-band mag
1	16 37 33.7	+29 48 19.0	18.04 ± 0.11	16.36 ± 0.02	14.54 ± 0.05
2	16 37 28.4	+29 47 05.6	16.97 ± 0.07	15.71 ± 0.02	13.95 ± 0.04
3	16 37 31.9	+29 46 53.6	16.41 ± 0.05	16.12 ± 0.02	15.31 ± 0.05
4	16 37 39.4	+29 49 05.6	16.22 ± 0.05	15.88 ± 0.02	15.07 ± 0.05
5	16 37 31.0	+29 49 36.4	17.65 ± 0.09	17.03 ± 0.03	−−
6	16 37 40.4	+29 48 03.4	18.62 ± 0.14	18.21 ± 0.04	17.38 ± 0.06
7	16 37 39.5	+29 46 07.7	15.99 ± 0.04	15.66 ± 0.02	−−
8	16 37 26.6	+29 47 34.5	14.57 ± 0.02	14.24 ± 0.02	13.54 ± 0.04
9	16 37 44.8	+29 48 25.3	13.11 ± 0.02	12.82 ± 0.02	−−

Table 3.3: Log of Spectroscopic data obtained at the 10.4m GTC.

Start Time (UT)	Exp Time (s)	Grism	Obs. Range (Å)	Slit width (”)
06-Jun 2013-22:23:50.5	1 x 450	R1000B	3,650 – 7,750	1.2
06-Jun 2013-22:32:18.1	1 x 450	R500R	4,750 – 10,300	1.2
07-Jun 2013-02:10:09.7	2 x 1,200	R2500I	7,320 – 10,100	1.0

Near-IR bservations were conducted on July 22 at the 3.5m telescope (+ OMEGA 2000) at the German-Spanish Calar Alto (CAHA) Observatory, with a 5,400s overall exposure time in the H-band. The photometric calibration is based on the observation of the standard S889-E (Persson *et al.*, 1998) at an airmass similar to the GRB field. The photometric results of the afterglow are tabulated in Table 3.1.

3.2.2.2 Spectroscopy

Starting 1.3 hr post-burst, optical spectra were obtained on 6 June 2013 with the 10.4m GTC using the R1000B and R500R grisms (1×450 s exposures) and R2500I ($2 \times 1{,}200$ s exposures) of the OSIRIS imaging spectrograph. The later one provides a nominal resolution of ~ 120 km s^{-1}. The log is given in Table 3.3. The 1” wide slit was positioned on the location of the transient source and a 2×2 binning mode was used. The GTC spectra were reduced and calibrated following standard procedures using custom tools based on IRAF and Python. Standard spectrophotometric stars used for flux calibration were Feige 92 for observations for the R1000B grism and Ross 640 for the prisms R500R and R2500I, taken the same night. All spectra were scaled in flux to correct for slit losses using the photometry of the corresponding acquisition images. The final wavelength calibration is on a vacuum scale, appropriate for the application of rest-frame UV atomic data.

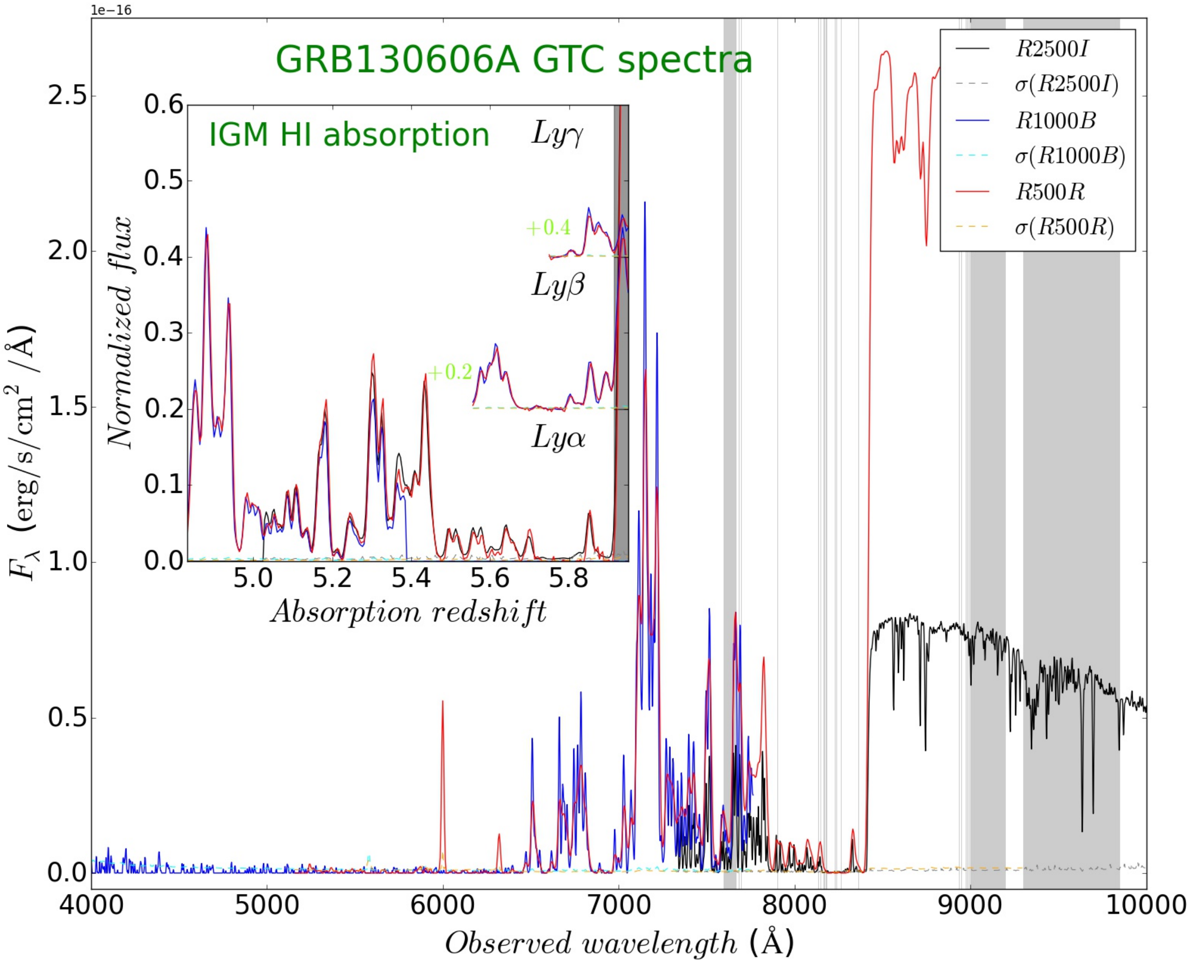

Figure 3.3: The 10.4m GTC spectra. We plot in the main panel flux-calibrated observations detailed in Table 3.3. Strong absorption by intergalactic hydrogen in the line of sight is causing the apparent low optical flux observed in the Lyman-α forest region (below 8,400 Å). In the embedded panel we show the corresponding redshift of the IGM absorption.

Table 3.4: Flux densities measured at Plateau de Bure Interferometer.

Time (days post-burst)	Flux density [mJy]	Frequency [GHz]
3.30	1.45 ± 0.15	86.7
7.50	0.03 ± 0.13	86.7

3.2.3 Millimetre observations

Target-of-Opportunity millimetre observations were carried out at the Plateau de Bure Interferometer (PdBI Guilloteau *et al.*, 1992). It was pointed to the GRB 130606A location on two occasions in its compact 6 antenna configuration. The millimetre counterpart was detected 3.30 days after the GRB onset with a high (~10) S/N ratio, on the phase center coordinates (J2000, R.A. = RA: 16:37:35.13; Dec: +29:47:46.5). The results of UV-plane point source fits to the phase center are given in Table 3.4.

The millimetre afterglow was detected with a flux density of ~1.5 mJy at 3 mm, confirming the detection earlier reported at centimetre wavelengths (Laskar *et al.*, 2013b). The source became undetectable by June 14.

3.3 Results

Hereafter we consider $H_0 = 73$ km s^{-1} Mpc^{-1}, Ω_Λ= 0.73 $\Omega_m = 0.27$. At the redshift of z = 5.9135 (see below), the light travel time was 12,350 Gyr, the age of the Universe at this redshift was 0.95 Gyr and the luminosity distance is 56,365 Mpc.

3.3.1 The initial bulk Lorentz factor

The 0.6m BOOTES-2/TELMA and 1.23m CAHA colours show clear signs of a high-redshift drop-out (V-$R > 2.2$ in the CAHA case). From the optical light curve depicted in Fig. 3.1, the optical flux ($F_{opt} \propto t^{\alpha}$) exhibits a rising phase toward an optical maximum at $\sim$ 7.5 minutes after the BAT trigger. A rising temporal index $\alpha_1 \sim 1.2$ and decaying temporal index of $\alpha_2 \sim$ -1.25 are derived, with a break around t $\sim$ 450 s. The interstellar medium (ISM) case predicts the rising index to be $\sim$ 2 whereas a wind profile (WIND) case predicts it to be $\sim$ 0.5 (Panaitescu & Vestrand, 2011). These values have not been seen in many of the observed cases at early times, possibly due to the early emission being a combination of multiple components such as early time energy injection. Using Eq. 4 of (Rykoff *et al.*, 2009) and for s $\sim$ 4, the peak time t_{peak} is $\sim$ 350 s. Assuming that the

Table 3.5: Spectral fitting analysis for the *Swift*/XRT X-ray data assuming N$_H$ (Gal) = 2×10^{20} cm^{-2}.

Time Interval (after T_0 [s]) (after T_0 [s])	N_H(intr.) [10^{22} cm^{-2}]	Γ	$F_X(unabsorbed)$	χ^2/dof
78-89	10^{+6}_{-5}	$1.10^{+0.13}_{-0.12}$	$3.25^{+0.22}_{-0.24} \times 10^{-}09$	42/43
115-200	$4.1^{+1.1}_{-1.0}$	$1.24^{+0.04}_{-0.04}$	$2.10^{+0.06}_{-0.06} \times 10^{-}09$	241/225
200-300	$8.3^{+1.0}_{-1.0}$	$1.60^{+0.03}_{-0.03}$	$2.61^{+0.05}_{-0.05} \times 10^{-}09$	324/296
300-500	$3.5^{+0.7}_{-0.6}$	$1.81^{+0.04}_{-0.04}$	$8.88^{+0.25}_{-0.22} \times 10^{-}10$	285/244
78-200	$5.1^{+1.1}_{-1.0}$	$1.22^{+0.04}_{-0.04}$	$2.85^{+0.09}_{-0.08} \times 10^{-}09$	261/259
500-1000	<1.4	$1.62^{+0.09}_{-0.09}$	$1.07^{+0.05}_{-0.12} \times 10^{-}10$	24/28
1000-10000	<3	$1.92^{+0.15}_{-0.14}$	$8.4^{+0.7}_{-0.7} \times 10^{-}12$	26/26
10000-30000	<1.1	$1.87^{+0.15}_{-0.14}$	$2.7^{+0.3}_{-0.3} \times 10^{-}12$	27/27
30000-300000	<1	$2.03^{+0.20}_{-0.13}$	$2.9^{+0.2}_{-0.4} \times 10^{-}13$	10/13
500-300000	<0.5	$1.81^{+0.07}_{-0.06}$	$1.81^{+0.08}_{-0.07} \times 10^{-}12$	65/89

early optical emission is the onset of the forward shock emission, the value of t_{peak} in the rest frame can be used (i.e. $t_{peak}/(1+z)$) to calculate the initial bulk Lorentz factors for the ISM and WIND cases for the GRB environment, following (Melandri *et al.*, 2010). We also consider the isotropic energy released in GRB 130606A (at z ∼ 5.91) to be 28.3 ± 0.5 in units of 10^{52} ergs (Golenetskii *et al.*, 2013). Thus, for $E_{52} \sim 28.3$ and $t_{peak} \sim$ 350 s, the bulk Lorentz factor in the ISM case is $\Gamma_0 \sim 185$, whereas in the case of WIND, $\Gamma_0 \sim 65$. Γ_0 can be also estimated from (Ghirlanda *et al.*, 2012), giving $\Gamma_0 \sim 160$ for the ISM case and $\Gamma_0 \sim 70$ for the WIND case. Using the statistical relations from Liang *et al.* (2010) and Lü *et al.* (2012), we find $\Gamma_0 \sim 185$ and ∼ 220 respectively for the ISM and WIND cases. The post-peak data of the optical light curve exhibits a temporal decay index $\alpha_{opt} \sim 1.3$ along with a superimposed variability.

3.3.2 Temporal and spectral evolution during the Swift observation

Swift/XRT observations showed a high hydrogen column density decreasing with time, which can be interpreted as a time-dependent photoionization of the local circumburst medium, within a compact and dense environment, as found in only a few cases.

The XRT light curve (Fig. 3.1) reveals noticeable variations in the observed count rate that can be divided into 4 segments. The results from the time resolved spectral analysis from the X-ray emission of GRB 130606A are given in Table 3.5. The dependence of the flux on frequency, ν, and time t, is described through this section and in Table 3.5 by F_ν

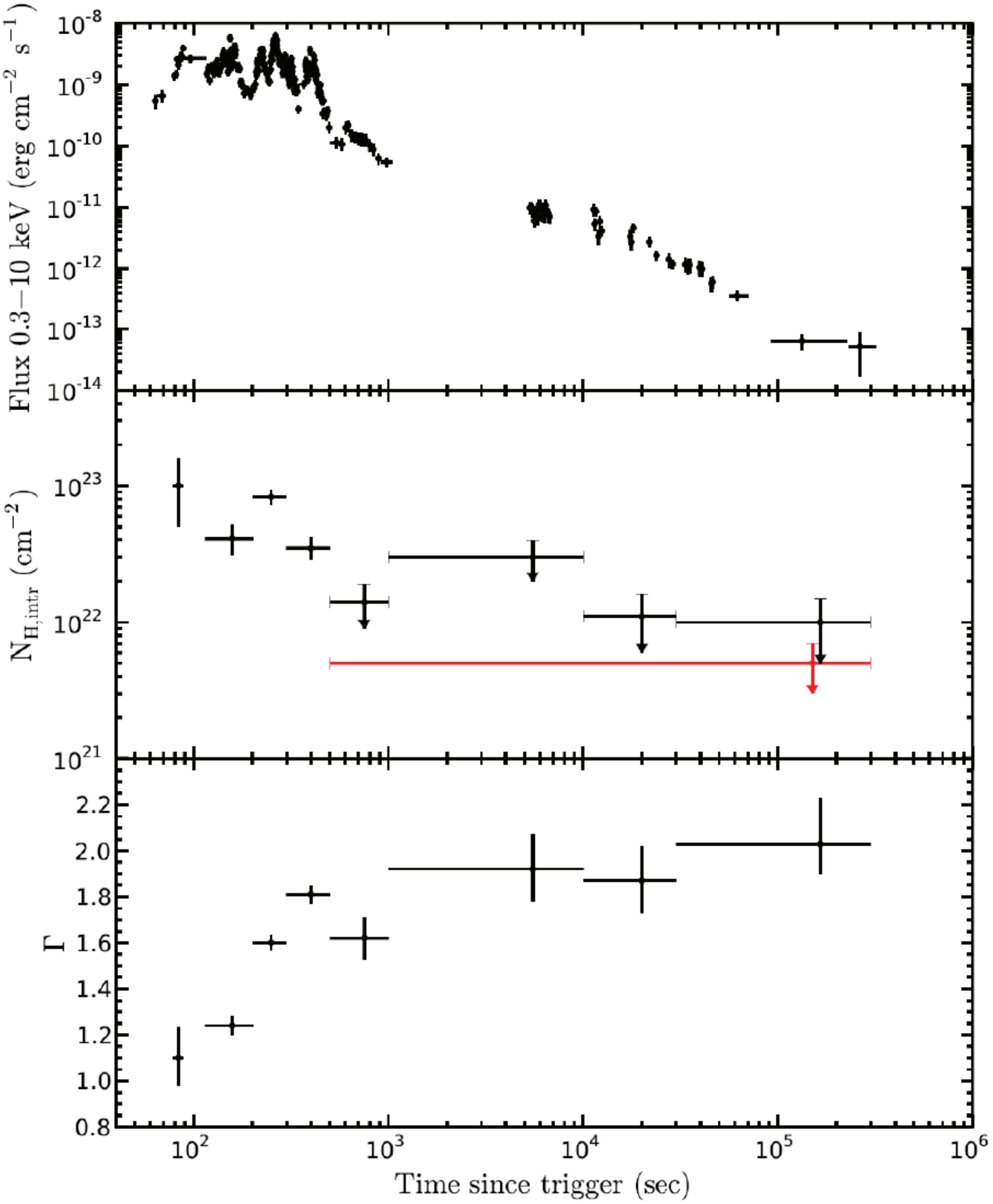

Figure 3.4: X-ray light curve for the GRB 130606A afterglow and variations in the power-law index and column density as a function of time. Upper panel: The X-ray afterglow light curve. Middle panel: The decrease of the column density as the gamma/X-ray emission decreases. Lower panel: The variation of the power-law index Γ with respect to the X-ray luminosity showing that the spectrum gets progressively harder as the flux increases. 1σ error bars are shown.

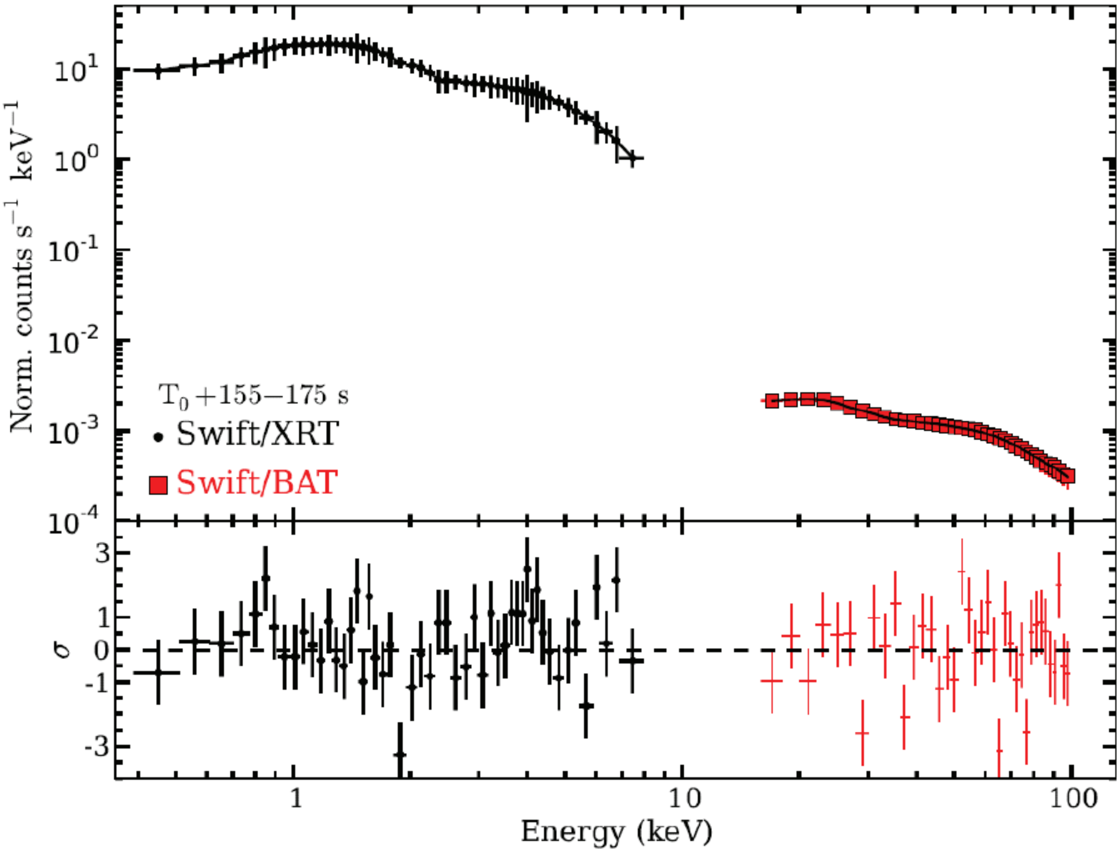

Figure 3.5: The GRB 130606A *Swift*/BAT and *Swift*/XRT spectrum. A simple power-law function (black line) yields a formally acceptable fit (χ^2 /d.o.f. = 1.29). The inclusion of a thermal component provides negligible improvement (χ^2 /d.o.f. = 1.26). 1σ error bars are shown.

$\propto \nu^{-\beta}$ $t^{-\alpha}$ where $\beta = \Gamma - 1$. Thus, we find the following distinct episodes:

I) Beginning of XRT observations up to $\sim T_0$+759 s. This segment is dominated by flaring activity from internal shocks as part of the prompt emission. The combined *Swift*/BAT-XRT X-ray spectrum in the interval T_0 + 155s to T_0 + 175s can be fit using a simple absorbed power law model (χ^2/d.o.f. = 1.29), and the addition of a thermal component has negligible effect (χ^2/d.o.f. = 1.26). The best fit model (Fig. 3.5) has a hydrogen column density $(4 \pm 2) \times 10^{22}\,\mathrm{cm}^{-2}$ and a photon index $\Gamma = 1.03 \pm 0.02$.

II) T_0+759 s to T_0+1300 s. This is characterised by a fast decay with temporal index, α_X=3 ± 1, consistent with high-latitude emission (Genet & Granot, 2009) at the end of the prompt emission (α_X= 2+β_X), where $\alpha_X = 0.62 \pm 0.09$.

III) T_0+1300 s to T_0+1.6 × 10^4 s. During this segment, the X-ray count-rate decay is consistent with a temporal decay index of α_X =0.66 ± 0.20. This plateau phase is typically associated with late activity from the central engine (Zhang, 2007). The end of this plateau phase at T_0+1.6 × 10^4 s seems to be achromatic when comparing the X-ray and i-band light curves (Fig. 3.1) as expected at the end of late activity from the central engine. The closure relations modified with an energy injection parameter, q (Zhang *et al.*, 2006), are consistent with an homogeneous environment (ISM) with $q = 0.5 \pm 0.4$ when ν_x ¡ ν_c. This value is consistent with previous measurements of q (Curran *et al.*, 2009; Zhang *et al.*, 2006). The electron spectral index inferred during this segment is $p = 2.84 \pm 0.30$, consistent within 1σ with the distribution of values of p presented by Curran *et al.* (2010) and Starling *et al.* (2008). The wind model when ν_x ¡ ν_c with late energy injection is rejected for GRB 130606A since the q-parameter inferred is q¡0 which does not have physical meaning. The cases when ν_x ¿ ν_c in the ISM or wind model are also rejected since result in p¡2 for which the closure relations are no longer valid. Finally, the optical temporal decay index $\alpha_{opt} \sim 1.3$ is consistent with α_X during this time interval.

IV) T_0+1.6 × 10^4 s to T_0+3 × 10^5s. In this segment, the decay (α_X =1.86 ± 0.20) is consistent with forward shock emission when ν_x ¡ ν_c. The closure relation between the temporal and spectral index in the case of an ISM model for ν_x ¡ ν_c is $\alpha = 3\beta/2 = 1.55 \pm 0.30$ consistent with the observed α_X. For a wind environment, the relationship can be re-written as α=(3β+1)/2=2.03 ± 0.30 which is also consistent with the observed temporal decay. However, the wind environment was tentatively rejected in the previous segment and may not be necessary to explain the afterglow emission of GRB 130606A. The electron spectral index obtained in this segment is, p = 3.0 ± 0.4. This value is consistent with the electron spectral index inferred in the previous segment. It should be noted that during this segment there seems to be small variability in the X-ray light curve in the form of a micro-flare peaking at $\sim T_0$+4 × 10^4 s. As shown in Fig. 3.4 GRB 130606A shows significant variation in the photon index, Γ and N_H column density throughout the X-ray observations. The variation of Γ with respect to the X-ray luminosity shows that the spectrum gets progressively softer as the flux decreases.

The intrinsic column density N_H is well constrained while the central engine remains active (first 500 s since trigger) implying high levels of photoionization of the local high-density medium. During this time, the observed intrinsic N_H is almost 3 orders of magnitude higher than the galactic column density at these coordinates. Once the prompt emission ends, the intrinsic N_H decreases abruptly and no excess with respect to the galactic value can be found for the remainder of the X-ray observations. This can be interpreted as a time-dependent photoionization of the local circumburst medium, within a compact and dense environment, only found in a few GRBs such as GRB 980329 (Lazzati & Perna, 2002) and GRB 000528 (Frontera *et al.*, 2004).

3.3.3 The GRB 130606A host galaxy

3.3.4 Hydrogen abundance

The GTC combined spectrum exhibits a huge IGM absorption which can difficult the determination of the $N(\text{H I})$ due to the host galaxy (e.g. Totani *et al.*, 2014). In order to determine the column density of the host, we normalised the spectra with a simple power law and fitted the red damping wing of the Lyα absorption, finding $z = 5.913$ and $\log N(\text{H I}) = 19.85 \pm 0.15$. The fit of this damped feature was performed using the same prescription and tools as in Sánchez-Ramírez *et al.* (2016) (see Fig. 2.2). Due to the huge IGM absorption we could not use higher order Lyman series lines to better constrain the host $N(\text{H I})$. This value is in good agreement with three independent data-sets (Chornock *et al.*, 2013; Hartoog *et al.*, 2015; Totani *et al.*, 2014). The associated system is therefore technically classified as a sub-DLA.

3.3.5 Metal abundances

A series of absorption lines due to different ions (N V, Si II, Si II*, O I, C II, and C II*) are detected at the same redshift of the Lyα feature. A plot of the GTC spectrum and line identifications is provided in Fig. 3.7. We measured the equivalent widths (EWs) of the lines fitting Gaussians profiles and computing the sum over the line model. This approximation is in our case valid, as discussed in section **ref**. Results for the host galaxy lines are presented in Table 3.6. With the redshifts obtained by the line fitting, we are able to refine the redshift up to $z = 5.9130 \pm 0.0004$.

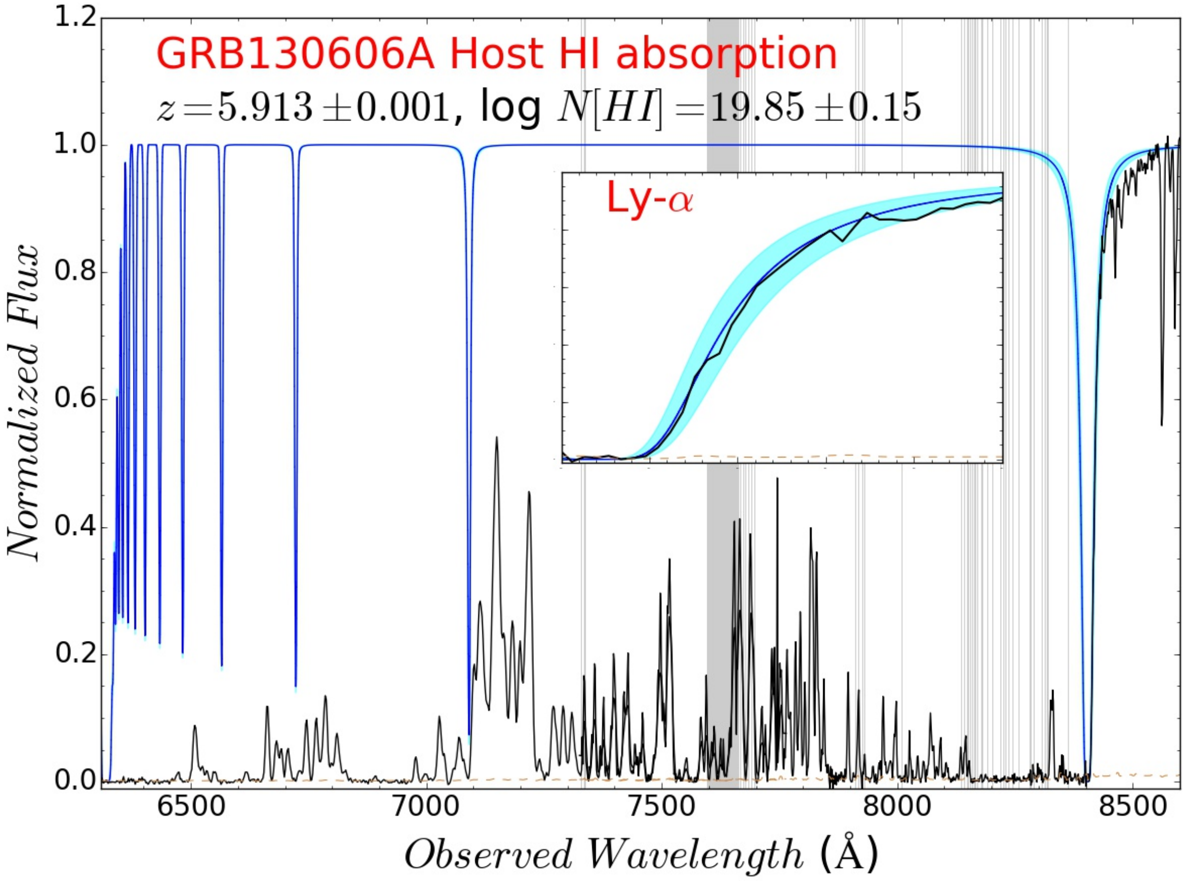

Figure 3.6: The $N(\mathrm{H\,I})$ fit to the GTC (+ OSIRIS) spectrum of GRB 130606A. Taken on June 7, 2013, the figure shows the data (black solid line) and the best fit damped profile (solid red line). The derived column density is log N (H I) = 19.85, together with the fits for log N (H I) = 19.70 and 20.00 (dashed red lines).

Table 3.6: EW measurements for the GRB 130606A host galaxy from the afterglow spectrum.

Feature	Wavelength	z	EW	eEW
NVλ1239	8562.92	5.9122	0.417	0.001
NVλ1243	8590.33	5.9121	0.248	0.003
SiIIλ1560	8713.795	5.9134	0.407	0.003
OIλ1302	9002.57	5.9135	0.185	0.004
CIIλ1335	9225.59	5.9130	0.367	0.003
CII*λ1336	9234.37	5.9135	0.156	0.004
SiIVλ1394	9635.38	5.9132	1.081	0.012
SiIVλ1403	9697.37	5.9130	6.04	0.04

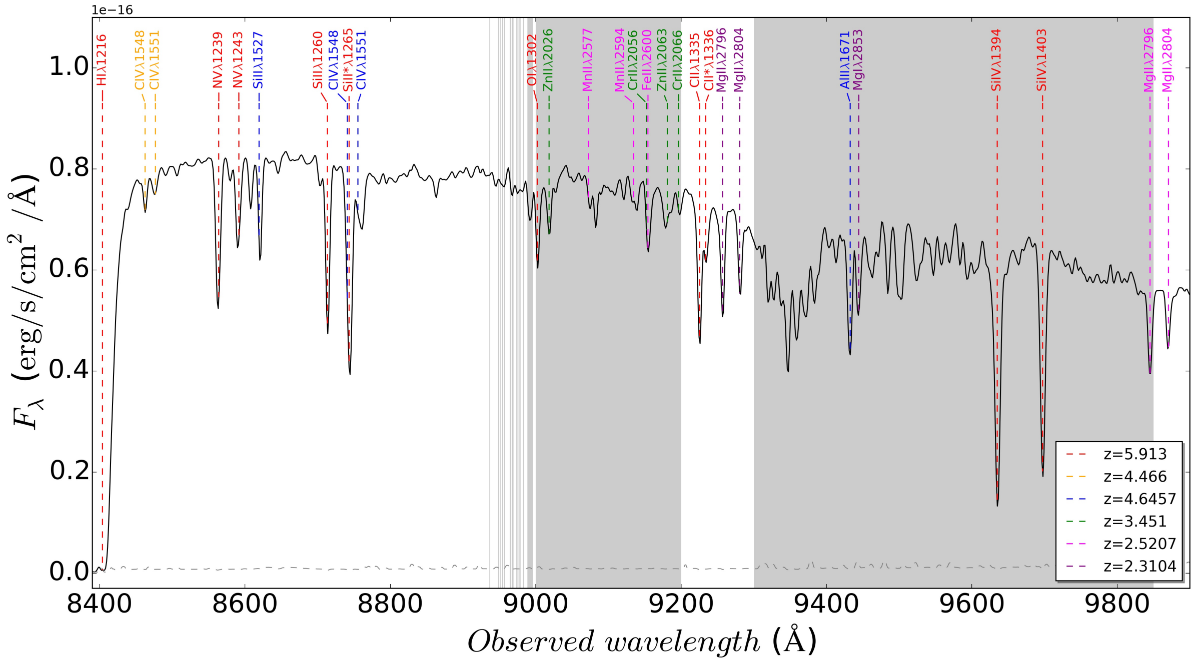

Figure 3.7: The identified lines in the R2500I 10.4m GTC spectrum ∼ 6 hr post-burst. The noise spectrum (dotted line) is also plotted. Each system is labelled as indicated in the legend.

3.3.6 Metallicity

The high signal-to-noise ratio (SNR) of the GTC spectrum permitted a search for relatively weak metal lines, and offers an improvement over some of the limits measured by Chornock *et al.* (2013).

In the case of sulphur, the triplet at 1250, 1253, 1259 Åcan be used. Significant absorption is detected at the position of the weakest of these three lines (1250 Å), but the lack of absorption at 1253 Å indicates that the absorption is likely from a contaminating source. Based on the non-detection of the S IIλ1253 line, we determine an observed frame 3σ EW limit ¡ 0.157 Å(assuming a FWHM = 3.4 Åand a S/N of 65 in the S IIline region) which corresponds to 0.023 Åin the rest frame. The rest-frame EW limit yields $\log N[S]$ < 14.17. Assuming a solar $[S/H]_\odot = 4.85$ (from Asplund *et al.*, 2009), this gives a 3σ upper limit [S/H] < -0.82, which is 0.3 dex (a factor of ∼2) deeper than the sulphur limit obtained by Chornock *et al.* (2013).

In addition to the upper limit to the sulphur abundance, we can determine lower limits to the abundances of oxygen and silicon. The limiting silicon abundance is determined from the mildly saturated Si IIλ1260 line with a rest frame EW=0.35 Å, yielding [Si/H] > -1.80, without consideration of ionization or dust depletion corrections. The oxygen

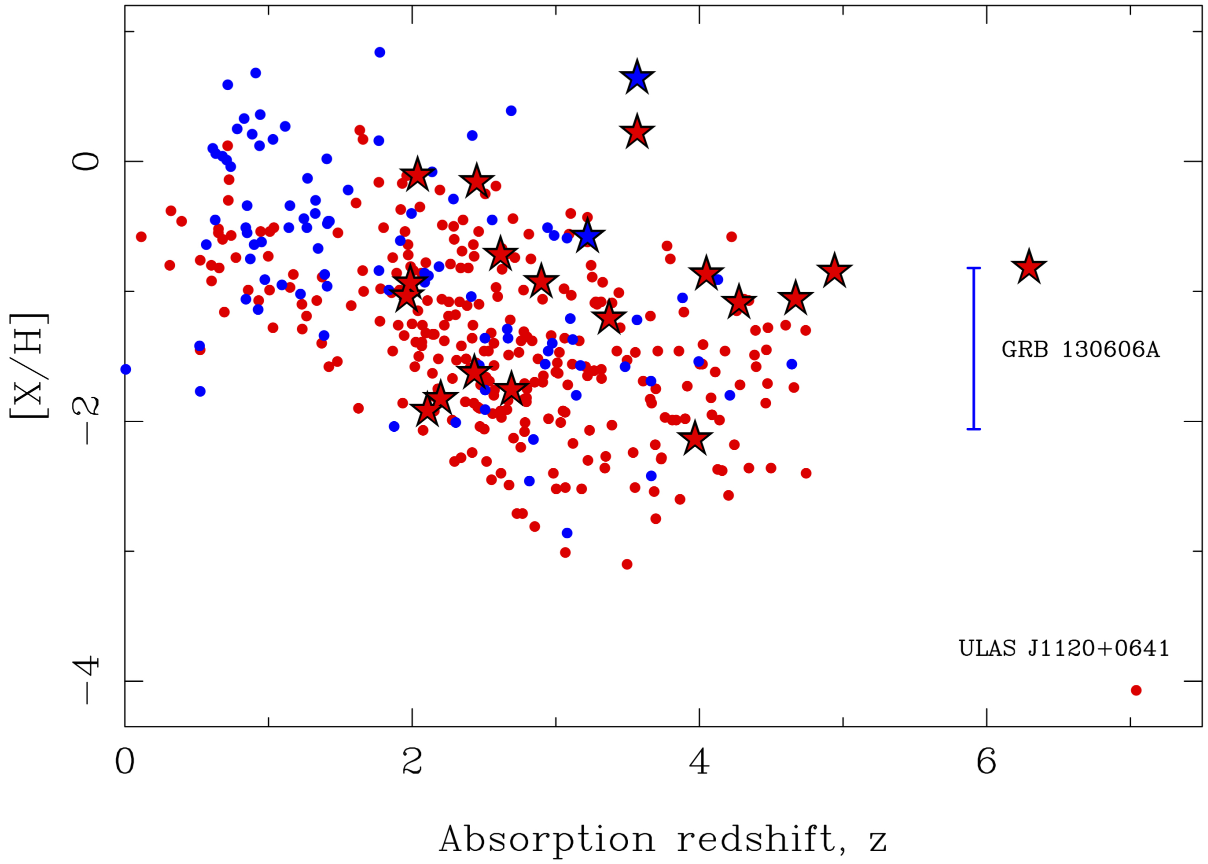

Figure 3.8: The metallicity ([X/H]) as a function of redshift is shown for a compilation of QSO-DLAs (circles; Berg *et al.*, 2015b) and GRB-DLAs (stars; Schady *et al.*, 2011; Thöne *et al.*, 2013), including the location for GRB 130606A at z = 5.9 (blue error bar) and ULAS J1120+0641 at z ∼ 7 (Simcoe *et al.*, 2012). The GRB 130606A sub-DLA is the 2nd highest redshift burst with a measured GRB-DLA metallicity and only the third GRB absorber with sub-DLA HI column density. Blue colours are used for $\log N(\mathrm{H\,I}) < 20.3$ and red is used for $\log N(\mathrm{H\,I}) \geq 20.3$. In order of preference for any given absorber, Zn, S, O, Si, Fe+0.4 dex is our choice of metallicity indicator, where the 0.4 offset for Fe accounts for typical dust depletion.

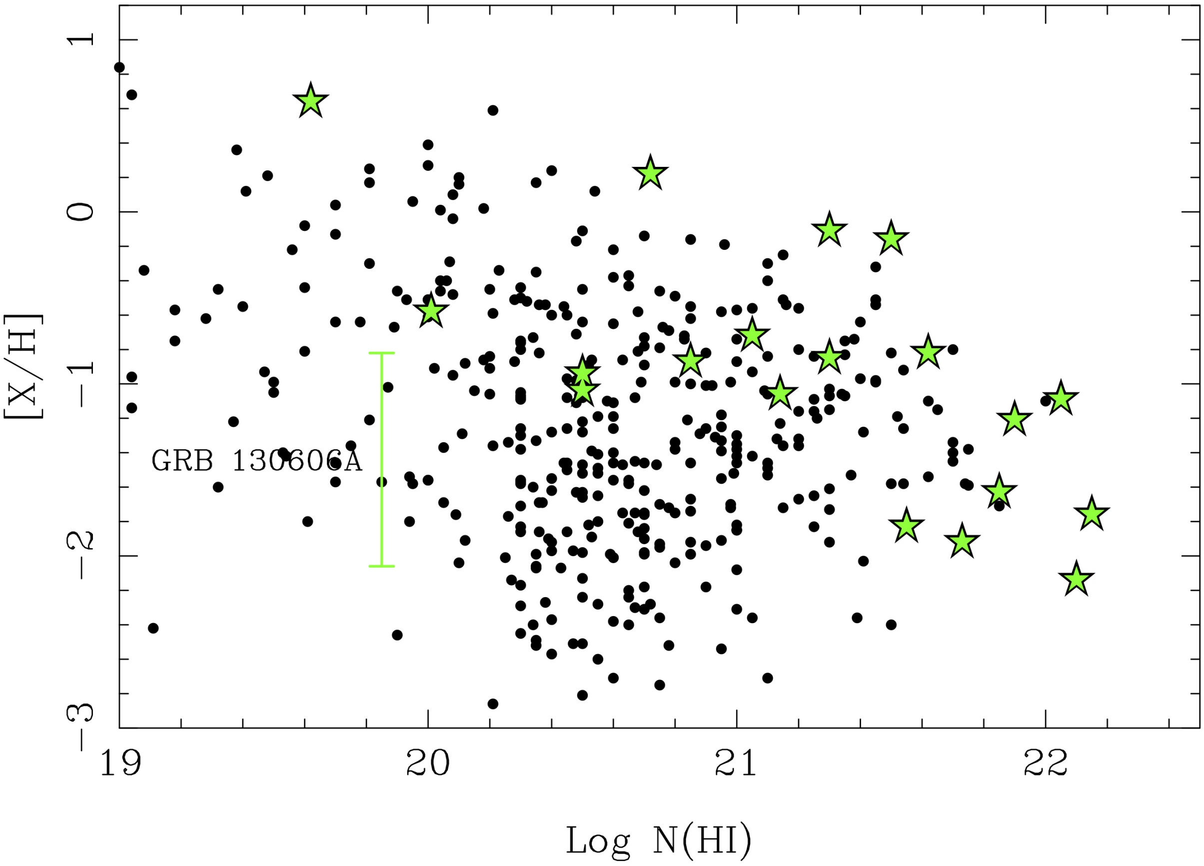

Figure 3.9: The metallicity of a GRB sample (green stars) versus $N(\mathrm{H\,I})$ compared to a sample of DLAs (black dots). The location for GRB 130606A (green error bar) is also plotted.

abundance is determined from the O Iλ1302 Å line, which is also likely to be partly saturated despite its modest EW (0.2Å). The fact that O I does not require an ionization correction and O does not deplete, means that this is one of the best lines from which to obtain an accurate metallicity. The major uncertainty here is that it is close to a small noise feature on the red side which might lead to an over-estimate of the oxygen abundance at the 0.1 dex level. Taking these factors into account, we determine [O/H]≥-2.06. The Si and O limits are consistent to within 0.1 dex of the values independently derived (from different spectra) by Chornock *et al.* (2013). Combined with the upper limit from sulphur, we can constrain the metallicity within a factor of about 10, in the range from ∼1/7 to ∼1/60 of solar.

For a more comprehensive study of the abundances, we refer to Hartoog *et al.* (2015). Furthermore, we also point out that it is very likely that the gas is partially ionized: strong high-ionization lines (such as Si IV and N V) are present at the redshift of the absorber.

3.3.7 Intervening systems

The GTC optical spectrum shows a variety of absorption lines at different redshifts (Table 3.7). We detect on our spectrum 5 intervening systems at redshifts $z_1 = 4.6457 \pm 0.0004$, $z_2 = 4.4660 \pm 0.0001$, $z_3 = 4.4510 \pm 0.0005$, $z_4 = 2.5207 \pm 0.0004$, and $z_5 = 2.3104 \pm 0.0001$.

3.3.8 IGM absorption

We analysed the ionisation state of the IGM using the Gunn & Peterson (1965) optical depth, defined as $\tau_{GP}^{eff} = -\ln(\mathcal{T})$, where $\mathcal{T}$ is the average transmission in a redshift bin. Following Songaila & Cowie (2002) and Songaila (2004) we normalised the GTC spectrum by fitting a power law to the continuum, and divided it into redshift bins of 0.1 between $z = 4.9$ and $z = 5.8$. The results are presented in Fig. 4.1 and in Table 4.1.

Results are consistent with quasar measurements Fan *et al.* (2006); Songaila (2004).

It has been suggested that a better fit to the GRB 130606A is achieved when including an IGM contribution to model the Lyα red damping wing (Totani *et al.*, 2014, 2016).

Table 3.7: EW measurements for the systems detected on the GRB 130606A afterglow spectrum.

Feature	Wavelength	z	EW	eEW
SiIIλ1527	8607.85	4.6467	0.251	0.004
CIVλ1551	8754.144	4.6450	0.294	0.005
AlIIλ1671	9432.25	4.6454	0.554	0.016
CIVλ1548	8462.85	4.4662	0.086	0.004
CIVλ1551	8475.9	4.4658	0.079	0.002
ZnIIλ2026	9018.74	3.4512	0.200	0.011
ZnIIλ2063	9178.76	3.4500	0.209	0.007
CrIIλ2066	9198.15	3.4518	0.112	0.002
MnIIλ2577	9074.60	2.5215	0.162	0.003
MnIIλ2594	9132.97	2.5201	0.108	0.003
MgIIλ2796	9845.20	2.5207	0.591	0.003
MgIIλ2804	9869.96	2.5205	0.364	0.003
MgIIλ2796	9257.33	2.3105	0.538	0.003
MgIIλ2804	9281.26	2.3106	0.396	0.006
MgIλ2853	9443.95	2.3102	0.568	0.012

Table 3.8: IGM absorption towards GRB 140515A.

z	$\mathfrak{T}$	τ_{GP}^{eff}
4.90	0.2469	1.40
5.00	0.0577	2.85
5.10	0.0574	2.86
5.20	0.0700	2.66
5.30	0.1154	2.16
5.40	0.1176	2.14
5.50	0.0249	3.69
5.60	0.0215	3.84
5.70	0.0136	4.30
5.80	0.0012	6.71

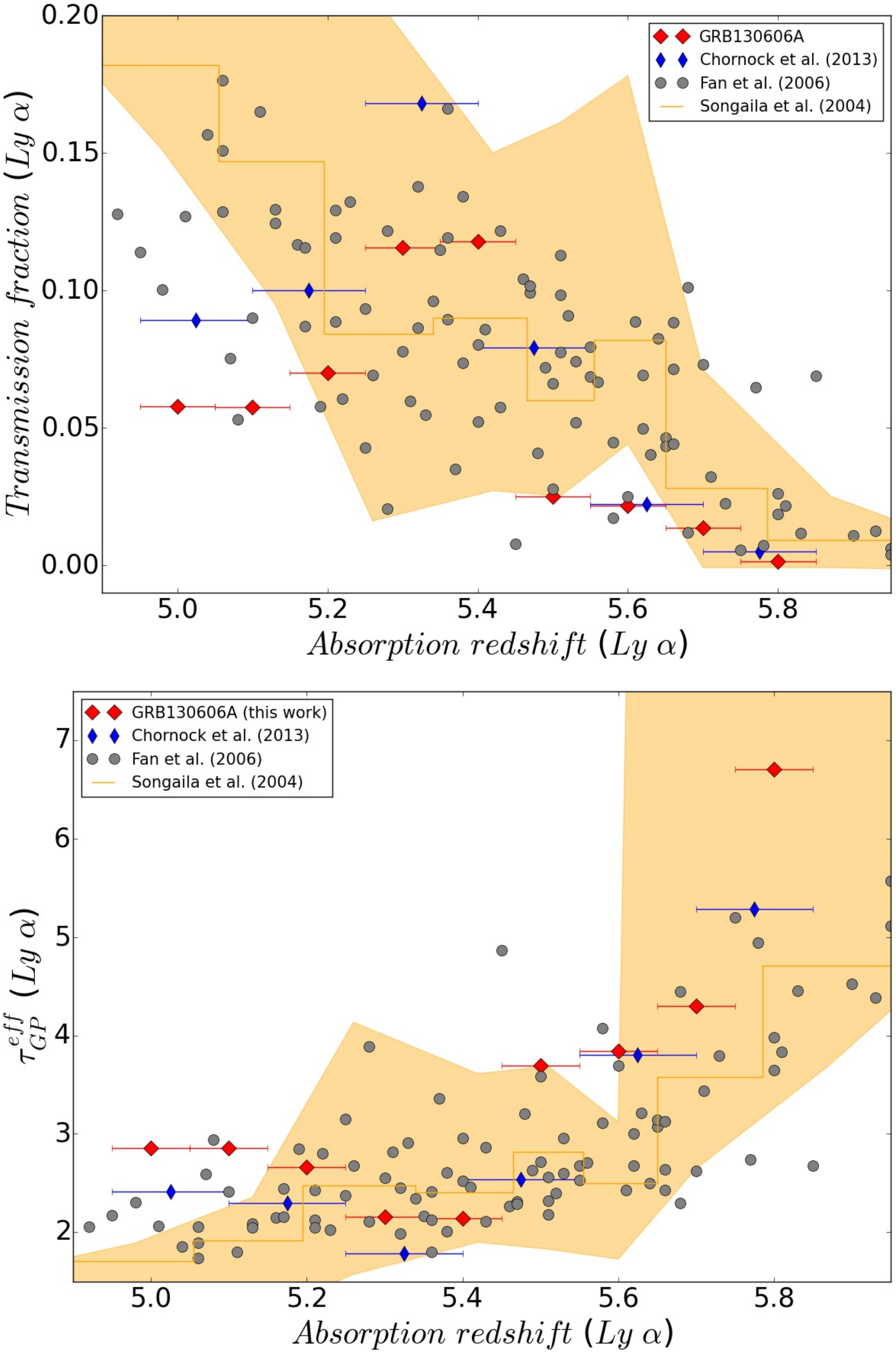

Figure 3.10: Lyα forest transmission (upper plot) and effective optical depth (bottom) in the line of sight to GRB 130606A compared with previous GRB and QSO works. The coloured area shows the optical depth found by Songaila (2004) while grey points are measurements from Fan *et al.* (2006) with sample of quasars.

3.4 Conclusions

- With an initial Lorentz bulk factor in the range $\Gamma_0 \sim$ 65-220, the X-ray afterglow evolution can be explained by a time-dependent photoionization of the local circumburst medium, within a compact and dense environment.

- The host galaxy has a sub-DLA with $\log N(\mathrm{H\,I}) = 19.85 \pm 0.15$, and a metallicity content in the range from ∼1/7 to ∼1/60 of solar.

- In order to place the chemistry of the GRB sub-DLA in context with other high z absorbers, both Fig. 3.8 and Fig. 3.9 show the metallicity of a compilation of GRB host galaxy absorption systems (GRB-DLAs) compared to quasars with DLA and sub-DLAs (QSO-DLAs), combining the data reported in the literature (Berg *et al.*, 2015b; Schady *et al.*, 2011; Thöne *et al.*, 2013). The GRB 130606A sub-DLA is a rare find: the second highest redshift burst with a measured GRB-DLA metallicity and only the third GRB absorber with sub-DLA HI column density. At z ¿ 5, the only other object known then with lower metallicity is the ULAS J1120+0641 DLA at z ∼ 7 (Simcoe *et al.*, 2012). However, the DLA towards ULAS J1120+0641 is close to the redshift of the quasar and its metallicity is determined from a stacked spectrum, both of which complicate its interpretation (Ellison *et al.*, 2010, 2011).

- We note that GRB 130606A, given the non-zero metal content of the host, might have originated from a non-Pop III progenitor star, but whether its afterglow light penetrated material that was pre-enriched by Pop III nucleosynthesis at even higher redshifts (Wang *et al.*, 2012) remains uncertain. Indeed several possibilities for the death of the first stars have recently been suggested by theoretical models (Bromm, 2013). A high value of C/O is predicted to be a signature of Pop III stellar enrichment (Fabbian *et al.*, 2009). A handful of DLAs in the metallicity range -2 to -3 (1/100 to 1/1000 of the Sun's metallicity) have C/O measurements (Cooke *et al.*, 2011a; Ellison *et al.*, 2010) and all but one (towards the quasar QSO J0035-0918) have [C/O] ¡ 0 (Cooke *et al.*, 2011a). Unfortunately, we cannot impose any constraint on this ratio as both species are likely saturated.

- Events such as GRB 130606A at z = 5.91, and future ones at z ¿ 10, offer an exciting new window into pre-galactic metal enrichment in these very high redshift galaxies. These bright lighthouses constitute a significant step forward towards using these sources as beacons for measuring abundances at such early times. New GRB missions, equipped with on-board near-IR detectors, and coupled to state-of-the-art instruments built for the largest diameter ground-based telescopes, will allow us to study the first stars that fundamentally transformed the Universe only a few hundred million years after the Big Bang.

Chapter 4

GRB140515A

Adapted from "The high-redshift gamma-ray burst GRB 140515A. A comprehensive X-ray and optical study"

— Melandri, Bernardini, D'Avanzo, Sánchez-Ramírez et al.,
A&A, 2015

4.1 Introduction

A better understanding of the chemical enrichment and evolution of the high-redshift universe is one of the fundamental goals of modern astrophysics. High redshift surveys have been performed by means of wide field surveys of bright quasars (e.g. Fan, 2012) or deep field analyses to identify distant galaxies by their drop-out (e.g. Bouwens *et al.*, 2014). The identification of high-redshift Gamma-Ray Bursts (GRBs) add a different and profitable views of the distant universe. With respect to other probes, GRBs have many advantages: (i) they are detected at higher redshifts; (ii) they are independent on the galaxy brightness; (iii) they do not suffer of usual biases affecting optical/NIR surveys; (iv) they reside in average cosmic regions. High-z GRBs can provide fundamental, and in some cases unique, information about the early stages of structure formation and the properties of the galaxies in which they blow up. For example, GRBs can be used to trace the cosmic star formation rate (Ishida *et al.*, 2011; Kistler *et al.*, 2009; Robertson & Ellis, 2012), to pinpoint high-z galaxies and explore their metal and dust content (Elliott *et al.*, 2015; Salvaterra *et al.*, 2013; Tanvir *et al.*, 2012), and to shed light on the re-ionization history (Gallerani *et al.*, 2008; McQuinn *et al.*, 2008), to constrain the dark matter particle mass (de Souza *et al.*, 2013a) and the amount of non-Gaussianity present in the primordial density field (Maio *et al.*, 2012), and to measure the level of the local inter-galactic radiation field (Inoue *et al.*, 2010). Additionally, they could also provide direct and/or indirect evidences for the existence of the first, massive, metal-free stars, the so-called Population III stars (Campisi *et al.*, 2011; de Souza *et al.*, 2013b; Ma *et al.*, 2015; Toma *et al.*, 2011; Wang *et al.*, 2012).

Since the launch of the *Swift* satellite (Gehrels *et al.*, 2004) 8 events have been identified at redshift greater than ~ 6, and for 5 of them spectroscopic redshift was secured, including in the list GRB 140515A that we are discussing in this paper. Remarkably, some of them showed fairly bright early-time afterglows, even detectable by small robotic telescopes (e.g. GRB 050904; Boër *et al.*, 2006; Tagliaferri *et al.*, 2005).

4.2 Observations

4.2.1 GTC spectrum

We obtained spectroscopy of the afterglow of GRB 140515A with OSIRIS (Cepa *et al.*, 2000) at the 10.4m Gran Telescopio Canarias (de Ugarte Postigo *et al.*, 2014). The observations were obtained between 22:37:31 UT and 00:09:46 UT (mean epoch 14.184

hr after the GRB onset) with 0.6″ seeing and consisted of 3 × 1800 s exposures. We used the R2500I VPH grism, which covers the range between 7330 and 10000 Å at a resolution of ∼1600 using a 1″ slit.

The data were reduced in a standard way (bias subtraction, pixel-to-pixel response correction, cosmic ray removal, wavelength calibration, 1D extraction, flux calibration, and combination of spectra) using self-made routines based on IRAF (Tody, 1993). The resulting combined GTC spectrum shows a strong continuum above ∼ 8900 Å, where the signal-to-noise ratio is ∼ 20 per pixel, or ∼ 40 per resolution element.

4.2.2 X-shooter spectrum

We observed the field of GRB 140515A with the X-shooter spectrograph mounted at the ESO/VLT using the nodding mode with 1 × 2 binning. The spectrum was acquired on 2014 May 16, starting at 00:42:43 UT (∼ 15.5 hr after the GRB onset) and consisted of 2x4x600 s exposures, for a total integration time of 4800 s on source, covering the range between ∼3000 and ∼ 24000 Å. The mid expose time is 16.3 hr (∼ 0.68 d) after the GRB trigger. The final reduced spectrum has a signal-to-noise ratio of ∼ 3 per pixel[1], with a seeing of ∼ 0.9″ (measured from combined 2D spectrum in the VIS and NIR arms). The flux calibration of the X-shooter, which is problematic in general, is uncertain due to unavailable standard spectrophotometric star in the night when the observations were done and because the photometric observations, which could be used to check the quality of calibration, have rather high errors at this epoch. Thus, as the photometric observations at this epoch have rather high errors, it is not possible to use them to reliably rescale the spectrum.

4.3 Results

4.3.1 Lyα forest constraints on the IGM

We analysed the ionisation state of the IGM using the Gunn & Peterson (1965) optical depth, defined as $\tau_{GP}^{eff} = -\ln(\mathfrak{T})$, where $\mathfrak{T}$ the average transmission in a redshift bin. Following Songaila & Cowie (2002) and Songaila (2004) we normalised the GTC spectrum (as its signal-to-noise ratio, SNR, is better than the X-shooter one, see section 3.4.4) by fitting a power law to the continuum, and divided it into redshift bins of 0.1 between

---

[1] The quoted difference in S/N between the GTC and X-shooter spectra is due partly to the different pixel size of the two instruments and partly to the better observing conditions of the GTC observation.

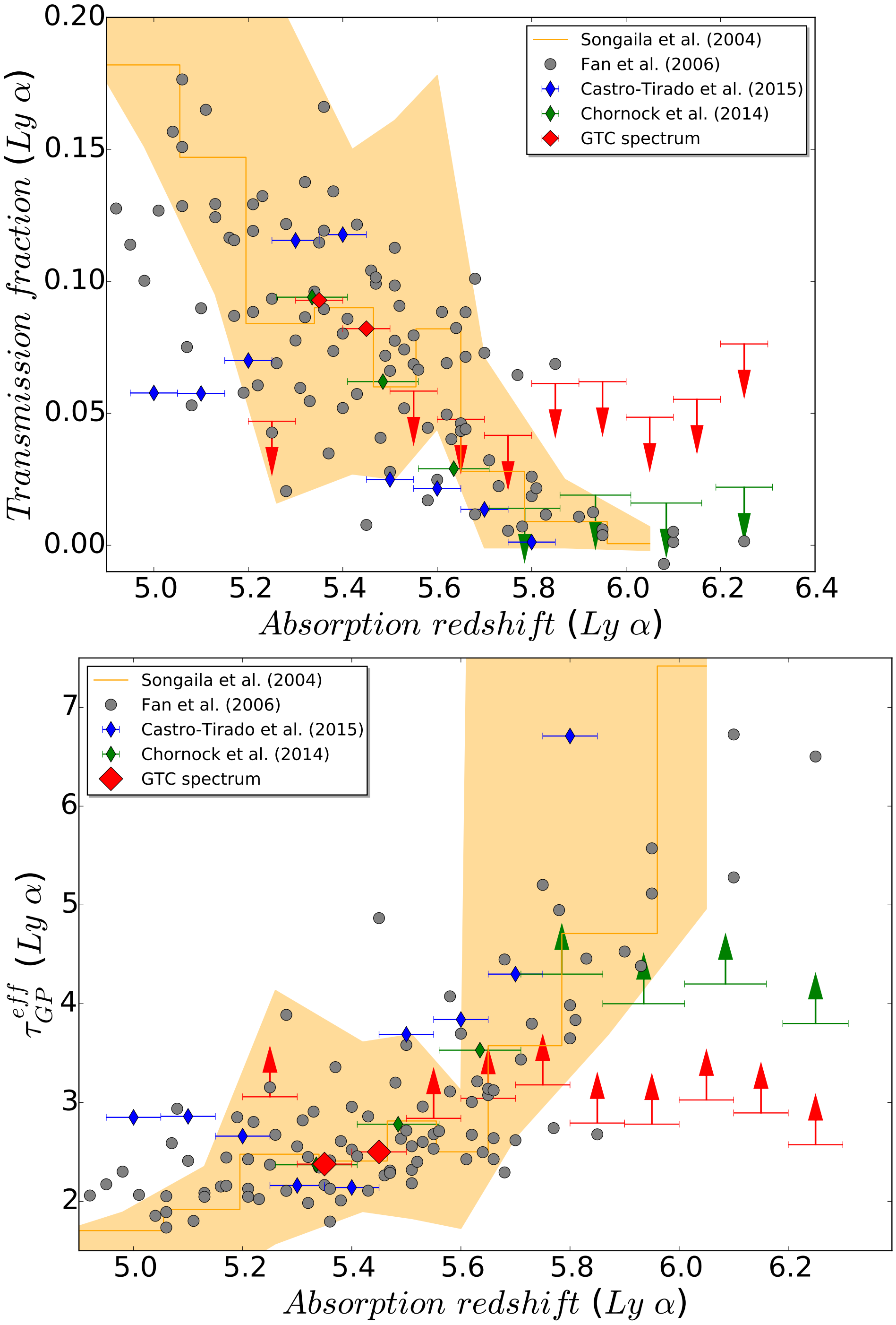

Figure 4.1: Lyα forest transmission (upper plot) and effective optical depth (bottom) in the line of sight to GRB 140515A compared with previous GRB and QSO works. The coloured area shows the optical depth found by Songaila (2004) while grey points are measurements from Fan *et al.* (2006) with sample of quasars.

Table 4.1: IGM absorption towards GRB 140515A.

z	$\mathcal{T}$	lim($\mathcal{T}$)	τ_{GP}^{eff}	lim(τ_{GP}^{eff})
5.25	–	0.0594	–	2.82
5.35	0.1174	0.0709	2.14	2.65
5.45	0.1038	0.0767	2.27	2.57
5.55	–	0.0739	–	2.61
5.65	–	0.0604	–	2.81
5.75	–	0.0527	–	2.94
5.85	–	0.0775	–	2.56
5.95	–	0.0784	–	2.55
6.05	–	0.0614	–	2.79
6.15	–	0.0700	–	2.66
6.25	–	0.0965	–	2.34

$z = 5.2$ and $z = 6.3$. The results are presented in Fig. 4.1 and in Table 4.1.

We only see sky line residuals up to $z \sim 5.5$, above which we can just give detection limits based on the noise spectrum. Our limits are less restrictive than the ones presented by Chornock *et al.* (2014) due to the lower SNR, but show the same behaviour (Fig. 4.1). Results coming from both GRB 140515A and GRB 130606A (Castro-Tirado *et al.*, 2013a; Chornock *et al.*, 2013; Hartoog *et al.*, 2015) are consistent with quasar measurements Fan *et al.* (2006); Songaila (2004).

4.3.2 Lyα red damping wing fitting

We tried to fit the strongest feature seen in the spectrum (at ~ 8900 Å) to an absorption Lyman-α feature with a Voigt profile. Following Chornock *et al.* (2014), we first computed a Voigt model using the same constraints, obtaining inconsistent results. This could be due to the fact that they do not seem to consider the instrumental profile, whose effect on the Ly-α feature is not negligible at this resolution when $\log(N_{\rm HI}) \lesssim 19$. Looking at Fig. 4.2, we can observe the residuals of a sky line subtraction few angstroms blue-wards the wing, precisely at the zone crucial to fit a Voigt model. After a careful inspection on the 2D images of both GTC and X-shooter instruments, we concluded that there is no flux at this zone. Consequently, the wing profile is too sharp to get a satisfactory fit, suggesting that the absorption is dominated by the IGM and that the host absorption is masked.

We then built up IGM models following the prescription of Miralda-Escudé (1998), fixing the lower redshift value to $z = 6.0$ because the contribution to the wing shape below this redshift is negligible (it starts to be important closer to the host). Our best fit, with $z = 6.3298 \pm 0.0004$ and a fraction of neutral hydrogen $x_{HI} \leq 0.002$, is shown in Fig. 4.2. We caution that due to the sharpness of the wing, the few points we have because of GTC resolution, and the sky line next to the absorption, any formal constraints on these quantities would be unreliable, so the values should be interpreted as the most plausible estimations that we can obtain from the data. Moreover, especially by the fact that z cannot be determined by metal lines, hybrid models cannot offer a more accurate fit than the one showed in Fig. 4.2, so no constraints on the host HI abundance can be derived from this event (for further discussion, see Miralda-Escudé, 1998). However, due to the sharpness of the red damping wing, it is obvious that the neutral hydrogen present in the IGM cannot mask neither the presence of a DLA nor a subDLA, as their damping wings would be easily identified. Consequently, we can establish a conservative upper limit of $\log(N_{\rm HI}) \lesssim 18.5$ for the HI abundance in the host galaxy of GRB 140515A. As shown in Fig. 4.2, the fraction of neutral hydrogen derived from this analysis is in good agreement with the model by Gnedin & Kaurov (2014), and it provides a very relevant observational constraint.

Last, we estimated the 3σ upper limits on the observer-frame equivalent width (EW) for the Si IIλ1260, O Iλ1302, and C IIλ1334. We find a value of 0.67 Å, 1.06 Å, and 1.30 Å, respectively. These estimates are a factor ~ 2 more stringent of what reported by Chornock *et al.* (2014), resulting to upper limits on the gas-phase abundances of [Si/H] $\lesssim -1.4$, [O/H] $\lesssim -1.1$, and [C/H] $\lesssim -1.0$. Furthermore, these lines are weaker than the average rest-frame EWs observed for a typical GRB. In fact, the strength of those lines compared to the average GRB spectrum that can be estimated with the use of the line strength parameter (LSP, as defined in de Ugarte Postigo et al. 2012), is LSP < -3.15, < -3.89, and < -2.88, respectively. This means that these lines are very weak and that GRB 140515A exploded in a relatively low density environment. However, our limits on the metals abundances do not allow us to put a stringent limit on the metallicity of the progenitor.

4.4 Discussion

4.4.1 Pop III or enriched Pop II progenitor

GRB 140515A shows evidence of long lasting central-engine activity up to $\sim 10^4$ s after the burst event. Its redshift ($z > 6$) could suggest a Pop III star progenitor. These type of massive stars ($M \geq 100 M_\odot$), that formed in the early universe at low metallicity

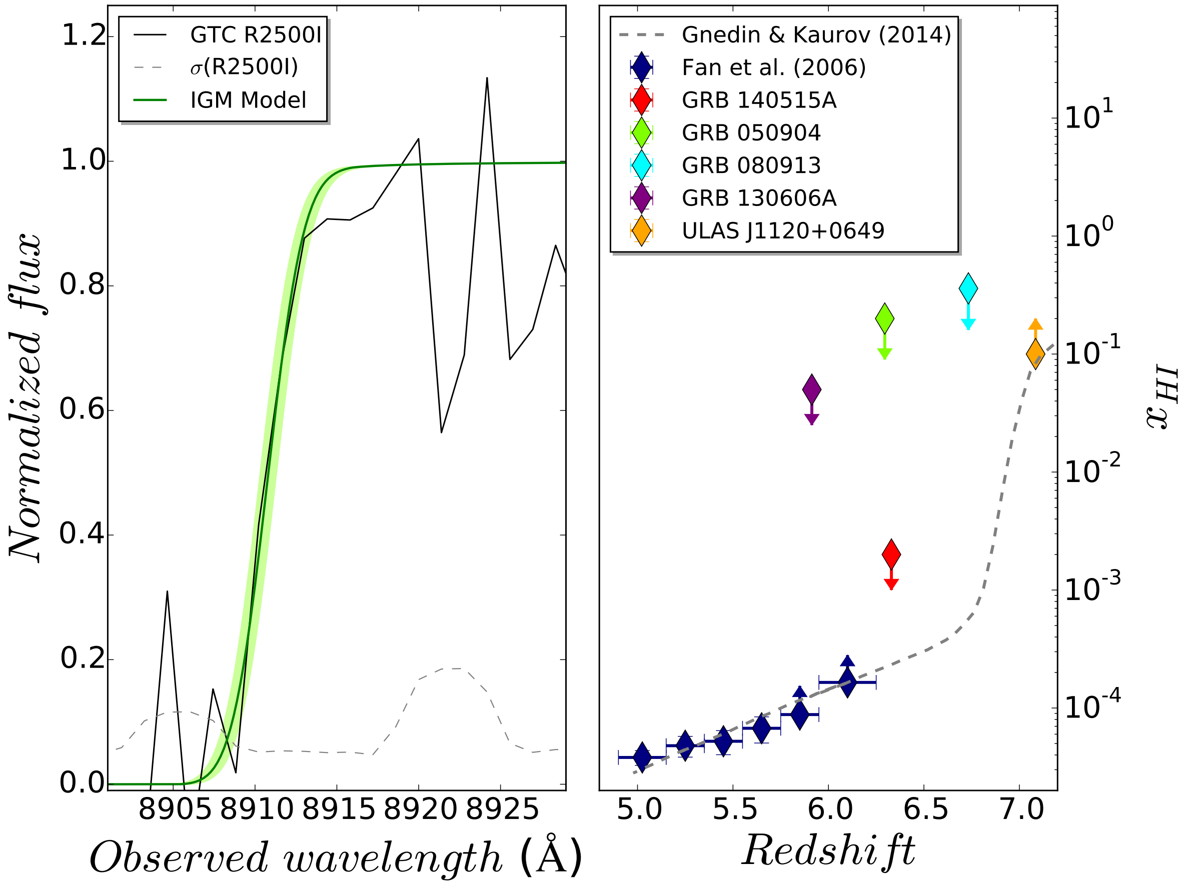

Figure 4.2: *Left*: Best IGM damping wing fit to the spectrum of GRB 140515A. *Right*: Redshift evolution of the hydrogen neutral fraction. The dotted line shows the Gnedin & Kaurov (2014) model, and points (see legend) the observational measurements of this quantity. Points with arrows are lower/upper limits.

($Z \leq 10^{-4}$), have been also proposed as progenitor of the so-called ultra-long GRBs, i.e. GRB 111209A (Gendre *et al.*, 2013), GRB 121027A (Hou *et al.*, 2014), and GRB 130925A (Willingale *et al.*, 2014).

In this scenario, the long duration is the results of the time needed for the accretion and collapse mechanisms. In the hypothesis of such a GRB progenitor one should expect to detect a very low density environment with a density profile dominated by the IGM. Another expectation for such massive collapsing stars is a long-lasting blackbody emission component in their spectra, with a typical average rest-frame temperature of $kT_{\rm BB} \sim 0.5$ keV (Piro *et al.*, 2014). This thermal emission would be in principle detectable by BAT and/or XRT if the redshift of the event is low.

In the case of GRB 140515A observations do support the idea of a low density environment with negligible contribution from the host galaxy, but there are no hints for a particularly low value of the metallicity (see Section 3.4.3). Moreover, being at such a high-z we do not expect to detect the blackbody component with *Swift* instruments. Indeed we tested this possibility (see Section 3.1) but we did not find any improvement of the fit with the inclusion of a blackbody component in the prompt emission spectrum. Therefore, the hypothesis that GRB 140515A originated from a Pop III star (or even from a Pop II star with environment enriched by Pop III stars) is unlikely.

4.4.2 Reionization and escape fraction of ionizing radiation

The distribution of intrinsic column densities of GRB hosts can be used to constrain the average escape fraction of ionizing radiation from the hosts (Chen *et al.*, 2007), under the assumption that GRB sightlines, taken as an ensemble, sample random lines-of-sight from star forming regions in GRB hosts. At intermediate redshifts ($z > 2$) the sample of GRB hosts from Chen *et al.* (2007) indicates that only in about 5% of all cases one expects a GRB sightline with $\log(N_{\rm HI}) < 18.5$. With GRB 140515A being only 1 out of 7 GRBS with $z > 6$ (and only 1 out of 3 with measured HI column densities), it appears that high redshift GRB hosts may have, on average, lower HI column densities and, hence, higher escape fractions than their lower redshift counterparts.

More quantitatively, the Kolmogorov-Smirnov test for the two distributions of HI column densities - first from Chen *et al.* (2007) and the second of four $z > 5.9$ GRBs with measured $N_{\rm HI}$ values - shows that the two distributions are consistent with only 9% probability. That probability raises to 30% if GRB 140515A is excluded. The importance of constraining the escape fractions in reionization sources is obvious, so a larger sample of $z > 6$ GRBs with measured HI column densities would be highly desirable.

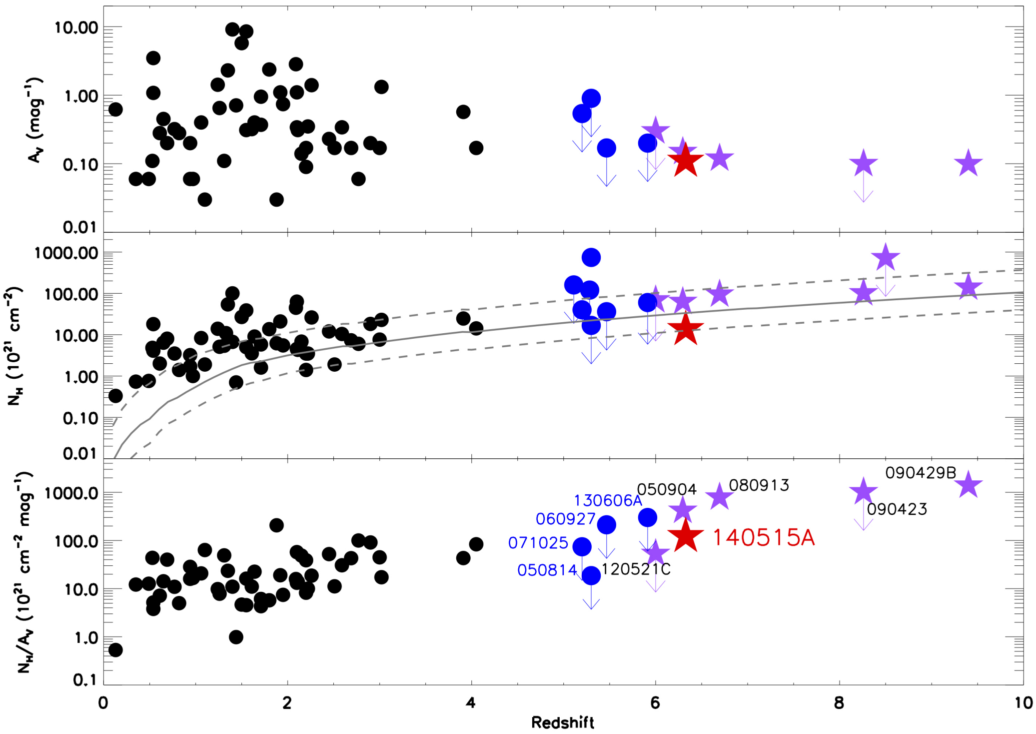

Figure 4.3: A_V, N_H, and N_H/A_V ratio as a function of redshift. Black points are from Covino et al. (2013) for events with $z \lesssim 4$, while the remaining events (blue circles, purple stars) are listed in Table 4.2. GRB 140515A is marked with a red star. The solid/dashed gray lines in the middle panel represent the effect of the intervening material along the line of sight (see Campana *et al.*, 2015; Salvaterra, 2015).

Table 4.2: Absorption properties of the GRBs with $z \geq 5$ (for the events marked with * the redshift was estimated photometrically). References: 1) Evans et al. 2010; 2) Perley et al. 2010; 3) Jakobsson et al. 2006; 4) Covino et al. 2013; 5) Salvaterra 2015; 6) Hartoog et al. 2014; 7) Totani et al. 2006; 8) This work.

GRB	z	log(N_{HI})	log($N_{H,X}$)	A_V	Ref.
		[cm^{-2}]	[10^{21} cm^{-2}]	[mag]	
060522	5.11	–	< 160	–	1
071025	$\leq 5.2^{*}$	–	49 ± 19	< 0.54	1, 2
140304A	5.283	–	< 120	–	1
050814	5.3	–	< 16.8	< 0.9	3, 1
131227A	5.3	–	520^{+220}_{-190}	–	1
060927	5.467	–	< 36	< 0.17	4, 1
130606A	5.913	19.93	< 30	< 0.2	5, 6
120521C	6.0^{*}	–	< 60	< 0.3	5
050904	6.295	21.6	63^{+34}_{-29}	0.15 ± 0.07	5,7
140515A	6.327	< 18.5	$13.5^{+12.2}_{-10.8}$	0.11 ± 0.02	8
080913	6.695	19.84	95^{+89}_{-77}	0.12 ± 0.03	5
090423	8.26	–	102^{+49}_{-54}	< 0.1	5
120923A	8.5^{*}	–	< 720	–	5
090429B	9.4^{*}	–	140 ± 10	0.10 ± 0.02	5

Such a sample would also serve as a direct test of reionization at $z > 6$, where constraints from high redshift quasars become scarce. A significant advantage of GRBs over quasars is in their low or negligible bias. While bright quasars, likely, do reside in the most massive, highly biased dark matter halos, GRBs hosts at high-z seem to sample the general galaxy population. Hence, constraints for the neutral hydrogen fraction obtained from the analysis of the IGM damping wing profile in the absorption spectra of GRB hosts can be expected to be more reliable than the analogous constraints from the quasar proximity zones.

In addition, constraints on the mean neutral fraction from observations of QSO proximity zones are, typically, lower limits (neutral fraction can be larger if a quasar lifetime is longer) (Bolton *et al.*, 2011; Robertson *et al.*, 2013, 2015), while constraints from GRBs are upper limits. Hence, the two observational probes are highly complementary to each other (this is demonstrated by red and orange diamonds in Fig. 4.2).

4.5 Conclusions

- We presented the multi-band spectroscopic and temporal analysis of the high-z GRB 140515A. The overall observed temporal properties of this burst, including the broad X-ray bump detected at late times, could be explained in the context of a standard afterglow model, although this requires an unusually flat index of the electron energy spectrum ($p = 1.67$).

- Another possible interpretation is to assume that an additional component (e.g. related to long-lasting central engine activity) is dominating the X-ray emission. In the latter case, the broad band observations can be explained using a more typical value of the spectral index for the injected electron spectrum ($p = 2.1$). Our modelling in this case shows that the central engine activity should cease at late times ($\sim 2 \times 10^5$ s), when the X-ray afterglow starts to dominate the emission.

- In both scenarios the cooling frequency is expected to be between the optical and the X-ray energy bands ($\nu_c \sim 2 \times 10^{16}$ Hz) and the average rest-frame circum-burst extinction ($\mathrm{A_V} \sim 0.1$) resulted to be typical of high-z bursts.

- Our detailed spectral analysis provided a best estimate of the neutral hydrogen fraction of the IGM towards the burst of $x_{HI} \leq 0.002$ and a conservative upper limit of the HI abundance in the GRB host galaxy of $N_{\mathrm{HI}} \lesssim 10^{18.5}$ cm^{-2}. These values are slightly different from the ones estimated by Chornock et al. (2014b).

- In addition, the spectral absorption lines observed in our spectra are the weakest lines ever observed in GRB afterglows (de Ugarte Postigo *et al.*, 2012a), suggesting that GRB 140515A happened in a very low density environment. However, our upper limits on the gas-phase abundances, coupled with the fact that we cannot establish the exact metal-to-dust ratio, do not allow us to distinguish between metallicity in the range of $10^{-4} < [Z/H] < 0.1$. This makes the possible Pop III star origin for GRB 140515A uncertain and doubtful.

- For all high-z GRBs the contribution of the host galaxy was not negligible (Table 4.2). GRB 140515A is the first case when this does not happen, allowing us to give the best observational constrains on a theoretical model at $z > 6$.

PART III

ABSORPTION SYSTEMS IN THE LINE OF SIGHT TO QUASARS:

THE EVOLUTION OF NEUTRAL GAS IN DAMPED LYMAN ALPHA SYSTEMS

Chapter 1

Introduction

> *"We do not argue with the critic who urges that the stars are not hot enough for this process; we tell him to go and find a hotter place."*
>
> — ARTHUR EDDINGTON, *The Internal Constitution of Stars, 1926*

These sources are described in the next sections.

Measurements of $\Omega_{\rm HI}$, the mass density of atomic hydrogen gas scaled to the critical density, and its evolution with redshift offer cosmological constraints on several aspects of galaxy formation. The value of $\Omega_{\rm HI}$ at any epoch characterizes the instantaneous reservoir of cold, neutral gas available for star-formation integrated across the entire galaxy population. This constraint holds independently of the detailed association of individual DLAs to specific galaxy populations, i.e. $\Omega_{\rm HI}$ is a cosmic quantity (e.g. Wolfe *et al.*, 1995). It may serve, therefore, as an input to semi-analytic prescriptions for galaxy formation (e.g., Somerville & Davé, 2015). The time evolution of $\Omega_{\rm HI}$, meanwhile, tracks the global balance between the accretion of cold gas onto galaxies against the processes that consume and/or expel that gas (e.g. Davé *et al.*, 2013; Kereš *et al.*, 2012; Lilly *et al.*, 2013). As theorists continue to explore models to capture the complex processes of star-formation and feedback, $\Omega_{\rm HI}$ offers a cosmic check on their prescriptions. Indeed, there is apparent tension between previous $\Omega_{\rm HI}$ measurements and galaxy formation models that reproduce other key observables of the galactic population (Bird *et al.*, 2015; Somerville & Davé, 2015). We are hence motivated to assess $\Omega_{\rm HI}$ and the uncertainties in its estimation across cosmic time.

This cosmic evolution of $\Omega_{\rm HI}$ can be traced by combining surveys of damped Lyman alpha systems (DLAs) at moderate-to-high redshifts, with 21cm emission surveys at $z{\sim}0$. In recent years, there has been significant progress in refining measurements of $\Omega_{\rm HI}$ with both of these techniques, where large statistical samples have been crucial for addressing biases due to incompleteness. In the nearby universe the greatest uncertainty for the determination of $\Omega_{\rm HI}$ in early 21cm surveys was the faint end slope of the H I mass function (e.g. Rosenberg & Schneider, 2002; Zwaan *et al.*, 2003, 2005). The Arecibo L-band Fast ALFA (ALFALFA) survey (Giovanelli *et al.*, 2005) has now provided the $z{\sim}0$ benchmark for $\Omega_{\rm HI}$, based on over 10,000 galaxies in the local universe (Martin *et al.*, 2010). Extending the measurement of $\Omega_{\rm HI}$ to even $z \sim 0.1 - 0.2$ is extremely challenging for current 21 cm surveys. Nonetheless, stacking experiments have produced several estimates of $\Omega_{\rm HI}$ in this redshift range (Delhaize *et al.*, 2013; Lah *et al.*, 2007; Rhee *et al.*, 2013). Individual detections of 21 cm emission beyond $z = 0$ are growing, thanks to surveys such as CHILES (Fernández *et al.*, 2013) and HIGHz (Catinella & Cortese, 2015), although these surveys are not yet large or complete enough to give a statistical perspective on $\Omega_{\rm HI}$.

Fortunately, $\Omega_{\rm HI}$ in the higher redshift universe can be effectively measured in absorption, using DLA surveys. The objective of DLA surveys has largely been to assess the redshift evolution of $\Omega_{\rm HI}$, in comparison to the z=0 local benchmark. Early surveys of DLAs focused predominantly on the redshift range $2 < z_{\rm abs} < 3.0$ (e.g. Wolfe *et al.*, 1986, 1995). The lower bound of this redshift range was set by the accessibility of the Lyα line to ground based spectrographs, and the upper bound by the limited number of bright, high redshift quasars known at the time. Although these early surveys enabled a broad-brush measurement of $\Omega_{\rm HI}$, the limited redshift range and sample sizes were insufficient to study the evolution of the cosmic gas reservoir. Subsequent ground-based surveys were motivated to extend the redshift range to earlier epochs, and reported a tentative peak in $\Omega_{\rm HI}$ at $z \sim 3$ (Storrie-Lombardi & Wolfe, 2000; Storrie-Lombardi *et al.*, 1996a). As the size of DLA samples grew, improved statistics led to an upward revision of $\Omega_{\rm HI}$ at z>3.5 and evidence for a peak at z∼3 diminished; the mass density of H I in DLAs appeared to be consistent over the range of redshifts z∼ 2 – 5 (Péroux *et al.*, 2003, 2005). The apparent down-turn of $\Omega_{\rm HI}$ seen in earlier surveys seems likely to be caused by poor statistics at the survey limit (e.g. Prochaska & Herbert-Fort, 2004).

Despite these early surveys, the error bars on $\Omega_{\rm HI}$ remained substantial, and it was the advent of the Sloan Digital Sky Survey (SDSS) that led to the first truly robust measure of $\Omega_{\rm HI}$ redshift evolution. Several investigations, based on different SDSS data releases, have found a mildly decreasing $\Omega_{\rm HI}$ from z∼3.5 to 2 (e.g. Noterdaeme *et al.*, 2009, 2012; Prochaska & Herbert-Fort, 2004; Prochaska & Wolfe, 2009; Prochaska *et al.*, 2005). All of these works self-consistently show an evolution of at most a factor of two in this redshift range, an effect too subtle to be detectable in previous smaller surveys. Pushing to even higher redshifts, there again seemed to be tentative evidence of a downturn in $\Omega_{\rm HI}$ above z∼3.5 (Guimarães *et al.*, 2009; Songaila & Cowie, 2010). However, with a factor of eight increase in path length over previous compilations, Crighton *et al.* (2015) have shown that $\Omega_{\rm HI}$ evolution is statistically consistent (within the observational errors) with a power law of index 0.4 from $z = 5$ to the present day. The results of Crighton *et al.* (2015) therefore support a mild, but steady evolution in the neutral gas content of galaxies since early times.

Despite the uniform decline in $\Omega_{\rm HI}$ from high z to the present day proposed by Crighton *et al.* (2015), the value of $\Omega_{\rm HI}$ measured at $z = 5$ is formally consistent with the value measured by Rao *et al.* (2006) in the range $0.2 < z_{\rm abs} < 1.5$ (see Fig. 12 of Crighton *et al.*, 2015). A statistically plausible alternative picture to the steady decline of $\Omega_{\rm HI}$ is therefore one in which gas consumption was almost perfectly balanced by replenishment, with a statistically significant decrease (of a factor of two) only at the most recent epochs. One of the challenges in the interpretation of the data compilation presented by Crighton *et al.* (2015) is in the combination of surveys performed at different redshifts, and a homogeneous assessment of the error associated with $\Omega_{\rm HI}$.

In this paper we present a new survey for DLAs in the range $1.6 < z_{\rm abs} < 4.5$ and make a novel assessment of $\Omega_{\rm HI}$ as a function of redshift. Our sample combines DLAs from our own survey, with a compilation of literature absorbers that has been carefully checked for duplicates and errors. Rather than showing our new survey results in comparison with previous surveys at different redshifts, we maximize the statistical potential of decades of work by combining previous surveys together. Moreover, by quantifying $\Omega_{\rm HI}$ within a sliding redshift window, rather than in contiguous non-overlapping bins, and with a rigorous assessment of error propagation techniques, we are able to determine a holistic perspective of the atomic gas content of galaxies up to $z = 5$.

The paper is organized as follows. In Section 2 we describe the XQ-100 survey of 100 $z > 3.5$ quasars, and the detection of DLAs therein. The XQ-100 DLA sample is combined with various literature samples and compilations, as described in Section 3. Section 4 presents our statistical analysis, including the description of our technique to determine $\Omega_{\rm HI}$ evolution 'curves', a rigorous assessment of sources of error and the analysis of the column density distribution and line density functions.

In this work, we will use the term $\Omega_{\rm HI}^{\rm DLA}$, to mean the neutral hydrogen mass density in Damped Lyman α systems (i.e. the contribution to $\Omega_{\rm HI}$ from systems above the DLA column density threshold, $\log N(\text{H I}) \geq 20.3$) relative to the critical density. The total gas mass density is given by $\Omega_{\rm g}$, which requires a correction to $\Omega_{\rm HI}$ by the factor μ=1.3 to account for helium. Finally, we assume a flat ΛCDM cosmology with H_0=70.0 km s^{-1} Mpc^{-1}, Ω_m=0.3 and Ω_Λ=0.7.

1.1 An historical perspective of the QSO-DLA surveys

Wolfe *et al.* (1986, W86) The first systematic search for DLAs in optical QSO spectra was performed by Wolfe *et al.* (1986). In this first survey 47 absorption features were found, but in 11 cases the presence of damping wings was ruled out, starting to show the difficulties in DLA identification with low quality spectra.
Since then, many low-resolution surveys were conducted with the aim of increasing the statistical sample to constrain better the H Icontent and its evolution over the cosmic time (e.g. Lanzetta *et al.*, 1991; Storrie-Lombardi & Wolfe, 2000; Storrie-Lombardi *et al.*, 1996c; Wolfe *et al.*, 1995). The culmination of this first exiting epoch arrived with the analysis of Péroux *et al.* (2001, 2003, 2005) compilation. These works showed that there is little evolution in the H Icontent up to $z\sim$ 5, increasing its value from $z\sim$ 1.7 and peaking at $z\sim$ 3.5.

Motivated by the discovery of 21cm absorption in 2 of the 3 radio loud Quasi-Stellar Objects (QSOs) at z 2 known at the date, Wolfe *et al.* (1986) published the results of the first systematic search for damped Lyαsystems (DLAs) in optical QSO spectra, that they thought are H Idisks in spiral galaxies in the line of sight of these backlight sources. DLA definition was establish to be those absorbers with $N(\mathrm{H\,I}) > 2.0 \times 10^{20}$ cm^{-2}. The physical reason to do that is because this value is the threshold to keep the gas mainly neutral, needed to trigger star formation processes. In this first survey 47 features were found, but in 11 cases the presence of damping wings was ruled out, showing for the first time the difficulties in DLA identification in the Lyαforest with poor quality spectra.

Lanzetta *et al.* (1991, L91) With Lanzetta *et al.* (1991) the idea that DLAs are only spiral galaxies disks was rejected and they performed the first statistical analysis of the H Icontent as a function of redshift. Such a small sample only showed an slightly increase of H Icontent with z, but they realized that local star mass density is comparable to DLA density at $z \sim 2.5$, supporting that these systems could be tracers of the material available for star formation. Data from Wolfe *et al.* (1995) seemed to confirm a exponential evolution of H Icontent due to gas consumption by star formation.

With the venue of the high redshift surveys by Storrie-Lombardi & Wolfe (2000); Storrie-Lombardi *et al.* (1996c), ”closed box” hypothesis was clearly rejected, indicating that DLAs are only reservoirs for a fraction of the stars actually observed, and H Icontent seemed to fall at $z \sim 3.5$. This behaviour was confirmed by Péroux *et al.* (2001, 2003, 2005) using new data.

At this stage, a low resolution compilation of DLAs in the line of sight of bright QSOs (there is no dust bias, so this detail is irrelevant; Ellison *et al.*, 2001) was built up from the work of many authors using different instruments. As consequence, this is an inhomogeneous sample that can be affected by strong systematics related to the quality of the data and/or the different criteria and procedure followed by the researcher in order to classify an absorber as damped or as a blend of saturated lines.

With SDSS came a great chance to test and expand these results. Prochaska & Herbert-Fort (2004); Prochaska & Wolfe (2009); Prochaska *et al.* (2005) analized data releases 1, 3 and 5. Latest DLA catalog is still the largest one with visually confirmed features. They saw with this new homogeneous sample the same behavior on the evolution of H Icontent but in the highest redshift interval, where they see no $z \sim 3.5$ drop. Nevertheless, they noticed that the results at very high redshift are strongly dependent on the spectra SNR, and several more were enumerated that could bias the results. So new analyses are needed in order to understand better the H Ievolution at very high redshift and the reasons for this discrepancy between samples.

Noterdaeme *et al.* (2009, 2012) analyzed SDSS DR7 and DR9 in a completely automated fashion. They published the largest absorber catalog down to log N(H I)=20.0 so far and their results constrains very well H Ievolution up to $z \sim 3.5$. Nevertheless, we have to take into account that these DLAs are not visually confirmed; there are false detections due to the algorithm and corrections needed to compute $\Omega_{\rm HI}^{\rm DLA}$were quantified using mock spectra. But when code is tested at redshifts higher than 3.5 the systematics associated cannot be constrained properly due to the increase of line blending in the Lyαforest.

So using even independent methods to analyse SDSS data, authors find difficulties at zones where Lyαforest density is important. This conclusion leads to the need to a better understanding of the issues involving very high redshift sight-lines.

The first chance to compare an intermediate resolution DLA survey arrived with the work by Guimarães *et al.* (2009). They observed a sample of $z > 4$ QSOs with a resolution of $R \sim 4600$. Their results seem consistent with a $z \sim 3.5$ drop, but statistical uncertainties are too high to establish anything.

Chapter 2

XQ-100

Adapted from "The evolution of neutral gas in damped Lyman α systems from the XQ-100 survey"

— Sánchez-Ramírez et al., *MNRAS, 2016*

In and out

2.1 The XQ-100 sample

The XQ-100 survey is an ESO Large Program (ESO ID 189.A-0424, P.I. S. Lopez) which obtained X-shooter spectra of 100 $3.5 < z < 4.7$ QSOs in the period between 10-02-2012 and 23-02-2014. X-shooter (Vernet *et al.*, 2011) is a triple-arm spectrograph which obtains moderate resolution spectra with complete wavelength coverage from $\sim 320 - 2500$ nm, permitting the simultaneous analysis of QSO absorption lines and emission features from the atmospheric cut-off to the near-IR. A full description of the XQ-100 survey characteristics, sample selection, observational set-up and data reduction is provided in Lopez et al. (in prep). We review only the basic features of the survey design and data here. In brief, the XQ-100 survey adopted slit widths of 0.9" (UVB arm) and 1.0" (VIS and NIR arms) to obtain spectra whose resolution ranged from $R \sim 5100 - 8800$. Exposure times ranged from $\sim$ 1700s to 3600s yielding a median signal-to-noise ratio (SNR) $\sim$ 30 per pixel. The data were reduced using a custom pipeline which provided a notable improvement in the removal of the near-IR sky emission with respect to the ESO provided pipeline. All of the 1-dimensional spectra (flux and wavelength calibrated) are made publically available (see Lopez et al. in prep for details on the data reduction and public data release). Higher order data products are also made available in the public repository: spectra corrected for telluric absorption and normalized spectra derived from a variety of continuum fitting methods.

In this paper, we make use of the basic 1D products and perform our own normalization of the continuum. This decision is driven by the sensitivity of the Lyα fit in the damping wings to the continuum placement. The nomalization of the spectra and Voigt profile fits were performed using an interactive interface that permits the user to simultaneously identify and fit the absorbers, and iterate on the continuum placement. The iterative procedure is required due to both the complexity of the Lyα forest, and the challenges associated with continuum placement over the broad damped profile, particularly in the shallow wing region (Prochaska *et al.*, 2003).

The fitting procedure can be summarized as follows. First, we estimated the continuum by manually identifying regions of apparently unabsorbed continuum flux throughout the Lyα forest and around the Lyα emission. A cubic spline was used to fit these points and make an initial normalization. Next, a Voigt profile with $\log N(\mathrm{H\,I})$=19.0 is moved through the forest range looking for DLA candidates. Although the canonical threshold for DLA classification is $\log N(\mathrm{H\,I})$=20.3, the lower threshold of our scan provides a conservative initial selection for assessment. It is also useful to identify these lower column density systems to aid with fits of blended absorbers. For each potential absorption system, a simultaneous fit of all Lyman series lines up to Lyϵ was performed, with adjustments to the continuum when necessary, in order to determine the HI column density and redshift of the absorber. Metal lines associated with each potential absorber were identified (in Berg et al., MNRAS **submmited**, we present a complete assessment of the abundances in the XQ-100 DLA sample), and in cases of uncertain fits (e.g. due to blends) the redshifts from the metal lines were used to inform the fits (but the metals are not used *a priori* to fix the redshifts for all absorbers). An example of our fits is shown in Figure 2.1; a full montage of all of the fits to our DLA sample is provided in the online version of this paper.

The conservative initial search threshold of $\log N(\text{H I})$=19.0 permits the identification of numerous absorbers whose $N(\text{H I})$ is below the traditional DLA threshold of $\log N(\text{H I})$=20.3, yet still exhibit damping wings that permit the accurate measurement of the HI content. These sub-DLAs have been the subject of targeted research (e.g. Zafar *et al.*, 2013) and are sometimes included explicitly (e.g. Guimarães *et al.*, 2009; Péroux *et al.*, 2005), or statistically (e.g. Crighton *et al.*, 2015) in the calculation of $\Omega_{\rm HI}$. Despite the ability of our dataset to identify absorbers down to at least $\log N(\text{H I})$=19.5, we do not include them in the present work (however, these absorbers are used to compute $f_{\rm HI}(N, X)$ and $\Omega_{\rm HI}^{\rm DLA}$ uncertainties). The motivation for this decision is one of homogeneity. Later in this work, we will combine the XQ-100 sample with other available surveys for DLAs at $z > 2$, in order to obtain the most statistically robust measure of $\Omega_{\rm HI}$ from $2 < z < 5.5$. Since many of the literature samples that we will make use of do not include sub-DLAs (often due to their more limited spectral resolution), we adopt the standard threshold of $\log N(\text{H I})$=20.3 for the DLA catalog presented here. However, in a separate future paper, we will present the identification of sub-DLAs, with column density completion functions and assess their contribution to both the neutral gas and metals at $z \sim 4$.

The final requirement for the DLA to be included in our XQ-100 statistical sample for the computation of $\Omega_{\rm HI}^{\rm DLA}$ is that its redshift be at least 5000 km s^{-1} from the background QSO in order to exclude the proximate DLA (PDLA) population. The PDLAs have been shown to exhibit different clustering properties (they are more prevalent than intervening systems, Ellison *et al.*, 2002; Prochaska *et al.*, 2008b; Russell *et al.*, 2006) and have also been suggested to manifest different metallicities and ionization conditions (Ellison *et al.*, 2010, 2011). These distinctions justify the exclusion of PDLAs from our statistical study of DLA gas content. These out-of-sample absorbers are flagged with a star in Table 2.1.

Our final XQ-100 DLA sample contains 38 absorbers with absorption redshifts ranging from 2.24 to 4.47. Of these DLAs, 27 are not duplicated in our combined literature sample and 22 are not in the catalog by Noterdaeme *et al.* (2012). Duplicated systems are flagged with a diamond in Table 2.1.

We compare in Figure 2.3 our fitted $N(\text{H I})$ values with previous estimates for some systems, where measurements have been made at a variety of spectral resolutions. Most of the DLAs in the Péroux *et al.* (2003) compilation, as well as those by Noterdaeme *et al.* (2012), are observed at $R < 2000$. The (Guimarães *et al.*, 2009) sample was observed with ESI, which has a comparable resolution to X-shooter. The 'high resolution' (HR Berg *et al.*, 2015a) data points have typical values of $R \sim 40,000$, observed with either HIRES on Keck or UVES on the VLT. There is a tendency for the XQ-100 fits to exceed those in the literature when the resolution of the latter is low. However, the agreement with high resolution measurements is generally excellent and well within the quoted uncertainties (typically 0.1 – 0.2 dex).

We also performed a further test to determine whether our XQ-100 measurements are reliable, or exhibit any systematic bias. Using the pairs of $(z, \log N(\text{H I}))$ values of our DLA sample and the number of Lyman series lines used to fit each pair, we injected synthetic absorbers into real XQ-100 spectra. In this way, we accurately represent the properties of the DLAs in our sample, and our ability to recover them for the noise and resolution properties of the data. We blindly measured the $\log N(\text{H I})$ of the synthetic absorbers using the same procedure as previously employed for real systems. The comparison between the real and measured column densities are shown in Figure 2.2. The agreement at high $\log N(\text{H I})$ is excellent. At moderate column densities, there is an increased scatter, mainly due to blending with sub-DLAs and Lyman limit systems, but most absorbers are accurately measured within 0.2 dex, and there is no systematic under or over-estimate.

2.2 Literature samples

Since the early work by Wolfe *et al.* (1986), numerous surveys have catalogued DLAs over a range of redshifts (e.g. Crighton *et al.*, 2015; Ellison *et al.*, 2001; Guimarães *et al.*, 2009; Lanzetta *et al.*, 1991; Neeleman *et al.*, 2016; Noterdaeme *et al.*, 2009, 2012; Péroux *et al.*, 2001; Prochaska & Herbert-Fort, 2004; Prochaska & Wolfe, 2009; Prochaska *et al.*, 2005; Rao *et al.*, 2006; Storrie-Lombardi & Wolfe, 2000; Storrie-Lombardi *et al.*, 1996c; Wolfe *et al.*, 1995) in order to trace the cosmic evolution of neutral hydrogen gas in galaxies. These surveys are extremely heterogenous and have been conducted with a variety of telescope apertures, both from space and on the ground, and at a range of spectral resolutions. There are also considerable duplications between surveys, and both the naming conventions and the presentation of the data in the literature mean that

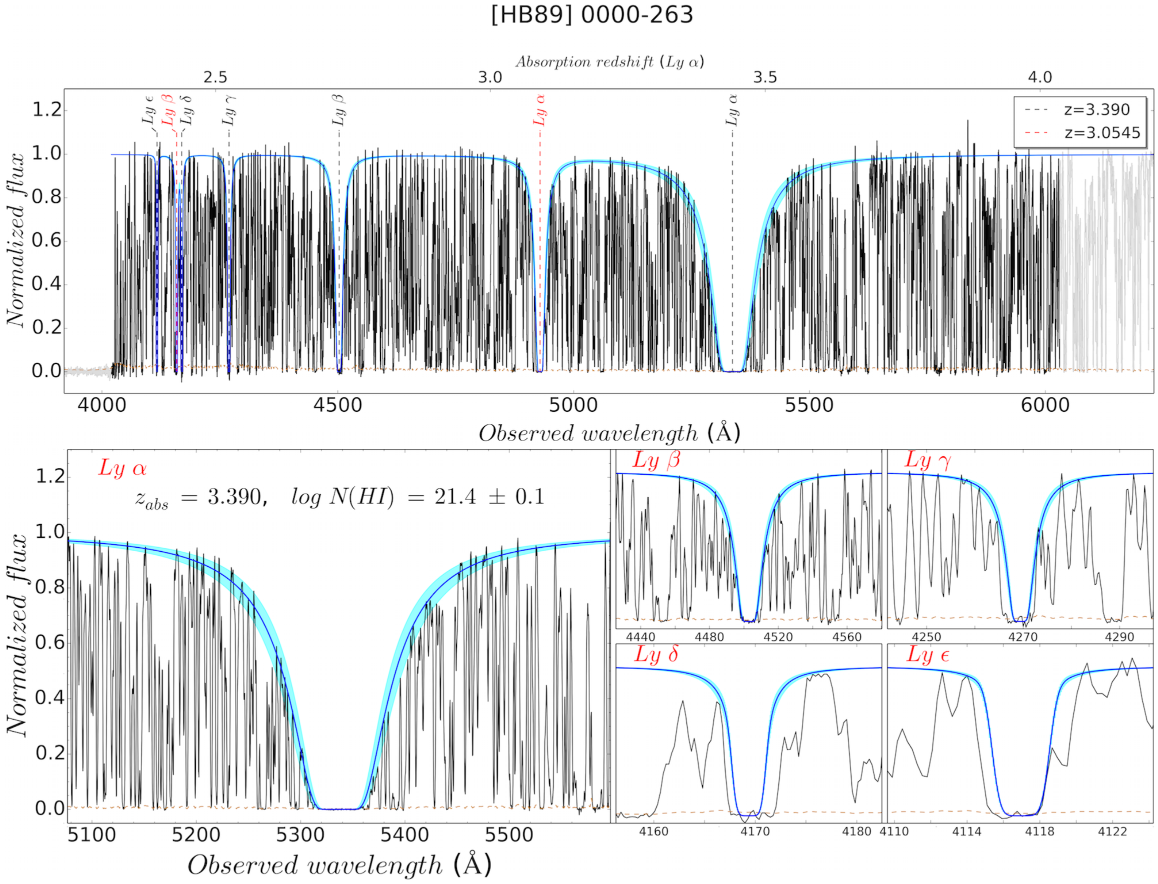

Figure 2.1: Example of normalized Lyα forest (upper panel) for the quasar [HB89] 0000-263. The part of the spectrum used for statistics is plotted in black and the rest in gray. The error spectrum is shown in brown. The model of all absorbers with log $N(\text{H I})\geq 19.5$ is drawn in blue with the 1σ error zone shaded in cyan. Each individual system is labeled with a specific color denoted in the legend box. However, only one of the absorbers, at $z = 3.390$, has an $N(\text{H I})$ above the DLA threshold and is included in our catalog. The fits to the higher order lines of this DLA are shown in the lower panels.

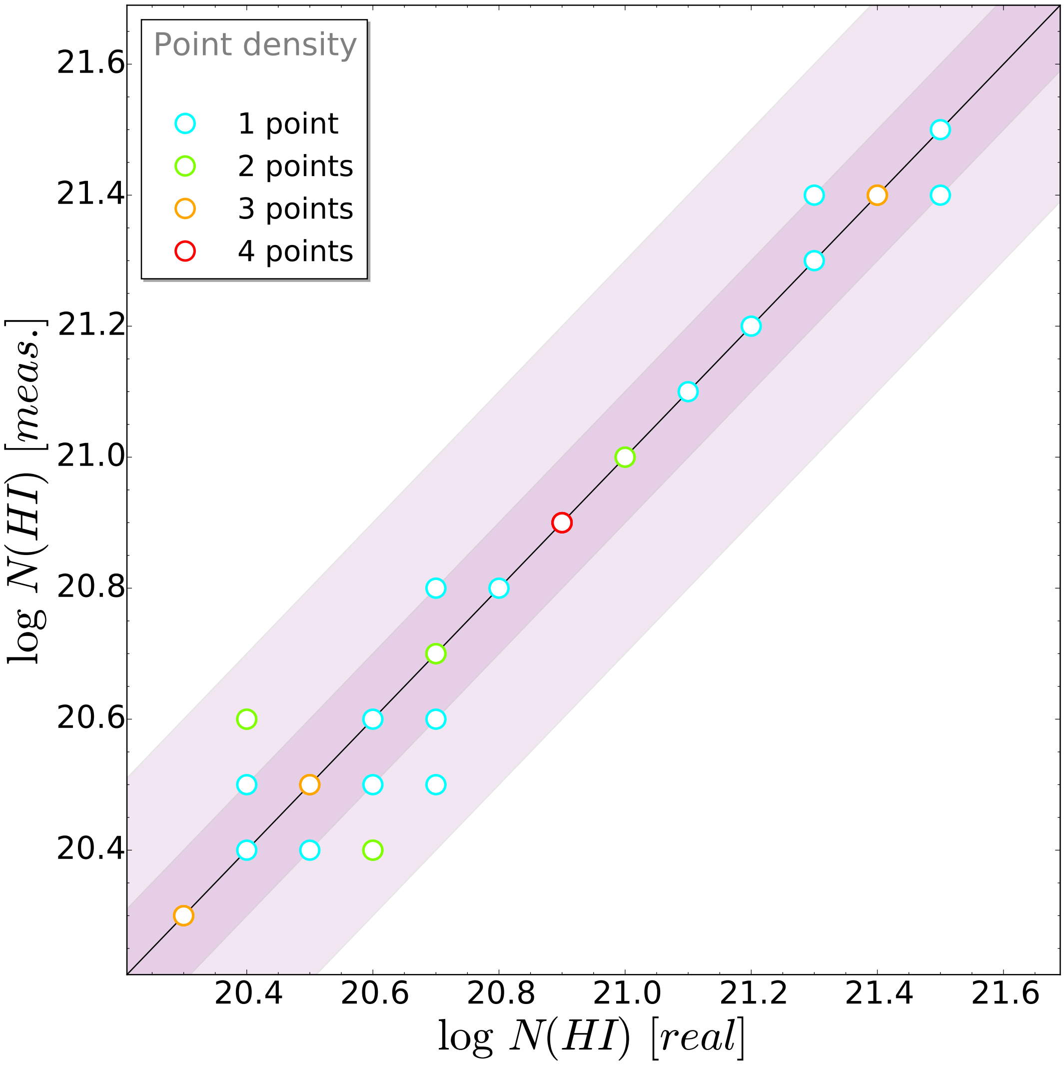

Figure 2.2: Comparison of our measurements of the synthetic DLAs inserted into XQ-100 data. The colour of the points represent the number of points that overlap due to matching log N(H I) for different redshift tests. Shaded purple regions show 0.1 dex and 0.3 dex intervals.

Table 2.1: **XQ-100 DLA catalog.**

Name	$z_{\rm em}$	$z_{\rm min}$	$z_{\rm max}$	$z_{\rm abs}$	$\log N(\mathrm{H\,I})$	$\epsilon[\log N(\mathrm{H\,I})]$	Lines covered
♢ [HB89] 0000-263	4.010	2.307	4.041	3.3900	21.40	0.10	Ly-α, Ly-β, Ly-γ, Ly-δ, Ly-ϵ
♠ [HB89] 0053-284	3.620	2.447	3.559				
[HB89] 0055-269	3.660	1.599	3.584				
BRI 0241-0146	4.050	2.743	3.972				
BR 0245-0608	4.240	2.891	4.147				
♢ BRI 0952-0115	4.430	2.907	4.329	4.0245	20.70	0.15	Ly-α, Ly-β, Ly-γ, Ly-δ
BR 1033-0327	4.510	2.899	4.440				
BRI 1108-0747	3.920	2.619	3.841				
[HB89] 1159+123	3.510	1.854	3.448				
BR 2212-1626	3.990	2.529	3.912				
BR 2213-6729	4.470	2.768	4.389				
BR 2248-1242	4.160	2.940	4.072				
♢ PKS B1418-064	3.690	2.356	3.611	3.4490	20.30	0.15	Ly-α, Ly-β, Ly-γ, Ly-δ, Ly-ϵ
BR J0006-6208	4.460	2.998	4.351	3.2030	20.90	0.15	Ly-α
				3.7750	21.00	0.20	Ly-α, Ly-β
BR J0030-5129	4.170	2.529	4.088				
★ PSS J0034+1639	4.29	2.9813	4.2396	4.2835	21.00	0.10	Ly-α, Ly-β, Ly-γ, Ly-δ, Ly-ϵ
★				4.2523	20.60	0.10	Ly-α, Ly-β, Ly-γ, Ly-δ, Ly-ϵ
				3.7550	20.40	0.15	Ly-α, Ly-β
SDSS J004219.74-102009.4	3.880	2.488	3.783				
BRI J0048-2442	4.150	2.587	4.000				
♠ PMN J0100-2708	3.520	2.192	3.471				
♢ BRI J0113-2803	4.300	2.784	4.227	3.1060	21.20	0.10	Ly-α
PSS J0117+1552	4.240	2.364	4.157				
PSS J0121+0347	4.130	2.546	4.041				
♢ SDSS J0124+0044	3.840	2.077	3.758	2.2610	20.70	0.15	Ly-α
♢ PSS J0132+1341	4.160	2.833	4.067	3.9360	20.40	0.15	Ly-α, Ly-β, Ly-γ, Ly-δ
♢ PSS J0133+0400	4.150	2.850	4.100	3.6920	20.70	0.10	Ly-α, Ly-β
♢				3.7725	20.70	0.10	Ly-α, Ly-β
BRI J0137-4224	3.970	2.513	3.889				
SDSS J015339.60-001104.8	4.190	2.825	4.110				
PSS J0211+1107	3.980	2.438	3.891				
PMN J0214-0518	3.990	2.554	3.895				
♢ BR J0234-1806	4.310	2.957	4.218	3.6930	20.40	0.15	Ly-α, Ly-β
PSS J0248+1802	4.420	2.858	4.350				
♢ SDSS J025518.57+004847.4	4.010	2.702	3.921	3.9145	21.50	0.10	Ly-α, Ly-β, Ly-γ, Ly-δ, Ly-ϵ
♢				3.2555	20.90	0.10	Ly-α
♢ BR J0307-4945	4.720	3.130	4.622	4.4665	20.60	0.10	Ly-α, Ly-β, Ly-γ, Ly-δ, Ly-ϵ
				3.5910	20.50	0.15	Ly-α
BR J0311-1722	4.040	2.562	3.951				
BR 0401-1711	4.230	2.858	4.141				
BR J0415-4357	4.070	2.800	3.990	3.8080	20.50	0.20	Ly-α, Ly-β, Ly-γ
♢ BR 0424-2209	4.320	2.751	4.242	2.9825	21.40	0.15	Ly-α
BR 0523-3345	4.410	2.817	4.297				
BR J0529-3526	4.410	2.817	4.329				
BR J0529-3552	4.170	2.825	4.087	3.6840	20.40	0.15	Ly-α, Ly-β
BR J0714-6455	4.460	2.776	4.374				
♢ SDSS J074711.15+273903.3	4.170	2.710	4.049	3.4235	20.90	0.10	Ly-α, Ly-β
♢				3.9010	20.60	0.15	Ly-α, Ly-β, Ly-γ, Ly-δ, Ly-ϵ
SDSS J075552.41+134551.1	3.670	2.085	3.587				
★ SDSS J080050.27+192058.9	3.96	2.7264	3.899	3.9465	20.40	0.10	Ly-α, Ly-β, Ly-γ, Ly-δ, Ly-ϵ
SDSS J081855.78+095848.0	3.670	2.406	3.580	3.3060	21.00	0.10	Ly-α, Ly-β, Ly-γ
SDSS J083322.50+095941.2	3.750	2.044	3.639				
SDSS J083510.92+065052.8	3.990	2.735	3.925				
SDSS J083941.45+031817.0	4.250	2.883	4.144				
SDSS J092041.76+072544.0	3.640	2.060	3.570	2.2380	20.90	0.15	Ly-α
SDSS J093556.91+002255.6	3.750	2.249	3.669				
SDSS J093714.48+082858.6	3.700	2.118	3.626				
SDSS J095937.11+131215.4	4.060	2.702	4.008				

Table 2.2: XQ-100 DLA catalog.

Name	$z_{\rm em}$	$z_{\rm min}$	$z_{\rm max}$	$z_{\rm abs}$	$\log N(\mathrm{H\,I})$	$\epsilon[\log N(\mathrm{H\,I})]$	Lines covered
SDSS J101347.29+065015.6	3.790	2.397	3.729				
♠ SDSS J101818.45+054822.8	3.520	2.299	3.441				
SDSS J102040.62+092254.2	3.640	2.093	3.564	2.5920	21.50	0.10	Ly-α
♠ SDSS J102456.61+181908.7	3.530	2.159	3.450	2.2980	21.30	0.10	Ly-α
SDSS J103221.11+092748.9	3.990	2.619	3.903				
SDSS J103446.54+110214.5	4.270	2.422	4.183				
SDSS J103730.33+213531.3	3.630	1.665	3.550				
SDSS J103732.38+070426.2	4.100	2.225	4.043				
SDSS J104234.01+195718.6	3.640	2.044	3.554				
SDSS J105340.75+010335.6	3.650	1.937	3.587				
SDSS J105434.17+021551.9	3.970	2.603	3.889				
SDSS J105705.37+191042.8	4.100	2.661	4.044	3.3735	20.30	0.10	Ly-α, Ly-β
◇ SDSS J105858.38+124554.9	4.330	2.570	4.253	3.4315	20.60	0.10	Ly-α, Ly-β
SDSS J110352.73+100403.1	3.610	2.200	3.531				
SDSS J110855.47+120953.3	3.670	2.447	3.601	3.5460	20.80	0.15	Ly-α, Ly-β, Ly-γ, Ly-δ, Ly-ϵ
◇				3.3965	20.70	0.10	Ly-α, Ly-β, Ly-γ
SDSS J111008.61+024458.0	4.120	2.364	4.062				
SDSS J111701.89+131115.4	3.620	2.208	3.546				
SDSS J112617.40-012632.6	3.610	2.225	3.558				
SDSS J112634.28-012436.9	3.740	2.430	3.687				
SDSS J113536.40+084218.9	3.830	1.780	3.755				
♠ SDSS J120210.08-005425.4	3.590	2.159	3.517				
SDSS J124837.31+130440.9	3.720	2.315	3.644				
SDSS J124957.23-015928.8	3.630	2.406	3.553				
SDSS J130452.57+023924.8	3.650	2.257	3.572				
SDSS J131242.87+084105.1	3.740	2.027	3.653	2.6600	20.50	0.10	Ly-α, Ly-β
2MASSi J1320299-052335	3.700	1.904	3.640				
SDSS J132346.05+140517.6	4.040	2.241	3.971				
BR J1330-2522	3.950	2.282	3.867				
SDSS J133150.69+101529.4	3.850	2.323	3.772				
♠ SDSS J133254.51+005250.6	3.510	2.323	3.434				
SDSS J133653.44+024338.1	3.800	1.887	3.722				
SDSS J135247.98+130311.5	3.700	2.035	3.629				
SDSS J1401+0244	4.440	2.916	4.319				
♠ SDSS J141608.39+181144.0	3.590	2.266	3.518				
♠ SDSS J144250.12+092001.5	3.530	1.780	3.458				
SDSS J144516.46+095836.0	3.520	1.599	3.487				
SDSS J150328.88+041949.0	3.660	2.118	3.615				
♠◇ SDSS J151756.18+051103.5	3.560	2.249	3.480	2.6885	21.40	0.10	Ly-α
♠ SDSS J152436.08+212309.1	3.610	2.052	3.525				
SDSS J154237.71+095558.8	3.990	2.257	3.904				
SDSS J155255.03+100538.3	3.730	2.529	3.644	3.6010	21.10	0.10	Ly-α, Ly-β, Ly-γ, Ly-δ, Ly-ϵ
SDSS J1621-0042	3.700	2.101	3.634				
◇ SDSS J163319.63+141142.0	4.330	2.438	4.277	2.8820	20.30	0.15	Ly-α
CGRaBS J1658-0739	3.740	2.537	3.671				
◇ PSS J1723+2243	4.520	3.056	4.440	3.6980	20.50	0.10	Ly-α
◇ 2MASSi J2239536-055219	4.560	2.949	4.465	4.0805	20.60	0.10	Ly-α, Ly-β, Ly-γ, Ly-δ
◇ PSS J2344+0342	4.240	2.693	4.162	3.2200	21.30	0.10	Ly-α
BR J2349-3712	4.210	2.850	4.133				

★ = PDLA, ◇ = DLA already identified in a previous survey, ♠ = Color biased sight-line.

Table 2.3: Abbreviations used for literature samples.

Id	Reference
P03	Péroux *et al.* (2003)
Z05	Zwaan *et al.* (2005)
R06	Rao *et al.* (2006)
PW09	Prochaska & Wolfe (2009)
B12	Braun (2012)
D13	Delhaize *et al.* (2013)
R13	Rhee *et al.* (2013)
C15	Crighton *et al.* (2015)
N15	Neeleman *et al.* (2016)

assembling a combined sample is a considerable challenge. Nonetheless, in this work we have attempted to assemble such a combined sample from the major DLA catalogs that are currently available, focusing on $z > 2$, the redshift range where ground-based surveys have most effectively contributed. We review these catalogs in turn below.

For comparison purposes, we also use Noterdaeme *et al.* (2012, hereafter N12) data in the high redshift range, Rao *et al.* (2006, hereafter R06) and Neeleman *et al.* (2016, hereafter N15) for intermediate redshifts and the 21cm samples from the local Universe by Rhee *et al.* (2013, hereafter R13), Delhaize *et al.* (2013, hereafter D13), Zwaan *et al.* (2005, hereafter Z05), and Braun (2012, hereafter B12). For reference, all abbreviations for the literature catalogs used in this work are summarized in Table 2.3.

2.2.1 The Peroux et al. (2003) compilation

A compilation of approximately the first decade and a half of DLA surveys is presented by Péroux *et al.* (2003), hereafter the P03 sample. The P03 sample combines the high redshift DLA survey of Péroux *et al.* (2001) with DLAs from 25 separate papers, several of which are themselves compilations from other surveys. Based on their statistical sample of 713 quasars and 114 DLAs, this sample was used by Péroux *et al.* (2003, 2005) to conclude that the total amount of neutral gas is conserved from z=2 to z∼5.

In the process of duplication checking (described in more detail in Section 2.2.5) and checking the original references of the P03 compilation, we noted a number of inconsistencies with the original reference papers, such as the values of emission redshifts adopted for the computation of absorption statistics. We checked each of these inconsistencies manually, and concluded that they are likely due to typographical errors, and we have corrected

Table 2.4: Modifications to the P03 catalog

Id	Comment
BR B0331-1622	$\equiv$ BR J0334-1612. Removed.
BR B0401-1711	$\equiv$ BR J0403-1703. Removed.
Q 0007-000	$\equiv$ Q 0007-0004. Removed.
Q 1600+0729	$\equiv$ BR J1603+0721. Removed.
Q 0101-3025	$z_{\rm em}$ changed from 4.073 to 3.164.
Q 0041-2607	$z_{\rm em}$ changed from 2.79 to 2.46.
Q 0201+3634	$z_{\rm em}$ changed from 2.49 to 2.912.
Q 2359-0216	$z_{\rm em}$ changed from 2.31 to 2.81.
MG 1559+1405	Reference not found. Removed.
MG 2254+0227	Reference not found. Removed.

them, as summarized in Table 2.4. We also identified 4 QSOs that are duplicates, but with different names, within the P03 compilation; the duplicated sightlines have been removed. In two cases, we could not find the original reference for a given QSO, and were therefore unable to verify the properties of the QSO/absorber; these two sightlines were also removed from the sample. We summarize all of the modifications made to the P03 compilation in Table 2.4. We recomputed $z_{\rm max}$ to be 5000 km s^{-1} bluewards of $z_{\rm em}$, in order to be consistent with the threshold set for the XQ-100 sample.

2.2.2 The Prochaska & Wolfe (2009) SDSS DLA sample

Prochaska & Wolfe (2009, hereafter PW09) used automated search algorithms to identify DLAs in the Sloan Digital Sky Survey Data Release 5 (SDSS DR5). A SNR requirement of 4 was adopted, and DLAs are included in their statistical sample if they are at least 3000 km s^{-1} from the background QSO. DLAs have also been identified in more recent data releases, specifically the DR7 (Noterdaeme *et al.*, 2009) and DR9 (Noterdaeme *et al.*, 2012), the former of which has a public catalog of identified DLAs. However, our computation of $\Omega_{\rm HI}^{\rm DLA}$ requires additional details of the minimum and maximum redshifts of the DLA search for every sightline, which is not available for the DR7 and DR9 samples. The DR5 sample of PW09 is therefore the largest of the individual literature samples considered in this work, containing 7472 QSOs with 738 DLAs. We do, however, compare the results of our combined sample to that of Noterdaeme *et al.* (2012) later in this paper.

PW09 find that the mass density of neutral gas has decreased by a factor of about two between redshifts of 3.5 and 2.5. A similar rate of gas content decline was determined from the later SDSS data releases by Noterdaeme *et al.* (2009, 2012). However, Noterdaeme *et al.* (2009) suggest that the analysis of PW09 may be biased against the detection of the lowest redshift DLAs, which could be rectified by implementing a velocity buffer to the minimum redshift used to compute DLA statistics. We implement this buffer, which has a value of 10,000 km s^{-1}, at the low redshift end of each SDSS spectrum. The new values of $z_{\rm min}$ listed in Table **??**, which describes our final combined DLA sample, include this velocity buffer. We also recomputed $z_{\rm max}$ to be 5000 km s^{-1} bluer than $z_{\rm em}$, for consistency with the XQ-100 sample.

2.2.3 The Guimaraes et al. (2009) sample

The broad Lyα wings of DLAs, and high absorber equivalent widths means that these galaxy scale absorbers can be easily detected in relatively low resolution spectra. Indeed, most surveys have been performed at typical resolutions of $R \sim 1000$ - 2000. However, there are advantages to pursuing absorption line surveys at higher resolution, such as the ability to push down to the sub-DLA regime (e.g., O'Meara *et al.*, 2007; Zafar *et al.*, 2013) and to assess the increasing potential for contamination (blends) at higher redshifts. The trade-off is, of course, the increased exposure times necessary to reach a fixed SNR.

Guimarães *et al.* (2009, hereafter G09) presented the first systematic DLA survey for $\Omega_{\rm HI}^{\rm DLA}$measurements performed with an intermediate resolution spectrograph, namely the Echellette Spectrograph and Imager (ESI, mounted at the 10m Keck telescope, Sheinis *et al.*, 2002). ESI's resolution ($R \sim 4500$) is quite similar to that of X-shooter. However, the most notable difference between the two instruments is the wavelength coverage. Whereas X-shooter extends from the atmospheric cut-off to the K-band, ESI has no coverage below 4000 Å and a greatly reduced efficiency from $\sim 4000 - 4300$ Å.

A total of 99 QSOs (77 considered for their statistical analysis) with emission redshifts ranging from z=4 to z=6.3 were observed by G09, leading to the detection of 100 absorbers with $\log N(\text{H I})$>19.5, of which 40 are DLAs. DLAs at least 5000 km s^{-1} from the QSO redshift were included in the statistical sample. Based on the DLA sample, G09 find that there is a decline in $\Omega_{\rm HI}$ at $z > 3.5$. This decline is also present if the sub-DLAs (which increase the total gas mass density by about 30 per cent) are combined with the DLAs. The discrepancy with the results of Prochaska & Wolfe (2009) is suggested by G09 to come from the difficulties in establishing the damping nature of the systems with the high density Lyα forest in this very high redshift range. However, generations of previous surveys have demonstrated that low number statistics at the redshift boundary of the survey can also lead to an apparent turnover of $\Omega_{\rm HI}$. Of the 40 DLAs in the G09 sample,

Table 2.5: Data-sets included to build up our combined sample.

Id	No. QSOs	No. DLAs	No. PDLAs [1]	$\sum \Delta X_i$
XQ100	100	38	3	536
G09	68	34	0	378
GGG	154	43	0	553
PW09	4983	559	50	8529
P03	397	68	0	1494
CS	5702	742	53	10434

there are 6 duplicates with the XQ-100 sample.

2.2.4 The Crighton et al. (2015) sample

The Giant Gemini GMOS (GGG) survey observed 163 $z > 4.4$ QSOs with GMOS-N and GMOS-S at the Gemini Observatory (Worseck *et al.*, 2014). Like the G09 sample, the main focus of the GGG DLA sample was the assessment of $\Omega_{\rm HI}$ at high redshifts. However, the GMOS spectra are of significantly lower resolution than the ESI spectra used by G09 and Crighton *et al.* (2015) carefully assess the contamination by both false positives (blends) and missed DLAs through a variety of blind tests and comparisons with repeated observations at higher spectral resolution. Despite potential concerns of blending and low resolution, Crighton *et al.* (2015) conclude that the required correction factors are minimal. DLAs are included in the GGG statistical sample if they are at least 5000 km s^{-1} from the background QSO.

Although Crighton *et al.* (2015) are not able to accurately identify and fit sub-DLAs, in their estimate of $\Omega_{\rm HI}$ they make a uniform correction for the contribution of these lower column density systems. We do not make this correction *a priori*, but rather use the DLA catalog of Crighton *et al.* (2015) directly in our combined sample. At $z_{\rm abs}\sim5$, the $\Omega_{\rm HI}$ derived from GGG is formally consistent with the SDSS measurements of Noterdaeme *et al.* (2012) at $z\sim 3$. However, a power law of the form $(1+z)^{0.4}$, describing a slowly decreasing $\Omega_{\rm HI}$ towards lower redshifts is consistent with data spanning $0 < z < 5$.

2.2.5 The combined sample

The reviews provided above highlight the sensitivity of $\Omega_{\rm HI}^{\rm DLA}$ to a variety of possible systematics, including blending/contamination, SNR, robust definitions of the search path

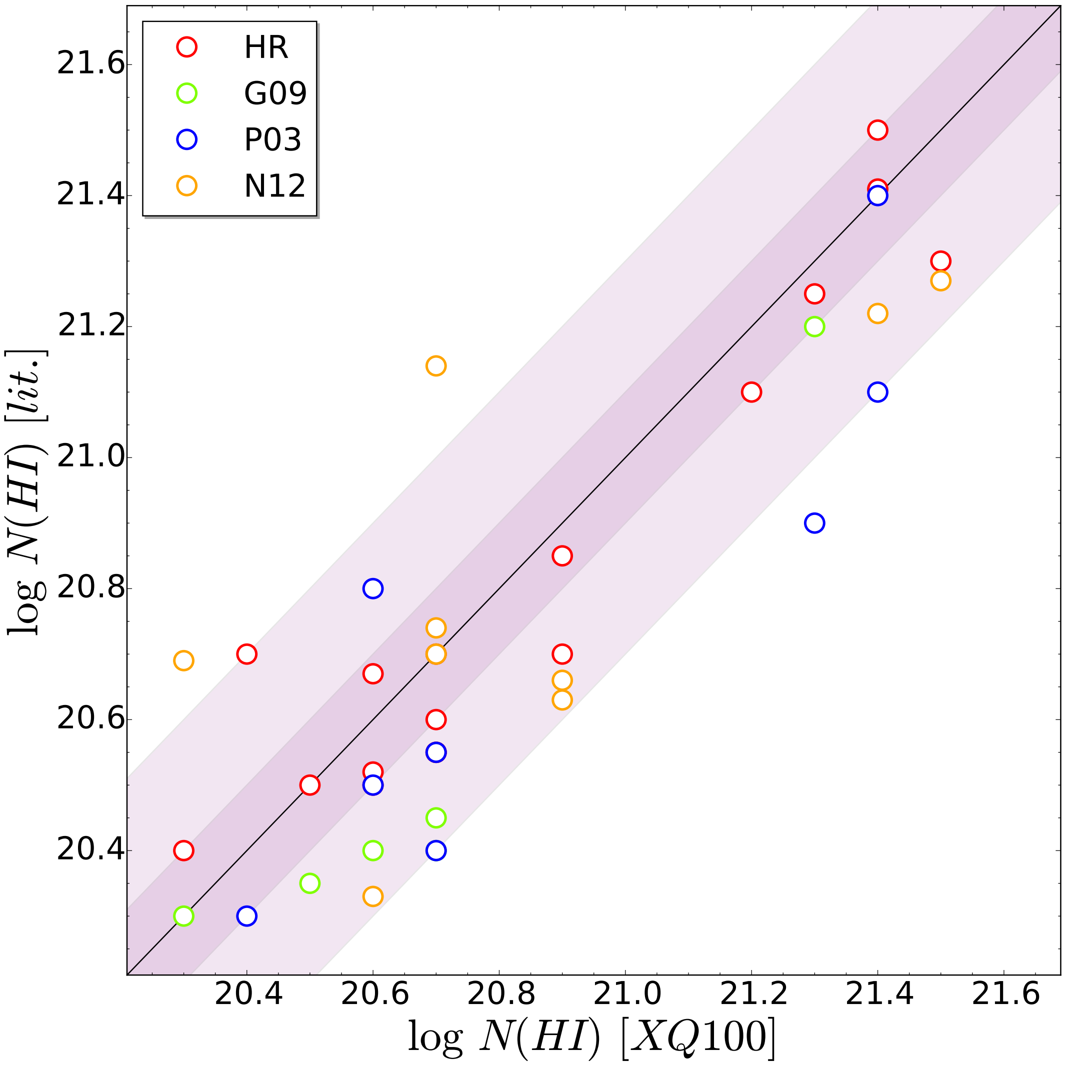

Figure 2.3: Comparison of our XQ-100 measurements with previous estimates. Shaded purple regions show 0.1 dex and 0.3 dex intervals.

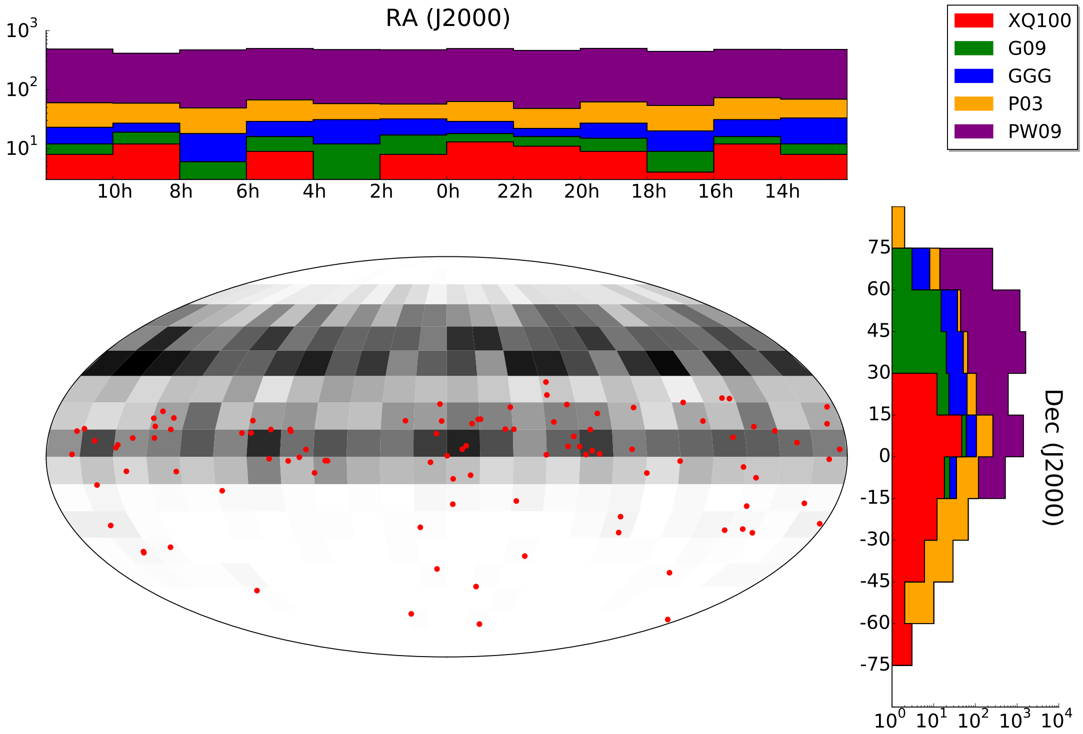

Figure 2.4: Sky position of the QSOs in the total combined sample. 1D histograms for each celestial coordinate and a 2D histogram density plot on the celestial globe are presented. The gray scale 2D histogram for the combined sample density plot represents the number of sources per surface unit (150 sq degrees), ranging from 0 (white) to 58 (black). The mean number of quasars per surface unit is 13.2. The red points over-plotted are the positions of the XQ-100 QSOs. The propensity of northern sky coverage is driven by the SDSS.

and, perhaps most importantly, sample size. Since the few, rare, high N(H I) absorbers contribute to $\Omega_{\rm HI}$ (and $\Omega_{\rm HI}^{\rm DLA}$) appreciably, large samples are required to statistically assess $\Omega_{\rm HI}$ at any given redshift. We have therefore combined the major surveys and compilations described above, in order to minimize fluctuations in the determination of $\Omega_{\rm HI}$ due to inadequate sampling of the column density distribution function.

Prior to combining the literature samples and the XQ-100 sample, it is necessary to check for, and remove, duplicate DLAs. Duplication checking was achieved by obtaining the sky coordinates and redshift of all quasars in all samples from NED, SIMBAD or SDSS, since naming conventions between surveys are heterogeneous. For the join procedure, we made XQ-100 the initial base sample. The catalogs were assessed in the order listed in Table 2.5, which was adopted as an approximate ranking of spectral quality (SNR and resolution). The base sample was compared with each subsequent catalog in Table 2.5 by performing a coordinate cross-matching with a positional tolerance of 10”. All matches were removed from the last table and the resulting combined (duplicate free) catalog was used as the base table for the next iteration (i.e. with the next catalog in Table 2.5).

In Table **??** we present the final combined sample (CS) with all duplicates removed. The final combined sample contains a total of 742 DLAs, spanning a redshift from 1.673 to 5.015. A comparison of the sky positions of the combined literature sample and the XQ-100 sample is shown in Figure 2.4.

2.3 Formalism

The formalism to treat cosmic H Icontent as a function of redshift was first introduced by Lanzetta *et al.* (1991). For more details, see, e.g., Wolfe *et al.* (2005), Prochaska *et al.* (2005), Rao *et al.* (2006), and Zafar *et al.* (2013).

Let the number of absorbers per sightline between $(N,\ N + dN)$ and $(z,\ z + dz)$ be

$$d^2\mathcal{N}(N, z) = n_{co}(N, z)dNA(N, z)(1 + z)^3 c\frac{dt}{dz}dz \tag{2.1}$$

where $n_{co}(N, z)dN$ is the quantity that ideally we would look for, i.e., the comoving density of systems between $(N,\ N + dN)$ at z, and $A(N, z)$ the comoving absorption cross section. This product is written explicitly to express that we cannot infer directly these quantities.

The absorption distance dX is conveniently defined by imposing that a non-evolving population has a constant frequency

$$dX \equiv \frac{H_0}{H(z)}(1+z)^2 dz \tag{2.2}$$

where

$$H(z) = H_0 \left[\Omega_m(1+z)^3 + (1-\Omega_m-\Omega_\Lambda)(1+z)^2 + \Omega_\Lambda\right]^{1/2}$$

Using relations 2.1 and 2.15

$$d^2\mathcal{N}(N,X) = f_{HI}(N,X)dNdX \tag{2.3}$$

being

$$f_{HI}(N,X) \equiv \left(\frac{c}{H_0}\right) n_{co}(N,X)A(N,X) \tag{2.4}$$

the differential column density distribution, that describes the evolution of absorption systems as a function of column density and redshift. The discrete limit can be expressed as

$$f_{HI}(N,X) = \frac{m}{\Delta N \sum\limits_i \Delta X_i} \tag{2.5}$$

where m is the number of systems in a column density bin ΔN within a total absorption path surveyed $\sum\limits_i \Delta X_i$.

The absorber line density is defined as the zeroth moment of $d^2\mathcal{N}(N,X)$

$$\ell(X) \equiv \frac{d^2\mathcal{N}(N,X)}{dX} = \int\limits_{N_{min}}^{N_{max}} dN f_{HI}(N,X) \tag{2.6}$$

This is the number of absorbers per unit absorption path length

$$\ell(X) = \frac{m}{\sum\limits_i \Delta X_i} \tag{2.7}$$

.

The number density, $n(z)$, defined in the way that $n(z)dz$ is the number of absorbers in the redshift interval between z and $z + dz$.

$$n(z) = \frac{m}{\sum\limits_i \Delta z_i} \tag{2.8}$$

Therefore, this is a pure empirical quantity but physically meaningless. In this frame, and taking into account that $n(z)dz \equiv \ell(X)dX$, the non evolution curve can be expressed by

$$n(z) = n_0(1+z)^2 \left(\frac{H_0}{H(z)}\right) \tag{2.9}$$

where $n_0 \equiv n(z=0) = n_{co}(0)A(0)$.

The gas mass density as a function of the critical density (ρ_{crit}) is defined as the first moment of $d^2\mathcal{N}(N, X)$

$$\Omega_g(X) = \frac{H_0}{c}\frac{\mu m_H}{\rho_{crit}} \int\limits_{N_{min}}^{N_{max}} f_{HI}(N,X)NdN \tag{2.10}$$

where μ is the mean molecular weight. In the discrete limit,

$$\int\limits_{N_{min}}^{N_{max}} f_{HI}(N,z)NdN = \frac{\sum_j N_j}{\sum_i \Delta X_i} \tag{2.11}$$

2.4 Results

2.4.1 Redshift path coverage

We begin our analysis by computing the redshift path covered by both the individual samples described in the previous section, as well as for the combined sample. Although we will ultimately use only the combined sample for our determination of $\Omega_{\rm HI}$, it is instructive to see how the various sub-samples contribute as a function of redshift.

The cumulative number of sightlines that could contain an absorber at a given redshift is defined as (Lanzetta *et al.*, 1991)

$$g(z) = \sum_i H(z^i_{max} - z)H(z - z^i_{min}) \tag{2.12}$$

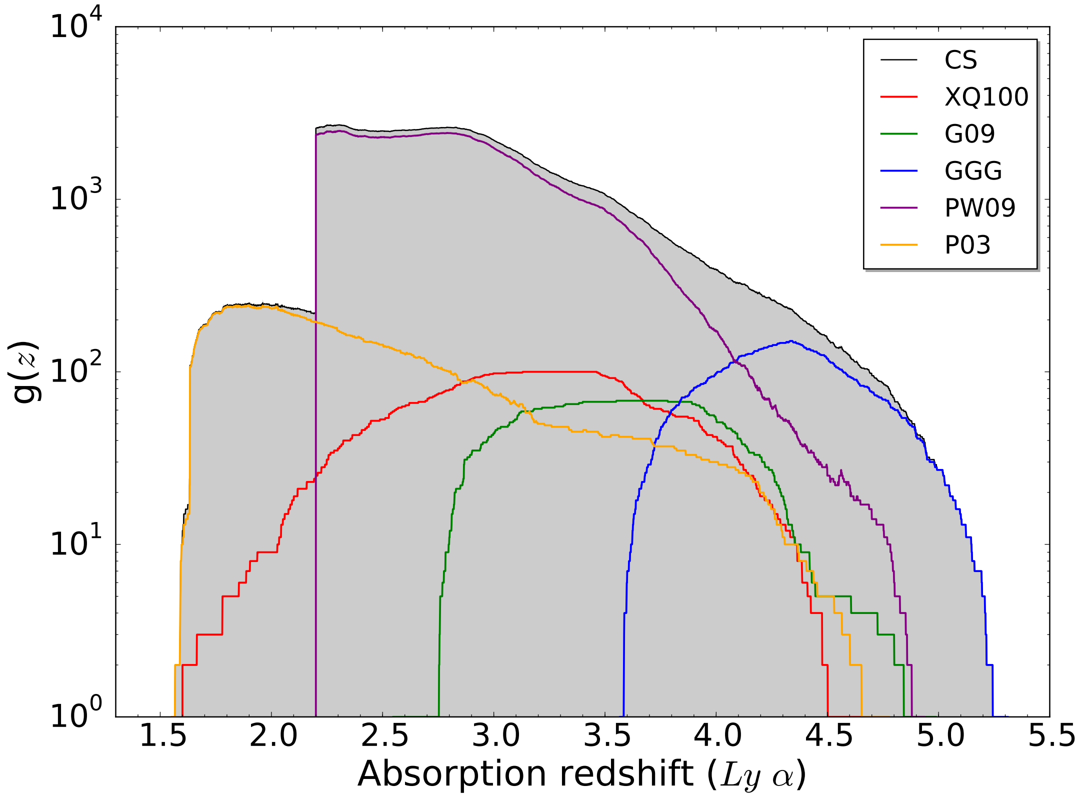

Figure 2.5: Redshift path for all samples used in this work and for the total combined sample (CS).

where H is the Heaviside function. Then, the total redshift path surveyed is

$$\Delta z = \int_0^\infty g(z)dz = \sum_i (z^i_{max} - z^i_{min}) \tag{2.13}$$

For the XQ-100 sample, the lower limit z^i_{min} for the i^{th} quasar was chosen as the minimum redshift where the SNR> 7.5. This SNR threshold was determined from our data as a conservative value where we start to easily identify damping wings. As described in Section 2.1, the maximum DLA search redshift, z^i_{max}, was set conservatively to be 5000 km s^{-1} bluewards of z^i_{em}.

The resulting XQ-100 $g(z)$ curve is shown in Fig. 2.5 together with the data of the other samples used in this paper. For the rest of the samples, we kept published $z_{\rm min}$ but we recomputed $z_{\rm max}$ to be 5000 km s^{-1} bluewards $z_{\rm em}$. This accounts also for possible uncertainties in the determination of emission redshifts, which are inhomogeneously computed (see, e.g., Hewett & Wild, 2010, and references therein). The 5000 km s^{-1} threshold therefore provides a safe buffer against the inclusion of PDLAs that are likely to affect our statistical sample.

Fig. 2.5 demonstrates the complementarity of the various previous surveys and the advantage of combining them all together. The XQ-100 survey probes from z=1.6 up to z=4.5, with the majority of the absorption path in the z=[3.0-3.5] range. The previous moderate resolution DLA survey by G09 extends to slightly higher redshifts than XQ-100. However, due to ESI's lack of blue sensitivity and the emission redshift distribution of this sample, there is no absorption path coverage below $z \sim 2.7$. The PW09 sample dominates at moderate redshifts, but the P03 sample and GGG samples are major contributors at the lowest and highest redshifts, respectively.

2.4.2 DLA distribution function

The differential column density distribution, that represents the number of absorbers between N and N+dN and z and z+dz, is defined (Lanzetta *et al.*, 1991) as

$$f_{HI}(N, X)dNdX = \frac{m}{\Delta N \sum_i \Delta X_i} dNdX \tag{2.14}$$

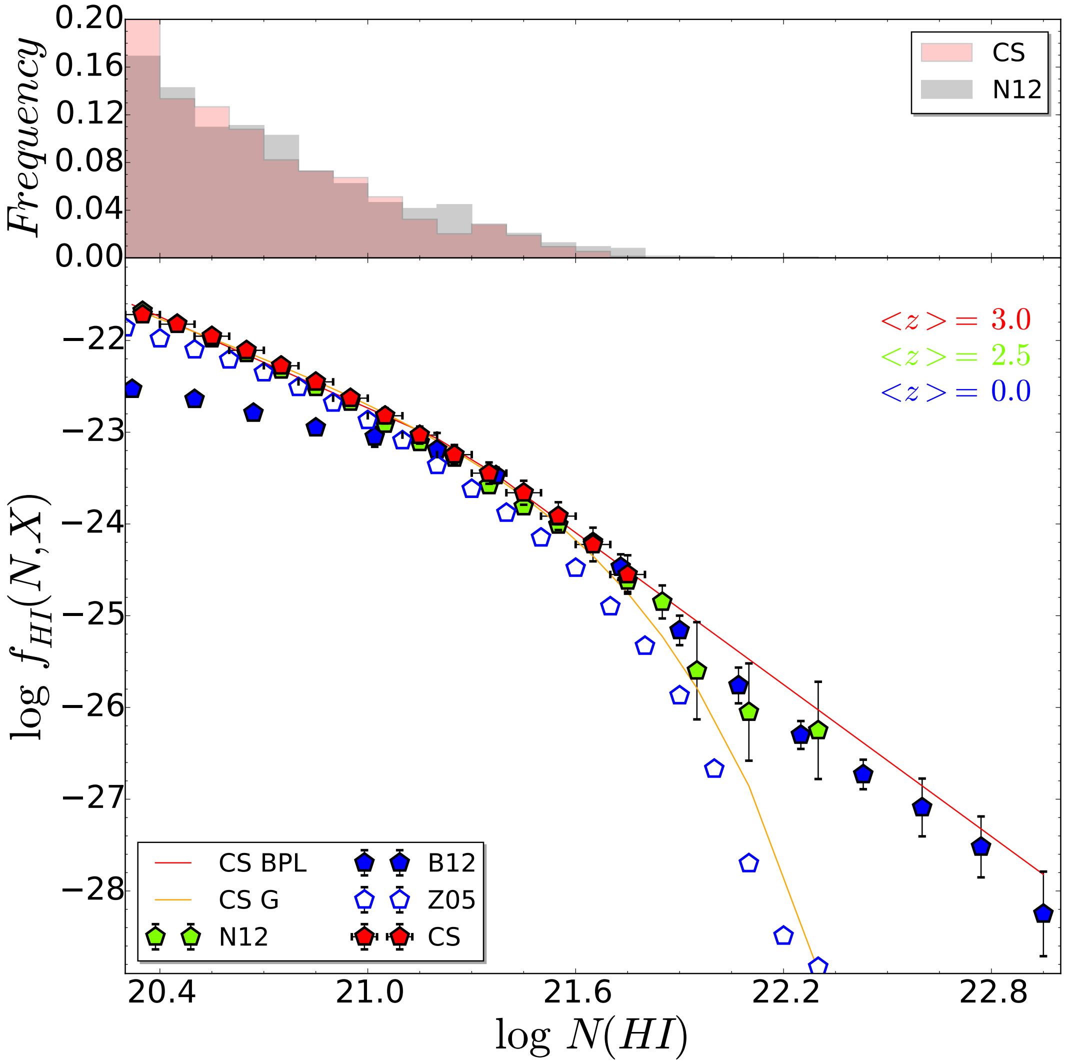

Figure 2.6: Sample frequency and distribution function for the whole combined sample compared with N12 (at similar mean redshift) and Z05+B12 representing the local universe. Model fits to a broken powerlaw (BPL, red) and a gamma function (G, orange) are also plotted.

Table 2.6: Column density distribution (binned evaluations) for the complete CS ($< z >= 2.99$), and split in 2 and 3 redshift bins

log N(H I)	log $f_{\rm HI}(N,X)$					
	z=2.99	z=2.57	z=3.47	z=2.44	z=2.95	z=3.69
20.3	-21.72 ± 0.05	-21.79 ± 0.08	-21.66 ± 0.07	-21.82 ± 0.1	-21.69 ± 0.08	-21.66 ± 0.08
20.4	-21.82 ± 0.05	-21.89 ± 0.08	-21.76 ± 0.07	-21.91 ± 0.1	-21.81 ± 0.09	-21.76 ± 0.08
20.5	-21.95 ± 0.06	-22.02 ± 0.08	-21.89 ± 0.07	-22.04 ± 0.1	-21.96 ± 0.09	-21.88 ± 0.08
20.6	-22.11 ± 0.06	-22.17 ± 0.09	-22.05 ± 0.08	-22.18 ± 0.1	-22.13 ± 0.1	-22.02 ± 0.09
20.7	-22.28 ± 0.06	-22.33 ± 0.09	-22.23 ± 0.08	-22.35 ± 0.11	-22.31 ± 0.11	-22.19 ± 0.1
20.8	-22.45 ± 0.07	-22.51 ± 0.1	-22.4 ± 0.09	-22.53 ± 0.12	-22.48 ± 0.12	-22.36 ± 0.1
20.9	-22.63 ± 0.07	-22.7 ± 0.11	-22.56 ± 0.09	-22.74 ± 0.14	-22.65 ± 0.13	-22.53 ± 0.11
21.0	-22.82 ± 0.08	-22.92 ± 0.12	-22.74 ± 0.1	-22.94 ± 0.15	-22.84 ± 0.14	-22.71 ± 0.12
21.1	-23.03 ± 0.09	-23.13 ± 0.14	-22.95 ± 0.12	-23.13 ± 0.16	-23.07 ± 0.16	-22.92 ± 0.14
21.2	-23.24 ± 0.11	-23.32 ± 0.15	-23.18 ± 0.13	-23.28 ± 0.17	-23.31 ± 0.18	-23.14 ± 0.15
21.3	-23.45 ± 0.12	-23.49 ± 0.16	-23.41 ± 0.15	-23.43 ± 0.18	-23.56 ± 0.19	-23.35 ± 0.17
21.4	-23.66 ± 0.13	-23.68 ± 0.17	-23.63 ± 0.17	-23.61 ± 0.19	-23.78 ± 0.21	-23.55 ± 0.18
21.5	-23.92 ± 0.15	-23.92 ± 0.19	-23.88 ± 0.19	-23.85 ± 0.2	-23.99 ± 0.21	-23.78 ± 0.2
21.6	-24.22 ± 0.18	-24.2 ± 0.21	-24.16 ± 0.21	-24.11 ± 0.22	-24.2 ± 0.22	-24.03 ± 0.21
21.7	-24.56 ± 0.21	—	-24.41 ± 0.22	—	—	-24.27 ± 0.22

where m is the number of systems in a column density bin and the absorption distance

$$\Delta X = \int_{z_{\rm min}}^{z_{\rm max}} \frac{H_0}{H(z)}(1+z)^2 dz \tag{2.15}$$

is a quantity conveniently defined to give the distribution values in a comoving frame.

The results for the whole sample, as well as fits for the sample split in 2 or 3 different redshift bins are tabulated in Table 2.6. In Figure 2.6 we present the sample frequency and the distribution function of the combined sample in bins of 0.1 dex. We also compare our points with the results from the SDSS/BOSS by N12, and with the samples from the local Universe by B12 and Z05. Our bias-corrected values for the combined sample[1] are in very good agreement with N12 results, although the size of our sample is not large enough to have many absorbers with column densities higher than log N(H I)∼21.7. The combined sample is also in good agreement with B12 at the high column density end (N(H I) $>$ 21), but the B12 sample has a paucity of low column density systems compared to the combined sample and N12. However, the B12 sample is limited to a small number of Local group galaxies and does not widely sample the low redshift universe. At the low column density end of the distribution function, DLA surveys are in much better agreement with Z05.

We have fitted a broken power law (e.g. Prochaska & Wolfe, 2009) to our binned data using the Nelder-Mead algorithm:

$$f_{\rm HI}(N,X) = \begin{cases} k_d \left(\frac{N}{N_d}\right)^{\alpha_{1d}} & N < N_d \\ k_d \left(\frac{N}{N_d}\right)^{\alpha_{2d}} & N \geq N_d \end{cases} \tag{2.16}$$

and a gamma function (e.g. Péroux *et al.*, 2003)

$$f_{\rm HI}(N,X) = k_g \left(\frac{N}{N_g}\right)^{\alpha_g} e^{N/N_g} \tag{2.17}$$

The coefficients from the distribution function fits are given in Table 2.7. Both expressions reproduce well our observed points, but when extrapolating to the highest column densities the broken power law describes much better the N12 and B12 distributions. The gamma function appears to significantly under-predict the frequency of the highest column density absorbers at high redshift. We note that these results are also consistent with the exponent $\alpha_2 \sim -3$ expected by Wolfe *et al.* (1995) for self-similar ‘disks’.

---

[1] We explain the bias correction method in detail in section 2.4.3

2.4.3 Hydrogen mass density ($\Omega_{\rm HI}$) curves

The main objective of the current work is to assess the redshift evolution of the gas mass density $\Omega_{\rm HI}$, which is defined as the first moment of the distribution function

$$\Omega_{\rm HI} = \frac{H_0}{c}\frac{m_H}{\rho_c}\int_{N_{min}}^{N_{max}} N f_{HI}(N, X) dN \tag{2.18}$$

where $\rho_c = 3H_0^2/8\pi G$ is the critical density for which the spatial geometry of the universe is flat. Usually, the discrete limit

$$\int_{N_{min}}^{N_{max}} N f_{HI}(N, z) dN = \frac{\sum_j N_j}{\sum_i \Delta X_i} \tag{2.19}$$

where i refers to the QSO and j to the DLA, is taken to compute this quantity. Here, we are assuming that the sample represents properly the real population characteristics and/or the errors coming from this discretization are negligible compared with the sampling errors. We will check these assumptions in section 2.4.3.2. For the computation of $\Omega_{\rm HI}^{\rm DLA}$, log N_{min} is taken to be 20.3.

2.4.3.1 Error estimations

The error bars associated with $\Omega_{\rm HI}^{\rm DLA}$ may arise from several uncertainties. Here, we consider two main sources of uncertainty: the error associated with the fitted N(H I) of a given DLA (which includes uncertainties associated with the continuum fitting), and limited sampling of the complete column density distribution function. The relative importance of these errors, and attempts to quantify them, have been varied in the literature. It is therefore instructive to compare various methods of error estimation, in order to quantify their relative magnitude.

In some early work, (e.g. Ellison *et al.*, 2001; Storrie-Lombardi *et al.*, 1996b) a common approach to determine the error on $\Omega_{\rm HI}^{\rm DLA}$ was to assume the sampling process followed a Poisson distribution (hereafter the 'P method'). This means that we are assuming a probability function of the form $P(X) = e^{-\lambda}\frac{\lambda^x}{x!}$ for finding absorbers with column density N(H I) within the total absorption path ΔX. Under this assumption, the error on $\Omega_{\rm HI}^{\rm DLA}$

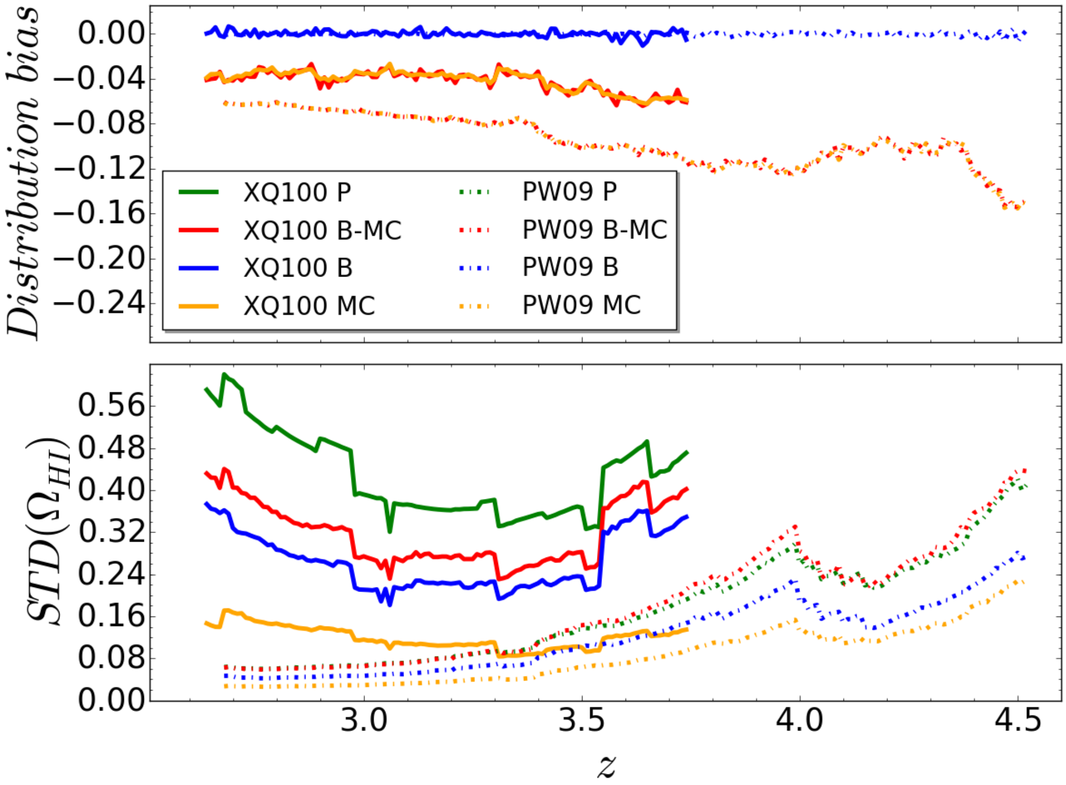

Figure 2.7: Representation of the standard deviation (lower panel) and statistical distribution bias (upper panel) as a function of redshift for the XQ-100 and PW09 samples. The y-axis represents deviations in $\Omega_{\rm HI}\times10^3$.

is propagated as

$$\Delta\Omega_{\text{HI}}^{\text{DLA}} = \Omega_{\text{HI}}^{\text{DLA}} \frac{\sqrt{\sum_{i=1}^{p} N_i^2}}{\sum_{i=1}^{p} N_i}. \tag{2.20}$$

An alternative approach is to use a bootstrap re-sampling (hereafter 'B method') of the observations in a given redshift bin (e.g. Crighton *et al.*, 2015). The bootstrap method consists of building up a large number of $\Omega_{\text{HI}}^{\text{DLA}}$ values ($N_{\text{re-samples}} = 10,000$ in our computations) that resamples, with replacement, the observed DLA sample in a given redshift bin. If the observed DLA 'pool' is large enough, and is a good representation of the population properties, then each bootstrap realization is analogous to performing another independent DLA survey with the same total absorption path and redshift interval. Then, this large set of simulated observations provides an easy way of computing the mean $\Omega_{\text{HI}}^{\text{DLA}}$, its standard deviation and the distribution bias (the difference between the computed $\Omega_{\text{HI}}^{\text{DLA}}$ from the originally measured DLA distribution and the resampled $\Omega_{\text{HI}}^{\text{DLA}}$ distribution mean). Although they provide a useful estimator of the uncertainties associated with survey size and the sampling of the column density distribution function, neither the P method nor the B method account for the fit uncertainties on an individual DLA.

In order to assess the uncertainty due to errors on the $N(\text{H I})$ fitting, a Monte Carlo approach may be adopted (hereafter, the 'MC method'). In this approach, the $\Omega_{\text{HI}}^{\text{DLA}}$ for the original sample of DLAs is recomputed 10,000 times, but the value of $N(\text{H I})$ is perturbed on each iteration, by drawing values from within the Gaussian error distribution defined by the 1σ errors of the fit. We note the possibility of a 'boundary bias' in the application of the MC method. This bias can occur because DLAs that are barely above the limiting $N(\text{H I})$ threshold of 20.3 may be lost from the re-sampled distribution after they are perturbed within their error distribution. In order that this sample migration occurs equally in the other direction (absorbers just below the $\log N(\text{H I}) = 20.3$ being boosted into the re-sampled distribution) we include in our error analysis tests all absorbers that have been identified in our sample, down to a limiting column density of $\log N(\text{H I}) = 19.5$.

It is also possible to combine the uncertainties associated with population sampling (epitomized with the B method) and the fit uncertainties (MC method). In the 'B-MC method', the bootstrap re-sampling of the original population additionally includes the perturbation of each $N(\text{H I})$ within its Gaussian error distribution.

In Figure 2.7 we compare the standard deviations (lower panel) and bias distributions

(i.e. the difference between the actual $\Omega_{\rm HI}^{\rm DLA}$ computed for the original observed sample and the value derived from sampling either the population or its errors, top panel) of the various error estimation techniques. Note that the P method does not entail re-sampling, so there is no measure of bias for this technique. The error curves are computed using a fixed ΔX=2.5 (we will discuss in the following subsection different approaches to binning). Due to the different characteristics of the surveys that comprise our combined sample, such as sample size and spectral resolution, it is useful to compare the errors from the different estimation techniques for some of the separate sub-samples. In Fig. 2.7 we therefore show the error estimate comparisons for PW09 and XQ-100. The former is the largest component of our combined sample and will hence best sample the underlying N(H I) distribution. However, this sample has a relatively relaxed SNR threshold (SNR $>$ 4) and was constructed from moderate resolution spectra. Conversely, the XQ-100 sample is of modest size, but has both relatively high spectral resolution and SNR. Moreover, the wide wavelength coverage of X-shooter permits the simultaneous fitting of higher order Lyman lines. These factors are all advantageous for the reduction of N(H I) fitting uncertainties.

Fig. 2.7 reveals several interesting features of the different error estimators. The P method generally exhibits the largest standard deviations of the four techniques investigated, particularly for smaller samples. Moreover, without any re-sampling, it is difficult to explicitly test the effect of sample size, and the P method does not account at all for errors in N(H I). The technique that best captures the uncertainties in the N(H I) fit is the MC method. From the lower panel of Fig. 2.7 it can be seen that the MC errors of PW09 are smaller than XQ-100, even though the fit uncertainties are generally smaller in the latter sample. The much greater size of the PW09 sample can apparently largely compensate for the slightly poorer fit accuracy. Comparing a subset of the PW09 survey with a size matched to XQ-100 would lead to larger uncertainties in the former. An important and non negligible effect that can be seen in the upper panel of Fig. 2.7 is that any variant of the MC technique (i.e. either with or without bootstrapping) always yields a negative bias, i.e. the simulated $\Omega_{\rm HI}^{\rm DLA}$ is usually greater than the original. This is due to the error distribution which is asymmetric in linear space.

We now consider the contribution of population sampling to the error estimate, as encapsulated by the bootstrap B method. For an infinitely large survey that fully samples the underlying population, the error due to incomplete sampling becomes negligible and the error is dominated by the uncertainties in the individual N(H I) measurements. In smaller surveys, the sampling error becomes dominant. We can see this effect by comparing the large PW09 sample to the more modest sized XQ-100 sample in the lower panel of Fig. 2.7. Here, we see that the error from the sampling alone (B method) is approximately twice that of the fitting errors alone (MC method) for the XQ-100 sample. However, the fitting errors approach the sampling errors for the much larger PW09 sample. In general, the larger the sample, the more important is the relative contribution of the fitting uncertainties, compared to population sampling alone. Therefore, where XQ-100 is dominated by the sampling uncertainties, sampling and fitting uncertainties contribute at a similar level in PW09. In contrast to the MC techniques, the top panel of Fig. 2.7 shows that the B method does not lead to a bias in the re-sampled distributions, as it considers perfect determinations of the column densities.

A combination of sampling and fitting errors seems to be required by our data, so we conclude that the best resampling technique to compute statistics is the B-MC method. However, since we have shown that the B-MC resampled distribution is biased (and could have non-negligible skewness), the standard deviation alone is an inadequate representation of the uncertainties. We have therefore computed the 68 and 95 per cent confidence intervals, using the so-called bootstrap bias corrected accelerated method (BCa, Efron, 1987) on the B-MC resampled $\Omega_{\rm HI}^{\rm DLA}$. In this non-parametric approach, the results are less affected by skewed distributions, and with this technique the bias mentioned before is also taken into account.

2.4.3.2 Binning techniques

In order to study the redshift evolution of $\Omega_{\rm HI}^{\rm DLA}$, there are two common procedures used in the literature to bin the observed data as a function of redshift. The first, and most common, is to select contiguous, and often equally spaced, z-intervals based on the characteristics of the sample (e.g., Noterdaeme *et al.*, 2012; Prochaska & Wolfe, 2009). This aproach has the advantage of being intuitive and computationally straight-forward. However, if the redshift path is very uneven, it can lead to large variations in the statistical uncertainties in $\Omega_{\rm HI}$ as a function of redshift. The alternative method is to set the redshift intervals of each $\Omega_{\rm HI}$ bin such that it uniformly samples the total absorption path (e.g., Guimarães *et al.*, 2009; Noterdaeme *et al.*, 2009). The redshift bin sizes may therefore be heterogeneous, but each bin is statistically similar. However, both of these methods adopt contiguous, non-overlapping bins to discretize the data.

In this work, we take a different approach. Instead of computing $\Omega_{\rm HI}^{\rm DLA}$ in contiguous, non-overlapping intervals, we sample the redshift distribution finely using a sliding redshift window to compute an $\Omega_{\rm HI}^{\rm DLA}(z)$ 'curve'. The computation of $\Omega_{\rm HI}^{\rm DLA}$ is still based on the summation of $N(\rm H\,I)$ between a given $z_{\rm min}$ and $z_{\rm max}$. However, we consider all $z_{\rm min}$ and $z_{\rm max}$ pairs over the full redshift range of our sample, beginning at the minimum redshift where $g(z)>0$, and incrementing $z_{\rm min}$ by 0.001. The $z_{\rm max}$ at each point in the $\Omega_{\rm HI}^{\rm DLA}$curve can be computed analogously to the two traditional methods described above: In the

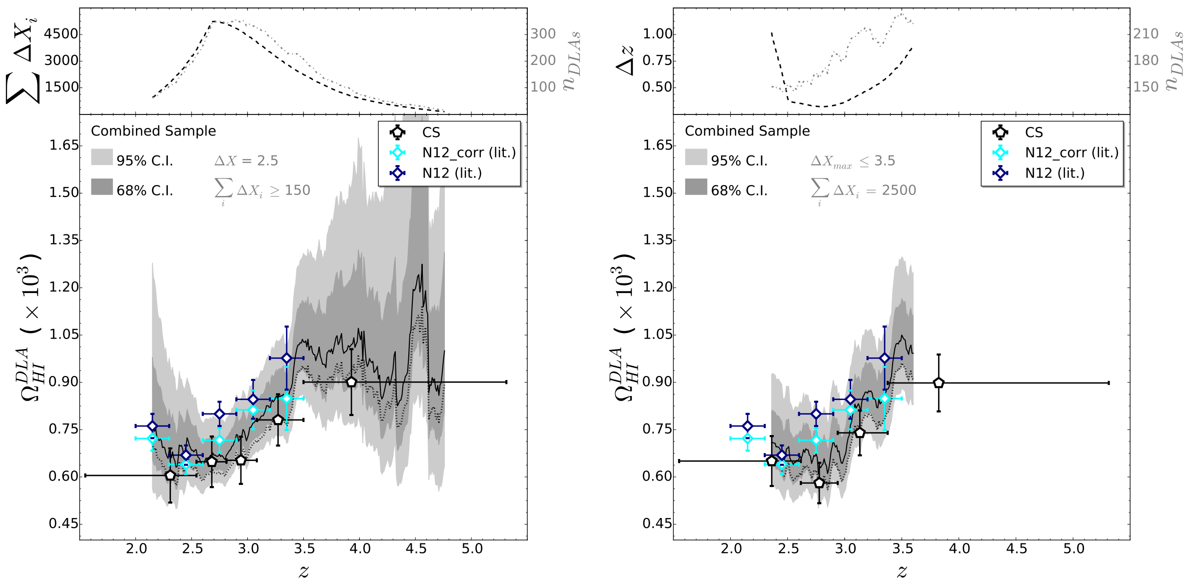

Figure 2.8: $\Omega_{\rm HI}^{\rm DLA}$curves for the combined sample using fixed comoving redshift intervals (left) and fixed total absorption path (right). 68 and 95 per cent confidence intervals derived from the BCa technique are shown in the shaded regions. Black line is the uncorrected curve. For comparison, we show the high column density correction applied to N12 results in order to have in both samples a maximum column density contribution of $\log N(\text{H I})$=21.75, and the conventional representation of discrete bias-uncorrected $\Omega_{\rm HI}^{\rm DLA}$ points for the combined sample. Upper subpanel for each plot represents the redshift range or the total absorption path probed to build up the curve (black) and the number of DLAs used for the computations (grey).

first technique, we simply define the $z_{\rm max}$ of each $\Omega_{\rm HI}^{\rm DLA}$ curve point to be $z_{\rm max}$=$z_{\rm min}$+Δz, where Δz is determined by imposing a constant ΔX (in the example below, we use ΔX = 2.5) and using eq. 2.15. The resulting mean redshift of the interval is weighted by the $g(z)$ curve. As a result of the weighting procedure, several ($z_{\rm min}$, $z_{\rm max}$) pairs can lead to a computation of $\Omega_{\rm HI}^{\rm DLA}$ at the same mean z; when this occurs, we take the median $\Omega_{\rm HI}^{\rm DLA}$ of the duplications. Although simple in its approach, the uneven distribution of redshift coverage in our sample leads to some redshift intervals being better sampled than others. The second approach mitigates this effect by setting the $z_{\rm max}$ dynamically for each $z_{\rm min}$, so that each (z, $\Omega_{\rm HI}^{\rm DLA}$) point has the same total absorption path contributing to it (in the example below, we use $\Sigma\ \Delta X$ = 2500). In this approach, we compute the z for each redshift interval by again weighting for the $g(z)$ curve in that interval. As with the first method, when multiple ($z_{\rm min}$, $z_{\rm max}$) pairs lead more than one bin to have the same mean redshift, we take the median $\Omega_{\rm HI}^{\rm DLA}$ of the duplications.

In Figure 2.8 we compare both binning methods for computing $\Omega_{\rm HI}^{\rm DLA}$ for the final combined sample, where the grey shaded regions show the 68 and 95 per cent confidence intervals determined from the BCa method described in the previous subsection. The $\Omega_{\rm HI}^{\rm DLA}$ curves are shown in the main (lower) panels and the upper panels show absorption paths/intervals (black dashed line) and number of DLAs (grey dotted line) as a function of z. The first conclusion we can draw from a comparison of the curves in Figure 2.8 is that both binning methods yield curves of $\Omega_{\rm HI}^{\rm DLA}$ that are statistically equivalent in the range $2.2 < z < 3.6$ where they can both be computed. In both cases, there is a scatter whose magnitude is inversely proportional to the number of absorbers used to compute statistics. This scatter originates from the limited sampling that draws different absorber distributions for each computed point. This effect is especially evident when high column density absorbers are included or not in a given bin. Therefore, although using a fixed total absorption path (right panel) theoretically smooths any uneven sampling, the contribution of the SDSS dominates in the redshift range where both techniques can be applied and the statistics are relatively uniform anyway. One of the most notable differences between the binning methods shown in Figure 2.8 is that a fixed total absorption path (right panel) greatly restricts the redshift range over which the curve can be computed. This is due to ‘running out’ of redshift path as the curve is built up towards higher z. This truncation can be mitigated by reducing the choice of $\Sigma\ \Delta X$, although in turn this is a compromise in the uncertainty. Using a fixed ΔX interval is therefore our preferred binning method.

Having constructed the $\Omega_{\rm HI}^{\rm DLA}$ curves, that we tabulate for the CS in Table **??** for ease of reproduction, it is interesting to compare the results to the more classical binning approach. For the combined sample, the binned-uncorrected values are shown with black symbols in Fig. 2.8, as well as the bias-uncorrected curve plotted in black. Different redshift bins select different DLAs, which cause the small variations between both uncorrected data points and curve. Larger effects are corrected when taking into account fitting uncertainties, as we can observe when comparing the uncorrected curve with BCa confidence intervals. However, when we plot together these intervals and the N12 points (dark blue), the latter are systematically above (although still consistent within the confidence intervals) the values for the CS.

We investigate whether the values measured by N12 are higher due to a more complete sampling of the high column density end of the distribution function by those authors, i.e. whether the combined sample's incompleteness at high $N(\mathrm{H\,I})$ may cause an under-estimate of $\Omega_{\mathrm{HI}}^{\mathrm{DLA}}$. For this purpose, we also computed $\Omega_{\mathrm{HI}}^{\mathrm{DLA}}$ by integrating $f_{\mathrm{HI}}(N,X)$. In Table 2.7 we show the results of integrating up to $\log N(\mathrm{H\,I})$=21.7 (the upper limit of our DLA sample, denoted in the table by ^{max}) and to $\log N(\mathrm{H\,I})$=∞. We observe, as expected, a very good agreement between our summed $\Omega_{\mathrm{HI}}^{\mathrm{DLA}}$ (e.g. 0.97 $\times10^{-3}$ for the redshift unbinned CS) and the partially integrated one (0.94 $\times10^{-3}$), being inside the derived confidence intervals for all bins. However, the difference between the partial and fully integrated values (1.16×10^{-3} for the full combined sample) indicates that our values may still be under-estimated due to our limited sample size. Our confidence intervals are actually rigorous as long as the bootstrap hypothesis is fulfilled, but we remark the fact that this technique cannot infer the information on the real population that is not contained in the combined sample. This hypothesis could be true if the contribution of the absorbers with higher column densities than $\log N(\mathrm{H\,I})\sim$21.7 (in our case) is negligible. However, the extrapolated broken power law fit results, supported by N12 (and B12) observations, suggest that these absorbers play an important role ($\approx$ 20%) in the value of the hydrogen gas mass density. If we impose the same maximum $\log N(\mathrm{H\,I}) = 21.7$ threshold for the N12 sample as applies to the combined sample, integrating the $f_{\mathrm{HI}}(N,X)$ for the SDSS/BOSS sample yields a slightly lower value of $\Omega_{\mathrm{HI}}^{\mathrm{DLA}}$ that is now nicely consistent with the combined sample (cyan points in Fig. 2.8), confirming the equivalency of both samples over their common redshift range.

2.4.4 DLA incidence rate

The DLA incidence rate $\ell(X)$, or line density, is defined as the zeroth moment of $f_{\mathrm{HI}}(N,X)$

$$\ell(X)dX = \int_{N_{min}}^{N_{max}} f_{HI}(N,z)dNdX \tag{2.21}$$

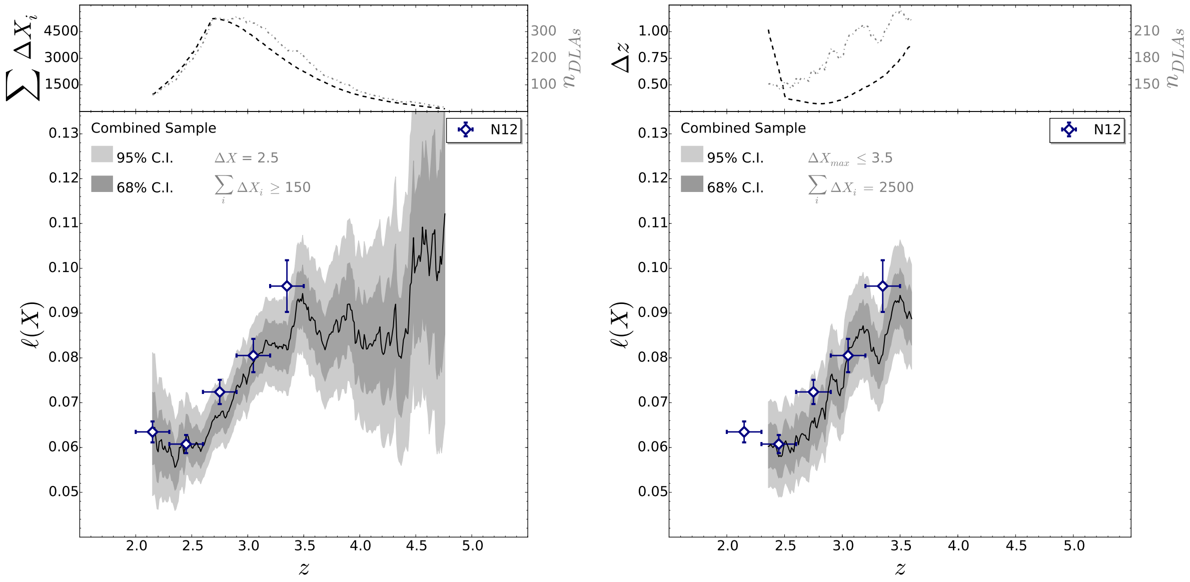

Figure 2.9: $\ell(X)$ curves for the combined sample using fixed comoving redshift intervals (left) and fixed total absorption path (right). 68 and 95 per cent confidence intervals are derived assiming a Poisson distribution. Solid line represents the value computed directly from eq. 2.22

Its discrete limit, commonly used to compute this quantity, is given by

$$\ell(X) = \frac{m}{\sum_i \Delta X_i} \tag{2.22}$$

i.e., it is the number of DLAs found per unit comoving redshift path.

In this analysis, for the error estimation we assumed a Poisson distribution. This is because the main variation we can expect using the B-MC technique is from the effect of the low $N(\mathrm{H\,I})$ absorbers crossing the DLA limit from one side to the other. However, the major source of uncertainty in the column density distribution function is from the poor sampling of the highest column density absorbers. We show line density curves in Figure 2.9, built up using the same binning techniques as for $\Omega_{\mathrm{HI}}^{\mathrm{DLA}}$. Here, we can observe again an excellent agreement with the N12 results: from $z \sim 2$ to 3.5 where the samples overlap a significant increase in the line density of DLAs is seen. At higher redshifts, the limited statistics prevent us from distinguishing whether $\ell(X)$ continues to rise, or flattens, although a steep evolution is not supported by the current dataset (Crighton *et al.*, 2015).

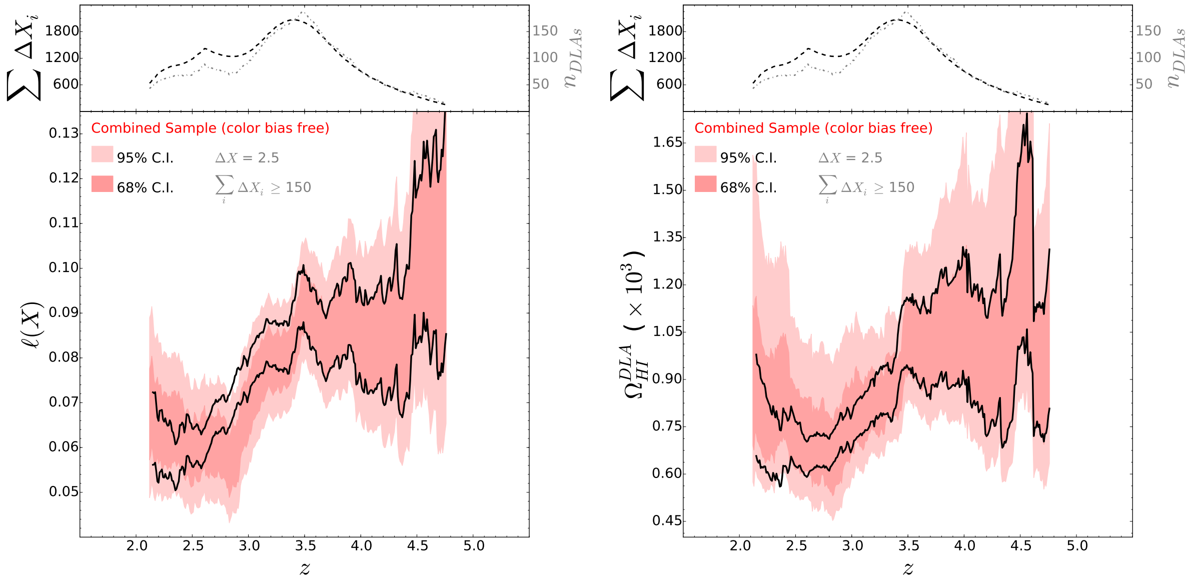

Figure 2.10: $\ell(X)$ (left) and $\Omega_{\rm HI}^{\rm DLA}$(right) curves for our color bias free sub-sample. The solid black lines represent the full CS 68% confidence limits.

2.5 Discussion

We have presented a new survey for DLAs based on spectra obtained for the XQ-100 survey, an X-shooter Large Program to observe 100 $z > 3.5$ QSOs (Lopez et al. A&A **submitted**). The 38 DLAs identified in the XQ-100 sample are combined with major literature samples compiled over the last ~ 20 years, with close attention paid to duplications, yielding a total of 742 DLAs over a redshift range of approximately $1.6 < z < 5.0$. The total redshift path of the combined sample is $\Delta X = 10{,}434$. We have described a thorough assessment of error estimators, and the relative contributions of fitting and sampling errors appropriate for our combined sample. A novel technique for binning the DLA statistics is presented, which yields continuous $\Omega_{\rm HI}^{\rm DLA}$ 'curves' rather than discretized binned values. A comparison with the limited redshift range covered by the Noterdaeme *et al.* (2012) sample of DLAs in the SDSS/BOSS indicates that, despite the large size of our total sample, $\Omega_{\rm HI}^{\rm DLA}$ may still be under-estimated due to the absence of very high column density ($\log N(\text{H I}) > 21.7$) DLAs. Looking at Table 2.7, extrapolation of the whole combined sample indicates that the missing contribution of these absorbers is ~20% for our sample. However, this correction could be redshift-dependent. Statistics at large column densities are too poor when splitting the sample, and this could also lead to incorrect extrapolations, as inferred from Table 2.7. Consequently, yet larger samples are needed in order to precisely constrain the impact of high column density DLAs on $\Omega_{\rm HI}$ evolution.

On the other hand, low column density DLAs are sufficiently well sampled to offer nar-

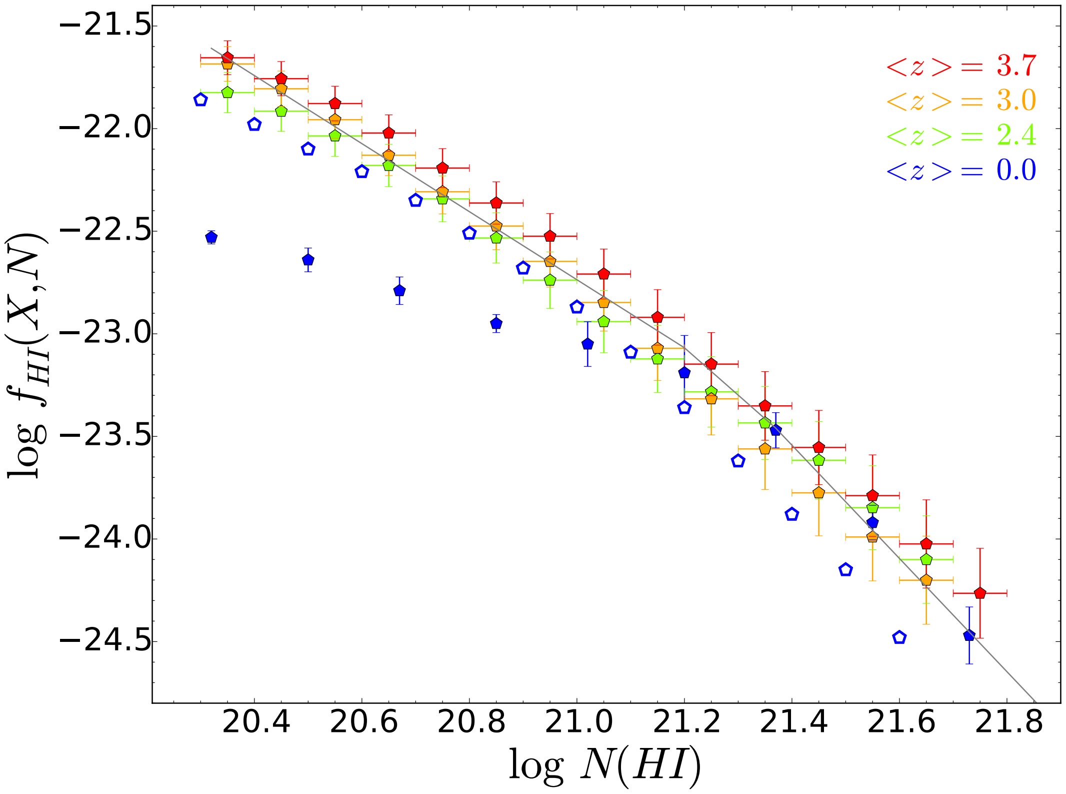

Figure 2.11: Column density distribution function of the CS 3 redshift bins compared with N12 (green points), B12 (filled blue points) and Z05 (unfilled blue points). The black line is the broken power law (BPL) fit of the whole CS.

row $\Omega_{\rm HI}^{\rm DLA}$ confidence intervals. This means that relatively small effects in sample selection that have been previously neglected could now become important. One such example is the false positives/negatives issue, that might represent an important systematic uncertainty. Results from Crighton *et al.* (2015) and the excellent agreement within our CS and N12 distribution functions, that were obtained using different methods, suggest that still we are not able to distinguish this effect from the sampling uncertainties.

Another source of error could be due to the SDSS color-selection of QSOs (see Prochaska *et al.*, 2009; Worseck & Prochaska, 2011). In order to investigate this effect, we built up a sub-sample of our CS composed only of 'safe' quasars, i.e., we excluded 10 biased XQ-100 QSOs (flagged in Table 2.1 with spades), SDSS quasars not flagged as selected by its FIRST counterpart with $2.7 < z_{\rm em} < 3.6$, and the P03 sample. Results are shown in Figure 2.10. We observe that, at this sample size (3152 QSOs and 402 DLAs), there is no strong evidence of the effects of this bias in $\Omega_{\rm HI}^{\rm DLA}$. However, from the $\ell(X)$ plot we can see a small decrease in the incidence rate at $z{\sim}2.8$, consistent with what we might expect, and suggesting that this color bias could be important in larger samples.

Table 2.7: Double power law fitting parameters and first moment of the $f_{\mathrm{HI}}(N,X)$. All values of $\Omega_{\mathrm{HI}}^{\mathrm{DLA}}$ are in units of 10^{-3}

z	z_{min}	z_{max}	n_{abs}	ΔX	log N_d	log k_d	α_{1d}	α_{2d}	${\Omega_{\mathrm{HI}}^{\mathrm{DLA}}}^{max}_{d}$	${\Omega_{\mathrm{HI}}^{\mathrm{DLA}}}^{\infty}_{d}$	$\Omega_{\mathrm{HI}}^{\mathrm{DLA}}$	$\Omega_{\mathrm{HI}}^{\mathrm{DLA}}$68% C.I.
2.99	1.550	5.313	742	10434	21.27	-23.18	-1.66	-2.77	0.94	1.16	0.97	0.93 - 1.03
2.57	1.550	2.947	318	5219	21.27	-23.26	-1.67	-2.41	0.60	1.02	0.65	0.60 - 0.71
3.47	2.947	5.313	424	5219	21.27	-23.12	-1.65	-2.74	0.83	1.05	0.85	0.80 - 0.92
2.44	1.550	2.732	208	3482	21.27	-23.26	-1.63	-2.16	0.62	1.65	0.67	0.61 - 0.74
2.95	2.732	3.207	235	3482	21.27	-23.26	-1.77	-2.64	0.63	0.86	0.64	0.58 - 0.70
3.69	3.207	5.313	300	3482	21.27	-23.08	-1.62	-2.53	0.93	1.34	0.95	0.88 - 1.05

In Fig. 2.11 we investigate whether the column density distribution function varies with redshift by comparing our $f_{\rm HI}(N,X)$ results split in 3 redshift bins with Z05 and B12 representing the local universe. Although the error bars for the 3 redshift bins of the CS overlap, there is a systematic trend for lower redshift intervals to have a lower normalization of $f_{\rm HI}(N,X)$ for moderate and low column density absorbers ($\log N({\rm H\,I}) < 20.9$). At high $N({\rm H\,I})$ there is more scatter amongst the points, due to poorer statistics, such that it is not possible to conclude if the evolution extends over the full column density range.

In Fig. 2.12 we plot the $\Omega_{\rm HI}^{\rm DLA}$ curve we derived down to $z \sim 2$, together with DLA surveys conducted at lower redshift (see Neeleman *et al.*, 2016; Rao *et al.*, 2006, and references therein) and $\Omega_{\rm HI}$ from 21 cm emission surveys (the different selection techniques, sparse sampling at intermediate z, and contrast in measurement techniques mean that it is not appropriate to combine these measurements into our computation of the $\Omega_{\rm HI}^{\rm DLA}$ curve).

A critical debate in the literature, that has been ongoing since the first measurements of $\Omega_{\rm HI}^{\rm DLA}$, is whether or not this quantity evolves with redshift. In order to *statistically* investigate whether the data favors (or not) an evolution of the H I content in the universe over cosmic time, we performed the following test: For each non overlapping redshift point of the CS split in 5 bins with the same ΔX, we randomly selected one value of $\Omega_{\rm HI}^{\rm DLA}$ from its probability distribution. This was repeated using the $\Omega_{\rm HI}^{\rm DLA}$ curve, in order to compare the impact of using either our new 'curve' methodology with traditional binning. In order to include intermediate redshift DLA surveys or local 21cm emission surveys in our re-samples, we draw $\Omega_{\rm HI}^{\rm DLA}$ (or $\Omega_{\rm HI}$) points assuming a Gaussian distribution within the quoted 1 σ error bars of those works. For surveys with extended redshift coverage (i.e. R06 and N15) we also re-sampled evenly across the quoted range in z, using the same Δz sampling as for the CS curve. After each re-sampling of the $\Omega_{\rm HI}^{\rm DLA}$ curve, we performed a linear regression and computed the slope and Pearson's correlation coefficient, r, which tests for the significance of a correlation between two quantities (in this case, z and $\Omega_{\rm HI}^{\rm DLA}$). We tabulate in Table 2.8 the distribution of the slopes and r for 100,000 iterations. Figure 2.13 considers only the CS, whereas Figure 2.14 include either intermediate or low redshift data.

Considering first only the CS, we observe a significant correlation for the whole sample, as shown by the red-to-yellow histograms, spanning approximately $2 < z < 5$. In Table 2.8 we can observe that the significance of the results depends on the redshift sampling of the $\Omega_{\rm HI}^{\rm DLA}$ results, since the larger the z range, the greater the degrees of freedom we have. We therefore also establish the significance of this correlation, finding $\geq 3\sigma$ **to be** independent of binning/sampling method. We note that in the z-range from 2.5 to

3.5, where our statistics are best, the slopes and r distributions are independent of the Δz chosen. From the curve analysis, the correlation is driven mostly by the data in the z-range from 2.5 to 3.5, where the median correlation coefficient is $r = 0.8$ (blue and cyan histograms). Taken together, the positive slopes and r values indicate significant redshift evolution in $\Omega_{\rm HI}^{\rm DLA}$ within these redshift ranges. However, when considering only redshifts greater than 3.5 (orange histograms), the data do not show a significant correlation, although the statistics in this high redshift regime are considerably poorer. The large confidence intervals associated with the $\Omega_{\rm HI}^{\rm DLA}$ curve at $z > 3.5$ could be masking some mild evolution.

In upper panels of Figure 2.14 we now include R06 ($0.11 < z < 1.6$, purple histograms) and N15 ($0.01 < z < 1.7$, green histograms) data. If we use the R06 statistics to represent intermediate redshift DLAs, in combination with the CS, the correlation coefficient (median $r = 0.0$) and slope (median value = 0.0) favors no evolution across the entire redshift range from $0.1 < z < 5$. Conversely, if the low value of $\Omega_{\rm HI}^{\rm DLA}$ reported by N15 is adopted, the evolution is very significant ($\geq 6.5\sigma$, with median $r = 0.9$ and slope = 0.24×10^{-3}). The N15 and R06 samples both have important limitations. On the one hand, the results from R06 are based on the incidence of Mg II, a pre-selection technique which may bias the high column density end of $f_{\rm HI}(N, X)$ towards higher values (see Neeleman *et al.*, 2016, and references therein). On the other hand, the N15 statistics are too poor to fully sample the column density distribution function and they had to correct their measurements assuming N12's $f_{\rm HI}(N, X)$ to include contribution by missing DLAs with $\log N(\rm H\,I)>21.0$.

Given the relatively small sample sizes of DLAs at intermediate redshifts, and the potential biases and uncertainties described above, we next test for evolution by combining the CS with $z \sim 0$ measurements of $\Omega_{\rm HI}$. However, even for the local universe, H I measurements are not absent of concerns on possible systematics, and Fig. 2.12 shows a factor of two disagreement between surveys. For example, Braun (2012) claims that current low-z measurements are strongly biased due to resolution effects, as the densest H I clouds are much smaller than the typical spatial resolution and no self-absorption correction, which is important in this case, can be computed from the data-cubes. This effect was pointed out previously by Zwaan *et al.* (2005), but with their data-set they were not able to find significant deviations. However, Braun (2012) builds up the local distribution function using high-resolution images ($\sim 100pc$) of only three galaxies, assuming that the cloud distribution is representative of the whole local Universe, which may not be accurate. We therefore repeat the evolution test, combining the CS with either R13 or B12, which show the lowest and and highest measurements of $\Omega_{\rm HI}$ respectively in the local universe. In the lower panels of Fig. 2.14 we show the distribution of slopes (left

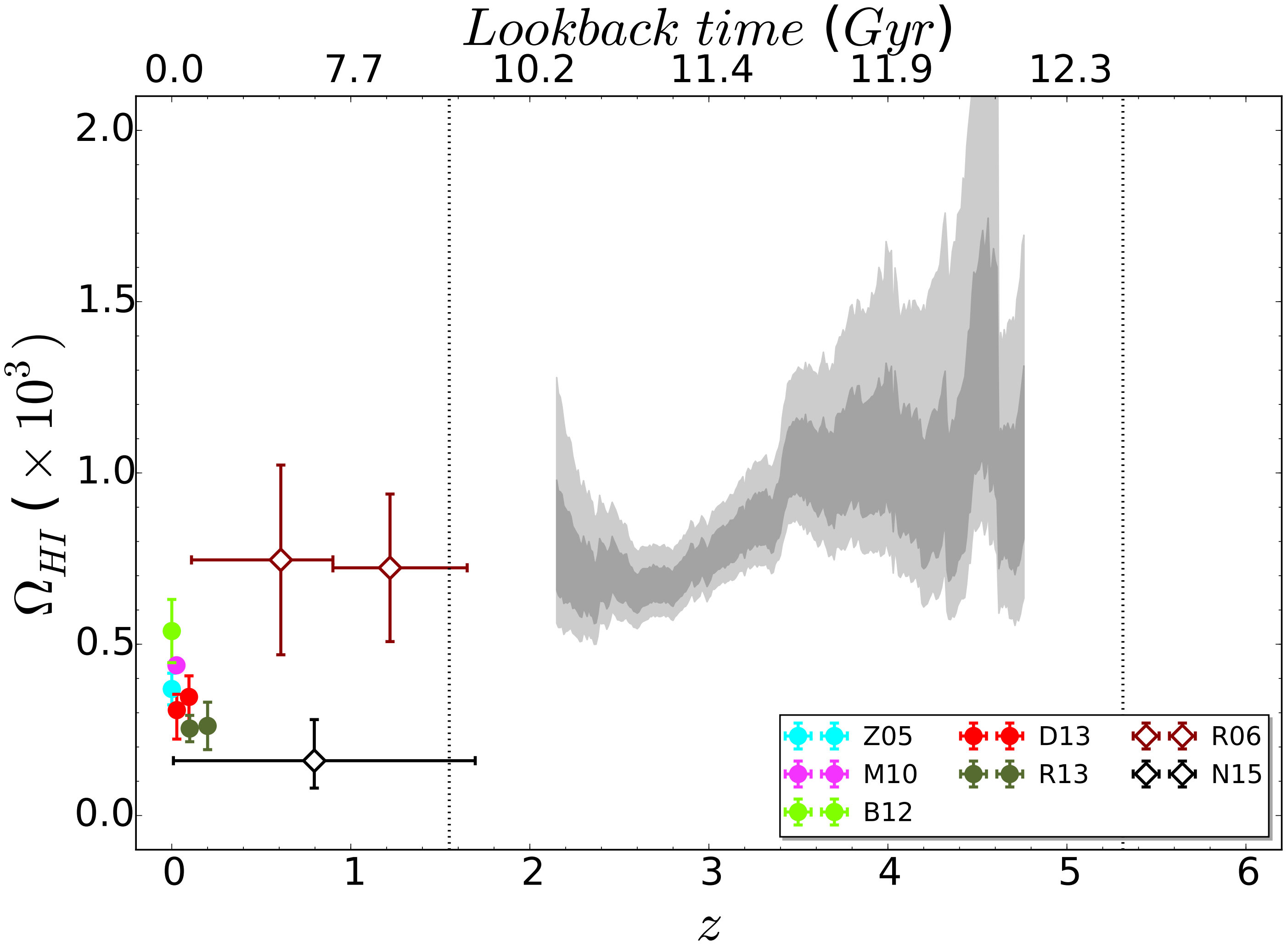

Figure 2.12: Evolution of the atomic HI gas in galaxies over the cosmic time. Data from 21cm emission line surveys (circles) and from QSO absorption systems (squares) are plotted. Empty points represents $\Omega_{\rm HI}^{\rm DLA}$ and filled $\Omega_{\rm HI}$. Vertical lines are the redshift limits of our combined sample. The data for the CS curve is tabulated in Table **??**.

panel) and correlation coefficients (right panel) for the 100,000 resamplings when the CS is combined with either R13 (olive green histogram) or B12 (grey histogram). Although the $\Omega_{\rm HI}$ values reported by these two works differ by a factor of two, when combined with the CS both exhibit a statistically significant correlation between $\Omega_{\rm HI}$ and z; in both cases the median correlation coefficient is $r = 0.6$ with a significance $\geq 3\sigma$. The median slopes are also very similar, $\sim 0.17 \times 10^{-3}$, which correspond to a factor of ~ 4 decrease in $\Omega_{\rm HI}$ between $z = 5$ and $z = 0$.

Despite decades of effort in compiling ever larger samples, our assessment of the galactic gas reservoir in DLAs is still limited by the missing high density absorbers and the traditional $N(\text{H I})$ definition at $\log N(\text{H I}) = 20.3$. It has been argued (e.g. Péroux *et al.*, 2005) that, particularly at high redshifts, sub-DLAs ($\log N(\text{H I}) > 19.0$) could contribute significantly to the atomic hydrogen budget. Crighton *et al.* (2015) made a statistical 20 per cent correction for sub-DLAs in their study of $z > 3.5$ DLAs, based on results from Noterdaeme *et al.* (2009); O'Meara *et al.* (2007); Prochaska *et al.* (2010); Zafar *et al.* (2013). The suggested redshift dependence of a sub-DLA correction means that a uniform correction to account for lower column density absorbers is not appropriate for our combined sample. Moreover, the majority of DLA surveys that comprise our combined sample were conducted at insufficient resolution to robustly identify sub-DLAs, such that a 'manual' assessment of the sub-DLA contribution to each is not possible. Although a redshift dependent sub-DLA correction could produce some changes in the $\Omega_{\rm HI}$ curve shape, existing results indicate that this factor is unlikely to dramatically change the picture that we presented in this work. In a future paper we will identify and investigate the nature of the sub-DLAs in the XQ-100 sample.

In closing, we note that the quality of the XQ-100 spectra are sufficient, both in terms of SNR and resolution, to directly determine elemental abundances for the DLAs presented here. There are numerous DLAs of interest amongst the sample, including a candidate very metal poor DLA, several PDLAs, and some cases of multiple DLAs that lie very close in velocity space along a single line of sight. All of these categories have been proposed to be chemically interesting (e.g. Cooke *et al.*, 2011b; Ellison & Lopez, 2001; Ellison *et al.*, 2010, 2011; Lopez & Ellison, 2003). In Berg et al. (in prep) we study the chemical abundances of all the XQ-100 DLAs, with a particular focus on these special cases, in the context of a large literature sample.

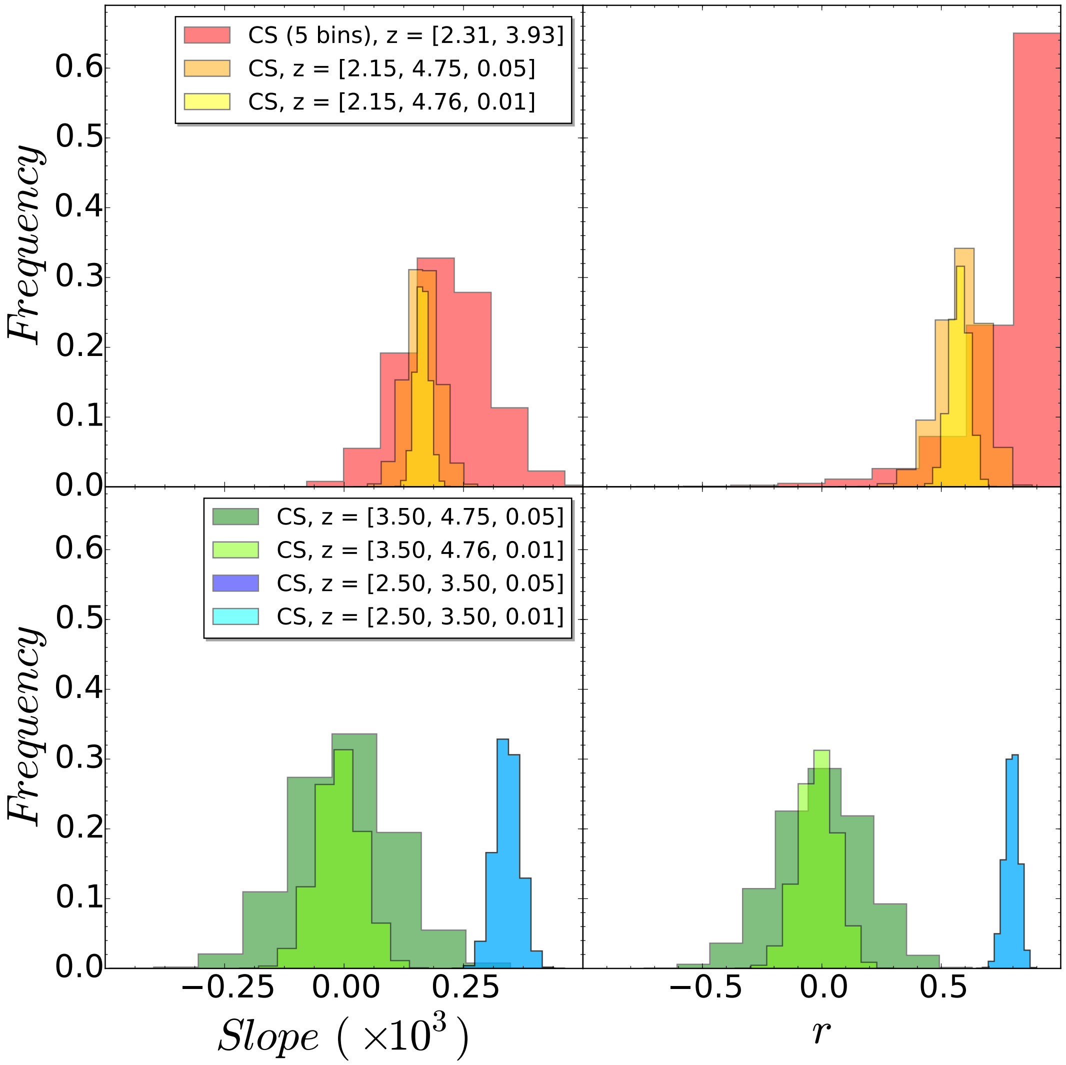

Figure 2.13: Histograms of the results of the evolution test for different redshift ranges of the CS split in 5 non overlapping bins (top panels), and the CS curve (bottom panels). Redshifts intervals in the legend have the format $[z_{\rm min},\, z_{\rm max}]$ (bins) or $[z_{\rm min},\, z_{\rm max},\, \Delta z]$ (curves). The left hand panels show the distribution of slopes from a linear regression of 100,000 re-sampled Ω curves; the right hand panels show the distributions of the Pearson correlation coefficients, r. Different colored histograms indicate different samples and redshift ranges, as given in the Figure legends.

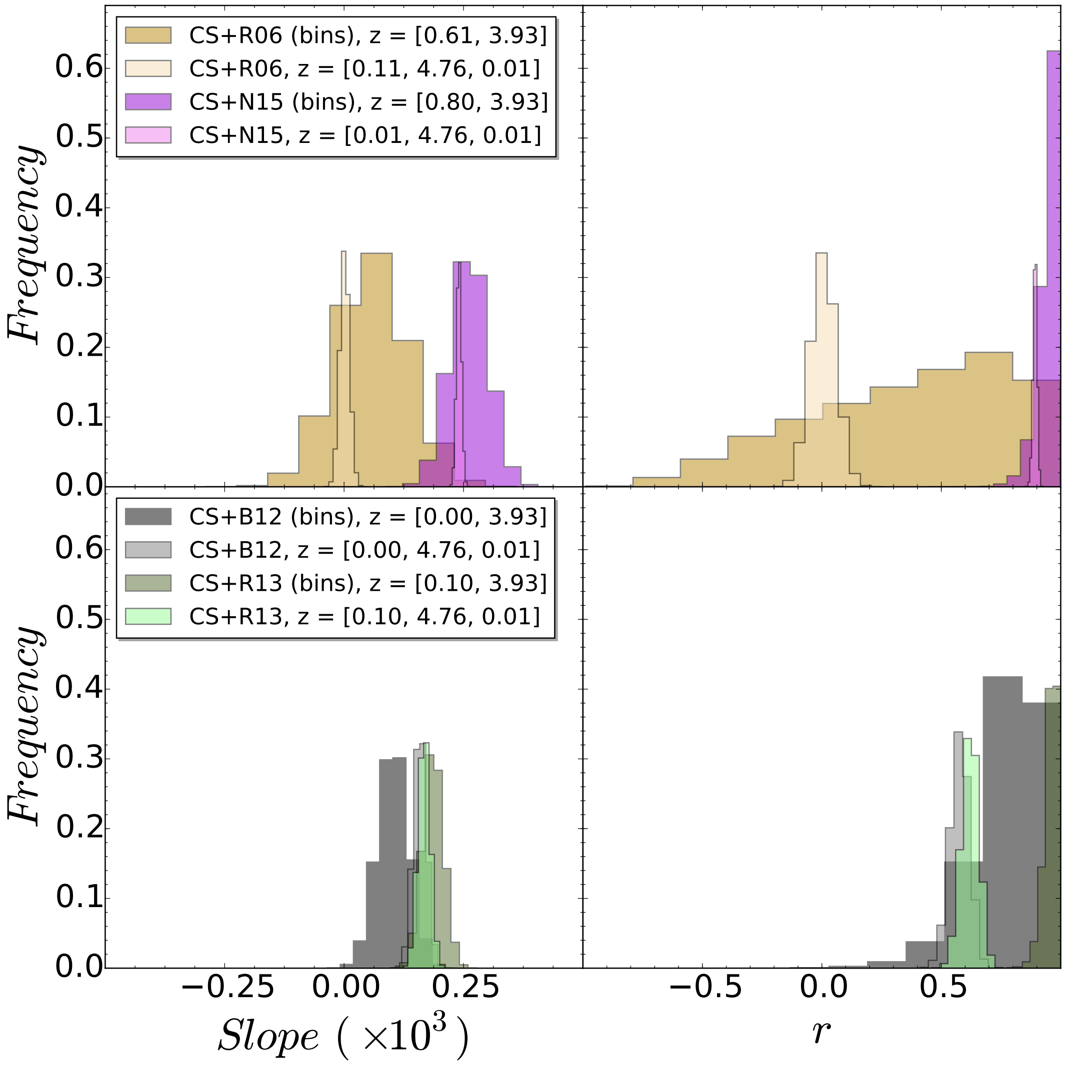

Figure 2.14: Version of Figure 2.13 with histograms of the results of the evolution test for the CS plus intermediate redshift samples (top panels), and local 21cm samples (bottom panels).

Table 2.8: Results of the evolution tests for 3 cases: non overlapping curves, $\Omega_{\rm HI}^{\rm DLA}$ curve with Δz=0.01 and its resampled version with Δz=0.05. Slopes are in units of 10^{-3}

	Non overlapping points			$\Delta z = 0.05$			$\Delta z = 0.01$		
Sample	Slope	r	σ	Slope	r	σ	Slope	r	σ
CS	0.21 ± 0.09	0.86 ± 0.19	3.0	0.16 ± 0.03	0.59 ± 0.09	5.0	0.16 ± 0.01	0.58 ± 0.04	11.0
CS ($z \geq 3.5$)	—	—	—	0.00 ± 0.11	0.00 ± 0.18	0.0	-0.01 ± 0.05	-0.01 ± 0.08	0.0
CS ($2.5 \leq z \leq 3.5$)	—	—	—	0.34 ± 0.03	0.80 ± 0.03	9.0	0.34 ± 0.03	0.80 ± 0.03	21.0
CS + R06	0.06 ± 0.07	0.42 ± 0.42	1.0	—	—	—	0.00 ± 0.01	0.0 ± 0.05	0.0
CS + N15	0.26 ± 0.04	0.95 ± 0.04	6.5	—	—	—	0.24 ± 0.01	0.89 ± 0.01	41.0
CS + B12	0.10 ± 0.03	0.80 ± 0.14	3.0	—	—	—	0.16 ± 0.01	0.58 ± 0.04	11.0
CS + R13	0.19 ± 0.02	0.96 ± 0.03	8.0	—	—	—	0.17 ± 0.01	0.62 ± 0.04	13.0

Chapter 3

Conclusions

3.1 Conclusions

Based on the results of the XQ-100 survey, we report the detection of 38 intervening DLAs identified towards 100 $z > 3.5$ QSOs. This sample has been combined, after exhaustive checking for duplications and errors, with a literature sample of DLA surveys spanning the last ~ 20 years. The final combined sample contains 742 DLAs spanning the redshift range from $z \sim 1.6$ to 5. We present statistical measures of the column density distribution function ($f_{\rm HI}(N, X)$, Fig 2.6), DLA number density ($\ell(X)$, Fig. 2.9), and the DLA HI gas content ($\Omega_{\rm HI}^{\rm DLA}$, Fig. 2.12), and present a thorough estimation of errors and potential biases (such as colour selection and incomplete sampling of the high column density end) on these quantities. The main focus of this paper is the evolution of $\Omega_{\rm HI}^{\rm DLA}$, and we present a novel technique for computing this quantity as a continuous function of redshift, with confidence intervals computed at every redshift point. In order to statistically assess whether there is evolution in $\Omega_{\rm HI}^{\rm DLA}$ over cosmic time, we perform a bootstrap re-sampling of the $\Omega_{\rm HI}^{\rm DLA}$ curve and compute the slope and correlation coefficients (r) of 100,000 iterations. For the combined sample, the most significant $\Omega_{\rm HI}^{\rm DLA}$ redshift evolution (median $r = 0.8$) is found for the interval $2.5 < z < 3.5$. However, at higher redshifts, the median slope of the bootstrap iterations is zero and median $r = 0.0$, indicating no significant evolution, but improved statistics above $z \sim 3.5$ are still required to confirm this. Assessing evolution in $\Omega_{\rm HI}^{\rm DLA}$ down to lower redshifts is found to be highly dependent on the choice of sample used for the evolution test. Combining the CS with the intermediate redshift sample of DLAs from Rao *et al.* (2006) yields a median correlation coefficient $r = 0$, indicating that the cosmic gas density is not strongly evolving from $z \sim 0.1$ to 5. However, this picture is challenged by an alternative survey for $0 < z < 1.6$ absorbers by Neeleman *et al.* (2016) who find an $\Omega_{\rm HI}^{\rm DLA}$ value a factor of five lower than R06. Adopting the N15 value of $\Omega_{\rm HI}^{\rm DLA}$ results in a highly significant evolution of galactic gas content (median correlation coefficient $r = 0.9$). A more consistent picture is obtained when the CS is combined with $z \sim 0$ surveys. Although these surveys exhibit a factor of $\sim$ two variation in their quoted $\Omega_{\rm HI}$, both the highest (Braun, 2012) and lowest (Rhee *et al.*, 2013) yield a statistically significant ($r = 0.6$) redshift evolution when combined with the high redshift data. The median slope obtained from out bootstrap re-sampling is $\sim 0.17 \times 10^{-3}$, corresponding to a factor of ~ 4 decrease in $\Omega_{\rm HI}$ from $z = 5$ to $z = 0$. Therefore, the greatest uncertainty in $\Omega_{\rm HI}$ measurements is in the intermediate redshift regime, which is currently beyond the reach of most 21cm surveys, but still poorly sampled by DLA studies. An accurate measure of $\Omega_{\rm HI}^{\rm DLA}$ at redshifts between 0.1 and 2 is therefore clearly of the utmost importance. Upcoming surveys with the Square Kilometre Array (SKA, Staveley-Smith & Oosterloo, 2015) and its pathfinders present an exciting prospect for resolving the current uncertainty in the gas content of galaxies since $z \sim 1.5$.

THESIS CONCLUSIONS

Chapter 1

Conclusions

- We present an extensive follow-up of the afterglow of GRB 110715A in 17 bands ranging from a few seconds up to 74 days after the trigger. The line of sight is affected by strong foreground Galactic extinction, which complicated the follow-up and the analysis of the data.

- GRB 110715A had a very bright afterglow at all wavelengths, although its intrinsic luminosity is not exceptional.

- Optical/nIR spectroscopy obtained with X-shooter shows weak absorption features at a redshift of $z = 0.8224$ with no resolved velocity components ($\lesssim 30$ km s^{-1}). Absorption line ratios indicate a low ionization environment, confirmed by the rare detection of Ca I.

- Deep late imaging reveals a faint host galaxy with an absolute magnitude of $\mathrm{M}_B =$ -18.2. This is consistent with the weak absorption features detected in the spectrum.

- We attempted to model the broadband data with a fireball model based on the prescription of Jóhannesson *et al.* (2006). The best model implies a forward shock evolving through a wind environment with a termination shock. In spite of describing roughly the behavior of the afterglow, none of the models is able to get a statistically acceptable fit. This shows the need for better broadband sampling and more complex models to accurately describe the physics of GRB afterglows. There are several works that explore other possibilities, such as magneto-hydrodynamic simulations (van Eerten *et al.*, 2012), which was satisfactorily used, e.g., in Guidorzi *et al.* (2014); Ryan *et al.* (2015); Zhang *et al.* (2015), or central engine activities (Zhang *et al.*, 2014). These and other effects might be considered together in future works to get a more accurate view of the GRB afterglow physics.

- Radio and sub-mm, along with X-ray observations, have been proven to be the most constraining bands for the afterglow modeling. We were limited by sensitivity for a long time in the crucial wavelength range of sub-mm, but now that ALMA is available, we have a good chance of getting high-quality data for a larger number of GRBs. This new, current and future facilities will allow us to probe the emission mechanisms in greater detail than previously possible, and will be determinant in the evolution of the GRB afterglow models.

- We detect a Damped Lyman-α system at $z = 5.2821 \pm 0.1$ on the optical spectra towards GRB 140304A. This is the third farthest DLA detected to date. The Voigt profile fitting give a column density value of $\log N(\mathrm{H\,I}) = 21.8 \pm 0.1$.

- There are several absorption lines at the same redshift as the Lyα absorption due to S, Si, O, and C, as well as at least one C IV intervening system.

- We measured the EW of the lines and compared them with the results from de Ugarte Postigo *et al.* (2012a), finding that the 41% of the sample has weaker features.

- We estimated the metal abundances of the S II and Si II* ions by using a novel technique based on the CoG method and the Bayesian inference, finding acceptable results.

- We obtained $[S/H] = -1.13^{+0.10}_{-0.07}$, a value consistent with the non evolution picture of the metal content in star forming regions up to $z{\sim}5$.

- With an initial Lorentz bulk factor in the range $\Gamma_0 \sim$ 65-220, the X-ray afterglow evolution can be explained by a time-dependent photoionization of the local circum-burst medium, within a compact and dense environment.

- The host galaxy has a sub-DLA with $\log N(\mathrm{H\,I}) = 19.85 \pm 0.15$, and a metallicity content in the range from ∼1/7 to ∼1/60 of solar.

- In order to place the chemistry of the GRB sub-DLA in context with other high z absorbers, both Fig. 3.8 and Fig. 3.9 show the metallicity of a compilation of GRB host galaxy absorption systems (GRB-DLAs) compared to quasars with DLA and sub-DLAs (QSO-DLAs), combining the data reported in the literature (Berg *et al.*, 2015b; Schady *et al.*, 2011; Thöne *et al.*, 2013). The GRB 130606A sub-DLA is a rare find: the second highest redshift burst with a measured GRB-DLA metallicity and only the third GRB absorber with sub-DLA HI column density. At z ¿ 5, the only other object known then with lower metallicity is the ULAS J1120+0641 DLA at z ∼ 7 (Simcoe *et al.*, 2012). However, the DLA towards ULAS J1120+0641 is close to the redshift of the quasar and its metallicity is determined from a stacked spectrum, both of which complicate its interpretation (Ellison *et al.*, 2010, 2011).

- We note that GRB 130606A, given the non-zero metal content of the host, might have originated from a non-Pop III progenitor star, but whether its afterglow light penetrated material that was pre-enriched by Pop III nucleosynthesis at even higher redshifts (Wang *et al.*, 2012) remains uncertain. Indeed several possibilities for the death of the first stars have recently been suggested by theoretical models (Bromm, 2013). A high value of C/O is predicted to be a signature of Pop III stellar enrichment (Fabbian *et al.*, 2009). A handful of DLAs in the metallicity range -2 to -3 (1/100 to 1/1000 of the Sun's metallicity) have C/O measurements (Cooke *et al.*, 2011a; Ellison *et al.*, 2010) and all but one (towards the quasar QSO J0035-0918) have [C/O] ¡ 0 (Cooke *et al.*, 2011a). Unfortunately, we cannot impose any constraint on this ratio as both species are likely saturated.

- Events such as GRB 130606A at z = 5.91, and future ones at z ¿ 10, offer an exciting new window into pre-galactic metal enrichment in these very high redshift galaxies. These bright lighthouses constitute a significant step forward towards using these sources as beacons for measuring abundances at such early times. New GRB missions, equipped with on-board near-IR detectors, and coupled to state-of-the-art instruments built for the largest diameter ground-based telescopes, will allow us to study the first stars that fundamentally transformed the Universe only a few hundred million years after the Big Bang.

- We presented the multi-band spectroscopic and temporal analysis of the high-z GRB 140515A. The overall observed temporal properties of this burst, including the broad X-ray bump detected at late times, could be explained in the context of a standard afterglow model, although this requires an unusually flat index of the electron energy spectrum ($p = 1.67$).

- Another possible interpretation is to assume that an additional component (e.g. related to long-lasting central engine activity) is dominating the X-ray emission. In the latter case, the broad band observations can be explained using a more typical value of the spectral index for the injected electron spectrum ($p = 2.1$). Our modelling in this case shows that the central engine activity should cease at late times ($\sim 2 \times 10^5$ s), when the X-ray afterglow starts to dominate the emission.

- In both scenarios the cooling frequency is expected to be between the optical and the X-ray energy bands ($\nu_c \sim 2 \times 10^{16}$ Hz) and the average rest-frame circum-burst extinction ($\mathrm{A_V} \sim 0.1$) resulted to be typical of high-z bursts.

- Our detailed spectral analysis provided a best estimate of the neutral hydrogen fraction of the IGM towards the burst of $x_{HI} \leq 0.002$ and a conservative upper limit of the HI abundance in the GRB host galaxy of $N_{\mathrm{HI}} \lesssim 10^{18.5}$ cm^{-2}. These values are slightly different from the ones estimated by Chornock et al. (2014b).

- In addition, the spectral absorption lines observed in our spectra are the weakest lines ever observed in GRB afterglows (de Ugarte Postigo *et al.*, 2012a), suggesting that GRB 140515A happened in a very low density environment. However, our upper limits on the gas-phase abundances, coupled with the fact that we cannot establish the exact metal-to-dust ratio, do not allow us to distinguish between metallicity in the range of $10^{-4} < [Z/H] < 0.1$. This makes the possible Pop III star origin for GRB 140515A uncertain and doubtful.

- For all high-z GRBs the contribution of the host galaxy was not negligible (Table 4.2). GRB 140515A is the first case when this does not happen, allowing us to give the best observational constrains on a theoretical model at $z > 6$.

- Based on the results of the XQ-100 survey, we report the detection of 38 intervening DLAs identified towards 100 $z > 3.5$ QSOs.

- This sample has been combined, after exhaustive checking for duplications and errors, with a literature sample of DLA surveys spanning the last ~ 20 years. The final combined sample contains 742 DLAs spanning the redshift range from $z \sim 1.6$ to 5.

- We present statistical measures of the column density distribution function ($f_{\mathrm{HI}}(N, X)$, Fig 2.6), DLA number density ($\ell(X)$, Fig. 2.9), and the DLA HI gas content ($\Omega_{\mathrm{HI}}^{\mathrm{DLA}}$, Fig. 2.12), and present a thorough estimation of errors and potential biases (such as colour selection and incomplete sampling of the high column density end) on these quantities.

- The main focus of this paper is the evolution of $\Omega_{\mathrm{HI}}^{\mathrm{DLA}}$, and we present a novel technique for computing this quantity as a continuous function of redshift, with confidence intervals computed at every redshift point.

- In order to statistically assess whether there is evolution in $\Omega_{\mathrm{HI}}^{\mathrm{DLA}}$ over cosmic time, we perform a bootstrap re-sampling of the $\Omega_{\mathrm{HI}}^{\mathrm{DLA}}$ curve and compute the slope and correlation coefficients (r) of 100,000 iterations. For the combined sample, the most significant $\Omega_{\mathrm{HI}}^{\mathrm{DLA}}$ redshift evolution (median $r = 0.8$) is found for the interval $2.5 < z < 3.5$. However, at higher redshifts, the median slope of the bootstrap iterations is zero and median $r = 0.0$, indicating no significant evolution, but improved statistics above $z \sim 3.5$ are still required to confirm this.

- Assessing evolution in $\Omega_{\rm HI}^{\rm DLA}$ down to lower redshifts is found to be highly dependent on the choice of sample used for the evolution test. Combining the CS with the intermediate redshift sample of DLAs from Rao *et al.* (2006) yields a median correlation coefficient $r = 0$, indicating that the cosmic gas density is not strongly evolving from $z \sim 0.1$ to 5. However, this picture is challenged by an alternative survey for $0 < z < 1.6$ absorbers by Neeleman *et al.* (2016) who find an $\Omega_{\rm HI}^{\rm DLA}$ value a factor of five lower than R06. Adopting the N15 value of $\Omega_{\rm HI}^{\rm DLA}$ results in a highly significant evolution of galactic gas content (median correlation coefficient $r = 0.9$).

- A more consistent picture is obtained when the CS is combined with $z \sim 0$ surveys. Although these surveys exhibit a factor of $\sim$ two variation in their quoted $\Omega_{\rm HI}$, both the highest (Braun, 2012) and lowest (Rhee *et al.*, 2013) yield a statistically significant ($r = 0.6$) redshift evolution when combined with the high redshift data. The median slope obtained from out bootstrap re-sampling is $\sim 0.17 \times 10^{-3}$, corresponding to a factor of ~ 4 decrease in $\Omega_{\rm HI}$ from $z = 5$ to $z = 0$.

- Therefore, the greatest uncertainty in $\Omega_{\rm HI}$ measurements is in the intermediate redshift regime, which is currently beyond the reach of most 21cm surveys, but still poorly sampled by DLA studies. An accurate measure of $\Omega_{\rm HI}^{\rm DLA}$ at redshifts between 0.1 and 2 is therefore clearly of the utmost importance. Upcoming surveys with the Square Kilometre Array (SKA, Staveley-Smith & Oosterloo, 2015) and its pathfinders present an exciting prospect for resolving the current uncertainty in the gas content of galaxies since $z \sim 1.5$.

APPENDICES

Appendix A

Follow up of GRB 110715A

Table A.1: Broad band multiwavelength observations of GRB 110715A.

T - T_0 [days]	Flux [Jy]	AB [mag]	Band
0.00094	$(1.32 \pm 0.33) \times 10^{-04}$	$18.60^{+0.24}_{-0.31}$	XRT 2 keV
0.00096	$(1.52 \pm 0.37) \times 10^{-04}$	$18.44^{+0.24}_{-0.31}$	XRT 2 keV
0.00098	$(1.12 \pm 0.27) \times 10^{-04}$	$18.78^{+0.24}_{-0.31}$	XRT 2 keV
0.00100	$(1.01 \pm 0.25) \times 10^{-04}$	$18.89^{+0.24}_{-0.31}$	XRT 2 keV
0.00103	$(1.13 \pm 0.26) \times 10^{-04}$	$18.77^{+0.23}_{-0.29}$	XRT 2 keV
0.00114	$(1.19 \pm 0.17) \times 10^{-04}$	$18.71^{+0.15}_{-0.17}$	XRT 2 keV
0.00116	$(0.86 \pm 0.13) \times 10^{-04}$	$19.06^{+0.16}_{-0.18}$	XRT 2 keV
0.00119	$(1.16 \pm 0.17) \times 10^{-04}$	$18.74^{+0.15}_{-0.18}$	XRT 2 keV
0.00121	$(0.83 \pm 0.12) \times 10^{-04}$	$19.10^{+0.15}_{-0.18}$	XRT 2 keV
0.00124	$(0.92 \pm 0.14) \times 10^{-04}$	$18.99^{+0.16}_{-0.18}$	XRT 2 keV
0.00127	$(1.13 \pm 0.17) \times 10^{-04}$	$18.76^{+0.15}_{-0.18}$	XRT 2 keV
0.00129	$(1.14 \pm 0.17) \times 10^{-04}$	$18.75^{+0.15}_{-0.18}$	XRT 2 keV
0.00132	$(0.85 \pm 0.12) \times 10^{-04}$	$19.08^{+0.15}_{-0.18}$	XRT 2 keV
0.00134	$(0.90 \pm 0.14) \times 10^{-04}$	$19.01^{+0.16}_{-0.19}$	XRT 2 keV
0.00138	$(0.79 \pm 0.12) \times 10^{-04}$	$19.16^{+0.16}_{-0.18}$	XRT 2 keV
0.00140	$(1.04 \pm 0.15) \times 10^{-04}$	$18.85^{+0.15}_{-0.18}$	XRT 2 keV
0.00143	$(0.86 \pm 0.13) \times 10^{-04}$	$19.06^{+0.16}_{-0.18}$	XRT 2 keV
0.00146	$(0.86 \pm 0.12) \times 10^{-04}$	$19.06^{+0.15}_{-0.18}$	XRT 2 keV
0.00149	$(1.17 \pm 0.17) \times 10^{-04}$	$18.73^{+0.15}_{-0.18}$	XRT 2 keV
0.00151	$(0.89 \pm 0.13) \times 10^{-04}$	$19.03^{+0.15}_{-0.18}$	XRT 2 keV
0.00154	$(0.82 \pm 0.12) \times 10^{-04}$	$19.11^{+0.16}_{-0.18}$	XRT 2 keV
0.00157	$(0.94 \pm 0.14) \times 10^{-04}$	$18.97^{+0.16}_{-0.18}$	XRT 2 keV
0.00160	$(1.04 \pm 0.15) \times 10^{-04}$	$18.86^{+0.16}_{-0.18}$	XRT 2 keV

Table A.1: continued.

T - T_0 [days]	Flux [Jy]	AB [mag]	Band
0.00163	$(0.82 \pm 0.12) \times 10^{-04}$	$19.11^{+0.15}_{-0.18}$	XRT 2 keV
0.00165	$(0.89 \pm 0.13) \times 10^{-04}$	$19.02^{+0.15}_{-0.18}$	XRT 2 keV
0.00168	$(0.89 \pm 0.13) \times 10^{-04}$	$19.02^{+0.16}_{-0.18}$	XRT 2 keV
0.00171	$(0.97 \pm 0.14) \times 10^{-04}$	$18.93^{+0.15}_{-0.18}$	XRT 2 keV
0.00174	$(0.89 \pm 0.13) \times 10^{-04}$	$19.02^{+0.15}_{-0.18}$	XRT 2 keV
0.00177	$(0.71 \pm 0.10) \times 10^{-04}$	$19.28^{+0.16}_{-0.18}$	XRT 2 keV
0.00181	$(0.72 \pm 0.10) \times 10^{-04}$	$19.26^{+0.15}_{-0.18}$	XRT 2 keV
0.00184	$(0.98 \pm 0.14) \times 10^{-04}$	$18.93^{+0.15}_{-0.18}$	XRT 2 keV
0.00187	$(0.78 \pm 0.11) \times 10^{-04}$	$19.17^{+0.15}_{-0.18}$	XRT 2 keV
0.00190	$(6.45 \pm 0.99) \times 10^{-05}$	$19.38^{+0.16}_{-0.18}$	XRT 2 keV
0.00194	$(1.03 \pm 0.15) \times 10^{-04}$	$18.87^{+0.15}_{-0.18}$	XRT 2 keV
0.00196	$(0.94 \pm 0.14) \times 10^{-04}$	$18.96^{+0.15}_{-0.18}$	XRT 2 keV
0.00199	$(0.89 \pm 0.13) \times 10^{-04}$	$19.02^{+0.15}_{-0.18}$	XRT 2 keV
0.00202	$(0.83 \pm 0.12) \times 10^{-04}$	$19.11^{+0.15}_{-0.18}$	XRT 2 keV
0.00205	$(0.83 \pm 0.12) \times 10^{-04}$	$19.10^{+0.15}_{-0.18}$	XRT 2 keV
0.00208	$(0.66 \pm 0.10) \times 10^{-04}$	$19.35^{+0.15}_{-0.18}$	XRT 2 keV
0.00212	$(0.75 \pm 0.11) \times 10^{-04}$	$19.21^{+0.15}_{-0.18}$	XRT 2 keV
0.00216	$(0.68 \pm 0.10) \times 10^{-04}$	$19.32^{+0.16}_{-0.18}$	XRT 2 keV
0.00220	$(5.39 \pm 0.82) \times 10^{-05}$	$19.57^{+0.16}_{-0.18}$	XRT 2 keV
0.00224	$(0.84 \pm 0.13) \times 10^{-04}$	$19.10^{+0.16}_{-0.18}$	XRT 2 keV
0.00227	$(0.92 \pm 0.13) \times 10^{-04}$	$18.99^{+0.15}_{-0.18}$	XRT 2 keV
0.00230	$(0.95 \pm 0.14) \times 10^{-04}$	$18.96^{+0.15}_{-0.18}$	XRT 2 keV
0.00232	$(0.75 \pm 0.11) \times 10^{-04}$	$19.21^{+0.15}_{-0.18}$	XRT 2 keV
0.00236	$(0.81 \pm 0.12) \times 10^{-04}$	$19.12^{+0.15}_{-0.18}$	XRT 2 keV
0.00239	$(0.68 \pm 0.10) \times 10^{-04}$	$19.32^{+0.15}_{-0.18}$	XRT 2 keV
0.00243	$(0.77 \pm 0.11) \times 10^{-04}$	$19.19^{+0.15}_{-0.18}$	XRT 2 keV
0.00247	$(6.15 \pm 0.97) \times 10^{-05}$	$19.43^{+0.16}_{-0.19}$	XRT 2 keV
0.00251	$(0.65 \pm 0.10) \times 10^{-04}$	$19.36^{+0.16}_{-0.18}$	XRT 2 keV
0.00254	$(0.76 \pm 0.11) \times 10^{-04}$	$19.19^{+0.15}_{-0.18}$	XRT 2 keV
0.00258	$(6.54 \pm 0.99) \times 10^{-05}$	$19.36^{+0.15}_{-0.18}$	XRT 2 keV
0.00263	$(5.24 \pm 0.79) \times 10^{-05}$	$19.60^{+0.15}_{-0.18}$	XRT 2 keV
0.00267	$(6.14 \pm 0.94) \times 10^{-05}$	$19.43^{+0.16}_{-0.18}$	XRT 2 keV
0.00271	$(0.67 \pm 0.10) \times 10^{-04}$	$19.33^{+0.16}_{-0.18}$	XRT 2 keV
0.00274	$(0.79 \pm 0.12) \times 10^{-04}$	$19.16^{+0.16}_{-0.18}$	XRT 2 keV

Table A.1: continued.

T - T_0 [days]	Flux [Jy]	AB [mag]	Band
0.00278	$(5.62 \pm 0.87) \times 10^{-05}$	$19.53^{+0.16}_{-0.18}$	XRT 2 keV
0.00283	$(5.57 \pm 0.85) \times 10^{-05}$	$19.54^{+0.16}_{-0.18}$	XRT 2 keV
0.00286	$(0.78 \pm 0.11) \times 10^{-04}$	$19.17^{+0.15}_{-0.18}$	XRT 2 keV
0.00290	$(5.61 \pm 0.85) \times 10^{-05}$	$19.53^{+0.15}_{-0.18}$	XRT 2 keV
0.00295	$(6.29 \pm 0.93) \times 10^{-05}$	$19.40^{+0.15}_{-0.18}$	XRT 2 keV
0.00299	$(0.67 \pm 0.10) \times 10^{-04}$	$19.34^{+0.15}_{-0.18}$	XRT 2 keV
0.00303	$(5.45 \pm 0.82) \times 10^{-05}$	$19.56^{+0.15}_{-0.18}$	XRT 2 keV
0.00307	$(6.60 \pm 0.98) \times 10^{-05}$	$19.35^{+0.15}_{-0.18}$	XRT 2 keV
0.00311	$(5.83 \pm 0.91) \times 10^{-05}$	$19.49^{+0.16}_{-0.18}$	XRT 2 keV
0.00315	$(0.67 \pm 0.10) \times 10^{-04}$	$19.34^{+0.15}_{-0.18}$	XRT 2 keV
0.00319	$(0.92 \pm 0.13) \times 10^{-04}$	$18.99^{+0.15}_{-0.18}$	XRT 2 keV
0.00322	$(0.68 \pm 0.10) \times 10^{-04}$	$19.31^{+0.15}_{-0.18}$	XRT 2 keV
0.00326	$(6.04 \pm 0.91) \times 10^{-05}$	$19.45^{+0.15}_{-0.18}$	XRT 2 keV
0.00330	$(4.68 \pm 0.87) \times 10^{-05}$	$19.72^{+0.19}_{-0.22}$	XRT 2 keV
0.00334	$(4.32 \pm 0.80) \times 10^{-05}$	$19.81^{+0.19}_{-0.22}$	XRT 2 keV
0.00337	$(4.63 \pm 0.85) \times 10^{-05}$	$19.74^{+0.18}_{-0.22}$	XRT 2 keV
0.00341	$(0.70 \pm 0.10) \times 10^{-04}$	$19.29^{+0.16}_{-0.18}$	XRT 2 keV
0.00345	$(4.67 \pm 0.73) \times 10^{-05}$	$19.73^{+0.16}_{-0.19}$	XRT 2 keV
0.00350	$(6.61 \pm 0.98) \times 10^{-05}$	$19.35^{+0.15}_{-0.18}$	XRT 2 keV
0.00354	$(4.41 \pm 0.82) \times 10^{-05}$	$19.79^{+0.19}_{-0.23}$	XRT 2 keV
0.00358	$(0.68 \pm 0.10) \times 10^{-04}$	$19.31^{+0.15}_{-0.18}$	XRT 2 keV
0.00362	$(6.26 \pm 0.93) \times 10^{-05}$	$19.41^{+0.15}_{-0.18}$	XRT 2 keV
0.00366	$(4.26 \pm 0.79) \times 10^{-05}$	$19.83^{+0.19}_{-0.22}$	XRT 2 keV
0.00370	$(4.39 \pm 0.80) \times 10^{-05}$	$19.79^{+0.18}_{-0.22}$	XRT 2 keV
0.00374	$(6.09 \pm 0.93) \times 10^{-05}$	$19.44^{+0.16}_{-0.18}$	XRT 2 keV
0.00378	$(5.63 \pm 0.84) \times 10^{-05}$	$19.52^{+0.15}_{-0.18}$	XRT 2 keV
0.00383	$(5.72 \pm 0.85) \times 10^{-05}$	$19.51^{+0.15}_{-0.18}$	XRT 2 keV
0.00387	$(6.16 \pm 0.96) \times 10^{-05}$	$19.43^{+0.16}_{-0.18}$	XRT 2 keV
0.00391	$(5.30 \pm 0.84) \times 10^{-05}$	$19.59^{+0.16}_{-0.19}$	XRT 2 keV
0.00396	$(0.81 \pm 0.12) \times 10^{-04}$	$19.13^{+0.15}_{-0.18}$	XRT 2 keV
0.00399	$(4.43 \pm 0.80) \times 10^{-05}$	$19.78^{+0.18}_{-0.22}$	XRT 2 keV
0.00403	$(5.09 \pm 0.78) \times 10^{-05}$	$19.63^{+0.16}_{-0.18}$	XRT 2 keV
0.00408	$(5.66 \pm 0.84) \times 10^{-05}$	$19.52^{+0.15}_{-0.18}$	XRT 2 keV
0.00412	$(0.81 \pm 0.12) \times 10^{-04}$	$19.13^{+0.16}_{-0.18}$	XRT 2 keV

Table A.1: continued.

T - T_0 [days]	Flux [Jy]	AB [mag]	Band
0.00416	$(5.45 \pm 0.81) \times 10^{-05}$	$19.56^{+0.15}_{-0.18}$	XRT 2 keV
0.00421	$(3.61 \pm 0.70) \times 10^{-05}$	$20.01^{+0.19}_{-0.24}$	XRT 2 keV
0.00425	$(4.36 \pm 0.83) \times 10^{-05}$	$19.80^{+0.19}_{-0.23}$	XRT 2 keV
0.00429	$(4.61 \pm 0.88) \times 10^{-05}$	$19.74^{+0.19}_{-0.23}$	XRT 2 keV
0.00433	$(4.56 \pm 0.81) \times 10^{-05}$	$19.75^{+0.18}_{-0.21}$	XRT 2 keV
0.00436	$(0.91 \pm 0.13) \times 10^{-04}$	$19.01^{+0.15}_{-0.18}$	XRT 2 keV
0.00439	$(6.52 \pm 0.98) \times 10^{-05}$	$19.36^{+0.15}_{-0.18}$	XRT 2 keV
0.00443	$(5.33 \pm 0.81) \times 10^{-05}$	$19.58^{+0.16}_{-0.18}$	XRT 2 keV
0.00448	$(4.75 \pm 0.86) \times 10^{-05}$	$19.71^{+0.18}_{-0.22}$	XRT 2 keV
0.00452	$(4.95 \pm 0.73) \times 10^{-05}$	$19.66^{+0.15}_{-0.18}$	XRT 2 keV
0.00457	$(4.21 \pm 0.76) \times 10^{-05}$	$19.84^{+0.18}_{-0.22}$	XRT 2 keV
0.00461	$(5.57 \pm 0.85) \times 10^{-05}$	$19.54^{+0.16}_{-0.18}$	XRT 2 keV
0.00465	$(4.67 \pm 0.76) \times 10^{-05}$	$19.73^{+0.17}_{-0.19}$	XRT 2 keV
0.00470	$(5.70 \pm 0.90) \times 10^{-05}$	$19.51^{+0.16}_{-0.19}$	XRT 2 keV
0.00474	$(3.99 \pm 0.74) \times 10^{-05}$	$19.90^{+0.19}_{-0.22}$	XRT 2 keV
0.00479	$(3.07 \pm 0.57) \times 10^{-05}$	$20.18^{+0.19}_{-0.22}$	XRT 2 keV
0.00484	$(4.63 \pm 0.84) \times 10^{-05}$	$19.74^{+0.18}_{-0.22}$	XRT 2 keV
0.00488	$(4.74 \pm 0.86) \times 10^{-05}$	$19.71^{+0.18}_{-0.22}$	XRT 2 keV
0.00491	$(3.45 \pm 0.64) \times 10^{-05}$	$20.06^{+0.19}_{-0.22}$	XRT 2 keV
0.00496	$(4.48 \pm 0.81) \times 10^{-05}$	$19.77^{+0.18}_{-0.22}$	XRT 2 keV
0.00500	$(4.79 \pm 0.74) \times 10^{-05}$	$19.70^{+0.16}_{-0.18}$	XRT 2 keV
0.00505	$(5.45 \pm 0.81) \times 10^{-05}$	$19.56^{+0.15}_{-0.18}$	XRT 2 keV
0.00510	$(4.29 \pm 0.78) \times 10^{-05}$	$19.82^{+0.18}_{-0.22}$	XRT 2 keV
0.00513	$(4.77 \pm 0.89) \times 10^{-05}$	$19.70^{+0.19}_{-0.22}$	XRT 2 keV
0.00518	$(3.77 \pm 0.70) \times 10^{-05}$	$19.96^{+0.19}_{-0.22}$	XRT 2 keV
0.00522	$(4.03 \pm 0.73) \times 10^{-05}$	$19.89^{+0.18}_{-0.22}$	XRT 2 keV
0.00526	$(4.51 \pm 0.90) \times 10^{-05}$	$19.76^{+0.20}_{-0.24}$	XRT 2 keV
0.00530	$(4.82 \pm 0.76) \times 10^{-05}$	$19.69^{+0.16}_{-0.19}$	XRT 2 keV
0.00534	$(4.84 \pm 0.79) \times 10^{-05}$	$19.69^{+0.17}_{-0.19}$	XRT 2 keV
0.00539	$(5.47 \pm 0.82) \times 10^{-05}$	$19.56^{+0.15}_{-0.18}$	XRT 2 keV
0.00544	$(5.24 \pm 0.80) \times 10^{-05}$	$19.60^{+0.16}_{-0.18}$	XRT 2 keV
0.00548	$(4.81 \pm 0.89) \times 10^{-05}$	$19.69^{+0.19}_{-0.22}$	XRT 2 keV
0.00552	$(4.36 \pm 0.81) \times 10^{-05}$	$19.80^{+0.19}_{-0.22}$	XRT 2 keV
0.00555	$(4.70 \pm 0.85) \times 10^{-05}$	$19.72^{+0.18}_{-0.22}$	XRT 2 keV

Table A.1: continued.

T - T_0 [days]	Flux [Jy]	AB [mag]	Band
0.00559	$(4.00 \pm 0.74) \times 10^{-05}$	$19.90^{+0.19}_{-0.22}$	XRT 2 keV
0.00563	$(4.75 \pm 0.88) \times 10^{-05}$	$19.71^{+0.19}_{-0.22}$	XRT 2 keV
0.00567	$(3.56 \pm 0.66) \times 10^{-05}$	$20.02^{+0.19}_{-0.22}$	XRT 2 keV
0.00573	$(3.06 \pm 0.55) \times 10^{-05}$	$20.19^{+0.18}_{-0.22}$	XRT 2 keV
0.04349	$(0.67 \pm 0.15) \times 10^{-05}$	$21.83^{+0.22}_{-0.28}$	XRT 2 keV
0.04392	$(0.71 \pm 0.16) \times 10^{-05}$	$21.77^{+0.22}_{-0.28}$	XRT 2 keV
0.04433	$(0.89 \pm 0.18) \times 10^{-05}$	$21.53^{+0.21}_{-0.26}$	XRT 2 keV
0.04600	$(0.72 \pm 0.16) \times 10^{-05}$	$21.75^{+0.22}_{-0.27}$	XRT 2 keV
0.04639	$(0.57 \pm 0.13) \times 10^{-05}$	$22.00^{+0.22}_{-0.28}$	XRT 2 keV
0.04689	$(0.48 \pm 0.10) \times 10^{-05}$	$22.20^{+0.22}_{-0.27}$	XRT 2 keV
0.04731	$(0.95 \pm 0.20) \times 10^{-05}$	$21.46^{+0.21}_{-0.26}$	XRT 2 keV
0.04778	$(0.56 \pm 0.12) \times 10^{-05}$	$22.03^{+0.22}_{-0.27}$	XRT 2 keV
0.04818	$(0.81 \pm 0.17) \times 10^{-05}$	$21.63^{+0.21}_{-0.26}$	XRT 2 keV
0.04864	$(0.52 \pm 0.11) \times 10^{-05}$	$22.11^{+0.22}_{-0.28}$	XRT 2 keV
0.04915	$(0.54 \pm 0.11) \times 10^{-05}$	$22.07^{+0.21}_{-0.27}$	XRT 2 keV
0.04954	$(0.67 \pm 0.15) \times 10^{-05}$	$21.83^{+0.22}_{-0.28}$	XRT 2 keV
0.04997	$(0.50 \pm 0.11) \times 10^{-05}$	$22.14^{+0.22}_{-0.28}$	XRT 2 keV
0.05039	$(0.75 \pm 0.16) \times 10^{-05}$	$21.71^{+0.21}_{-0.26}$	XRT 2 keV
0.05088	$(5.83 \pm 0.95) \times 10^{-06}$	$21.99^{+0.16}_{-0.19}$	XRT 2 keV
0.05217	$(0.61 \pm 0.13) \times 10^{-05}$	$21.93^{+0.22}_{-0.28}$	XRT 2 keV
0.05255	$(0.51 \pm 0.11) \times 10^{-05}$	$22.13^{+0.22}_{-0.28}$	XRT 2 keV
0.05312	$(0.56 \pm 0.12) \times 10^{-05}$	$22.02^{+0.22}_{-0.27}$	XRT 2 keV
0.05385	$(0.50 \pm 0.11) \times 10^{-05}$	$22.16^{+0.22}_{-0.27}$	XRT 2 keV
0.05444	$(3.64 \pm 0.83) \times 10^{-06}$	$22.50^{+0.22}_{-0.28}$	XRT 2 keV
0.05523	$(3.46 \pm 0.78) \times 10^{-06}$	$22.55^{+0.22}_{-0.28}$	XRT 2 keV
0.05601	$(4.22 \pm 0.92) \times 10^{-06}$	$22.34^{+0.22}_{-0.27}$	XRT 2 keV
0.05668	$(4.28 \pm 0.93) \times 10^{-06}$	$22.32^{+0.21}_{-0.27}$	XRT 2 keV
0.05741	$(4.20 \pm 0.94) \times 10^{-06}$	$22.34^{+0.22}_{-0.28}$	XRT 2 keV
0.05811	$(0.45 \pm 0.10) \times 10^{-05}$	$22.27^{+0.22}_{-0.28}$	XRT 2 keV
0.05872	$(4.40 \pm 0.96) \times 10^{-06}$	$22.29^{+0.21}_{-0.27}$	XRT 2 keV
0.05922	$(3.57 \pm 0.79) \times 10^{-06}$	$22.52^{+0.22}_{-0.27}$	XRT 2 keV
0.05997	$(3.31 \pm 0.74) \times 10^{-06}$	$22.60^{+0.22}_{-0.28}$	XRT 2 keV
0.06064	$(0.46 \pm 0.10) \times 10^{-05}$	$22.25^{+0.22}_{-0.28}$	XRT 2 keV
0.06121	$(3.53 \pm 0.80) \times 10^{-06}$	$22.53^{+0.22}_{-0.28}$	XRT 2 keV

Table A.1: continued.

T - T_0 [days]	Flux [Jy]	AB [mag]	Band
0.06174	$(0.83 \pm 0.18) \times 10^{-05}$	$21.60^{+0.22}_{-0.27}$	XRT 2 keV
0.06215	$(4.16 \pm 0.94) \times 10^{-06}$	$22.35^{+0.22}_{-0.28}$	XRT 2 keV
0.06289	$(0.48 \pm 0.10) \times 10^{-05}$	$22.20^{+0.22}_{-0.28}$	XRT 2 keV
0.06354	$(3.49 \pm 0.78) \times 10^{-06}$	$22.54^{+0.22}_{-0.28}$	XRT 2 keV
0.06425	$(4.47 \pm 0.97) \times 10^{-06}$	$22.28^{+0.21}_{-0.27}$	XRT 2 keV
0.06480	$(3.95 \pm 0.88) \times 10^{-06}$	$22.41^{+0.22}_{-0.28}$	XRT 2 keV
0.06530	$(0.58 \pm 0.13) \times 10^{-05}$	$22.00^{+0.22}_{-0.28}$	XRT 2 keV
0.06583	$(4.32 \pm 0.97) \times 10^{-06}$	$22.31^{+0.22}_{-0.28}$	XRT 2 keV
0.06662	$(2.71 \pm 0.60) \times 10^{-06}$	$22.82^{+0.22}_{-0.27}$	XRT 2 keV
0.06741	$(3.62 \pm 0.77) \times 10^{-06}$	$22.50^{+0.21}_{-0.26}$	XRT 2 keV
0.06851	$(2.73 \pm 0.61) \times 10^{-06}$	$22.81^{+0.22}_{-0.27}$	XRT 2 keV
0.06946	$(2.87 \pm 0.65) \times 10^{-06}$	$22.75^{+0.22}_{-0.28}$	XRT 2 keV
0.07010	$(0.53 \pm 0.11) \times 10^{-05}$	$22.10^{+0.22}_{-0.28}$	XRT 2 keV
0.07062	$(3.75 \pm 0.86) \times 10^{-06}$	$22.46^{+0.22}_{-0.28}$	XRT 2 keV
0.07184	$(2.88 \pm 0.48) \times 10^{-06}$	$22.75^{+0.17}_{-0.20}$	XRT 2 keV
0.10980	$(2.17 \pm 0.48) \times 10^{-06}$	$23.06^{+0.22}_{-0.28}$	XRT 2 keV
0.11042	$(1.71 \pm 0.37) \times 10^{-06}$	$23.32^{+0.22}_{-0.27}$	XRT 2 keV
0.11120	$(1.56 \pm 0.35) \times 10^{-06}$	$23.42^{+0.22}_{-0.28}$	XRT 2 keV
0.11193	$(1.58 \pm 0.35) \times 10^{-06}$	$23.41^{+0.22}_{-0.28}$	XRT 2 keV
0.11261	$(2.37 \pm 0.52) \times 10^{-06}$	$22.96^{+0.22}_{-0.27}$	XRT 2 keV
0.11334	$(1.12 \pm 0.25) \times 10^{-06}$	$23.77^{+0.22}_{-0.28}$	XRT 2 keV
0.11413	$(2.87 \pm 0.63) \times 10^{-06}$	$22.76^{+0.22}_{-0.27}$	XRT 2 keV
0.11504	$(2.15 \pm 0.48) \times 10^{-06}$	$23.07^{+0.22}_{-0.28}$	XRT 2 keV
0.11581	$(1.37 \pm 0.31) \times 10^{-06}$	$23.56^{+0.22}_{-0.28}$	XRT 2 keV
0.11658	$(1.98 \pm 0.44) \times 10^{-06}$	$23.16^{+0.22}_{-0.27}$	XRT 2 keV
0.11730	$(1.65 \pm 0.37) \times 10^{-06}$	$23.36^{+0.22}_{-0.28}$	XRT 2 keV
0.11814	$(0.98 \pm 0.22) \times 10^{-06}$	$23.93^{+0.22}_{-0.28}$	XRT 2 keV
0.13186	$(0.73 \pm 0.18) \times 10^{-06}$	$24.24^{+0.25}_{-0.32}$	XRT 2 keV
0.13330	$(0.79 \pm 0.18) \times 10^{-06}$	$24.16^{+0.23}_{-0.29}$	XRT 2 keV
0.13474	$(0.82 \pm 0.19) \times 10^{-06}$	$24.12^{+0.23}_{-0.29}$	XRT 2 keV
0.13635	$(0.78 \pm 0.17) \times 10^{-06}$	$24.17^{+0.22}_{-0.28}$	XRT 2 keV
0.13772	$(1.36 \pm 0.30) \times 10^{-06}$	$23.56^{+0.22}_{-0.28}$	XRT 2 keV
0.13898	$(1.05 \pm 0.21) \times 10^{-06}$	$23.84^{+0.20}_{-0.25}$	XRT 2 keV
0.25983	$(0.48 \pm 0.18) \times 10^{-06}$	$24.70^{+0.36}_{-0.54}$	XRT 2 keV

Table A.1: continued.

T - T_0 [days]	Flux [Jy]	AB [mag]	Band
0.26627	$(0.55 \pm 0.13) \times 10^{-06}$	$24.54^{+0.24}_{-0.30}$	XRT 2 keV
0.31187	$(0.73 \pm 0.16) \times 10^{-06}$	$24.25^{+0.22}_{-0.27}$	XRT 2 keV
0.33105	$(0.44 \pm 0.12) \times 10^{-06}$	$24.79^{+0.26}_{-0.35}$	XRT 2 keV
0.33321	$(0.42 \pm 0.10) \times 10^{-06}$	$24.85^{+0.25}_{-0.32}$	XRT 2 keV
0.33549	$(0.54 \pm 0.12) \times 10^{-06}$	$24.57^{+0.23}_{-0.29}$	XRT 2 keV
0.33776	$(0.54 \pm 0.12) \times 10^{-06}$	$24.58^{+0.22}_{-0.28}$	XRT 2 keV
0.40383	$(0.47 \pm 0.12) \times 10^{-06}$	$24.72^{+0.26}_{-0.34}$	XRT 2 keV
0.40566	$(0.45 \pm 0.11) \times 10^{-06}$	$24.77^{+0.24}_{-0.31}$	XRT 2 keV
0.45723	$(0.86 \pm 0.14) \times 10^{-06}$	$24.06^{+0.17}_{-0.20}$	XRT 2 keV
0.57836	$(0.52 \pm 0.11) \times 10^{-06}$	$24.61^{+0.22}_{-0.28}$	XRT 2 keV
0.58062	$(1.05 \pm 0.20) \times 10^{-06}$	$23.85^{+0.19}_{-0.23}$	XRT 2 keV
0.64780	$(4.40 \pm 0.86) \times 10^{-07}$	$24.79^{+0.19}_{-0.24}$	XRT 2 keV
0.72256	$(0.48 \pm 0.12) \times 10^{-06}$	$24.70^{+0.25}_{-0.33}$	XRT 2 keV
0.72491	$(3.14 \pm 0.82) \times 10^{-07}$	$25.16^{+0.25}_{-0.33}$	XRT 2 keV
0.72717	$(0.68 \pm 0.14) \times 10^{-06}$	$24.32^{+0.22}_{-0.27}$	XRT 2 keV
0.72970	$(3.35 \pm 0.89) \times 10^{-07}$	$25.09^{+0.26}_{-0.34}$	XRT 2 keV
0.73196	$(0.48 \pm 0.11) \times 10^{-06}$	$24.71^{+0.24}_{-0.30}$	XRT 2 keV
0.73420	$(0.51 \pm 0.11) \times 10^{-06}$	$24.64^{+0.22}_{-0.27}$	XRT 2 keV
0.77934	$(0.44 \pm 0.11) \times 10^{-06}$	$24.79^{+0.26}_{-0.33}$	XRT 2 keV
0.78148	$(0.48 \pm 0.12) \times 10^{-06}$	$24.70^{+0.25}_{-0.33}$	XRT 2 keV
0.78472	$(4.29 \pm 0.80) \times 10^{-07}$	$24.82^{+0.19}_{-0.23}$	XRT 2 keV
0.80328	$(2.59 \pm 0.62) \times 10^{-07}$	$25.37^{+0.23}_{-0.30}$	XRT 2 keV
0.84682	$(0.40 \pm 0.10) \times 10^{-06}$	$24.89^{+0.25}_{-0.33}$	XRT 2 keV
0.84933	$(3.44 \pm 0.90) \times 10^{-07}$	$25.06^{+0.25}_{-0.33}$	XRT 2 keV
0.85203	$(0.42 \pm 0.11) \times 10^{-06}$	$24.84^{+0.25}_{-0.33}$	XRT 2 keV
0.85436	$(0.65 \pm 0.14) \times 10^{-06}$	$24.36^{+0.22}_{-0.28}$	XRT 2 keV
0.85720	$(2.72 \pm 0.72) \times 10^{-07}$	$25.31^{+0.26}_{-0.34}$	XRT 2 keV
0.86086	$(3.07 \pm 0.80) \times 10^{-07}$	$25.18^{+0.25}_{-0.33}$	XRT 2 keV
0.86342	$(0.45 \pm 0.10) \times 10^{-06}$	$24.77^{+0.22}_{-0.28}$	XRT 2 keV
0.86671	$(0.44 \pm 0.11) \times 10^{-06}$	$24.80^{+0.25}_{-0.32}$	XRT 2 keV
0.86912	$(0.41 \pm 0.10) \times 10^{-06}$	$24.87^{+0.25}_{-0.33}$	XRT 2 keV
0.87115	$(0.49 \pm 0.11) \times 10^{-06}$	$24.68^{+0.23}_{-0.30}$	XRT 2 keV
0.87428	$(0.50 \pm 0.11) \times 10^{-06}$	$24.66^{+0.23}_{-0.29}$	XRT 2 keV
0.91337	$(0.42 \pm 0.11) \times 10^{-06}$	$24.83^{+0.25}_{-0.33}$	XRT 2 keV

Table A.1: continued.

T - T_0 [days]	Flux [Jy]	AB [mag]	Band
0.91523	$(0.40 \pm 0.10) \times 10^{-06}$	$24.90^{+0.25}_{-0.33}$	XRT 2 keV
0.91831	$(4.92 \pm 0.92) \times 10^{-07}$	$24.67^{+0.19}_{-0.23}$	XRT 2 keV
0.93483	$(0.49 \pm 0.12) \times 10^{-06}$	$24.68^{+0.24}_{-0.31}$	XRT 2 keV
0.93714	$(0.46 \pm 0.11) \times 10^{-06}$	$24.74^{+0.24}_{-0.32}$	XRT 2 keV
0.94023	$(3.92 \pm 0.80) \times 10^{-07}$	$24.92^{+0.20}_{-0.25}$	XRT 2 keV
0.99305	$(3.64 \pm 0.95) \times 10^{-07}$	$25.00^{+0.25}_{-0.33}$	XRT 2 keV
0.99520	$(0.51 \pm 0.12) \times 10^{-06}$	$24.64^{+0.24}_{-0.31}$	XRT 2 keV
0.99923	$(2.07 \pm 0.55) \times 10^{-07}$	$25.61^{+0.26}_{-0.33}$	XRT 2 keV
1.00297	$(3.62 \pm 0.94) \times 10^{-07}$	$25.00^{+0.25}_{-0.33}$	XRT 2 keV
1.00541	$(3.60 \pm 0.94) \times 10^{-07}$	$25.01^{+0.25}_{-0.33}$	XRT 2 keV
1.00778	$(0.52 \pm 0.13) \times 10^{-06}$	$24.60^{+0.24}_{-0.31}$	XRT 2 keV
1.04741	$(2.96 \pm 0.78) \times 10^{-07}$	$25.22^{+0.25}_{-0.33}$	XRT 2 keV
1.05969	$(2.34 \pm 0.41) \times 10^{-07}$	$25.48^{+0.18}_{-0.21}$	XRT 2 keV
1.11522	$(3.01 \pm 0.63) \times 10^{-07}$	$25.20^{+0.21}_{-0.26}$	XRT 2 keV
1.25089	$(2.67 \pm 0.74) \times 10^{-07}$	$25.34^{+0.27}_{-0.35}$	XRT 2 keV
1.26804	$(0.52 \pm 0.13) \times 10^{-06}$	$24.61^{+0.24}_{-0.31}$	XRT 2 keV
1.27128	$(2.27 \pm 0.62) \times 10^{-07}$	$25.51^{+0.27}_{-0.35}$	XRT 2 keV
1.27480	$(3.49 \pm 0.81) \times 10^{-07}$	$25.04^{+0.23}_{-0.29}$	XRT 2 keV
1.31466	$(2.92 \pm 0.76) \times 10^{-07}$	$25.24^{+0.25}_{-0.33}$	XRT 2 keV
1.33864	$(1.85 \pm 0.38) \times 10^{-07}$	$25.73^{+0.21}_{-0.26}$	XRT 2 keV
1.38285	$(1.57 \pm 0.41) \times 10^{-07}$	$25.91^{+0.25}_{-0.33}$	XRT 2 keV
1.40841	$(2.35 \pm 0.61) \times 10^{-07}$	$25.47^{+0.25}_{-0.33}$	XRT 2 keV
1.46118	$(2.08 \pm 0.36) \times 10^{-07}$	$25.60^{+0.17}_{-0.21}$	XRT 2 keV
1.73381	$(1.42 \pm 0.28) \times 10^{-07}$	$26.02^{+0.20}_{-0.24}$	XRT 2 keV
1.80608	$(1.05 \pm 0.26) \times 10^{-07}$	$26.35^{+0.24}_{-0.32}$	XRT 2 keV
1.87122	$(1.72 \pm 0.45) \times 10^{-07}$	$25.81^{+0.25}_{-0.33}$	XRT 2 keV
1.87530	$(2.06 \pm 0.52) \times 10^{-07}$	$25.62^{+0.25}_{-0.32}$	XRT 2 keV
2.00743	$(1.85 \pm 0.39) \times 10^{-07}$	$25.73^{+0.21}_{-0.26}$	XRT 2 keV
2.28136	$(1.21 \pm 0.24) \times 10^{-07}$	$26.20^{+0.20}_{-0.24}$	XRT 2 keV
2.78891	$(0.80 \pm 0.14) \times 10^{-07}$	$26.64^{+0.18}_{-0.22}$	XRT 2 keV
2.97775	$(0.63 \pm 0.12) \times 10^{-07}$	$26.90^{+0.19}_{-0.24}$	XRT 2 keV
3.62113	$(0.67 \pm 0.14) \times 10^{-07}$	$26.83^{+0.22}_{-0.27}$	XRT 2 keV
3.80739	$(0.78 \pm 0.15) \times 10^{-07}$	$26.66^{+0.20}_{-0.24}$	XRT 2 keV
4.38666	$(0.43 \pm 0.10) \times 10^{-07}$	$27.33^{+0.23}_{-0.29}$	XRT 2 keV

Table A.1: continued.

T - T_0 [days]	Flux [Jy]	AB [mag]	Band
4.70026	$(0.43 \pm 0.11) \times 10^{-07}$	$27.31^{+0.26}_{-0.34}$	XRT 2 keV
4.84931	$(0.48 \pm 0.13) \times 10^{-07}$	$27.20^{+0.27}_{-0.36}$	XRT 2 keV
6.02367	$(2.50 \pm 0.75) \times 10^{-08}$	$27.91^{+0.29}_{-0.39}$	XRT 2 keV
6.70266	$(2.78 \pm 0.73) \times 10^{-08}$	$27.79^{+0.25}_{-0.33}$	XRT 2 keV
7.62593	$(2.28 \pm 0.59) \times 10^{-08}$	$28.01^{+0.25}_{-0.33}$	XRT 2 keV
8.92297	$(1.42 \pm 0.41) \times 10^{-08}$	$28.52^{+0.28}_{-0.38}$	XRT 2 keV
9.80520	$(1.27 \pm 0.78) \times 10^{-08}$	$28.64^{+0.52}_{-1.05}$	XRT 2 keV
0.04936	¡ 0.60×10^{-05}	¿ 21.95	UVOT uvw2
0.06599	¡ 0.74×10^{-05}	¿ 21.72	UVOT uvw2
7.64330	¡ 0.88×10^{-06}	¿ 24.03	UVOT uvw2
0.05411	¡ 0.86×10^{-05}	¿ 21.56	UVOT uvm2
0.07073	¡ 0.11×10^{-04}	¿ 21.23	UVOT uvm2
8.71353	¡ 0.21×10^{-05}	¿ 23.07	UVOT uvm2
0.05648	¡ 0.98×10^{-05}	¿ 21.42	UVOT uvw1
0.07232	¡ 0.42×10^{-05}	¿ 22.32	UVOT uvw1
0.11407	¡ 0.61×10^{-05}	¿ 21.92	UVOT uvw1
6.10495	¡ 0.41×10^{-06}	¿ 24.85	UVOT uvw1
9.64872	¡ 0.42×10^{-06}	¿ 24.82	UVOT uvw1
0.00394	$(1.02 \pm 0.13) \times 10^{-04}$	$18.88^{+0.15}_{-0.13}$	UVOT u
0.00474	$(0.93 \pm 0.11) \times 10^{-04}$	$18.98^{+0.14}_{-0.12}$	UVOT u
0.00551	$(0.63 \pm 0.11) \times 10^{-04}$	$19.41^{+0.23}_{-0.19}$	UVOT u
0.05886	$(1.10 \pm 0.42) \times 10^{-05}$	$21.30^{+0.53}_{-0.36}$	UVOT u
0.13530	$(1.00 \pm 0.21) \times 10^{-05}$	$21.40^{+0.26}_{-0.21}$	UVOT u
0.28371	¡ 0.16×10^{-04}	¿ 20.83	UVOT u
0.36449	¡ 0.26×10^{-04}	¿ 20.36	UVOT u
0.45115	¡ 0.24×10^{-04}	¿ 20.43	UVOT u
0.61076	¡ 0.13×10^{-04}	¿ 21.07	UVOT u
0.78153	¡ 0.14×10^{-04}	¿ 21.01	UVOT u
1.00808	$(0.93 \pm 0.34) \times 10^{-05}$	$21.48^{+0.50}_{-0.34}$	UVOT u
1.37423	¡ 0.53×10^{-05}	¿ 22.09	UVOT u
1.86113	¡ 0.15×10^{-04}	¿ 20.92	UVOT u
2.27112	¡ 0.19×10^{-04}	¿ 20.70	UVOT u
2.86062	¡ 0.37×10^{-05}	¿ 22.48	UVOT u
7.01244	¡ 0.40×10^{-05}	¿ 22.39	UVOT u

Table A.1: continued.

T - T_0 [days]	Flux [Jy]	AB [mag]	Band
0.00323	$(33.15 \pm 0.76) \times 10^{-05}$	17.60 ± 0.03	UVOT b
0.04392	$(0.54 \pm 0.16) \times 10^{-04}$	$19.56^{+0.39}_{-0.29}$	UVOT b
0.06123	$(5.11 \pm 0.97) \times 10^{-05}$	$19.63^{+0.23}_{-0.19}$	UVOT b
2.51402	$(4.51^{+0.40}_{-0.37}) \times 10^{-06}$	22.26 ± 0.09	GROND g'
4.49622	$(2.47^{+0.14}_{-0.13}) \times 10^{-06}$	22.92 ± 0.06	GROND g'
4.52934	$(2.55 \pm 0.13) \times 10^{-06}$	22.88 ± 0.05	GROND g'
6.50292	$(1.40^{+0.19}_{-0.17}) \times 10^{-06}$	23.53 ± 0.14	GROND g'
8.52834	$(0.75^{+0.11}_{-0.10}) \times 10^{-06}$	24.21 ± 0.15	GROND g'
606.83450	¡ 0.31×10^{-06}	¿ 25.15	GROND g'
0.00121	$(3.22 \pm 0.28) \times 10^{-04}$	$17.63^{+0.10}_{-0.09}$	UVOT white
0.00132	$(2.54 \pm 0.24) \times 10^{-04}$	$17.89^{+0.11}_{-0.10}$	UVOT white
0.00144	$(2.49 \pm 0.24) \times 10^{-04}$	$17.91^{+0.11}_{-0.10}$	UVOT white
0.00156	$(2.27 \pm 0.22) \times 10^{-04}$	$18.01^{+0.12}_{-0.10}$	UVOT white
0.00167	$(2.01 \pm 0.21) \times 10^{-04}$	$18.14^{+0.12}_{-0.11}$	UVOT white
0.00179	$(1.91 \pm 0.20) \times 10^{-04}$	$18.20^{+0.13}_{-0.11}$	UVOT white
0.00190	$(1.84 \pm 0.20) \times 10^{-04}$	$18.24^{+0.13}_{-0.11}$	UVOT white
0.00202	$(1.71 \pm 0.19) \times 10^{-04}$	$18.32^{+0.13}_{-0.12}$	UVOT white
0.00214	$(1.58 \pm 0.18) \times 10^{-04}$	$18.40^{+0.14}_{-0.12}$	UVOT white
0.00225	$(1.26 \pm 0.17) \times 10^{-04}$	$18.65^{+0.16}_{-0.14}$	UVOT white
0.00237	$(1.50 \pm 0.18) \times 10^{-04}$	$18.46^{+0.14}_{-0.13}$	UVOT white
0.00248	$(1.50 \pm 0.18) \times 10^{-04}$	$18.46^{+0.14}_{-0.13}$	UVOT white
0.00260	$(1.19 \pm 0.16) \times 10^{-04}$	$18.71^{+0.16}_{-0.14}$	UVOT white
0.00271	$(1.08 \pm 0.15) \times 10^{-04}$	$18.82^{+0.17}_{-0.15}$	UVOT white
0.00283	$(1.34 \pm 0.17) \times 10^{-04}$	$18.58^{+0.15}_{-0.14}$	UVOT white
0.04698	$(2.01 \pm 0.32) \times 10^{-05}$	$20.64^{+0.19}_{-0.16}$	UVOT white
0.06360	$(1.80 \pm 0.30) \times 10^{-05}$	$20.76^{+0.20}_{-0.17}$	UVOT white
0.28542	$(1.10 \pm 0.17) \times 10^{-05}$	$21.30^{+0.19}_{-0.16}$	UVOT white
0.33267	$(1.24 \pm 0.22) \times 10^{-05}$	$21.17^{+0.21}_{-0.18}$	UVOT white
0.43672	$(1.68 \pm 0.26) \times 10^{-05}$	$20.84^{+0.19}_{-0.16}$	UVOT white
0.61474	$(0.70 \pm 0.13) \times 10^{-05}$	$21.79^{+0.23}_{-0.19}$	UVOT white
0.78835	$(7.52 \pm 0.65) \times 10^{-06}$	$21.71^{+0.10}_{-0.09}$	UVOT white
0.98959	$(8.63 \pm 0.67) \times 10^{-06}$	$21.56^{+0.09}_{-0.08}$	UVOT white
1.22145	$(5.75 \pm 0.91) \times 10^{-06}$	$22.00^{+0.19}_{-0.16}$	UVOT white
1.44721	$(0.31 \pm 0.10) \times 10^{-05}$	$22.68^{+0.43}_{-0.31}$	UVOT white

Table A.1: continued.

T - T_0 [days]	Flux [Jy]	AB [mag]	Band
1.86317	$(3.28 \pm 0.73) \times 10^{-06}$	$22.61^{+0.27}_{-0.22}$	UVOT white
2.27295	$(0.43 \pm 0.11) \times 10^{-05}$	$22.31^{+0.35}_{-0.26}$	UVOT white
2.86442	$(1.21 \pm 0.61) \times 10^{-06}$	$23.69^{+0.77}_{-0.44}$	UVOT white
3.88343	$(1.29 \pm 0.49) \times 10^{-06}$	$23.62^{+0.53}_{-0.35}$	UVOT white
4.60764	$(0.76 \pm 0.46) \times 10^{-06}$	$24.20^{+1.02}_{-0.52}$	UVOT white
5.39492	¡ 0.87×10^{-05}	¿ 21.54	UVOT white
0.00099	$(1.79 \pm 0.24) \times 10^{-03}$	$15.77^{+0.16}_{-0.14}$	UVOT v
0.05173	$(0.81 \pm 0.20) \times 10^{-04}$	$19.13^{+0.31}_{-0.24}$	UVOT v
0.06835	$(0.64 \pm 0.19) \times 10^{-04}$	$19.38^{+0.39}_{-0.29}$	UVOT v
0.26973	$(0.41 \pm 0.10) \times 10^{-04}$	$19.87^{+0.32}_{-0.25}$	UVOT v
0.36934	$(0.59 \pm 0.10) \times 10^{-04}$	$19.47^{+0.22}_{-0.18}$	UVOT v
0.47368	¡ 0.14×10^{-03}	¿ 18.47	UVOT v
0.80018	$(2.40 \pm 0.58) \times 10^{-05}$	$20.45^{+0.30}_{-0.24}$	UVOT v
1.00463	$(4.13 \pm 0.69) \times 10^{-05}$	$19.86^{+0.20}_{-0.17}$	UVOT v
1.37053	$(2.99 \pm 0.80) \times 10^{-05}$	$20.21^{+0.34}_{-0.26}$	UVOT v
1.86764	$(1.91 \pm 0.60) \times 10^{-05}$	$20.70^{+0.42}_{-0.30}$	UVOT v
2.27620	¡ 0.26×10^{-04}	¿ 20.34	UVOT v
2.87012	$(1.34 \pm 0.51) \times 10^{-05}$	$21.08^{+0.52}_{-0.35}$	UVOT v
2.51402	$(14.76^{+0.68}_{-0.65}) \times 10^{-06}$	20.98 ± 0.05	GROND r'
4.49622	$(6.91^{+0.21}_{-0.20}) \times 10^{-06}$	21.80 ± 0.03	GROND r'
4.52934	$(6.58^{+0.22}_{-0.21}) \times 10^{-06}$	21.85 ± 0.04	GROND r'
6.50292	$(3.39^{+0.21}_{-0.20}) \times 10^{-06}$	22.57 ± 0.07	GROND r'
8.52834	$(2.00^{+0.21}_{-0.19}) \times 10^{-06}$	23.15 ± 0.11	GROND r'
606.83450	¡ 0.56×10^{-06}	¿ 24.52	GROND r'
2.51402	$(2.92 \pm 0.10) \times 10^{-05}$	20.24 ± 0.04	GROND i'
4.49622	$(13.20^{+0.46}_{-0.44}) \times 10^{-06}$	21.10 ± 0.04	GROND i'
4.52934	$(13.05^{+0.44}_{-0.43}) \times 10^{-06}$	21.11 ± 0.04	GROND i'
6.50292	$(6.72^{+0.55}_{-0.51}) \times 10^{-06}$	21.83 ± 0.09	GROND i'
8.52834	$(4.51^{+0.48}_{-0.43}) \times 10^{-06}$	22.26 ± 0.11	GROND i'
606.83450	¡ 0.10×10^{-05}	¿ 23.86	GROND i'
750.94580	$(0.70^{+0.28}_{-0.20}) \times 10^{-07}$	26.78 ± 0.36	FORS Ic
2.51402	$(4.65^{+0.19}_{-0.18}) \times 10^{-05}$	19.73 ± 0.04	GROND z'
4.49622	$(19.41^{+0.82}_{-0.79}) \times 10^{-06}$	20.68 ± 0.05	GROND z'
4.52934	$(19.92^{+0.73}_{-0.70}) \times 10^{-06}$	20.65 ± 0.04	GROND z'

Table A.1: continued.

T - T_0 [days]	Flux [Jy]	AB [mag]	Band
6.50292	$(9.88^{+0.77}_{-0.71}) \times 10^{-06}$	21.41 ± 0.08	GROND z'
8.52834	$(0.75^{+0.10}_{-0.09}) \times 10^{-05}$	21.71 ± 0.14	GROND z'
606.83450	¡ 0.15×10^{-05}	¿ 23.44	GROND z'
2.51402	$(8.47^{+0.64}_{-0.59}) \times 10^{-05}$	19.08 ± 0.08	GROND J
4.49622	$(0.43^{+0.11}_{-0.09}) \times 10^{-04}$	19.82 ± 0.24	GROND J
4.52934	$(0.46^{+0.10}_{-0.08}) \times 10^{-04}$	19.75 ± 0.22	GROND J
6.50292	$(2.09^{+0.51}_{-0.41}) \times 10^{-05}$	20.60 ± 0.24	GROND J
8.52834	$(1.09^{+0.30}_{-0.24}) \times 10^{-05}$	21.31 ± 0.27	GROND J
38.46488	¡ 0.10×10^{-04}	¿ 21.34	GROND J
606.83450	¡ 0.12×10^{-04}	¿ 21.13	GROND J
2.51402	$(1.41 \pm 0.10) \times 10^{-04}$	18.53 ± 0.08	GROND H
4.49622	$(0.67^{+0.10}_{-0.09}) \times 10^{-04}$	19.34 ± 0.15	GROND H
4.52934	$(0.67^{+0.11}_{-0.10}) \times 10^{-04}$	19.33 ± 0.17	GROND H
6.50292	$(3.10^{+0.77}_{-0.61}) \times 10^{-05}$	20.17 ± 0.24	GROND H
8.52834	$(2.29^{+0.49}_{-0.41}) \times 10^{-05}$	20.50 ± 0.21	GROND H
38.46488	¡ 0.14×10^{-04}	¿ 20.98	GROND H
606.83450	¡ 0.18×10^{-04}	¿ 20.75	GROND H
2.51402	$(1.85^{+0.14}_{-0.13}) \times 10^{-04}$	18.23 ± 0.08	GROND K
4.49622	$(0.81^{+0.10}_{-0.09}) \times 10^{-04}$	19.12 ± 0.13	GROND K
4.52934	$(0.85^{+0.10}_{-0.09}) \times 10^{-04}$	19.08 ± 0.12	GROND K
6.50292	$(0.38^{+0.13}_{-0.10}) \times 10^{-04}$	19.95 ± 0.32	GROND K
8.52834	$(0.30^{+0.18}_{-0.11}) \times 10^{-04}$	20.22 ± 0.52	GROND K
38.46488	¡ 0.22×10^{-04}	¿ 20.54	GROND K
606.83450	¡ 0.21×10^{-04}	¿ 20.58	GROND K
1.42000	$(1.10 \pm 0.20) \times 10^{-02}$	$13.80^{+0.18}_{-0.22}$	APEX 345 GHz
3.57000	$(6.30 \pm 0.70) \times 10^{-03}$	$14.40^{+0.11}_{-0.13}$	ALMA 345 GHz
2.00400	$(5.10 \pm 0.90) \times 10^{-04}$	$17.13^{+0.18}_{-0.21}$	ATCA 44 GHz
2.94500	$(20.50 \pm 0.50) \times 10^{-04}$	15.62 ± 0.03	ATCA 44 GHz
11.73800	$(18.90 \pm 0.80) \times 10^{-04}$	$15.71^{+0.04}_{-0.05}$	ATCA 44 GHz
17.52100	$(11.80 \pm 0.80) \times 10^{-04}$	$16.22^{+0.07}_{-0.08}$	ATCA 44 GHz
32.33500	$(6.50 \pm 0.90) \times 10^{-04}$	$16.87^{+0.14}_{-0.16}$	ATCA 44 GHz
74.33000	$(3.50 \pm 0.10) \times 10^{-04}$	17.54 ± 0.03	ATCA 44 GHz
3.97200	$(7.30 \pm 0.60) \times 10^{-04}$	16.74 ± 0.09	ATCA 18 GHz
4.06700	$(7.90 \pm 0.40) \times 10^{-04}$	$16.66^{+0.05}_{-0.06}$	ATCA 18 GHz

Table A.1: continued.

T - T_0 [days]	Flux [Jy]	AB [mag]	Band
10.72300	$(14.70 \pm 0.60) \times 10^{-04}$	$15.98^{+0.04}_{-0.05}$	ATCA 18 GHz
17.55100	$(11.00 \pm 0.30) \times 10^{-04}$	16.30 ± 0.03	ATCA 18 GHz
41.52600	$(5.10 \pm 0.90) \times 10^{-04}$	$17.13^{+0.18}_{-0.21}$	ATCA 18 GHz
74.36700	$(6.70 \pm 0.40) \times 10^{-04}$	$16.83^{+0.06}_{-0.07}$	ATCA 18 GHz
3.99200	$(4.40 \pm 0.40) \times 10^{-04}$	$17.29^{+0.09}_{-0.10}$	ATCA 9 GHz
17.59600	$(5.80 \pm 0.40) \times 10^{-04}$	$16.99^{+0.07}_{-0.08}$	ATCA 9 GHz
18.51700	$(8.30 \pm 0.70) \times 10^{-04}$	$16.60^{+0.09}_{-0.10}$	ATCA 9 GHz
41.55500	$(5.10 \pm 0.70) \times 10^{-04}$	$17.13^{+0.14}_{-0.16}$	ATCA 9 GHz
3.99200	$(5.30 \pm 0.30) \times 10^{-04}$	17.09 ± 0.06	ATCA 5.5 GHz
4.70000	$(4.00 \pm 0.50) \times 10^{-04}$	$17.39^{+0.13}_{-0.15}$	ATCA 5.5 GHz
12.67900	$(4.30 \pm 0.40) \times 10^{-04}$	$17.32^{+0.10}_{-0.11}$	ATCA 5.5 GHz
17.59600	$(6.20 \pm 0.30) \times 10^{-04}$	16.92 ± 0.05	ATCA 5.5 GHz
18.51700	$(4.80 \pm 0.40) \times 10^{-04}$	17.20 ± 0.09	ATCA 5.5 GHz
41.55500	$(2.90 \pm 0.50) \times 10^{-04}$	$17.74^{+0.17}_{-0.21}$	ATCA 5.5 GHz

Appendix B

Goodness of fits

B.1 Fit to all bands, except UV, MW extinction corrected

CM Model

Band	χ^2	d.o.f.	χ^2_{red}	χ^2_{frac}	$\chi^2_{frac,color}$	$\chi^2_{red,frac}$	$\chi^2_{red,frac,color}$
XRT 2 keV	655	267	2.45	28.38	100.00	0.80	100.00
UVOT uvw2	0	0	0.00	0.00	0.00	0.00	0.00
UVOT uvm2	0	0	0.00	0.00	0.00	0.00	0.00
UVOT uvw1	0	0	0.00	0.00	0.00	0.00	0.00
UVOT u	0	0	0.00	0.00	0.00	0.00	0.00
UVOT b	47	2	23.36	2.02	4.17	7.67	17.92
GROND g'	110	4	27.42	4.75	9.78	9.00	21.04
UVOT white	671	29	23.14	29.08	59.86	7.59	17.75
UVOT v	122	9	13.57	5.29	10.90	4.45	10.41
GROND r'	101	4	25.34	4.39	9.04	8.31	19.43
GROND i'	11	4	2.76	0.48	0.99	0.91	2.12
GROND z'	20	4	5.08	0.88	1.81	1.67	3.90
GROND J	9	4	2.37	0.41	0.85	0.78	1.82
GROND H	20	4	5.04	0.87	1.80	1.66	3.87
GROND K	9	4	2.27	0.39	0.81	0.74	1.74
APEX+ALMA 345 GHz	69	1	68.71	2.98	12.92	22.55	39.97
ATCA 44 GHz	120	5	23.98	5.20	22.55	7.87	13.95
ATCA 18 GHz	217	5	43.38	9.40	40.80	14.24	25.24
ATCA 9 GHz	79	3	26.49	3.44	14.95	8.69	15.41
ATCA 5.5 GHz	47	5	9.33	2.02	8.77	3.06	5.43

TS Model

Band	χ^2	d.o.f.	χ^2_{red}	χ^2_{frac}	$\chi^2_{frac,color}$	$\chi^2_{red,frac}$	$\chi^2_{red,frac,color}$
XRT 2 keV	535	267	2.00	24.19	100.00	0.57	100.00
UVOT uvw2	0	0	0.00	0.00	0.00	0.00	0.00
UVOT uvm2	0	0	0.00	0.00	0.00	0.00	0.00
UVOT uvw1	0	0	0.00	0.00	0.00	0.00	0.00
UVOT u	0	0	0.00	0.00	0.00	0.00	0.00
UVOT b	20	2	9.84	0.89	1.80	2.79	6.08
GROND g'	177	4	44.37	8.03	16.19	12.57	27.41
UVOT white	492	29	16.95	22.24	44.84	4.80	10.47
UVOT v	81	9	8.98	3.66	7.37	2.54	5.55
GROND r'	223	4	55.86	10.11	20.38	15.83	34.51
GROND i'	36	4	9.06	1.64	3.31	2.57	5.60
GROND z'	35	4	8.78	1.59	3.20	2.49	5.43
GROND J	9	4	2.14	0.39	0.78	0.61	1.32
GROND H	16	4	3.95	0.71	1.44	1.12	2.44
GROND K	8	4	1.92	0.35	0.70	0.54	1.19
APEX+ALMA 345 GHz	77	1	77.01	3.48	13.30	21.82	40.73
ATCA 44 GHz	121	5	24.24	5.48	20.93	6.87	12.82
ATCA 18 GHz	239	5	47.79	10.81	41.26	13.54	25.28
ATCA 9 GHz	87	3	29.05	3.94	15.05	8.23	15.36
ATCA 5.5 GHz	55	5	10.97	2.48	9.47	3.11	5.80

WM Model

Band	χ^2	d.o.f.	χ^2_{red}	χ^2_{frac}	$\chi^2_{frac,color}$	$\chi^2_{red,frac}$	$\chi^2_{red,frac,color}$
XRT 2 keV	698	267	2.61	20.15	100.00	0.51	100.00
UVOT uvw2	0	0	0.00	0.00	0.00	0.00	0.00
UVOT uvm2	0	0	0.00	0.00	0.00	0.00	0.00
UVOT uvw1	0	0	0.00	0.00	0.00	0.00	0.00
UVOT u	0	0	0.00	0.00	0.00	0.00	0.00
UVOT b	135	2	67.52	3.90	6.71	13.16	21.08
GROND g'	249	4	62.19	7.18	12.36	12.12	19.42
UVOT white	943	29	32.50	27.22	46.83	6.33	10.15
UVOT v	97	9	10.76	2.80	4.81	2.10	3.36
GROND r'	378	4	94.52	10.92	18.78	18.42	29.51
GROND i'	101	4	25.21	2.91	5.01	4.91	7.87
GROND z'	77	4	19.35	2.23	3.85	3.77	6.04
GROND J	13	4	3.31	0.38	0.66	0.65	1.03
GROND H	13	4	3.36	0.39	0.67	0.65	1.05
GROND K	6	4	1.62	0.19	0.32	0.32	0.51
APEX+ALMA 345 GHz	37	1	36.63	1.06	4.87	7.14	19.26
ATCA 44 GHz	253	5	50.66	7.31	33.66	9.87	26.64
ATCA 18 GHz	333	5	66.53	9.60	44.20	12.97	34.98
ATCA 9 GHz	78	3	25.87	2.24	10.31	5.04	13.61
ATCA 5.5 GHz	52	5	10.48	1.51	6.96	2.04	5.51

B.2 Fit to all bands, including MW extinction

CM Model

Band	χ^2	d.o.f.	χ^2_{red}	χ^2_{frac}	$\chi^2_{frac,color}$	$\chi^2_{red,frac}$	$\chi^2_{red,frac,color}$
XRT 2 keV	658	267	2.46	26.49	100.00	0.51	100.00
UVOT uvw2	0	0	0.00	0.00	0.00	0.00	0.00
UVOT uvm2	0	0	0.00	0.00	0.00	0.00	0.00
UVOT uvw1	0	0	0.00	0.00	0.00	0.00	0.00
UVOT u	62	5	12.49	2.51	5.43	2.58	5.53
UVOT b	37	2	18.52	1.49	3.22	3.83	8.19
GROND g'	194	4	48.53	7.82	16.88	10.04	21.47
UVOT white	262	29	9.05	10.56	22.81	1.87	4.00
UVOT v	79	9	8.80	3.19	6.89	1.82	3.89
GROND r'	279	4	69.82	11.24	24.29	14.44	30.88
GROND i'	82	4	20.52	3.30	7.14	4.24	9.08
GROND z'	78	4	19.50	3.14	6.78	4.03	8.63
GROND J	22	4	5.50	0.89	1.91	1.14	2.43
GROND H	33	4	8.22	1.32	2.86	1.70	3.64
GROND K	21	4	5.13	0.83	1.79	1.06	2.27
APEX+ALMA 345 GHz	142	1	141.66	5.70	20.96	29.29	55.55
ATCA 44 GHz	187	5	37.47	7.54	27.72	7.75	14.69
ATCA 18 GHz	140	5	28.06	5.65	20.76	5.80	11.00
ATCA 9 GHz	49	3	16.34	1.97	7.25	3.38	6.41
ATCA 5.5 GHz	157	5	31.50	6.34	23.30	6.51	12.35

TS Model

Band	χ^2	d.o.f.	χ^2_{red}	χ^2_{frac}	$\chi^2_{frac,color}$	$\chi^2_{red,frac}$	$\chi^2_{red,frac,color}$
XRT 2 keV	512	267	1.92	20.98	100.00	0.45	100.00
UVOT uvw2	0	0	0.00	0.00	0.00	0.00	0.00
UVOT uvm2	0	0	0.00	0.00	0.00	0.00	0.00
UVOT uvw1	0	0	0.00	0.00	0.00	0.00	0.00
UVOT u	102	5	20.31	4.16	7.64	4.75	8.89
UVOT b	18	2	9.20	0.75	1.38	2.15	4.03
GROND g'	227	4	56.79	9.32	17.08	13.29	24.86
UVOT white	431	29	14.85	17.66	32.37	3.47	6.50
UVOT v	78	9	8.64	3.19	5.85	2.02	3.78
GROND r'	320	4	80.00	13.12	24.06	18.72	35.02
GROND i'	69	4	17.18	2.82	5.17	4.02	7.52
GROND z'	57	4	14.15	2.32	4.26	3.31	6.19
GROND J	8	4	2.09	0.34	0.63	0.49	0.91
GROND H	14	4	3.39	0.56	1.02	0.79	1.49
GROND K	7	4	1.83	0.30	0.55	0.43	0.80
APEX+ALMA 345 GHz	82	1	81.71	3.35	13.69	19.12	41.46
ATCA 44 GHz	125	5	24.91	5.11	20.86	5.83	12.64
ATCA 18 GHz	242	5	48.40	9.92	40.53	11.32	24.56
ATCA 9 GHz	92	3	30.73	3.78	15.44	7.19	15.60
ATCA 5.5 GHz	57	5	11.31	2.32	9.47	2.65	5.74

WM Model

Band	χ^2	d.o.f.	χ^2_{red}	χ^2_{frac}	$\chi^2_{frac,color}$	$\chi^2_{red,frac}$	$\chi^2_{red,frac,color}$
XRT 2 keV	601	267	2.25	2.94	100.00	0.05	100.00
UVOT uvw2	0	0	0.00	0.00	0.00	0.00	0.00
UVOT uvm2	0	0	0.00	0.00	0.00	0.00	0.00
UVOT uvw1	0	0	0.00	0.00	0.00	0.00	0.00
UVOT u	978	5	195.54	4.78	5.15	3.92	4.18
UVOT b	3887	2	1943.45	18.99	20.49	38.99	41.59
GROND g'	1695	4	423.65	8.28	8.93	8.50	9.07
UVOT white	4407	29	151.98	21.53	23.24	3.05	3.25
UVOT v	300	9	33.29	1.46	1.58	0.67	0.71
GROND r'	3671	4	917.77	17.93	19.35	18.41	19.64
GROND i'	2200	4	550.06	10.75	11.60	11.03	11.77
GROND z'	1533	4	383.16	7.49	8.08	7.69	8.20
GROND J	121	4	30.34	0.59	0.64	0.61	0.65
GROND H	89	4	22.25	0.43	0.47	0.45	0.48
GROND K	87	4	21.79	0.43	0.46	0.44	0.47
APEX+ALMA 345 GHz	140	1	139.88	0.68	15.51	2.81	45.20
ATCA 44 GHz	244	5	48.77	1.19	27.05	0.98	15.76
ATCA 18 GHz	171	5	34.19	0.84	18.96	0.69	11.05
ATCA 9 GHz	129	3	43.09	0.63	14.34	0.86	13.93
ATCA 5.5 GHz	218	5	43.54	1.06	24.14	0.87	14.07

B.3 Fit to all bands except UV, including MW extinction

CM Model

Band	χ^2	d.o.f.	χ^2_{red}	χ^2_{frac}	$\chi^2_{frac,color}$	$\chi^2_{red,frac}$	$\chi^2_{red,frac,color}$
XRT 2 keV	655	267	2.45	27.24	100.00	0.52	100.00
UVOT uvw2	0	0	0.00	0.00	0.00	0.00	0.00
UVOT uvm2	0	0	0.00	0.00	0.00	0.00	0.00
UVOT uvw1	0	0	0.00	0.00	0.00	0.00	0.00
UVOT u	0	0	0.00	0.00	0.00	0.00	0.00
UVOT b	43	2	21.42	1.78	3.97	4.56	10.01
GROND g'	191	4	47.73	7.94	17.71	10.16	22.31
UVOT white	255	29	8.80	10.61	23.67	1.87	4.11
UVOT v	81	9	9.05	3.38	7.55	1.93	4.23
GROND r'	274	4	68.46	11.38	25.39	14.57	31.99
GROND i'	81	4	20.22	3.36	7.50	4.30	9.45
GROND z'	77	4	19.36	3.22	7.18	4.12	9.05
GROND J	22	4	5.52	0.92	2.05	1.18	2.58
GROND H	33	4	8.28	1.38	3.07	1.76	3.87
GROND K	21	4	5.16	0.86	1.91	1.10	2.41
APEX+ALMA 345 GHz	140	1	140.20	5.83	20.87	29.84	55.34
ATCA 44 GHz	183	5	36.50	7.59	27.17	7.77	14.41
ATCA 18 GHz	144	5	28.75	5.98	21.40	6.12	11.35
ATCA 9 GHz	51	3	17.11	2.13	7.64	3.64	6.75
ATCA 5.5 GHz	154	5	30.78	6.40	22.91	6.55	12.15

TS Model

Band	χ^2	d.o.f.	χ^2_{red}	χ^2_{frac}	$\chi^2_{frac,color}$	$\chi^2_{red,frac}$	$\chi^2_{red,frac,color}$
XRT 2 keV	510	267	1.91	22.15	100.00	0.48	100.00
UVOT uvw2	0	0	0.00	0.00	0.00	0.00	0.00
UVOT uvm2	0	0	0.00	0.00	0.00	0.00	0.00
UVOT uvw1	0	0	0.00	0.00	0.00	0.00	0.00
UVOT u	0	0	0.00	0.00	0.00	0.00	0.00
UVOT b	19	2	9.46	0.82	1.58	2.38	4.73
GROND g'	219	4	54.82	9.53	18.32	13.78	27.41
UVOT white	432	29	14.90	18.78	36.10	3.75	7.45
UVOT v	78	9	8.71	3.41	6.55	2.19	4.35
GROND r'	304	4	75.94	13.20	25.37	19.09	37.97
GROND i'	63	4	15.64	2.72	5.23	3.93	7.82
GROND z'	52	4	13.11	2.28	4.38	3.29	6.55
GROND J	8	4	2.08	0.36	0.69	0.52	1.04
GROND H	14	4	3.49	0.61	1.17	0.88	1.75
GROND K	7	4	1.85	0.32	0.62	0.47	0.93
APEX+ALMA 345 GHz	81	1	81.41	3.54	13.70	20.47	41.57
ATCA 44 GHz	126	5	25.13	5.46	21.15	6.32	12.83
ATCA 18 GHz	243	5	48.61	10.56	40.92	12.22	24.82
ATCA 9 GHz	89	3	29.75	3.88	15.03	7.48	15.19
ATCA 5.5 GHz	55	5	10.93	2.38	9.20	2.75	5.58

WM Model

Band	χ^2	d.o.f.	χ^2_{red}	χ^2_{frac}	$\chi^2_{frac,color}$	$\chi^2_{red,frac}$	$\chi^2_{red,frac,color}$
XRT 2 keV	590	267	2.21	3.06	100.00	0.05	100.00
UVOT uvw2	0	0	0.00	0.00	0.00	0.00	0.00
UVOT uvm2	0	0	0.00	0.00	0.00	0.00	0.00
UVOT uvw1	0	0	0.00	0.00	0.00	0.00	0.00
UVOT u	0	0	0.00	0.00	0.00	0.00	0.00
UVOT b	3813	2	1906.53	19.78	21.43	40.30	43.13
GROND g'	1670	4	417.56	8.66	9.39	8.83	9.45
UVOT white	4361	29	150.38	22.62	24.51	3.18	3.40
UVOT v	305	9	33.94	1.58	1.72	0.72	0.77
GROND r'	3632	4	908.09	18.84	20.41	19.20	20.55
GROND i'	2184	4	546.00	11.33	12.27	11.54	12.35
GROND z'	1527	4	381.78	7.92	8.58	8.07	8.64
GROND J	122	4	30.57	0.63	0.69	0.65	0.69
GROND H	91	4	22.68	0.47	0.51	0.48	0.51
GROND K	90	4	22.48	0.47	0.51	0.48	0.51
APEX+ALMA 345 GHz	142	1	142.01	0.74	15.90	3.00	46.06
ATCA 44 GHz	263	5	52.69	1.37	29.51	1.11	17.09
ATCA 18 GHz	167	5	33.32	0.86	18.66	0.70	10.81
ATCA 9 GHz	121	3	40.36	0.63	13.56	0.85	13.09
ATCA 5.5 GHz	200	5	39.96	1.04	22.37	0.84	12.96

B.4 Fit to all bands except UV, MW extinction corrected, White shifted to V

CM Model

Band	χ^2	d.o.f.	χ^2_{red}	χ^2_{frac}	$\chi^2_{frac,color}$	$\chi^2_{red,frac}$	$\chi^2_{red,frac,color}$
XRT 2 keV	666	267	2.49	33.34	100.00	0.91	100.00
UVOT uvw2	0	0	0.00	0.00	0.00	0.00	0.00
UVOT uvm2	0	0	0.00	0.00	0.00	0.00	0.00
UVOT uvw1	0	0	0.00	0.00	0.00	0.00	0.00
UVOT u	0	0	0.00	0.00	0.00	0.00	0.00
UVOT b	62	2	30.81	3.08	7.51	11.20	29.12
GROND g’	70	4	17.44	3.49	8.50	6.34	16.48
UVOT v+white	518	35	14.80	25.93	63.14	5.38	13.99
GROND r’	42	4	10.47	2.10	5.11	3.81	9.90
GROND i’	26	4	6.44	1.29	3.14	2.34	6.09
GROND z’	39	4	9.87	1.98	4.81	3.59	9.33
GROND J	15	4	3.78	0.76	1.84	1.37	3.57
GROND H	32	4	8.01	1.60	3.90	2.91	7.57
GROND K	17	4	4.18	0.84	2.04	1.52	3.95
APEX+ALMA 345 GHz	68	1	67.83	3.40	13.27	24.66	40.67
ATCA 44 GHz	119	5	23.84	5.97	23.32	8.67	14.30
ATCA 18 GHz	206	5	41.13	10.29	40.22	14.95	24.66
ATCA 9 GHz	77	3	25.64	3.85	15.04	9.32	15.37
ATCA 5.5 GHz	42	5	8.34	2.09	8.16	3.03	5.00

TS Model

Band	χ^2	d.o.f.	χ^2_{red}	χ^2_{frac}	$\chi^2_{frac,color}$	$\chi^2_{red,frac}$	$\chi^2_{red,frac,color}$
XRT 2 keV	570	267	2.14	29.48	100.00	0.68	100.00
UVOT uvw2	0	0	0.00	0.00	0.00	0.00	0.00
UVOT uvm2	0	0	0.00	0.00	0.00	0.00	0.00
UVOT uvw1	0	0	0.00	0.00	0.00	0.00	0.00
UVOT u	0	0	0.00	0.00	0.00	0.00	0.00
UVOT b	27	2	13.58	1.40	3.52	4.32	11.64
GROND g’	130	4	32.51	6.72	16.86	10.35	27.87
UVOT v+white	375	35	10.70	19.36	48.56	3.41	9.17
GROND r’	137	4	34.37	7.11	17.83	10.95	29.47
GROND i’	22	4	5.55	1.15	2.88	1.77	4.76
GROND z’	31	4	7.69	1.59	3.99	2.45	6.59
GROND J	12	4	3.12	0.64	1.62	0.99	2.67
GROND H	24	4	6.02	1.24	3.12	1.92	5.16
GROND K	12	4	3.12	0.65	1.62	1.00	2.68
APEX+ALMA 345 GHz	80	1	79.95	4.13	13.49	25.46	40.96
ATCA 44 GHz	128	5	25.65	6.63	21.63	8.17	13.14
ATCA 18 GHz	231	5	46.13	11.92	38.90	14.69	23.63
ATCA 9 GHz	95	3	31.65	4.91	16.02	10.08	16.21
ATCA 5.5 GHz	59	5	11.82	3.05	9.97	3.76	6.05

WM Model

Band	χ^2	d.o.f.	χ^2_{red}	χ^2_{frac}	$\chi^2_{frac,color}$	$\chi^2_{red,frac}$	$\chi^2_{red,frac,color}$
XRT 2 keV	729	267	2.73	27.88	100.00	0.63	100.00
UVOT uvw2	0	0	0.00	0.00	0.00	0.00	0.00
UVOT uvm2	0	0	0.00	0.00	0.00	0.00	0.00
UVOT uvw1	0	0	0.00	0.00	0.00	0.00	0.00
UVOT u	0	0	0.00	0.00	0.00	0.00	0.00
UVOT b	168	2	83.84	6.41	14.31	19.21	33.45
GROND g’	194	4	48.52	7.42	16.56	11.11	19.36
UVOT v+white	381	35	10.88	14.55	32.48	2.49	4.34
GROND r’	266	4	66.57	10.18	22.72	15.25	26.56
GROND i’	64	4	15.90	2.43	5.43	3.64	6.34
GROND z’	55	4	13.82	2.11	4.72	3.17	5.51
GROND J	15	4	3.78	0.58	1.29	0.86	1.51
GROND H	20	4	5.00	0.77	1.71	1.15	2.00
GROND K	9	4	2.33	0.36	0.79	0.53	0.93
APEX+ALMA 345 GHz	37	1	37.06	1.42	5.19	8.49	20.23
ATCA 44 GHz	222	5	44.50	8.51	31.14	10.19	24.29
ATCA 18 GHz	319	5	63.81	12.20	44.65	14.62	34.83
ATCA 9 GHz	80	3	26.61	3.05	11.17	6.10	14.53
ATCA 5.5 GHz	56	5	11.20	2.14	7.84	2.57	6.12

B.5 Fit to all bands except UV, including MW extinction, White shifted to V

CM Model

Band	χ^2	d.o.f.	χ^2_{red}	χ^2_{frac}	$\chi^2_{frac,color}$	$\chi^2_{red,frac}$	$\chi^2_{red,frac,color}$
XRT 2 keV	659	267	2.47	29.81	100.00	0.75	100.00
UVOT uvw2	0	0	0.00	0.00	0.00	0.00	0.00
UVOT uvm2	0	0	0.00	0.00	0.00	0.00	0.00
UVOT uvw1	0	0	0.00	0.00	0.00	0.00	0.00
UVOT u	197	5	39.40	8.91	18.91	12.02	24.97
UVOT b	80	2	40.01	3.62	7.68	12.21	25.36
GROND g’	54	4	13.44	2.43	5.16	4.10	8.52
UVOT v+white	510	35	14.56	23.07	48.93	4.45	9.23
GROND r’	24	4	5.94	1.07	2.28	1.81	3.76
GROND i’	43	4	10.67	1.93	4.10	3.26	6.76
GROND z’	56	4	14.12	2.56	5.42	4.31	8.95
GROND J	19	4	4.63	0.84	1.78	1.41	2.94
GROND H	39	4	9.66	1.75	3.71	2.95	6.12
GROND K	21	4	5.32	0.96	2.04	1.62	3.37
APEX+ALMA 345 GHz	68	1	68.27	3.09	13.41	20.84	40.78
ATCA 44 GHz	114	5	22.89	5.18	22.48	6.99	13.67
ATCA 18 GHz	205	5	41.02	9.28	40.29	12.52	24.50
ATCA 9 GHz	82	3	27.44	3.72	16.17	8.37	16.39
ATCA 5.5 GHz	39	5	7.79	1.76	7.65	2.38	4.65

TS Model

Band	χ^2	d.o.f.	χ^2_{red}	χ^2_{frac}	$\chi^2_{frac,color}$	$\chi^2_{red,frac}$	$\chi^2_{red,frac,color}$
XRT 2 keV	574	267	2.15	27.68	100.00	0.62	100.00
UVOT uvw2	0	0	0.00	0.00	0.00	0.00	0.00
UVOT uvm2	0	0	0.00	0.00	0.00	0.00	0.00
UVOT uvw1	0	0	0.00	0.00	0.00	0.00	0.00
UVOT u	145	5	29.02	6.99	16.45	8.38	20.65
UVOT b	35	2	17.38	1.68	3.94	5.02	12.36
GROND g'	97	4	24.18	4.66	10.97	6.98	17.20
UVOT v+white	367	35	10.50	17.71	41.66	3.03	7.47
GROND r'	87	4	21.63	4.17	9.81	6.24	15.38
GROND i'	32	4	7.93	1.53	3.60	2.29	5.64
GROND z'	46	4	11.39	2.20	5.16	3.29	8.10
GROND J	19	4	4.64	0.89	2.10	1.34	3.30
GROND H	35	4	8.80	1.70	3.99	2.54	6.26
GROND K	20	4	5.12	0.99	2.32	1.48	3.64
APEX+ALMA 345 GHz	83	1	83.49	4.02	13.50	24.10	40.98
ATCA 44 GHz	140	5	28.08	6.77	22.71	8.10	13.78
ATCA 18 GHz	233	5	46.57	11.22	37.66	13.44	22.85
ATCA 9 GHz	100	3	33.28	4.81	16.15	9.61	16.33
ATCA 5.5 GHz	62	5	12.34	2.97	9.98	3.56	6.05

WM Model

Band	χ^2	d.o.f.	χ^2_{red}	χ^2_{frac}	$\chi^2_{frac,color}$	$\chi^2_{red,frac}$	$\chi^2_{red,frac,color}$
XRT 2 keV	736	267	2.76	26.34	100.00	0.57	100.00
UVOT uvw2	0	0	0.00	0.00	0.00	0.00	0.00
UVOT uvm2	0	0	0.00	0.00	0.00	0.00	0.00
UVOT uvw1	0	0	0.00	0.00	0.00	0.00	0.00
UVOT u	231	5	46.16	8.26	16.88	9.50	15.37
UVOT b	219	2	109.27	7.82	15.99	22.48	36.39
GROND g'	159	4	39.64	5.67	11.60	8.16	13.20
UVOT v+white	382	35	10.92	13.67	27.95	2.25	3.64
GROND r'	202	4	50.44	7.22	14.76	10.38	16.80
GROND i'	56	4	13.97	2.00	4.09	2.87	4.65
GROND z'	56	4	13.98	2.00	4.09	2.88	4.66
GROND J	19	4	4.85	0.69	1.42	1.00	1.61
GROND H	29	4	7.21	1.03	2.11	1.48	2.40
GROND K	15	4	3.81	0.55	1.12	0.78	1.27
APEX+ALMA 345 GHz	43	1	42.76	1.53	6.19	8.80	23.37
ATCA 44 GHz	201	5	40.29	7.21	29.14	8.29	22.02
ATCA 18 GHz	310	5	61.96	11.08	44.81	12.75	33.85
ATCA 9 GHz	79	3	26.37	2.83	11.44	5.43	14.41
ATCA 5.5 GHz	58	5	11.63	2.08	8.41	2.39	6.36

B.6 Fit to optical/nIR bands except UV, MW extinction corrected, White shifted to V

CM Model

Band	χ^2	d.o.f.	χ^2_{red}	χ^2_{frac}	$\chi^2_{frac,color}$	$\chi^2_{red,frac}$	$\chi^2_{red,frac,color}$
XRT 2 keV	2355	267	8.82	3.82	100.00	0.07	100.00
UVOT uvw2	0	0	0.00	0.00	0.00	0.00	0.00
UVOT uvm2	0	0	0.00	0.00	0.00	0.00	0.00
UVOT uvw1	0	0	0.00	0.00	0.00	0.00	0.00
UVOT u	0	0	0.00	0.00	0.00	0.00	0.00
UVOT b	530	2	265.07	0.86	21.84	2.04	38.74
GROND g'	441	4	110.25	0.71	18.17	0.85	16.11
UVOT v+white	249	35	7.11	0.40	10.26	0.05	1.04
GROND r'	719	4	179.71	1.16	29.62	1.39	26.27
GROND i'	286	4	71.48	0.46	11.78	0.55	10.45
GROND z'	179	4	44.73	0.29	7.37	0.34	6.54
GROND J	10	4	2.60	0.02	0.43	0.02	0.38
GROND H	3	4	0.71	0.00	0.12	0.01	0.10
GROND K	10	4	2.53	0.02	0.42	0.02	0.37
APEX+ALMA 345 GHz	96	1	96.32	0.16	0.17	0.74	0.78
ATCA 44 GHz	10694	5	2138.87	17.32	18.78	16.50	17.43
ATCA 18 GHz	14475	5	2894.94	23.45	25.42	22.33	23.59
ATCA 9 GHz	6049	3	2016.36	9.80	10.62	15.55	16.43
ATCA 5.5 GHz	25633	5	5126.67	41.52	45.01	39.54	41.77

TS Model

Band	χ^2	d.o.f.	χ^2_{red}	χ^2_{frac}	$\chi^2_{frac,color}$	$\chi^2_{red,frac}$	$\chi^2_{red,frac,color}$
XRT 2 keV	5253	267	19.67	20.97	100.00	0.42	100.00
UVOT uvw2	0	0	0.00	0.00	0.00	0.00	0.00
UVOT uvm2	0	0	0.00	0.00	0.00	0.00	0.00
UVOT uvw1	0	0	0.00	0.00	0.00	0.00	0.00
UVOT u	0	0	0.00	0.00	0.00	0.00	0.00
UVOT b	1147	2	573.70	4.58	24.95	12.12	42.94
GROND g'	727	4	181.64	2.90	15.80	3.84	13.60
UVOT v+white	455	35	12.99	1.81	9.88	0.27	0.97
GROND r'	1274	4	318.59	5.09	27.71	6.73	23.85
GROND i'	597	4	149.35	2.38	12.99	3.16	11.18
GROND z'	364	4	91.08	1.45	7.92	1.92	6.82
GROND J	23	4	5.87	0.09	0.51	0.12	0.44
GROND H	5	4	1.19	0.02	0.10	0.03	0.09
GROND K	6	4	1.55	0.02	0.13	0.03	0.12
APEX+ALMA 345 GHz	365	1	364.97	1.46	2.40	7.71	10.81
ATCA 44 GHz	9519	5	1903.88	37.99	62.62	40.23	56.37
ATCA 18 GHz	4747	5	949.36	18.95	31.22	20.06	28.11
ATCA 9 GHz	335	3	111.79	1.34	2.21	2.36	3.31
ATCA 5.5 GHz	236	5	47.27	0.94	1.55	1.00	1.40

WM Model

Band	χ^2	d.o.f.	χ^2_{red}	χ^2_{frac}	$\chi^2_{frac,color}$	$\chi^2_{red,frac}$	$\chi^2_{red,frac,color}$
XRT 2 keV	74001	267	277.16	28.98	100.00	0.66	100.00
UVOT uvw2	0	0	0.00	0.00	0.00	0.00	0.00
UVOT uvm2	0	0	0.00	0.00	0.00	0.00	0.00
UVOT uvw1	0	0	0.00	0.00	0.00	0.00	0.00
UVOT u	0	0	0.00	0.00	0.00	0.00	0.00
UVOT b	3703	2	1851.64	1.45	24.95	4.43	44.92
GROND g'	1921	4	480.34	0.75	12.94	1.15	11.65
UVOT v+white	2328	35	66.52	0.91	15.68	0.16	1.61
GROND r'	3630	4	907.45	1.42	24.45	2.17	22.02
GROND i'	1999	4	499.75	0.78	13.47	1.20	12.12
GROND z'	1186	4	296.41	0.46	7.99	0.71	7.19
GROND J	57	4	14.30	0.02	0.39	0.03	0.35
GROND H	13	4	3.19	0.00	0.09	0.01	0.08
GROND K	8	4	2.06	0.00	0.06	0.00	0.05
APEX+ALMA 345 GHz	3424	1	3424.35	1.34	2.06	8.19	9.16
ATCA 44 GHz	72236	5	14447.16	28.29	43.39	34.57	38.64
ATCA 18 GHz	60029	5	12005.82	23.51	36.05	28.73	32.11
ATCA 9 GHz	10142	3	3380.58	3.97	6.09	8.09	9.04
ATCA 5.5 GHz	20665	5	4132.95	8.09	12.41	9.89	11.05

B.7 Fit to radio/submm bands

CM Model

Band	χ^2	d.o.f.	χ^2_{red}	χ^2_{frac}	$\chi^2_{frac,color}$	$\chi^2_{red,frac}$	$\chi^2_{red,frac,color}$
XRT 2 keV	12976	267	48.60	62.34	100.00	2.86	100.00
UVOT uvw2	0	0	0.00	0.00	0.00	0.00	0.00
UVOT uvm2	0	0	0.00	0.00	0.00	0.00	0.00
UVOT uvw1	0	0	0.00	0.00	0.00	0.00	0.00
UVOT u	630	5	125.94	3.03	8.56	7.41	8.42
UVOT b	1824	2	912.06	8.76	24.79	53.64	60.98
GROND g'	311	4	77.74	1.49	4.23	4.57	5.20
UVOT white	3411	29	117.61	16.39	46.35	6.92	7.86
UVOT v	242	9	26.85	1.16	3.28	1.58	1.80
GROND r'	542	4	135.53	2.60	7.37	7.97	9.06
GROND i'	206	4	51.58	0.99	2.80	3.03	3.45
GROND z'	150	4	37.48	0.72	2.04	2.20	2.51
GROND J	17	4	4.19	0.08	0.23	0.25	0.28
GROND H	8	4	2.09	0.04	0.11	0.12	0.14
GROND K	18	4	4.60	0.09	0.25	0.27	0.31
APEX+ALMA 345 GHz	66	1	66.18	0.32	13.80	3.89	42.45
ATCA 44 GHz	103	5	20.67	0.50	21.55	1.22	13.26
ATCA 18 GHz	182	5	36.50	0.88	38.05	2.15	23.40
ATCA 9 GHz	53	3	17.68	0.25	11.06	1.04	11.34
ATCA 5.5 GHz	74	5	14.90	0.36	15.53	0.88	9.56

TS Model

Band	χ^2	d.o.f.	χ^2_{red}	χ^2_{frac}	$\chi^2_{frac,color}$	$\chi^2_{red,frac}$	$\chi^2_{red,frac,color}$
XRT 2 keV	36206	267	135.60	51.66	100.00	1.62	100.00
UVOT uvw2	0	0	0.00	0.00	0.00	0.00	0.00
UVOT uvm2	0	0	0.00	0.00	0.00	0.00	0.00
UVOT uvw1	0	0	0.00	0.00	0.00	0.00	0.00
UVOT u	378	5	75.54	0.54	1.13	0.90	0.93
UVOT b	597	2	298.45	0.85	1.79	3.57	3.68
GROND g'	3250	4	812.47	4.64	9.72	9.71	10.02
UVOT white	1594	29	54.97	2.27	4.77	0.66	0.68
UVOT v	285	9	31.62	0.41	0.85	0.38	0.39
GROND r'	9461	4	2365.14	13.50	28.30	28.27	29.18
GROND i'	9176	4	2294.10	13.09	27.45	27.42	28.31
GROND z'	6690	4	1672.58	9.55	20.01	19.99	20.64
GROND J	671	4	167.86	0.96	2.01	2.01	2.07
GROND H	784	4	195.88	1.12	2.34	2.34	2.42
GROND K	545	4	136.14	0.78	1.63	1.63	1.68
APEX+ALMA 345 GHz	35	1	35.17	0.05	7.72	0.42	28.04
ATCA 44 GHz	117	5	23.32	0.17	25.59	0.28	18.59
ATCA 18 GHz	157	5	31.40	0.22	34.46	0.38	25.03
ATCA 9 GHz	46	3	15.49	0.07	10.20	0.19	12.35
ATCA 5.5 GHz	100	5	20.07	0.14	22.03	0.24	16.00

WM Model

Band	χ^2	d.o.f.	χ^2_{red}	χ^2_{frac}	$\chi^2_{frac,color}$	$\chi^2_{red,frac}$	$\chi^2_{red,frac,color}$
XRT 2 keV	50851	267	190.45	30.28	100.00	0.66	100.00
UVOT uvw2	0	0	0.00	0.00	0.00	0.00	0.00
UVOT uvm2	0	0	0.00	0.00	0.00	0.00	0.00
UVOT uvw1	0	0	0.00	0.00	0.00	0.00	0.00
UVOT u	836	5	167.20	0.50	0.72	0.58	0.58
UVOT b	3104	2	1552.22	1.85	2.66	5.35	5.41
GROND g'	12176	4	3043.99	7.25	10.44	10.49	10.60
UVOT white	5015	29	172.94	2.99	4.30	0.60	0.60
UVOT v	784	9	87.12	0.47	0.67	0.30	0.30
GROND r'	34104	4	8526.12	20.31	29.24	29.38	29.70
GROND i'	31013	4	7753.35	18.47	26.59	26.71	27.01
GROND z'	22759	4	5689.77	13.55	19.51	19.60	19.82
GROND J	2265	4	566.20	1.35	1.94	1.95	1.97
GROND H	2608	4	651.95	1.55	2.24	2.25	2.27
GROND K	1973	4	493.27	1.18	1.69	1.70	1.72
APEX+ALMA 345 GHz	44	1	43.81	0.03	10.23	0.15	34.25
ATCA 44 GHz	98	5	19.57	0.06	22.85	0.07	15.29
ATCA 18 GHz	164	5	32.75	0.10	38.24	0.11	25.60
ATCA 9 GHz	54	3	18.12	0.03	12.70	0.06	14.16
ATCA 5.5 GHz	68	5	13.69	0.04	15.98	0.05	10.70

B.8 Fit to X-rays + optical/nIR bands, MW extinction corrected, White shifted to V

CM Model

Band	χ^2	d.o.f.	χ^2_{red}	χ^2_{frac}	$\chi^2_{frac,color}$	$\chi^2_{red,frac}$	$\chi^2_{red,frac,color}$
XRT 2 keV	502	267	1.88	0.86	100.00	0.02	100.00
UVOT uvw2	0	0	0.00	0.00	0.00	0.00	0.00
UVOT uvm2	0	0	0.00	0.00	0.00	0.00	0.00
UVOT uvw1	0	0	0.00	0.00	0.00	0.00	0.00
UVOT u	128	5	25.59	0.22	14.05	0.21	16.16
UVOT b	40	2	20.07	0.07	4.41	0.16	12.68
GROND g'	180	4	44.99	0.31	19.77	0.36	28.42
UVOT v+white	329	35	9.41	0.56	36.17	0.08	5.94
GROND r'	188	4	47.02	0.32	20.66	0.38	29.70
GROND i'	22	4	5.62	0.04	2.47	0.05	3.55
GROND z'	10	4	2.57	0.02	1.13	0.02	1.62
GROND J	2	4	0.48	0.00	0.21	0.00	0.31
GROND H	9	4	2.25	0.02	0.99	0.02	1.42
GROND K	1	4	0.31	0.00	0.14	0.00	0.19
APEX+ALMA 345 GHz	19	1	19.50	0.03	0.03	0.16	0.16
ATCA 44 GHz	10132	5	2026.37	17.34	17.77	16.35	16.56
ATCA 18 GHz	14694	5	2938.89	25.15	25.78	23.71	24.02
ATCA 9 GHz	6143	3	2047.80	10.52	10.78	16.52	16.74
ATCA 5.5 GHz	26018	5	5203.66	44.54	45.64	41.98	42.53

TS Model

Band	χ^2	d.o.f.	χ^2_{red}	χ^2_{frac}	$\chi^2_{frac,color}$	$\chi^2_{red,frac}$	$\chi^2_{red,frac,color}$
XRT 2 keV	462	267	1.73	2.42	100.00	0.04	100.00
UVOT uvw2	0	0	0.00	0.00	0.00	0.00	0.00
UVOT uvm2	0	0	0.00	0.00	0.00	0.00	0.00
UVOT uvw1	0	0	0.00	0.00	0.00	0.00	0.00
UVOT u	506	5	101.25	2.65	10.53	2.35	7.42
UVOT b	1202	2	600.88	6.29	24.99	13.94	44.06
GROND g'	636	4	158.97	3.33	13.22	3.69	11.66
UVOT v+white	513	35	14.66	2.69	10.67	0.34	1.08
GROND r'	1137	4	284.19	5.95	23.63	6.59	20.84
GROND i'	497	4	124.18	2.60	10.33	2.88	9.10
GROND z'	303	4	75.75	1.59	6.30	1.76	5.55
GROND J	13	4	3.20	0.07	0.27	0.07	0.23
GROND H	1	4	0.32	0.01	0.03	0.01	0.02
GROND K	2	4	0.52	0.01	0.04	0.01	0.04
APEX+ALMA 345 GHz	119	1	118.95	0.62	0.86	2.76	4.04
ATCA 44 GHz	7987	5	1597.42	41.81	57.75	37.05	54.23
ATCA 18 GHz	3489	5	697.81	18.26	25.23	16.19	23.69
ATCA 9 GHz	631	3	210.46	3.31	4.56	4.88	7.15
ATCA 5.5 GHz	1604	5	320.87	8.40	11.60	7.44	10.89

WM Model

Band	χ^2	d.o.f.	χ^2_{red}	χ^2_{frac}	$\chi^2_{frac,color}$	$\chi^2_{red,frac}$	$\chi^2_{red,frac,color}$
XRT 2 keV	567	267	2.12	0.87	100.00	0.01	100.00
UVOT uvw2	0	0	0.00	0.00	0.00	0.00	0.00
UVOT uvm2	0	0	0.00	0.00	0.00	0.00	0.00
UVOT uvw1	0	0	0.00	0.00	0.00	0.00	0.00
UVOT u	50	5	9.96	0.08	4.83	0.07	5.50
UVOT b	45	2	22.43	0.07	4.35	0.15	12.38
GROND g'	146	4	36.49	0.22	14.16	0.25	20.15
UVOT v+white	385	35	11.01	0.59	37.37	0.08	6.08
GROND r'	171	4	42.87	0.26	16.64	0.29	23.67
GROND i'	58	4	14.50	0.09	5.62	0.10	8.00
GROND z'	66	4	16.62	0.10	6.45	0.11	9.18
GROND J	27	4	6.77	0.04	2.63	0.05	3.74
GROND H	47	4	11.85	0.07	4.60	0.08	6.54
GROND K	35	4	8.63	0.05	3.35	0.06	4.76
APEX+ALMA 345 GHz	1353	1	1352.59	2.07	2.12	9.29	9.41
ATCA 44 GHz	25033	5	5006.56	38.26	39.22	34.38	34.82
ATCA 18 GHz	25496	5	5099.26	38.97	39.94	35.02	35.47
ATCA 9 GHz	3972	3	1324.00	6.07	6.22	9.09	9.21
ATCA 5.5 GHz	7978	5	1595.52	12.19	12.50	10.96	11.10

B.9 Fit to X-rays + radio/submm bands

CM Model

Band	χ^2	d.o.f.	χ^2_{red}	χ^2_{frac}	$\chi^2_{frac,color}$	$\chi^2_{red,frac}$	$\chi^2_{red,frac,color}$
XRT 2 keV	636	267	2.38	21.09	100.00	0.48	100.00
UVOT uvw2	0	0	0.00	0.00	0.00	0.00	0.00
UVOT uvm2	0	0	0.00	0.00	0.00	0.00	0.00
UVOT uvw1	0	0	0.00	0.00	0.00	0.00	0.00
UVOT u	186	5	37.16	6.16	9.83	7.51	11.35
UVOT b	78	2	39.14	2.60	4.14	7.91	11.95
GROND g'	8	4	2.02	0.27	0.43	0.41	0.62
UVOT white	647	29	22.32	21.46	34.24	4.51	6.82
UVOT v	115	9	12.74	3.80	6.06	2.58	3.89
GROND r'	63	4	15.63	2.07	3.31	3.16	4.77
GROND i'	278	4	69.46	9.21	14.70	14.04	21.22
GROND z'	274	4	68.43	9.08	14.48	13.83	20.90
GROND J	59	4	14.77	1.96	3.13	2.99	4.51
GROND H	106	4	26.40	3.50	5.59	5.34	8.06
GROND K	77	4	19.36	2.57	4.10	3.91	5.91
APEX+ALMA 345 GHz	71	1	71.29	2.36	14.57	14.41	43.25
ATCA 44 GHz	106	5	21.14	3.50	21.60	4.27	12.83
ATCA 18 GHz	202	5	40.39	6.70	41.26	8.16	24.50
ATCA 9 GHz	74	3	24.78	2.47	15.19	5.01	15.04
ATCA 5.5 GHz	36	5	7.22	1.20	7.38	1.46	4.38

TS Model

Band	χ^2	d.o.f.	χ^2_{red}	χ^2_{frac}	$\chi^2_{frac,color}$	$\chi^2_{red,frac}$	$\chi^2_{red,frac,color}$
XRT 2 keV	499	267	1.87	15.75	100.00	0.30	100.00
UVOT uvw2	0	0	0.00	0.00	0.00	0.00	0.00
UVOT uvm2	0	0	0.00	0.00	0.00	0.00	0.00
UVOT uvw1	0	0	0.00	0.00	0.00	0.00	0.00
UVOT u	73	5	14.54	2.30	3.42	2.31	3.26
UVOT b	58	2	29.19	1.84	2.75	4.64	6.55
GROND g'	393	4	98.26	12.41	18.48	15.63	22.06
UVOT white	398	29	13.73	12.57	18.72	2.18	3.08
UVOT v	82	9	9.06	2.57	3.83	1.44	2.03
GROND r'	681	4	170.13	21.49	32.00	27.05	38.19
GROND i'	241	4	60.26	7.61	11.33	9.58	13.53
GROND z'	175	4	43.70	5.52	8.22	6.95	9.81
GROND J	10	4	2.40	0.30	0.45	0.38	0.54
GROND H	7	4	1.73	0.22	0.33	0.28	0.39
GROND K	10	4	2.50	0.32	0.47	0.40	0.56
APEX+ALMA 345 GHz	80	1	79.75	2.52	14.73	12.68	43.94
ATCA 44 GHz	107	5	21.45	3.39	19.81	3.41	11.82
ATCA 18 GHz	229	5	45.73	7.22	42.24	7.27	25.20
ATCA 9 GHz	71	3	23.61	2.24	13.09	3.75	13.01
ATCA 5.5 GHz	55	5	10.96	1.73	10.12	1.74	6.04

WM Model

Band	χ^2	d.o.f.	χ^2_{red}	χ^2_{frac}	$\chi^2_{frac,color}$	$\chi^2_{red,frac}$	$\chi^2_{red,frac,color}$
XRT 2 keV	612	267	2.29	15.93	100.00	0.33	100.00
UVOT uvw2	0	0	0.00	0.00	0.00	0.00	0.00
UVOT uvm2	0	0	0.00	0.00	0.00	0.00	0.00
UVOT uvw1	0	0	0.00	0.00	0.00	0.00	0.00
UVOT u	291	5	58.15	7.57	11.31	8.37	11.62
UVOT b	404	2	202.15	10.53	15.72	29.08	40.40
GROND g'	72	4	17.93	1.87	2.79	2.58	3.58
UVOT white	984	29	33.93	25.63	38.27	4.88	6.78
UVOT v	121	9	13.49	3.16	4.72	1.94	2.70
GROND r'	112	4	27.95	2.91	4.35	4.02	5.59
GROND i'	181	4	45.36	4.73	7.06	6.52	9.06
GROND z'	188	4	46.93	4.89	7.30	6.75	9.38
GROND J	59	4	14.85	1.55	2.31	2.14	2.97
GROND H	91	4	22.84	2.38	3.55	3.29	4.56
GROND K	67	4	16.82	1.75	2.62	2.42	3.36
APEX+ALMA 345 GHz	61	1	60.92	1.59	9.28	8.76	31.65
ATCA 44 GHz	169	5	33.82	4.40	25.76	4.86	17.57
ATCA 18 GHz	246	5	49.18	6.40	37.46	7.07	25.55
ATCA 9 GHz	93	3	31.08	2.43	14.20	4.47	16.15
ATCA 5.5 GHz	87	5	17.46	2.27	13.30	2.51	9.07

B.10 Fit to optical/nIR + radio/submm band, MW extinction corrected, White shifted to V

CM Model

Band	χ^2	d.o.f.	χ^2_{red}	χ^2_{frac}	$\chi^2_{frac,color}$	$\chi^2_{red,frac}$	$\chi^2_{red,frac,color}$
XRT 2 keV	4983	267	18.66	67.20	100.00	2.62	100.00
UVOT uvw2	0	0	0.00	0.00	0.00	0.00	0.00
UVOT uvm2	0	0	0.00	0.00	0.00	0.00	0.00
UVOT uvw1	0	0	0.00	0.00	0.00	0.00	0.00
UVOT u	213	5	42.66	2.88	11.50	6.00	8.67
UVOT b	349	2	174.64	4.71	18.83	24.56	35.47
GROND g'	246	4	61.39	3.31	13.23	8.63	12.47
UVOT v+white	217	35	6.21	2.93	11.72	0.87	1.26
GROND r'	460	4	115.11	6.21	24.82	16.19	23.38
GROND i'	172	4	43.11	2.33	9.29	6.06	8.76
GROND z'	144	4	36.10	1.95	7.78	5.08	7.33
GROND J	16	4	3.97	0.21	0.86	0.56	0.81
GROND H	11	4	2.82	0.15	0.61	0.40	0.57
GROND K	25	4	6.31	0.34	1.36	0.89	1.28
APEX+ALMA 345 GHz	98	1	98.38	1.33	17.06	13.84	49.18
ATCA 44 GHz	149	5	29.85	2.01	25.88	4.20	14.92
ATCA 18 GHz	123	5	24.60	1.66	21.32	3.46	12.29
ATCA 9 GHz	45	3	15.02	0.61	7.81	2.11	7.51
ATCA 5.5 GHz	161	5	32.21	2.17	27.93	4.53	16.10

TS Model

Band	χ^2	d.o.f.	χ^2_{red}	χ^2_{frac}	$\chi^2_{frac,color}$	$\chi^2_{red,frac}$	$\chi^2_{red,frac,color}$
XRT 2 keV	11133	267	41.70	65.44	100.00	2.67	100.00
UVOT uvw2	0	0	0.00	0.00	0.00	0.00	0.00
UVOT uvm2	0	0	0.00	0.00	0.00	0.00	0.00
UVOT uvw1	0	0	0.00	0.00	0.00	0.00	0.00
UVOT u	404	5	80.78	2.37	7.49	5.17	5.93
UVOT b	990	2	494.75	5.82	18.35	31.66	36.31
GROND g'	662	4	165.55	3.89	12.28	10.59	12.15
UVOT v+white	960	35	27.43	5.64	17.81	1.76	2.01
GROND r'	1257	4	314.20	7.39	23.31	20.10	23.06
GROND i'	626	4	156.40	3.68	11.60	10.01	11.48
GROND z'	425	4	106.30	2.50	7.89	6.80	7.80
GROND J	29	4	7.26	0.17	0.54	0.46	0.53
GROND H	14	4	3.45	0.08	0.26	0.22	0.25
GROND K	25	4	6.27	0.15	0.47	0.40	0.46
APEX+ALMA 345 GHz	69	1	69.09	0.41	14.16	4.42	43.53
ATCA 44 GHz	124	5	24.76	0.73	25.38	1.58	15.60
ATCA 18 GHz	184	5	36.81	1.08	37.72	2.36	23.19
ATCA 9 GHz	44	3	14.67	0.26	9.02	0.94	9.24
ATCA 5.5 GHz	67	5	13.39	0.39	13.72	0.86	8.44

WM Model

Band	χ^2	d.o.f.	χ^2_{red}	χ^2_{frac}	$\chi^2_{frac,color}$	$\chi^2_{red,frac}$	$\chi^2_{red,frac,color}$
XRT 2 keV	6917	267	25.91	82.62	100.00	7.23	100.00
UVOT uvw2	0	0	0.00	0.00	0.00	0.00	0.00
UVOT uvm2	0	0	0.00	0.00	0.00	0.00	0.00
UVOT uvw1	0	0	0.00	0.00	0.00	0.00	0.00
UVOT u	129	5	25.72	1.54	16.51	7.18	15.37
UVOT b	53	2	26.41	0.63	6.78	7.37	15.78
GROND g’	123	4	30.82	1.47	15.83	8.60	18.41
UVOT v+white	154	35	4.40	1.84	19.78	1.23	2.63
GROND r’	194	4	48.49	2.32	24.90	13.53	28.97
GROND i’	50	4	12.40	0.59	6.37	3.46	7.41
GROND z’	49	4	12.21	0.58	6.27	3.41	7.29
GROND J	11	4	2.71	0.13	1.39	0.76	1.62
GROND H	9	4	2.30	0.11	1.18	0.64	1.37
GROND K	8	4	1.92	0.09	0.99	0.54	1.15
APEX+ALMA 345 GHz	29	1	29.16	0.35	4.31	8.14	17.66
ATCA 44 GHz	243	5	48.58	2.90	35.93	13.56	29.43
ATCA 18 GHz	289	5	57.84	3.45	42.78	16.14	35.04
ATCA 9 GHz	49	3	16.38	0.59	7.27	4.57	9.92
ATCA 5.5 GHz	66	5	13.13	0.78	9.71	3.66	7.95

B.11 Fit to all bands without early optical data, MW extinction corrected, White shifted to V

CM Model

Band	χ^2	d.o.f.	χ^2_{red}	χ^2_{frac}	$\chi^2_{frac,color}$	$\chi^2_{red,frac}$	$\chi^2_{red,frac,color}$
XRT 2 keV	567	155	3.66	25.46	100.00	0.80	100.00
UVOT uvw2	0	0	0.00	0.00	0.00	0.00	0.00
UVOT uvm2	0	0	0.00	0.00	0.00	0.00	0.00
UVOT uvw1	0	0	0.00	0.00	0.00	0.00	0.00
UVOT u	93	3	30.99	4.17	8.24	6.81	11.57
UVOT b	26	1	25.60	1.15	2.27	5.62	9.56
GROND g’	246	4	61.56	11.05	21.82	13.52	22.99
UVOT v+white	204	21	9.73	9.16	18.10	2.14	3.63
GROND r’	375	4	93.84	16.84	33.25	20.61	35.04
GROND i’	97	4	24.35	4.37	8.63	5.35	9.09
GROND z’	70	4	17.54	3.15	6.22	3.85	6.55
GROND J	7	4	1.80	0.32	0.64	0.40	0.67
GROND H	5	4	1.18	0.21	0.42	0.26	0.44
GROND K	5	4	1.20	0.21	0.42	0.26	0.45
APEX+ALMA 345 GHz	87	1	86.82	3.90	16.29	19.07	47.23
ATCA 44 GHz	147	5	29.33	6.58	27.52	6.44	15.96
ATCA 18 GHz	161	5	32.29	7.24	30.30	7.09	17.56
ATCA 9 GHz	58	3	19.49	2.62	10.97	4.28	10.60
ATCA 5.5 GHz	79	5	15.90	3.57	14.92	3.49	8.65

TS Model

Band	χ^2	d.o.f.	χ^2_{red}	χ^2_{frac}	$\chi^2_{frac,color}$	$\chi^2_{red,frac}$	$\chi^2_{red,frac,color}$
XRT 2 keV	347	155	2.24	11.60	100.00	0.33	100.00
UVOT uvw2	0	0	0.00	0.00	0.00	0.00	0.00
UVOT uvm2	0	0	0.00	0.00	0.00	0.00	0.00
UVOT uvw1	0	0	0.00	0.00	0.00	0.00	0.00
UVOT u	64	3	21.33	2.14	3.07	3.12	4.20
UVOT b	8	1	8.25	0.28	0.40	1.21	1.63
GROND g’	445	4	111.18	14.89	21.36	16.27	21.90
UVOT v+white	121	21	5.76	4.05	5.81	0.84	1.14
GROND r’	817	4	204.19	27.35	39.23	29.89	40.23
GROND i’	342	4	85.57	11.46	16.44	12.53	16.86
GROND z’	247	4	61.74	8.27	11.86	9.04	12.16
GROND J	13	4	3.27	0.44	0.63	0.48	0.64
GROND H	7	4	1.68	0.22	0.32	0.25	0.33
GROND K	18	4	4.61	0.62	0.89	0.67	0.91
APEX+ALMA 345 GHz	67	1	67.08	2.25	12.03	9.82	38.69
ATCA 44 GHz	108	5	21.53	3.60	19.31	3.15	12.42
ATCA 18 GHz	260	5	52.08	8.72	46.70	7.62	30.04
ATCA 9 GHz	61	3	20.44	2.05	11.00	2.99	11.79
ATCA 5.5 GHz	61	5	12.23	2.05	10.96	1.79	7.05

WM Model

Band	χ^2	d.o.f.	χ^2_{red}	χ^2_{frac}	$\chi^2_{frac,color}$	$\chi^2_{red,frac}$	$\chi^2_{red,frac,color}$
XRT 2 keV	473	155	3.05	13.89	100.00	0.43	100.00
UVOT uvw2	0	0	0.00	0.00	0.00	0.00	0.00
UVOT uvm2	0	0	0.00	0.00	0.00	0.00	0.00
UVOT uvw1	0	0	0.00	0.00	0.00	0.00	0.00
UVOT u	137	3	45.64	4.02	6.67	6.47	9.24
UVOT b	52	1	51.52	1.51	2.51	7.31	10.43
GROND g’	377	4	94.30	11.07	18.36	13.38	19.09
UVOT v+white	344	21	16.38	10.10	16.75	2.32	3.32
GROND r’	669	4	167.21	19.64	32.57	23.72	33.86
GROND i’	249	4	62.23	7.31	12.12	8.83	12.60
GROND z’	183	4	45.82	5.38	8.92	6.50	9.28
GROND J	17	4	4.29	0.50	0.84	0.61	0.87
GROND H	12	4	2.90	0.34	0.56	0.41	0.59
GROND K	14	4	3.60	0.42	0.70	0.51	0.73
APEX+ALMA 345 GHz	28	1	27.82	0.82	3.16	3.95	13.37
ATCA 44 GHz	334	5	66.84	9.81	38.00	9.48	32.13
ATCA 18 GHz	401	5	80.28	11.78	45.64	11.39	38.59
ATCA 9 GHz	74	3	24.73	2.18	8.44	3.51	11.89
ATCA 5.5 GHz	42	5	8.38	1.23	4.76	1.19	4.03

B.12 Fit to all bands after 0.5 days, MW extinction corrected, White shifted to V

CM Model

Band	χ^2	d.o.f.	χ^2_{red}	χ^2_{frac}	$\chi^2_{frac,color}$	$\chi^2_{red,frac}$	$\chi^2_{red,frac,color}$
XRT 2 keV	108	65	1.65	6.13	100.00	0.38	100.00
UVOT uvw2	0	0	0.00	0.00	0.00	0.00	0.00
UVOT uvm2	0	0	0.00	0.00	0.00	0.00	0.00
UVOT uvw1	0	0	0.00	0.00	0.00	0.00	0.00
UVOT u	0	0	0.00	0.02	0.02	0.00	0.00
UVOT b	0	0	0.00	0.00	0.00	0.00	0.00
GROND g’	302	4	75.46	17.22	27.37	17.24	28.30
UVOT v+white	52	13	4.01	2.97	4.72	0.92	1.50
GROND r’	480	4	119.96	27.37	43.50	27.40	44.98
GROND i’	150	4	37.58	8.57	13.63	8.58	14.09
GROND z’	102	4	25.48	5.81	9.24	5.82	9.55
GROND J	8	4	1.97	0.45	0.71	0.45	0.74
GROND H	3	4	0.63	0.14	0.23	0.14	0.24
GROND K	6	4	1.59	0.36	0.58	0.36	0.60
APEX+ALMA 345 GHz	67	1	67.20	3.83	12.39	15.35	39.65
ATCA 44 GHz	137	5	27.34	7.80	25.20	6.25	16.13
ATCA 18 GHz	212	5	42.46	12.11	39.14	9.70	25.05
ATCA 9 GHz	54	3	18.09	3.10	10.00	4.13	10.67
ATCA 5.5 GHz	72	5	14.39	4.11	13.27	3.29	8.49

TS Model

Band	χ^2	d.o.f.	χ^2_{red}	χ^2_{frac}	$\chi^2_{frac,color}$	$\chi^2_{red,frac}$	$\chi^2_{red,frac,color}$
XRT 2 keV	121	65	1.86	4.62	100.00	0.29	100.00
UVOT uvw2	0	0	0.00	0.00	0.00	0.00	0.00
UVOT uvm2	0	0	0.00	0.00	0.00	0.00	0.00
UVOT uvw1	0	0	0.00	0.00	0.00	0.00	0.00
UVOT u	0	0	0.00	0.01	0.02	0.00	0.00
UVOT b	0	0	0.00	0.00	0.00	0.00	0.00
GROND g’	439	4	109.86	16.80	22.80	17.07	23.32
UVOT v+white	61	13	4.71	2.34	3.18	0.73	1.00
GROND r’	802	4	200.52	30.66	41.62	31.15	42.56
GROND i’	339	4	84.77	12.96	17.60	13.17	17.99
GROND z’	242	4	60.61	9.27	12.58	9.42	12.87
GROND J	15	4	3.81	0.58	0.79	0.59	0.81
GROND H	7	4	1.86	0.28	0.39	0.29	0.39
GROND K	20	4	4.96	0.76	1.03	0.77	1.05
APEX+ALMA 345 GHz	60	1	59.86	2.29	10.53	9.30	35.05
ATCA 44 GHz	117	5	23.39	4.47	20.58	3.63	13.70
ATCA 18 GHz	270	5	53.92	10.30	47.44	8.38	31.57
ATCA 9 GHz	69	3	23.15	2.65	12.22	3.60	13.55
ATCA 5.5 GHz	52	5	10.48	2.00	9.22	1.63	6.14

WM Model

Band	χ^2	d.o.f.	χ^2_{red}	χ^2_{frac}	$\chi^2_{frac,color}$	$\chi^2_{red,frac}$	$\chi^2_{red,frac,color}$
XRT 2 keV	194	65	2.99	2.37	100.00	0.15	100.00
UVOT uvw2	0	0	0.00	0.00	0.00	0.00	0.00
UVOT uvm2	0	0	0.00	0.00	0.00	0.00	0.00
UVOT uvw1	0	0	0.00	0.00	0.00	0.00	0.00
UVOT u	8	0	0.00	0.09	0.11	0.00	0.00
UVOT b	0	0	0.00	0.00	0.00	0.00	0.00
GROND g'	1349	4	337.14	16.43	18.86	16.90	19.79
UVOT v+white	478	13	36.74	5.82	6.68	1.84	2.16
GROND r'	2666	4	666.47	32.49	37.28	33.41	39.13
GROND i'	1502	4	375.38	18.30	20.99	18.82	22.04
GROND z'	982	4	245.55	11.97	13.73	12.31	14.42
GROND J	79	4	19.82	0.97	1.11	0.99	1.16
GROND H	44	4	10.92	0.53	0.61	0.55	0.64
GROND K	45	4	11.35	0.55	0.63	0.57	0.67
APEX+ALMA 345 GHz	125	1	125.49	1.53	14.60	6.29	43.54
ATCA 44 GHz	218	5	43.62	2.66	25.38	2.19	15.13
ATCA 18 GHz	188	5	37.64	2.29	21.90	1.89	13.06
ATCA 9 GHz	120	3	39.92	1.46	13.93	2.00	13.85
ATCA 5.5 GHz	208	5	41.57	2.53	24.19	2.08	14.42

Appendix C

Light Curves

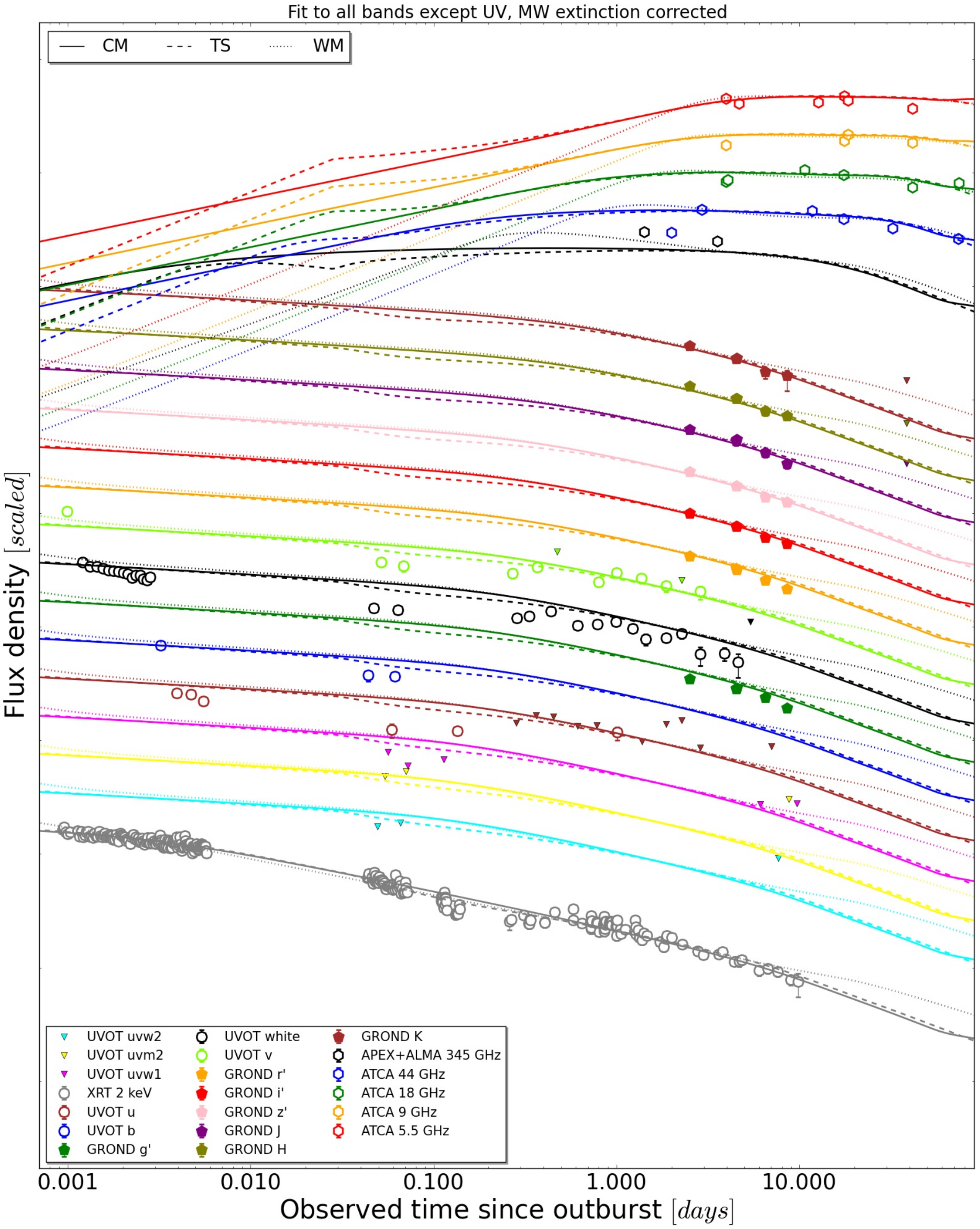
Fit to all bands except UV, MW extinction corrected
CM
TS
WM
Flux density [scaled]
Observed time since outburst [days]
0.001
0.010
0.100
1.000
10.000
UVOT uvw2
UVOT uvm2
UVOT uvw1
XRT 2 keV
UVOT u
UVOT b
GROND g'
UVOT white
UVOT v
GROND r'
GROND i'
GROND z'
GROND J
GROND H
GROND K
APEX+ALMA 345 GHz
ATCA 44 GHz
ATCA 18 GHz
ATCA 9 GHz
ATCA 5.5 GHz

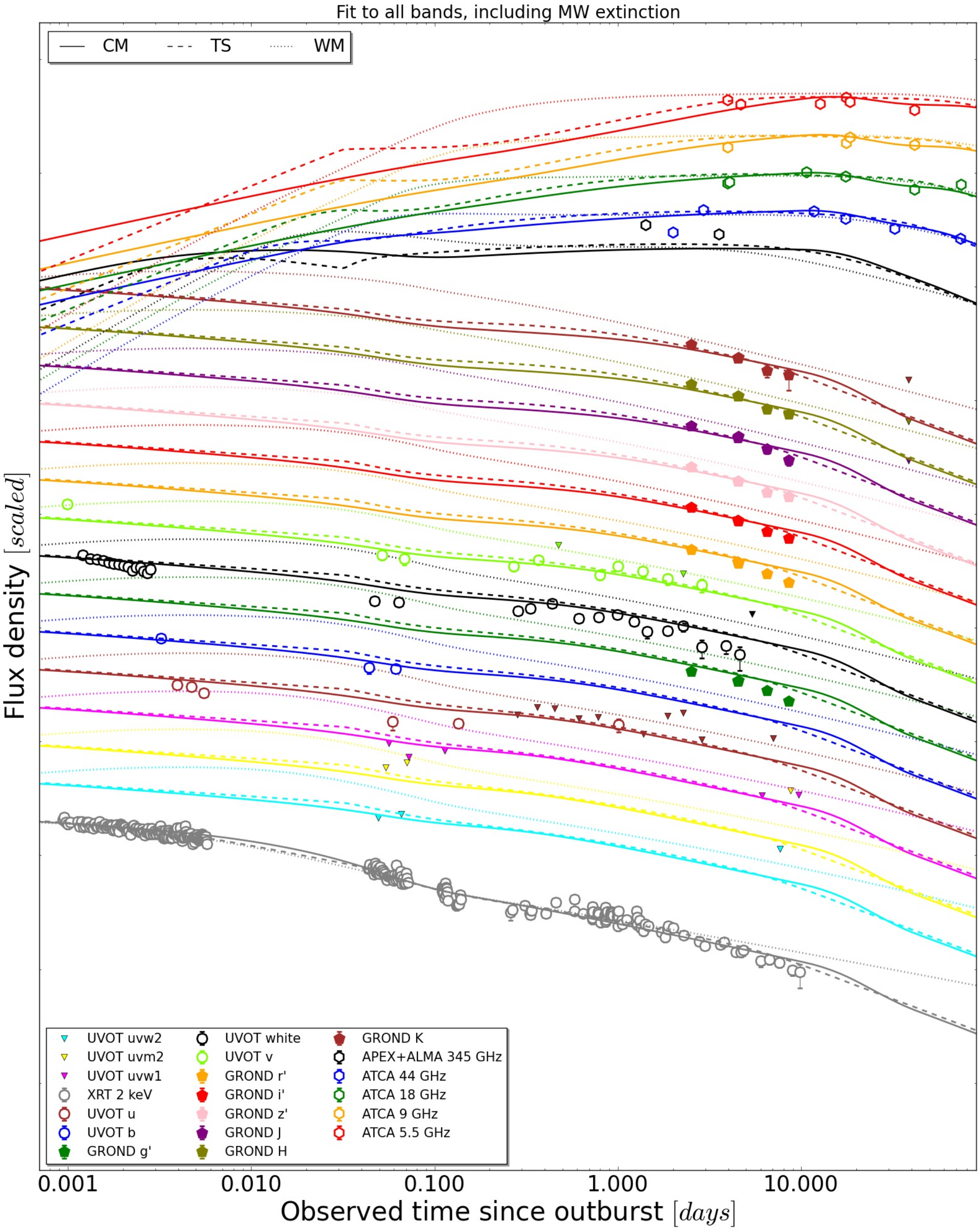
Fit to all bands, including MW extinction
CM
TS
WM
Flux density [scaled]
Observed time since outburst [days]
0.001
0.010
0.100
1.000
10.000
UVOT uvw2
UVOT uvm2
UVOT uvw1
XRT 2 keV
UVOT u
UVOT b
GROND g'
UVOT white
UVOT v
GROND r'
GROND i'
GROND z'
GROND J
GROND H
GROND K
APEX+ALMA 345 GHz
ATCA 44 GHz
ATCA 18 GHz
ATCA 9 GHz
ATCA 5.5 GHz

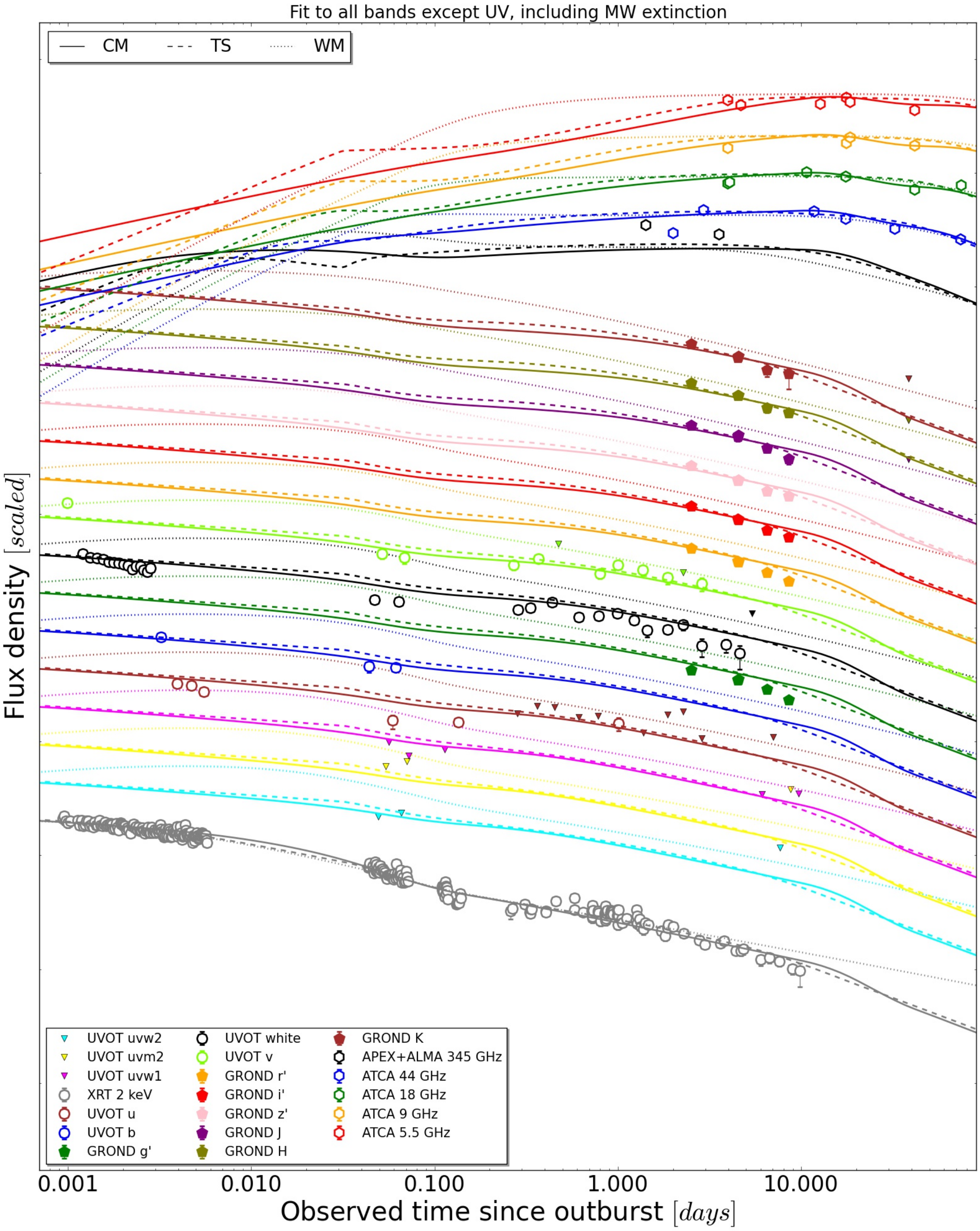
Fit to all bands except UV, including MW extinction
CM
TS
WM
Flux density [scaled]
Observed time since outburst [days]
0.001
0.010
0.100
1.000
10.000
UVOT uvw2
UVOT uvm2
UVOT uvw1
XRT 2 keV
UVOT u
UVOT b
GROND g'
UVOT white
UVOT v
GROND r'
GROND i'
GROND z'
GROND J
GROND H
GROND K
APEX+ALMA 345 GHz
ATCA 44 GHz
ATCA 18 GHz
ATCA 9 GHz
ATCA 5.5 GHz

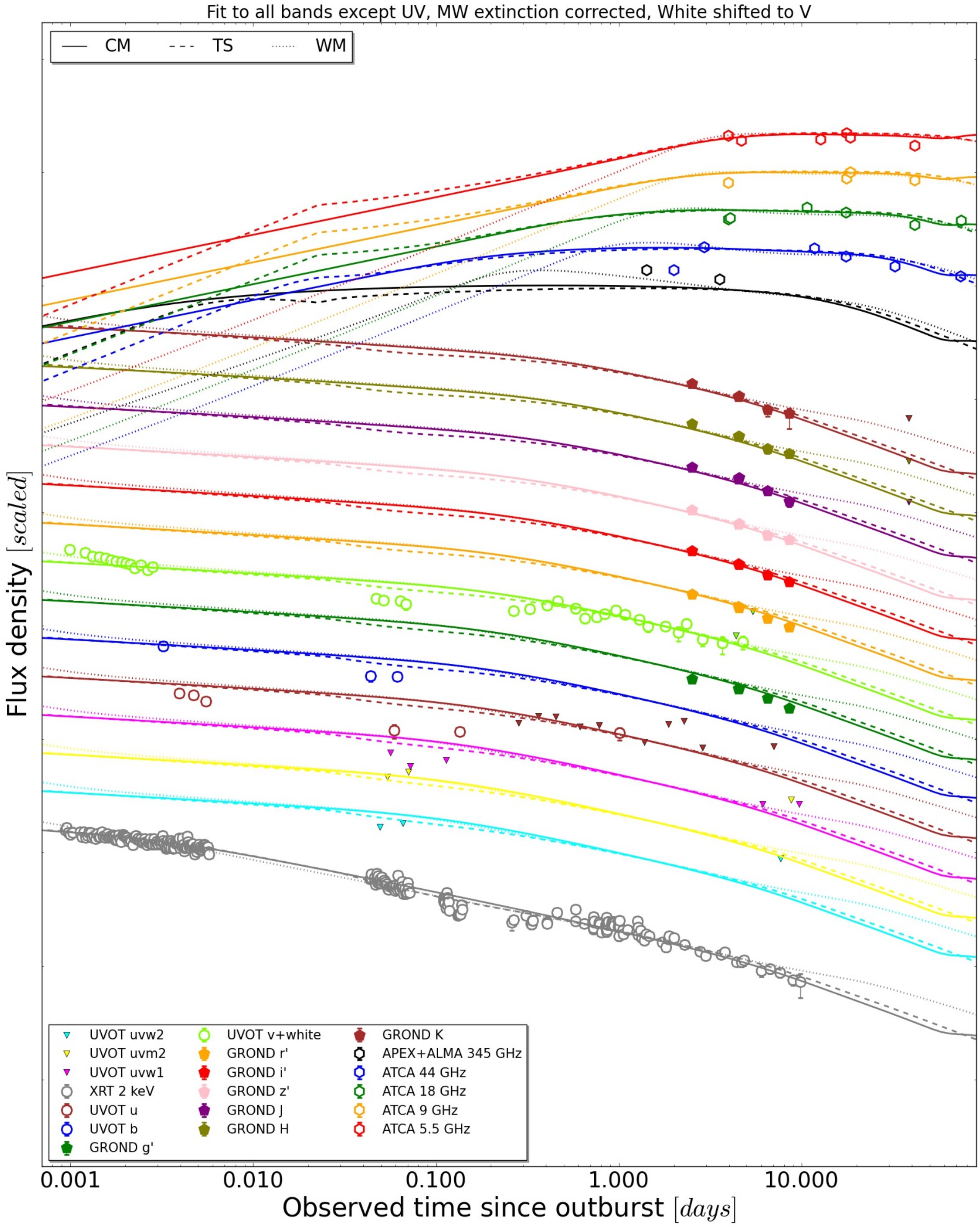
Fit to all bands except UV, MW extinction corrected, White shifted to V
CM
TS
WM
Flux density [scaled]
Observed time since outburst [days]
0.001
0.010
0.100
1.000
10.000
UVOT uvw2
UVOT uvm2
UVOT uvw1
XRT 2 keV
UVOT u
UVOT b
GROND g'
UVOT v+white
GROND r'
GROND i'
GROND z'
GROND J
GROND H
GROND K
APEX+ALMA 345 GHz
ATCA 44 GHz
ATCA 18 GHz
ATCA 9 GHz
ATCA 5.5 GHz

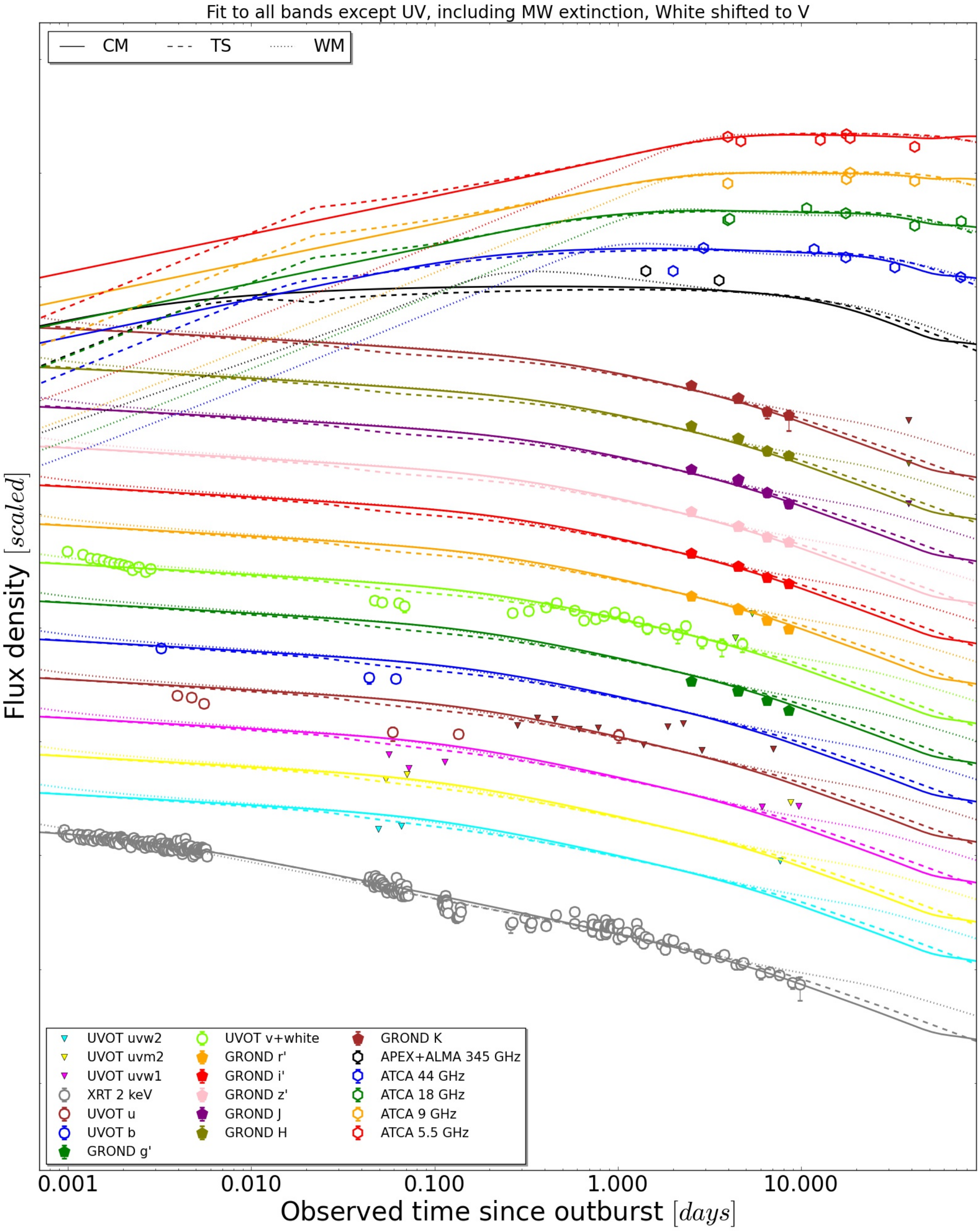
Fit to all bands except UV, including MW extinction, White shifted to V
CM
TS
WM
Flux density [scaled]
Observed time since outburst [days]
0.001
0.010
0.100
1.000
10.000
UVOT uvw2
UVOT uvm2
UVOT uvw1
XRT 2 keV
UVOT u
UVOT b
GROND g'
UVOT v+white
GROND r'
GROND i'
GROND z'
GROND J
GROND H
GROND K
APEX+ALMA 345 GHz
ATCA 44 GHz
ATCA 18 GHz
ATCA 9 GHz
ATCA 5.5 GHz

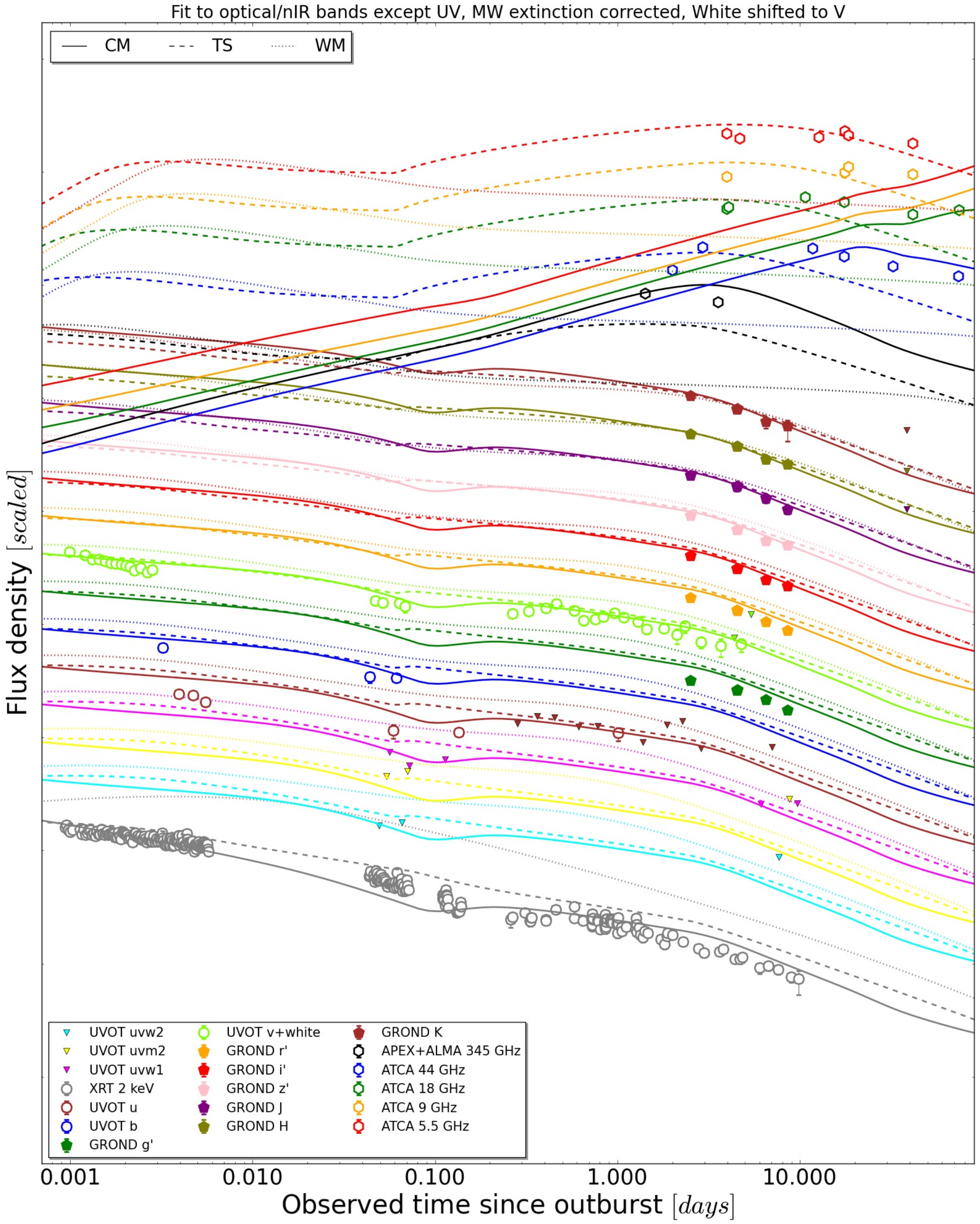
Fit to optical/nIR bands except UV, MW extinction corrected, White shifted to V
CM
TS
WM
Flux density [scaled]
Observed time since outburst [days]
0.001
0.010
0.100
1.000
10.000
UVOT uvw2
UVOT uvm2
UVOT uvw1
XRT 2 keV
UVOT u
UVOT b
GROND g'
UVOT v+white
GROND r'
GROND i'
GROND z'
GROND J
GROND H
GROND K
APEX+ALMA 345 GHz
ATCA 44 GHz
ATCA 18 GHz
ATCA 9 GHz
ATCA 5.5 GHz

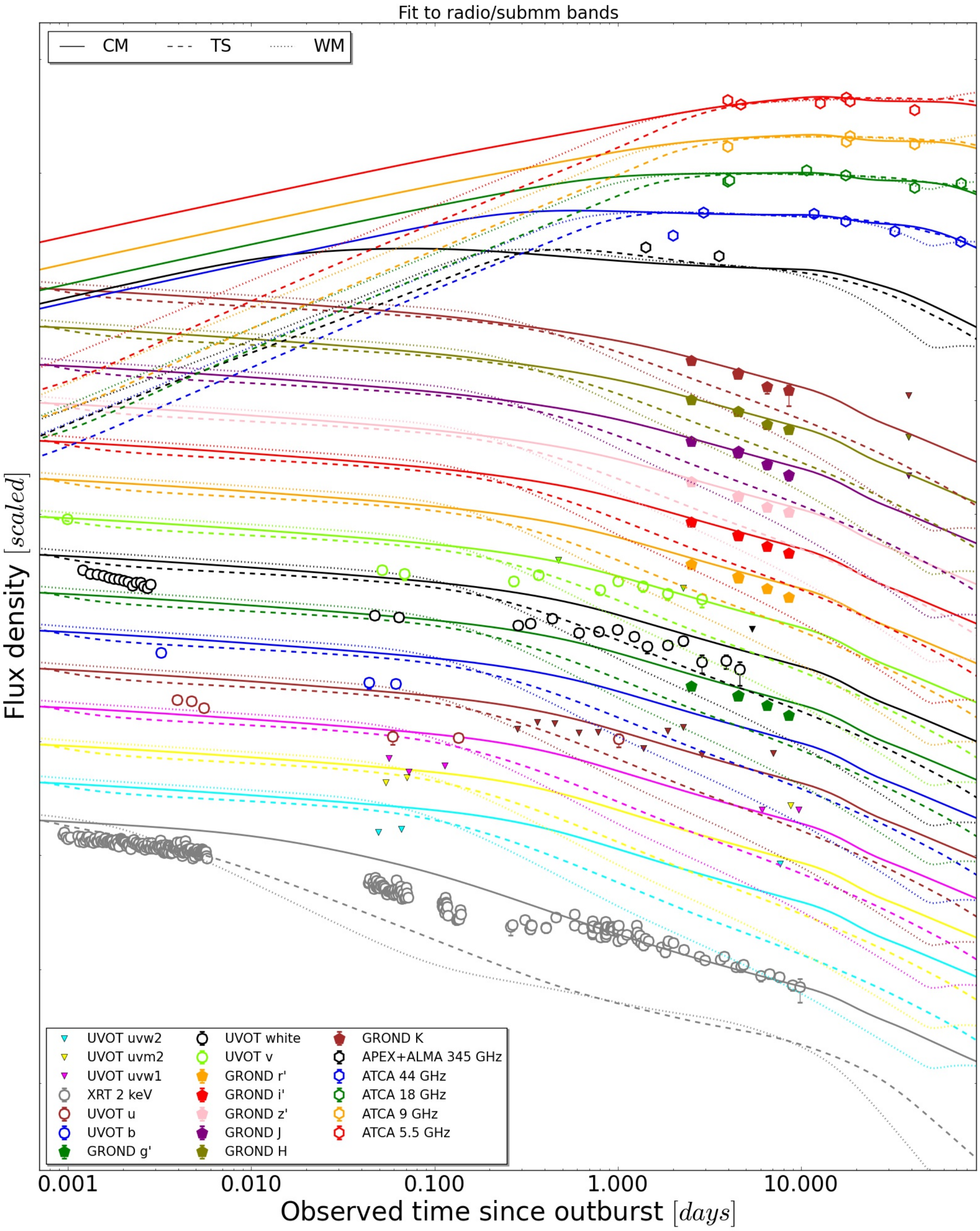
Fit to radio/submm bands
CM
TS
WM
Flux density [scaled]
Observed time since outburst [days]
0.001
0.010
0.100
1.000
10.000
UVOT uvw2
UVOT uvm2
UVOT uvw1
XRT 2 keV
UVOT u
UVOT b
GROND g'
UVOT white
UVOT v
GROND r'
GROND i'
GROND z'
GROND J
GROND H
GROND K
APEX+ALMA 345 GHz
ATCA 44 GHz
ATCA 18 GHz
ATCA 9 GHz
ATCA 5.5 GHz

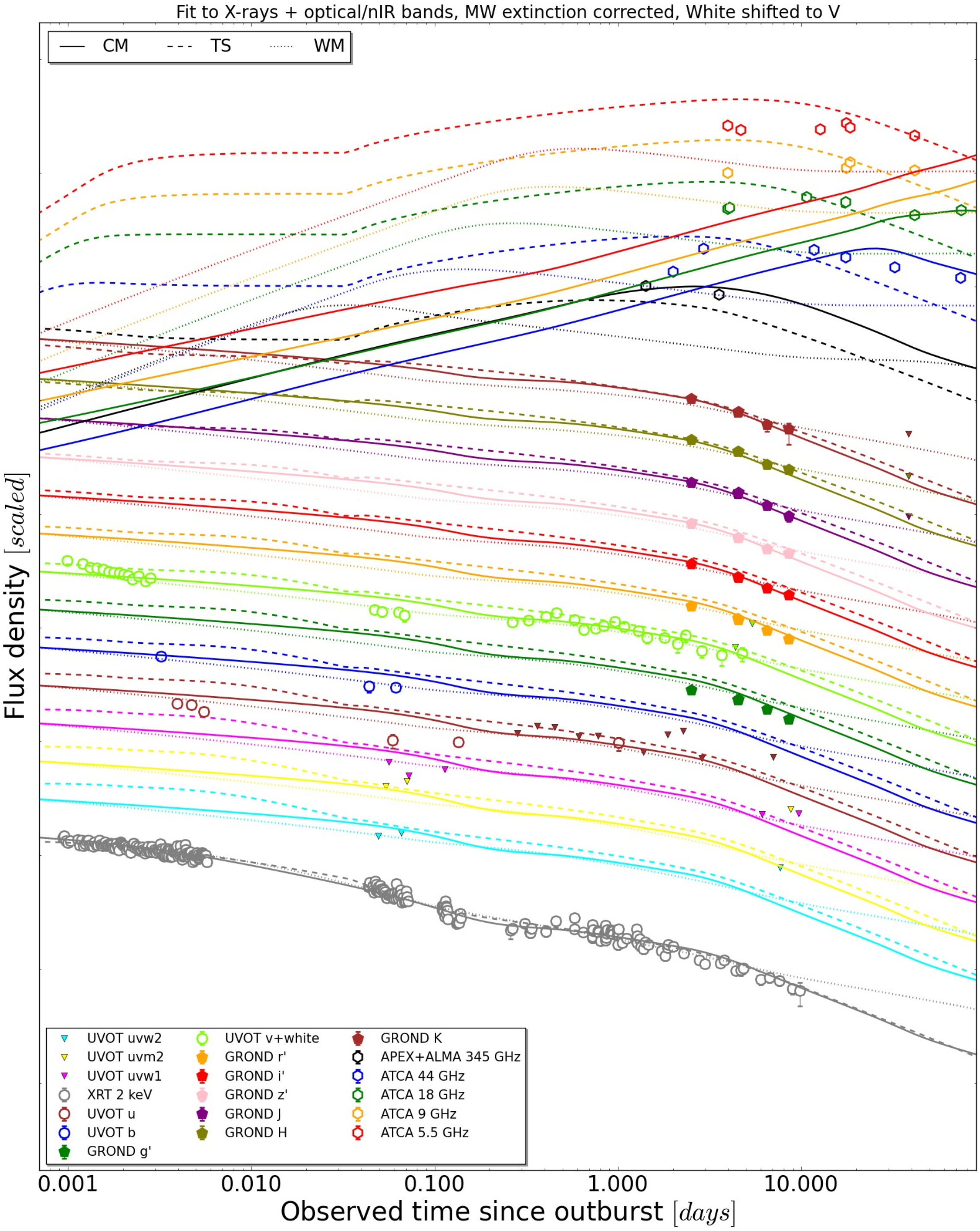
Fit to X-rays + optical/nIR bands, MW extinction corrected, White shifted to V
CM
TS
WM
Flux density [scaled]
Observed time since outburst [days]
0.001
0.010
0.100
1.000
10.000
UVOT uvw2
UVOT uvm2
UVOT uvw1
XRT 2 keV
UVOT u
UVOT b
GROND g'
UVOT v+white
GROND r'
GROND i'
GROND z'
GROND J
GROND H
GROND K
APEX+ALMA 345 GHz
ATCA 44 GHz
ATCA 18 GHz
ATCA 9 GHz
ATCA 5.5 GHz

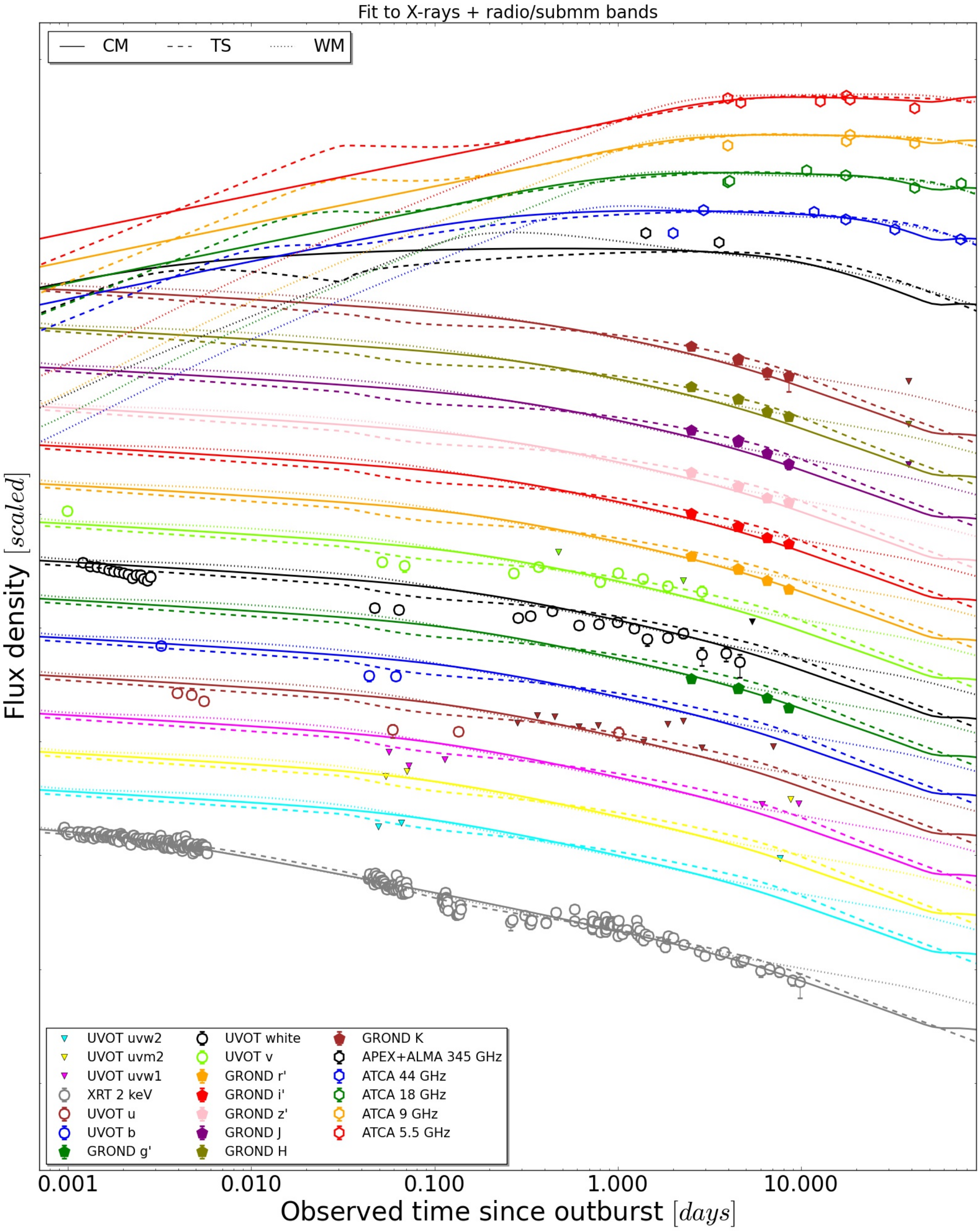
Fit to X-rays + radio/submm bands
CM
TS
WM
Flux density [scaled]
Observed time since outburst [days]
0.001
0.010
0.100
1.000
10.000
UVOT uvw2
UVOT uvm2
UVOT uvw1
XRT 2 keV
UVOT u
UVOT b
GROND g'
UVOT white
UVOT v
GROND r'
GROND i'
GROND z'
GROND J
GROND H
GROND K
APEX+ALMA 345 GHz
ATCA 44 GHz
ATCA 18 GHz
ATCA 9 GHz
ATCA 5.5 GHz

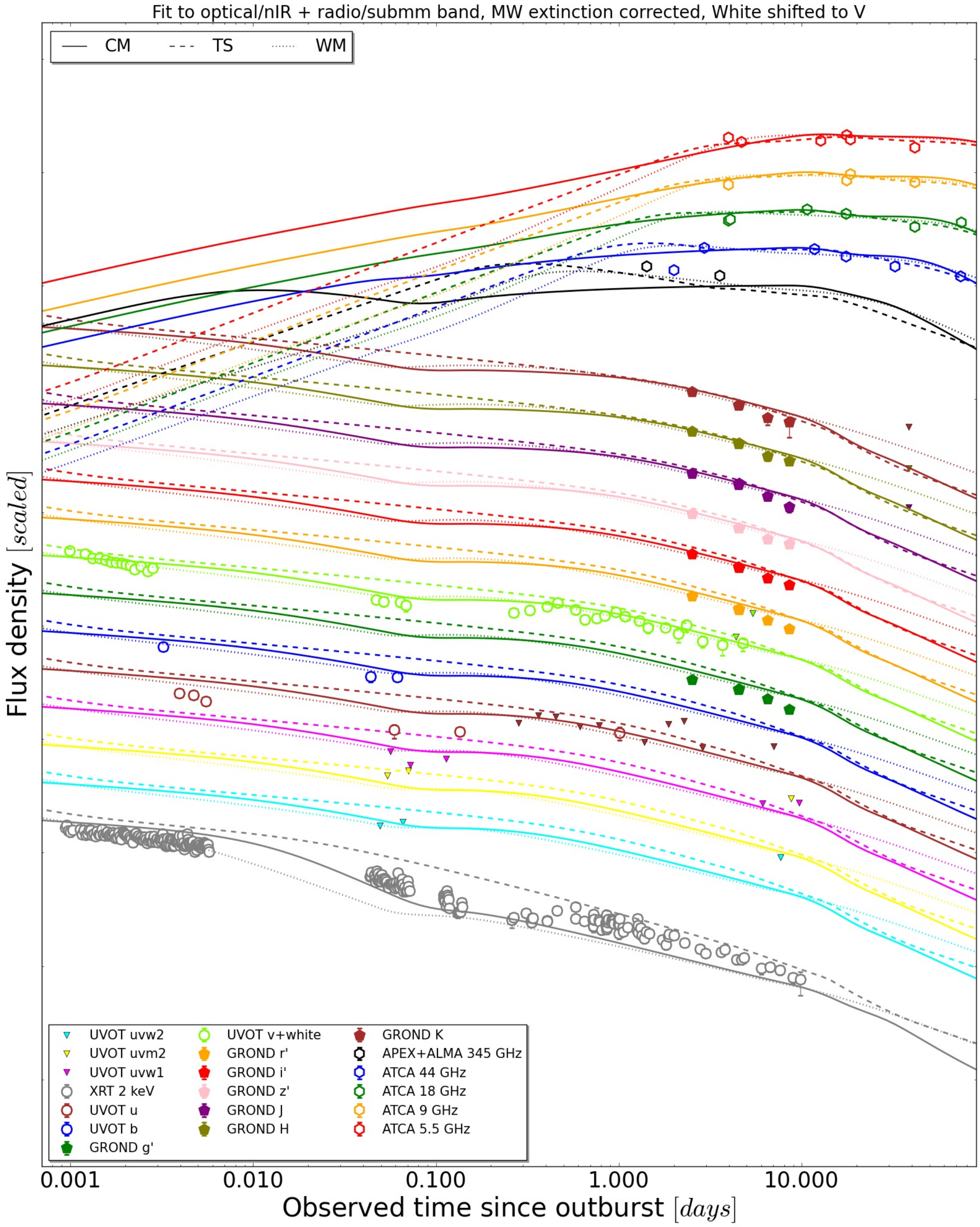
Fit to optical/nIR + radio/submm band, MW extinction corrected, White shifted to V
CM
TS
WM
UVOT uvw2
UVOT uvm2
UVOT uvw1
XRT 2 keV
UVOT u
UVOT b
GROND g'
UVOT v+white
GROND r'
GROND i'
GROND z'
GROND J
GROND H
GROND K
APEX+ALMA 345 GHz
ATCA 44 GHz
ATCA 18 GHz
ATCA 9 GHz
ATCA 5.5 GHz
Flux density $[scaled]$
0.001
0.010
0.100
1.000
10.000
Observed time since outburst $[days]$

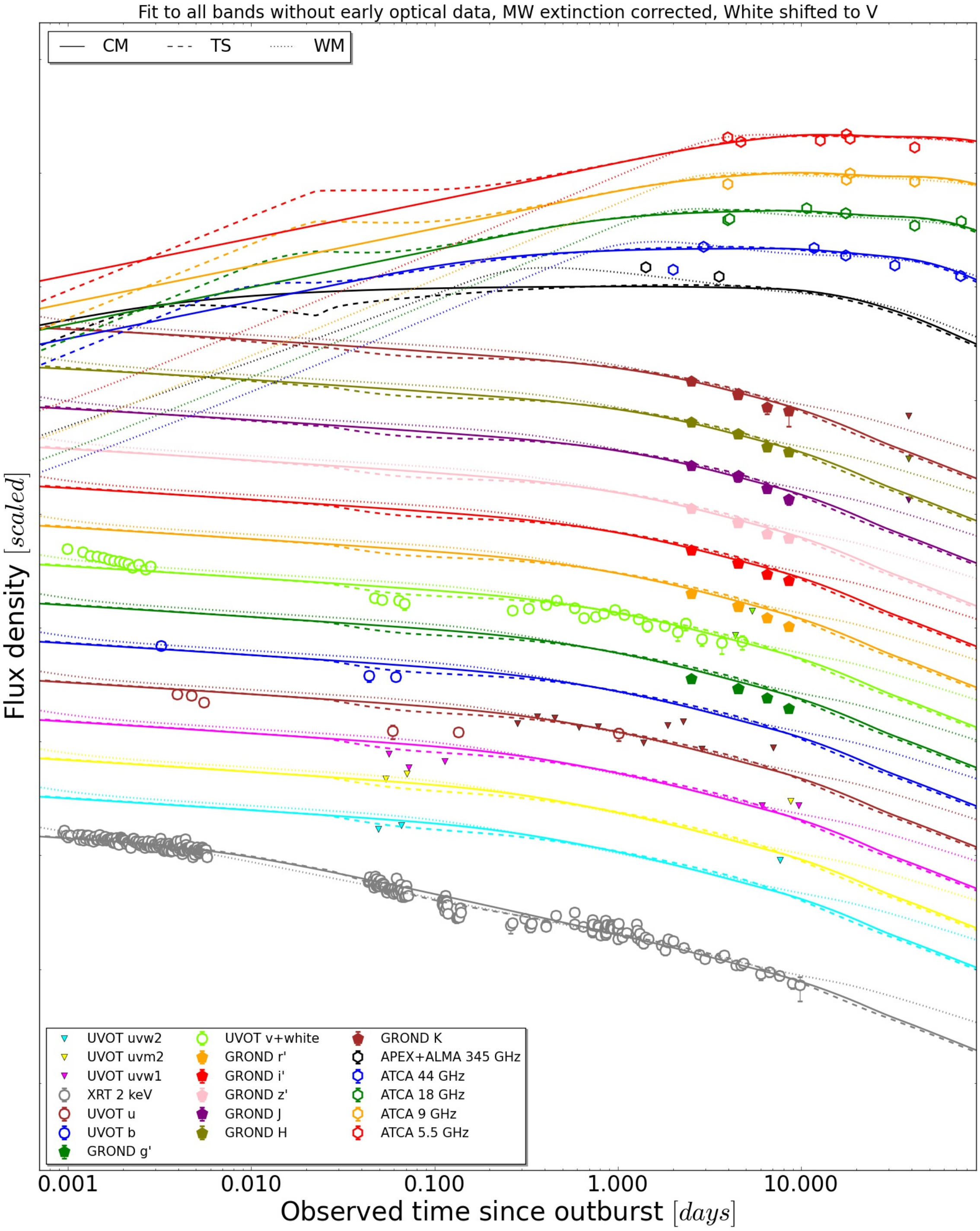
Fit to all bands without early optical data, MW extinction corrected, White shifted to V
CM
TS
WM
Flux density [scaled]
Observed time since outburst [days]
0.001
0.010
0.100
1.000
10.000
UVOT uvw2
UVOT uvm2
UVOT uvw1
XRT 2 keV
UVOT u
UVOT b
GROND g'
UVOT v+white
GROND r'
GROND i'
GROND z'
GROND J
GROND H
GROND K
APEX+ALMA 345 GHz
ATCA 44 GHz
ATCA 18 GHz
ATCA 9 GHz
ATCA 5.5 GHz

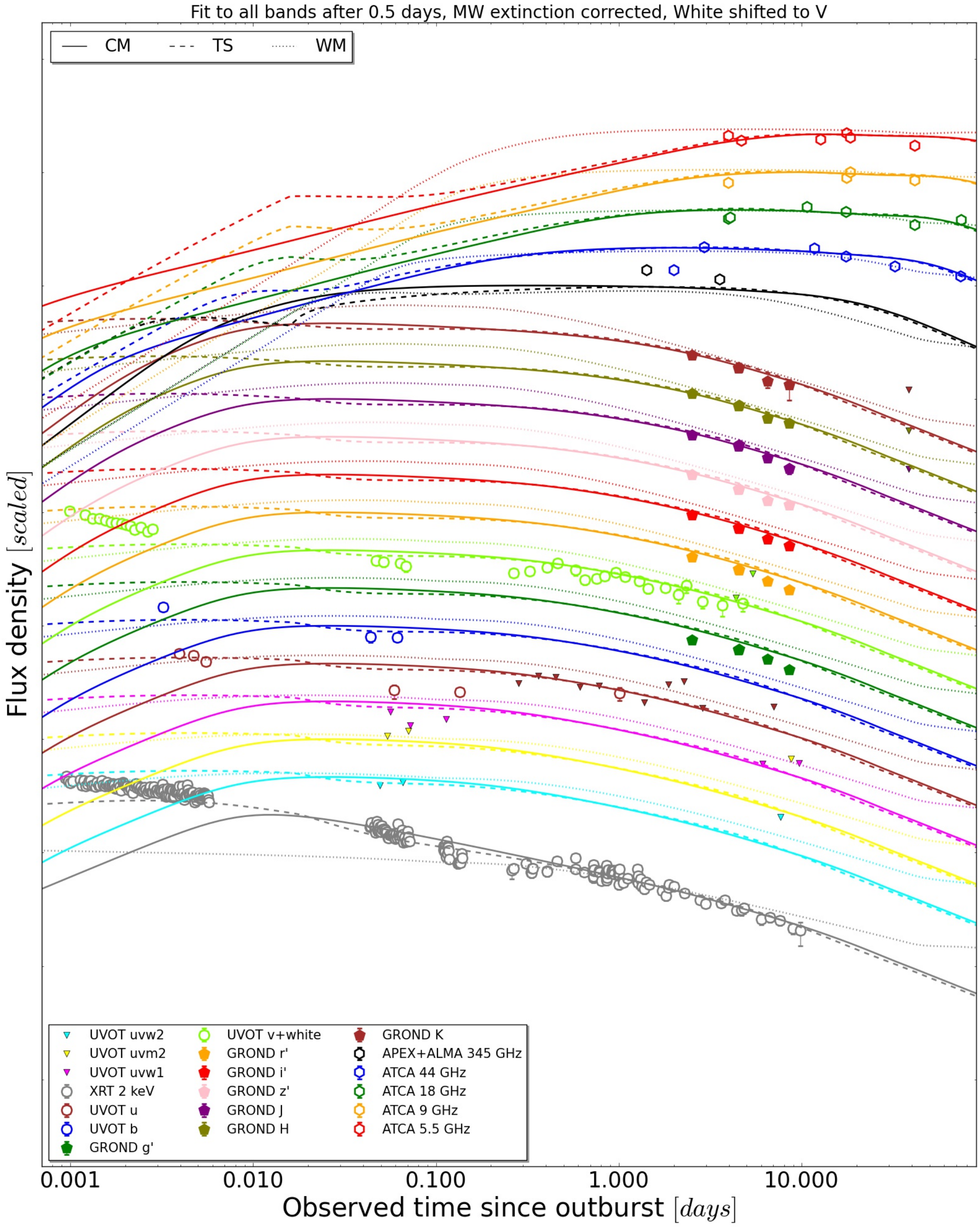
Fit to all bands after 0.5 days, MW extinction corrected, White shifted to V
CM
TS
WM
Flux density [scaled]
Observed time since outburst [days]
0.001
0.010
0.100
1.000
10.000
UVOT uvw2
UVOT uvm2
UVOT uvw1
XRT 2 keV
UVOT u
UVOT b
GROND g'
UVOT v+white
GROND r'
GROND i'
GROND z'
GROND J
GROND H
GROND K
APEX+ALMA 345 GHz
ATCA 44 GHz
ATCA 18 GHz
ATCA 9 GHz
ATCA 5.5 GHz

Appendix D

Spectral Energy Distributions

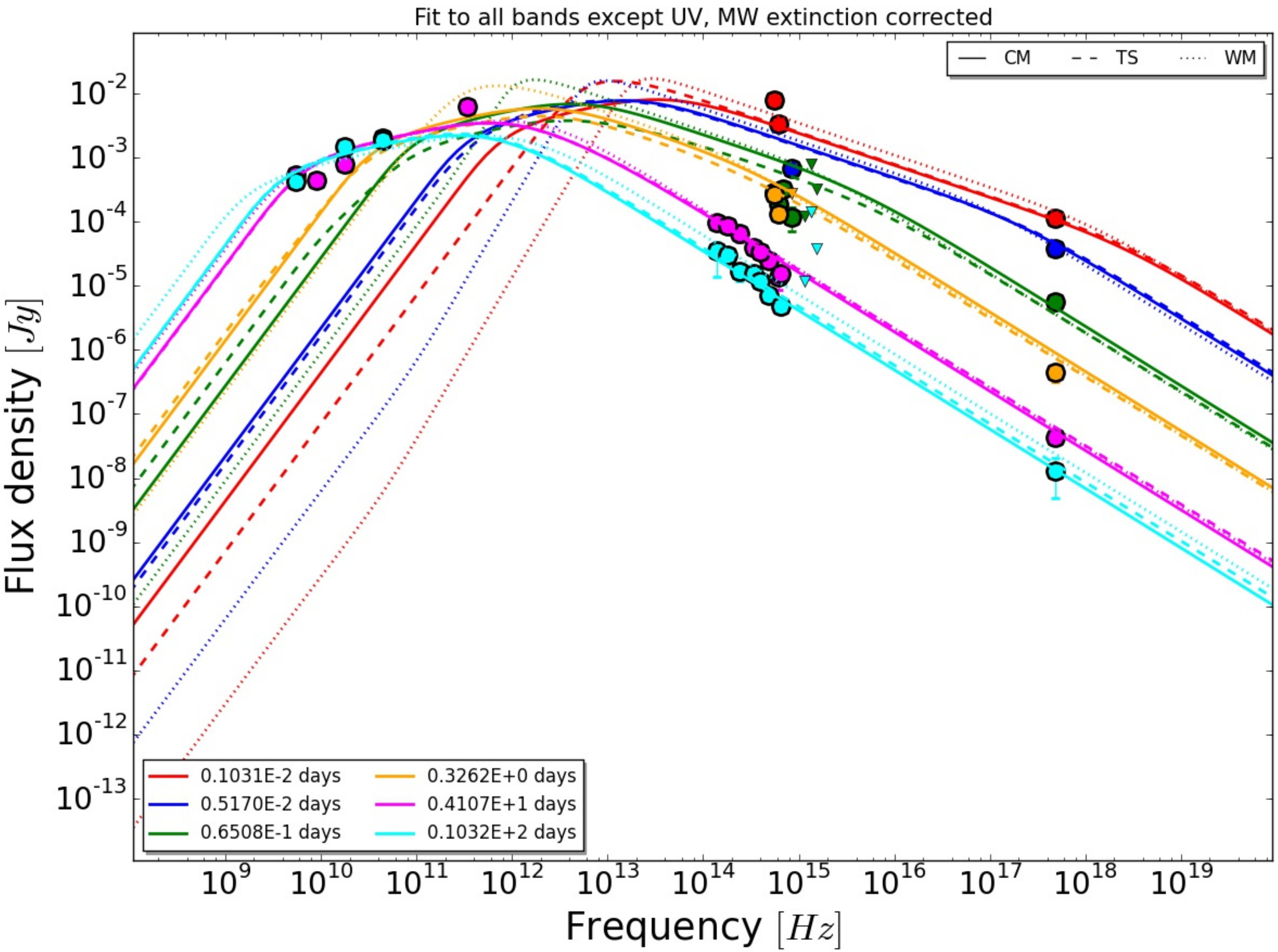
Fit to all bands except UV, MW extinction corrected
CM
TS
WM
Flux density $[Jy]$
10^{-2}
10^{-3}
10^{-4}
10^{-5}
10^{-6}
10^{-7}
10^{-8}
10^{-9}
10^{-10}
10^{-11}
10^{-12}
10^{-13}
0.1031E-2 days
0.5170E-2 days
0.6508E-1 days
0.3262E+0 days
0.4107E+1 days
0.1032E+2 days
10^{9}
10^{10}
10^{11}
10^{12}
10^{13}
10^{14}
10^{15}
10^{16}
10^{17}
10^{18}
10^{19}
Frequency $[Hz]$

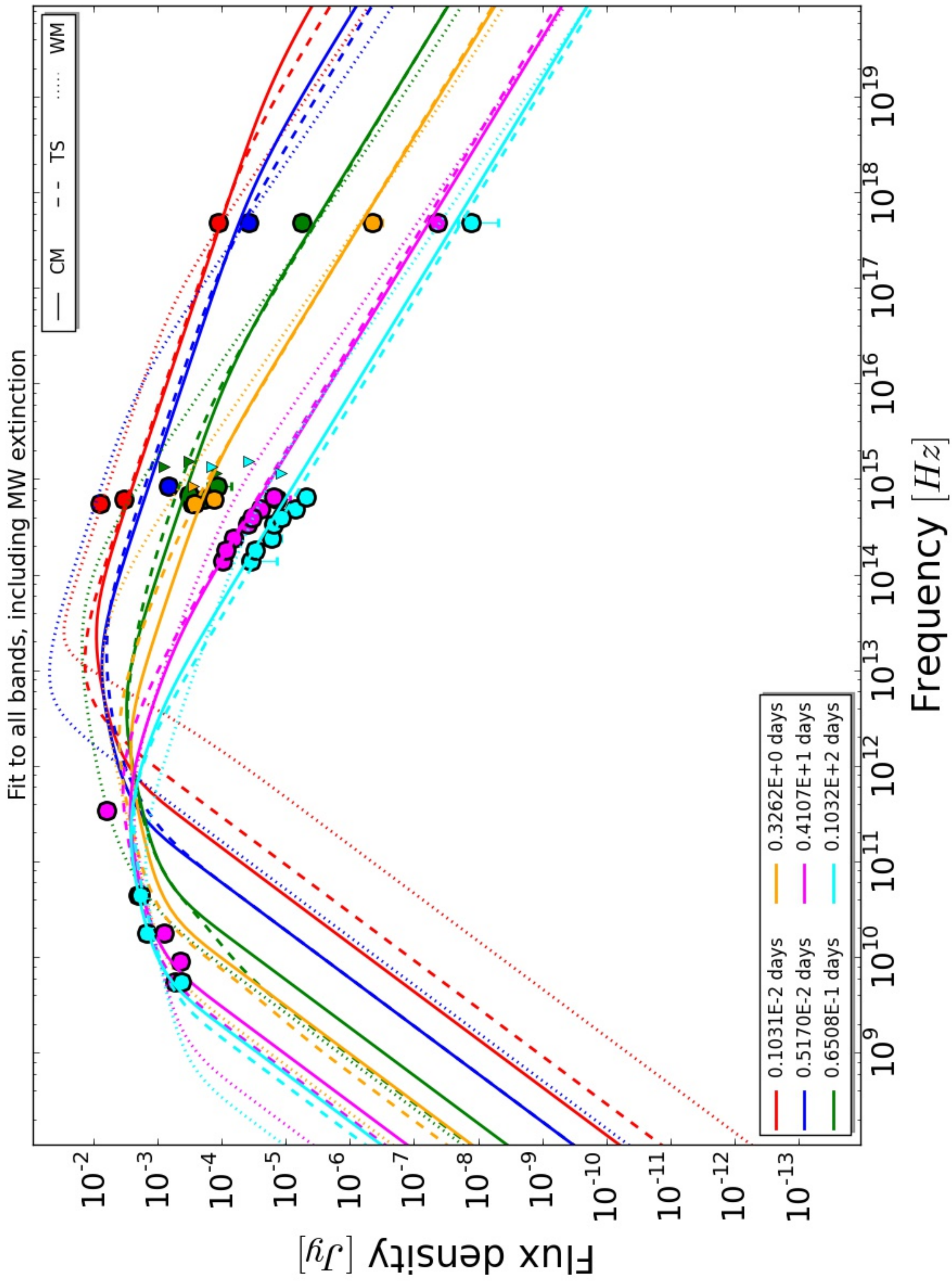
Fit to all bands, including MW extinction
CM
TS
WM
0.1031E-2 days
0.5170E-2 days
0.6508E-1 days
0.3262E+0 days
0.4107E+1 days
0.1032E+2 days
Frequency [Hz]
Flux density [Jy]
10^{9}
10^{10}
10^{11}
10^{12}
10^{13}
10^{14}
10^{15}
10^{16}
10^{17}
10^{18}
10^{19}
10^{-2}
10^{-3}
10^{-4}
10^{-5}
10^{-6}
10^{-7}
10^{-8}
10^{-9}
10^{-10}
10^{-11}
10^{-12}
10^{-13}

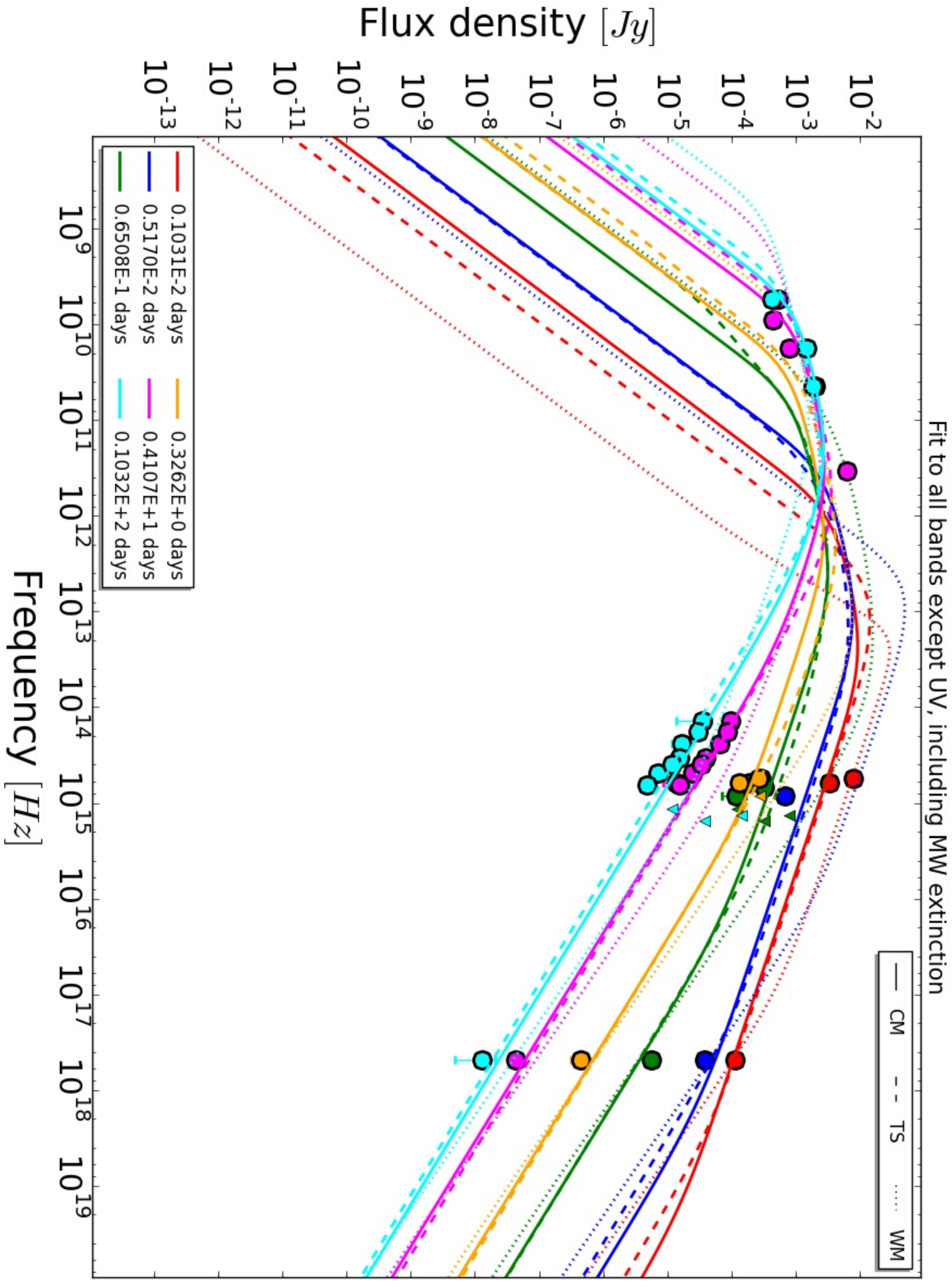
Fit to all bands except UV, including MW extinction
Flux density [Jy]
10^-2
10^-3
10^-4
10^-5
10^-6
10^-7
10^-8
10^-9
10^-10
10^-11
10^-12
10^-13
Frequency [Hz]
10^9
10^10
10^11
10^12
10^13
10^14
10^15
10^16
10^17
10^18
10^19
— CM
-- TS
···· WM
0.1031E-2 days
0.5170E-2 days
0.6508E-1 days
0.3262E+0 days
0.4107E+1 days
0.1032E+2 days

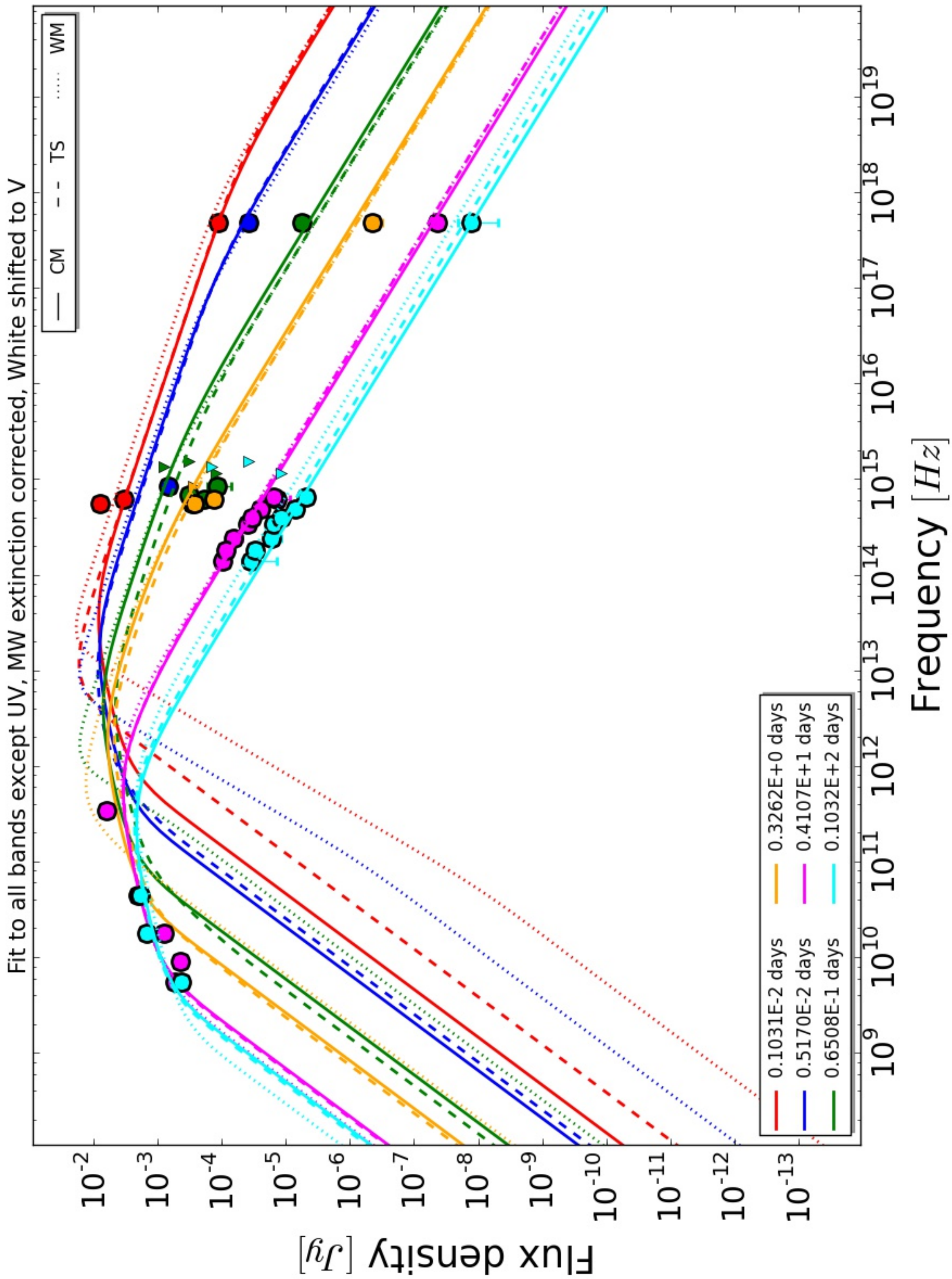
Fit to all bands except UV, MW extinction corrected, White shifted to V
— CM
- - TS
····· WM
0.1031E-2 days
0.5170E-2 days
0.6508E-1 days
0.3262E+0 days
0.4107E+1 days
0.1032E+2 days
Flux density [Jy]
Frequency [Hz]
10^-2
10^-3
10^-4
10^-5
10^-6
10^-7
10^-8
10^-9
10^-10
10^-11
10^-12
10^-13
10^9
10^10
10^11
10^12
10^13
10^14
10^15
10^16
10^17
10^18
10^19

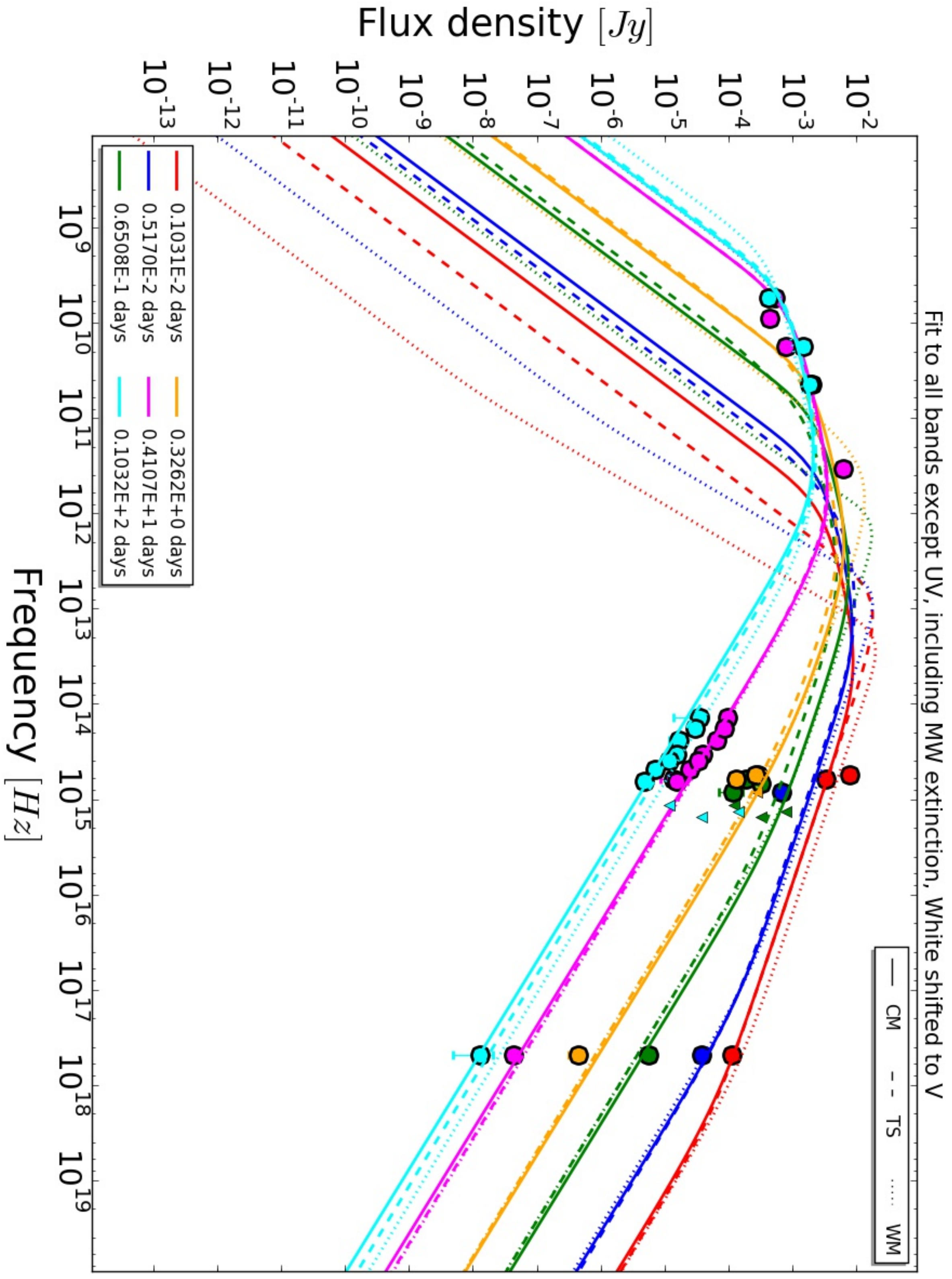
Fit to all bands except UV, including MW extinction, White shifted to V
Flux density $[Jy]$
10^{-2}
10^{-3}
10^{-4}
10^{-5}
10^{-6}
10^{-7}
10^{-8}
10^{-9}
10^{-10}
10^{-11}
10^{-12}
10^{-13}
Frequency $[Hz]$
10^{9}
10^{10}
10^{11}
10^{12}
10^{13}
10^{14}
10^{15}
10^{16}
10^{17}
10^{18}
10^{19}
0.1031E-2 days
0.5170E-2 days
0.6508E-1 days
0.3262E+0 days
0.4107E+1 days
0.1032E+2 days
— CM
-- TS
···· WM

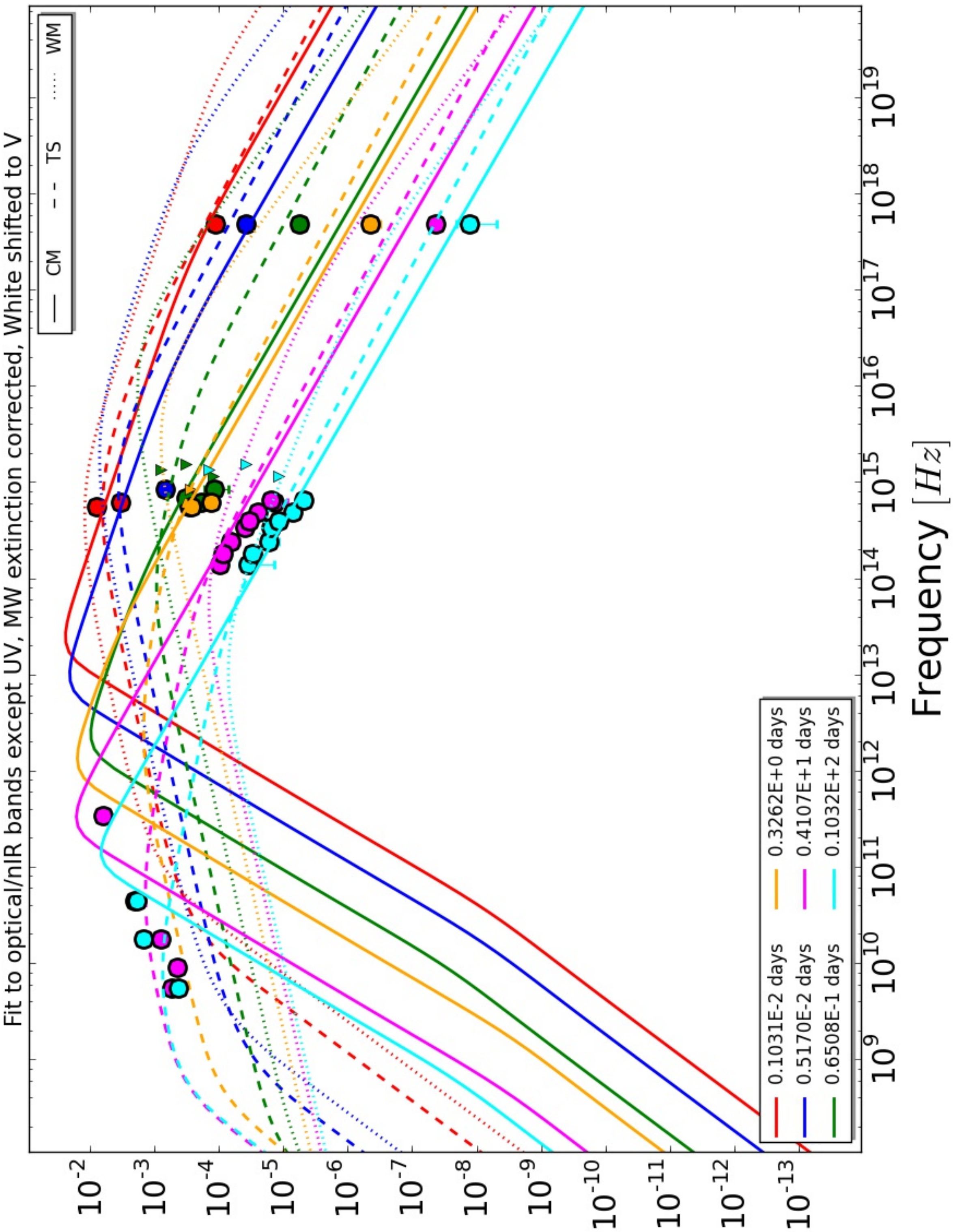
Fit to optical/nIR bands except UV, MW extinction corrected, White shifted to V
CM
TS
WM
0.1031E-2 days
0.5170E-2 days
0.6508E-1 days
0.3262E+0 days
0.4107E+1 days
0.1032E+2 days
Frequency [Hz]
Flux density [Jy]
10^9
10^10
10^11
10^12
10^13
10^14
10^15
10^16
10^17
10^18
10^19
10^-2
10^-3
10^-4
10^-5
10^-6
10^-7
10^-8
10^-9
10^-10
10^-11
10^-12
10^-13

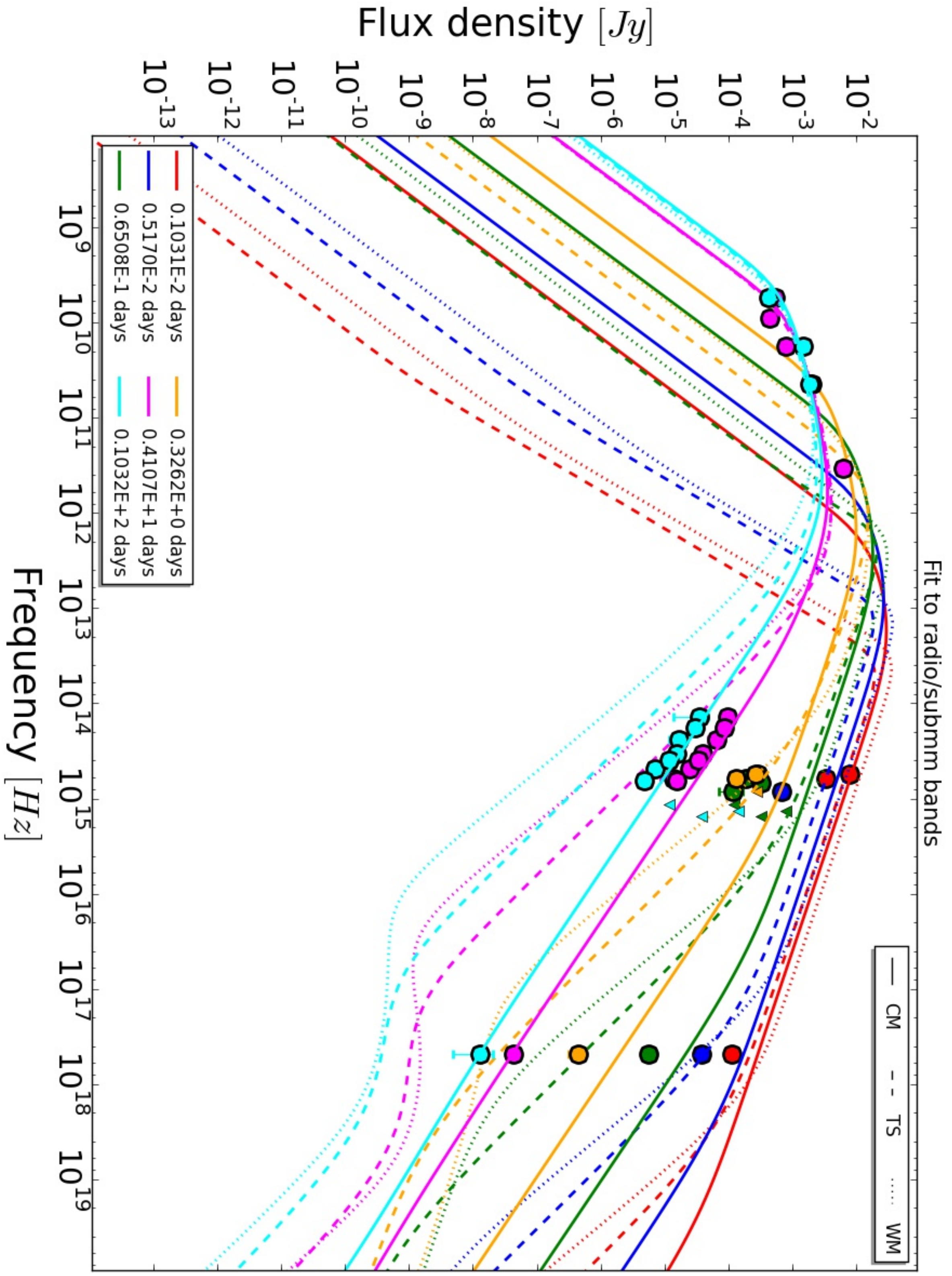
Fit to radio/submm bands
Flux density [Jy]
Frequency [Hz]
10^-13
10^-12
10^-11
10^-10
10^-9
10^-8
10^-7
10^-6
10^-5
10^-4
10^-3
10^-2
10^9
10^10
10^11
10^12
10^13
10^14
10^15
10^16
10^17
10^18
10^19
0.1031E-2 days
0.5170E-2 days
0.6508E-1 days
0.3262E+0 days
0.4107E+1 days
0.1032E+2 days
CM
TS
WM

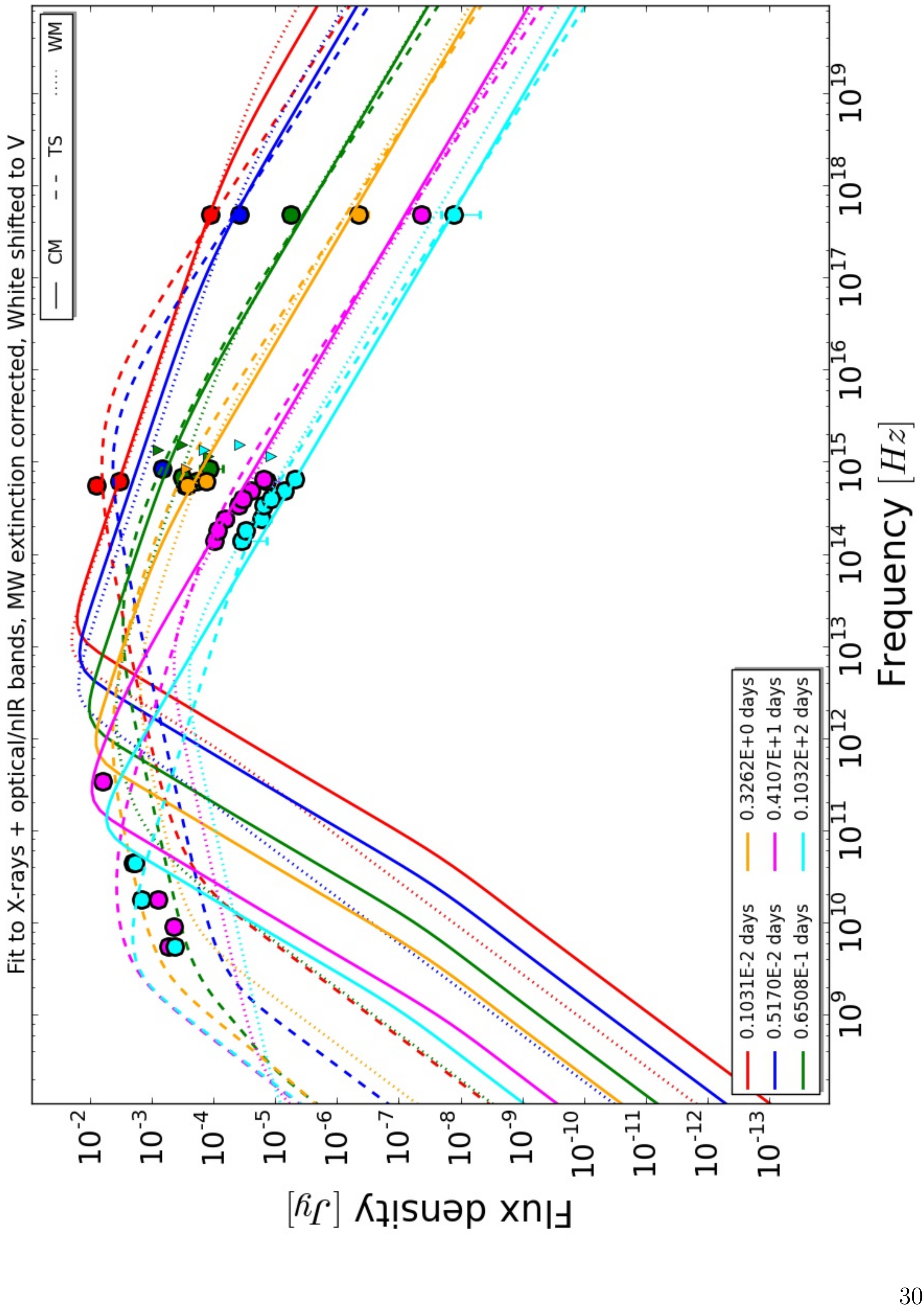
Fit to X-rays + optical/nIR bands, MW extinction corrected, White shifted to V
CM
TS
WM
0.1031E-2 days
0.5170E-2 days
0.6508E-1 days
0.3262E+0 days
0.4107E+1 days
0.1032E+2 days
Frequency [Hz]
Flux density [Jy]
10^{9}
10^{10}
10^{11}
10^{12}
10^{13}
10^{14}
10^{15}
10^{16}
10^{17}
10^{18}
10^{19}
10^{-2}
10^{-3}
10^{-4}
10^{-5}
10^{-6}
10^{-7}
10^{-8}
10^{-9}
10^{-10}
10^{-11}
10^{-12}
10^{-13}

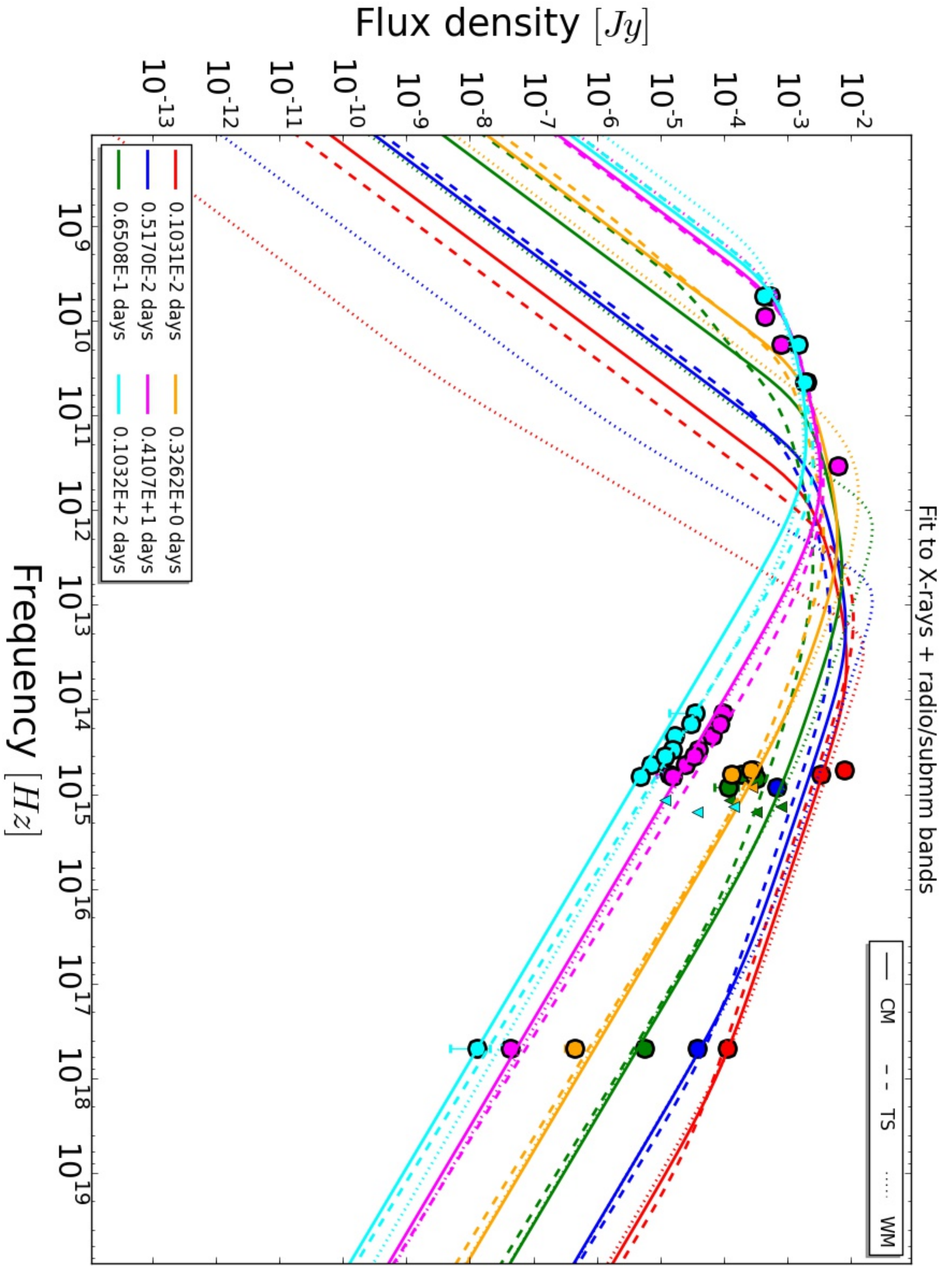
Fit to X-rays + radio/submm bands
Flux density $[Jy]$
Frequency $[Hz]$
10^{-13}
10^{-12}
10^{-11}
10^{-10}
10^{-9}
10^{-8}
10^{-7}
10^{-6}
10^{-5}
10^{-4}
10^{-3}
10^{-2}
10^{9}
10^{10}
10^{11}
10^{12}
10^{13}
10^{14}
10^{15}
10^{16}
10^{17}
10^{18}
10^{19}
0.1031E-2 days
0.5170E-2 days
0.6508E-1 days
0.3262E+0 days
0.4107E+1 days
0.1032E+2 days
CM
TS
WM

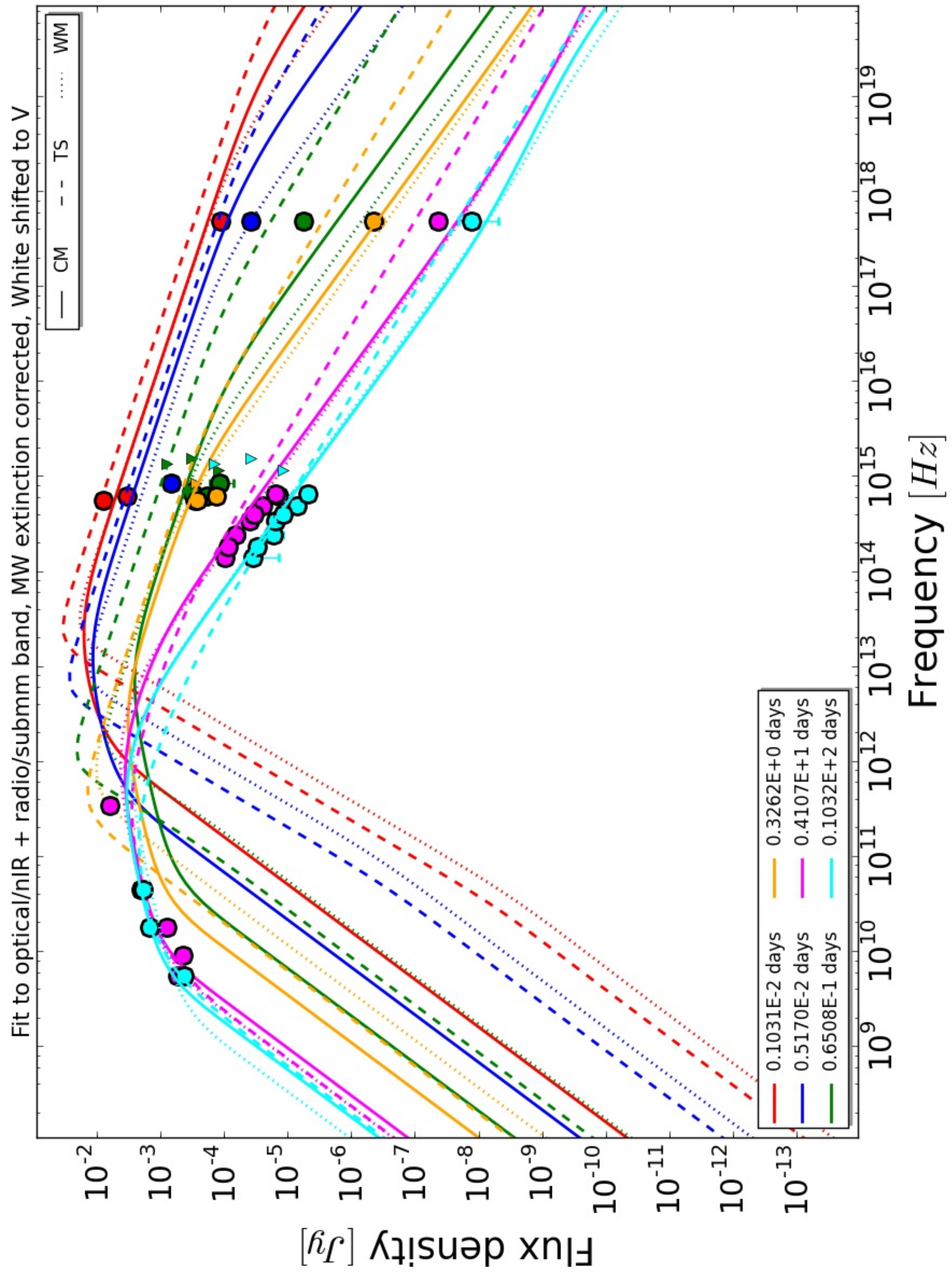
Fit to optical/nIR + radio/submm band, MW extinction corrected, White shifted to V
CM
TS
WM
0.1031E-2 days
0.5170E-2 days
0.6508E-1 days
0.3262E+0 days
0.4107E+1 days
0.1032E+2 days
Flux density $[Jy]$
Frequency $[Hz]$
10^{-2}
10^{-3}
10^{-4}
10^{-5}
10^{-6}
10^{-7}
10^{-8}
10^{-9}
10^{-10}
10^{-11}
10^{-12}
10^{-13}
10^{9}
10^{10}
10^{11}
10^{12}
10^{13}
10^{14}
10^{15}
10^{16}
10^{17}
10^{18}
10^{19}

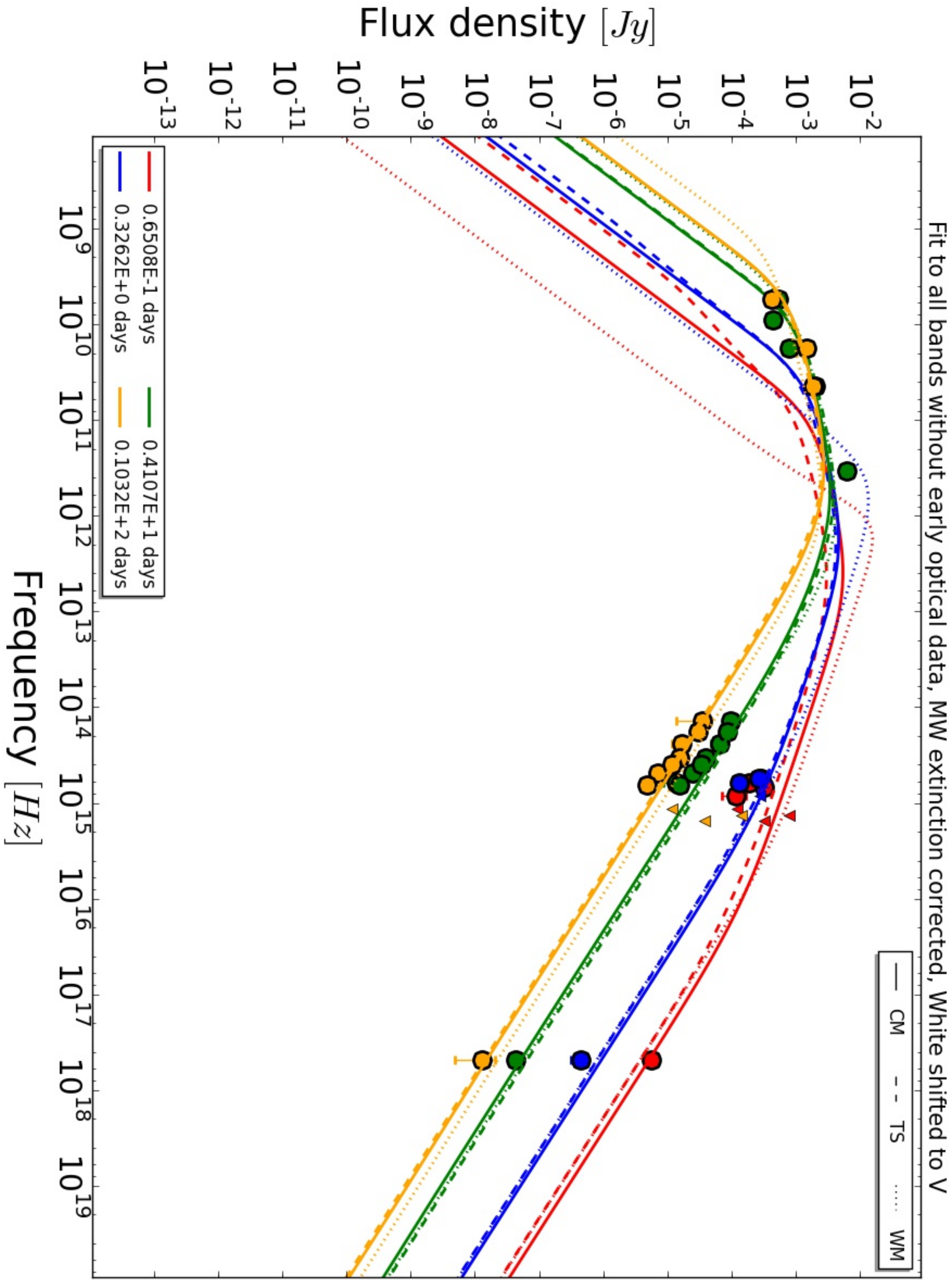
Fit to all bands without early optical data, MW extinction corrected, White shifted to V
Flux density $[Jy]$
10^{-13}
10^{-12}
10^{-11}
10^{-10}
10^{-9}
10^{-8}
10^{-7}
10^{-6}
10^{-5}
10^{-4}
10^{-3}
10^{-2}
Frequency $[Hz]$
10^{9}
10^{10}
10^{11}
10^{12}
10^{13}
10^{14}
10^{15}
10^{16}
10^{17}
10^{18}
10^{19}
0.6508E-1 days
0.3262E+0 days
0.4107E+1 days
0.1032E+2 days
— CM
- - TS
···· WM

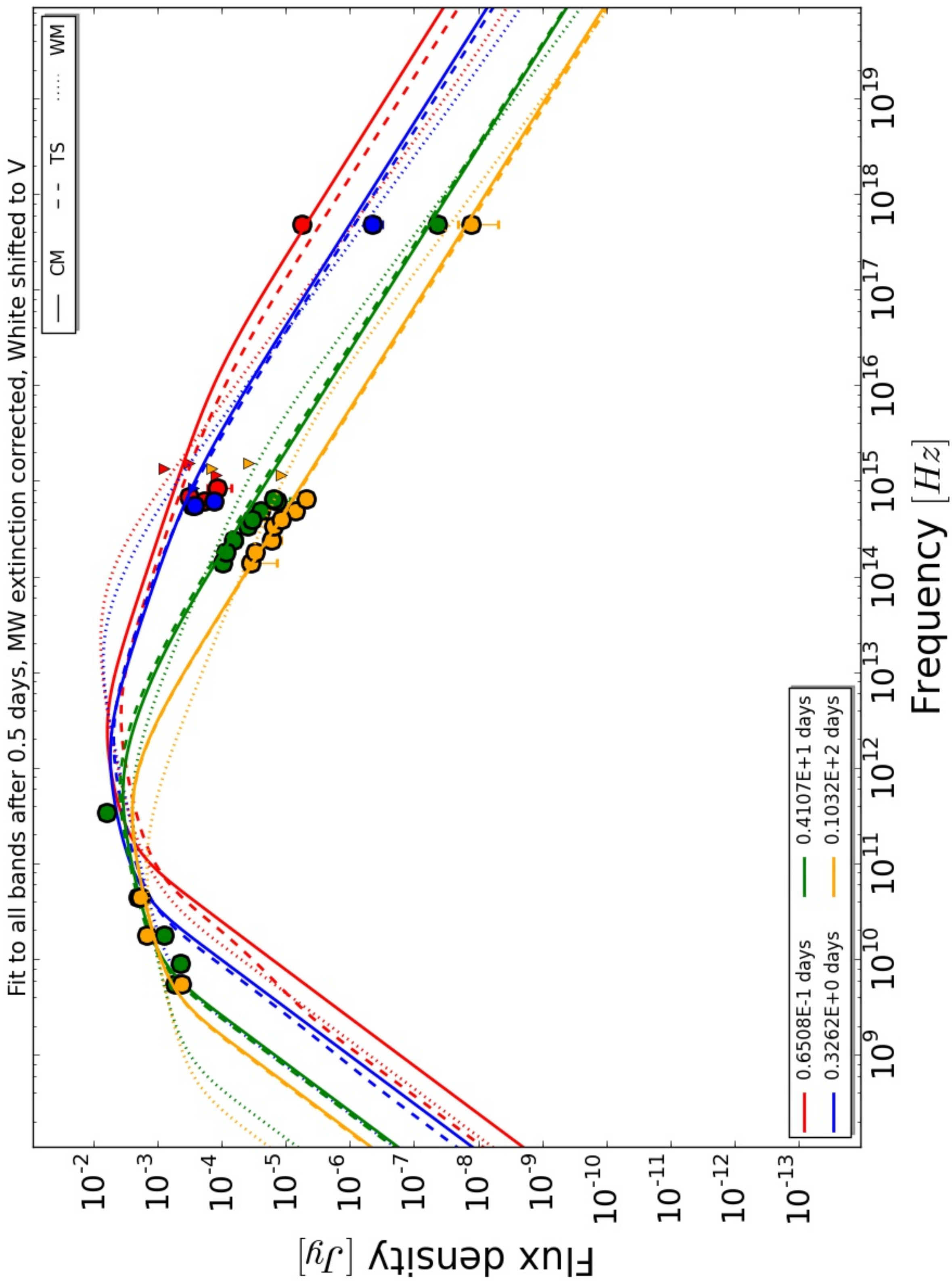
Fit to all bands after 0.5 days, MW extinction corrected, White shifted to V
CM
TS
WM
0.6508E-1 days
0.3262E+0 days
0.4107E+1 days
0.1032E+2 days
Flux density $[Jy]$
Frequency $[Hz]$
10^{-2}
10^{-3}
10^{-4}
10^{-5}
10^{-6}
10^{-7}
10^{-8}
10^{-9}
10^{-10}
10^{-11}
10^{-12}
10^{-13}
10^{9}
10^{10}
10^{11}
10^{12}
10^{13}
10^{14}
10^{15}
10^{16}
10^{17}
10^{18}
10^{19}

Appendix E

Marginals 1D

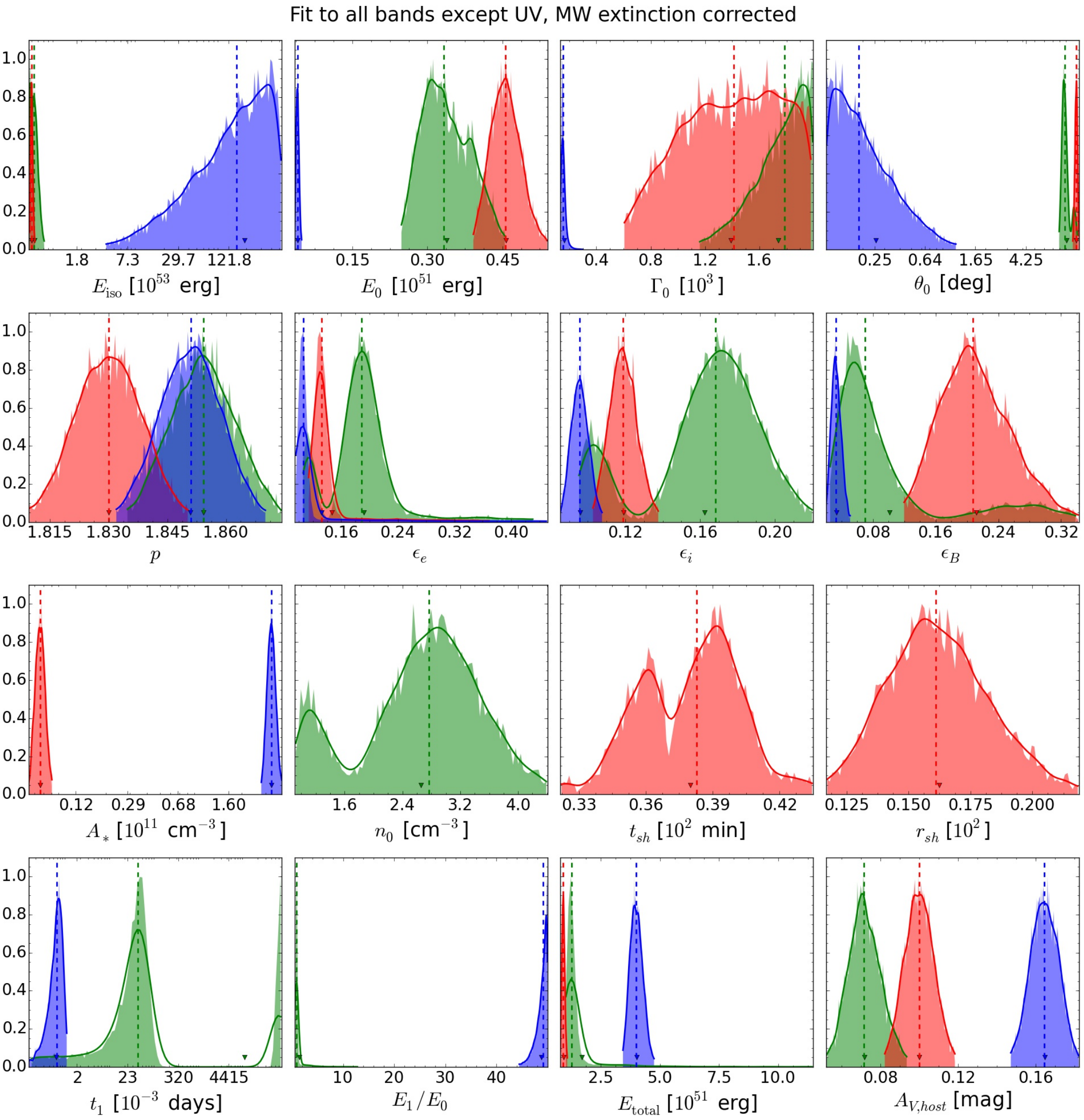
Fit to all bands except UV, MW extinction corrected
1.0
0.8
0.6
0.4
0.2
0.0
1.8
7.3
29.7
121.8
$E_{\rm iso}$ [10^{53} erg]
0.15
0.30
0.45
E_0 [10^{51} erg]
0.4
0.8
1.2
1.6
Γ_0 [10^3]
0.25
0.64
1.65
4.25
θ_0 [deg]
1.815
1.830
1.845
1.860
p
0.16
0.24
0.32
0.40
ϵ_e
0.12
0.16
0.20
ϵ_i
0.08
0.16
0.24
0.32
ϵ_B
0.12
0.29
0.68
1.60
A_* [10^{11} cm^{-3}]
1.6
2.4
3.2
4.0
n_0 [cm^{-3}]
0.33
0.36
0.39
0.42
t_{sh} [10^2 min]
0.125
0.150
0.175
0.200
r_{sh} [10^2]
2
23
320
4415
t_1 [10^{-3} days]
10
20
30
40
E_1/E_0
2.5
5.0
7.5
10.0
$E_{\rm total}$ [10^{51} erg]
0.08
0.12
0.16
$A_{V,host}$ [mag]

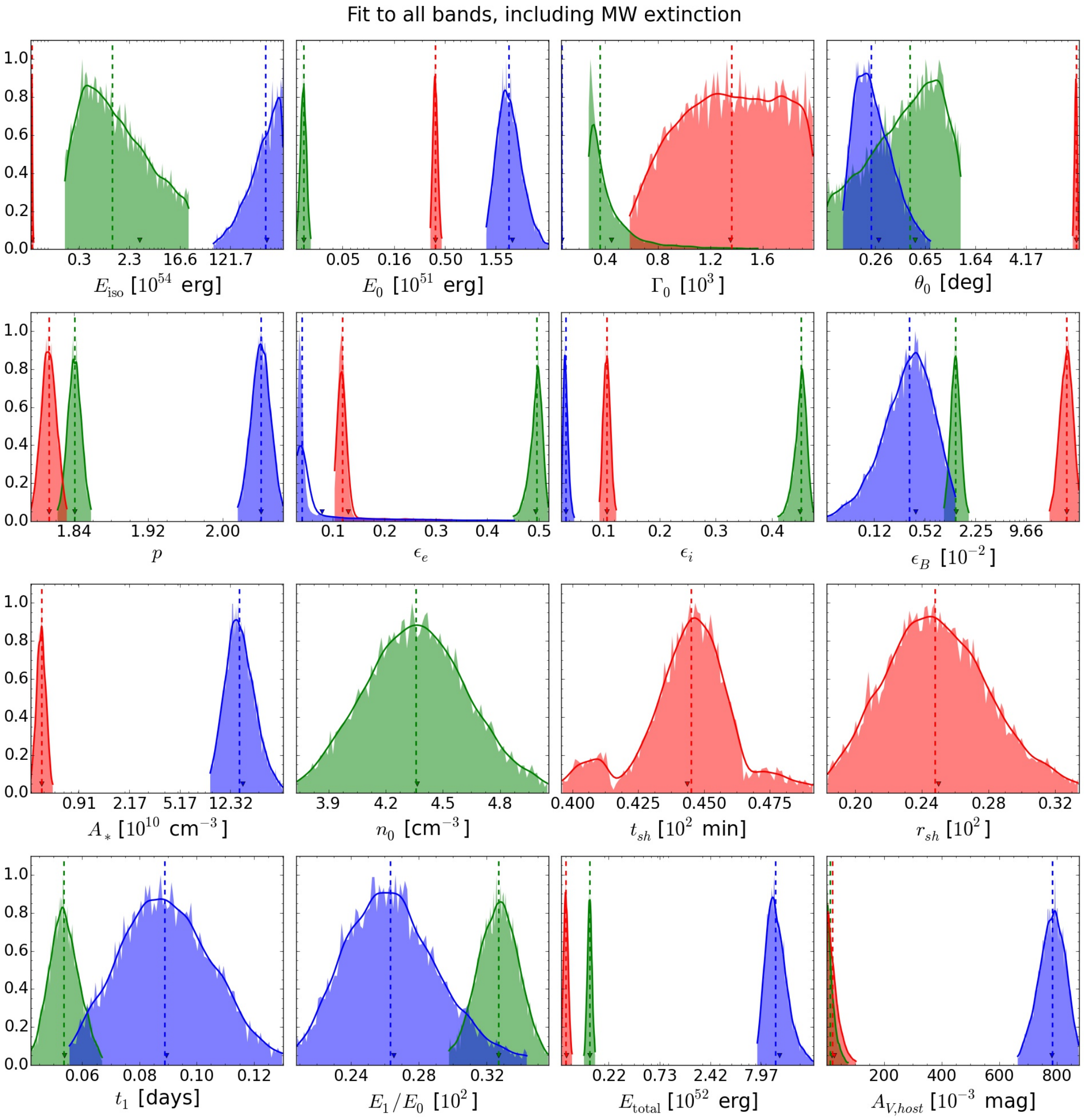
Fit to all bands, including MW extinction
1.0
0.8
0.6
0.4
0.2
0.0
0.3
2.3
16.6
121.7
$E_{\rm iso}$ [10^{54} erg]
0.05
0.16
0.50
1.55
E_0 [10^{51} erg]
0.4
0.8
1.2
1.6
Γ_0 [10^3]
0.26
0.65
1.64
4.17
θ_0 [deg]
1.84
1.92
2.00
p
0.1
0.2
0.3
0.4
0.5
ϵ_e
0.1
0.2
0.3
0.4
ϵ_i
0.12
0.52
2.25
9.66
ϵ_B [10^{-2}]
0.91
2.17
5.17
12.32
A_* [10^{10} cm^{-3}]
3.9
4.2
4.5
4.8
n_0 [cm^{-3}]
0.400
0.425
0.450
0.475
t_{sh} [10^2 min]
0.20
0.24
0.28
0.32
r_{sh} [10^2]
0.06
0.08
0.10
0.12
t_1 [days]
0.24
0.28
0.32
E_1/E_0 [10^2]
0.22
0.73
2.42
7.97
$E_{\rm total}$ [10^{52} erg]
200
400
600
800
$A_{V,host}$ [10^{-3} mag]

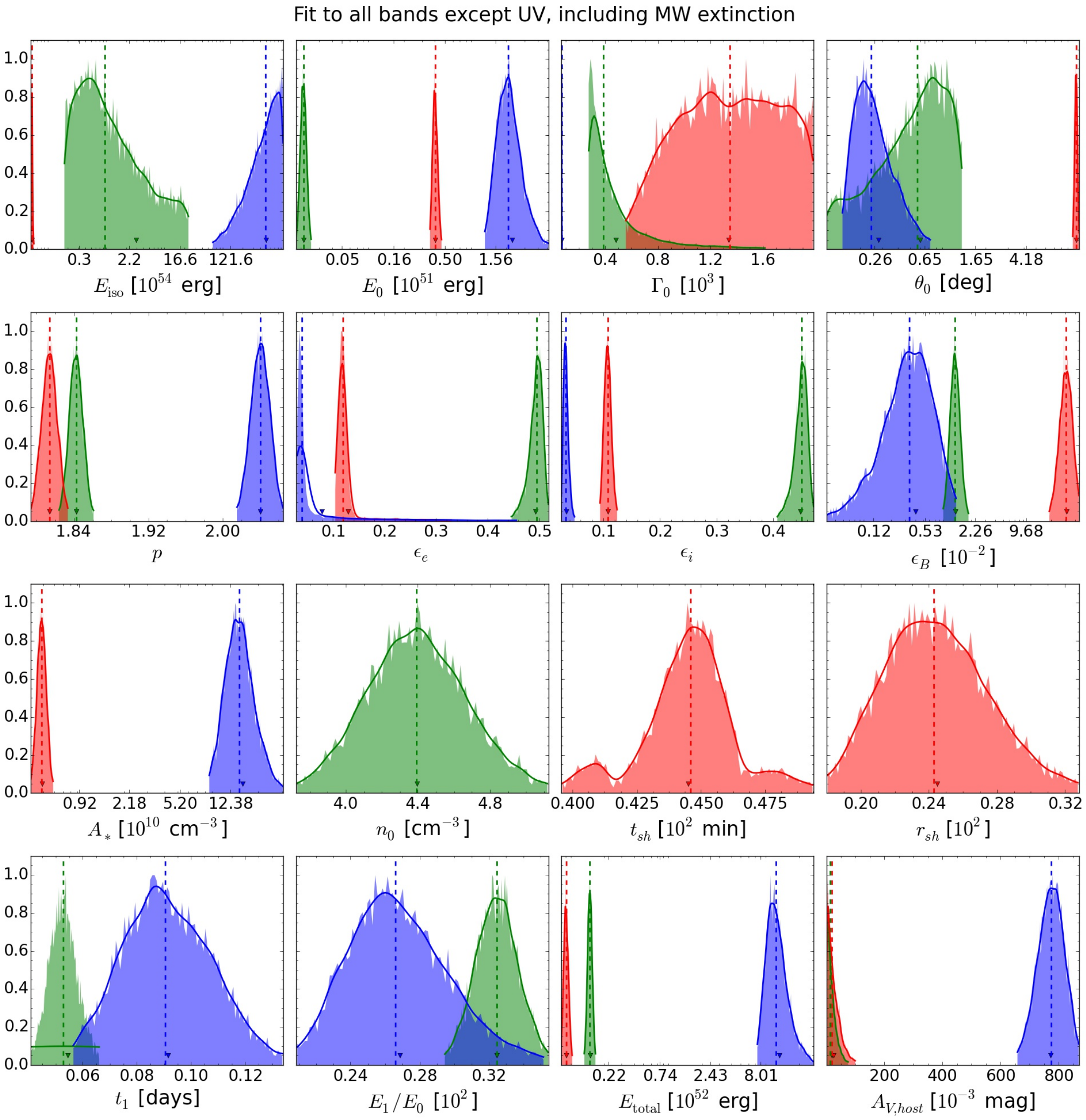
Fit to all bands except UV, including MW extinction
0.0
0.2
0.4
0.6
0.8
1.0
0.3
2.2
16.6
121.6
$E_{\rm iso}$ [10^{54} erg]
0.05
0.16
0.50
1.56
E_0 [10^{51} erg]
0.4
0.8
1.2
1.6
Γ_0 [10^3]
0.26
0.65
1.65
4.18
θ_0 [deg]
1.84
1.92
2.00
p
0.1
0.2
0.3
0.4
0.5
ϵ_e
0.1
0.2
0.3
0.4
ϵ_i
0.12
0.53
2.26
9.68
ϵ_B [10^{-2}]
0.92
2.18
5.20
12.38
A_* [10^{10} cm^{-3}]
4.0
4.4
4.8
n_0 [cm^{-3}]
0.400
0.425
0.450
0.475
t_{sh} [10^2 min]
0.20
0.24
0.28
0.32
r_{sh} [10^2]
0.06
0.08
0.10
0.12
t_1 [days]
0.24
0.28
0.32
E_1/E_0 [10^2]
0.22
0.74
2.43
8.01
$E_{\rm total}$ [10^{52} erg]
200
400
600
800
$A_{V,host}$ [10^{-3} mag]

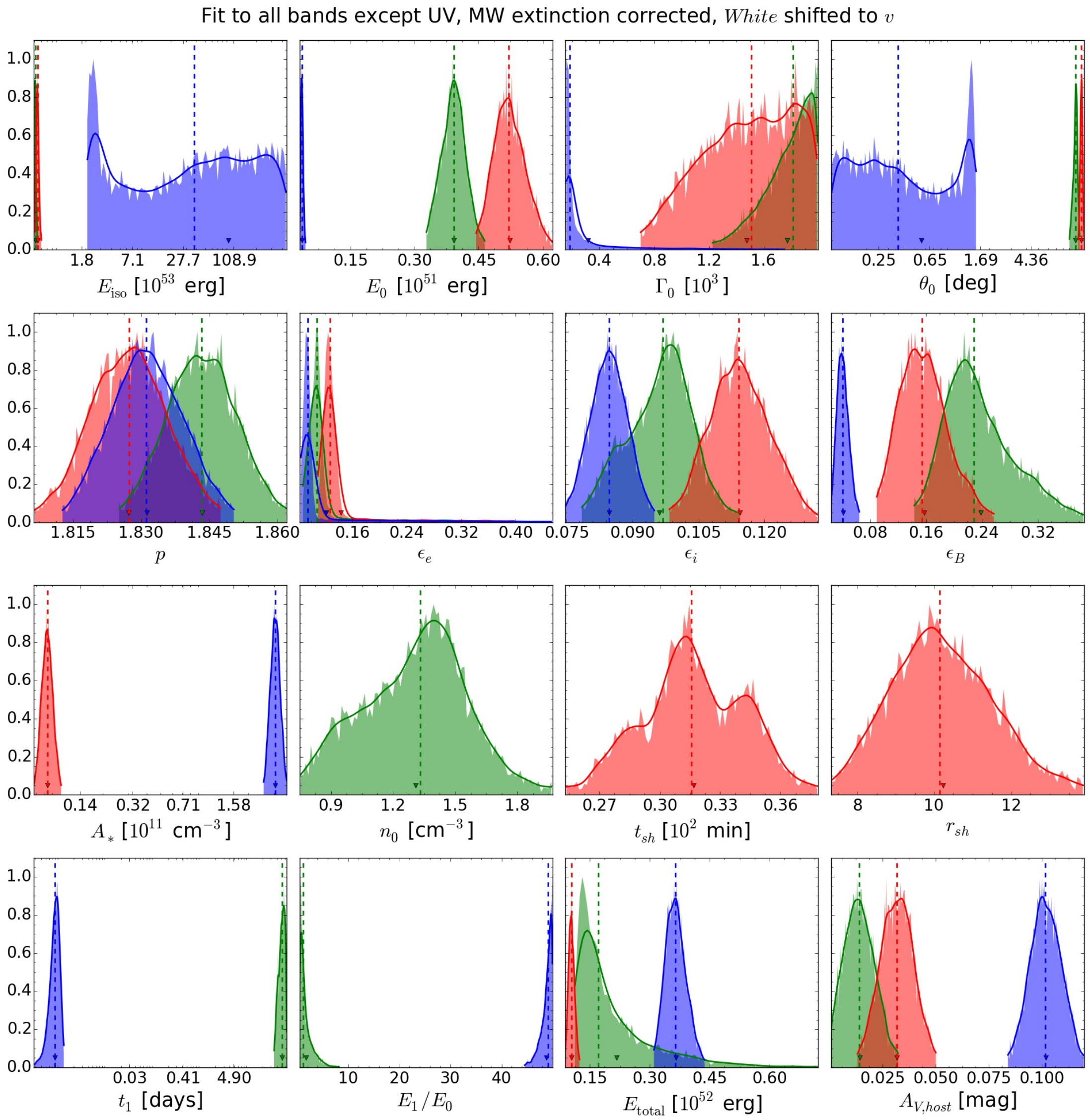
Fit to all bands except UV, MW extinction corrected, $White$ shifted to v

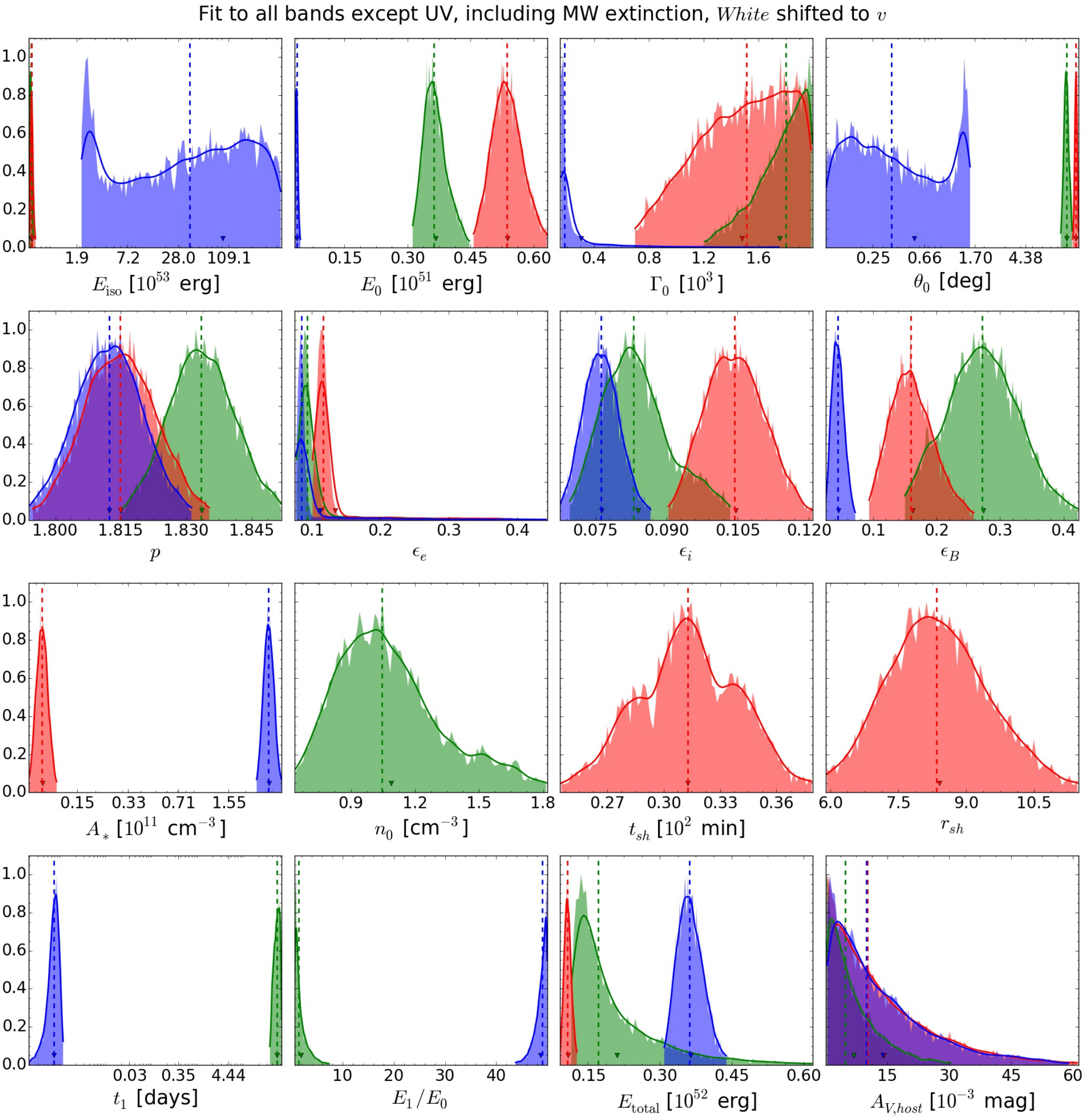
Fit to all bands except UV, including MW extinction, $White$ shifted to v
1.0
0.8
0.6
0.4
0.2
0.0
1.9
7.2
28.0
109.1
$E_{\rm iso}$ [10^{53} erg]
0.15
0.30
0.45
0.60
E_0 [10^{51} erg]
0.4
0.8
1.2
1.6
Γ_0 [10^3]
0.25
0.66
1.70
4.38
θ_0 [deg]
1.800
1.815
1.830
1.845
p
0.1
0.2
0.3
0.4
ϵ_e
0.075
0.090
0.105
0.120
ϵ_i
0.1
0.2
0.3
0.4
ϵ_B
0.15
0.33
0.71
1.55
A_* [10^{11} cm^{-3}]
0.9
1.2
1.5
1.8
n_0 [cm^{-3}]
0.27
0.30
0.33
0.36
t_{sh} [10^2 min]
6.0
7.5
9.0
10.5
r_{sh}
0.03
0.35
4.44
t_1 [days]
10
20
30
40
E_1/E_0
0.15
0.30
0.45
0.60
$E_{\rm total}$ [10^{52} erg]
15
30
45
60
$A_{V,host}$ [10^{-3} mag]

Fit to optical/nIR bands except UV, MW extinction corrected, *White* shifted to v

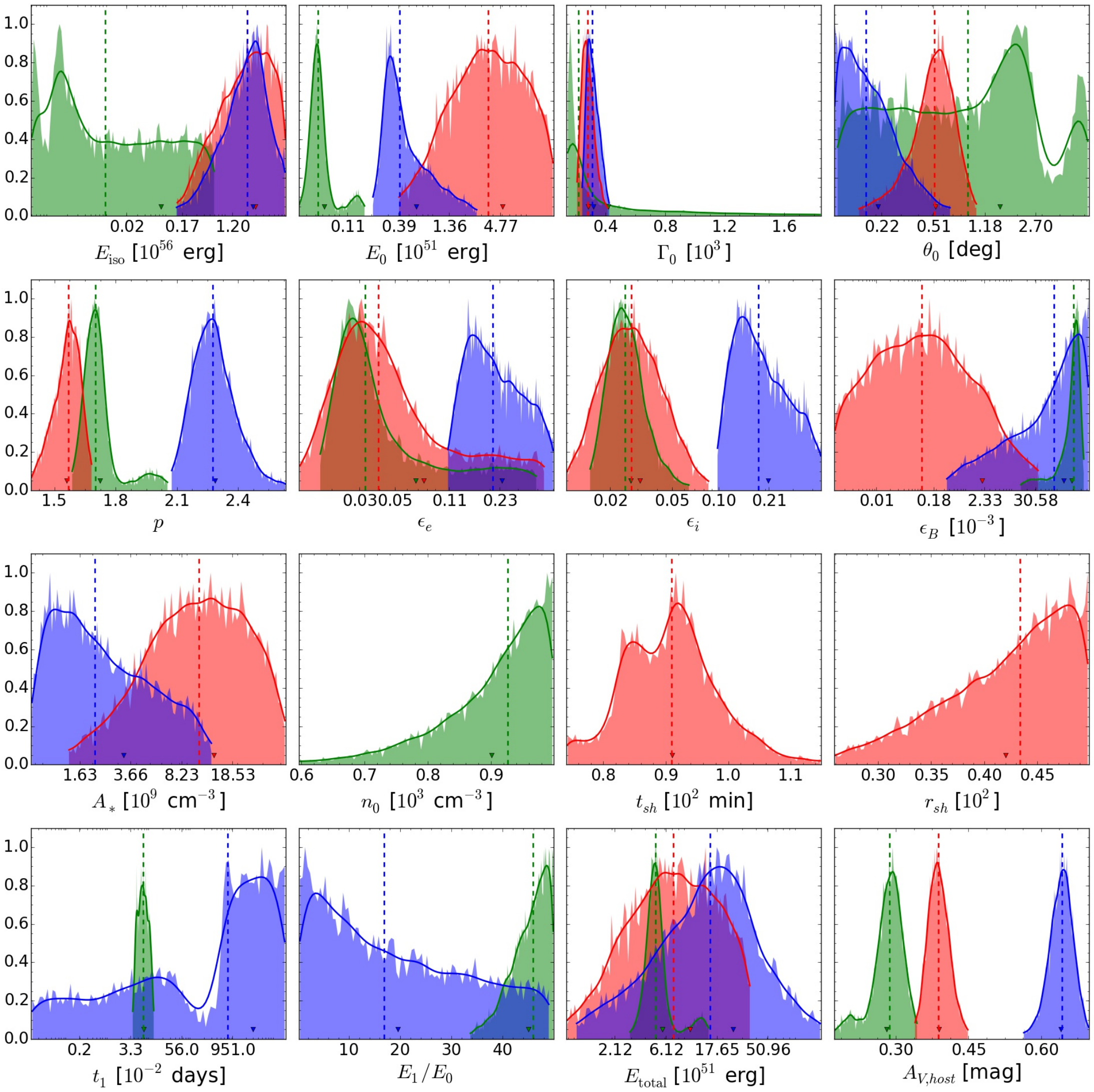

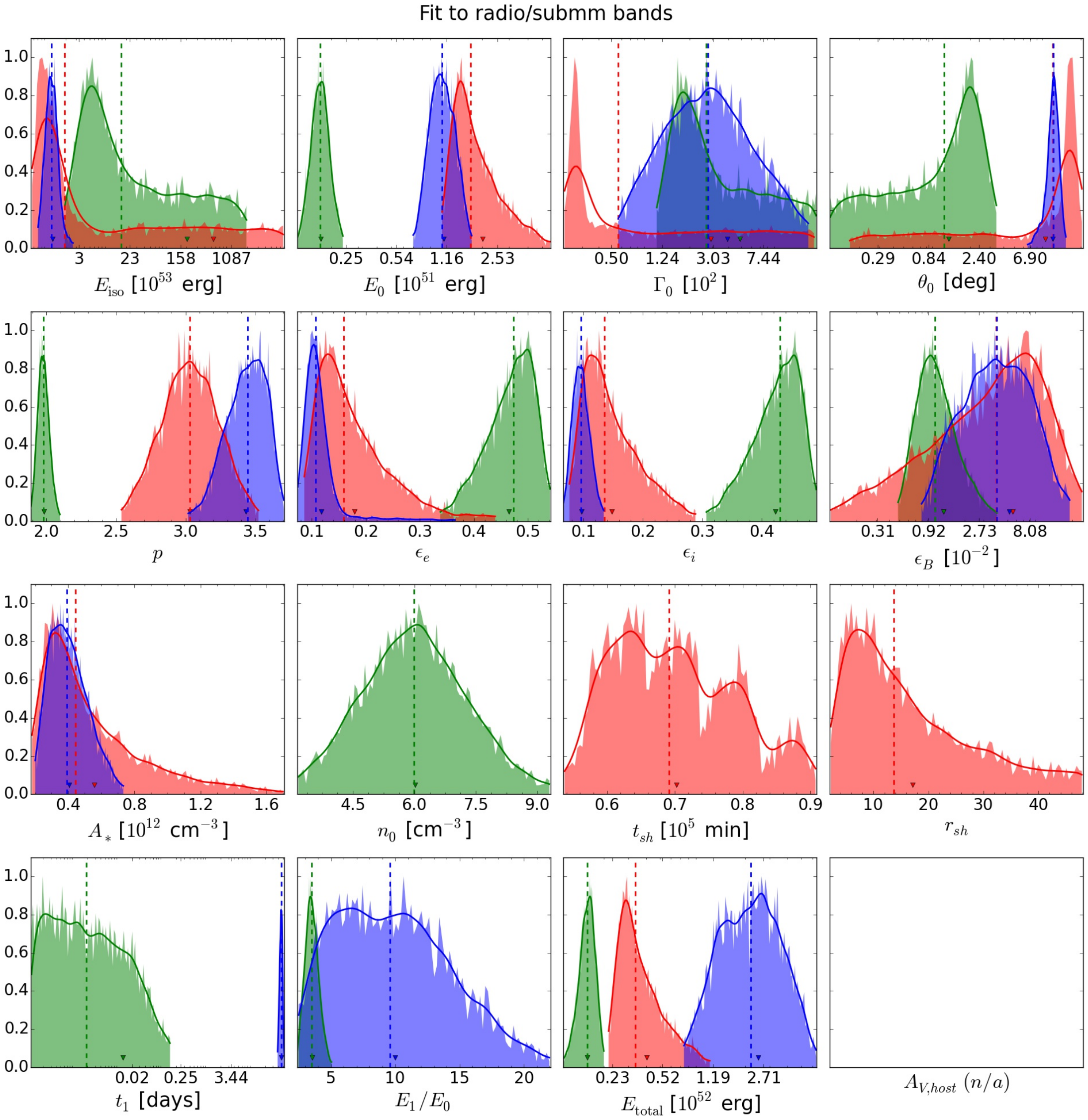
Fit to radio/submm bands
1.0
0.8
0.6
0.4
0.2
0.0
3
23
158
1087
E_{iso} [10^{53} erg]
0.25
0.54
1.16
2.53
E_0 [10^{51} erg]
0.50
1.24
3.03
7.44
Γ_0 [10^2]
0.29
0.84
2.40
6.90
θ_0 [deg]
2.0
2.5
3.0
3.5
p
0.1
0.2
0.3
0.4
0.5
ϵ_e
0.1
0.2
0.3
0.4
ϵ_i
0.31
0.92
2.73
8.08
ϵ_B [10^{-2}]
0.4
0.8
1.2
1.6
A_* [10^{12} cm^{-3}]
4.5
6.0
7.5
9.0
n_0 [cm^{-3}]
0.6
0.7
0.8
0.9
t_{sh} [10^5 min]
10
20
30
40
r_{sh}
0.02
0.25
3.44
t_1 [days]
5
10
15
20
E_1/E_0
0.23
0.52
1.19
2.71
E_{total} [10^{52} erg]
$A_{V,host}$ (n/a)

Fit to X-rays + optical/nIR bands, MW extinction corrected, $White$ shifted to v

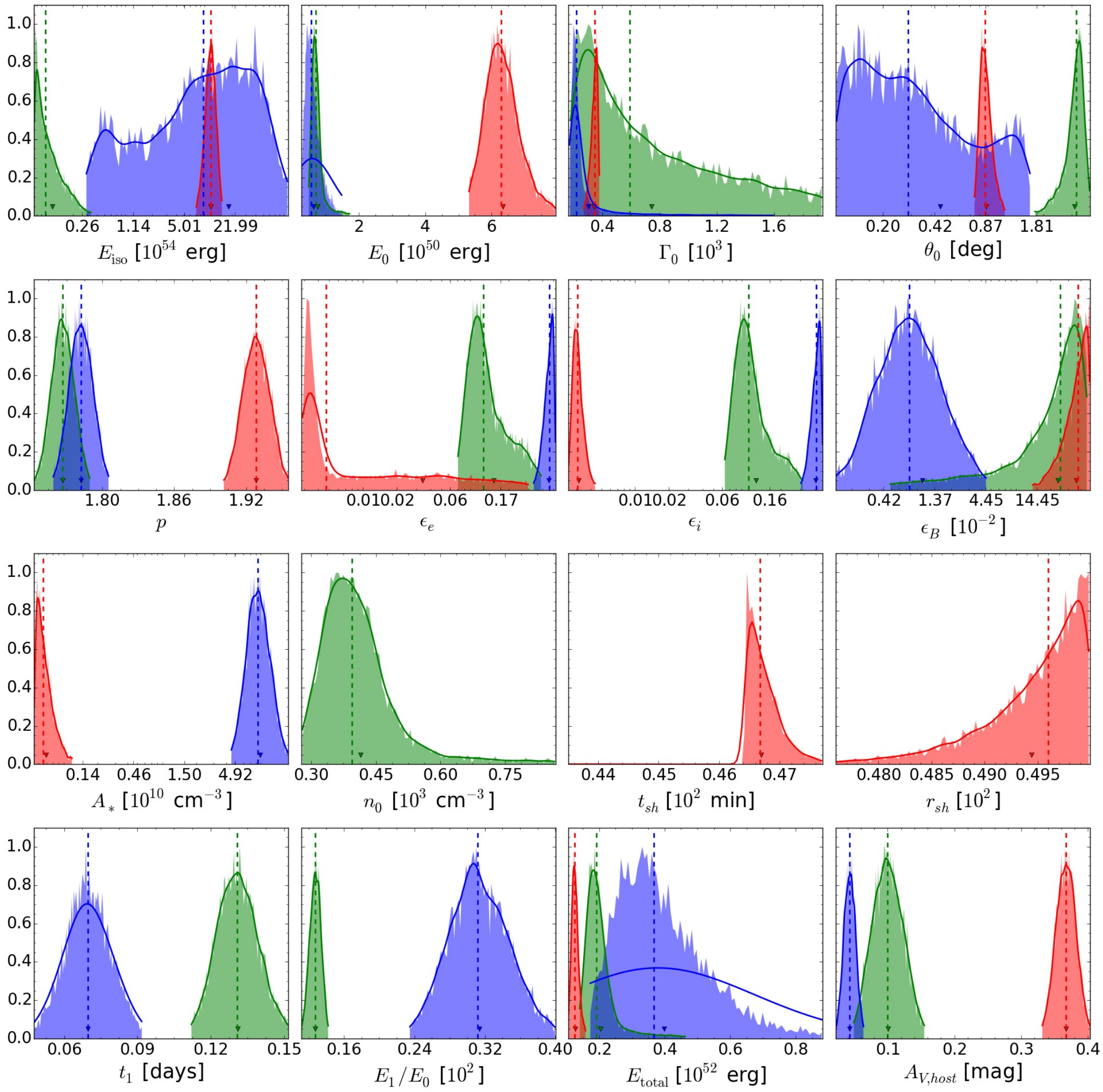

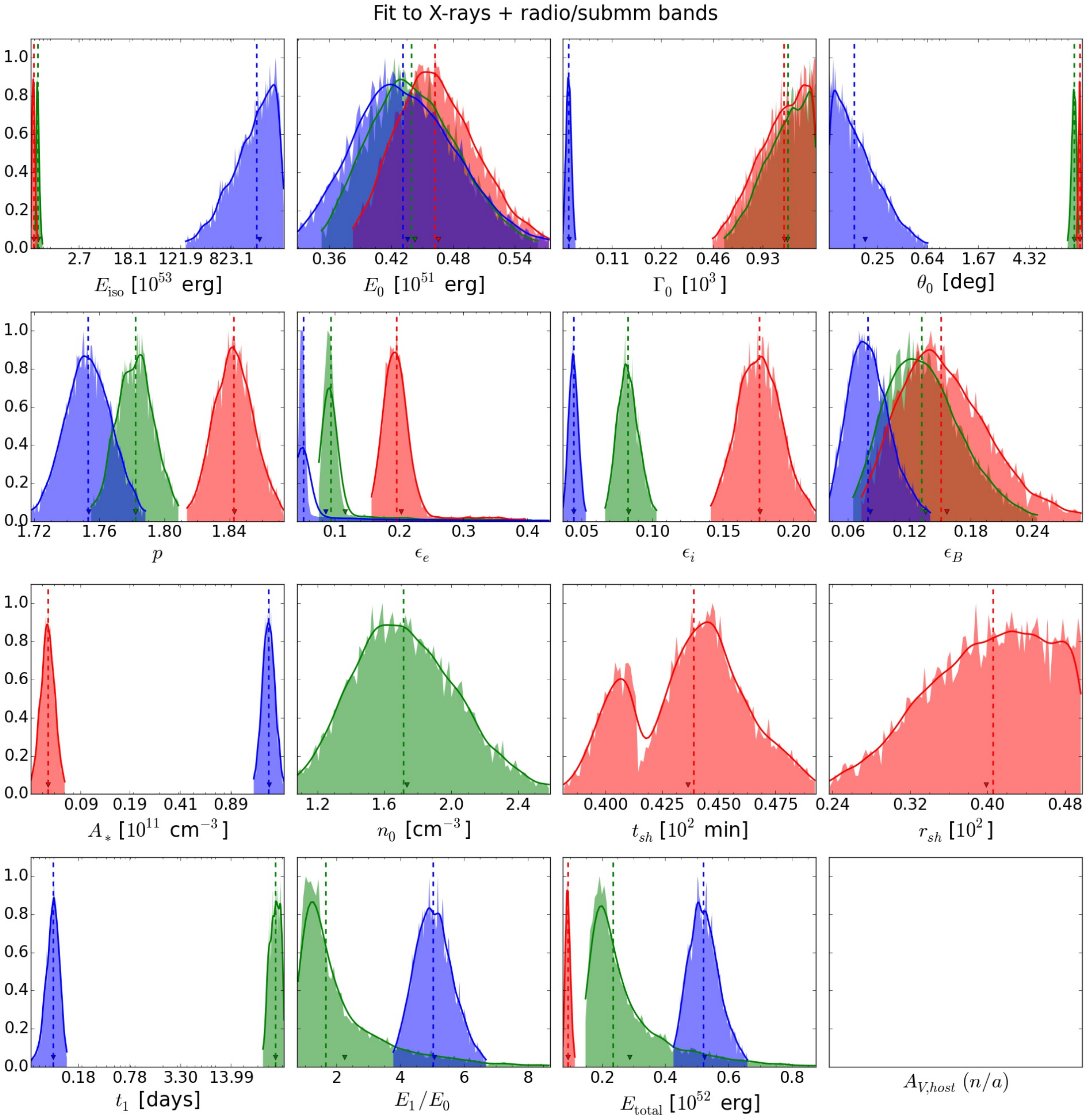

Fit to X-rays + radio/submm bands

Fit to optical/nIR + radio/submm band, MW extinction corrected, $White$ shifted to v

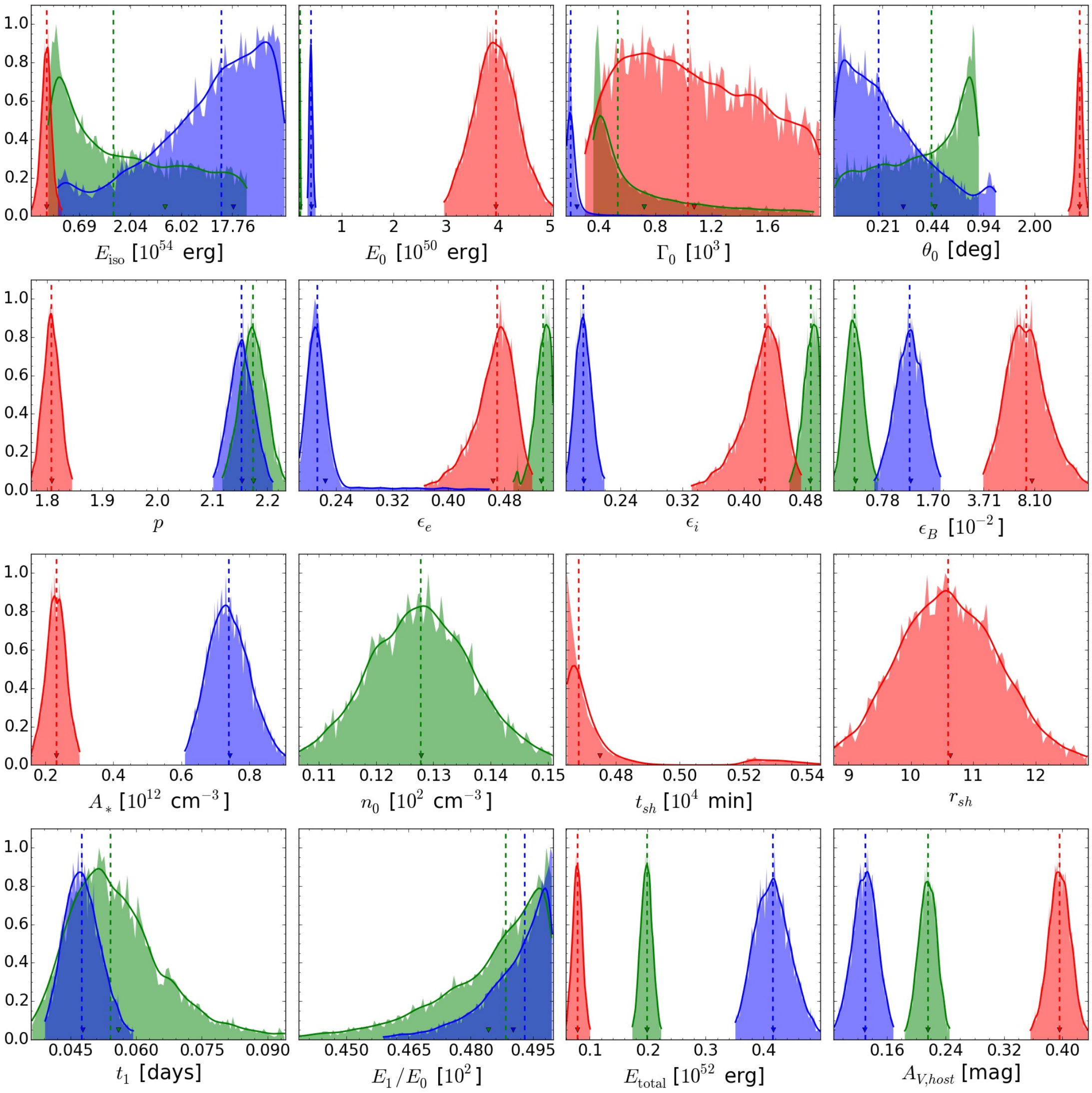

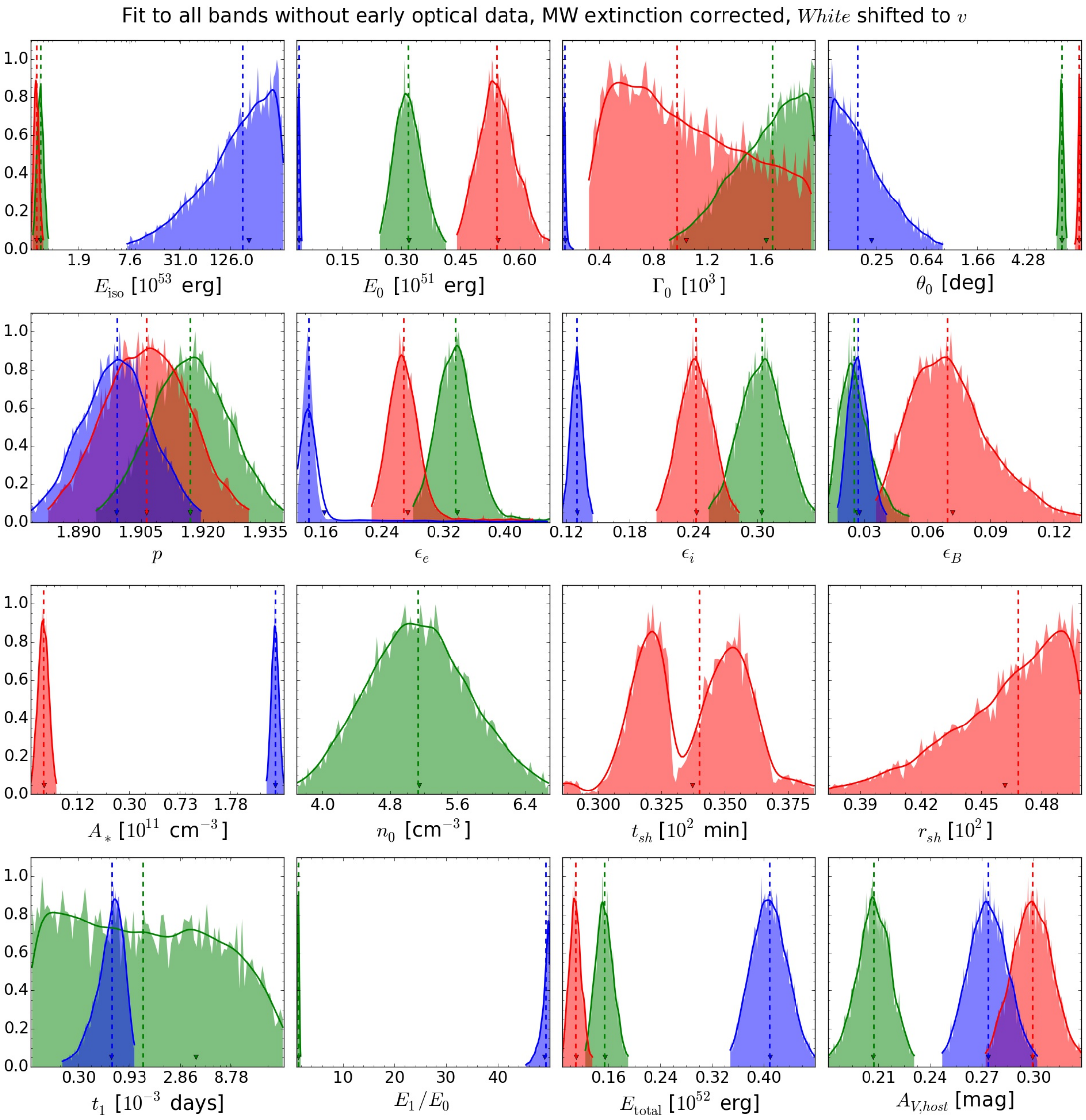

Fit to all bands without early optical data, MW extinction corrected, $White$ shifted to v

Fit to all bands after 0.5 days, MW extinction corrected, *White* shifted to *v*

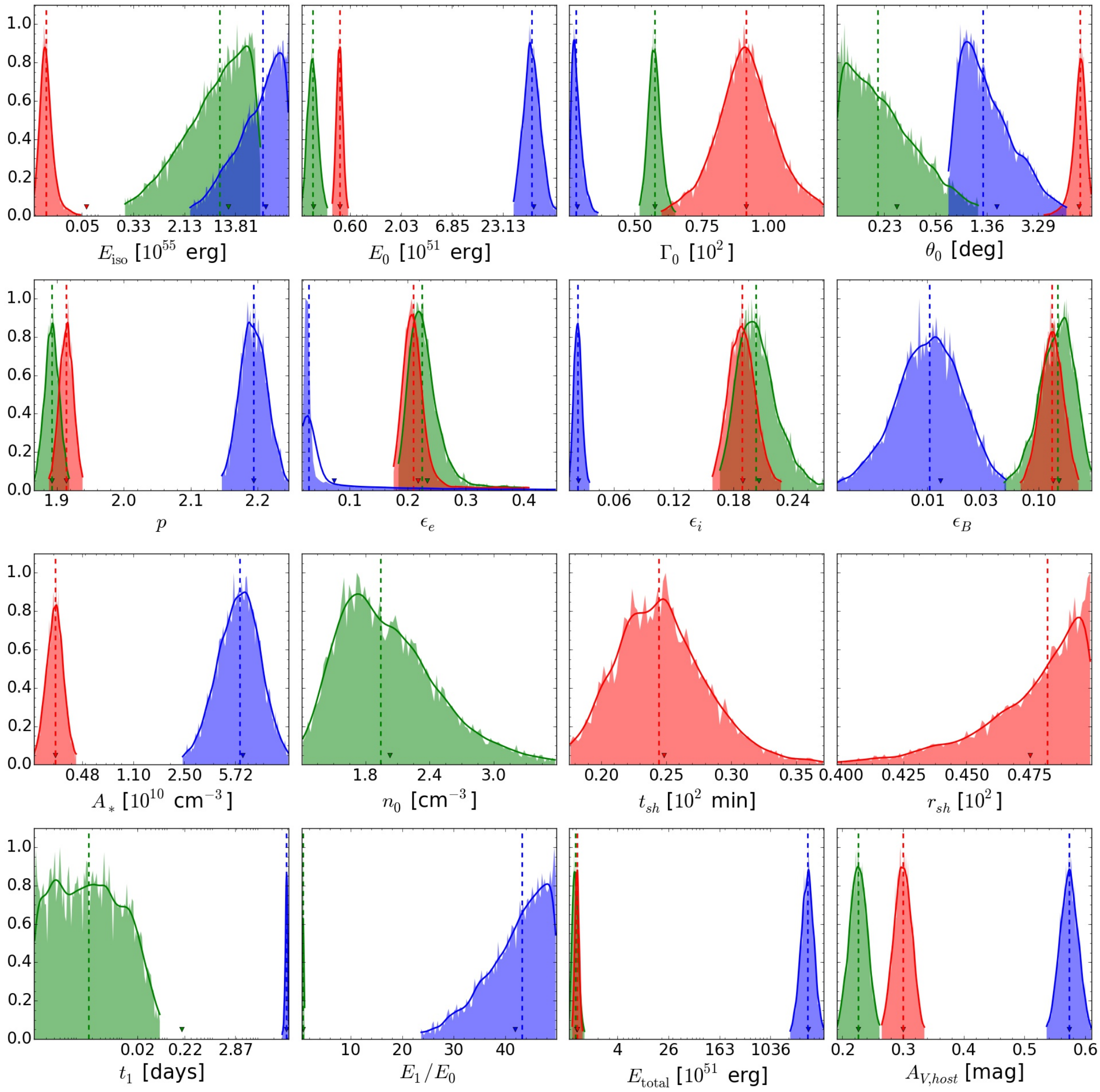

Appendix F

Marginals 2D

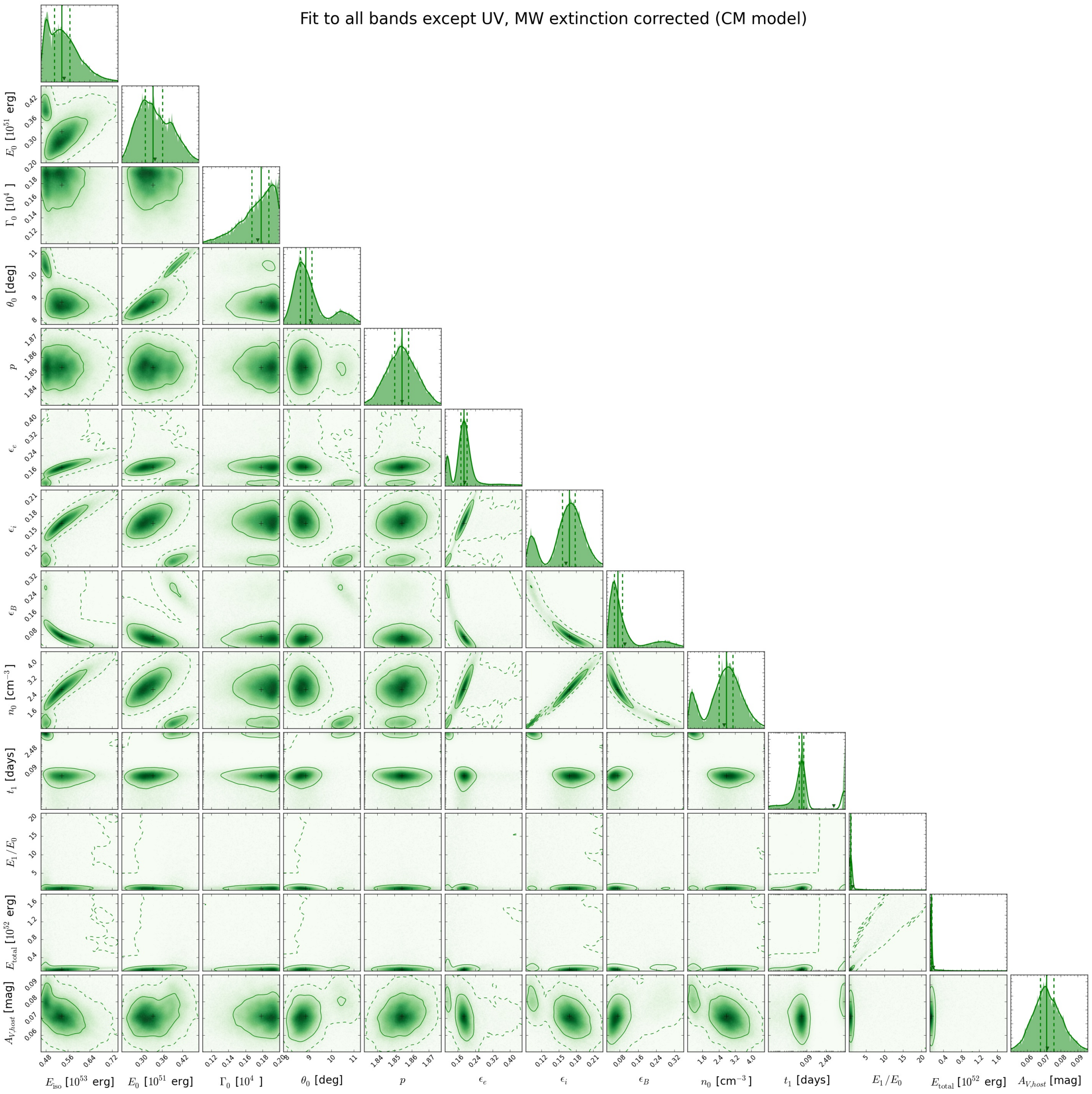
Fit to all bands except UV, MW extinction corrected (CM model)
$E_{\rm iso}$ [10^{53} erg]
E_0 [10^{51} erg]
Γ_0 [10^4]
θ_0 [deg]
p
ϵ_e
ϵ_i
ϵ_B
n_0 [cm^{-3}]
t_1 [days]
E_1/E_0
$E_{\rm total}$ [10^{52} erg]
$A_{V,host}$ [mag]

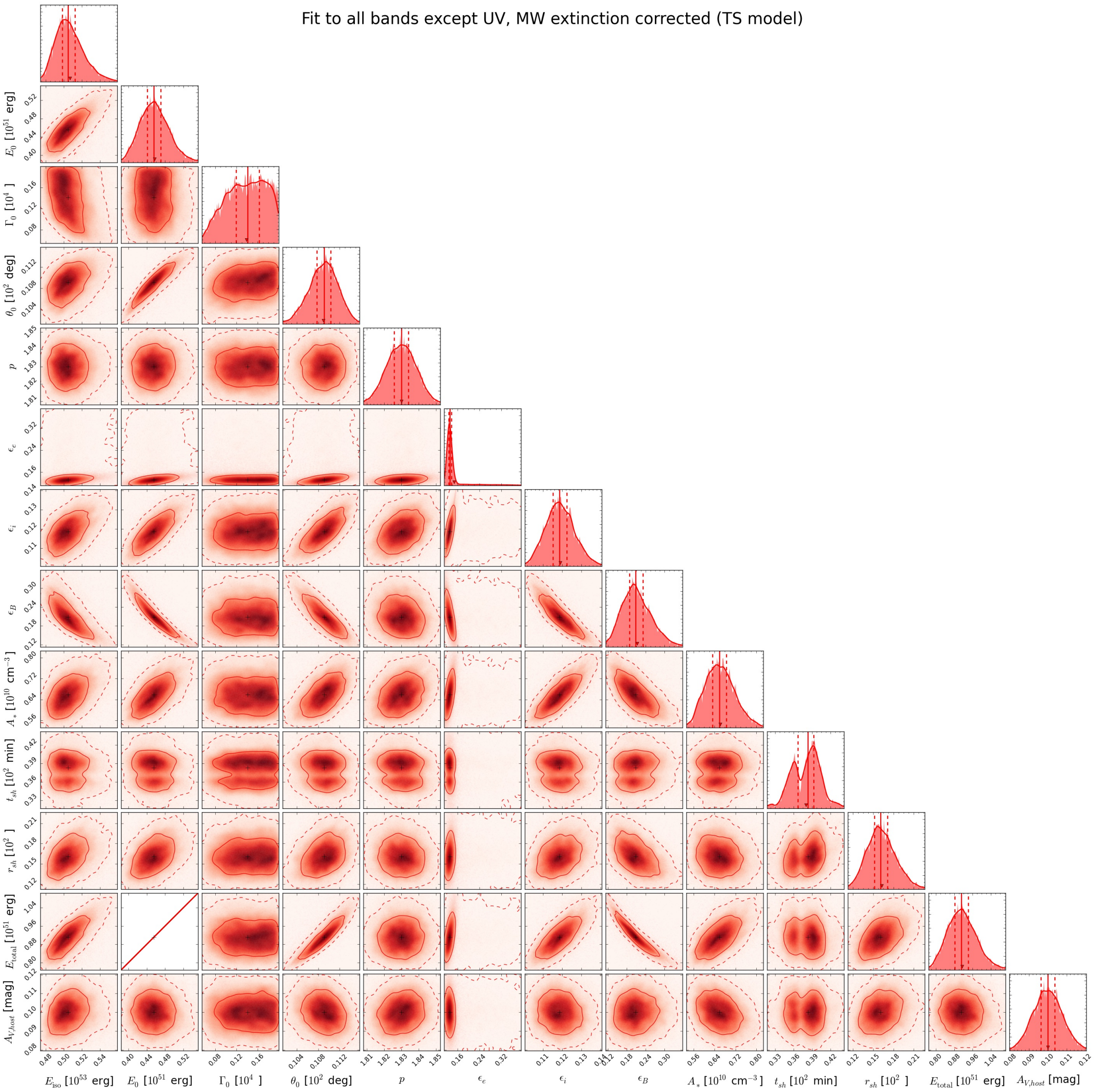
Fit to all bands except UV, MW extinction corrected (TS model)

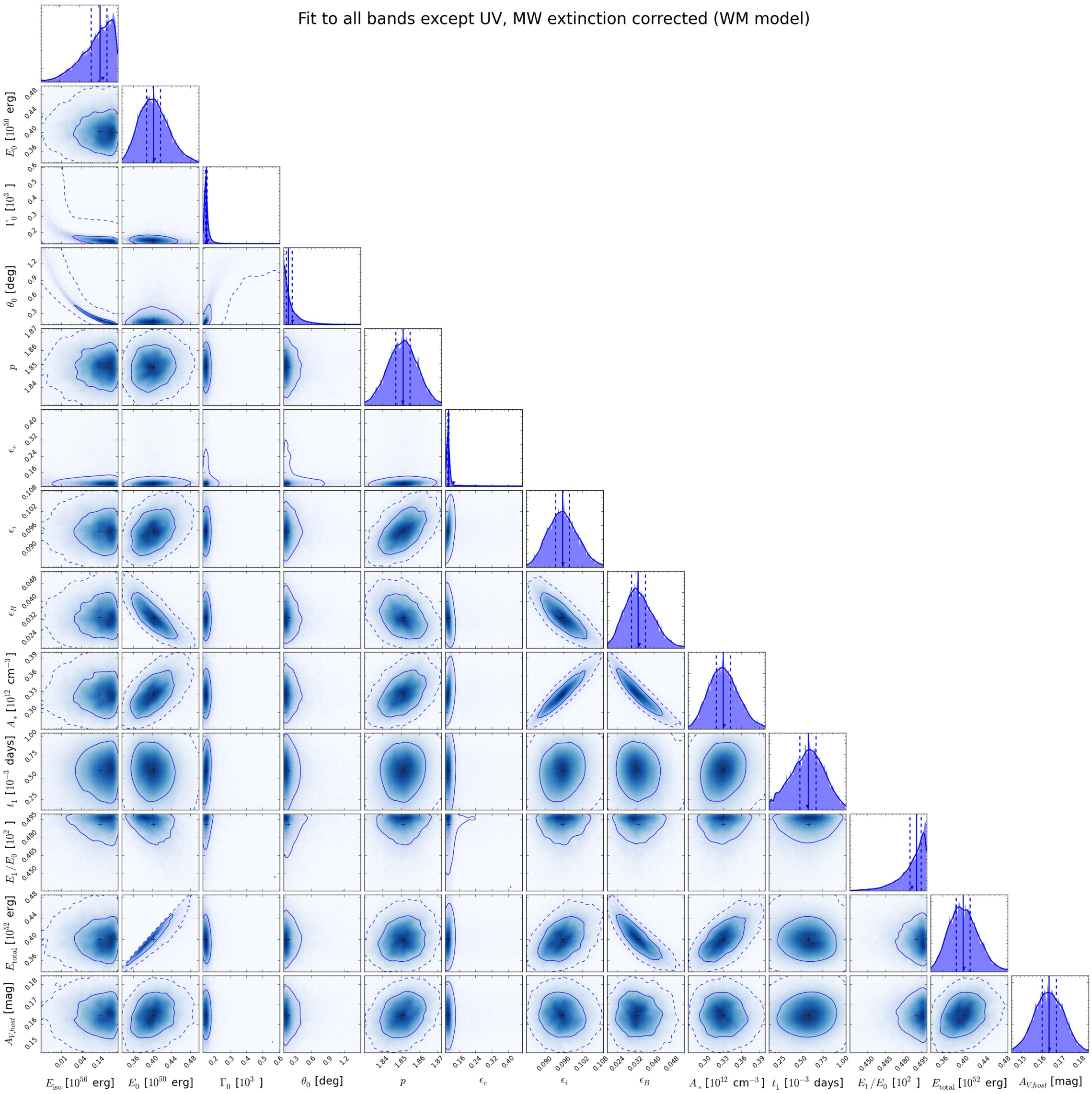
Fit to all bands except UV, MW extinction corrected (WM model)
E_0 [10^{50} erg]
Γ_0 [10^3]
θ_0 [deg]
p
ϵ_e
ϵ_i
ϵ_B
A_* [10^{12} cm^{-3}]
t_1 [10^{-3} days]
E_1/E_0 [10^2]
$E_{\rm total}$ [10^{52} erg]
$A_{V,host}$ [mag]
$E_{\rm iso}$ [10^{56} erg]

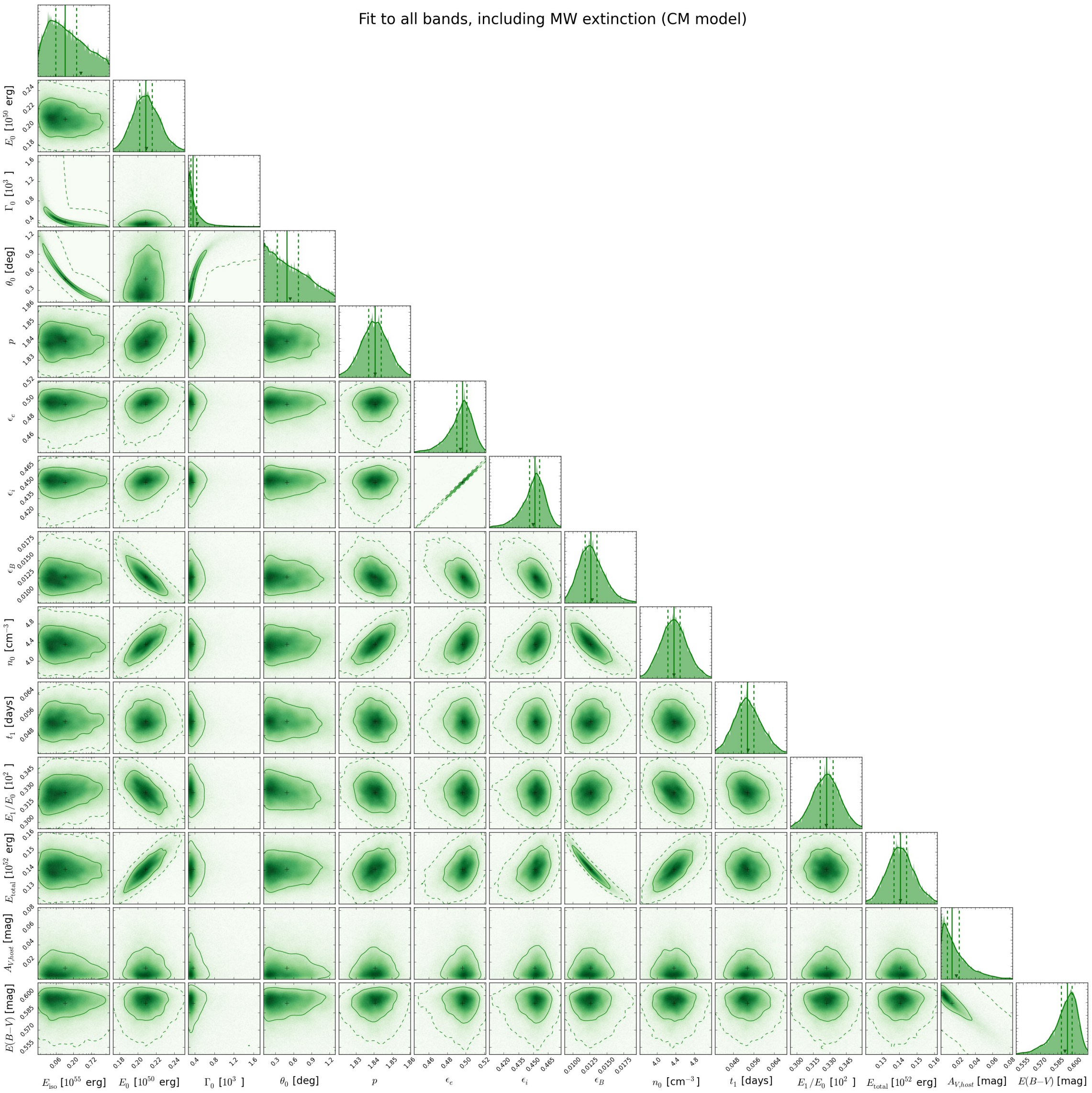
Fit to all bands, including MW extinction (CM model)
$E_{\rm iso}$ [10^{55} erg]
E_0 [10^{50} erg]
Γ_0 [10^3]
θ_0 [deg]
p
ϵ_e
ϵ_i
ϵ_B
n_0 [cm^{-3}]
t_1 [days]
E_1/E_0 [10^2]
$E_{\rm total}$ [10^{52} erg]
$A_{V,host}$ [mag]
$E(B-V)$ [mag]

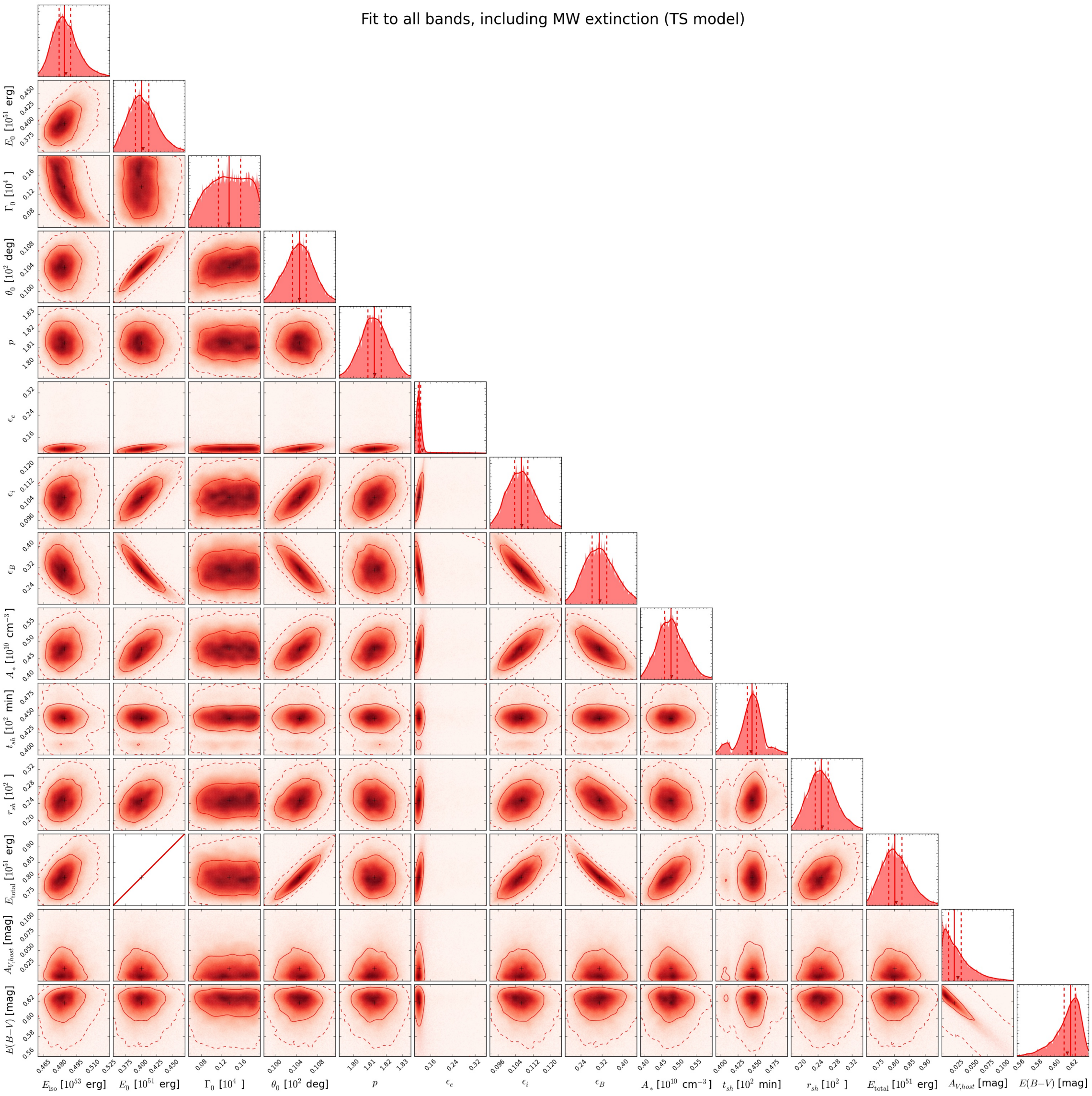

Fit to all bands, including MW extinction (TS model)

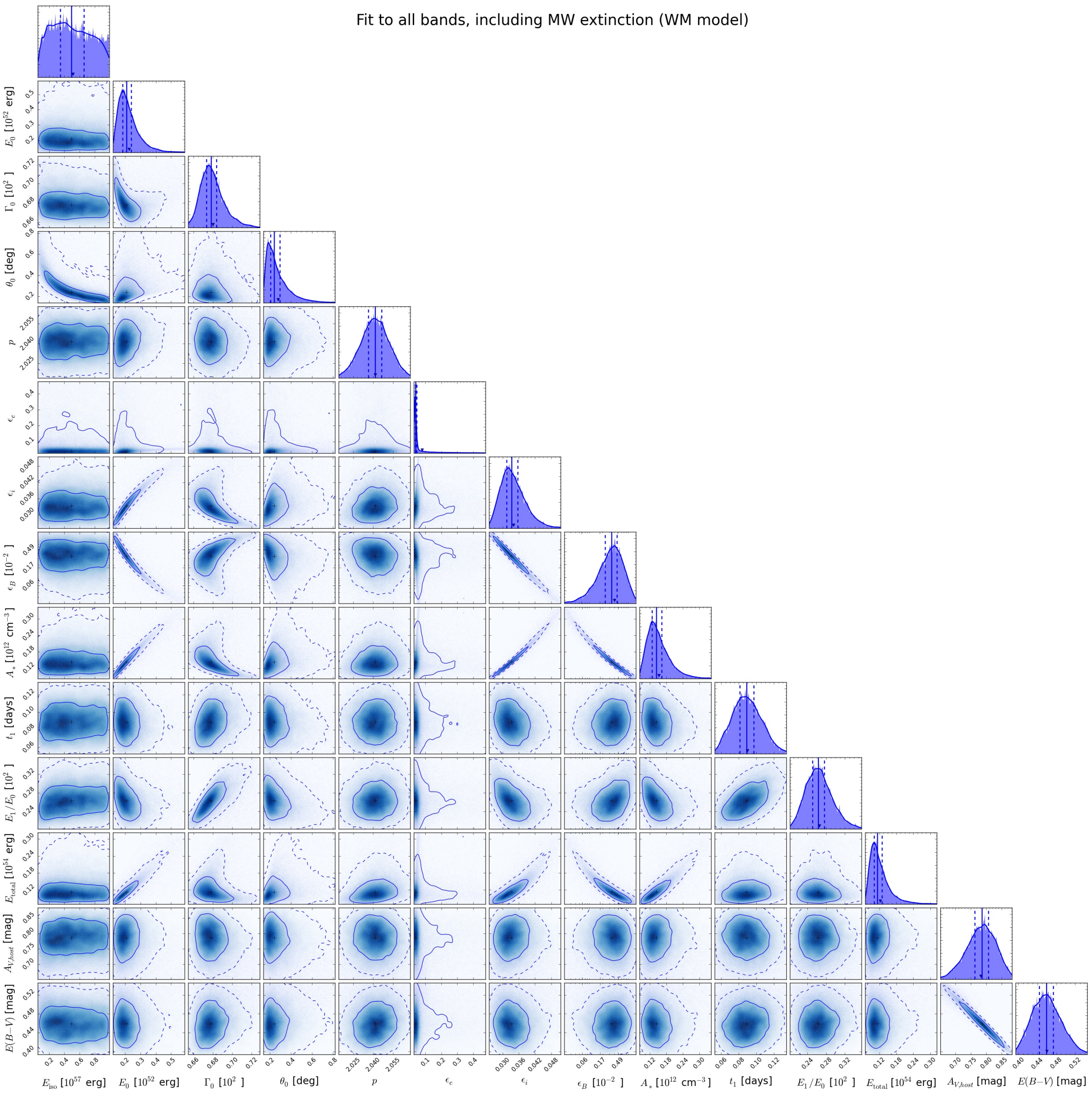
Fit to all bands, including MW extinction (WM model)

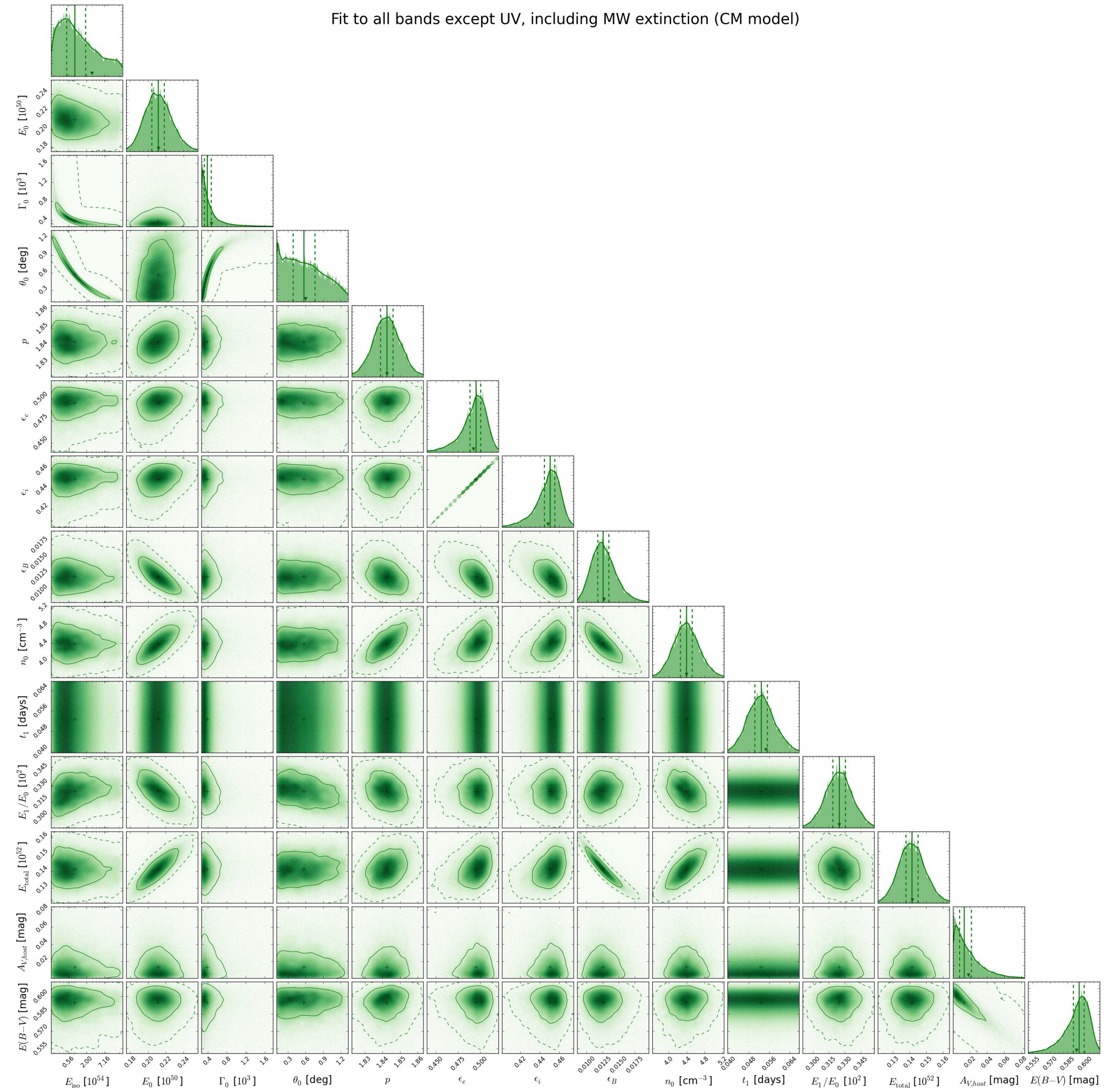
Fit to all bands except UV, including MW extinction (CM model)
$E_{\rm iso}$ [10^{54}]
E_0 [10^{50}]
Γ_0 [10^3]
θ_0 [deg]
p
ϵ_e
ϵ_i
ϵ_B
n_0 [cm^{-3}]
t_1 [days]
E_1/E_0 [10^2]
$E_{\rm total}$ [10^{52}]
$A_{V,host}$ [mag]
$E(B-V)$ [mag]

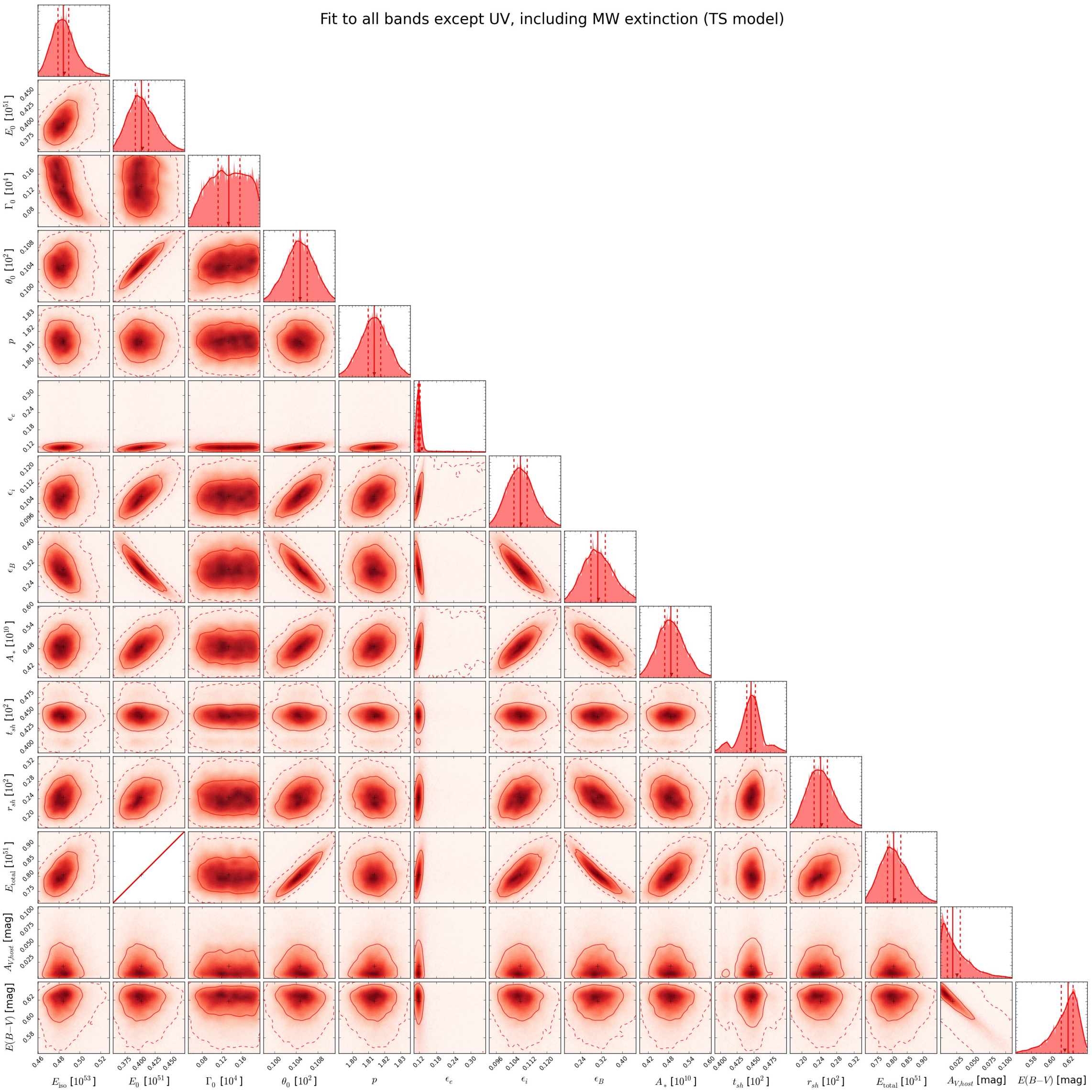
Fit to all bands except UV, including MW extinction (TS model)
E_0 [10^{51}]
Γ_0 [10^4]
θ_0 [10^2]
p
ϵ_e
ϵ_i
ϵ_B
A_* [10^{10}]
t_{sh} [10^2]
r_{sh} [10^2]
$E_{\rm total}$ [10^{51}]
$A_{V,host}$ [mag]
$E(B-V)$ [mag]
0.46 0.48 0.50 0.52
$E_{\rm iso}$ [10^{53}]
0.375 0.400 0.425 0.450
E_0 [10^{51}]
0.08 0.12 0.16
Γ_0 [10^4]
0.100 0.104 0.108
θ_0 [10^2]
1.80 1.81 1.82 1.83
p
0.12 0.18 0.24 0.30
ϵ_e
0.096 0.104 0.112 0.120
ϵ_i
0.24 0.32 0.40
ϵ_B
0.42 0.48 0.54 0.60
A_* [10^{10}]
0.400 0.425 0.450 0.475
t_{sh} [10^2]
0.20 0.24 0.28 0.32
r_{sh} [10^2]
0.75 0.80 0.85 0.90
$E_{\rm total}$ [10^{51}]
0.025 0.050 0.075 0.100
$A_{V,host}$ [mag]
0.58 0.60 0.62
$E(B-V)$ [mag]

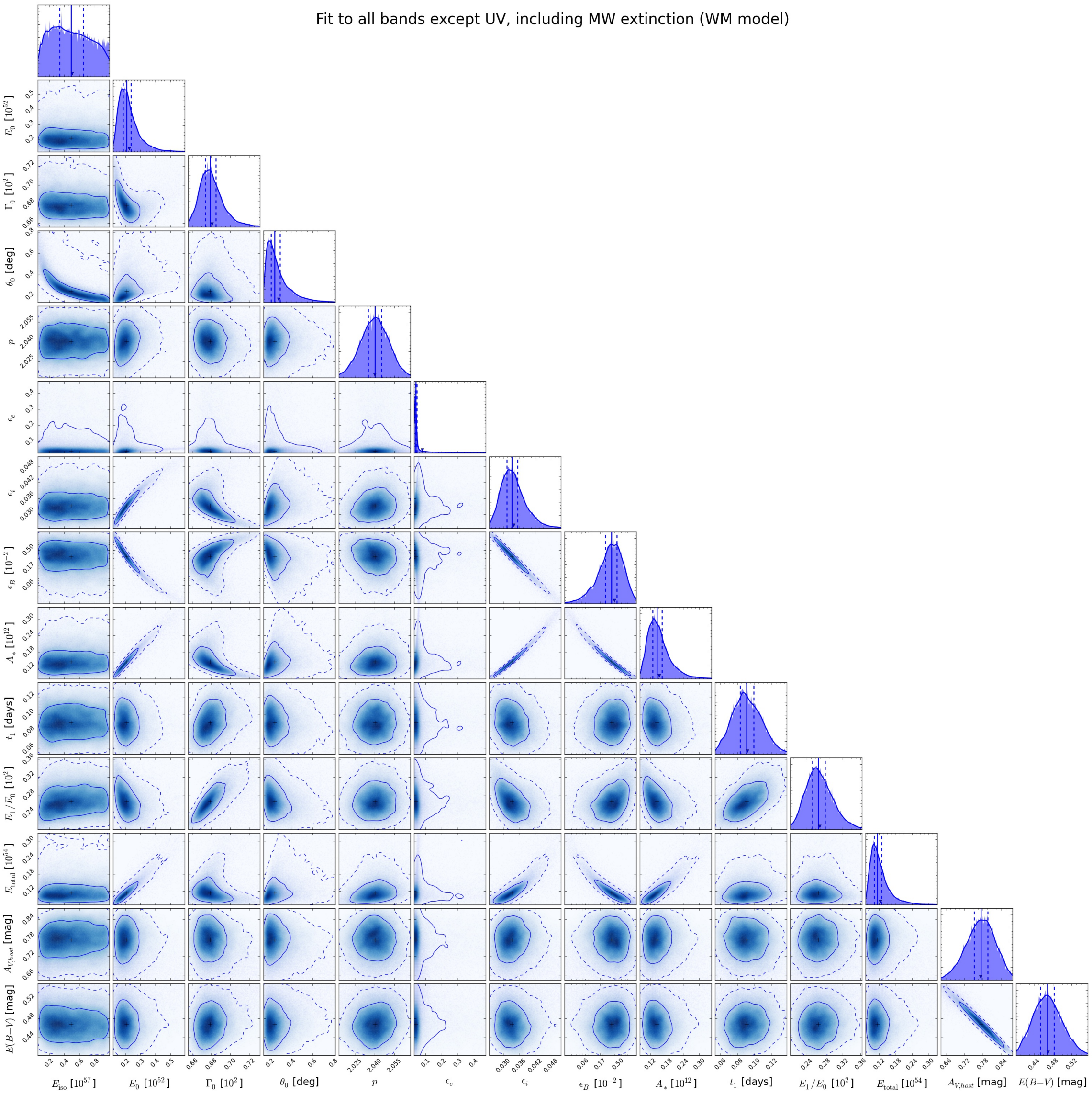
Fit to all bands except UV, including MW extinction (WM model)
$E_{\rm iso}$ [10^{57}]
E_0 [10^{52}]
Γ_0 [10^2]
θ_0 [deg]
p
ϵ_e
ϵ_i
ϵ_B [10^{-2}]
A_* [10^{12}]
t_1 [days]
E_1/E_0 [10^2]
$E_{\rm total}$ [10^{54}]
$A_{V,host}$ [mag]
$E(B-V)$ [mag]

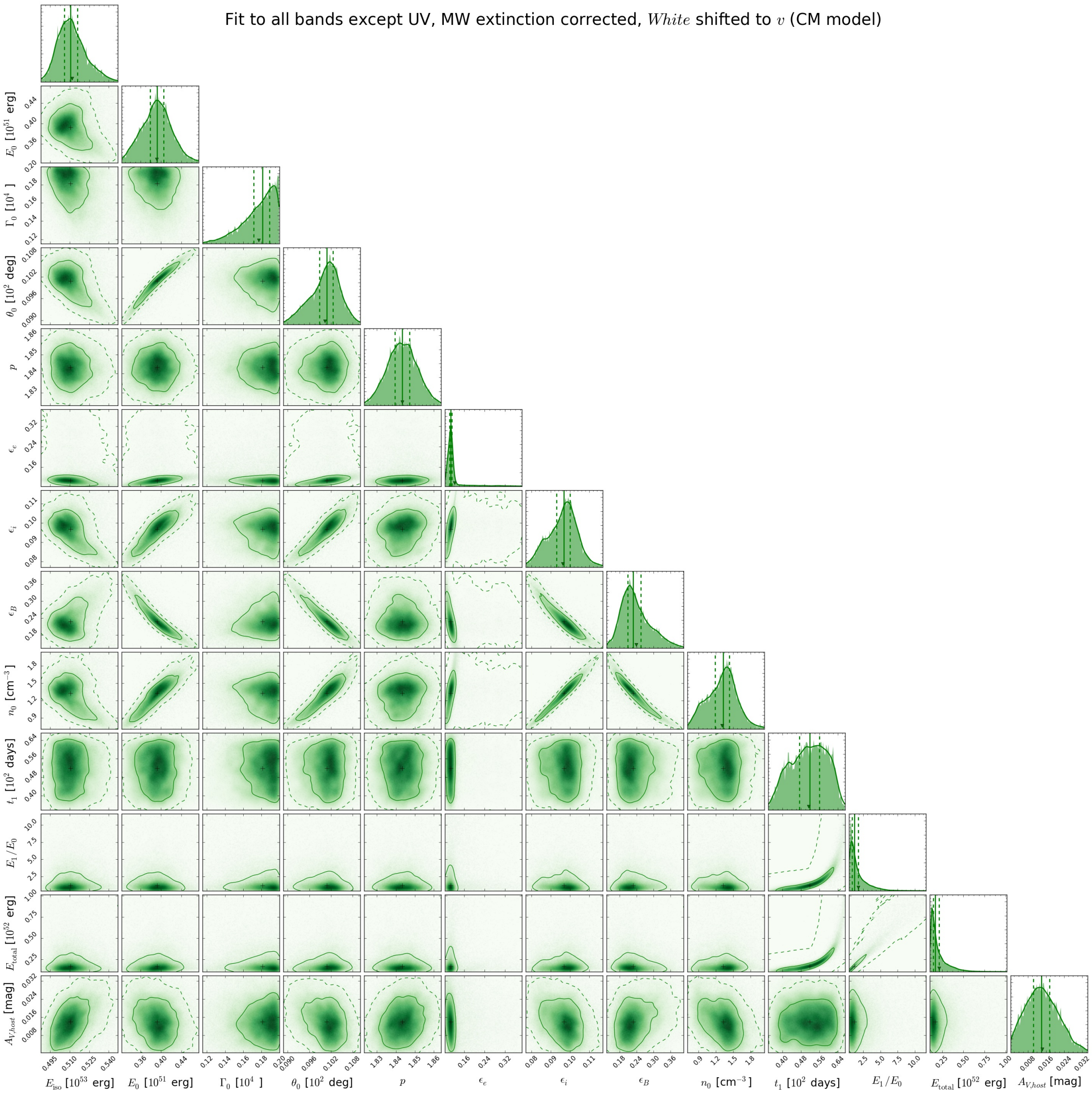

Fit to all bands except UV, MW extinction corrected, $White$ shifted to v (CM model)

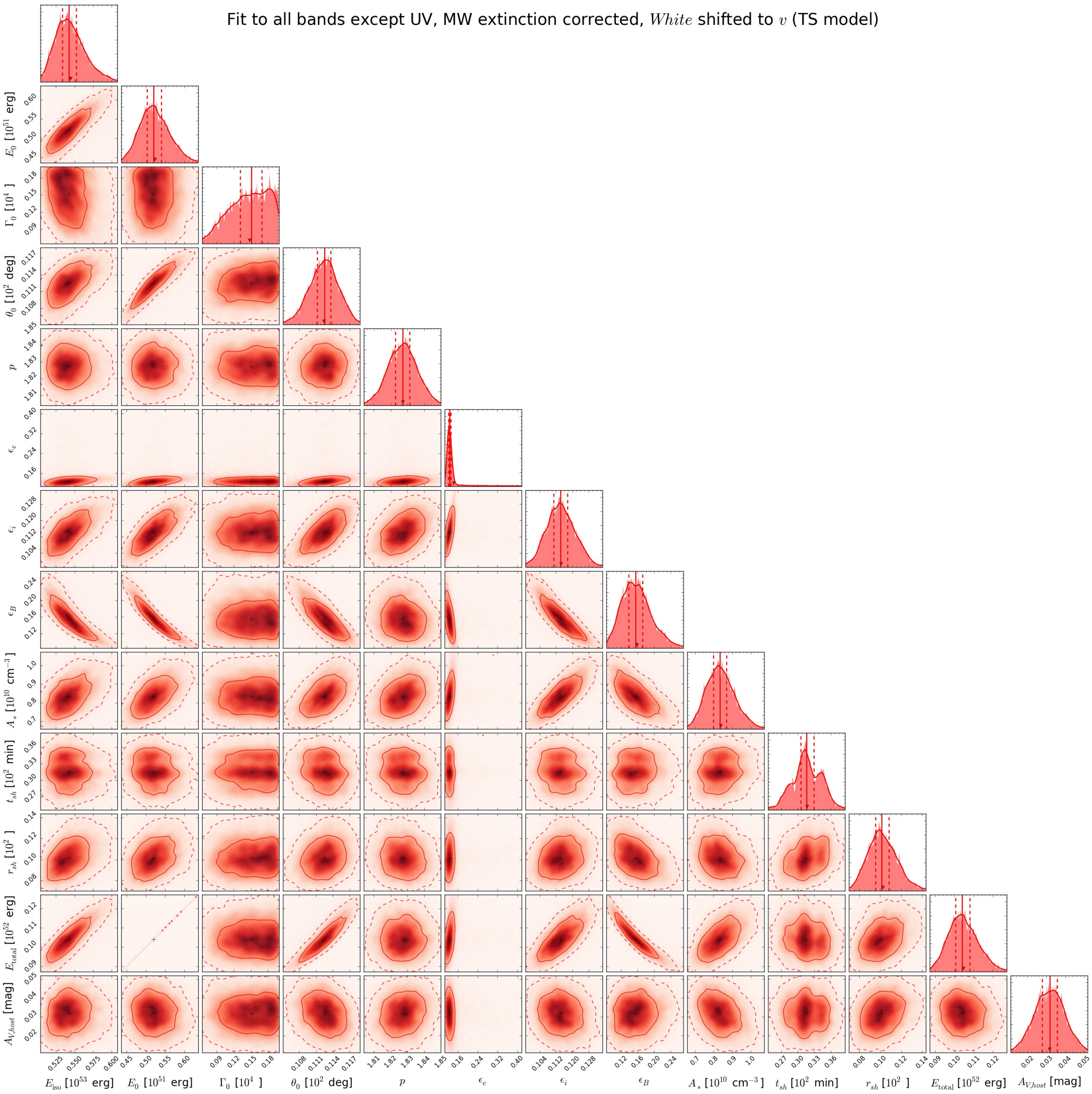
Fit to all bands except UV, MW extinction corrected, $White$ shifted to v (TS model)

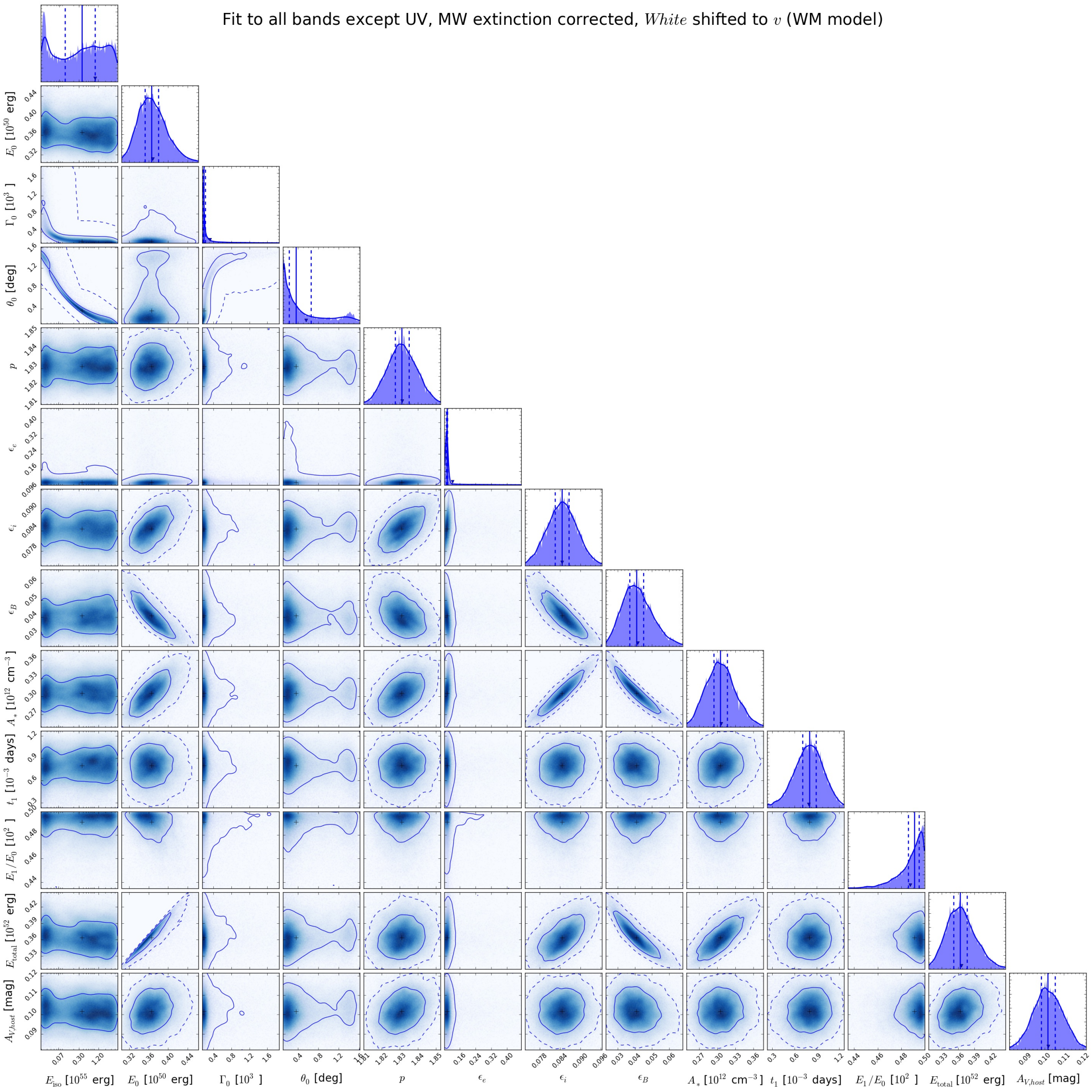
Fit to all bands except UV, MW extinction corrected, $White$ shifted to v (WM model)
E_{iso} [10^{55} erg]
E_0 [10^{50} erg]
Γ_0 [10^3]
θ_0 [deg]
p
ϵ_e
ϵ_i
ϵ_B
A_* [10^{12} cm^{-3}]
t_1 [10^{-3} days]
E_1/E_0 [10^2]
E_{total} [10^{52} erg]
$A_{V,host}$ [mag]

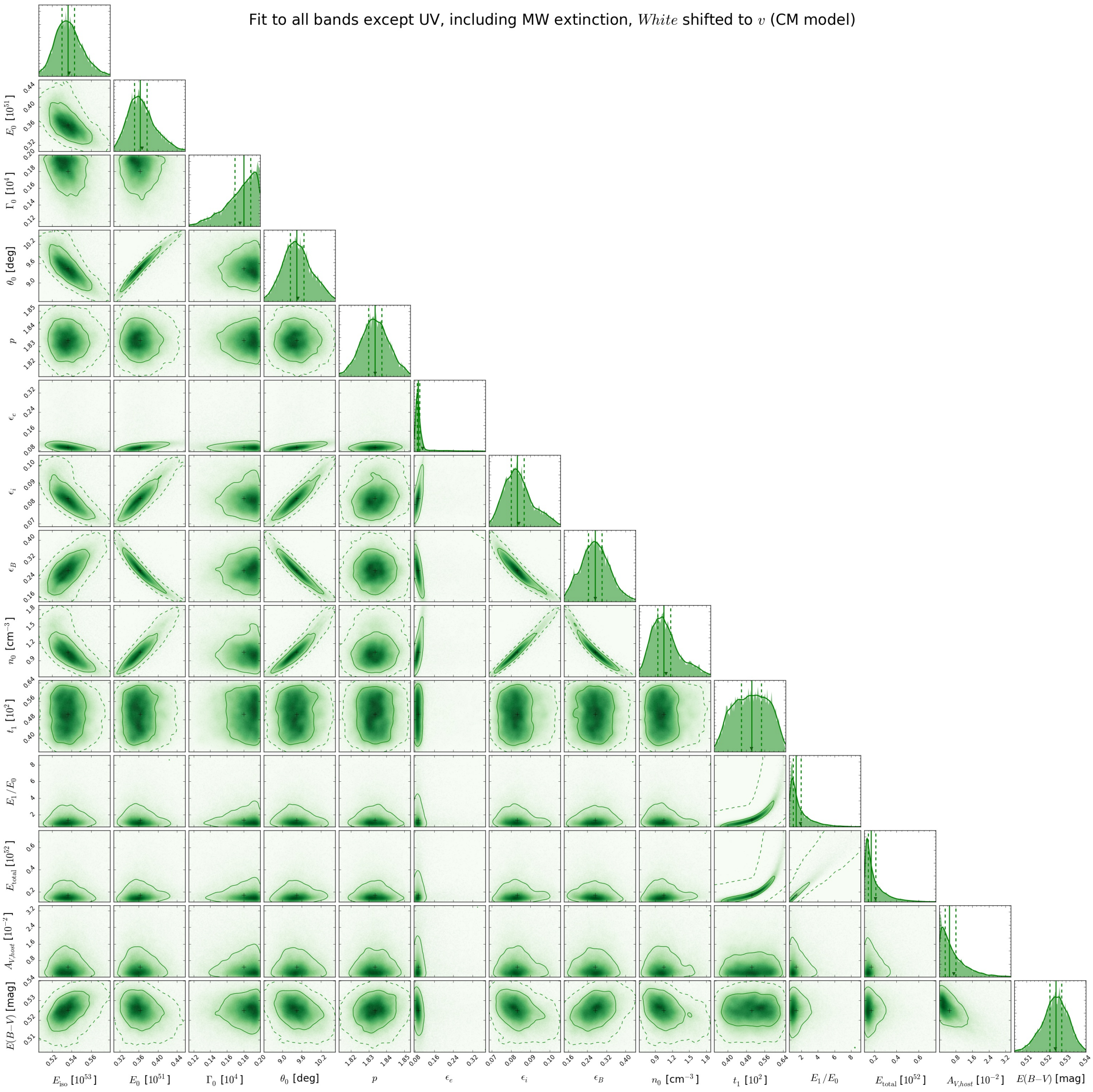

Fit to all bands except UV, including MW extinction, $White$ shifted to v (CM model)

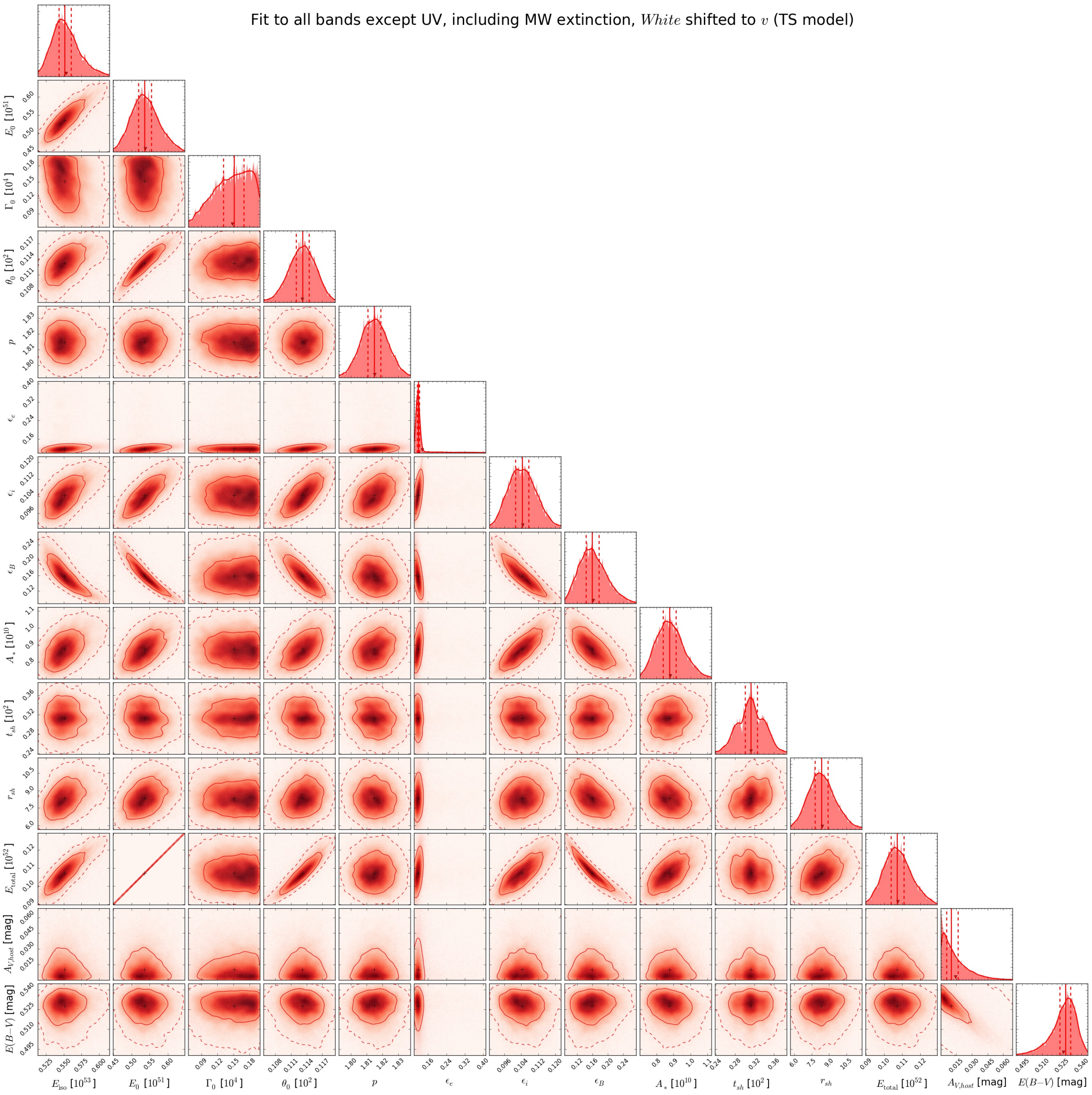

Fit to all bands except UV, including MW extinction, $White$ shifted to v (TS model)

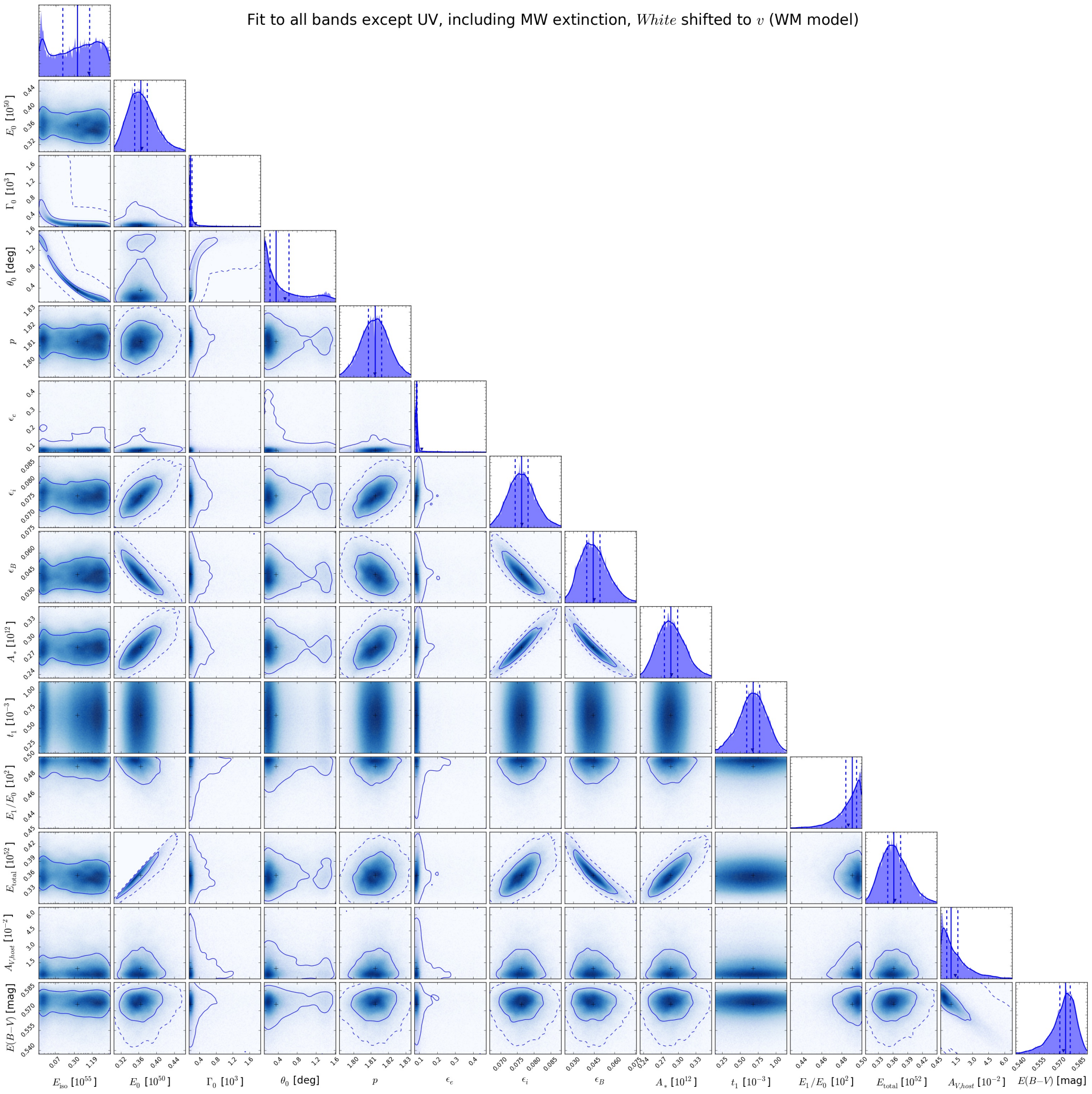

Fit to all bands except UV, including MW extinction, $White$ shifted to v (WM model)

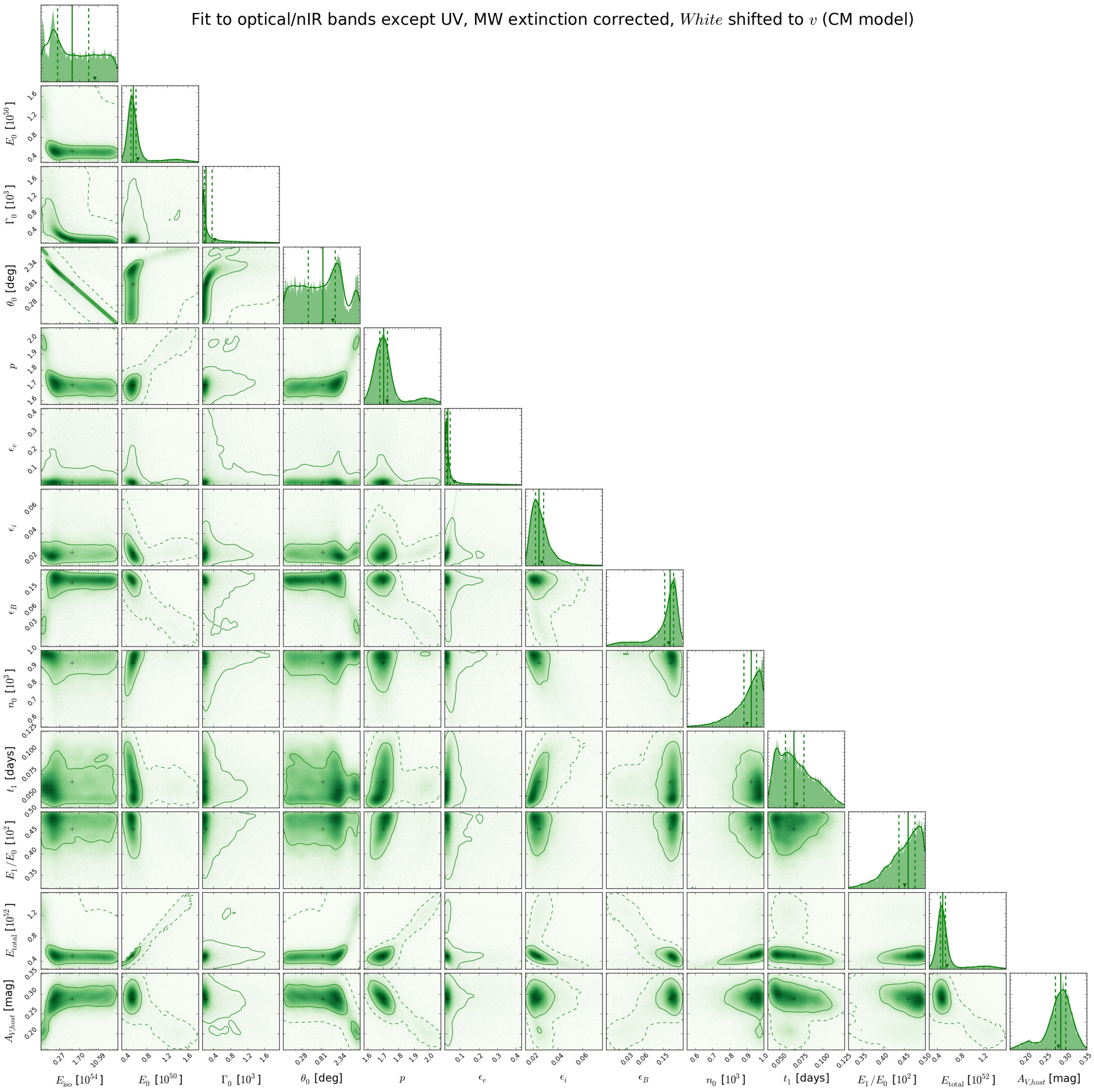
Fit to optical/nIR bands except UV, MW extinction corrected, $White$ shifted to v (CM model)
$E_{\rm iso}$ $[10^{54}]$
E_0 $[10^{50}]$
Γ_0 $[10^3]$
θ_0 [deg]
p
ϵ_e
ϵ_i
ϵ_B
n_0 $[10^3]$
t_1 [days]
E_1/E_0 $[10^2]$
$E_{\rm total}$ $[10^{52}]$
$A_{V,host}$ [mag]

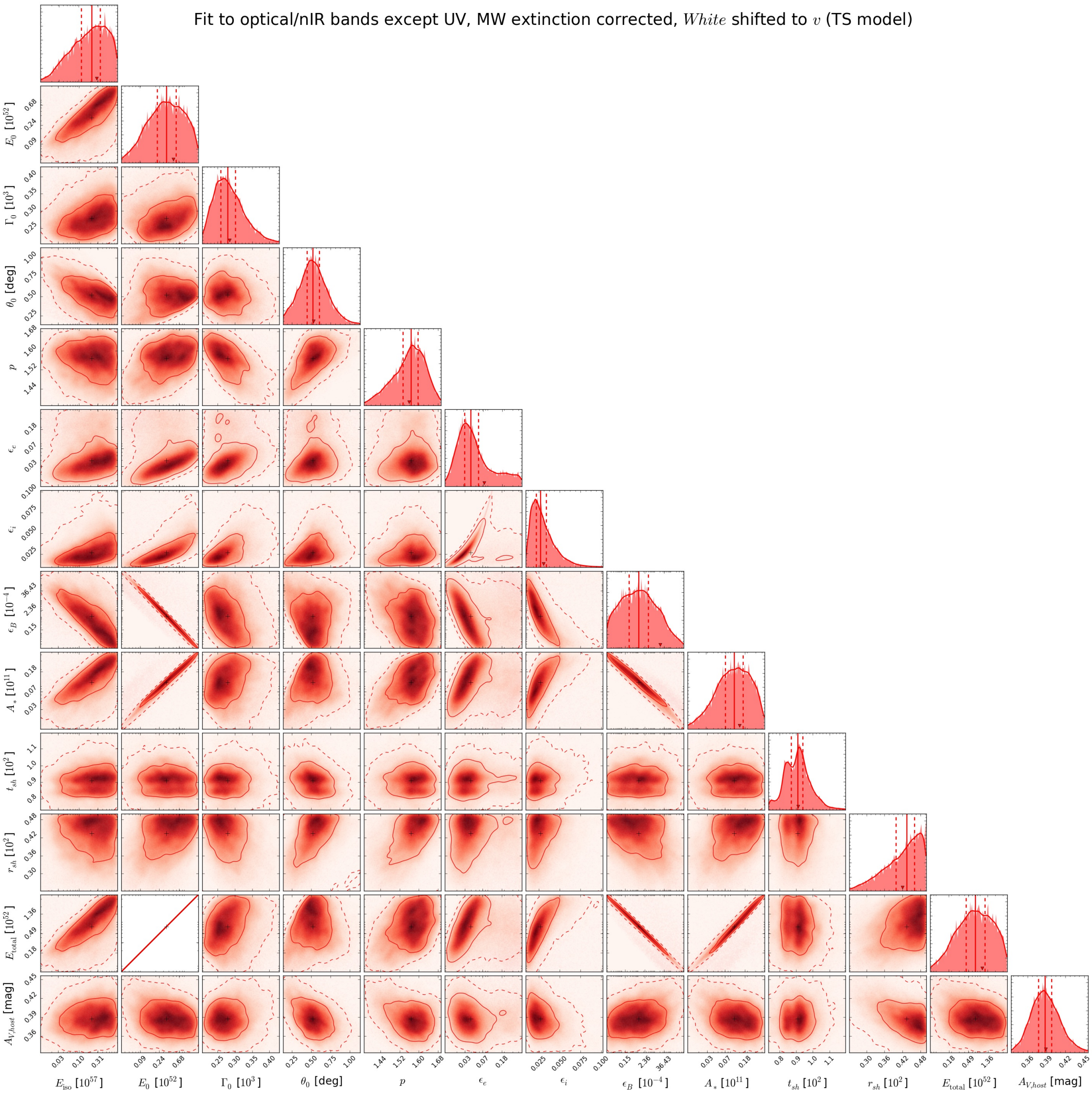

Fit to optical/nIR bands except UV, MW extinction corrected, $White$ shifted to v (TS model)

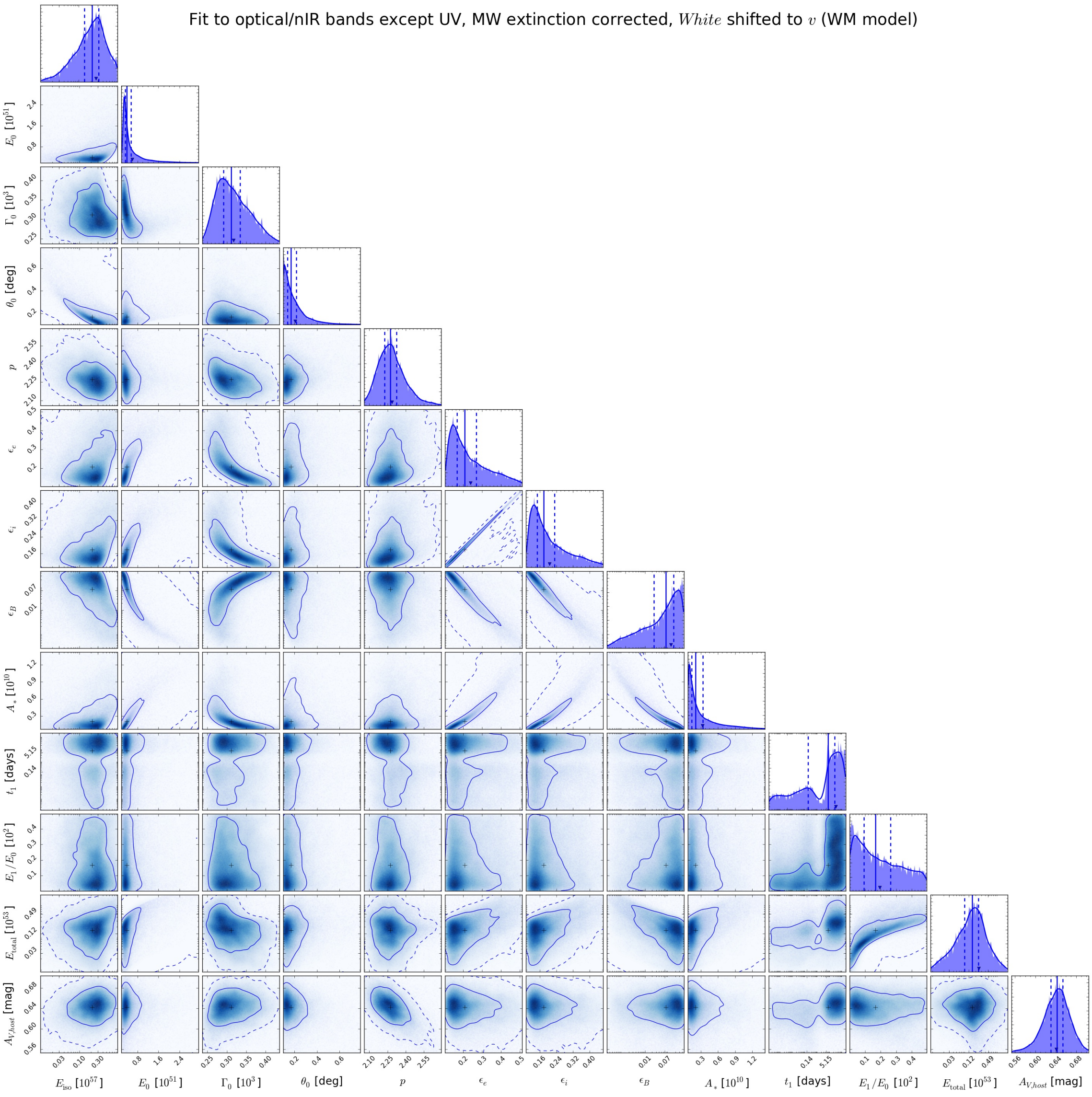
Fit to optical/nIR bands except UV, MW extinction corrected, $White$ shifted to v (WM model)
E_0 [10^{51}]
Γ_0 [10^3]
θ_0 [deg]
p
ϵ_e
ϵ_i
ϵ_B
A_* [10^{10}]
t_1 [days]
E_1/E_0 [10^2]
$E_{\rm total}$ [10^{53}]
$A_{V,host}$ [mag]
$E_{\rm iso}$ [10^{57}]

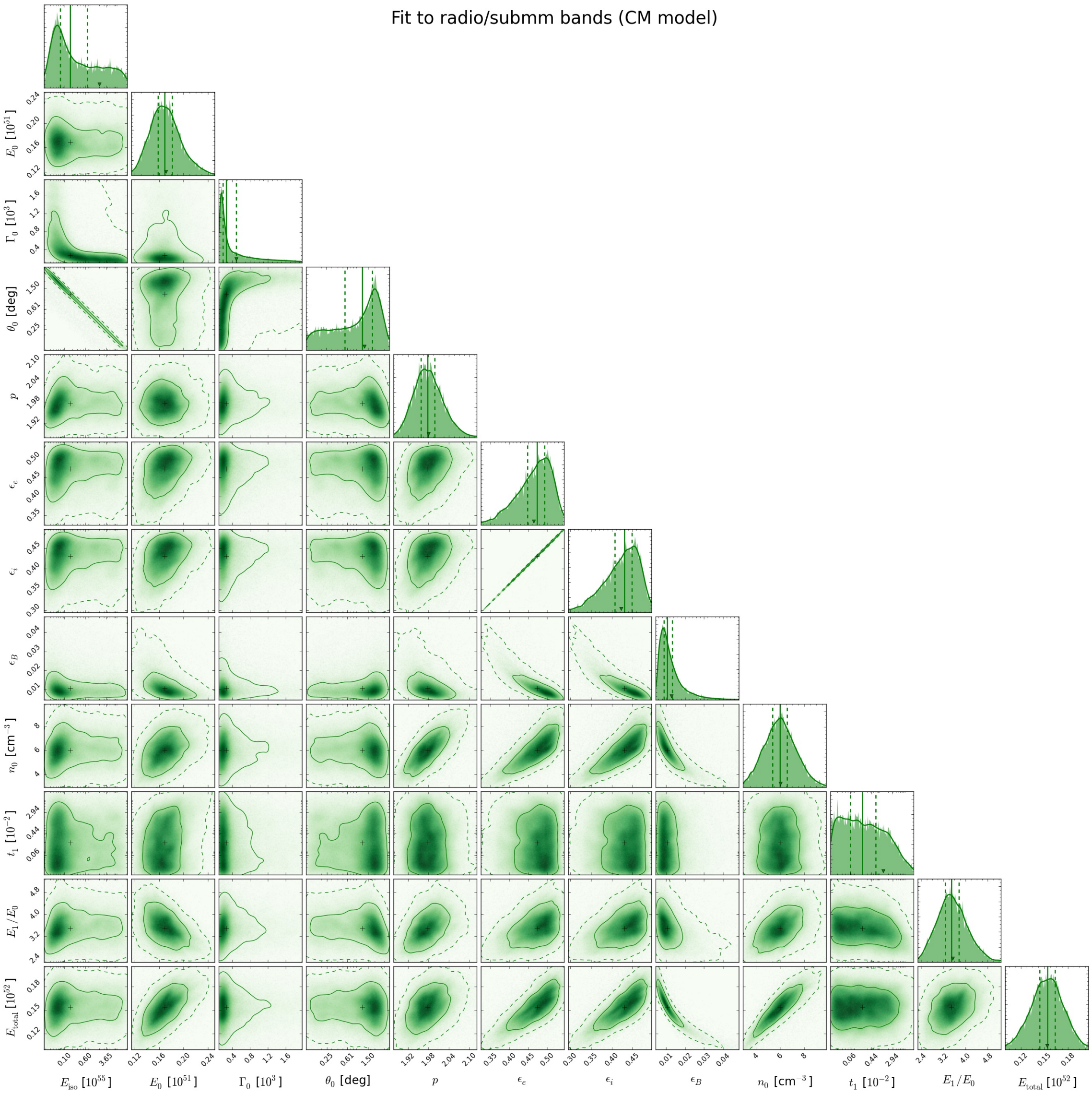
Fit to radio/submm bands (CM model)
$E_{\rm iso}$ [10^{55}]
E_0 [10^{51}]
Γ_0 [10^3]
θ_0 [deg]
p
ϵ_e
ϵ_i
ϵ_B
n_0 [cm^{-3}]
t_1 [10^{-2}]
E_1/E_0
$E_{\rm total}$ [10^{52}]
0.10
0.60
3.65
0.12
0.16
0.20
0.24
0.4
0.8
1.2
1.6
0.25
0.61
1.50
1.92
1.98
2.04
2.10
0.35
0.40
0.45
0.50
0.30
0.01
0.02
0.03
0.04
4
6
8
0.06
0.44
2.94
2.4
3.2
4.0
4.8
0.12
0.15
0.18

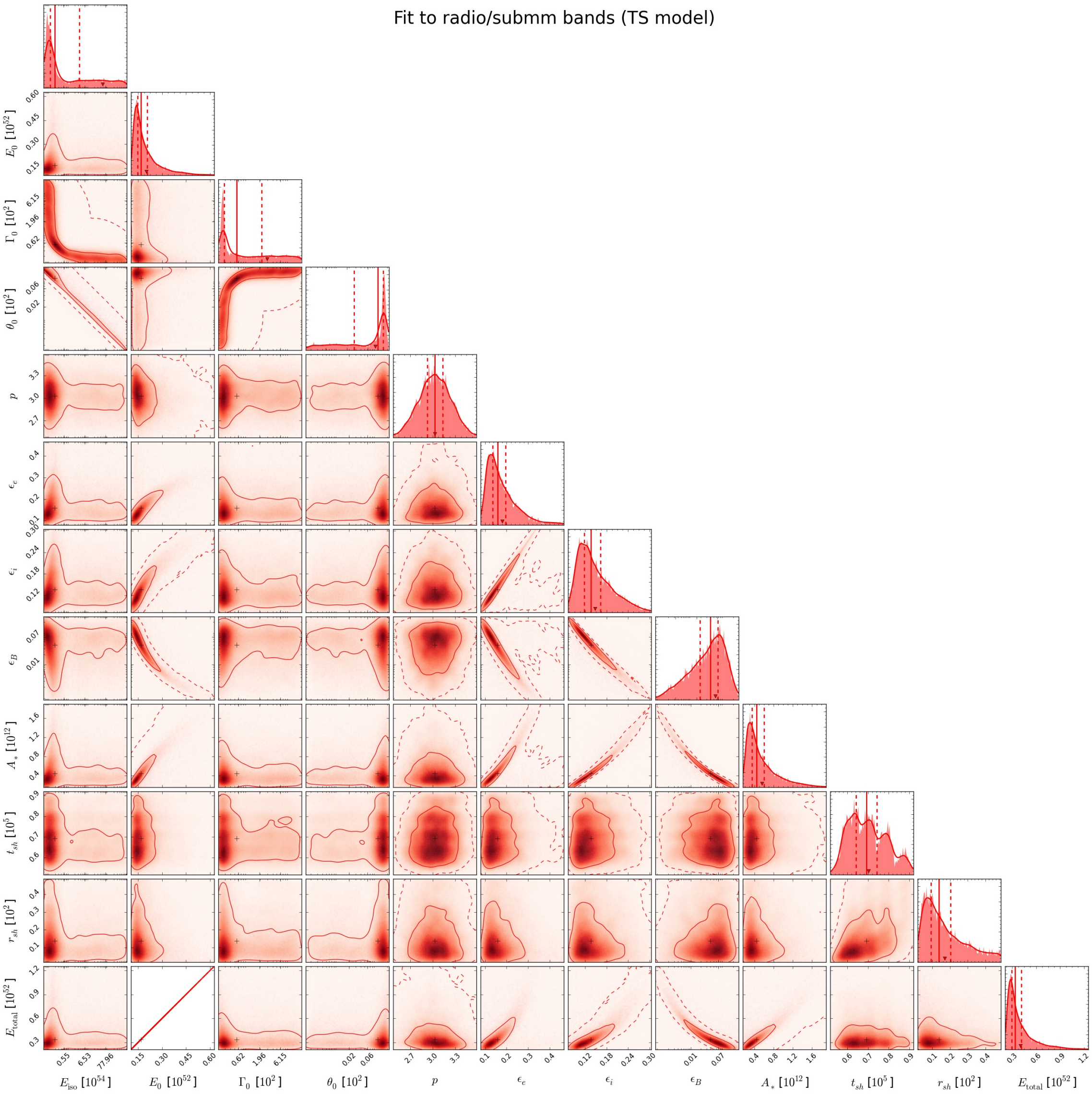
Fit to radio/submm bands (TS model)
E_0 [10^{52}]
Γ_0 [10^2]
θ_0 [10^2]
p
ϵ_e
ϵ_i
ϵ_B
A_* [10^{12}]
t_{sh} [10^5]
r_{sh} [10^2]
$E_{\rm total}$ [10^{52}]
$E_{\rm iso}$ [10^{54}]
0.55
6.53
77.96
0.15
0.30
0.45
0.60
0.62
1.96
6.15
0.02
0.06
2.7
3.0
3.3
0.1
0.2
0.3
0.4
0.12
0.18
0.24
0.30
0.01
0.07
0.4
0.8
1.2
1.6
0.6
0.7
0.8
0.9
0.3
0.6
0.9
1.2

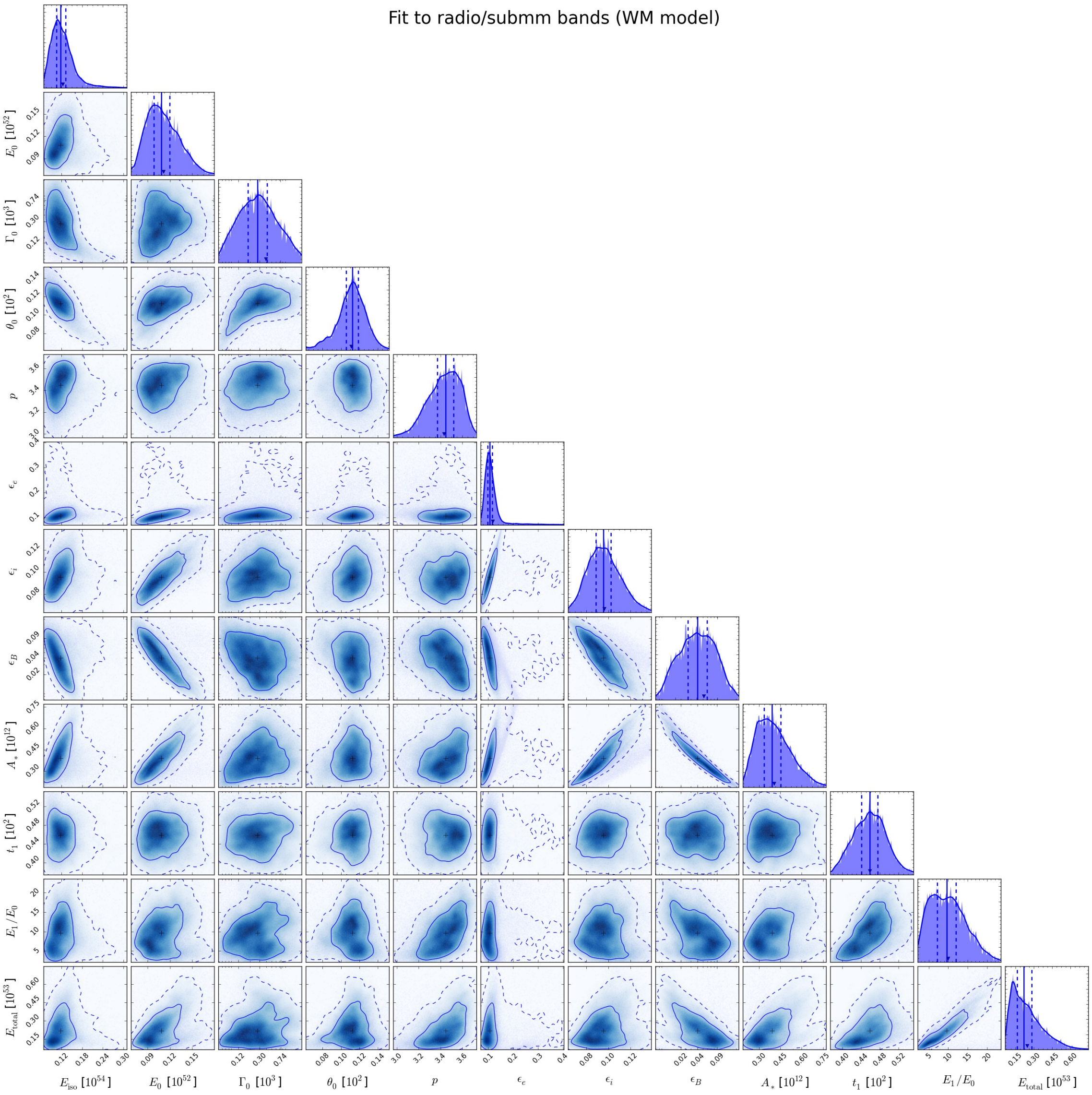

Fit to radio/submm bands (WM model)

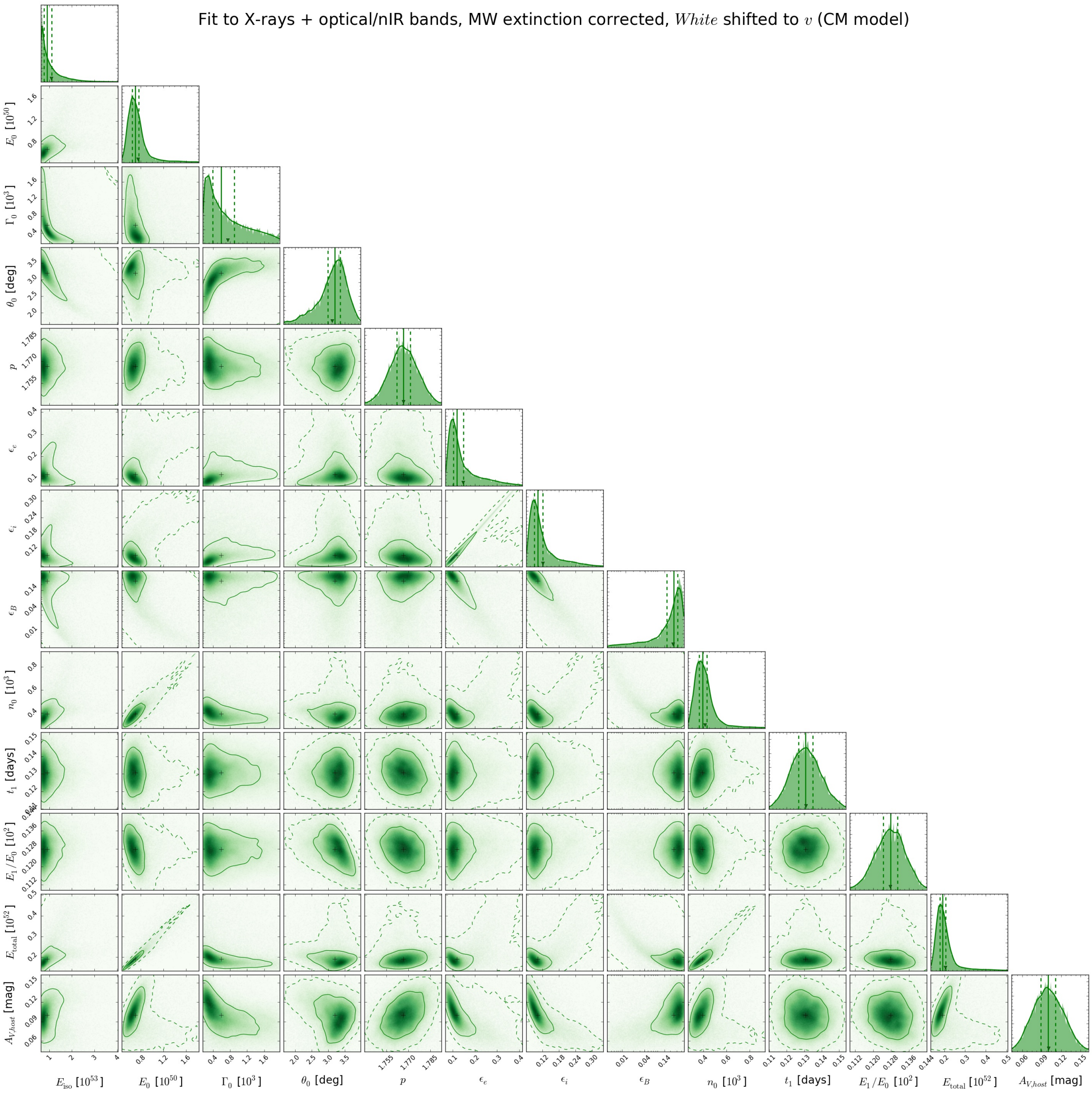
Fit to X-rays + optical/nIR bands, MW extinction corrected, $White$ shifted to v (CM model)

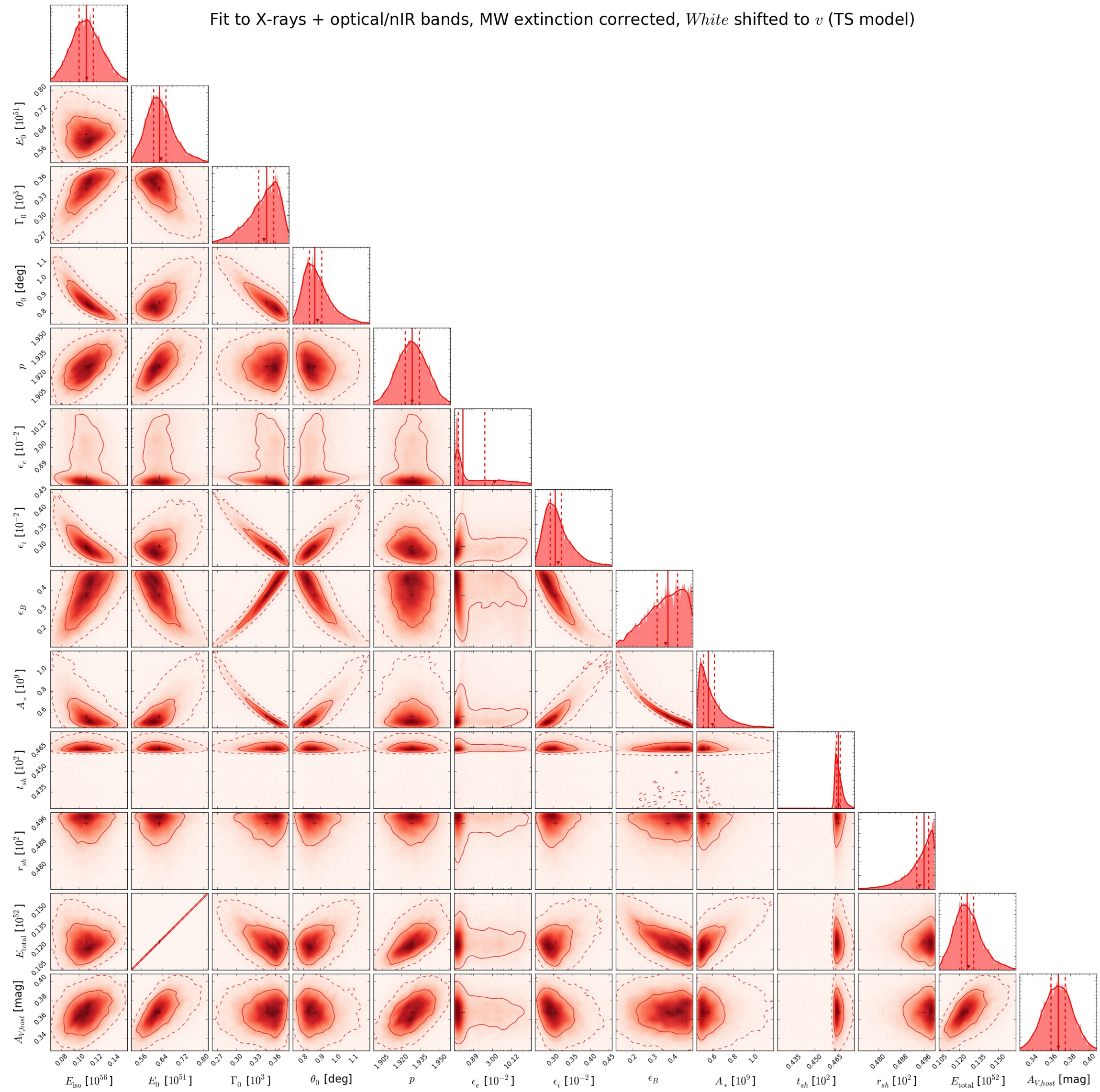
Fit to X-rays + optical/nIR bands, MW extinction corrected, $White$ shifted to v (TS model)

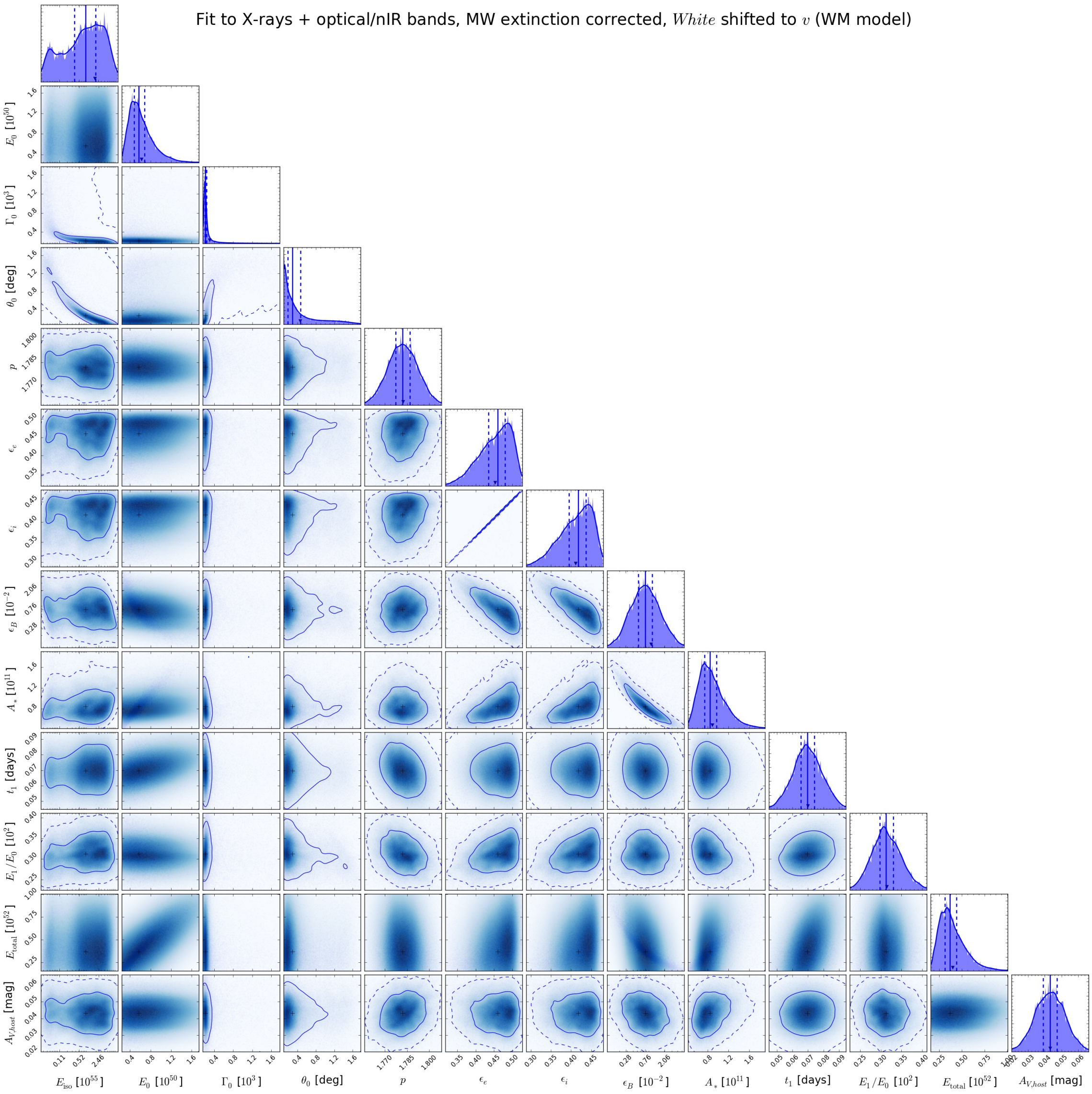

Fit to X-rays + optical/nIR bands, MW extinction corrected, $White$ shifted to v (WM model)

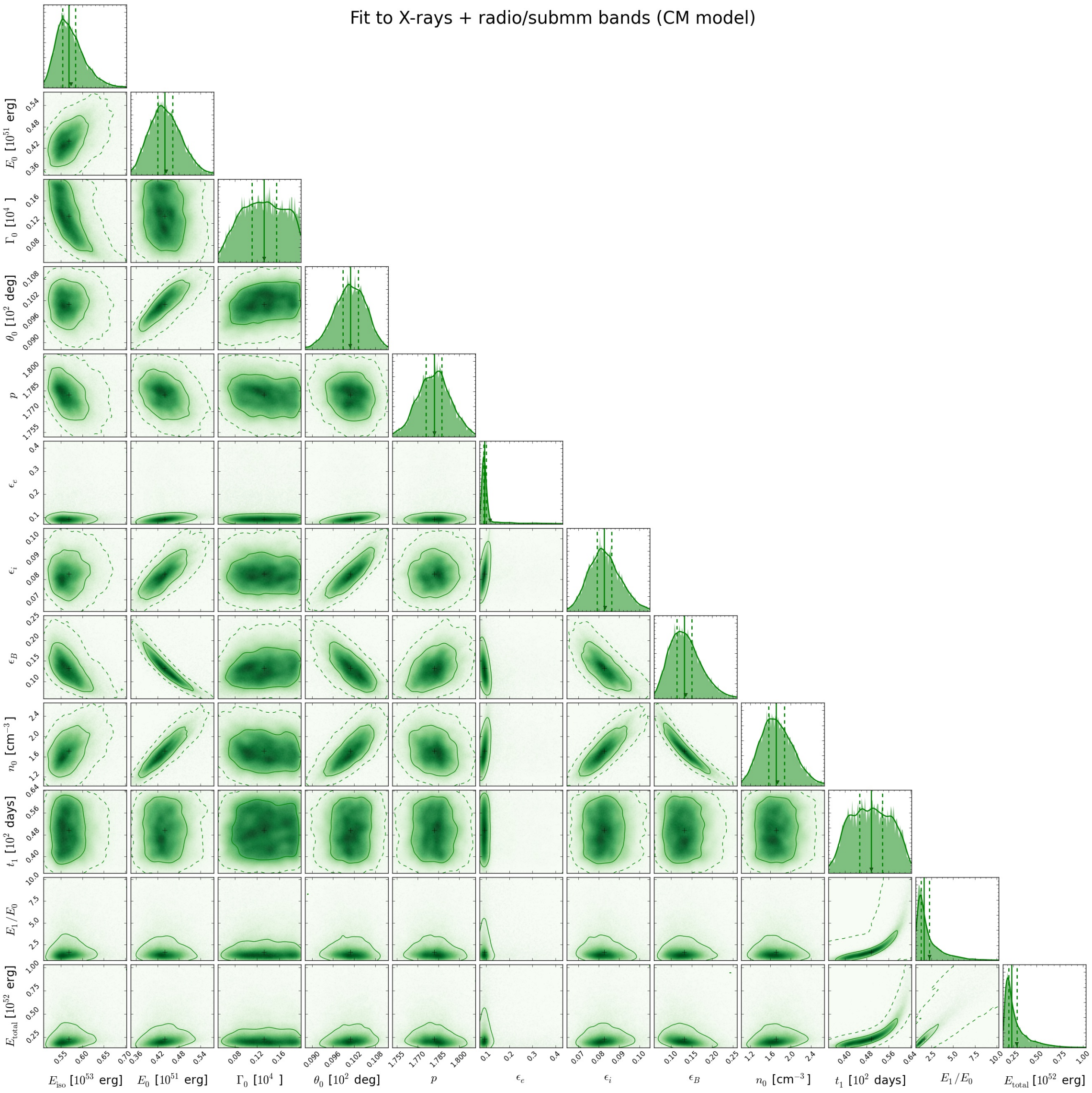
Fit to X-rays + radio/submm bands (CM model)
$E_{\rm iso}$ [10^{53} erg]
E_0 [10^{51} erg]
Γ_0 [10^4]
θ_0 [10^2 deg]
p
ϵ_e
ϵ_i
ϵ_B
n_0 [cm^{-3}]
t_1 [10^2 days]
E_1/E_0
$E_{\rm total}$ [10^{52} erg]

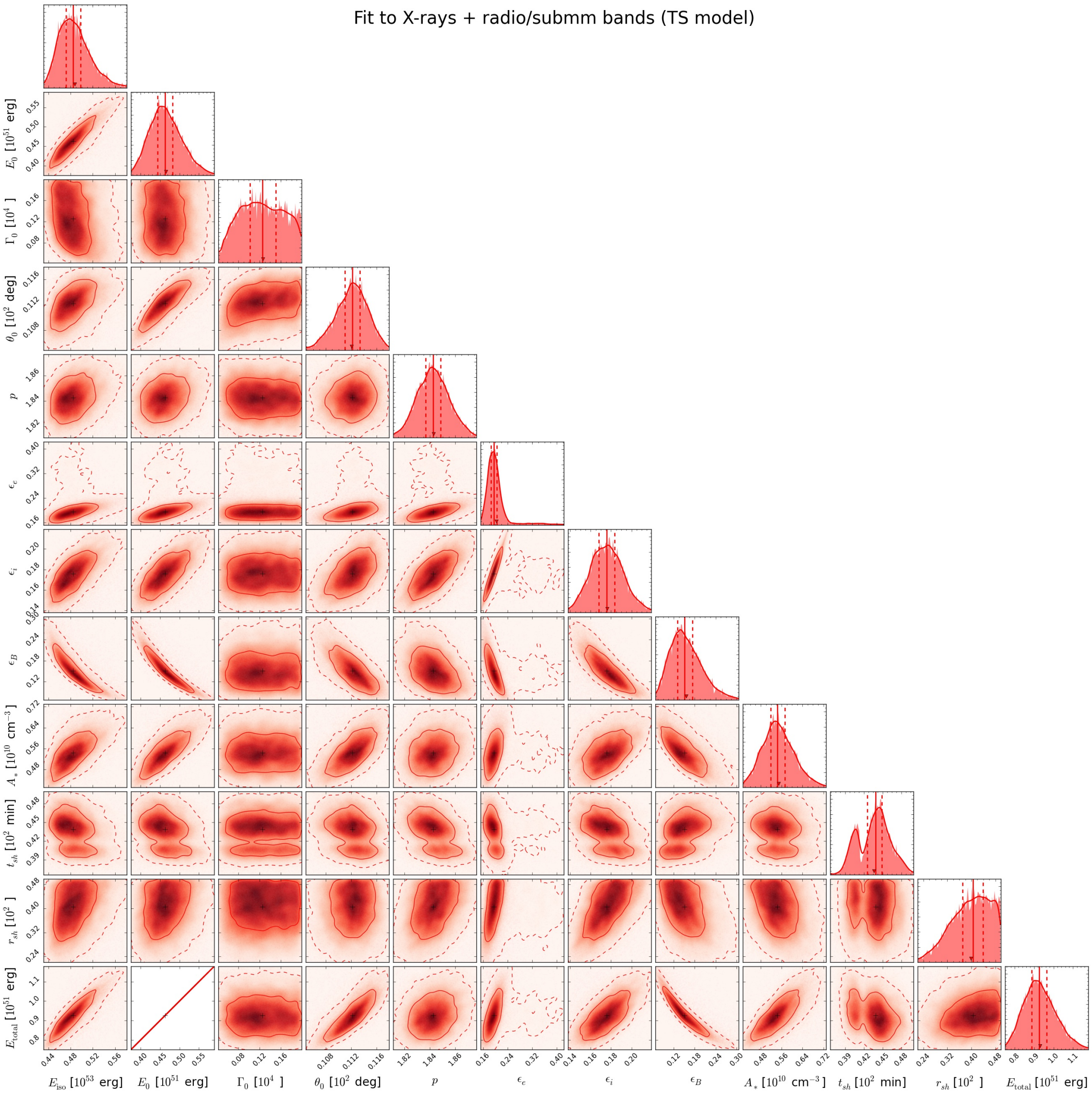
Fit to X-rays + radio/submm bands (TS model)
$E_{\rm iso}$ [10^{53} erg]
E_0 [10^{51} erg]
Γ_0 [10^4]
θ_0 [10^2 deg]
p
ϵ_e
ϵ_i
ϵ_B
A_* [10^{10} cm^{-3}]
t_{sh} [10^2 min]
r_{sh} [10^2]
$E_{\rm total}$ [10^{51} erg]

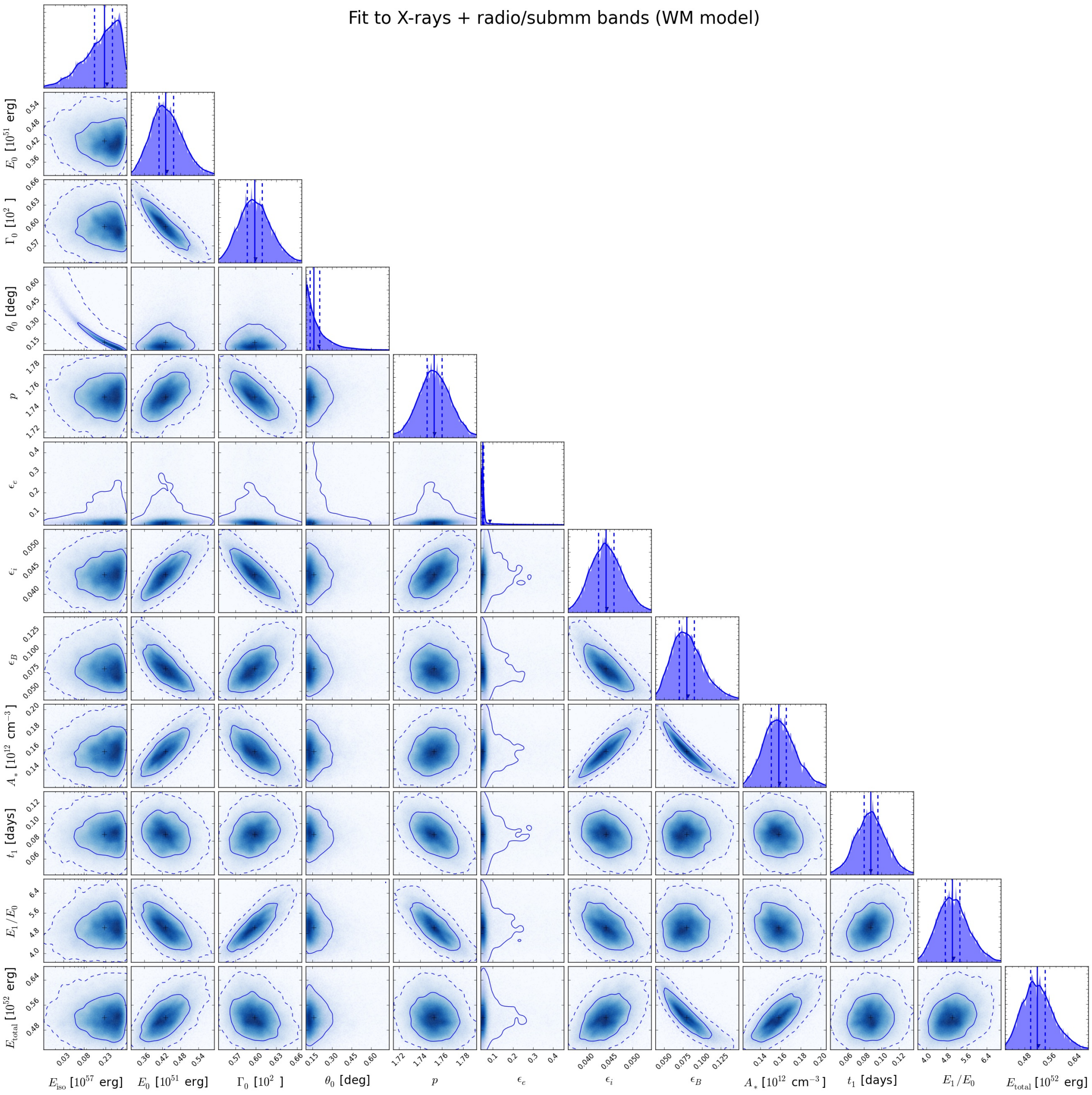
Fit to X-rays + radio/submm bands (WM model)
$E_{\rm iso}$ [10^{57} erg]
E_0 [10^{51} erg]
Γ_0 [10^2]
θ_0 [deg]
p
ϵ_e
ϵ_i
ϵ_B
A_* [10^{12} cm^{-3}]
t_1 [days]
E_1/E_0
$E_{\rm total}$ [10^{52} erg]
0.03
0.08
0.23
0.36
0.42
0.48
0.54
0.57
0.60
0.63
0.66
0.15
0.30
0.45
0.60
1.72
1.74
1.76
1.78
0.1
0.2
0.3
0.4
0.040
0.045
0.050
0.075
0.100
0.125
0.14
0.16
0.18
0.20
0.06
0.08
0.10
0.12
4.0
4.8
5.6
6.4
0.48
0.56
0.64

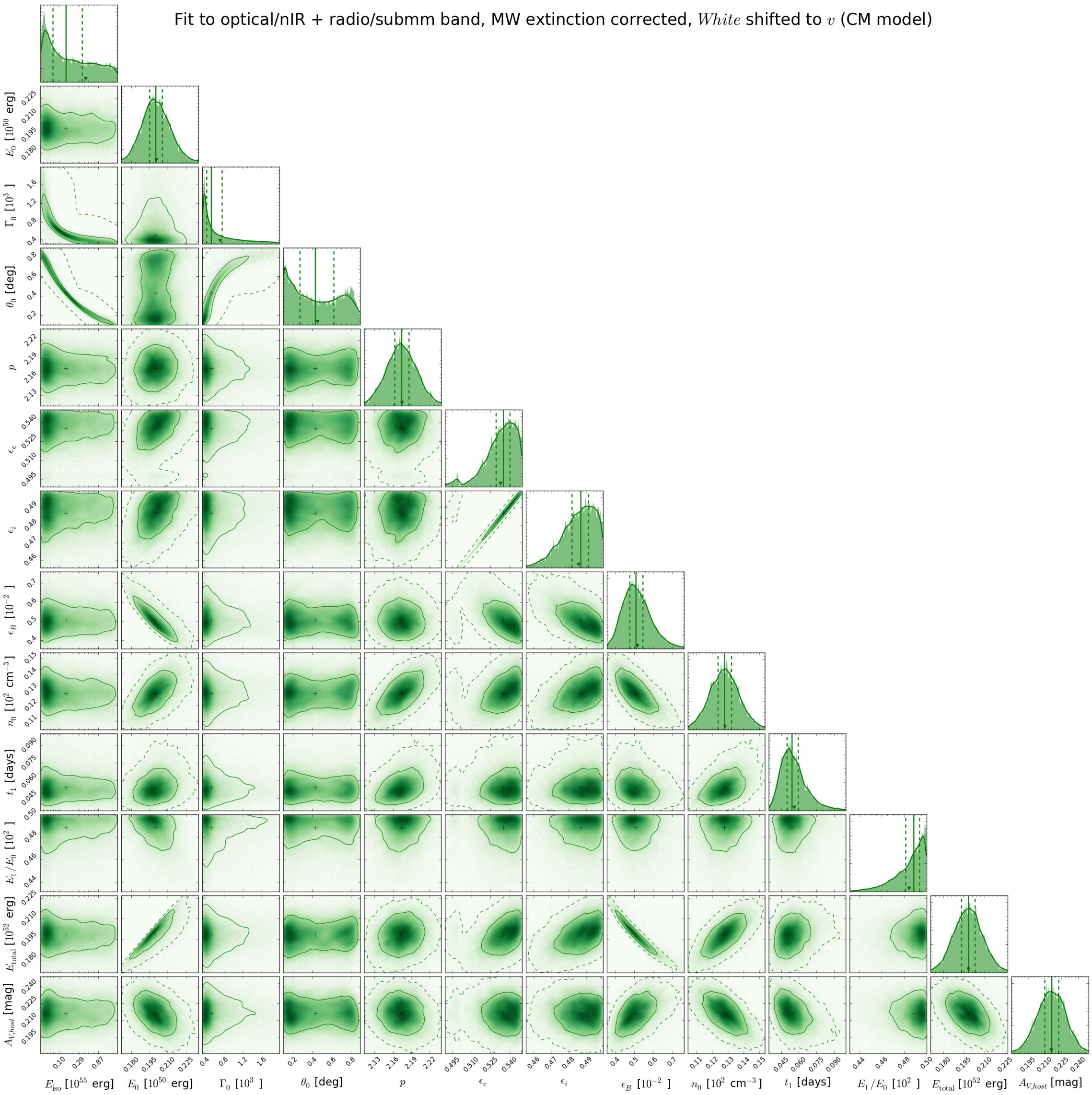
Fit to optical/nIR + radio/submm band, MW extinction corrected, $White$ shifted to v (CM model)
$E_{\rm iso}$ [10^{55} erg]
E_0 [10^{50} erg]
Γ_0 [10^3]
θ_0 [deg]
p
ϵ_e
ϵ_i
ϵ_B [10^{-2}]
n_0 [10^2 cm^{-3}]
t_1 [days]
E_1/E_0 [10^2]
$E_{\rm total}$ [10^{52} erg]
$A_{V,host}$ [mag]

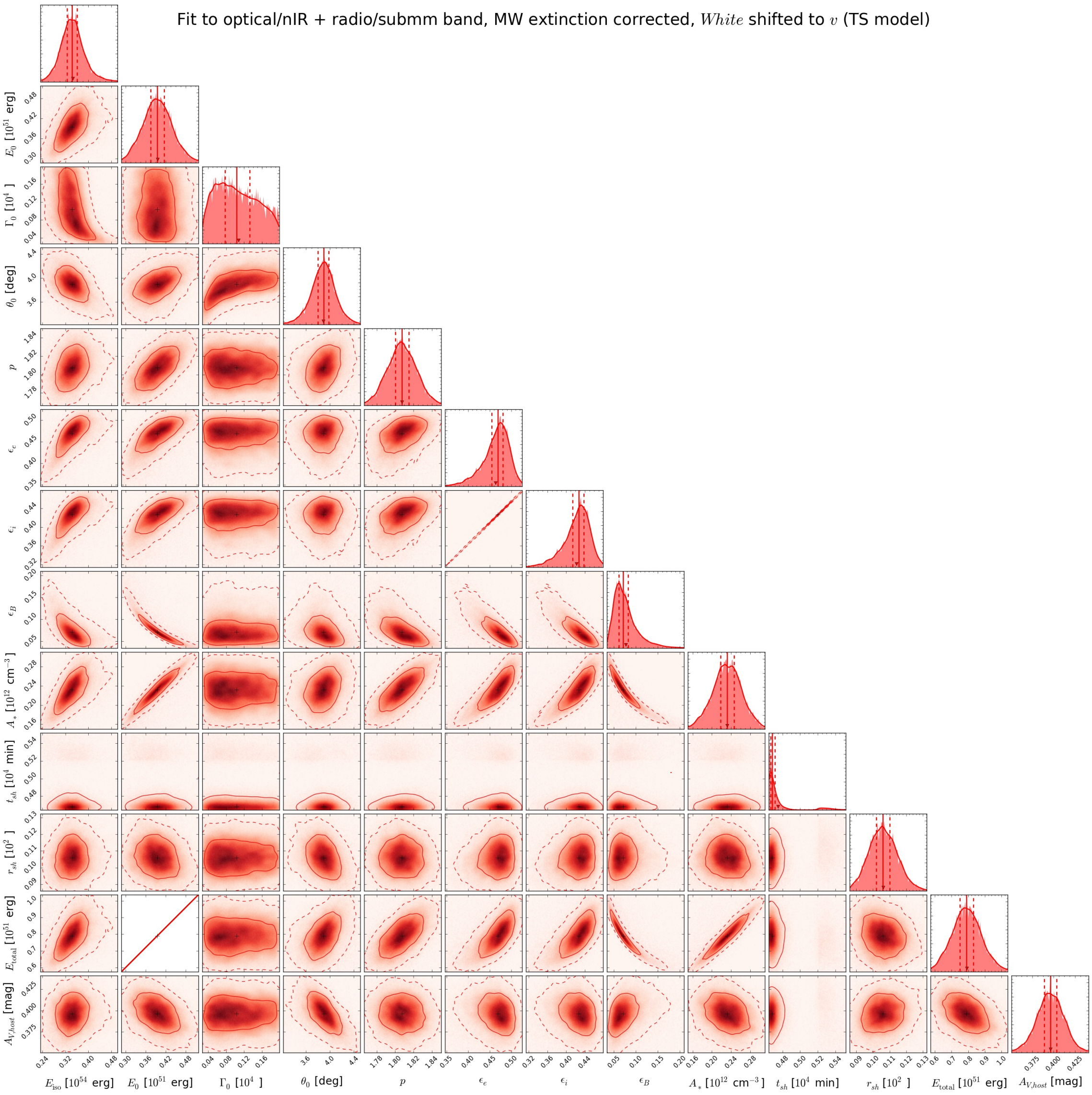
Fit to optical/nIR + radio/submm band, MW extinction corrected, $White$ shifted to v (TS model)
$E_{\rm iso}$ [10^{54} erg]
E_0 [10^{51} erg]
Γ_0 [10^4]
θ_0 [deg]
p
ϵ_e
ϵ_i
ϵ_B
A_* [10^{12} cm^{-3}]
t_{sh} [10^4 min]
r_{sh} [10^2]
$E_{\rm total}$ [10^{51} erg]
$A_{V,host}$ [mag]

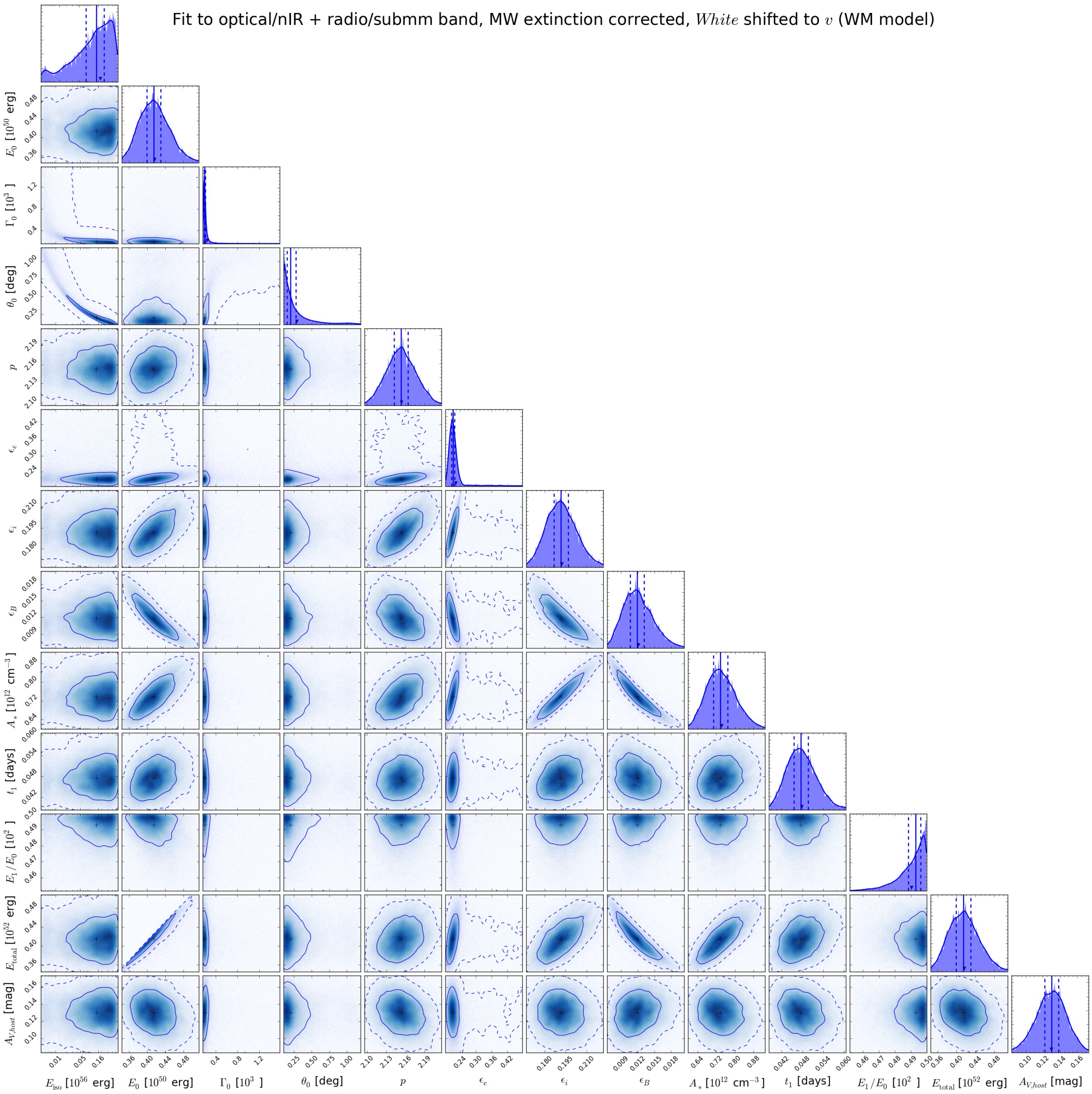
Fit to optical/nIR + radio/submm band, MW extinction corrected, $White$ shifted to v (WM model)

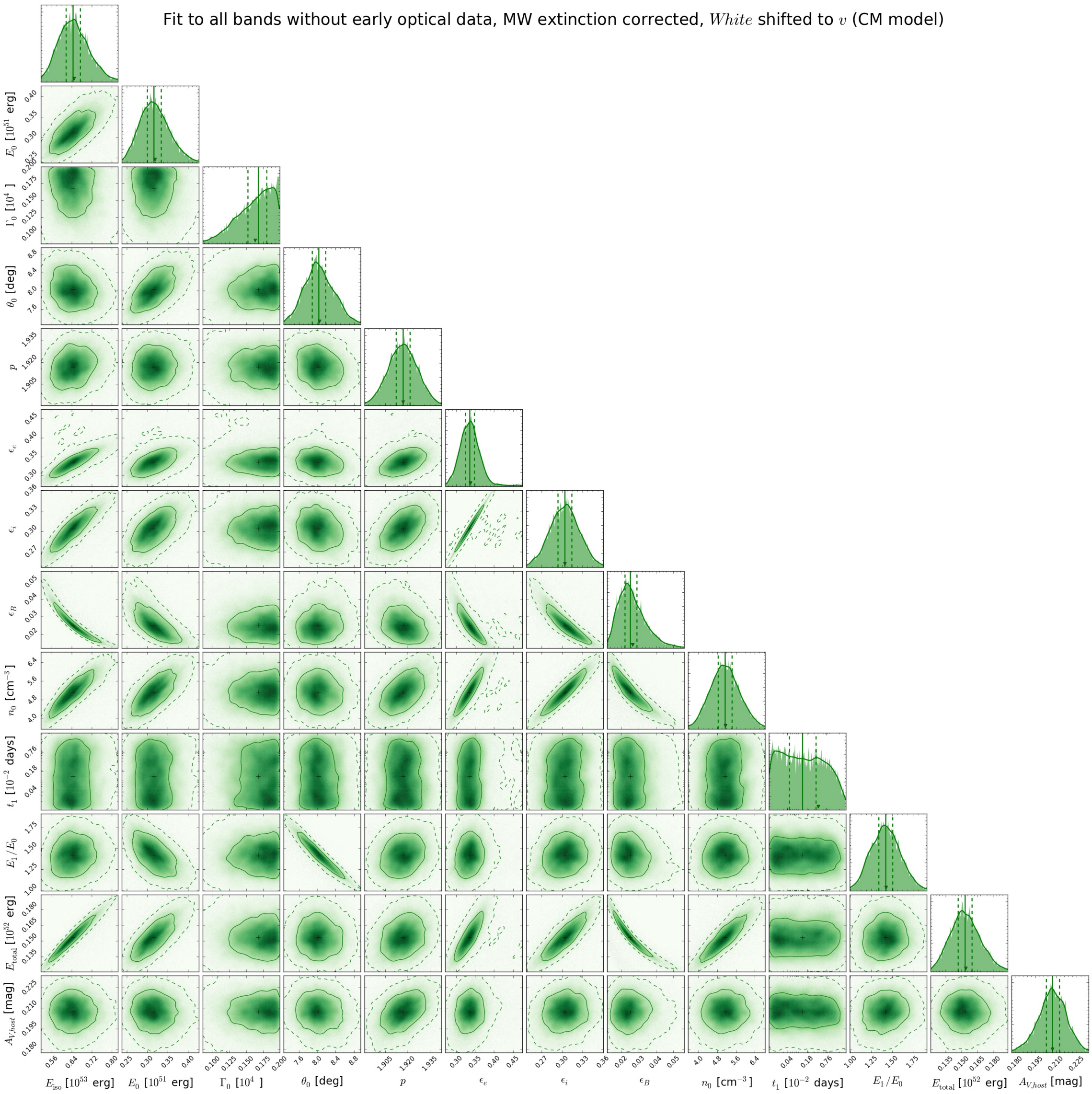

Fit to all bands without early optical data, MW extinction corrected, *White* shifted to v (CM model)

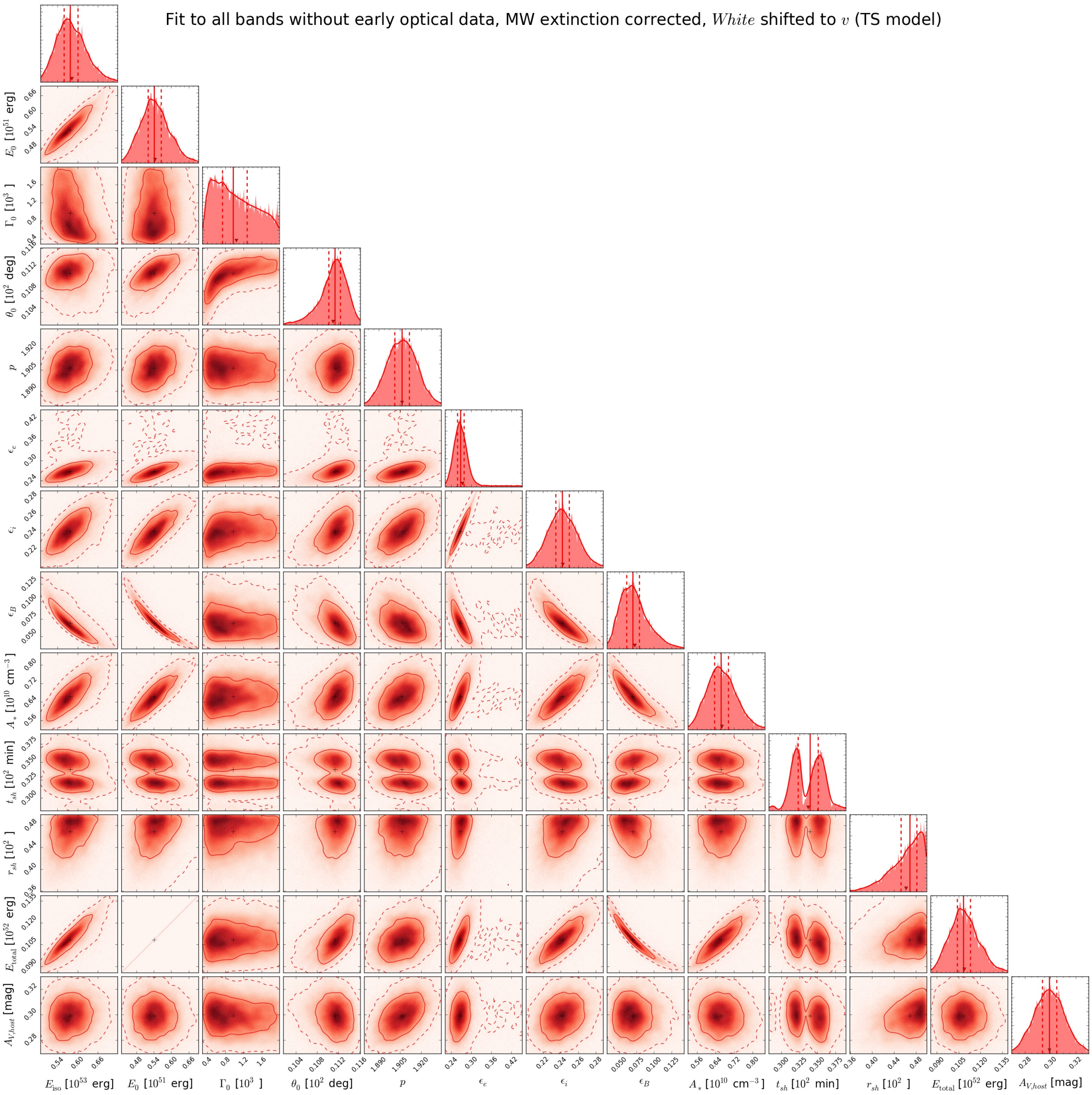

Fit to all bands without early optical data, MW extinction corrected, *White* shifted to v (TS model)

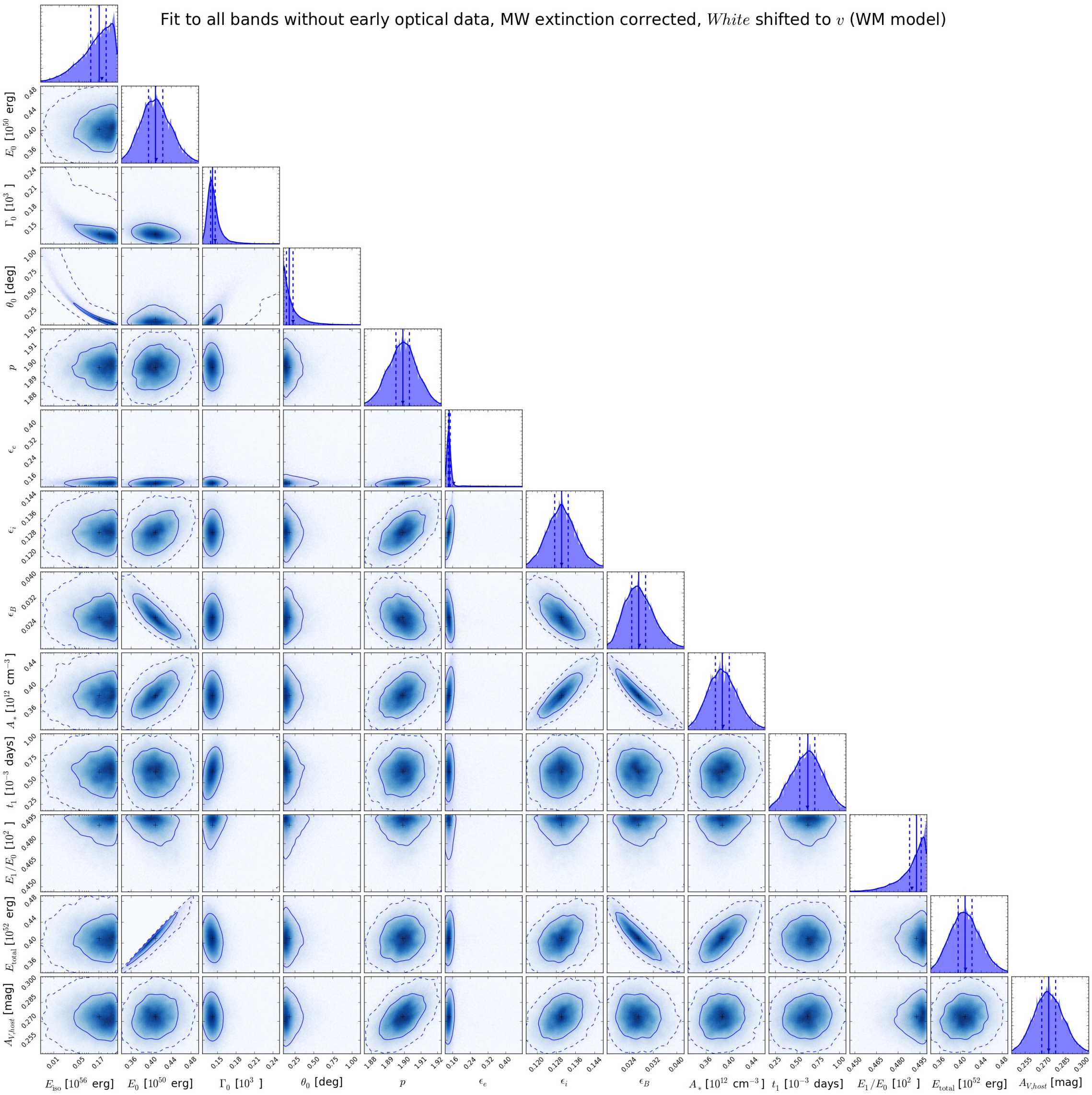

Fit to all bands without early optical data, MW extinction corrected, $White$ shifted to v (WM model)

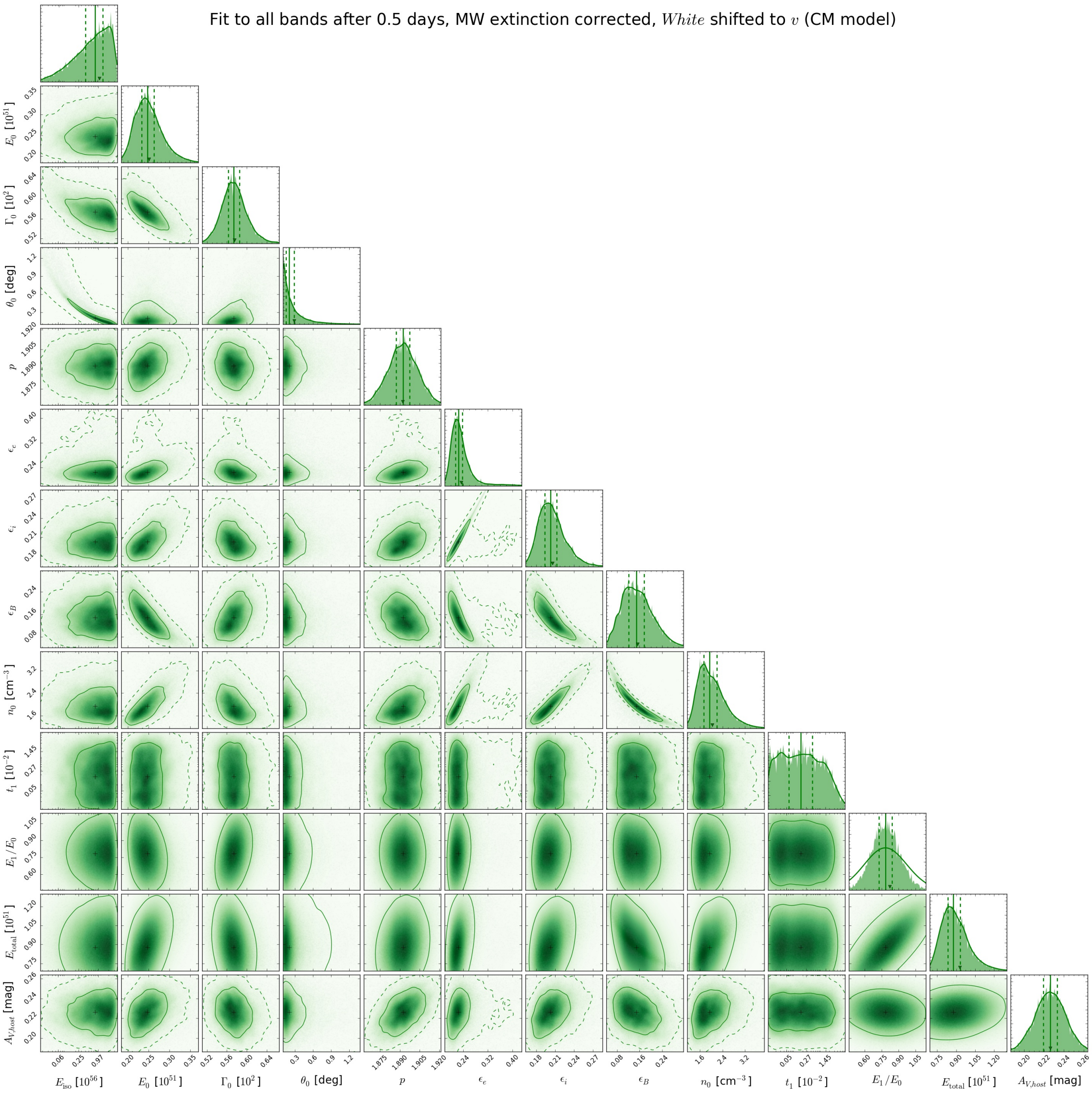

Fit to all bands after 0.5 days, MW extinction corrected, *White* shifted to v (CM model)

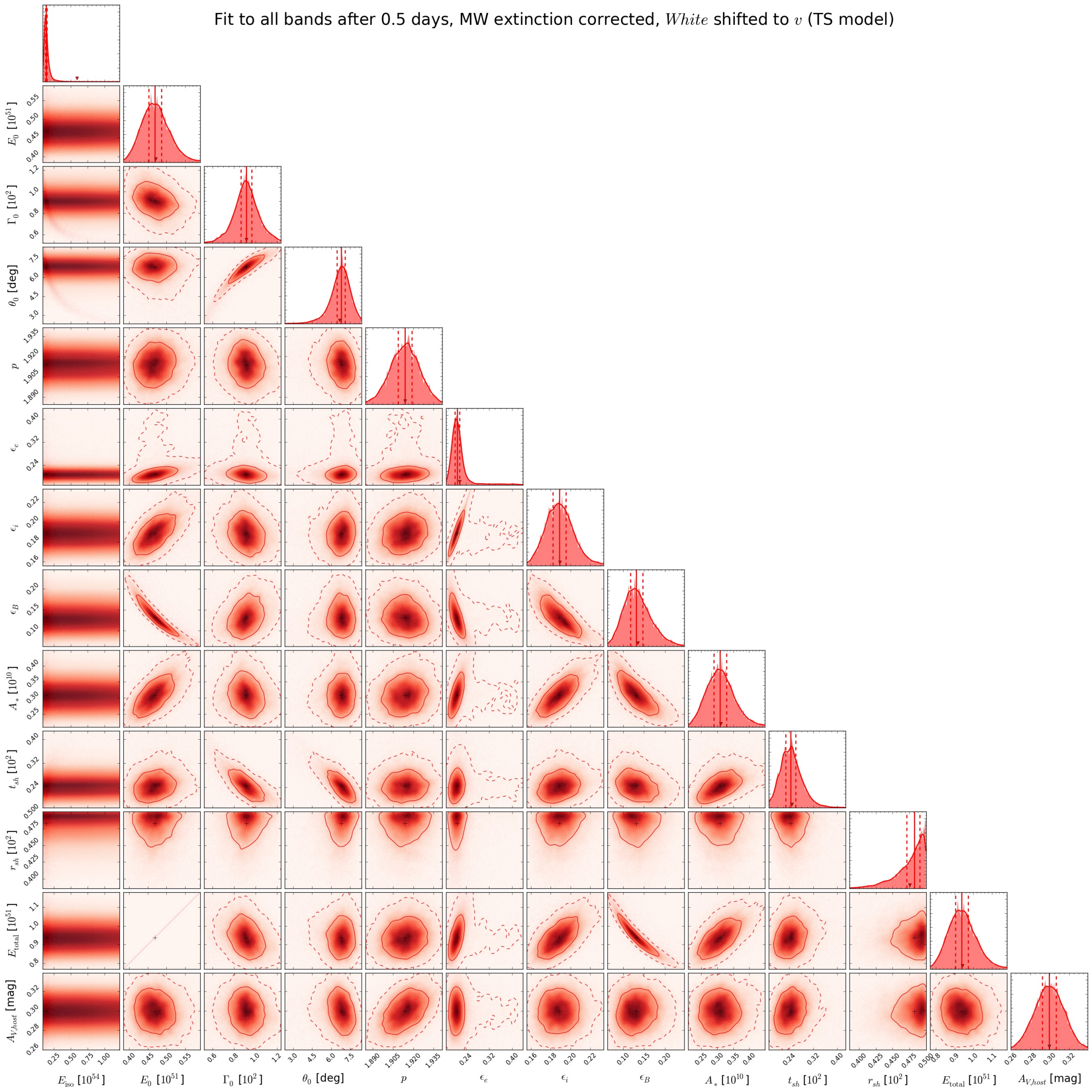
Fit to all bands after 0.5 days, MW extinction corrected, $White$ shifted to v (TS model)

Fit to all bands after 0.5 days, MW extinction corrected, $White$ shifted to v (WM model)

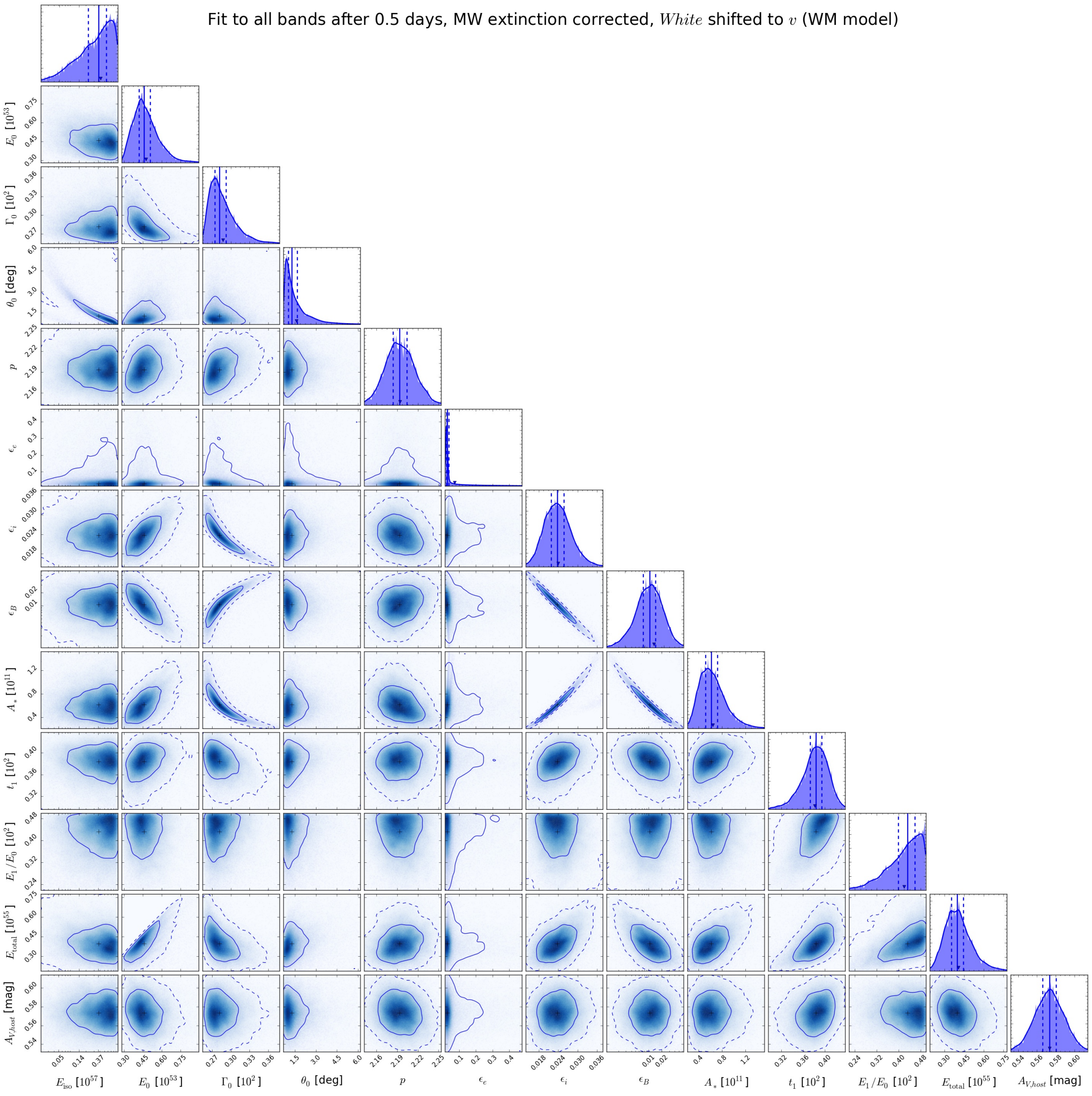

Appendix G

DLA fits

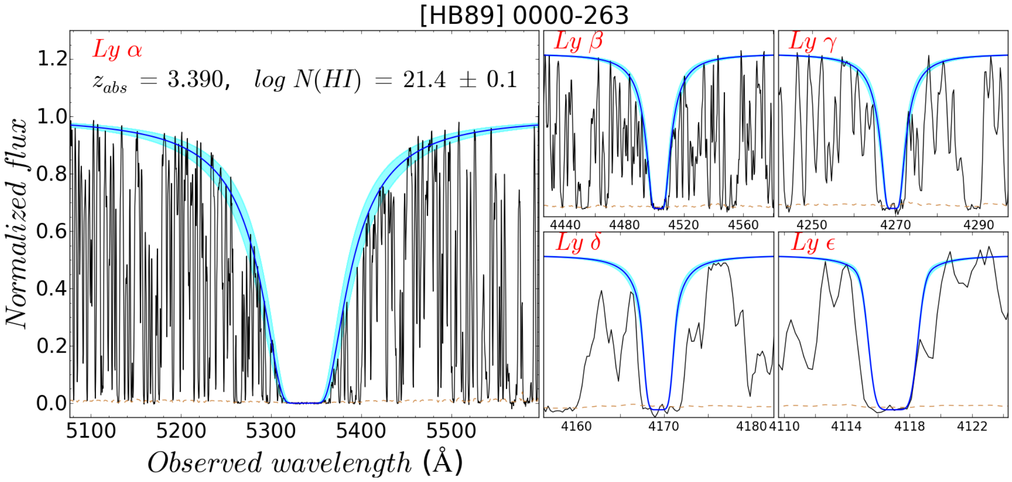

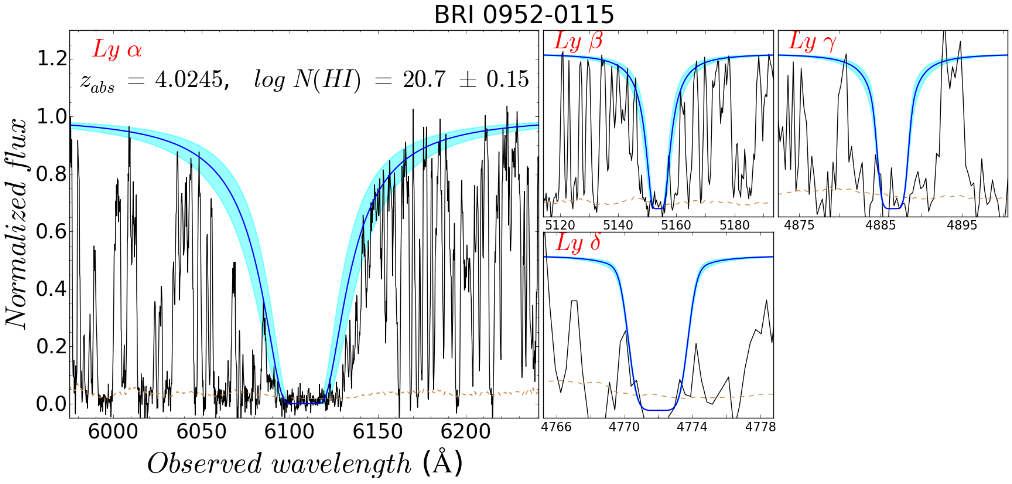

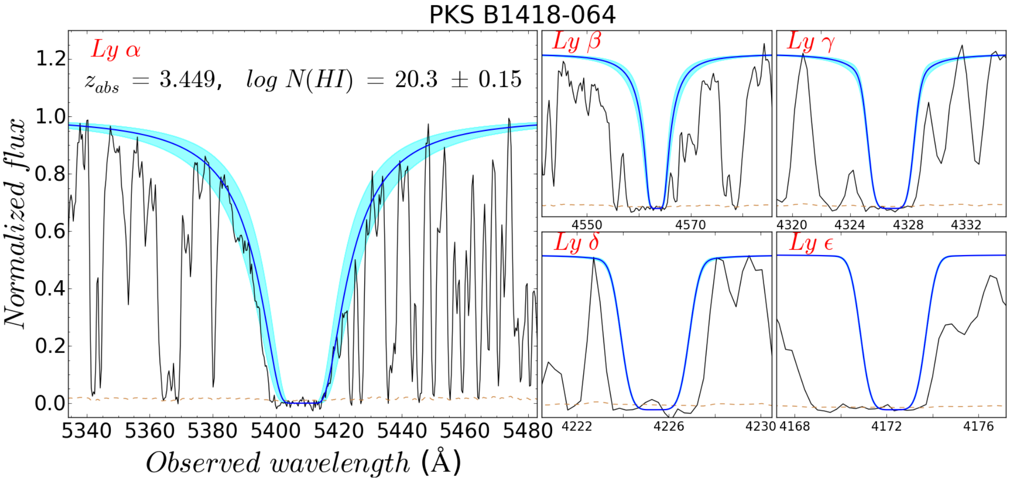
PKS B1418-064
Ly α
z_{abs} = 3.449, log N(HI) = 20.3 ± 0.15
Normalized flux
0.0
0.2
0.4
0.6
0.8
1.0
1.2
5340
5360
5380
5400
5420
5440
5460
5480
Observed wavelength (Å)
Ly β
4550
4570
Ly γ
4320
4324
4328
4332
Ly δ
4222
4226
4230
Ly ϵ
4168
4172
4176

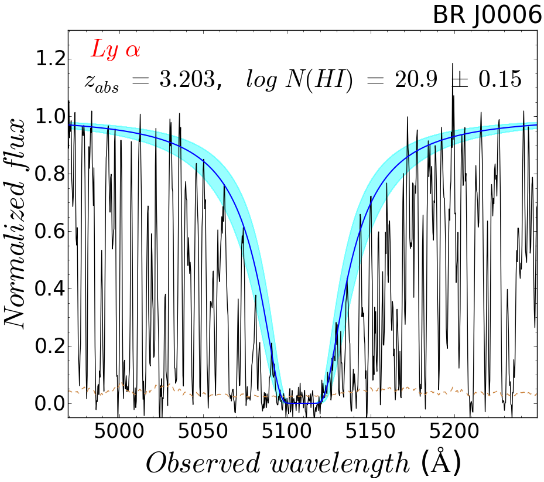
BR J0006-6208
Ly α
z_{abs} = 3.203, log N(HI) = 20.9 ± 0.15
Normalized flux
0.0
0.2
0.4
0.6
0.8
1.0
1.2
5000
5050
5100
5150
5200
Observed wavelength (Å)

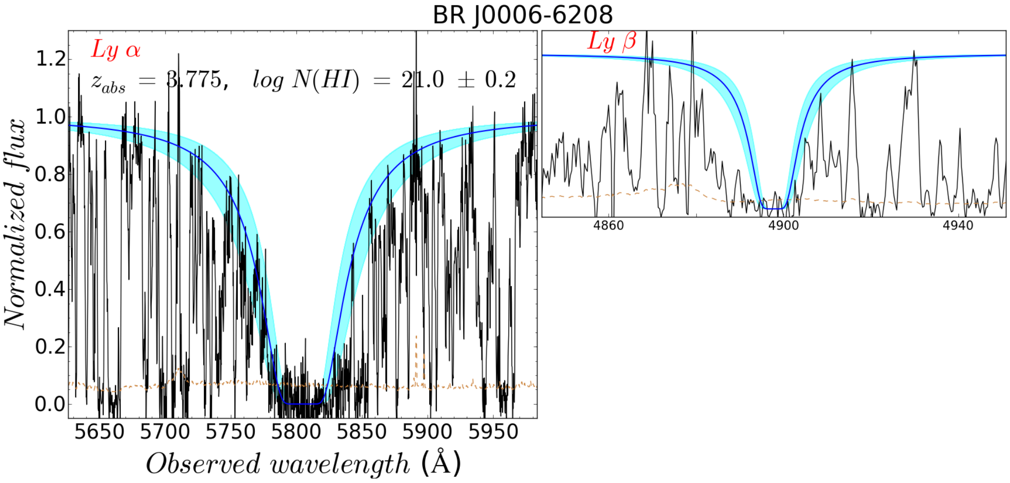
BR J0006-6208
Ly α
z_{abs} = 3.775, log N(HI) = 21.0 ± 0.2
Normalized flux
0.0
0.2
0.4
0.6
0.8
1.0
1.2
5650
5700
5750
5800
5850
5900
5950
Observed wavelength (Å)
Ly β
4860
4900
4940

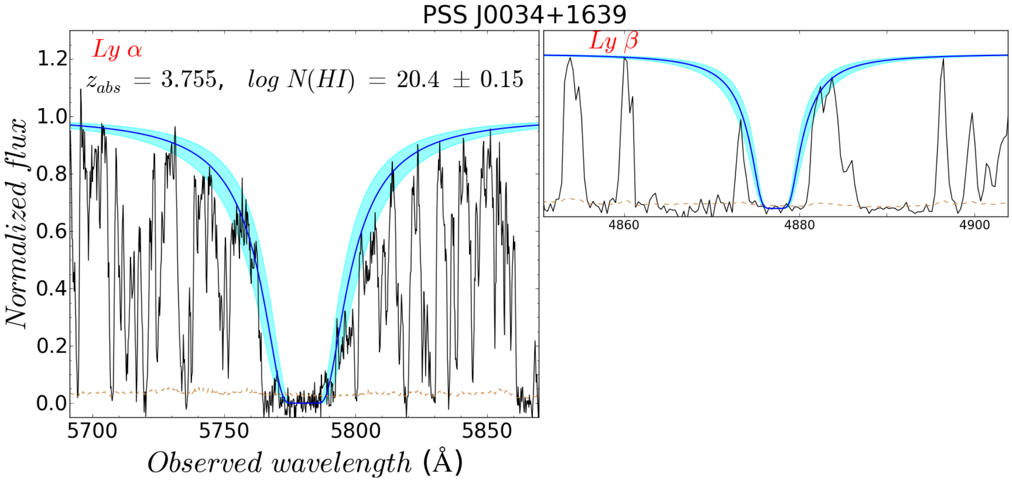
PSS J0034+1639
Ly α
z_{abs} = 3.755, log N(HI) = 20.4 ± 0.15
Normalized flux
0.0
0.2
0.4
0.6
0.8
1.0
1.2
5700
5750
5800
5850
Observed wavelength (Å)
Ly β
4860
4880
4900

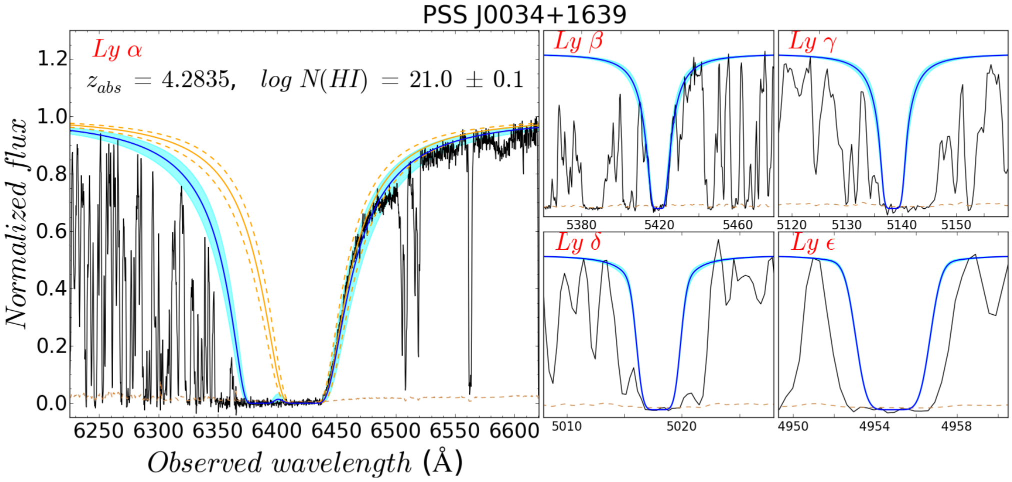
PSS J0034+1639
Ly α
z_{abs} = 4.2835, log N(HI) = 21.0 ± 0.1
Normalized flux
0.0
0.2
0.4
0.6
0.8
1.0
1.2
6250
6300
6350
6400
6450
6500
6550
6600
Observed wavelength (Å)
Ly β
5380
5420
5460
Ly γ
5120
5130
5140
5150
Ly δ
5010
5020
Ly ϵ
4950
4954
4958

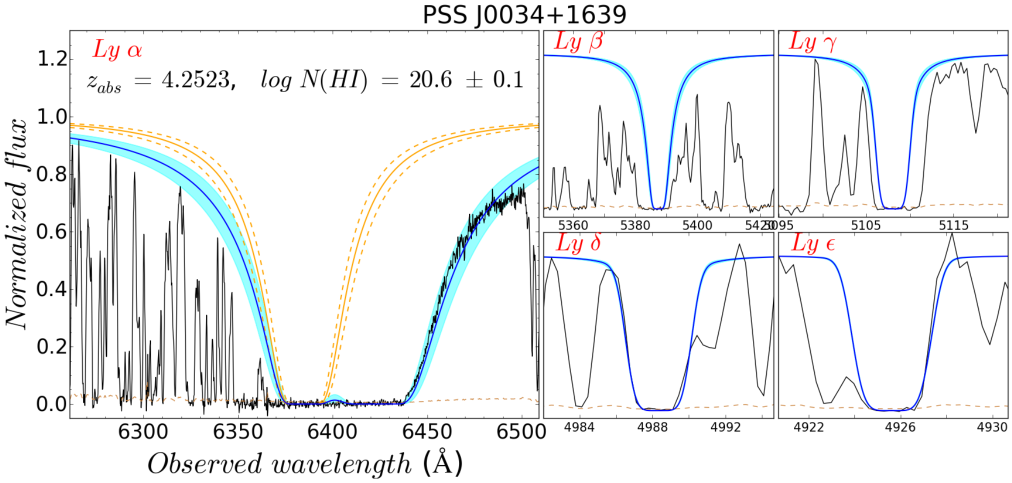
PSS J0034+1639
Ly α
z_{abs} = 4.2523, log N(HI) = 20.6 ± 0.1
Normalized flux
0.0
0.2
0.4
0.6
0.8
1.0
1.2
6300
6350
6400
6450
6500
Observed wavelength (Å)
Ly β
5360
5380
5400
5420
Ly γ
5095
5105
5115
Ly δ
4984
4988
4992
Ly ϵ
4922
4926
4930

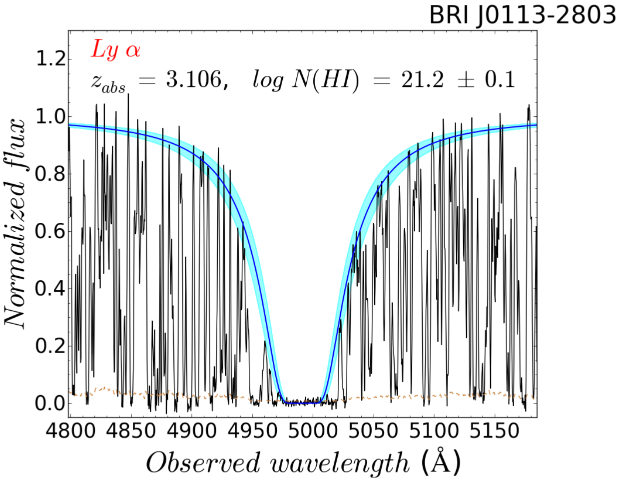
BRI J0113-2803
Ly α
z_{abs} = 3.106, log N(HI) = 21.2 ± 0.1
Normalized flux
1.2
1.0
0.8
0.6
0.4
0.2
0.0
4800 4850 4900 4950 5000 5050 5100 5150
Observed wavelength (Å)

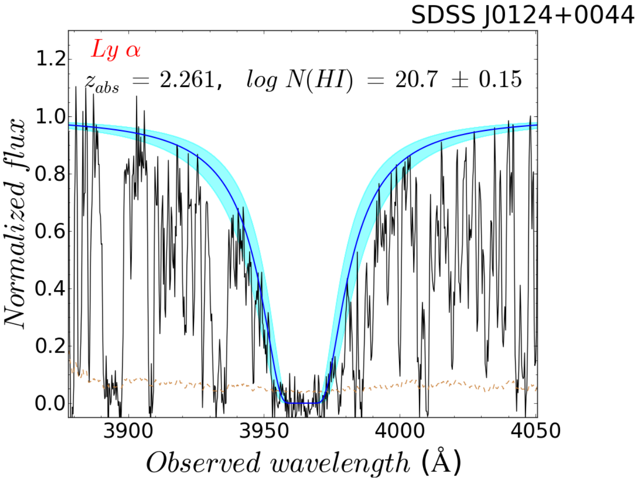
SDSS J0124+0044
Ly α
z_{abs} = 2.261, log N(HI) = 20.7 ± 0.15
Normalized flux
1.2
1.0
0.8
0.6
0.4
0.2
0.0
3900 3950 4000 4050
Observed wavelength (Å)

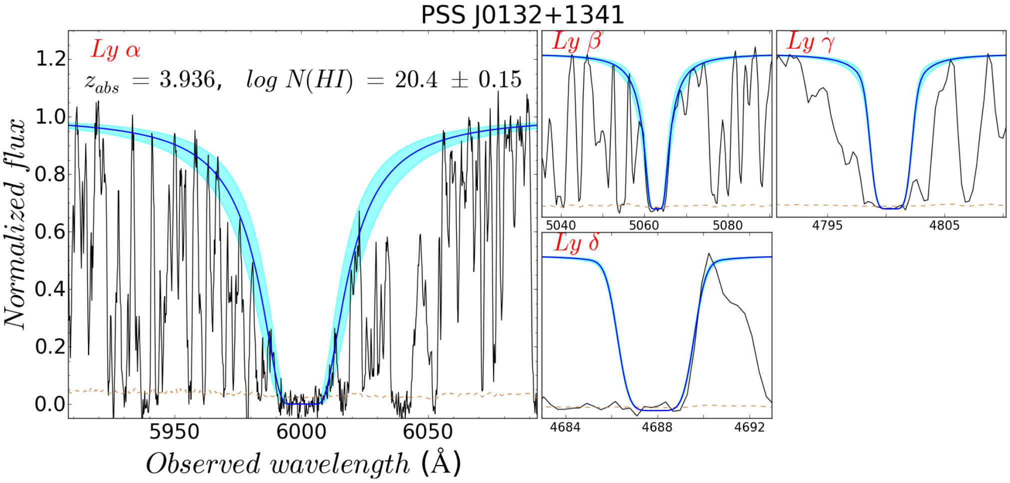
PSS J0132+1341
Ly α
z_{abs} = 3.936, log N(HI) = 20.4 ± 0.15
Normalized flux
1.2
1.0
0.8
0.6
0.4
0.2
0.0
5950 6000 6050
Observed wavelength (Å)
Ly β
5040 5060 5080
Ly γ
4795 4805
Ly δ
4684 4688 4692

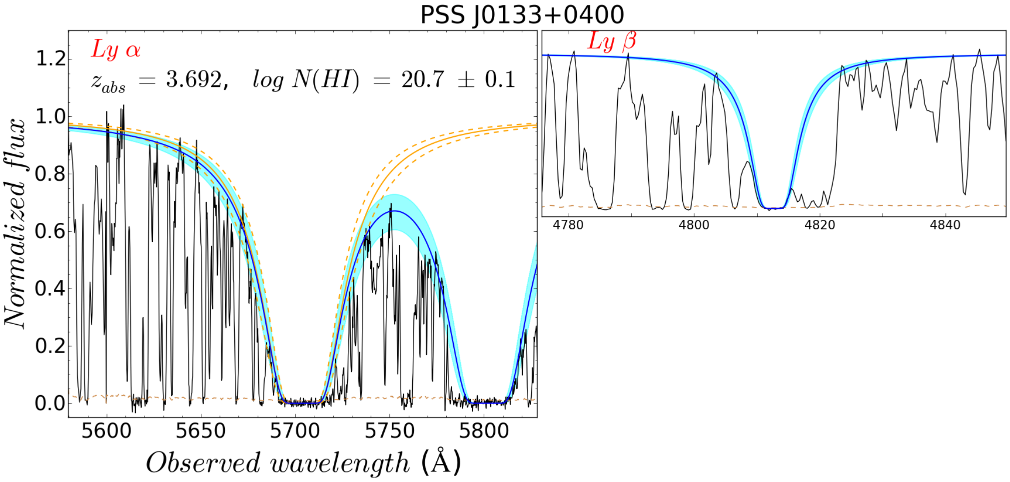
PSS J0133+0400
Ly α
z_{abs} = 3.692, log N(HI) = 20.7 ± 0.1
Normalized flux
0.0
0.2
0.4
0.6
0.8
1.0
1.2
5600
5650
5700
5750
5800
Observed wavelength (Å)
Ly β
4780
4800
4820
4840

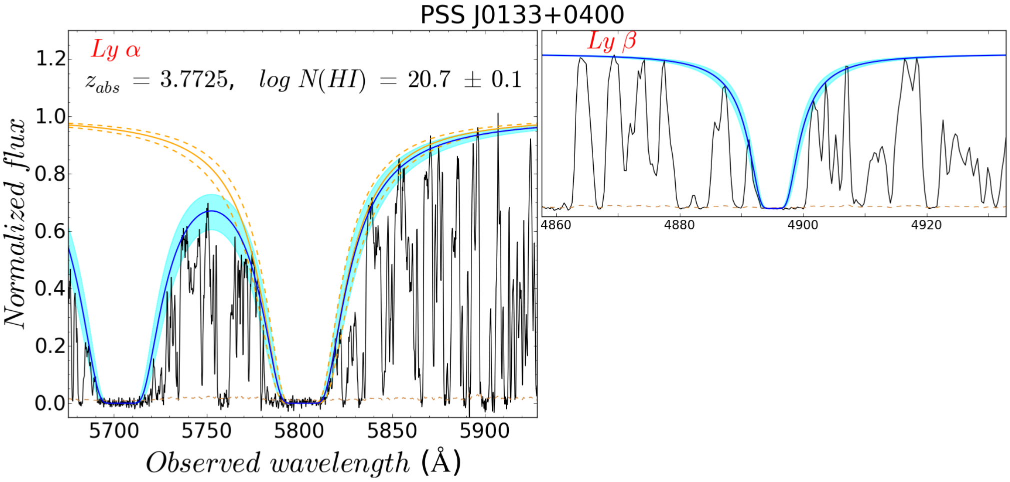
PSS J0133+0400
Ly α
z_{abs} = 3.7725, log N(HI) = 20.7 ± 0.1
Normalized flux
0.0
0.2
0.4
0.6
0.8
1.0
1.2
5700
5750
5800
5850
5900
Observed wavelength (Å)
Ly β
4860
4880
4900
4920

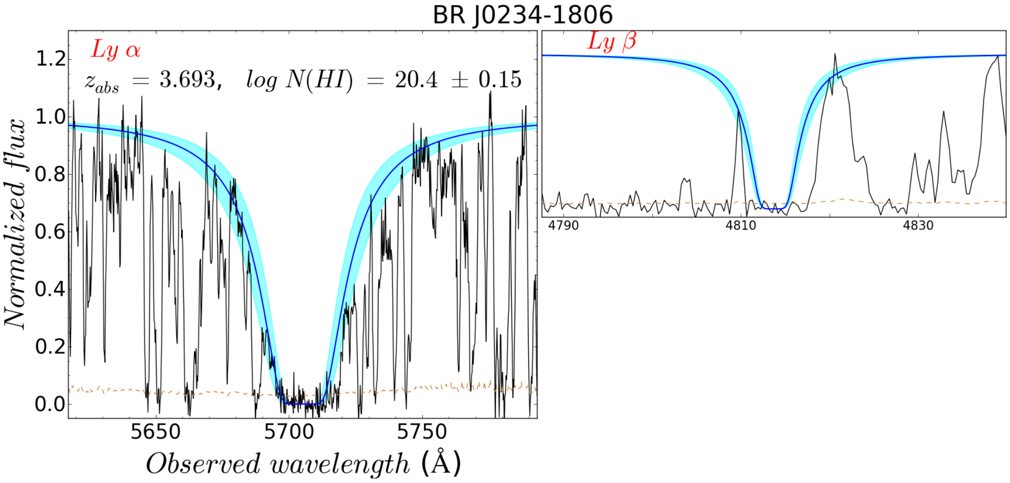
BR J0234-1806
Ly α
z_{abs} = 3.693, log N(HI) = 20.4 ± 0.15
Normalized flux
0.0
0.2
0.4
0.6
0.8
1.0
1.2
5650
5700
5750
Observed wavelength (Å)
Ly β
4790
4810
4830

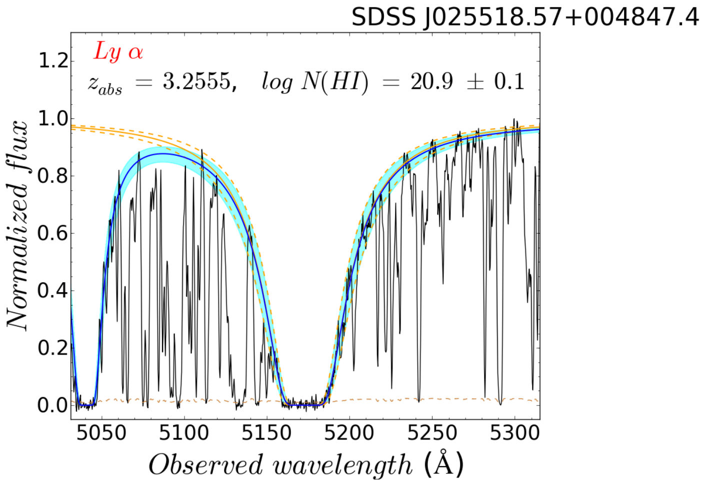
SDSS J025518.57+004847.4
Ly α
z_{abs} = 3.2555, log N(HI) = 20.9 ± 0.1
Normalized flux
Observed wavelength (Å)
0.0
0.2
0.4
0.6
0.8
1.0
1.2
5050
5100
5150
5200
5250
5300

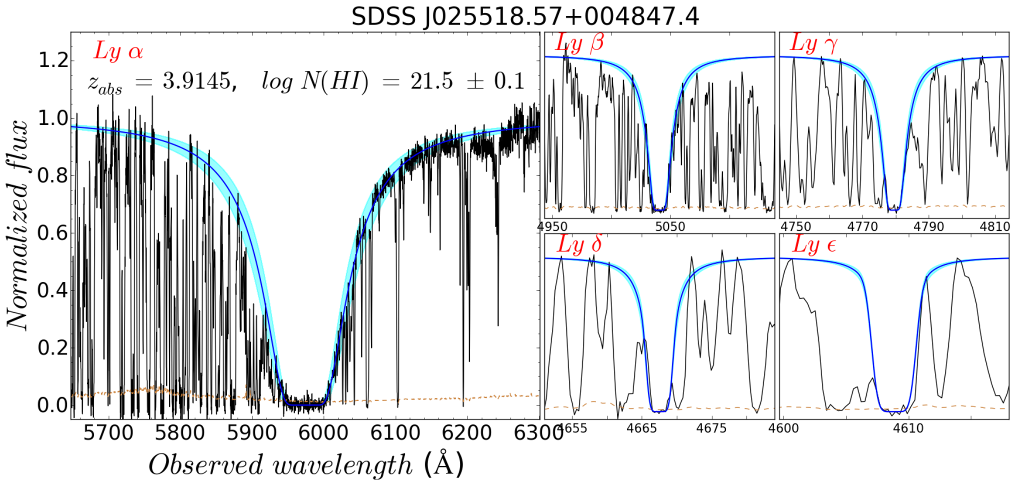
SDSS J025518.57+004847.4
Ly α
z_{abs} = 3.9145, log N(HI) = 21.5 ± 0.1
Normalized flux
Observed wavelength (Å)
0.0
0.2
0.4
0.6
0.8
1.0
1.2
5700
5800
5900
6000
6100
6200
6300
Ly β
4950
5050
Ly γ
4750
4770
4790
4810
Ly δ
4655
4665
4675
Ly ϵ
4600
4610

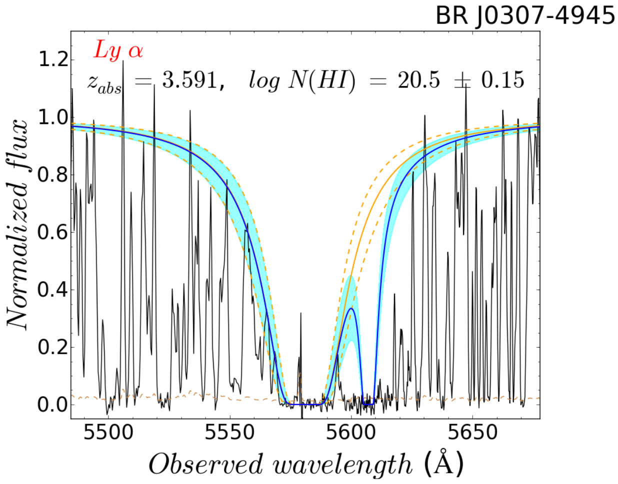
BR J0307-4945
Ly α
z_{abs} = 3.591, log N(HI) = 20.5 ± 0.15
Normalized flux
Observed wavelength (Å)
0.0
0.2
0.4
0.6
0.8
1.0
1.2
5500
5550
5600
5650

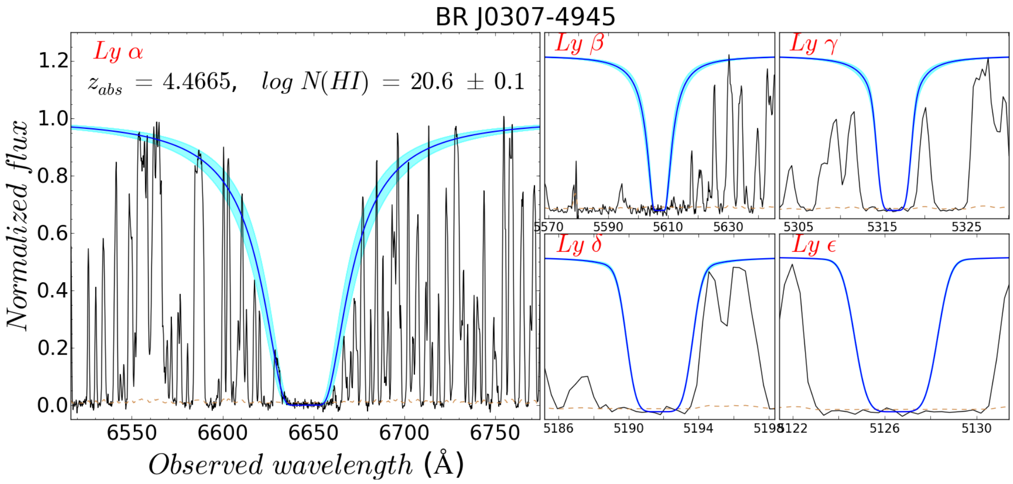
BR J0307-4945
Ly α
z_abs = 4.4665, log N(HI) = 20.6 ± 0.1
Normalized flux
Observed wavelength (Å)
0.0
0.2
0.4
0.6
0.8
1.0
1.2
6550
6600
6650
6700
6750
Ly β
5570
5590
5610
5630
Ly γ
5305
5315
5325
Ly δ
5186
5190
5194
5198
Ly ε
5122
5126
5130

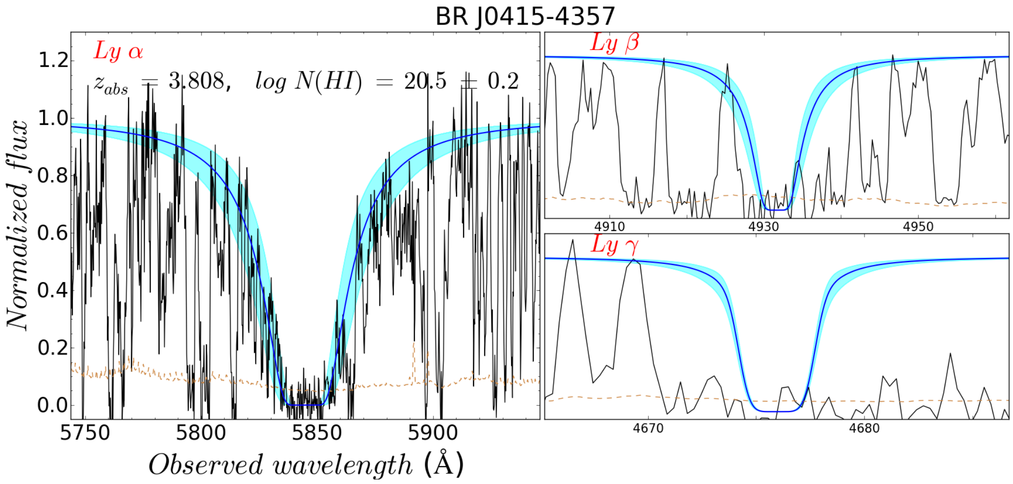
BR J0415-4357
Ly α
z_abs = 3.808, log N(HI) = 20.5 ± 0.2
Normalized flux
Observed wavelength (Å)
0.0
0.2
0.4
0.6
0.8
1.0
1.2
5750
5800
5850
5900
Ly β
4910
4930
4950
Ly γ
4670
4680

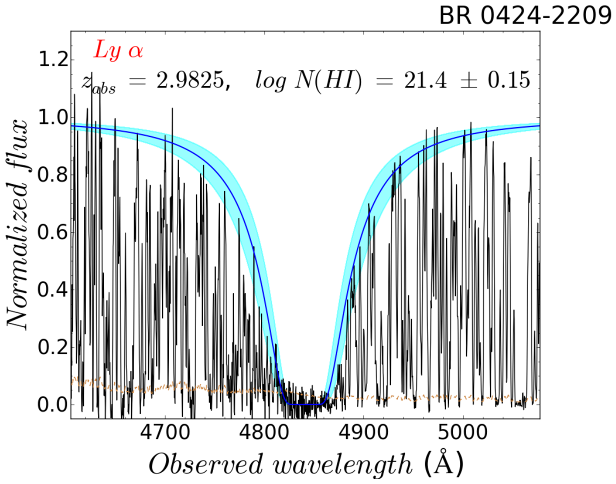
BR 0424-2209
Ly α
z_abs = 2.9825, log N(HI) = 21.4 ± 0.15
Normalized flux
Observed wavelength (Å)
0.0
0.2
0.4
0.6
0.8
1.0
1.2
4700
4800
4900
5000

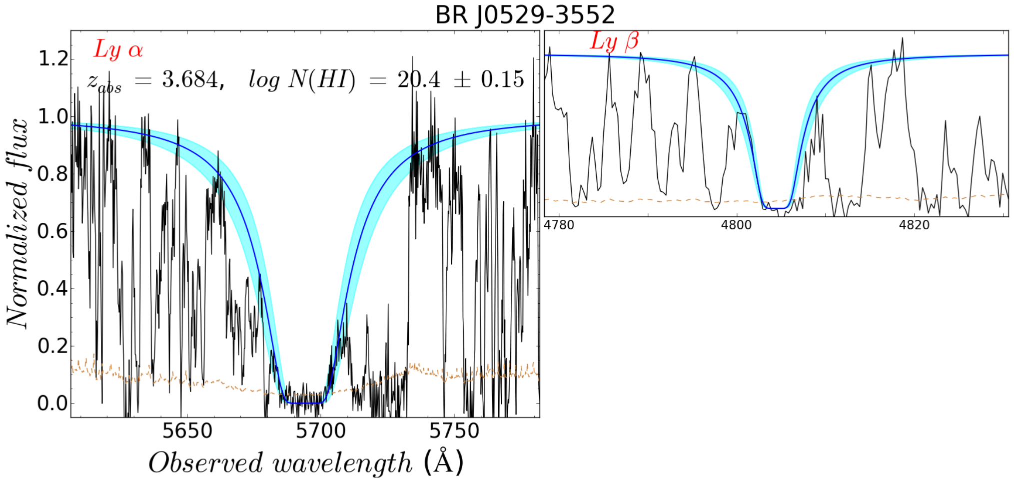
BR J0529-3552
Ly α
$z_{abs} = 3.684$, $log\ N(HI) = 20.4 \pm 0.15$
Normalized flux
0.0
0.2
0.4
0.6
0.8
1.0
1.2
5650
5700
5750
Observed wavelength (Å)
Ly β
4780
4800
4820

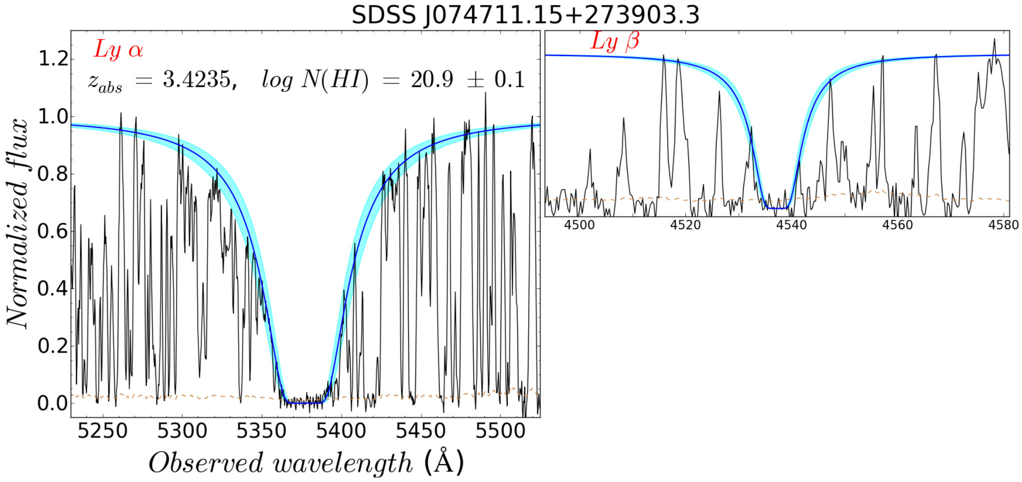
SDSS J074711.15+273903.3
Ly α
$z_{abs} = 3.4235$, $log\ N(HI) = 20.9 \pm 0.1$
Normalized flux
0.0
0.2
0.4
0.6
0.8
1.0
1.2
5250
5300
5350
5400
5450
5500
Observed wavelength (Å)
Ly β
4500
4520
4540
4560
4580

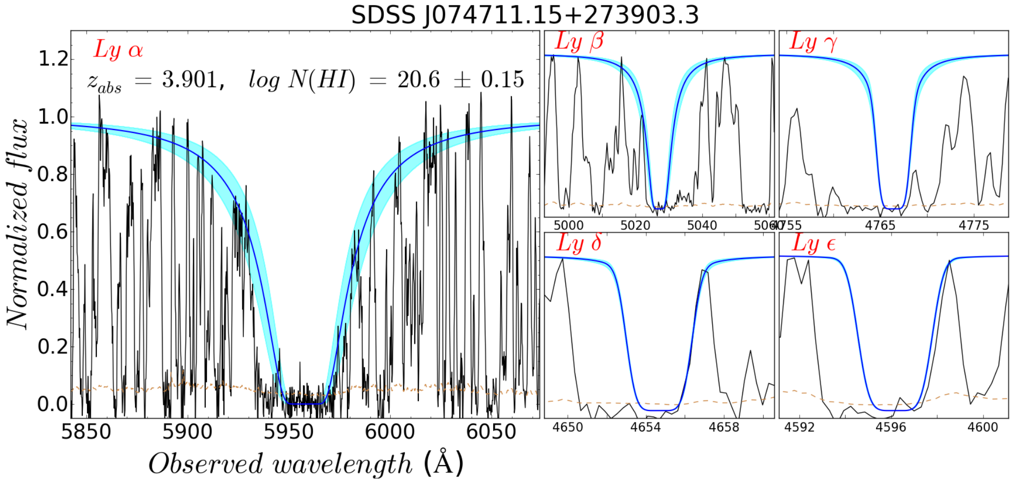
SDSS J074711.15+273903.3
Ly α
$z_{abs} = 3.901$, $log\ N(HI) = 20.6 \pm 0.15$
Normalized flux
0.0
0.2
0.4
0.6
0.8
1.0
1.2
5850
5900
5950
6000
6050
Observed wavelength (Å)
Ly β
5000
5020
5040
5060
Ly γ
4755
4765
4775
Ly δ
4650
4654
4658
Ly ϵ
4592
4596
4600

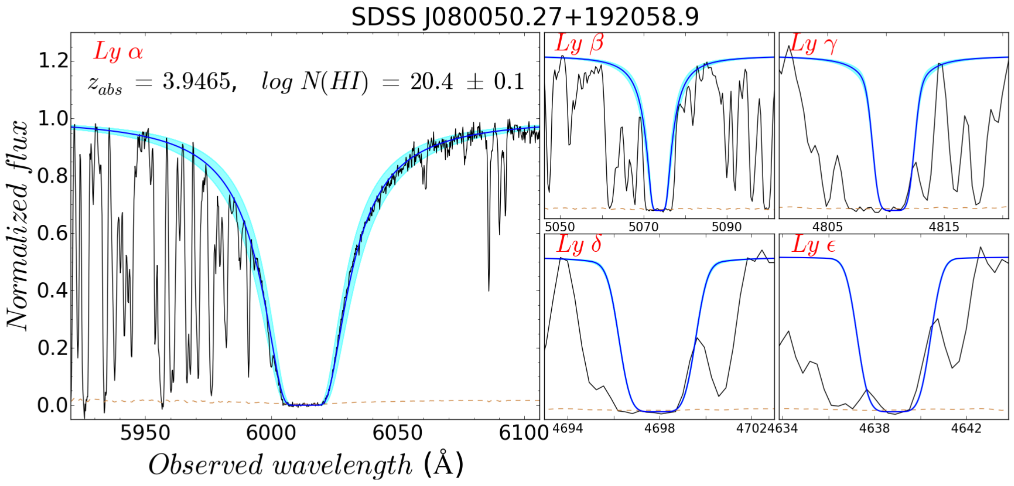
SDSS J080050.27+192058.9
Ly α
z_{abs} = 3.9465, log N(HI) = 20.4 ± 0.1
Normalized flux
Observed wavelength (Å)
0.0
0.2
0.4
0.6
0.8
1.0
1.2
5950
6000
6050
6100
Ly β
5050
5070
5090
Ly γ
4805
4815
Ly δ
4694
4698
4702
Ly ϵ
4634
4638
4642

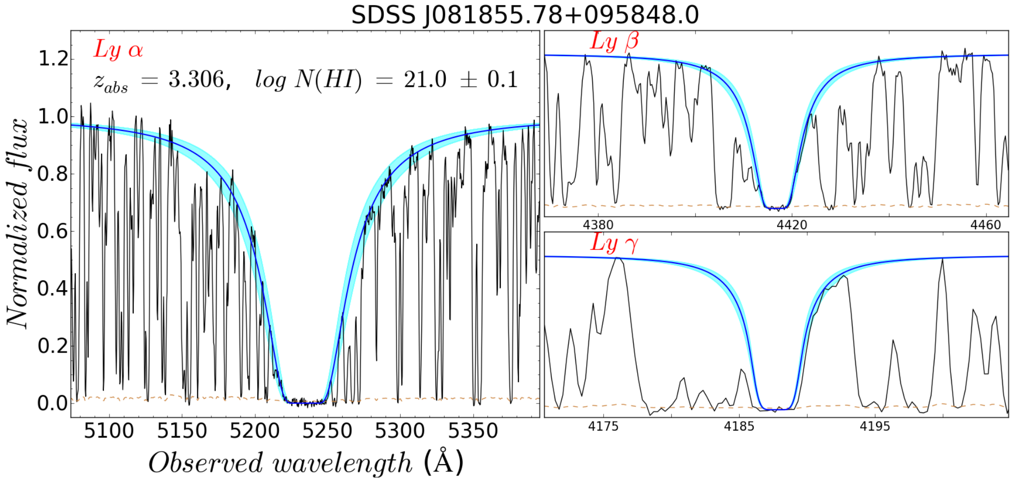
SDSS J081855.78+095848.0
Ly α
z_{abs} = 3.306, log N(HI) = 21.0 ± 0.1
Normalized flux
Observed wavelength (Å)
0.0
0.2
0.4
0.6
0.8
1.0
1.2
5100
5150
5200
5250
5300
5350
Ly β
4380
4420
4460
Ly γ
4175
4185
4195

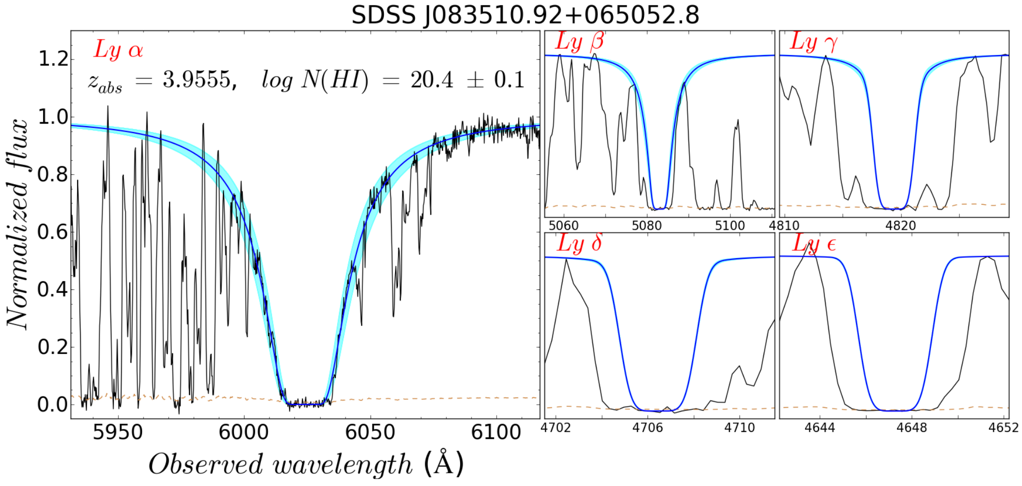
SDSS J083510.92+065052.8
Ly α
z_{abs} = 3.9555, log N(HI) = 20.4 ± 0.1
Normalized flux
Observed wavelength (Å)
0.0
0.2
0.4
0.6
0.8
1.0
1.2
5950
6000
6050
6100
Ly β
5060
5080
5100
Ly γ
4810
4820
Ly δ
4702
4706
4710
Ly ϵ
4644
4648
4652

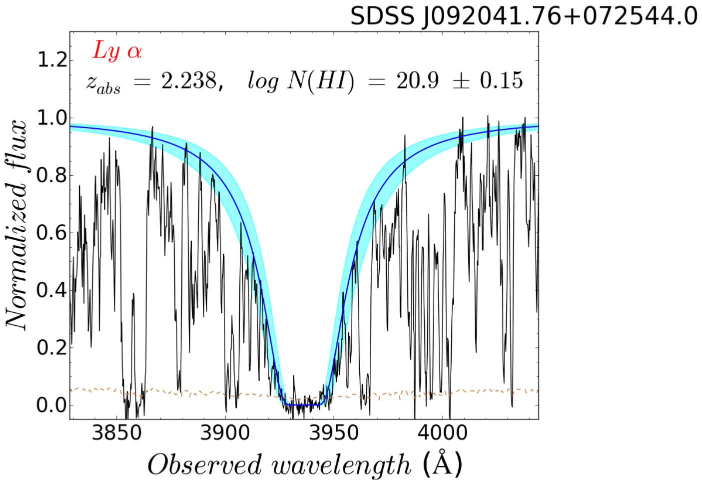
SDSS J092041.76+072544.0
Ly α
z_{abs} = 2.238, log N(HI) = 20.9 ± 0.15
Normalized flux
Observed wavelength (Å)
1.2
1.0
0.8
0.6
0.4
0.2
0.0
3850
3900
3950
4000

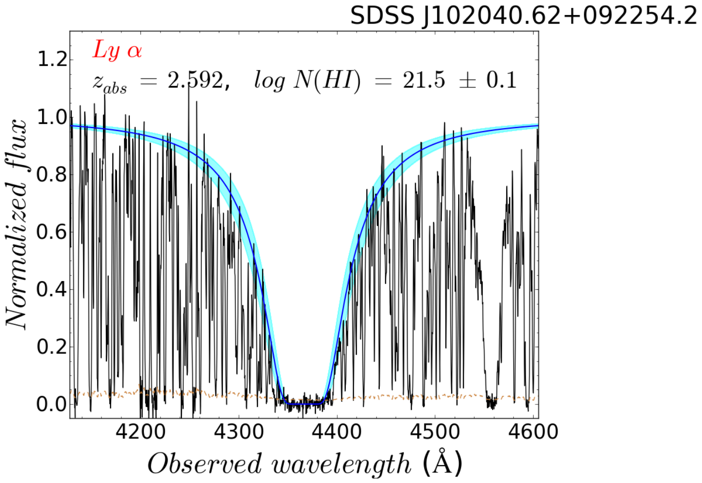
SDSS J102040.62+092254.2
Ly α
z_{abs} = 2.592, log N(HI) = 21.5 ± 0.1
Normalized flux
Observed wavelength (Å)
1.2
1.0
0.8
0.6
0.4
0.2
0.0
4200
4300
4400
4500
4600

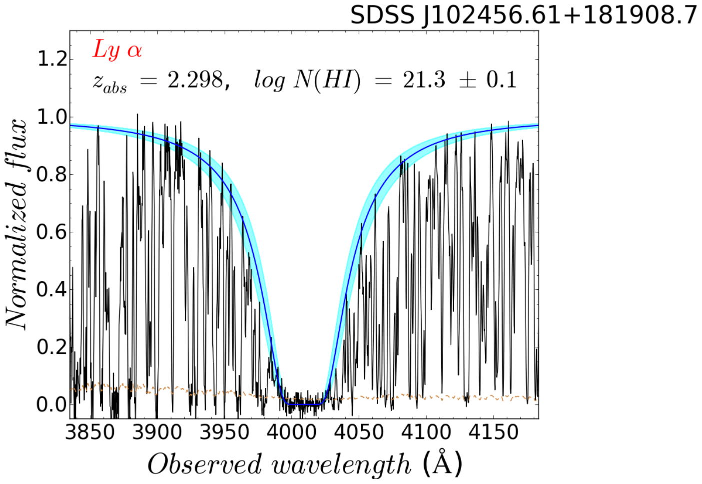
SDSS J102456.61+181908.7
Ly α
z_{abs} = 2.298, log N(HI) = 21.3 ± 0.1
Normalized flux
Observed wavelength (Å)
1.2
1.0
0.8
0.6
0.4
0.2
0.0
3850
3900
3950
4000
4050
4100
4150

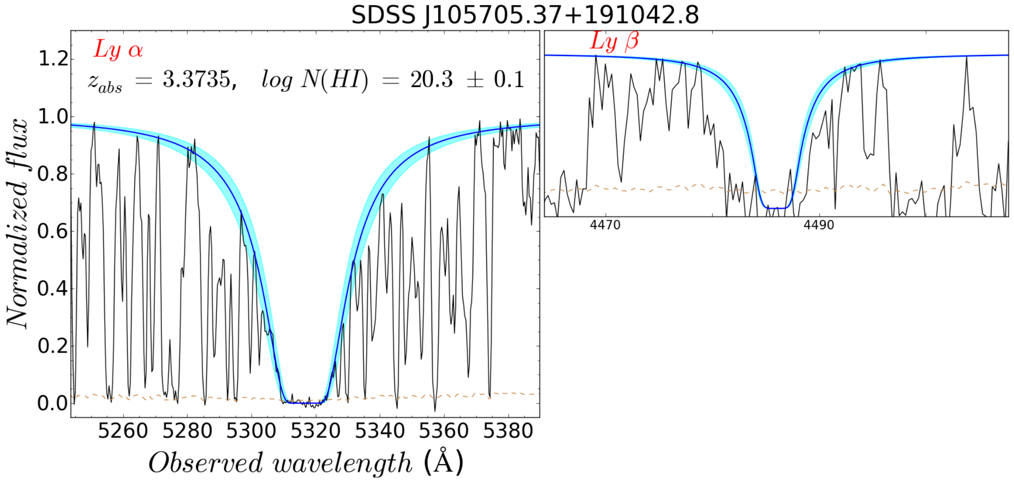
SDSS J105705.37+191042.8
Ly α
z_{abs} = 3.3735, log N(HI) = 20.3 ± 0.1
Normalized flux
0.0
0.2
0.4
0.6
0.8
1.0
1.2
5260
5280
5300
5320
5340
5360
5380
Observed wavelength (Å)
Ly β
4470
4490

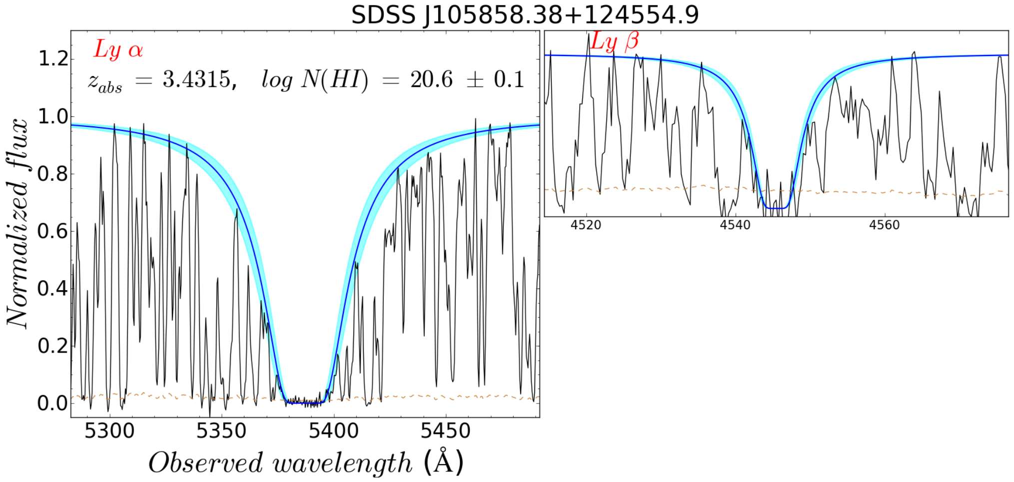
SDSS J105858.38+124554.9
Ly α
z_{abs} = 3.4315, log N(HI) = 20.6 ± 0.1
Normalized flux
0.0
0.2
0.4
0.6
0.8
1.0
1.2
5300
5350
5400
5450
Observed wavelength (Å)
Ly β
4520
4540
4560

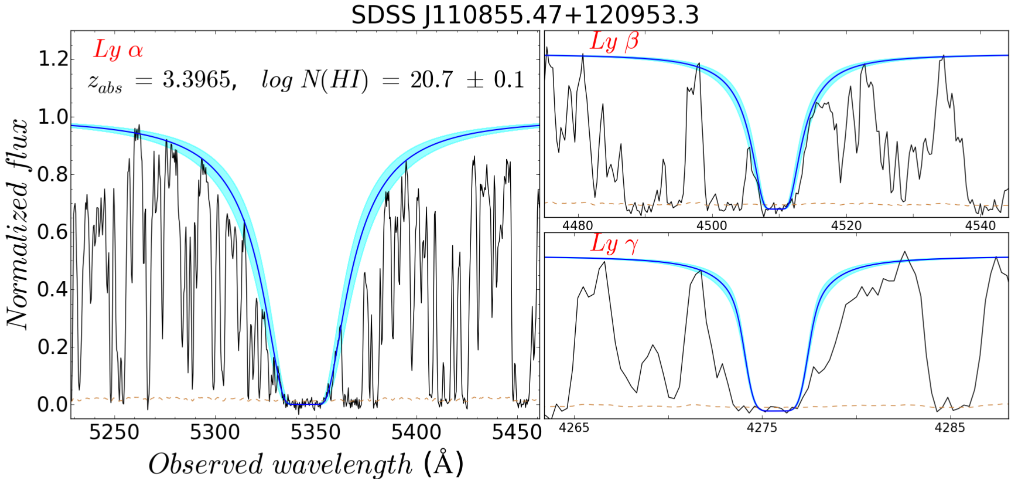
SDSS J110855.47+120953.3
Ly α
z_{abs} = 3.3965, log N(HI) = 20.7 ± 0.1
Normalized flux
0.0
0.2
0.4
0.6
0.8
1.0
1.2
5250
5300
5350
5400
5450
Observed wavelength (Å)
Ly β
4480
4500
4520
4540
Ly γ
4265
4275
4285

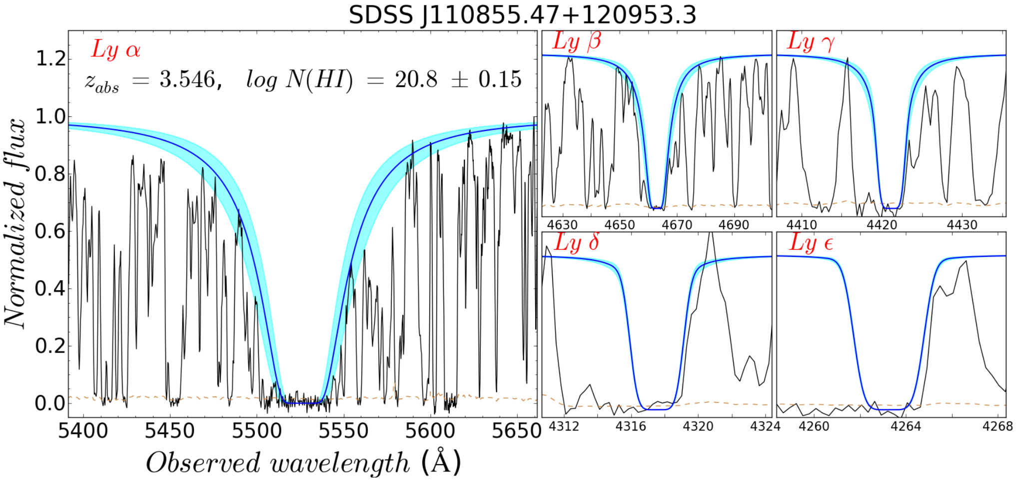
SDSS J110855.47+120953.3
Ly α
z_{abs} = 3.546, log N(HI) = 20.8 ± 0.15
Ly β
Ly γ
Ly δ
Ly ϵ
Normalized flux
Observed wavelength (Å)
0.0
0.2
0.4
0.6
0.8
1.0
1.2
5400
5450
5500
5550
5600
5650
4630
4650
4670
4690
4410
4420
4430
4312
4316
4320
4324
4260
4264
4268

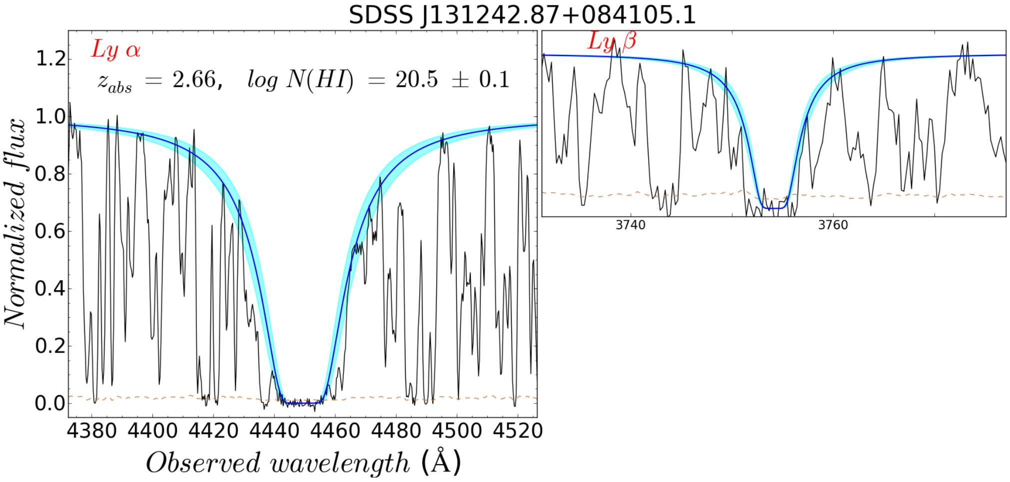
SDSS J131242.87+084105.1
Ly α
z_{abs} = 2.66, log N(HI) = 20.5 ± 0.1
Ly β
Normalized flux
Observed wavelength (Å)
0.0
0.2
0.4
0.6
0.8
1.0
1.2
4380
4400
4420
4440
4460
4480
4500
4520
3740
3760

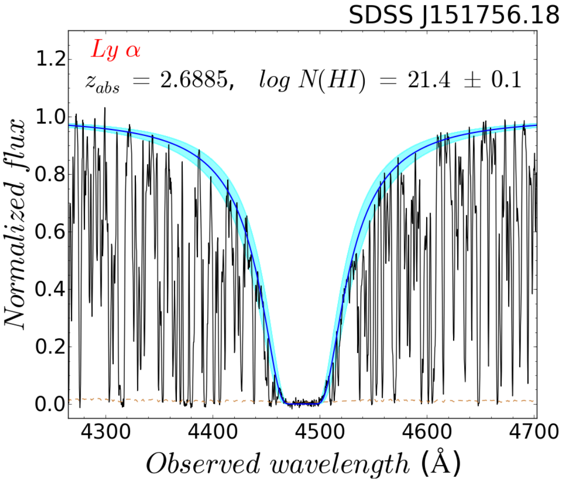
SDSS J151756.18+051103.5
Ly α
z_{abs} = 2.6885, log N(HI) = 21.4 ± 0.1
Normalized flux
Observed wavelength (Å)
0.0
0.2
0.4
0.6
0.8
1.0
1.2
4300
4400
4500
4600
4700

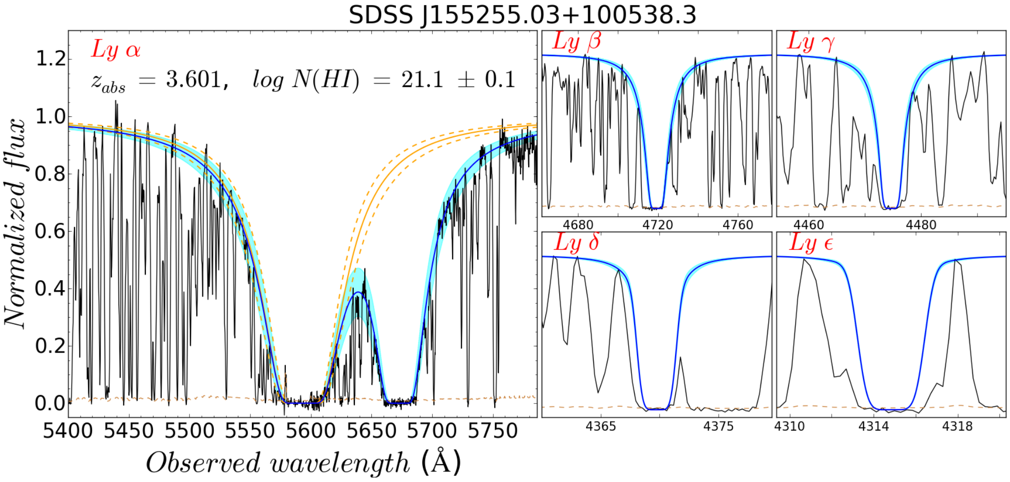
SDSS J155255.03+100538.3

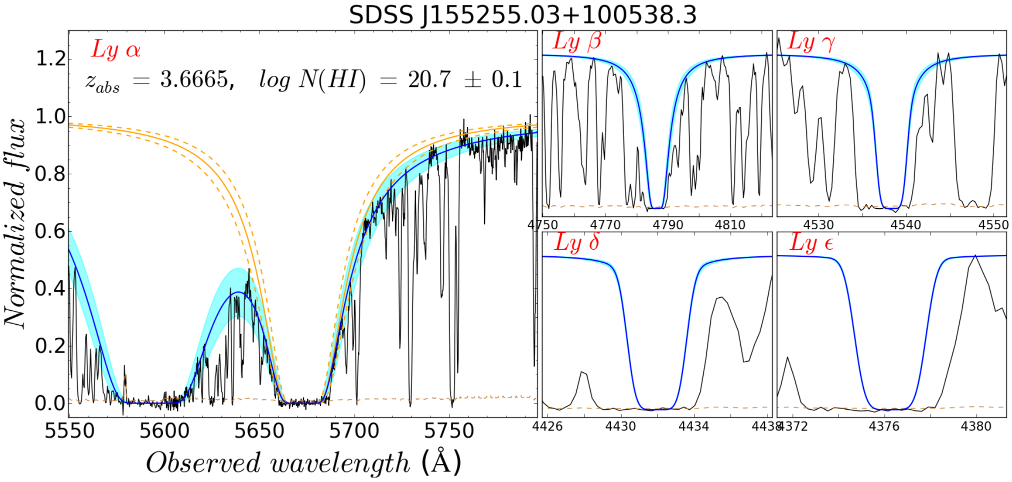
SDSS J155255.03+100538.3

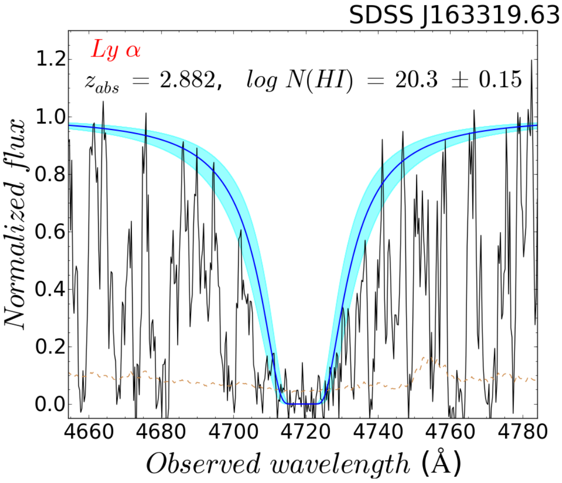
SDSS J163319.63+141142.0

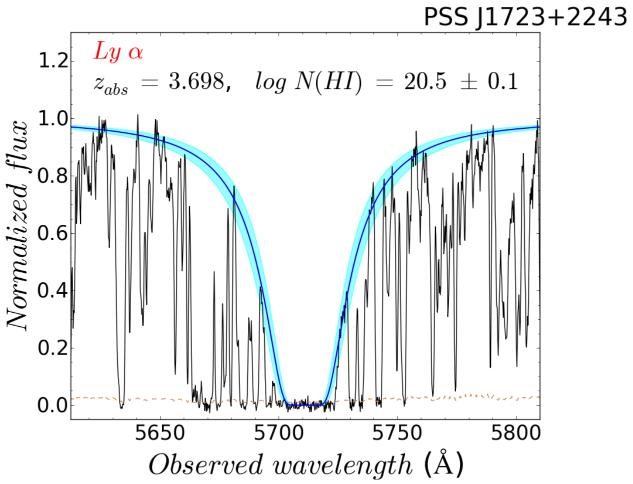
PSS J1723+2243
Ly α
z_{abs} = 3.698, log N(HI) = 20.5 ± 0.1
Normalized flux
0.0
0.2
0.4
0.6
0.8
1.0
1.2
5650
5700
5750
5800
Observed wavelength (Å)

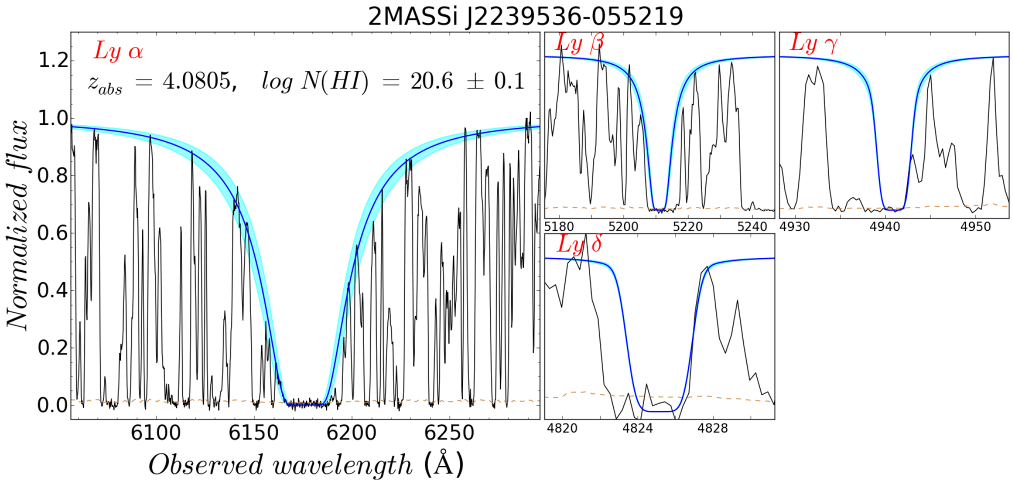
2MASSi J2239536-055219
Ly α
z_{abs} = 4.0805, log N(HI) = 20.6 ± 0.1
Normalized flux
0.0
0.2
0.4
0.6
0.8
1.0
1.2
6100
6150
6200
6250
Observed wavelength (Å)
Ly β
5180
5200
5220
5240
Ly γ
4930
4940
4950
Ly δ
4820
4824
4828

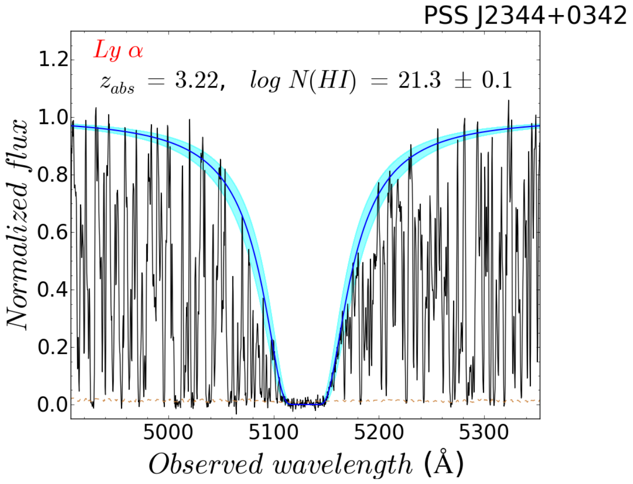
PSS J2344+0342
Ly α
z_{abs} = 3.22, log N(HI) = 21.3 ± 0.1
Normalized flux
0.0
0.2
0.4
0.6
0.8
1.0
1.2
5000
5100
5200
5300
Observed wavelength (Å)

BIBLIOGRAPHY

Thesis Refereed Publications

Z. Cano, A. de Ugarte Postigo, A. Pozanenko, N. Butler, C. C. Thöne, C. Guidorzi, T. Krühler, J. Gorosabel, P. Jakobsson, G. Leloudas, D. Malesani, J. Hjorth, A. Melandri, C. Mundell, K. Wiersema, P. D'Avanzo, S. Schulze, A. Gomboc, A. Johansson, W. Zheng, D. A. Kann, F. Knust, K. Varela, C. W. Akerlof, J. Bloom, O. Burkhonov, E. Cooke, J. A. de Diego, G. Dhungana, C. Farina, F. V. Ferrante, H. A. Flewelling, O. D. Fox, J. Fynbo, N. Gehrels, L. Georgiev, J. J. González, J. Greiner, T. Güver, O. Hartoog, N. Hatch, M. Jelinek, R. Kehoe, S. Klose, E. Klunko, D. Kopač, A. Kutyrev, Y. Krugly, W. H. Lee, A. Levan, V. Linkov, A. Matkin, N. Minikulov, I. Molotov, J. X. Prochaska, M. G. Richer, C. G. Román-Zúñiga, V. Rumyantsev, R. **Sánchez-Ramírez**, I. Steele, N. R. Tanvir, A. Volnova, A. M. Watson, D. Xu, and F. Yuan. A trio of gamma-ray burst supernovae:. GRB 120729A, GRB 130215A/SN 2013ez, and GRB 130831A/SN 2013fu. *A&A*, 568:A19, August 2014.

Z. Cano, A. de Ugarte Postigo, D. Perley, T. Krühler, R. Margutti, M. Friis, D. Malesani, P. Jakobsson, J. P. U. Fynbo, J. Gorosabel, J. Hjorth, R. **Sánchez-Ramírez**, S. Schulze, N. R. Tanvir, C. C. Thöne, and D. Xu. GRB 140606B/iPTF14bfu: detection of shock-breakout emission from a cosmological γ-ray burst? *MNRAS*, 452: 1535–1552, September 2015. doi: 10.1093/mnras/stv1327.

A. de Ugarte Postigo, J. P. U. Fynbo, C. C. Thöne, L. Christensen, J. Gorosabel, B. Milvang-Jensen, S. Schulze, P. Jakobsson, K. Wiersema, R. **Sánchez-Ramírez**, G. Leloudas, T. Zafar, D. Malesani, and J. Hjorth. The distribution of equivalent widths in long GRB afterglow spectra. *A&A*, 548:A11, December 2012a. doi: 10.1051/0004-6361/201219894. xxvi, 107, 108, 139, 141, 145, 146, 182, 240, 242

A. de Ugarte Postigo, A. Lundgren, S. Martín, D. Garcia-Appadoo, I. de Gregorio Monsalvo, A. Peck, M. J. Michałowski, C. C. Thöne, S. Campana, J. Gorosabel, N. R. Tanvir, K. Wiersema, A. J. Castro-Tirado, S. Schulze, C. De Breuck, G. Petitpas, J. Hjorth, P. Jakobsson, S. Covino, J. P. U. Fynbo, J. M. Winters, M. Bremer, A. J. Levan, A. Llorente, R. **Sánchez-Ramírez**, J. C. Tello, and R. Salvaterra. Pre-ALMA observations of GRBs in the mm/submm range. *A&A*, 538:A44, February 2012b. doi: 10.1051/0004-6361/201117848. xxv, 101, 105, 107

A. de Ugarte Postigo, S. Campana, C. C. Thöne, P. D'Avanzo, R. **Sánchez-Ramírez**, A. Melandri, J. Gorosabel, G. Ghirlanda, P. Veres, S. Martín, G. Petitpas, S. Covino, J. P. U. Fynbo, and A. J. Levan. The obscured hyper-energetic GRB 120624B hosted by a luminous compact galaxy at z = 2.20. *A&A*, 557:L18, September 2013. doi: 10.1051/0004-6361/201322065.

A. de Ugarte Postigo, C. C. Thöne, A. Rowlinson, R. García-Benito, A. J. Levan, J. Gorosabel, P. Goldoni, S. Schulze, T. Zafar, K. Wiersema, R. **Sánchez-Ramírez**, A. Melandri, P. D'Avanzo, S. Oates, V. D'Elia, M. De Pasquale, T. Krühler, A. J. van der Horst, D. Xu, D. Watson, S. Piranomonte, S. D. Vergani, B. Milvang-Jensen, L. Kaper, D. Malesani, J. P. U. Fynbo, Z. Cano, S. Covino, H. Flores, S. Greiss, F. Hammer, O. E. Hartoog, S. Hellmich, C. Heuser, J. Hjorth, P. Jakobsson, S. Mottola, M. Sparre, J. Sollerman, G. Tagliaferri, N. R. Tanvir, M. Vestergaard, and R. A. M. J. Wijers. Spectroscopy of the short-hard GRB 130603B. The host galaxy and environment of a compact object merger. *A&A*, 563:A62, March 2014. doi: 10.1051/0004-6361/201322985.

V. D'Elia, J. P. U. Fynbo, P. Goldoni, S. Covino, A. de Ugarte Postigo, C. Ledoux, F. Calura, J. Gorosabel, D. Malesani, F. Matteucci, R. **Sánchez-Ramírez**, S. Savaglio, A. J. Castro-Tirado, O. E. Hartoog, L. Kaper, T. Muñoz-Darias, E. Pian, S. Piranomonte, G. Tagliaferri, N. Tanvir, S. D. Vergani, D. J. Watson, and D. Xu. VLT/X-shooter spectroscopy of the GRB 120327A afterglow. *A&A*, 564:A38, April 2014. doi: 10.1051/0004-6361/201323057. 35

J. Elliott, T. Krühler, J. Greiner, S. Savaglio, F. Olivares, E. A. Rau, A. de Ugarte Postigo, R. **Sánchez-Ramírez**, K. Wiersema, P. Schady, D. A. Kann, R. Filgas, M. Nardini, E. Berger, D. Fox, J. Gorosabel, S. Klose, A. Levan, A. Nicuesa Guelbenzu, A. Rossi, S. Schmidl, V. Sudilovsky, N. R. Tanvir, and C. C. Thöne. The low-extinction afterglow in the solar-metallicity host galaxy of γ-ray burst 110918A. *A&A*, 556:A23, August 2013. doi: 10.1051/0004-6361/201220968.

P. A. Evans, R. Willingale, J. P. Osborne, P. T. O'Brien, N. R. Tanvir, D. D. Frederiks, V. D. Pal'shin, D. S. Svinkin, A. Lien, J. Cummings, S. Xiong, B.-B. Zhang, D. Götz, V. Savchenko, H. Negoro, S. Nakahira, K. Suzuki, K. Wiersema, R. L. C. Starling, A. J. Castro-Tirado, A. P. Beardmore, R. **Sánchez-Ramírez**, J. Gorosabel, S. Jeong, J. A. Kennea, D. N. Burrows, and N. Gehrels. GRB 130925A: an ultralong gamma ray burst with a dust-echo afterglow, and implications for the origin of the ultralong GRBs. *MNRAS*, 444:250–267, October 2014. 178

E. S. Gorbovskoy, G. V. Lipunova, V. M. Lipunov, V. G. Kornilov, A. A. Belinski, N. I. Shatskiy, N. V. Tyurina, D. A. Kuvshinov, P. V. Balanutsa, V. V. Chazov, A. Kuznetsov, D. S. Zimnukhov, M. V. Kornilov, A. V. Sankovich, A. Krylov, K. I. Ivanov, O. Chvalaev, V. A. Poleschuk, E. N. Konstantinov, O. A. Gress, S. A. Yazev, N. M. Budnev, V. V. Krushinski, I. S. Zalozhnich, A. A. Popov, A. G. Tlatov, A. V. Parhomenko, D. V. Dormidontov, V. Senik, V. V. Yurkov, Y. P. Sergienko, D. Varda, I. P. Kudelina, A. J. Castro-Tirado, J. Gorosabel, R. **Sánchez-Ramírez**, M. Jelinek, and J. C. Tello. Prompt, early and afterglow optical observations of five γ-ray bursts: GRB 100901A, GRB 100902A, GRB 100905A, GRB 100906A and GRB 101020A. *MNRAS*, 421:1874–1890, April 2012. doi: 10.1111/j.1365-2966.2012.20195.x.

E. S. Gorbovskoy, V. M. Lipunov, D. A. H. Buckley, V. G. Kornilov, P. V. Balanutsa, N. V. Tyurina, A. S. Kuznetsov, D. A. Kuvshinov, I. A. Gorbunov, D. Vlasenko, E. Popova, V. V. Chazov, S. Potter, M. Kotze, A. Y. Kniazev, O. A. Gress, N. M. Budnev, K. I. Ivanov, S. A. Yazev, A. G. Tlatov, V. A. Senik, D. V. Dormidontov, A. V. Parhomenko, V. V. Krushinski, I. S. Zalozhnich, R. A. Castro-Tirado, R. Sánchez-Ramírez, Y. P. Sergienko, A. Gabovich, V. V. Yurkov, H. Levato, C. Saffe, C. Mallamaci, C. Lopez, F. Podest, and V. V. Vladimirov. Early polarization observations of the optical emission of gamma-ray bursts: GRB 150301B and GRB 150413A. *MNRAS*, 455:3312–3318, January 2016. doi: 10.1093/mnras/stv2515.

J. Japelj, S. Covino, A. Gomboc, S. D. Vergani, P. Goldoni, J. Selsing, Z. Cano, V. D'Elia, H. Flores, J. P. U. Fynbo, F. Hammer, J. Hjorth, P. Jakobsson, L. Kaper, D. Kopač, T. Krühler, A. Melandri, S. Piranomonte, R. **Sánchez-Ramírez**, G. Tagliaferri, N. R. Tanvir, A. de Ugarte Postigo, D. Watson, and R. A. M. J. Wijers. Spectrophotometric analysis of gamma-ray burst afterglow extinction curves with X-Shooter. *A&A*, 579: A74, July 2015. doi: 10.1051/0004-6361/201525665. 33

S. Jeong, A. J. Castro-Tirado, M. Bremer, J. M. Winters, J. Gorosabel, S. Guziy, S. B. Pandey, M. Jelínek, R. **Sánchez-Ramírez**, I. V. Sokolov, N. V. Orekhova, A. S. Moskvitin, J. C. Tello, R. Cunniffe, O. Lara-Gil, S. R. Oates, D. Pérez-Ramírez, J. Bai, Y. Fan, C. Wang, and I. H. Park. The dark nature of GRB 130528A and its host galaxy. *A&A*, 569:A93, September 2014.

Z.-P. Jin, S. Covino, M. Della Valle, P. Ferrero, D. Fugazza, D. Malesani, A. Melandri, E. Pian, R. Salvaterra, D. Bersier, S. Campana, Z. Cano, A. J. Castro-Tirado, P. D'Avanzo, J. P. U. Fynbo, A. Gomboc, J. Gorosabel, C. Guidorzi, J. B. Haislip, J. Hjorth, S. Kobayashi, A. P. LaCluyze, G. Marconi, P. A. Mazzali, C. G. Mundell, S. Piranomonte, D. E. Reichart, R. **Sánchez-Ramírez**, R. J. Smith, I. A. Steele,

G. Tagliaferri, N. R. Tanvir, S. Valenti, S. D. Vergani, T. Vestrand, E. S. Walker, and P. Woźniak. GRB 081007 and GRB 090424: The Surrounding Medium, Outflows, and Supernovae. *ApJ*, 774:114, September 2013. doi: 10.1088/0004-637X/774/2/114.

D. Kopač, C. G. Mundell, J. Japelj, D. M. Arnold, I. A. Steele, C. Guidorzi, S. Dichiara, S. Kobayashi, A. Gomboc, R. M. Harrison, G. P. Lamb, A. Melandri, R. J. Smith, F. J. Virgili, A. J. Castro-Tirado, J. Gorosabel, A. Järvinen, R. Sánchez-Ramírez, S. R. Oates, and M. Jelínek. Limits on Optical Polarization during the Prompt Phase of GRB 140430A. *ApJ*, 813:1, November 2015. doi: 10.1088/0004-637X/813/1/1.

T. Krühler, C. Ledoux, J. P. U. Fynbo, P. M. Vreeswijk, S. Schmidl, D. Malesani, L. Christensen, A. De Cia, J. Hjorth, P. Jakobsson, D. A. Kann, L. Kaper, S. D. Vergani, P. M. J. Afonso, S. Covino, A. de Ugarte Postigo, V. D'Elia, R. Filgas, P. Goldoni, J. Greiner, O. E. Hartoog, B. Milvang-Jensen, M. Nardini, S. Piranomonte, A. Rossi, R. **Sánchez-Ramírez**, P. Schady, S. Schulze, V. Sudilovsky, N. R. Tanvir, G. Tagliaferri, D. J. Watson, K. Wiersema, R. A. M. J. Wijers, and D. Xu. Molecular hydrogen in the damped Lyman α system towards GRB 120815A at z = 2.36. *A&A*, 557:A18, September 2013. doi: 10.1051/0004-6361/201321772. xxii, 35, 36

T. Krühler, D. Malesani, J. P. U. Fynbo, O. E. Hartoog, J. Hjorth, P. Jakobsson, D. A. Perley, A. Rossi, P. Schady, S. Schulze, N. R. Tanvir, S. D. Vergani, K. Wiersema, P. M. J. Afonso, J. Bolmer, Z. Cano, S. Covino, V. D'Elia, A. de Ugarte Postigo, R. Filgas, M. Friis, J. F. Graham, J. Greiner, P. Goldoni, A. Gomboc, F. Hammer, J. Japelj, D. A. Kann, L. Kaper, S. Klose, A. J. Levan, G. Leloudas, B. Milvang-Jensen, A. Nicuesa Guelbenzu, E. Palazzi, E. Pian, S. Piranomonte, R. Sánchez-Ramírez, S. Savaglio, J. Selsing, G. Tagliaferri, P. M. Vreeswijk, D. J. Watson, and D. Xu. GRB hosts through cosmic time. VLT/X-Shooter emission-line spectroscopy of 96 γ-ray-burst-selected galaxies at $0.1 < z < 3.6$. *A&A*, 581:A125, September 2015. doi: 10.1051/0004-6361/201425561. 62

A. J. Levan, N. R. Tanvir, S. B. Cenko, D. A. Perley, K. Wiersema, J. S. Bloom, A. S. Fruchter, A. d. U. Postigo, P. T. O'Brien, N. Butler, A. J. van der Horst, G. Leloudas, A. N. Morgan, K. Misra, G. C. Bower, J. Farihi, R. L. Tunnicliffe, M. Modjaz, J. M. Silverman, J. Hjorth, C. Thöne, A. Cucchiara, J. M. C. Cerón, A. J. Castro-Tirado, J. A. Arnold, M. Bremer, J. P. Brodie, T. Carroll, M. C. Cooper, P. A. Curran, R. M. Cutri, J. Ehle, D. Forbes, J. Fynbo, J. Gorosabel, J. Graham, D. I. Hoffman, S. Guziy, P. Jakobsson, A. Kamble, T. Kerr, M. M. Kasliwal, C. Kouveliotou, D. Kocevski, N. M. Law, P. E. Nugent, E. O. Ofek, D. Poznanski, R. M. Quimby, E. Rol, A. J. Romanowsky, R. **Sánchez-Ramírez**, S. Schulze, N. Singh, L. van Spaandonk, R. L. C. Starling, R. G.

Strom, J. C. Tello, O. Vaduvescu, P. J. Wheatley, R. A. M. J. Wijers, J. M. Winters, and D. Xu. An Extremely Luminous Panchromatic Outburst from the Nucleus of a Distant Galaxy. *Science*, 333:199–, July 2011. doi: 10.1126/science.1207143.

A. J. Levan, N. R. Tanvir, R. L. C. Starling, K. Wiersema, K. L. Page, D. A. Perley, S. Schulze, G. A. Wynn, R. Chornock, J. Hjorth, S. B. Cenko, A. S. Fruchter, P. T. O'Brien, G. C. Brown, R. L. Tunnicliffe, D. Malesani, P. Jakobsson, D. Watson, E. Berger, D. Bersier, B. E. Cobb, S. Covino, A. Cucchiara, A. de Ugarte Postigo, D. B. Fox, A. Gal-Yam, P. Goldoni, J. Gorosabel, L. Kaper, T. Krühler, R. Karjalainen, J. P. Osborne, E. Pian, R. **Sánchez-Ramírez**, B. Schmidt, I. Skillen, G. Tagliaferri, C. Thöne, O. Vaduvescu, R. A. M. J. Wijers, and B. A. Zauderer. A New Population of Ultra-long Duration Gamma-Ray Bursts. *ApJ*, 781:13, January 2014. doi: 10.1088/0004-637X/781/1/13.

A. Melandri, M. G. Bernardini, P. D'Avanzo, R. **Sánchez-Ramírez**, F. Nappo, L. Nava, J. Japelj, A. de Ugarte Postigo, S. Oates, S. Campana, S. Covino, V. D'Elia, G. Ghirlanda, E. Gafton, G. Ghisellini, N. Gnedin, P. Goldoni, J. Gorosabel, T. Libbrecht, D. Malesani, R. Salvaterra, C. C. Thöne, S. D. Vergani, D. Xu, and G. Tagliaferri. The high-redshift gamma-ray burst GRB 140515A. A comprehensive X-ray and optical study. *A&A*, 581:A86, September 2015. doi: 10.1051/0004-6361/201526660.

T. Muñoz-Darias, A. de Ugarte Postigo, D. M. Russell, S. Guziy, J. Gorosabel, J. Casares, M. Armas Padilla, P. A. Charles, R. P. Fender, T. M. Belloni, F. Lewis, S. Motta, A. Castro-Tirado, C. G. Mundell, R. **Sánchez-Ramírez**, and C. C. Thöne. The optical counterpart of the bright X-ray transient Swift J1745-26. *MNRAS*, 432:1133–1137, June 2013. doi: 10.1093/mnras/stt532.

L. Resmi, K. Misra, G. Jóhannesson, A. J. Castro Tirado, J. Gorosabel, M. Jelínek, D. Bhattacharya, P. Kubánek, G. C. Anupama, A. Sota, D. K. Sahu, A. de Ugarte Postigo, S. B. Pandey, R. **Sánchez Ramírez**, M. Bremer, and R. Sagar. Comprehensive multiwavelength modelling of the afterglow of GRB 050525A. *MNRAS*, 427: 288–297, November 2012. doi: 10.1111/j.1365-2966.2012.21713.x. 109

T. Sakamoto, E. Troja, K. Aoki, S. Guiriec, M. Im, G. Leloudas, D. Malesani, A. Melandri, A. de Ugarte Postigo, Y. Urata, D. Xu, P. D'Avanzo, J. Gorosabel, Y. Jeon, R. **Sánchez-Ramírez**, M. I. Andersen, J. Bai, S. D. Barthelmy, M. S. Briggs, S. Foley, A. S. Fruchter, J. P. U. Fynbo, N. Gehrels, K. Huang, M. Jang, N. Kawai, H. Korhonen, J. Mao, J. P. Norris, R. D. Preece, J. L. Racusin, C. C. Thöne, K. Vida, and X. Zhao. Identifying the Location in the Host Galaxy of the Short

GRB 111117A with the Chandra Subarcsecond Position. *ApJ*, 766:41, March 2013. doi: 10.1088/0004-637X/766/1/41.

R. Sánchez-Ramírez, S. L. Ellison, J. X. Prochaska, T. A. M. Berg, S. López, V. D'Odorico, G. D. Becker, L. Christensen, G. Cupani, K. D. Denney, I. Pâris, G. Worseck, and J. Gorosabel. The evolution of neutral gas in damped Lyman α systems from the XQ-100 survey. *MNRAS*, 456:4488–4505, March 2016. doi: 10.1093/mnras/stv2732. xxvi, 138, 139, 162

S. Schulze, D. Malesani, A. Cucchiara, N. R. Tanvir, T. Krühler, A. de Ugarte Postigo, G. Leloudas, J. Lyman, D. Bersier, K. Wiersema, D. A. Perley, P. Schady, J. Gorosabel, J. P. Anderson, A. J. Castro-Tirado, S. B. Cenko, A. De Cia, L. E. Ellerbroek, J. P. U. Fynbo, J. Greiner, J. Hjorth, D. A. Kann, L. Kaper, S. Klose, A. J. Levan, S. Martín, P. T. O'Brien, K. L. Page, G. Pignata, S. Rapaport, R. **Sánchez-Ramírez**, J. Sollerman, I. A. Smith, M. Sparre, C. C. Thöne, D. J. Watson, D. Xu, F. E. Bauer, M. Bayliss, G. Björnsson, M. Bremer, Z. Cano, S. Covino, V. D'Elia, D. A. Frail, S. Geier, P. Goldoni, O. E. Hartoog, P. Jakobsson, H. Korhonen, K. Y. Lee, B. Milvang-Jensen, M. Nardini, A. Nicuesa Guelbenzu, M. Oguri, S. B. Pandey, G. Petitpas, A. Rossi, A. Sandberg, S. Schmidl, G. Tagliaferri, R. P. J. Tilanus, J. M. Winters, D. Wright, and E. Wuyts. GRB 120422A/SN 2012bz: Bridging the gap between low- and high-luminosity gamma-ray bursts. *A&A*, 566:A102, June 2014.

B. Sicardy, J. L. Ortiz, M. Assafin, E. Jehin, A. Maury, E. Lellouch, R. G. Hutton, F. Braga-Ribas, F. Colas, D. Hestroffer, J. Lecacheux, F. Roques, P. Santos-Sanz, T. Widemann, N. Morales, R. Duffard, A. Thirouin, A. J. Castro-Tirado, M. Jelínek, P. Kubánek, A. Sota, R. **Sánchez-Ramírez**, A. H. Andrei, J. I. B. Camargo, D. N. da Silva Neto, A. R. Gomes, R. V. Martins, M. Gillon, J. Manfroid, G. P. Tozzi, C. Harlingten, S. Saravia, R. Behrend, S. Mottola, E. G. Melendo, V. Peris, J. Fabregat, J. M. Madiedo, L. Cuesta, M. T. Eibe, A. Ullán, F. Organero, S. Pastor, J. A. de Los Reyes, S. Pedraz, A. Castro, I. de La Cueva, G. Muler, I. A. Steele, M. Cebrián, P. Montañés-Rodríguez, A. Oscoz, D. Weaver, C. Jacques, W. J. B. Corradi, F. P. Santos, W. Reis, A. Milone, M. Emilio, L. Gutiérrez, R. Vázquez, and H. Hernández-Toledo. A Pluto-like radius and a high albedo for the dwarf planet Eris from an occultation. *Nature*, 478:493–496, October 2011. doi: 10.1038/nature10550.

M. Sparre, O. E. Hartoog, T. Krühler, J. P. U. Fynbo, D. J. Watson, K. Wiersema, V. D'Elia, T. Zafar, P. M. J. Afonso, S. Covino, A. de Ugarte Postigo, H. Flores, P. Goldoni, J. Greiner, J. Hjorth, P. Jakobsson, L. Kaper, S. Klose, A. J. Levan, D. Malesani, B. Milvang-Jensen, M. Nardini, S. Piranomonte, J. Sollerman,

R. **Sánchez-Ramírez**, S. Schulze, N. R. Tanvir, S. D. Vergani, and R. A. M. J. Wijers. The Metallicity and Dust Content of a Redshift 5 Gamma-Ray Burst Host Galaxy. *ApJ*, 785:150, April 2014. doi: 10.1088/0004-637X/785/2/150.

J. C. Tello, A. J. Castro-Tirado, J. Gorosabel, D. Pérez-Ramírez, S. Guziy, R. **Sánchez-Ramírez**, M. Jelínek, P. Veres, and Z. Bagoly. Searching for Galactic sources in the Swift GRB catalog. Statistical analyses of the angular distributions of FREDs. *A&A*, 548:L7, December 2012. doi: 10.1051/0004-6361/201220527.

S. D. Vergani, H. Flores, S. Covino, D. Fugazza, J. Gorosabel, A. J. Levan, M. Puech, R. Salvaterra, J. C. Tello, A. de Ugarte Postigo, P. D'Avanzo, V. D'Elia, M. Fernández, J. P. U. Fynbo, G. Ghirlanda, M. Jelínek, A. Lundgren, D. Malesani, E. Palazzi, S. Piranomonte, M. Rodrigues, R. **Sánchez-Ramírez**, V. Terrón, C. C. Thöne, L. A. Antonelli, S. Campana, A. J. Castro-Tirado, P. Goldoni, F. Hammer, J. Hjorth, P. Jakobsson, L. Kaper, A. Melandri, B. Milvang-Jensen, J. Sollerman, G. Tagliaferri, N. R. Tanvir, K. Wiersema, and R. A. M. J. Wijers. GRB 091127/SN 2009nz and the VLT/X-shooter spectroscopy of its host galaxy: probing the faint end of the mass-metallicity relation. *A&A*, 535:A127, November 2011. doi: 10.1051/0004-6361/201117726. 38

L. P. Xin, A. Pozanenko, D. A. Kann, D. Xu, J. Gorosabel, G. Leloudas, J. Y. Wei, M. Andreev, S. F. Qin, M. Ibrahimov, X. H. Han, A. de Ugarte Postigo, Y. L. Qiu, J. S. Deng, A. Volnova, P. Jakobsson, A. J. Castro-Tirado, F. Aceituno, J. P. U. Fynbo, J. Wang, R. **Sanchez-Ramirez**, V. Kouprianov, W. K. Zheng, J. C. Tello, and C. Wu. The shallow-decay phase in both the optical and X-ray afterglows of Swift GRB 090529A: energy injection into a wind-type medium? *MNRAS*, 422:2044–2050, May 2012. doi: 10.1111/j.1365-2966.2012.20681.x.

D. Xu, A. de Ugarte Postigo, G. Leloudas, T. Krühler, Z. Cano, J. Hjorth, D. Malesani, J. P. U. Fynbo, C. C. Thöne, R. **Sánchez-Ramírez**, S. Schulze, P. Jakobsson, L. Kaper, J. Sollerman, D. J. Watson, A. Cabrera-Lavers, C. Cao, S. Covino, H. Flores, S. Geier, J. Gorosabel, S. M. Hu, B. Milvang-Jensen, M. Sparre, L. P. Xin, T. M. Zhang, W. K. Zheng, and Y. C. Zou. Discovery of the Broad-lined Type Ic SN 2013cq Associated with the Very Energetic GRB 130427A. *ApJ*, 776:98, October 2013. doi: 10.1088/0004-637X/776/2/98.

W. Zheng, R. F. Shen, T. Sakamoto, A. P. Beardmore, M. De Pasquale, X. F. Wu, J. Gorosabel, Y. Urata, S. Sugita, B. Zhang, A. Pozanenko, M. Nissinen, D. K. Sahu, M. Im, T. N. Ukwatta, M. Andreev, E. Klunko, A. Volnova, C. W. Akerlof, P. Anto, S. D. Barthelmy, A. Breeveld, U. Carsenty, S. Castillo-Carrión, A. J. Castro-Tirado, M. M. Chester, C. J. Chuang, R. Cunniffe, A. De Ugarte Postigo, R. Duffard,

H. Flewelling, N. Gehrels, T. Güver, S. Guziy, V. P. Hentunen, K. Y. Huang, M. Jelínek, T. S. Koch, P. Kubánek, P. Kuin, T. A. McKay, S. Mottola, S. R. Oates, P. O'Brien, M. Ohno, M. J. Page, S. B. Pandey, C. Pérez del Pulgar, W. Rujopakarn, E. Rykoff, T. Salmi, R. **Sánchez-Ramírez**, B. E. Schaefer, A. Sergeev, E. Sonbas, A. Sota, J. C. Tello, K. Yamaoka, S. A. Yost, and F. Yuan. Panchromatic Observations of the Textbook GRB 110205A: Constraining Physical Mechanisms of Prompt Emission and Afterglow. *ApJ*, 751:90, June 2012. doi: 10.1088/0004-637X/751/2/90. 73

Thesis Proceedings

A. J. Castro-Tirado, M. Bremer, J.-M. Winters, A. de Ugarte Postigo, J. Gorosabel, S. Guziy, D. Pérez-Ramírez, J. M. C. Cerón, C. Thöne, M. Jelínek, R. **Sánchez-Ramírez**, J. C. Tello, S. B. Pandey, and D. Bhattacharya. Millimetre Observations of Gamma-ray Bursts. In J. E. McEnery, J. L. Racusin, and N. Gehrels, editors, *American Institute of Physics Conference Series*, volume 1358 of *American Institute of Physics Conference Series*, pages 109–112, August 2011. doi: 10.1063/1.3621749.

A. J. Castro-Tirado, J. L. Gómez, I. Agudo, M. A. Guerrero, M. Bremer, J. M. Winters, J. Gorosabel, S. Guziy, M. Jelinek, J. C. Tello, R. **Sánchez-Ramírez**, D. Pérez-Ramírez, J. Reyes-Iturbide, I. H. Park, S. Jeong, and A. S. Pozanenko. The first months in the lifetime of the newly born jet associated to Swift J1644+57. In *European Physical Journal Web of Conferences*, volume 39 of *European Physical Journal Web of Conferences*, page 4002, December 2012a. doi: 10.1051/epjconf/20123904002.

A. J. Castro-Tirado, M. Jelínek, J. Gorosabel, P. Kubánek, R. Cunniffe, S. Guziy, O. Lara-Gil, O. Rabaza-Castillo, A. de Ugarte Postigo, R. **Sánchez-Ramírez**, J. C. Tello, V. Muñoz-Martínez, C. Pérez del Pulgar, S. Castillo-Carrión, J. M. Castro Cerón, T. d. J. Mateo Sanguino, R. Hudec, S. Vitek, B. A. de la Morena Carretero, J. A. Díaz Andreu, R. Fernández-Muñoz, D. Pérez-Ramírez, P. A. Yock, W. H. Allen, I. Bond, G. Christie, L. Sabau-Graziati, A. Castro, A. Pozanenko, J. Bai, Y. Fan, and C. Cui. Building the BOOTES world-wide Network of Robotic telescopes. In *Astronomical Society of India Conference Series*, volume 7 of *Astronomical Society of India Conference Series*, pages 313–320, 2012b.

A. J. Castro-Tirado, M. Bremer, J. M. Winters, J. C. Tello, S. B. Pandey, A. de Ugarte Postigo, J. Gorosabel, S. Guziy, M. Jelinek, R. **Sánchez-Ramírez**, D. Pérez-Ramírez, and J. M. Castro Cerón. Millimetre Observations of Gamma-ray Bursts at IRAM. In A. J. Castro-Tirado, J. Gorosabel, and I. H. Park, editors, *EAS Publications Series*, volume 61 of *EAS Publications Series*, pages 279–281, July 2013a. doi: 10.1051/eas/1361045.

A. J. Castro-Tirado, J. L. Gómez, I. Agudo, M. A. Guerrero, M. Bremer, J. M. Winters, J. Gorosabel, S. Guziy, A. de Ugarte Postigo, M. Jelínek, J. C. Tello, R. **Sánchez-Ramírez**, D. Pérez-Ramírez, J. Reyes-Iturbide, I. H. Park, S. Jeong, A. S. Pozanenko, and J. Acosta-Pulido. The first two months in the lifetime of the newly born jet associated to Swift J1644+57. In *Revista Mexicana de Astronomia y Astrofisica Conference Series*, volume 42 of *Revista Mexicana de Astronomia y Astrofisica Conference Series*, pages 36–37, May 2013b.

A. J. Castro-Tirado, J. L. Gómez, I. Agudo, M. A. Guerrero, M. Bremer, J. M. Winters, J. Gorosabel, R. **Sánchez-Ramírez**, S. Guziy, M. Jelinek, J. C. Tello, D. Pérez-Ramírez, J. Reyes-Iturbide, I. H. Park, S. Jeong, U. Bach, A. Kraussh, T. P. Krichbaumh, and A. S. Pozanenko. The first two years in the lifetime of the newly born jet associated to Sw J1644+57. In *European Physical Journal Web of Conferences*, volume 61 of *European Physical Journal Web of Conferences*, page 1003, December 2013c. doi: 10.1051/epjconf/20136101003.

A. J. Castro-Tirado, J. L. Gómez, I. Agudo, M. A. Guerrero, M. Bremer, J. M. Winters, J. Gorosabel, R. **Sánchez-Ramírez**, S. Guziy, M. Jelinek, J. C. Tello, D. Pérez-Ramírez, J. Reyes-Iturbide, I. H. Park, S. Jeong, and A. S. Pozanenko. The first months in the lifetime of the newly born jet associated to Swift J1644+57. In J. C. Guirado, L. M. Lara, V. Quilis, and J. Gorgas, editors, *Highlights of Spanish Astrophysics VII*, pages 185–189, May 2013d.

A. de Ugarte Postigo, A. Lundgren, S. Martín, D. García-Appadoo, I. de Gregorio Monsalvo, C. C. Thöne, J. Gorosabel, A. J. Castro-Tirado, R. **Sánchez-Ramírez**, and J. C. Tello. Observations of GRBs in the mm/submm range at the dawn of the ALMA era. In *Death of Massive Stars: Supernovae and Gamma-Ray Bursts*, volume 279 of *IAU Symposium*, pages 380–382, September 2012. doi: 10.1017/S1743921312013440.

A. de Ugarte Postigo, J. Gorosabel, C. C. Thöne, and R. **Sánchez-Ramírez**. The role of GTC in gamma-ray burst science. In *Revista Mexicana de Astronomia y Astrofisica Conference Series*, volume 42 of *Revista Mexicana de Astronomia y Astrofisica Conference Series*, pages 73–74, May 2013.

A. de Ugarte Postigo, M. Blazek, P. Janout, P. Sprimont, C. C. Thöne, J. Gorosabel, and R. **Sánchez-Ramírez**. GRBSpec: a multi-observatory database for gamma-ray burst spectroscopy. In *Society of Photo-Optical Instrumentation Engineers (SPIE) Conference Series*, volume 9152 of *Society of Photo-Optical Instrumentation Engineers (SPIE) Conference Series*, page 0, July 2014.

A. de Ugarte Postigo, J. P. U. Fynbo, C. C. Thöne, L. Christensen, J. Gorosabel, and R. **Sánchez-Ramírez**. Statistical study of the ISM of GRB hosts. *Highlights of Astronomy*, 16:620–620, March 2015. doi: 10.1017/S1743921314012496.

J. Gorosabel, P. Kubánek, O. Lara-Gil, M. Jelínek, S. Guziy, N. Morales, A. J. Castro-Tirado, A. de Ugarte Postigo, C. C. Thöne, J. C. Tello, R. **Sanchéz-Ramírez**, S. Castillo-Carrión, N. Huélamo, V. Terrón, J. L. Ortiz, M. Fernández, S. Mottola, S. Hellmich, G. Hahn, R. Cunniffe, V. Peris, and U. Carsenty. The 1.23m CAHA telescope: combining upgrades and scientific observations. In *Astronomical Society of India Conference Series*, volume 7 of *Astronomical Society of India Conference Series*, page 303, 2012.

J. Gorosabel, A. J. Castro-Tirado, A. de Ugarte Postigo, C. C. Thöne, R. **Sánchez-Ramírez**, D. Peréz-Ramírez, J. C. Tello, M. Jelínek, and S. Guziy. Observing GRB afterglows, SNe and their host galaxies with the 10.4 m Gran Telescopio Canarias (GTC). In A. J. Castro-Tirado, J. Gorosabel, and I. H. Park, editors, *EAS Publications Series*, volume 61 of *EAS Publications Series*, pages 235–239, July 2013a. doi: 10.1051/eas/1361035.

J. Gorosabel, A. de Ugarte Postigo, J. P. U. Fynbo, L. Christensen, C. C. Thöne, B. Milvang-Jensen, S. Schulze, P. Jakobsson, K. Wiersema, R. **Sánchez-Ramírez**, G. Leloudas, T. Zafar, D. Malesani, and Hjorth. The distribution of equivalent widths in GRB spectra. In J. C. Guirado, L. M. Lara, V. Quilis, and J. Gorgas, editors, *Highlights of Spanish Astrophysics VII*, pages 230–234, May 2013b.

S. Guziy, A. Castro-Tirado, M. Jelínek, J. Gorosabel, P. Kubánek, R. Cunniffe, O. Lara-Gil, O. Rabaza-Castillo, A. de Ugarte Postigo, R. **Sánchez-Ramírez**, J. Tello, C. Pérez del Pulgar, S. Castillo-Carrión, J. Castro Cerón, T. d. J. Mateo Sanguino, R. Hudec, S. Vitek, B. de la Morena Carretero, J. Díaz Andreu, R. Fernández-Muñoz, D. Pérez-Ramírez, P. Yock, W. Allen, I. Bond, I. Kheyfets, G. Christie, L. Sabau-Graziati, C. Cui, Y. Fan, and I. H. Park. GRBS Followed-up by the bootes network. In A. J. Castro-Tirado, J. Gorosabel, and I. H. Park, editors, *EAS Publications Series*, volume 61 of *EAS Publications Series*, pages 251–254, July 2013. doi: 10.1051/eas/1361038.

O. Lara-Gil, P. Kubanek, A. J. Castro-Tirado, J. Gorosabel, M. Jelinek, R. Cunniffe, S. Guziy, A. D. U. Postigo, R. **Sanchez-Ramirez**, and J. C. Tello. The RTS2 Web Interface. In S. Gajadhar, J. Walawender, R. Genet, C. Veillet, A. Adamson, J. Martinez, J. Melnik, T. Jenness, and N. Manset, editors, *Telescopes from Afar*, March 2011.

D. Pérez-Ramírez, J. P. Norris, J. Gorosabel, A. J. Castro-Tirado, L. Hernández-García, A. de Ugarte Postigo, S. Guziy, J. C. Tello, R. **Sánchez-Ramírez**, and P. Ferrero. A

GTC study of the afterglow and host galaxy of the short-duration GRB 100816A. In A. J. Castro-Tirado, J. Gorosabel, and I. H. Park, editors, *EAS Publications Series*, volume 61 of *EAS Publications Series*, pages 345–349, July 2013. doi: 10.1051/eas/1361055.

J. C. Tello, A. de Ugarte Postigo, R. **Sánchez-Ramírez**, M. Jelínek, J. Gorosabel, P. Kubánek, R. Cunniffe, S. Guziy, W. Allen, P. Yock, K.-Y. Lin, A. J. Castro-Tirado, R. Fernández, and C. Pérez del Pulgar. Bootes 3: first two years of GRB follow-ups in New Zealand. In *Astronomical Society of India Conference Series*, volume 7 of *Astronomical Society of India Conference Series*, page 79, 2012.

J. C. Tello, W. Allen, P. Yock, N. Rattenbury, J., M. Jelinek, J. Gorosabel, R. **Sánchez-Ramírez**, K.-Y. Lin, A. J. Castro-Tirado, and C. Pérez del Pulgar. BOOTES-3 Status. In *Revista Mexicana de Astronomia y Astrofisica Conference Series*, volume 45 of *Revista Mexicana de Astronomia y Astrofisica, vol. 27*, pages 12–, December 2014.

R. **Sánchez-Ramírez**, A. de Ugarte Postigo, J. Gorosabel, P. Hankcock, T. Murphy, A. Lundgren, D. A. Kann, I. de Gregorio Monsalvo, J. P. U. Fynbo, D. Garcia-Appadoo, S. Martín, A. Kamble, M. P. M. Kuin, S. R. Oates, A. J. Castro-Tirado, and J. Greiner. GRB110715A: Multifrequency study of the first gamma-ray burst observed with ALMA. In J. C. Guirado, L. M. Lara, V. Quilis, and J. Gorgas, editors, *Highlights of Spanish Astrophysics VII*, pages 399–404, May 2013a.

R. **Sánchez-Ramírez**, J. Gorosabel, A. de Ugarte Postigo, A. J. Castro-Tirado, C. C. Thöne, J. P. U. Fynbo, A. Cabrera-Lavers, S. Guziy, M. Jelínek, J. C. Tello, V. Peris, and D. Galadí-Enríquez. GRB 100316A: A Burst from a High Redshift Galaxy. In *Revista Mexicana de Astronomia y Astrofisica Conference Series*, volume 42 of *Revista Mexicana de Astronomia y Astrofisica Conference Series*, pages 113–113, May 2013b.

R. **Sánchez-Ramírez**, J. Gorosabel, A. de Ugarte Postigo, A. J. Castro-Tirado, C. C. Thöne, J. P. U. Fynbo, S. Guziy, M. Jelínek, J. C. Tello, V. Peris, and D. Galadí-Eníquez. GRB 100316A: an explosion at a high redshift galaxy. In J. C. Guirado, L. M. Lara, V. Quilis, and J. Gorgas, editors, *Highlights of Spanish Astrophysics VII*, pages 463–463, May 2013c.

R. **Sánchez-Ramírez**, P. Hancock, T. Murphy, A. de Ugarte Postigo, J. Gorosabel, D. A. Kann, C. C. Thöne, A. Lundgren, A. Kamble, S. R. Oates, J. P. U. Fynbo, I. de Gregorio Monsalvo, D. Garcia-Appadoo, S. Martín, N. P. M. Kuin, J. Greiner, and A. J. Castro-Tirado. GRB 110715A: Multiwavelength study of the first gamma-ray burst observed with ALMA. In A. J. Castro-Tirado, J. Gorosabel, and I. H. Park, editors, *EAS Publications Series*, volume 61 of *EAS Publications Series*, pages 267–269, July 2013d. doi: 10.1051/eas/1361042.

Thesis Circulars

F. Aceituno, R. **Sanchez-Ramirez**, A. de Ugarte Postigo, J. Gorosabel, and A. J. Castro-Tirado. GRB 120722A: 1.5m OSN i-band observations. *GRB Coordinates Network*, 13505:1, 2012.

F. J. Aceituno, A. J. Castro-Tirado, R. **Sanchez-Ramirez**, and J. Gorosabel. GRB 140428A: 1.5m OSN I-band detection. *GRB Coordinates Network*, 16182:1, 2014.

A. J. Castro-Tirado, R. **Sanchez-Ramirez**, J. Gorosabel, M. Jelinek, J. C. Tello, P. Ferrero, O. Lara-Gil, R. Cunniffe, D. Perez-Ramirez, P. Kubanek, J. M. Castro Ceron, S. Mottola, S. Hellmich, R. Fernandez-Munoz, V. F. Munoz-Martinez, L. Sabau-Graziati, A. Martin-Carrillo, J. Cepa, A. Tejero, and C. Alvarez-Iglesias. GRB 130606A: 10.4m GTC refined redshift z = 5.91. *GRB Coordinates Network*, 14796:1, 2013a. 149

A. J. Castro-Tirado, R. **Sanchez-Ramirez**, M. Jelinek, J. Gorosabel, J. C. Tello, P. Ferrero, O. Lara-Gil, R. Cunniffe, D. Perez-Ramirez, P. Kubanek, J. M. Castro Ceron, A. Fernandez-Soto, S. Mottola, S. Hellmich, R. Fernandez-Munoz, V. F. Munoz-Martinez, J. Cepa, and C. Alvarez-Iglesias. GRB 130606A: 10.4m GTC spectroscopy indicates z = 6.1. *GRB Coordinates Network*, 14790:1, 2013b. 149

A. J. Castro-Tirado, R. Cunniffe, R. **Sanchez-Ramirez**, J. Gorosabel, M. Jelinek, S. R. Oates, S. Jeong, J. R. Tello, and S. Pandey. GRB140703A: 10.4m GTC redshift. *GRB Coordinates Network*, 16505:1, 2014a.

A. J. Castro-Tirado, J. Gorosabel, S. Guziy, O. Rabaza, I. Syniavskyi, Y. Ivanov, R. Cunniffe, A. Gonzalez-Rodriguez, M. Jelinek, S. Jeong, O. Lara-Gil, S. R. Oates, R. **Sanchez-Ramirez**, and J. C. Tello. GRB 140614C: 1.23m CAHA (+EDIPO) observations. *GRB Coordinates Network*, 16410:1, 2014b.

A. J. Castro-Tirado, J. Gorosabel, J. C. Tello, R. Cunniffe, A. Gonzalez-Rodriguez, A. Sota, M. Jelinek, S. Jeong, O. Lara-Gil, S. R. Oates, R. **Sanchez-Ramirez**, P. Kubanek, and S. Pandey. GRB 140709A: BOOTES-2 and OSN optical observations. *GRB Coordinates Network*, 16554:1, 2014d.

A. J. Castro-Tirado, J. Gorosabel, J. C. Tello, R. Cunniffe, A. Gonzalez-Rodriguez, A. Sota, M. Jelinek, S. Jeong, O. Lara-Gil, S. R. Oates, R. **Sanchez-Ramirez**, P. Kubanek, and S. Pandey. GRB 140709A: 10.4m GTC optical decay. *GRB Coordinates Network*, 16564:1, 2014c.

A. J. Castro-Tirado, D. Galadí-Enríquez, F. Hoyos, A. Guijarro, R. **Sánchez-Ramírez**, M. Fernández, J. C. Tello, S. Jeong, and J. Maíz-Apellániz. ANTARES neutrino detection: CAHA photometry and spectroscopy of the Swift source. *The Astronomer's Telegram*, 7998:1, September 2015a.

A. J. Castro-Tirado, R. **Sanchez-Ramirez**, J. Gorosabel, and R. Scarpa. GRB 150101B: potential host galaxy redshift by GTC. *GRB Coordinates Network*, 17278:1, 2015b.

A. J. Castro-Tirado, R. **Sanchez-Ramirez**, G. Lombardi, and M. A. Rivero. GRB 150424A: 10.4m GTC spectroscopy. *GRB Coordinates Network*, 17758:1, 2015c.

R. Cunniffe, A. Gonzalez-Rodriguez, V. Casanova, M. Jelinek, S. Jeong, O. Lara-Gil, S. R. Oates, R. **Sanchez-Ramirez**, J. C. Tello, P. Kubanek, J. Gorosabel, and A. J. Castro-Tirado. GRB 140703A: BOOTES-2 and OSN optical observations. *GRB Coordinates Network*, 16504:1, 2014.

A. de Ugarte Postigo, P. Kubanek, J. C. Tello, R. **Sanchez-Ramirez**, M. Jelinek, R. Cunniffe, S. Guziy, J. Gorosabel, R. Fernandez-Munoz, S. Castillo-Carrion, L. Sabau-Graziati, C. Perez Del Pulgar, L. Sabau-Graziati, and A. J. Castro-Tirado. GRB 101112A: BOOTES-2/TELMA optical afterglow candidate. *GRB Coordinates Network*, 11398:1, 2010.

A. de Ugarte Postigo, J. C. Tello, V. Casanova, A. J. Castro-Tirado, R. **Sanchez-Ramirez**, J. Gorosabel, S. Guziy, and D. Malesani. GRB 110915B: afterglow candidate from OSN. *GRB Coordinates Network*, 12350:1, 2011.

A. de Ugarte Postigo, C. De Breuck, T. Stanke, C. Agurto, M. Valencia-S., A. Remy, F. Montenegro, J. Gorosabel, R. **Sanchez-Ramirez**, and J. P. U. Fynbo. GRB 120514A: APEX observations of the submm counterpart. *GRB Coordinates Network*, 13293:1, 2012a.

A. de Ugarte Postigo, R. **Sanchez-Ramirez**, T. Munoz-Darias, J. Gorosabel, C. C. Thoene, and A. Cabrera-Lavers. Swift J1745-26: Spectroscopy and imaging from GTC. *The Astronomer's Telegram*, 4388:1, September 2012b.

A. de Ugarte Postigo, Z. Cano, C. C. Thoene, J. Gorosabel, R. **Sanchez-Ramirez**, G. Leloudas, D. Xu, K. Wiersema, J. P. U. Fynbo, D. Malesani, J. Hjorth, P. Jakobsson, and O. E. Hartoog. Supernova 2013ez = GRB 130215A. *Central Bureau Electronic Telegrams*, 3637:1, August 2013a.

A. de Ugarte Postigo, N. Tanvir, R. **Sanchez-Ramirez**, C. C. Thoene, J. Gorosabel, and J. P. U. Fynbo. GRB 130420A: redshift from 10.4m GTC. *GRB Coordinates Network*, 14437:1, 2013b.

A. de Ugarte Postigo, C. C. Thoene, J. Gorosabel, R. **Sanchez-Ramirez**, J. P. U. Fynbo, and N. Tanvir. GRB130313A: optical observations from GTC. *GRB Coordinates Network*, 14302:1, 2013c.

A. de Ugarte Postigo, C. C. Thoene, J. Gorosabel, R. **Sanchez-Ramirez**, J. P. U. Fynbo, N. Tanvir, and C. A. Alvarez Iglesias. GRB 130418A: redshift from 10.4m GTC. *GRB Coordinates Network*, 14380:1, 2013d.

A. de Ugarte Postigo, C. C. Thoene, J. Gorosabel, R. **Sanchez-Ramirez**, J. P. U. Fynbo, N. R. Tanvir, A. Cabrera-Lavers, and A. Garcia. GRB 131108A: redshift from 10.4m GTC. *GRB Coordinates Network*, 15470:1, 2013e.

A. de Ugarte Postigo, C. C. Thoene, J. Gorosabel, R. **Sanchez-Ramirez**, G. Leloudas, Z. Cano, D. Xu, K. Wiersema, J. P. U. Fynbo, D. Malesani, J. Hjorth, P. Jakobsson, and O. E. Hartoog. GRB 130215A: detection of the SN with the 10.4m GTC. *GRB Coordinates Network*, 14303:1, 2013f.

A. de Ugarte Postigo, C. C. Thoene, R. **Sanchez-Ramirez**, J. Gorosabel, J. P. U. Fynbo, N. R. Tanvir, and C. A. Alvarez Iglesias. GRB 131030A: spectroscopy from 10.4m GTC. *GRB Coordinates Network*, 15408:1, 2013g.

A. de Ugarte Postigo, D. Xu, G. Leloudas, T. Kruehler, D. Malesani, J. Gorosabel, C. C. Thoene, R. **Sanchez-Ramirez**, S. Schulze, J. P. U. Fynbo, J. Hjorth, Z. Cano, P. Jakobsson, and A. Cabrera-Lavers. Supernova 2013cq = GRB 130427A. *Central Bureau Electronic Telegrams*, 3529:1, May 2013i.

A. de Ugarte Postigo, D. Xu, G. Leloudas, T. Kruehler, D. Malesani, J. Gorosabel, C. C. Thoene, R. **Sanchez-Ramirez**, S. Schulze, J. P. U. Fynbo, J. Hjorth, Z. Cano, P. Jakobsson, and A. Cabrera-Lavers. Supernova 2013cq = GRB 130427A. *Central Bureau Electronic Telegrams*, 3531:1, May 2013h.

A. de Ugarte Postigo, D. Xu, G. Leloudas, T. Kruehler, D. Malesani, J. Gorosabel, C. C. Thoene, R. **Sanchez-Ramirez**, S. Schulze, J. P. U. Fynbo, J. Hjorth, P. Jakobsson, and A. Cabrera-Lavers. GRB 130427A: spectroscopic detection of the SN from the 10.4m GTC. *GRB Coordinates Network*, 14646:1, 2013j.

A. de Ugarte Postigo, C. C. Thoene, D. Malesani, S. Schulze, R. **Sanchez-Ramirez**, J. Gorosabel, C. A. Alvarez Iglesias, J. Molgo, and M. Rivero. GRB141004A: Host galaxy redshift form GTC. *GRB Coordinates Network*, 16902:1, 2014.

A. de Ugarte Postigo, J. P. U. Fynbo, C. Thoene, N. R. Tanvir, R. **Sanchez-Ramirez**, J. Gorosabel, P. Pessev, C. Alvarez-Iglesias, and M. A. Rivero. GRB 150314A: Redshift from OSIRIS/GTC. *GRB Coordinates Network*, 17583:1, 2015.

J. Gorosabel, A. de Ugarte Postigo, S. Mottola, S. Hellmich, P. Ferrero, R. **Sanchez-Ramirez**, J. C. Tello, V. Casanova, R. Marti, and A. J. Castro-Tirado. Swift J1822.3-1606: Optical/NIR counterpart candidate. *The Astronomer's Telegram*, 3496:1, July 2011a.

J. Gorosabel, A. C. Lavers, R. **Sanchez-Ramirez**, A. de Ugarte Postigo, A. J. Levan, C. C. Thoene, N. R. Tanvir, A. J. Castro-Tirado, and P. Kubanek. GRB 111022B: 10.4m GTC z'-band observations. *GRB Coordinates Network*, 12494:1, 2011b.

J. Gorosabel, R. **Sanchez-Ramirez**, R. Gimeno, P. Montañes, and A. D. U. Postigo. MAXIJ1836-194: 1.23m CAHA I-band observations. *The Astronomer's Telegram*, 3673: 1, October 2011c.

J. Gorosabel, N. Huelamo, R. **Sanchez-Ramirez**, A. de Ugarte Postigo, T. Kruehler, A. J. Castro-Tirado, J. C. Tello, and M. Jelinek. GRB 120805A: 1.23m CAHA observations. *GRB Coordinates Network*, 13591:1, 2012a.

J. Gorosabel, M. Jelinek, C. Wang, C. Zurita, A. Sota, J. C. Tello, R. **Sanchez-Ramirez**, and A. J. Castro-Tirado. GRB 120729A: optical observations from OSN, BOOTES1/2 and IAC80. *GRB Coordinates Network*, 13550:1, 2012b.

J. Gorosabel, P. Kubanek, and R. **Sanchez-Ramirez**. GRB 120219A: 1.23m CAHA optical observations. *GRB Coordinates Network*, 12976:1, 2012c.

J. Gorosabel, A. de Ugarte Postigo, J. C. Tello, A. J. Castro-Tirado, J. Cepa, D. Jimenez-Mejias, R. Alonso, R. **Sanchez-Ramirez**, and V. Casanova. GRB 130502A: OSN and IAC80 i-band observations. *GRB Coordinates Network*, 14535:1, 2013a.

J. Gorosabel, A. de Ugarte Postigo, J. C. Tello, A. J. Castro-Tirado, J. Cepa, D. Jimenez-Mejias, J. L. D. Caballero, D. H. Ojados, and R. **Sanchez-Ramirez**. GRB 130504A: IAC80 optical candidate. *GRB Coordinates Network*, 14564:1, 2013b.

J. Gorosabel, J. C. Tello, M. Sanchez-Ramirez, M. Jelinek, and A. J. Castro-Tirado. GRB130313A: GTC early optical limits. *GRB Coordinates Network*, 14319:1, 2013c.

J. Gorosabel, A. de Ugarte Postigo, C. Thone, T. Munoz-Darias, R. **Sanchez-Ramirez**, and R. Scarpa. Swift Trigger 600114: Optical spectroscopy from GTC. *GRB Coordinates Network*, 16335:1, 2014a.

J. Gorosabel, R. **Sanchez-Ramirez**, S. Hellmich, and S. Mottola. GRB 141212A: 1.23m CAHA I-band observations. *GRB Coordinates Network*, 17167:1, 2014b.

S. Guziy, R. **Sanchez-Ramirez**, L. Monteagudo Narvion, O. Lara, M. Jelinek, P. Kubanek, Y. Fan, X. Zhao, J. Bai, C. Wang, Y. Xin, C. Cui, R. Cunniffe, A. J. Castro-Tirado, J. C. Tello, and J. Gorosabel. GRB 121123A: BOOTES-4 and IAC80 optical observations. *GRB Coordinates Network*, 13987:1, 2012b.

S. Guziy, R. **Sanchez-Ramirez**, L. Monteagudo Narvion, O. Lara, M. Jelinek, P. Kubanek, Y. Fan, X. Zhao, J. Bai, C. Wang, Y. Xin, C. Cui, R. Cunniffe, A. J. Castro-Tirado, J. C. Tello, and J. Gorosabel. GRB 121123A: BOOTES-4 optical observations. *GRB Coordinates Network*, 14026:1, 2012a.

S. Guziy, J. Gorosabel, A. J. Castro-Tirado, R. Cunniffe, M. Jelinek, S. Jeong, O. Lara-Gil, R. **Sanchez-Ramirez**, J. C. Tello, P. Kubanek, S. B. Pandey, Y. Fan, X. Zhao, J. Bai, C. Wang, Y. Xin, and C. Cui. GRB 140102A: BOOTES-4 early optical observations. *GRB Coordinates Network*, 15685:1, 2014.

O. E. Hartoog, D. Malesani, R. **Sanchez-Ramirez**, A. de Ugarte Postigo, A. J. Levan, J. P. U. Fynbo, P. M. Vreeswijk, and L. Kaper. GRB 140622A: VLT/X-shooter redshift. *GRB Coordinates Network*, 16437:1, 2014.

S. Jeong, R. **Sanchez-Ramirez**, A. J. Castro-Tirado, J. Gorosabel, M. Jelinek, J. C. Tello, P. Ferrero, O. Lara-Gil, R. Cunniffe, D. Perez-Ramirez, S. Guziy, J. M. Castro Ceron, A. Fernandez-Soto, J. Cepa, M. A. Rivero, and G. Gomez-Velarde. GRB 140304A: 10.4m GTC redshift z = 5.39. *GRB Coordinates Network*, 15922:1, 2014a.

S. Jeong, R. **Sanchez-Ramirez**, J. Gorosabel, and A. J. Castro-Tirado. GRB 140304A: 10.4m GTC refined redshift z = 5.283. *GRB Coordinates Network*, 15936:1, 2014b. 137

T. Kruehler, D. Xu, R. **Sanchez-Ramirez**, D. Malesani, J. Fynbo, and H. Flores. GRB130418A: VLT/X-shooter redshift confirmation. *GRB Coordinates Network*, 14390:1, 2013.

D. Malesani, A. de Ugarte Postigo, R. **Sanchez-Ramirez**, and J. P. U. Fynbo. GRB 120612A: optical observations. *GRB Coordinates Network*, 13363:1, 2012.

A. Moskvitin, R. Burenin, R. Uklein, V. Sokolov, R. **Sanchez-Ramirez**, J. Gorosabel, and A. J. Castro-Tirado. GRB 140629A: BTA redshift. *GRB Coordinates Network*, 16489:1, 2014.

A. d. U. Postigo, J. Gorosabel, C. C. Thoene, R. **Sanchez-Ramirez**, and D. Garcia-Alvarez. MLS121106:014420+082311: 10.4m GTC r-band observations. *The Astronomer's Telegram*, 4589:1, November 2012.

J. C. Tello, R. **Sanchez-Ramirez**, A. Sota, J. Gorosabel, and A. J. Castro-Tirado. GRB 100902A: 1.5m OSN i-band upper limits. *GRB Coordinates Network*, 11196:1, 2010.

J. C. Tello, R. Gimeno, J. Gorosabel, M. Jelinek, R. **Sanchez-Ramirez**, and A. J. Castro-Tirado. Swift trigger 535026: optical decay confirmation with IAC80 and BOOTES-2/TELMA. *GRB Coordinates Network*, 13835:1, 2012a.

J. C. Tello, R. **Sanchez-Ramirez**, J. Gorosabel, A. J. Castro-Tirado, P. Kubanek, W. Allen, P. Yock, and K.-Y. Lin. XRF 120118A: optical candidate. *GRB Coordinates Network*, 12851:1, 2012b.

J. C. Tello, R. **Sanchez-Ramirez**, J. Gorosabel, A. J. Castro-Tirado, M. A. Rivero, G. Gomez-Velarde, and A. Klotz. GRB 120326A: GTC redshift. *GRB Coordinates Network*, 13118:1, 2012c.

J. C. Tello, V. Casanova, J. Gorosabel, R. **Sanchez-Ramirez**, and M. Jelinek. GRB130612A OSN i-band observations. *GRB Coordinates Network*, 14881:1, 2013a.

J. C. Tello, M. Jelinek, J. Gorosabel, A. J. Castro-Tirado, and R. **Sanchez-Ramirez**. GRB130608A: BOOTES-2/TELMA upper limits. *GRB Coordinates Network*, 14829:1, 2013b.

J. C. Tello, R. **Sanchez-Ramirez**, J. Gorosabel, F. Aceituno, and A. Castro-Tirado. GRB130418A: OSN 1.5m fading afterglow detection. *GRB Coordinates Network*, 14385: 1, 2013c.

J. C. Tello, R. **Sanchez-Ramirez**, M. Jelinek, J. Gorosabel, W. Allen, P. Yock, P. Kubanek, and A. J. Castro-Tirado. GRB130315A BOOTES-3 optical limit. *GRB Coordinates Network*, 14312:1, 2013d.

J. C. Tello, R. **Sanchez-Ramirez**, M. Jelinek, J. Gorosabel, W. Allen, P. Yock, P. Kubanek, and A. J. Castro-Tirado. GRB130508A: BOOTES-3 optical limit. *GRB Coordinates Network*, 14609:1, 2013e.

R. **Sanchez-Ramirez**, J. C. Tello, A. Sota, J. Gorosabel, and A. J. Castro-Tirado. GRB 100901A: 1.5m OSN BVRI-band observations. *GRB Coordinates Network*, 11180:1, 2010.

R. **Sanchez-Ramirez**, J. Gorosabel, M. Cebrian, A. de Ugarte Postigo, P. Montanes, and A. R. Anton. GRB 111008A: IAC80 i-band observations. *GRB Coordinates Network*, 12432:1, 2011a.

R. **Sanchez-Ramirez**, N. Morales, J. Gorosabel, J. L. Ortiz, P. Kubanek, A. de Ugarte Postigo, and A. J. Castro-Tirado. GRB 110915A: 1.23m CAHA i-band observations. *GRB Coordinates Network*, 12342:1, 2011b.

R. **Sanchez-Ramirez**, A. de Ugarte Postigo, T. Kruehler, B. Milvang-Jensen, J. P. U. Fynbo, N. Tanvir, D. Malesani, S. Schulze, L. Kaper, and H. Flores. GRB 121201A: x-shooter redshift. *GRB Coordinates Network*, 14035:1, 2012a.

R. **Sanchez-Ramirez**, J. Gorosabel, A. J. Castro-Tirado, M. A. Rivero, and G. Gomez-Velarde. GRB 120327A: GTC redshift confirmation. *GRB Coordinates Network*, 13146:1, 2012b.

R. **Sanchez-Ramirez**, J. Gorosabel, A. de Ugarte Postigo, and J. M. Gonzalez Perez. GRB 120907A: spectroscopy from OSIRIS/GTC. *GRB Coordinates Network*, 13723:1, 2012c.

R. **Sanchez-Ramirez**, D. Jimenez Mejias, J. C. Tello, A. de Ugarte Postigo, and J. Gorosabel. GRB 120116A: IAC80 i-band observations. *GRB Coordinates Network*, 12837:1, 2012d.

R. **Sanchez-Ramirez**, G. Leloudas, A. de Ugarte Postigo, C. C. Thoene, J. Gorosabel, D. Malesani, S. Schulze, J. P. U. Fynbo, N. R. Tanvir, J. Hjorth, and D. Xu. GRB 120422A: SN identification from GTC. *GRB Coordinates Network*, 13281:1, 2012e.

R. **Sanchez-Ramirez**, A. J. Castro-Tirado, J. Gorosabel, F. J. Aceituno, E. Sonbas, E. Gogus, T. Guver, H. Kirbiyik, and D. Garcia-Alvarez. GRB 130603B: optical follow-up and independent GTC redshift determination and afterglow spectrum. *GRB Coordinates Network*, 14747:1, 2013a.

R. **Sanchez-Ramirez**, J. Gorosabel, A. J. Castro-Tirado, J. Cepa, and G. Gomez-Velarde. GRB 130518A: 10.4m GTC/OSIRIS redshift. *GRB Coordinates Network*, 14685:1, 2013b.

R. **Sanchez-Ramirez**, A. J. Castro-Tirado, F. Hoyos, and J. Aceituno. GRB 150413A: redshift determination with the 2.2m CAHA. *GRB Coordinates Network*, 17697:1, 2015.

C. C. Thoene, J. Gorosabel, A. de Ugarte Postigo, R. **Sanchez-Ramirez**, T. Munoz-Darias, S. Guziy, and A. J. Castro-Tirado. GRB 110328A / Swift J164449.3+573451: optical spectroscopy from GTC. *GRB Coordinates Network*, 11834:1, March 2011.

C. C. Thoene, A. de Ugarte Postigo, J. Gorosabel, R. **Sanchez-Ramirez**, J. P. U. Fynbo, and G. Gomez Velarde. GRB 120811C: redshift from OSIRIS/GTC. *GRB Coordinates Network*, 13628:1, 2012.

References

Abbott, B.P., Abbott, R., Abbott, T.D., Abernathy, M.R., Acernese, F., Ackley, K., Adams, C., Adams, T., Addesso, P., Adhikari, R.X., Adya, V.B., Affeldt, C., Agathos, M., Agatsuma, K., Aggarwal, N., Aguiar, O.D., Aiello, L., Ain, A., Ajith, P., Allen, B., Allocca, A., Altin, P.A., Anderson, S.B., Anderson, W.G., Arai, K., Arain, M.A., Araya, M.C., Arceneaux, C.C., Areeda, J.S., Arnaud, N., Arun, K.G., Ascenzi, S., Ashton, G., Ast, M., Aston, S.M., Astone, P., Aufmuth, P., Aulbert, C., Babak, S., Bacon, P., Bader, M.K.M., Baker, P.T., Baldaccini, F., Ballardin, G., Ballmer, S.W., Barayoga, J.C., Barclay, S.E., Barish, B.C., Barker, D., Barone, F., Barr, B., Barsotti, L., Barsuglia, M., Barta, D., Bartlett, J., Barton, M.A., Bartos, I., Bassiri, R., Basti, A., Batch, J.C., Baune, C., Bavigadda, V., Bazzan, M., Behnke, B., Bejger, M., Belczynski, C., Bell, A.S., Bell, C.J., Berger, B.K., Bergman, J., Bergmann, G., Berry, C.P.L., Bersanetti, D., Bertolini, A., Betzwieser, J., Bhagwat, S., Bhandare, R., Bilenko, I.A., Billingsley, G., Birch, J., Birney, R., Birnholtz, O., Biscans, S., Bisht, A., Bitossi, M., Biwer, C., Bizouard, M.A., Blackburn, J.K., Blair, C.D., Blair, D.G., Blair, R.M., Bloemen, S., Bock, O., Bodiya, T.P., Boër, M., Bogaert, G., Bogan, C., Bohe, A., Bojtos, P., Bond, C., Bondu, F., Bonnand, R., Boom, B.A., Bork, R., Boschi, V., Bose, S., Bouffanais, Y., Bozzi, A., Bradaschia, C., Brady, P.R., Braginsky, V.B., Branchesi, M., Brau, J.E., Briant, T., Brillet, A., Brinkmann, M., Brisson, V., Brockill, P., Brooks, A.F., Brown, D.A., Brown, D.D., Brown, N.M., Buchanan, C.C., Buikema, A., Bulik, T., Bulten, H.J., Buonanno, A., Buskulic, D., Buy, C., Byer, R.L., Cabero, M., Cadonati, L., Cagnoli, G., Cahillane, C., Bustillo, J.C., Callister, T., Calloni, E., Camp, J.B., Cannon, K.C., Cao, J., Capano, C.D., Capocasa, E., Carbognani, F., Caride, S., Diaz, J.C., Casentini, C., Caudill, S., Cavaglià, M., Cavalier, F., Cavalieri, R., Cella, G., Cepeda, C.B., Baiardi, L.C., Cerretani, G., Cesarini, E., Chakraborty, R., Chalermsongsak, T., Chamberlin, S.J., Chan, M., Chao, S., Charlton, P., Chassande-Mottin, E., Chen, H.Y., Chen, Y., Cheng, C., Chincarini, A., Chiummo, A., Cho, H.S., Cho, M., Chow, J.H., Christensen, N., Chu, Q., Chua, S., Chung, S., Ciani, G., Clara, F., Clark, J.A., Cleva, F., Coccia, E., Cohadon, P.F., Colla, A., Collette, C.G., Cominsky, L., Constancio, M., Conte, A., Conti, L., Cook, D., Corbitt, T.R., Cornish, N., Corsi, A., Cortese, S., Costa, C.A., Coughlin, M.W., Coughlin, S.B., Coulon, J.P., Countryman, S.T., Couvares, P., Cowan, E.E., Coward, D.M., Cowart, M.J., Coyne, D.C., Coyne, R., Craig, K., Creighton, J.D.E., Creighton, T.D., Cripe, J., Crowder, S.G., Cruise, A.M., Cumming, A., Cunningham, L., Cuoco, E., Canton, T.D., Danilishin, S.L., D'Antonio, S., Danzmann, K., Darman, N.S., Da Silva Costa, C.F., Dattilo, V., Dave, I., Daveloza, H.P., Davier, M., Davies, G.S., Daw, E.J., Day, R., De, S., DeBra, D., Debreczeni, G., Degallaix, J., De Laurentis, M., Deléglise, S., Del Pozzo, W., Denker, T., Dent, T., Dereli, H., Dergachev, V., DeRosa, R.T., De Rosa, R., DeSalvo, R., Dhurandhar, S., Díaz, M.C., Di Fiore, L., Di Giovanni, M., Di Lieto, A., Di Pace, S., Di Palma, I., Di Virgilio, A., Dojcinoski, G., Dolique, V., Donovan, F., Dooley, K.L., Doravari, S., Douglas, R., Downes, T.P., Drago, M., Drever, R.W.P., Driggers, J.C., Du, Z., Ducrot, M., Dwyer, S.E., Edo, T.B., Edwards, M.C., Effler, A., Eggenstein, H.B., Ehrens, P., Eichholz, J., Eikenberry, S.S., Engels, W., Essick, R.C., Etzel, T., Evans, M., Evans, T.M., Everett, R., Factourovich, M., Fafone, V., Fair, H., Fairhurst, S., Fan, X., Fang, Q., Farinon, S., Farr, B., Farr, W.M., Favata, M., Fays, M., Fehrmann, H., Fejer, M.M., Feldbaum, D., Ferrante, I., Ferreira, E.C., Ferrini, F., Fidecaro, F., Finn, L.S., Fiori, I., Fiorucci, D., Fisher, R.P., Flaminio, R., Fletcher, M., Fong, H., Fournier, J.D., Franco, S., Frasca, S., Frasconi, F., Frede, M., Frei, Z., Freise, A., Frey, R., Frey, V., Fricke, T.T., Fritschel, P. & Fro... (2016a). Observation of Gravitational Waves from a Binary Black Hole Merger. *Physical Review Letters*, **116**, 061102.

Abbott, B.P., Abbott, R., Abbott, T.D., Abernathy, M.R., Acernese, F., Ackley, K., Adams, C., Adams, T., Addesso, P., Adhikari, R.X., Adya, V.B., Affeldt, C., Agathos, M., Agatsuma, K., Aggarwal, N., Aguiar, O.D., Aiello, L., Ain, A., Ajith, P., Allen, B., Allocca, A., Altin, P.A., Anderson, S.B., Anderson, W.G., Arai, K., Araya, M.C., Arceneaux, C.C., Areeda, J.S., Arnaud, N., Arun, K.G., Ascenzi, S., Ashton, G., Ast, M., Aston, S.M., Astone, P., Aufmuth, P., Aulbert, C., Babak, S., Bacon, P., Bader, M.K.M., Baker, P.T., Baldaccini, F., Ballardin, G., Ballmer, S.W., Barayoga, J.C., Barclay, S.E., Barish, B.C., Barker, D., Barone, F., Barr, B., Barsotti, L., Barsuglia, M., Barta, D., Barthelmy, S.D., Bartlett, J., Bartos, I., Bassiri, R., Basti, A., Batch, J.C., Baune, C., Bavigadda, V., Bazzan, M., Behnke, B., Bejger, M., Bell, A.S., Bell, C.J., Berger, B.K., Bergman, J., Bergmann, G., Berry, C.P.L., Bersanetti, D., Bertolini, A., Betzwieser, J., Bhagwat, S., Bhandare, R., Bilenko, I.A., Billingsley, G., Birch, J., Birney, R., Biscans, S., Bisht, A., Bitossi, M., Biwer, C., Bizouard, M.A., Blackburn, J.K., Blair, C.D., Blair, D.G., Blair, R.M., Bloemen, S., Bock, O., Bodiya, T.P., Boër, M., Bogaert, G., Bogan, C., Bohe, A., Bojtos, P., Bond, C., Bondu, F., Bonnand, R., Boom, B.A., Bork, R., Boschi, V., Bose, S., Bouffanais, Y., Bozzi, A., Bradaschia, C., Brady, P.R., Braginsky, V.B., Branchesi, M., Brau, J.E., Briant, T., Brillet, A., Brinkmann, M., Brisson, V., Brockill, P., Brooks, A.F., Brown, D.A., Brown, D.D., Brown, N.M., Buchanan, C.C., Buikema, A., Bulik, T., Bulten, H.J., Buonanno, A., Buskulic, D., Buy, C., Byer, R.L., Cadonati, L., Cagnoli, G., Cahillane, C., Bustillo, J.C., Callister, T., Calloni, E., Camp, J.B., Cannon, K.C., Cao, J., Capano, C.D., Capocasa, E., Carbognani, F., Caride, S., Diaz, J.C., Casentini, C., Caudill, S., Cavaglià, M., Cavalier, F., Cavalieri, R., Cella, G., Cepeda, C.B., Baiardi, L.C., Cerretani, G., Cesarini, E., Chakraborty, R., Chalermsongsak, T., Chamberlin, S.J., Chan, M., Chao, S., Charlton, P., Chassande-Mottin, E., Chen, H.Y., Chen, Y., Cheng, C., Chincarini, A., Chiummo, A., Cho, H.S., Cho, M., Chow, J.H., Christensen, N., Chu, Q., Chua, S., Chung, S., Ciani, G., Clara, F., Clark, J.A., Cleva, F., Coccia, E., Cohadon, P.F., Colla, A., Collette, C.G., Cominsky, L., Constancio, M.J., Conte, A., Conti, L., Cook, D., Corbitt, T.R., Cornish, N., Corsi, A., Cortese, S., Costa, C.A., Coughlin, M.W., Coughlin, S.B., Coulon, J.P., Countryman, S.T., Couvares, P., Cowan, E.E., Coward, D.M., Cowart, M.J., Coyne, D.C., Coyne, R., Craig, K., Creighton, J.D.E., Cripe, J., Crowder, S.G., Cumming, A., Cunningham, L., Cuoco, E., Dal Canton, T., Danilishin, S.L., D'Antonio, S., Danzmann, K., Darman, N.S., Dattilo, V., Dave, I., Daveloza, H.P., Davier, M., Davies, G.S., Daw, E.J., Day, R., DeBra, D., Debreczeni, G., Degallaix, J., De Laurentis, M., Deléglise, S., Del Pozzo, W., Denker, T., Dent, T., Dereli, H., Dergachev, V., DeRosa, R.T., De Rosa, R., DeSalvo, R., Dhurandhar, S., Díaz, M.C., Di Fiore, L., Di Giovanni, M., Di Lieto, A., Di Pace, S., Di Palma, I., Di Virgilio, A., Dojcinoski, G., Dolique, V., Donovan, F., Dooley, K.L., Doravari, S., Douglas, R., Downes, T.P., Drago, M., Drever, R.W.P., Driggers, J.C., Du, Z., Ducrot, M., Dwyer, S.E., Edo, T.B., Edwards, M.C., Effler, A., Eggenstein, H.B., Ehrens, P., Eichholz, J., Eikenberry, S.S., Engels, W., Essick, R.C., Etzel, T., Evans, M., Evans, T.M., Everett, R., Factourovich, M., Fafone, V., Fair, H., Fairhurst, S., Fan, X., Fang, Q., Farinon, S., Farr, B., Farr, W.M., Favata, M., Fays, M., Fehrmann, H., Fejer, M.M., Ferrante, I., Ferreira, E.C., Ferrini, F., Fidecaro, F., Fiori, I., Fiorucci, D., Fisher, R.P., Flaminio, R., Fletcher, M., Fournier, J.D., Franco, S., Frasca, S., Frasconi, F., Frei, Z., Freise, A., Frey, R., Frey, V., Fricke, T.T., Fritschel, P., Frolov, V.V., Fulda, P., Fyffe, M., Gabbard, H.A.G., Gair, J.R., Gammaitoni, L., Gaonkar, S.G., Garufi, F., Gatto, A., Gaur, G., Gehrels, N., Gemme, G., Gendre, B., Genin, E. & Ge... (2016b). Localization and broadband follow-up of the gravitational-wave transient GW150914. *arXiv.org*, arXiv:1602.08492.

Abel, T., Bryan, G.L. & Norman, M.L. (2002). The Formation of the First Star in the Universe. *Science*, **295**, 93–98.

Achterberg, A., Gallant, Y.A., Kirk, J.G. & Guthmann, A.W. (2001). Particle acceleration by ultrarelativistic shocks: theory and simulations. *Monthly Notices of the Royal Astronomical Society*, **328**, 393–408.

Afonso, P.M.J., Kann, D.A., Nicuesa Guelbenzu, A., Krühler, T., Elliott, J. & Greiner, J. (2013). GRB 130606A: GROND detection of the Optical/NIR afterglow. *GRB Coordinates Network*, **1480**, 1.

Aihara, H., Allende Prieto, C., An, D., Anderson, S.F., Aubourg, É., Balbinot, E., Beers, T.C., Berlind, A.A., Bickerton, S.J., Bizyaev, D., Blanton, M.R., Bochanski, J.J., Bolton, A.S., Bovy, J., Brandt, W.N., Brinkmann, J., Brown, P.J., Brownstein, J.R., Busca, N.G., Campbell, H., Carr, M.A., Chen, Y., Chiappini, C., Comparat, J., Connolly, N., Cortes, M., Croft, R.A.C., Cuesta, A.J., da Costa, L.N., Davenport, J.R.A., Dawson, K.S., Dhital, S., Ealet, A., Ebelke, G.L., Edmondson, E.M., Eisenstein, D.J., Escoffier, S., Esposito, M., Evans, M.L., Fan, X., Femenía Castellá, B., Font-Ribera, A., Frinchaboy, P.M., Ge, J., Gillespie, B.A., Gilmore, G., González Hernández, J.I., Gott, J.R., Gould, A., Grebel, E.K., Gunn, J.E., Hamilton, J.C., Harding, P., Harris, D.W., Hawley, S.L., Hearty, F.R., Ho, S., Hogg, D.W., Holtzman, J.A., Honscheid, K., Inada, N., Ivans, I.I., Jiang, L., Johnson, J.A., Jordan, C., Jordan, W.P., Kazin, E.A., Kirkby, D., Klaene, M.A., Knapp, G.R., Kneib, J.P., Kochanek, C.S., Koesterke, L., Kollmeier, J.A., Kron, R.G., Lampeitl, H., Lang, D., Le Goff, J.M., Lee, Y.S., Lin, Y.T., Long, D.C., Loomis, C.P., Lucatello, S., Lundgren, B., Lupton, R.H., Ma, Z., MacDonald, N., Mahadevan, S., Maia, M.A.G., Makler, M., Malanushenko, E., Malanushenko, V., Mandelbaum, R., Maraston, C., Margala, D., Masters, K.L., McBride, C.K., McGehee, P.M., McGreer, I.D., Ménard, B., Miralda-Escudé, J., Morrison, H.L., Mullally, F., Muna, D., Munn, J.A., Murayama, H., Myers, A.D., Naugle, T., Neto, A.F., Nguyen, D.C., Nichol, R.C., O'Connell, R.W., Ogando, R.L.C., Olmstead, M.D., Oravetz, D.J., Padmanabhan, N., Palanque-Delabrouille, N., Pan, K., Pandey, P., Pâris, I., Percival, W.J., Petitjean, P., Pfaffenberger, R., Pforr, J., Phleps, S., Pichon, C., Pieri, M.M., Prada, F., Price-Whelan, A.M., Raddick, M.J., Ramos, B.H.F., Reylé, C., Rich, J., Richards, G.T., Rix, H.W., Robin, A.C., Rocha-Pinto, H.J., Rockosi, C.M., Roe, N.A., Rollinde, E., Ross, A.J., Ross, N.P., Rossetto, B.M., Sánchez, A.G., Sayres, C., Schlegel, D.J., Schlesinger, K.J., Schmidt, S.J., Schneider, D.P., Sheldon, E., Shu, Y., Simmerer, J., Simmons, A.E., Sivarani, T., Snedden, S.A., Sobeck, J.S., Steinmetz, M., Strauss, M.A., Szalay, A.S., Tanaka, M., Thakar, A.R., Thomas, D., Tinker, J.L., Tofflemire, B.M., Tojeiro, R., Tremonti, C.A., Vandenberg, J., Vargas Magaña, M., Verde, L., Vogt, N.P., Wake, D.A., Wang, J., Weaver, B.A., Weinberg, D.H., White, M., White, S.D.M., Yanny, B., Yasuda, N., Yèche, C. & Zehavi, I. (2011). The Eighth Data Release of the Sloan Digital Sky Survey: First Data from SDSS-III. *The Astrophysical Journal Supplement Series*, **193**, 29.

Amati, L., Frontera, F., Tavani, M., in't Zand, J.J.M., Antonelli, L.A., Costa, E., Feroci, M., Guidorzi, C., Heise, J., Masetti, N., Montanari, E., Nicastro, L., Palazzi, E., Pian, E., Piro, L. & Soffitta, P. (2002). Intrinsic spectra and energetics of BeppoSAX Gamma-Ray Bursts with known redshifts. *Astronomy and Astrophysics*, **390**, 81–89.

Arabsalmani, M., Møller, P., Fynbo, J.P.U., Christensen, L., Freudling, W., Savaglio, S. & Zafar, T. (2015). On the mass-metallicity relation, velocity dispersion, and gravitational well depth of GRB host galaxies. *Monthly Notices of the Royal Astronomical Society*, **446**, 990–999.

Asplund, M., Grevesse, N., Sauval, A.J. & Scott, P. (2009). The Chemical Composition of the Sun. *Annual Review of Astronomy and Astrophysics*, **47**, 481–522.

Band, D., Matteson, J., Ford, L., Schaefer, B., Palmer, D., Teegarden, B., Cline, T., Briggs, M.S., Paciesas, W., Pendleton, G.N., Fishman, G.J., Kouveliotou, C., Meegan, C., Wilson, R. & Lestrade, P. (1993). BATSE observations of gamma-ray burst spectra. I - Spectral diversity. *The Astrophysical Journal*, **413**, 281–292.

Barkana, R. & Loeb, A. (2001). In the beginning: the first sources of light and the reionization of the universe. *Physics Reports*, **349**, 125–238.

Barthelmy, S.D., Barbier, L.M., Cummings, J.R., Fenimore, E.E., Gehrels, N., Hullinger, D., Krimm, H.A., Markwardt, C.B., Palmer, D.M., Parsons, A., Sato, G., Suzuki, M., Takahashi, T., Tashiro, M. & Tueller, J. (2005). The Burst Alert Telescope (BAT) on the SWIFT Midex Mission. *Space Science Reviews*, **120**, 143–164.

Barthelmy, S.D., Baumgartner, W.H., Cummings, J.R., Fenimore, E.E., Gehrels, N., Krimm, H.A., Lien, A.Y., Markwardt, C.B., Palmer, D.M., Sakamoto, T., Sato, G., Stamatikos, M., Tueller, J. & Ukwatta, T.N. (2013). GRB 130606A, Swift-BAT refined analysis. *GRB Coordinates Network*, **1481**, 1.

Baum, W.A. (1962). Photoelectric Magnitudes and Red-Shifts. *Problems of Extra-Galactic Research*, **15**, 390–.

Bazin, G., Ruhlmann-Kleider, V., Palanque-Delabrouille, N., Rich, J., Aubourg, É., Astier, P., Balland, C., Basa, S., Carlberg, R.G., Conley, A., Fouchez, D., Guy, J., Hardin, D., Hook, I.M., Howell, D.A., Pain, R., Perrett, K., Pritchet, C.J., Regnault, N., Sullivan, M., Fourmanoit, N., González-Gaitán, S., Lidman, C., Perlmutter, S., Ripoche, P. & Walker, E.S. (2011). Photometric selection of Type Ia supernovae in the Supernova Legacy Survey. *Astronomy and Astrophysics*, **534**, A43.

Becker, R.H., Fan, X., White, R.L., Strauss, M.A., Narayanan, V.K., Lupton, R.H., Gunn, J.E., Annis, J., Bahcall, N.A., Brinkmann, J., Connolly, A.J., Csabai, I., Czarapata, P.C., Doi, M., Heckman, T.M., Hennessy, G.S., Ivezić, Ž., Knapp, G.R., Lamb, D.Q., McKay, T.A., Munn, J.A., Nash, T., Nichol, R., Pier, J.R., Richards, G.T., Schneider, D.P., Stoughton, C., Szalay, A.S., Thakar, A.R. & York, D.G. (2001). Evidence for Reionization at z˜6: Detection of a Gunn-Peterson Trough in a z=6.28 Quasar. *The Astronomical Journal*, **122**, 2850–2857.

Beckwith, S.V.W., Stiavelli, M., Koekemoer, A.M., Caldwell, J.A.R., Ferguson, H.C., Hook, R., Lucas, R.A., Bergeron, L.E., Corbin, M., Jogee, S., Panagia, N., Robberto, M., Royle, P., Somerville, R.S. & Sosey, M. (2006). The Hubble Ultra Deep Field. *The Astronomical Journal*, **132**, 1729–1755.

Belczynski, K., Bulik, T., Heger, A. & Fryer, C. (2007). The Lack of Gamma-Ray Bursts from Population III Binaries. *The Astrophysical Journal*, **664**, 986–999.

Berg, T.A.M., Ellison, S.L., Prochaska, J.X., Venn, K.A. & Dessauges-Zavadsky, M. (2015a). The chemistry of the most metal-rich damped Lyman α systems at z ˜ 2 - II. Context with the Local Group. *Monthly Notices of the Royal Astronomical Society*, **452**, 4326–4346.

Berg, T.A.M., Neeleman, M., Prochaska, J.X., Ellison, S.L. & Wolfe, A.M. (2015b). The Most Metal-rich Damped Lyα Systems at z gsim 1.5 I: The Data. *Publications of the Astronomical Society of Pacific*, **127**, 167–210.

Berger, E., Price, P.A., Cenko, S.B., Gal-Yam, A., Soderberg, A.M., Kasliwal, M., Leonard, D.C., Cameron, P.B., Frail, D.A., Kulkarni, S.R., Murphy, D.C., Krzeminski, W., Piran, T., Lee, B.L., Roth, K.C., Moon, D.S., Fox, D.B., Harrison, F.A., Persson, S.E., Schmidt, B.P., Penprase, B.E., Rich, J., Peterson, B.A. & Cowie, L.L. (2005). The afterglow and elliptical host galaxy of the short γ-ray burst GRB 050724. *Nature*, **438**, 988–990.

Bernardini, M.G., Ghirlanda, G., Campana, S., Covino, S., Salvaterra, R., Atteia, J.L., Burlon, D., Calderone, G., D'Avanzo, P., D'Elia, V., Ghisellini, G., Heussaff, V., Lazzati, D., Melandri, A., Nava, L., Vergani, S.D. & Tagliaferri, G. (2015). Comparing the spectral lag of short and long gamma-ray bursts and its relation with the luminosity. *Monthly Notices of the Royal Astronomical Society*, **446**, 1129–1138.

Bertin, E. & Arnouts, S. (1996). SExtractor: Software for source extraction. *Astronomy and Astrophysics Supplement*, **117**, 393–404.

Bird, S., Haehnelt, M., Neeleman, M., Genel, S., Vogelsberger, M. & Hernquist, L. (2015). Reproducing the kinematics of damped Lyman α systems. *Monthly Notices of the Royal Astronomical Society*, **447**, 1834–1846.

Blain, A.W., Frayer, D.T., Bock, J.J. & Scoville, N.Z. (2000). Millimetre/submillimetre-wave emission-line searches for high-redshift galaxies. *Monthly Notices of the Royal Astronomical Society*, **313**, 559–570.

Bloom, J.S., Kulkarni, S.R., Djorgovski, S.G., Eichelberger, A.C., Côté, P., Blakeslee, J.P., Odewahn, S.C., Harrison, F.A., Frail, D.A., Filippenko, A.V., Leonard, D.C., Riess, A.G., Spinrad, H., Stern, D., Bunker, A., Dey, A., Grossan, B., Perlmutter, S., Knop, R.A., Hook, I.M. & Feroci, M. (1999). The unusual afterglow of the γ-ray burst of 26 March 1998 as evidence for a supernova connection. *Nature*, **401**, 453–456.

Boër, M., Atteia, J.L., Damerdji, Y., Gendre, B., Klotz, A. & Stratta, G. (2006). Detection of a Very Bright Optical Flare from the Gamma-Ray Burst GRB 050904 at Redshift 6.29. *The Astrophysical Journal*, **638**, L71–L74.

Bolton, J.S., Haehnelt, M., Warren, S.J., Hewett, P.C., Mortlock, D.J., Venemans, B.P., McMahon, R.G. & Simpson, C. (2011). How neutral is the intergalactic medium surrounding the redshift z = 7.085 quasar ULAS J1120+0641? *Monthly Notices of the Royal Astronomical Society: Letters*, **416**, L70–L74.

Bouwens, R.J., Illingworth, G.D., Labbé, I., Oesch, P.A., Trenti, M., Carollo, C.M., van Dokkum, P.G., Franx, M., Stiavelli, M., González, V., Magee, D. & Bradley, L. (2011). A candidate redshift z˜10 galaxy and rapid changes in that population at an age of 500Myr. *Nature*, **469**, 504–507.

Bouwens, R.J., Bradley, L., Zitrin, A., Coe, D., Franx, M., Zheng, W., Smit, R., Host, O., Postman, M., Moustakas, L., Labbé, I., Carrasco, M., Molino, A., Donahue, M., Kelson, D.D., Meneghetti, M., Benitez, N., Lemze, D., Umetsu, K., Broadhurst, T., Moustakas, J., Rosati, P., Jouvel, S., Bartelmann, M., Ford, H., Graves, G., Grillo, C., Infante, L., Jimenez-Teja, Y., Lahav, O., Maoz, D., Medezinski, E., Melchior, P., Merten, J., Nonino, M., Ogaz, S. & Seitz, S. (2014). A Census of Star-forming Galaxies in the Z ˜ 9-10 Universe based on HST+Spitzer Observations over 19 Clash Clusters: Three Candidate Z ˜ 9-10 Galaxies and Improved Constraints on the Star Formation Rate Density at Z ˜ 9.2. *The Astrophysical Journal*, **795**, 126.

Bowler, R.A.A., Dunlop, J.S., McLure, R.J., McCracken, H.J., Milvang-Jensen, B., Furusawa, H., Fynbo, J.P.U., Le Fèvre, O., Holt, J., Ideue, Y., Ihara, Y., Rogers, A.B. & Taniguchi, Y. (2012). Discovery of bright z $\simeq$ 7 galaxies in the UltraVISTA survey. *Monthly Notices of the Royal Astronomical Society*, **426**, 2772–2788.

BOYLE, B.J., SHANKS, T., CROOM, S.M., SMITH, R.J., MILLER, L., LOARING, N. & HEYMANS, C. (2000). The 2dF QSO Redshift Survey - I. The optical luminosity function of quasi-stellar objects. *Monthly Notices of the Royal Astronomical Society*, **317**, 1014–1022.

BRAUN, R. (2012). Cosmological Evolution of Atomic Gas and Implications for 21 cm H I Absorption. *The Astrophysical Journal*, **749**, 87.

BREEVELD, A.A., LANDSMAN, W., HOLLAND, S.T., ROMING, P., KUIN, N.P.M. & PAGE, M.J. (2011). An Updated Ultraviolet Calibration for the Swift/UVOT. In *GAMMA RAY BURSTS 2010. AIP Conference Proceedings*, 373–376, Mullard Space Science Laboratory, University College London, Holmbury St. Mary, Dorking, Surrey RH5 6NT, UK, AIP.

BROMBERG, O., NAKAR, E. & PIRAN, T. (2011). Are Low-luminosity Gamma-Ray Bursts Generated by Relativistic Jets? *The Astrophysical Journal Letters*, **739**, L55.

BROMM, V. (2013). Formation of the first stars. *Reports on Progress in Physics*, **76**, 112901.

BROMM, V. & LARSON, R.B. (2004). The First Stars. *Annual Review of Astronomy and Astrophysics*, **42**, 79–118.

BROMM, V. & LOEB, A. (2003). The formation of the first low-mass stars from gas with low carbon and oxygen abundances. *Nature*, **425**, 812–814.

BROMM, V. & LOEB, A. (2006). High-Redshift Gamma-Ray Bursts from Population III Progenitors. *The Astrophysical Journal*, **642**, 382–388.

BROMM, V. & YOSHIDA, N. (2011). The First Galaxies. *Annual Review of Astronomy and Astrophysics*, **49**, 373–407.

BROMM, V., COPPI, P.S. & LARSON, R.B. (2002). The Formation of the First Stars. I. The Primordial Star-forming Cloud. *The Astrophysical Journal*, **564**, 23–51.

BROMM, V., YOSHIDA, N., HERNQUIST, L. & MCKEE, C.F. (2009). The formation of the first stars and galaxies. *Nature*, **459**, 49–54.

BURBIDGE, E.M., LYNDS, C.R. & BURBIDGE, G.R. (1966). On the Measurement and Interpretation of Absorption Features in the Spectrum of the Quasi-Stellar Object 3c 191. *The Astrophysical Journal*, **144**, 447.

Burrows, D.N., Hill, J.E., Nousek, J.A., Kennea, J.A., Wells, A.A., Osborne, J.P., Abbey, A.F., Beardmore, A.P., Mukerjee, K., Short, A.D.T., Chincarini, G., Campana, S., Citterio, O., Moretti, A., Pagani, C., Tagliaferri, G., Giommi, P., Capalbi, M., Tamburelli, F., Angelini, L., Cusumano, G., Bräuninger, H.W., Burkert, W. & Hartner, G.D. (2005). The Swift X-Ray Telescope. *Space Science Reviews*, **120**, 165–195.

Butler, N.R., Watson, A.M., Kutyrev, A., Lee, W.H., Richer, M.G., Klein, C., Fox, O., Prochaska, J.X., Bloom, J.S., Cucchiara, A., Troja, E., Littlejohns, O., Ramirez-Ruiz, E., de Diego, J.A., Georgiev, L., Gonzalez, J., Roman-Zuniga, C., Gehrels, N. & Moseley, H. (2013a). GRB 130606B: RATIR optical and NIR observations. *GRB Coordinates Network*, **1482**, 1.

Butler, N.R., Watson, A.M., Kutyrev, A., Lee, W.H., Richer, M.G., Klein, C., Fox, O., Prochaska, J.X., Bloom, J.S., Cucchiara, A., Troja, E., Littlejohns, O., Ramirez-Ruiz, E., de Diego, J.A., Georgiev, L., Gonzalez, J., Roman-Zuniga, C., Gehrels, N. & Moseley, H. (2013b). GRB 130606A: continued RATIR optical and NIR monitoring. *GRB Coordinates Network*, **1482**, 1.

Campana, S., Salvaterra, R., Ferrara, A. & Pallottini, A. (2015). Missing cosmic metals revealed by X-ray absorption towards distant sources. *Astronomy and Astrophysics*, **575**, A43.

Campisi, M.A., Maio, U., Salvaterra, R. & Ciardi, B. (2011). Population III stars and the long gamma-ray burst rate. *Monthly Notices of the Royal Astronomical Society*, **416**, 2760–2767.

Cano, Z., Bersier, D., Guidorzi, C., Margutti, R., Svensson, K.M., Kobayashi, S., Melandri, A., Wiersema, K., Pozanenko, A., van der Horst, A.J., Pooley, G.G., Fernandez-Soto, A., Castro-Tirado, A.J., de Ugarte Postigo, A., Im, M., Kamble, A.P., Sahu, D., Alonso-Lorite, J., Anupama, G.C., Bibby, J.L., Burgdorf, M.J., Clay, N., Curran, P.A., Fatkhullin, T.A., Fruchter, A.S., Garnavich, P., Gomboc, A., Gorosabel, J., Graham, J.F., Gurugubelli, U., Haislip, J.B., Huang, K., Huxor, A., Ibrahimov, M., Jeon, Y., Jeon, Y.B., Ivarsen, K., Kasen, D., Klunko, E., Kouveliotou, C., Lacluyze, A., Levan, A.J., Loznikov, V., Mazzali, P.A., Moskvitin, A.S., Mottram, C., Mundell, C.G., Nugent, P.E., Nysewander, M., O'Brien, P.T., Park, W.K., Peris, V., Pian, E., Reichart, D., Rhoads, J.E., Rol, E., Rumyantsev, V., Scowcroft, V., Shakhovskoy, D., Small, E., Smith, R.J., Sokolov, V.V., Starling, R.L.C., Steele, I., Strom, R.G., Tanvir, N.R., Tsapras, Y., Urata, Y., Vaduvescu, O., Volnova, A., Volvach, A., Wijers, R.A.M.J., Woosley, S.E. & Young, D.R. (2011). A tale of two GRB-SNe at a common redshift of z=0.54. *Monthly Notices of the Royal Astronomical Society*, **413**, 669–685.

Cardelli, J.A., Clayton, G.C. & Mathis, J.S. (1989). The relationship between infrared, optical, and ultraviolet extinction. *The Astrophysical Journal*, **345**, 245–256.

Casey, C.M., Scoville, N.Z., Sanders, D.B., Lee, N., Cooray, A., Finkelstein, S.L., Capak, P., Conley, A., de Zotti, G., Farrah, D., Fu, H., Le Floc'h, E., Ilbert, O., Ivison, R.J. & Takeuchi, T.T. (2014). Are Dusty Galaxies Blue? Insights on UV Attenuation from Dust-selected Galaxies. *The Astrophysical Journal*, **796**, 95.

Castro-Tirado, A.J. & Gorosabel, J. (1999). Optical observations of GRB afterglows: GRB 970508 and GRB 980326 revisited. *Astronomy and Astrophysics Supplement*, **138**, 449–450.

Castro-Tirado, A.J., Gorosabel, J., Heidt, J., Seitz, T., Thommes, E., Wolf, C., Lund, N., Pedersen, H., Costa, E., Frontera, F., Heise, J., in 't Zand, J., Bartolini, C., Guarnieri, A., Masetti, A., Piccioni, A. & Palazzi, E. (1997). GRB 970111 and GRB 970228. *Circulars of the International Astronomical Union*, **6598**, 2.

Castro-Tirado, A.J., Zapatero-Osorio, M.R., Caon, N., Cairos, L.M., Hjorth, J., Pedersen, H., Andersen, M.I., Gorosabel, J., Bartolini, C., Guarnieri, A., Piccioni, A., Frontera, F., Masetti, N., Palazzi, E., Pian, E., Greiner, J., Hudec, R., Sagar, R., Pandey, A.K., Mohan, V., Yadav, R.K.S., Nilakshi, N., Björnsson, G., Jakobsson, P., Burud, I., Courbin, F., Valentini, G., Piersimoni, A., Aceituno, J., Montoya, L.M., Pedraz, S., Gredel, R., Claver, C.F., Rector, T.A., Rhoads, J.E., Walter, F., Ott, J., Hippelein, H., Sanchez-Bejar, V., Gutierrez, C., Oscoz, A., Zhu, J., Chen, J., Zhang, H., Wei, J., Zhou, A., Guziy, S., Shlyapnikov, A., Heise, J., Costa, E., Feroci, M. & Piro, L. (1999). Decay of the GRB 990123 Optical Afterglow: Implications for the Fireball Model. *Science*, **283**, 2069–.

Castro-Tirado, A.J., Sokolov, V.V., Gorosabel, J., Castro Cerón, J.M., Greiner, J., Wijers, R.A.M.J., Jensen, B.L., Hjorth, J., Toft, S., Pedersen, H., Palazzi, E., Pian, E., Masetti, N., Sagar, R., Mohan, V., Pandey, A.K., Pandey, S.B., Dodonov, S.N., Fatkhullin, T.A., Afanasiev, V.L., Komarova, V.N., Moiseev, A.V., Hudec, R., Simon, V., Vreeswijk, P.M., Rol, E., Klose, S., Stecklum, B., Zapatero-Osorio, M.R., Caon, N., Blake, C., Wall, J., Heinlein, D., Henden, A.A., Benetti, S., Magazzù, A., Ghinassi, F., Tommasi, L., Bremer, M., Kouveliotou, C., Guziy, S., Shlyapnikov, A., Hopp, U., Feulner, G., Dreizler, S., Hartmann, D.H., Boehnhardt, H., Paredes, J.M., Martí, J., Xanthopoulos, E., Kristen, H.E., Smoker, J. & Hurley, K. (2001). The extraordinarily bright optical afterglow of GRB 991208 and its host galaxy. *Astronomy and Astrophysics*, **370**, 398–406.

Castro-Tirado, A.J., Møller, P., García-Segura, G., Gorosabel, J., Pérez, E., Solano, E., Barrado, D., Kouveliotou, C., Pedersen, H., Pian, E., Rol, E., Palazzi, E., Masetti, N., Andersen, M.I., Fruchter, A.S., Wijers, R.A.M.J. & van den Heuvel, E.P.J. (2010). GRB 021004: Tomography of a gamma-ray burst progenitor and its host galaxy. *Astronomy and Astrophysics*, **517**, A61.

Castro-Tirado, A.J., Sánchez-Ramírez, R., Ellison, S.L., Jelínek, M., Martín-Carrillo, A., Bromm, V., Gorosabel, J., Bremer, M., Winters, J.M., Hanlon, L., Meegan, S., Topinka, M., Pandey, S.B., Guziy, S., Jeong, S., Sonbas, E., Pozanenko, A.S., Cunniffe, R., Fernández-Muñoz, R., Ferrero, P., Gehrels, N., Hudec, R., Kubánek, P., Lara-Gil, O., Muñoz-Martínez, V.F., Pérez-Ramírez, D., Štrobl, J., Álvarez-Iglesias, C., Inasaridze, R., Rumyantsev, V., Volnova, A., Hellmich, S., Mottola, S., Castro Cerón, J.M., Cepa, J., Göğüş, E., Güver, T., Önal Taş, Ö., Park, I.H., Sabau-Graziati, L. & Tejero, A. (2013a). GRB 130606A within a sub-DLA at redshift 5.91. *arXiv.org*, 5631.

Castro-Tirado, A.J., Sánchez-Ramírez, R., Gorosabel, J., Jelínek, M., Tello, J.C., Ferrero, P., Lara-Gil, O., Cunniffe, R., Pérez-Ramírez, D., Kubánek, P., Castro Cerón, J.M., Mottola, S., Hellmich, S., Fernández-Muñoz, R., Muñoz-Martínez, V.F., Sabau-Graziati, L., Martín-Carrillo, A., Cepa, J., Tejero, A. & Álvarez-Iglesias, C. (2013b). GRB 130606A: 10.4m GTC refined redshift z = 5.91. *GRB Coordinates Network*, **1479**, 1. 149

Castro-Tirado, A.J., Sánchez-Ramírez, R., Jelínek, M., Gorosabel, J., Tello, J.C., Ferrero, P., Lara-Gil, O., Cunniffe, R., Pérez-Ramírez, D., Kubánek, P., Castro Cerón, J.M., Fernandez-Soto, A., Mottola, S., Hellmich, S., Fernández-Muñoz, R., Muñoz-Martínez, V.F., Cepa, J. & Álvarez-Iglesias, C. (2013c). GRB 130606A: 10.4m GTC spectroscopy indicates z = 6.1. *GRB Coordinates Network*, **1479**, 1. 149

Catinella, B. & Cortese, L. (2015). HIGHz: a survey of the most H I-massive galaxies at z ˜ 0.2. *Monthly Notices of the Royal Astronomical Society*, **446**, 3526–3544.

Cavallo, G. & Rees, M.J. (1978). A qualitative study of cosmic fireballs and gamma-ray bursts. *Monthly Notices of the Royal Astronomical Society*, **183**, 359–365.

Cen, R., Miralda-Escudé, J., Ostriker, J.P. & Rauch, M. (1994). Gravitational collapse of small-scale structure as the origin of the Lyman-alpha forest. *The Astrophysical Journal*, **437**, L9–L12.

Cepa, J., Aguiar, M., Escalera, V.G., Gonzalez-Serrano, I., Joven-Alvarez, E., Peraza, L., Rasilla, J.L., Rodriguez-Ramos, L.F., Gonzalez, J.J., Cobos Duenas, F.J., Sanchez, B., Tejada, C., Bland-Hawthorn, J., Militello, C. & Rosa, F. (2000). OSIRIS tunable imager and spectrograph. *Proc. SPIE Vol. 4008*, **4008**, 623–631.

Chandra, P. & Frail, D.A. (2012). A Radio-selected Sample of Gamma-Ray Burst Afterglows. *The Astrophysical Journal*, **746**, 156.

Chen, H.W. (2012). Near-infrared spectroscopy of gamma-ray burst host galaxies at z interpretations of afterglow absorption spectra. *Monthly Notices of the Royal Astronomical Society*, **419**, 3039–3047.

Chen, H.W., Prochaska, J.X. & Gnedin, N.Y. (2007). A New Constraint on the Escape Fraction in Distant Galaxies Using γ-Ray Burst Afterglow Spectroscopy. *The Astrophysical Journal*, **667**, L125–L128.

Chevalier, R.A. & Li, Z.Y. (1999). Gamma-Ray Burst Environments and Progenitors. *The Astrophysical Journal*, **520**, L29–L32.

Chevalier, R.A. & Li, Z.Y. (2000). Wind Interaction Models for Gamma-Ray Burst Afterglows: The Case for Two Types of Progenitors. *The Astrophysical Journal*, **536**, 195–212.

Chornock, R., Berger, E., Fox, D.B., Lunnan, R., Drout, M.R., Fong, W.f., Laskar, T. & Roth, K.C. (2013). GRB 130606A as a Probe of the Intergalactic Medium and the Interstellar Medium in a Star-forming Galaxy in the First Gyr after the Big Bang. *The Astrophysical Journal*, **774**, 26.

Chornock, R., Berger, E., Fox, D.B., Fong, W., Laskar, T. & Roth, K.C. (2014). GRB 140515A at z=6.33: Constraints on the End of Reionization From a Gamma-ray Burst in a Low Hydrogen Column Density Environment. *arXiv.org*, 7400.

Christensen, L., Fynbo, J.P.U., Prochaska, J.X., Thöne, C.C., de Ugarte Postigo, A. & Jakobsson, P. (2011). A High Signal-to-noise Ratio Composite Spectrum of Gamma-ray Burst Afterglows. *The Astrophysical Journal*, **727**, 73.

Ciardi, B. & Loeb, A. (2000). Expected Number and Flux Distribution of Gamma-Ray Burst Afterglows with High Redshifts. *The Astrophysical Journal*, **540**, 687–696.

Cline, T.L., Desai, U.D., Teegarden, B.J., Evans, W.D., Klebesadel, R.W., Laros, J.G., Barat, C., Hurley, K., Niel, M. & Weisskopf, M.C. (1982). Precise source location of the anomalous 1979 March 5 gamma-ray transient. *The Astrophysical Journal*, **255**, L45–L48.

Coe, D., Zitrin, A., Carrasco, M., Shu, X., Zheng, W., Postman, M., Bradley, L., Koekemoer, A., Bouwens, R., Broadhurst, T., Monna, A., Host, O., Moustakas, L.A., Ford, H., Moustakas, J., van der Wel, A., Donahue, M., Rodney, S.A., Benitez, N., Jouvel, S., Seitz, S., Kelson, D.D. & Rosati, P. (2013). CLASH: Three Strongly Lensed Images of a Candidate z $\approx$ 11 Galaxy. *The Astrophysical Journal*, **762**, 32.

Cooke, R.J., Pettini, M., Steidel, C.C., Rudie, G.C. & Jorgenson, R.A. (2011a). A carbon-enhanced metal-poor damped Lyα system: probing gas from Population III nucleosynthesis? *Monthly Notices of the Royal Astronomical Society*, **412**, 1047–1058.

Cooke, R.J., Pettini, M., Steidel, C.C., Rudie, G.C. & Nissen, P.E. (2011b). The most metal-poor damped Lyα systems: insights into chemical evolution in the very metal-poor regime. *Monthly Notices of the Royal Astronomical Society*, **417**, 1534–1558.

Covino, S., Rossi, E., Lazzati, D., Malesani, D. & Ghisellini, G. (2005). Gamma-Ray Bursts and Afterglow Polarisation. *INTERACTING BINARIES: Accretion*, **797**, 144–149.

Covino, S., Melandri, A., Salvaterra, R., Campana, S., Vergani, S.D., Bernardini, M.G., D'Avanzo, P., D'Elia, V., Fugazza, D., Ghirlanda, G., Ghisellini, G., Gomboc, A., Jin, Z.P., Krühler, T., Malesani, D., Nava, L., Sbarufatti, B. & Tagliaferri, G. (2013). Dust extinctions for an unbiased sample of gamma-ray burst afterglows. *Monthly Notices of the Royal Astronomical Society*, **432**, 1231–1244.

Crighton, N.H.M., Murphy, M.T., Prochaska, J.X., Worseck, G., Rafelski, M., Becker, G.D., Ellison, S.L., Fumagalli, M., Lopez, S., Meiksin, A. & O'Meara, J.M. (2015). The neutral hydrogen cosmological mass density at z = 5. *Monthly Notices of the Royal Astronomical Society*, **452**, 217–234.

Cucchiara, A., Fumagalli, M., Rafelski, M., Kocevski, D., Prochaska, J.X., Cooke, R.J. & Becker, G.D. (2015). Unveiling the Secrets of Metallicity and Massive Star Formation Using DLAs along Gamma-Ray Bursts. *The Astrophysical Journal*, **804**, 51.

Curran, P.A., Starling, R.L.C., van der Horst, A.J. & Wijers, R.A.M.J. (2009). Testing the blast wave model with Swift GRBs. *Monthly Notices of the Royal Astronomical Society*, **395**, 580–592.

Curran, P.A., Evans, P.A., De Pasquale, M., Page, M.J. & van der Horst, A.J. (2010). On the Electron Energy Distribution Index of Swift Gamma-ray Burst Afterglows. *The Astrophysical Journal Letters*, **716**, L135–L139.

Daigne, F. & Mochkovitch, R. (1998). Gamma-ray bursts from internal shocks in a relativistic wind: temporal and spectral properties. *Monthly Notices of the Royal Astronomical Society*, **296**, 275–286.

Davé, R., Katz, N., Oppenheimer, B.D., Kollmeier, J.A. & Weinberg, D.H. (2013). The neutral hydrogen content of galaxies in cosmological hydrodynamic simulations. *Monthly Notices of the Royal Astronomical Society*, **434**, 2645–2663.

De Cia, A., Ledoux, C., Fox, A.J., Smette, A., Petitjean, P. & Björnsson, G. (2012). Rapid-response mode VLT/UVES spectroscopy of super iron-rich gas exposed to GRB 080310. Evidence of ionization in action and episodic star formation in the host. *Astronomy and Astrophysics*, **545**, A64.

De Cia, A., Ledoux, C., Savaglio, S., Schady, P. & Vreeswijk, P.M. (2013). Dust-to-metal ratios in damped Lyman-α absorbers. Fresh clues to the origins of dust and optical extinction towards γ-ray bursts. *Astronomy and Astrophysics*, **560**, A88.

De Rosa, G., Decarli, R., Walter, F., Fan, X., Jiang, L., Kurk, J., Pasquali, A. & Rix, H.W. (2011). Evidence for Non-evolving Fe II/Mg II Ratios in Rapidly Accreting z ˜ 6 QSOs. *The Astrophysical Journal*, **739**, 56.

de Souza, R.S., Ciardi, B., Maio, U. & Ferrara, A. (2013a). Dark matter halo environment for primordial star formation. *Monthly Notices of the Royal Astronomical Society*, **428**, 2109–2117.

de Souza, R.S., Ishida, E.E.O., Johnson, J.L., Whalen, D.J. & Mesinger, A. (2013b). Detectability of the first cosmic explosions. *Monthly Notices of the Royal Astronomical Society*, **436**, 1555–1563.

de Ugarte Postigo, A., Castro-Tirado, A.J., Guziy, S., Gorosabel, J., Jóhannesson, G., Aloy, M.A., McBreen, S., Lamb, D.Q., Benitez, N., Jelínek, M., Pandey, S.B., Coe, D., Pérez-Ramírez, M.D., Aceituno, F.J., Alises, M., Acosta-Pulido, J.A., Gómez, G., López, R., Donaghy, T.Q., Nakagawa, Y.E., Sakamoto, T., Ricker, G.R., Hearty, F.R., Bayliss, M., Gyuk, G. & York, D.G. (2006). GRB 060121: Implications of a Short-/Intermediate-Duration γ-Ray Burst at High Redshift. *The Astrophysical Journal*, **648**, L83–L87.

de Ugarte Postigo, A., Fatkhullin, T.A., Jóhannesson, G., Gorosabel, J., Sokolov, V.V., Castro-Tirado, A.J., Balega, Y.Y., Spiridonova, O.I., Jelínek, M., Guziy, S., Pérez-Ramírez, D., Hjorth, J., Laursen, P., Bersier, D., Pandey, S.B., Bremer, M., Monfardini, A., Huang, K.Y., Urata, Y., Ip, W.H., Tamagawa, T., Kinoshita, D., Mizuno, T., Arai, Y., Yamagishi, H., Soyano, T., Usui, F., Tashiro, M., Abe, K., Onda, K., Aslan, Z., Khamitov, I., Ozisik, T., Kiziloğlu, Ü., Bikmaev, I., Sakhibullin, N., Burenin, R.A., Pavlinsky, M., Sunyaev, R., Bhattacharya, D., Kamble, A.P., Ishwara Chandra, C.H. & Trushkin, S.A. (2007). Extensive multiband study of the X-ray rich GRB 050408. A likely off-axis event with an intense energy injection. *Astronomy and Astrophysics*, **462**, L57–L60.

de Ugarte Postigo, A., Lundgren, A., Mac-Auliffe, F., Montenegro, F.M., Garcia-Appadoo, D., de Gregorio Monsalvo, I., Martín, S., de Breuk, C., Bergman, P., Hajigholi, M., Thöne, C.C., Gorosabel, J., Castro-Tirado, A.J., Fynbo, J.P.U. & Covino, S. (2011). GRB 110715A: APEX detection of the submm counterpart. *GRB Coordinates Network*, **1216**, 1.

de Ugarte Postigo, A., Fynbo, J.P.U., Thöne, C.C., Christensen, L., Gorosabel, J., Milvang-Jensen, B., Schulze, S., Jakobsson, P., Wiersema, K., Sánchez-Ramírez, R., Leloudas, G., Zafar, T., Malesani, D. & Hjorth, J. (2012a). The distribution of equivalent widths in long GRB afterglow spectra. *Astronomy and Astrophysics*, **548**, A11. xxvi, 107, 108, 139, 141, 145, 146, 182, 240, 242

de Ugarte Postigo, A., Lundgren, A., Martín, S., Garcia-Appadoo, D., de Gregorio Monsalvo, I., Peck, A., Michałowski, M.J., Thöne, C.C., Campana, S., Gorosabel, J., Tanvir, N.R., Wiersema, K., Castro-Tirado, A.J., Schulze, S., De Breuck, C., Petitpas, G., Hjorth, J., Jakobsson, P., Covino, S., Fynbo, J.P.U., Winters, J.M., Bremer, M., Levan, A.J., Llorente, A., Sánchez-Ramírez, R., Tello, J.C. & Salvaterra, R. (2012b). Pre-ALMA observations of GRBs in the mm/submm range. *Astronomy and Astrophysics*, **538**, A44. xxv, 101, 105, 107

de Ugarte Postigo, A., Gorosabel, J., Thöne, C.C., Cabrera-Lavers, A., Reverte, D. & Álvarez-Iglesias, C. (2014). GRB 140515A: Spectroscopy from the 10.4m GTC. *GRB Coordinates Network*, **1627**.

Delhaize, J., Meyer, M., Staveley-Smith, L. & Boyle, B.J. (2013). Detection of H I in distant galaxies using spectral stacking. *Monthly Notices of the Royal Astronomical Society*, **433**, 1398–1410.

D'Elia, V., Fynbo, J.P.U., Goldoni, P., Covino, S., de Ugarte Postigo, A., Ledoux, C., Calura, F., Gorosabel, J., Malesani, D., Matteucci, F., Sánchez-Ramírez, R., Savaglio, S., Castro-Tirado, A.J., Hartoog, O.E., Kaper, L., Muñoz-Darias, T., Pian, E., Piranomonte, S., Tagliaferri, G., Tanvir, N., Vergani, S.D., Watson, D.J. & Xu, D. (2014). VLT/X-shooter spectroscopy of the GRB 120327A afterglow. *Astronomy and Astrophysics*, **564**, A38. 35

D'Odorico, V., Cristiani, S., Romano, D., Granato, G.L. & Danese, L. (2004). Chemical abundances in QSO host galaxies and environments from narrow absorption line systems. *Monthly Notices of the Royal Astronomical Society*, **351**, 976–988.

Draine, B.T. & Hao, L. (2002). Gamma-Ray Burst in a Molecular Cloud: Destruction of Dust and H2 and the Emergent Spectrum. *The Astrophysical Journal*, **569**, 780–791.

Duncan, R.C. & Thompson, C. (1992). Formation of very strongly magnetized neutron stars - Implications for gamma-ray bursts. *The Astrophysical Journal*, **392**, L9–L13.

Dunkley, J., Spergel, D.N., Komatsu, E., Hinshaw, G., Larson, D., Nolta, M.R., Odegard, N., Page, L., Bennett, C.L., Gold, B., Hill, R.S., Jarosik, N., Weiland, J.L., Halpern, M., Kogut, A., Limon, M., Meyer, S.S., Tucker, G.S., Wollack, E. & Wright, E.L. (2009). Five-Year Wilkinson Microwave Anisotropy Probe (WMAP) Observations: Bayesian Estimation of Cosmic Microwave Background Polarization Maps. *The Astrophysical Journal*, **701**, 1804–1813.

Efron, B. (1987). Better Bootstrap Confidence Intervals. *Journal of the American Statistical Association*, **82**, 171–185.

Efron, B. & Petrosian, V. (1992). A simple test of independence for truncated data with applications to redshift surveys. *The Astrophysical Journal*, **399**, 345–352.

Elliott, J., Khochfar, S., Greiner, J. & Dalla Vecchia, C. (2015). The First Billion Years project: gamma-ray bursts at z ¿ 5. *Monthly Notices of the Royal Astronomical Society*, **446**, 4239–4249.

Ellis, R.S., Colless, M., Broadhurst, T., Heyl, J. & Glazebrook, K. (1996). Autofib Redshift Survey - I. Evolution of the galaxy luminosity function. *Monthly Notices of the Royal Astronomical Society*, **280**, 235–251.

Ellison, S.L. & Lopez, S. (2001). Unusual metal abundances in a pair of damped Lyman alpha systems at z ˜ 2. *Astronomy and Astrophysics*, **380**, 117–122.

Ellison, S.L., Yan, L., Hook, I.M., Pettini, M., Wall, J.V. & Shaver, P. (2001). The CORALS survey I: New estimates of the number density and gas content of damped Lyman alpha systems free from dust bias. *Astronomy and Astrophysics*, **379**, 393–406.

Ellison, S.L., Yan, L., Hook, I.M., Pettini, M., Wall, J.V. & Shaver, P. (2002). The CORALS survey. II. Clues to galaxy clustering around QSOs from zabs ˜ zem damped Lyman alpha systems. *Astronomy and Astrophysics*, **383**, 91–97.

Ellison, S.L., Prochaska, J.X., Hennawi, J.F., Lopez, S., Usher, C., Wolfe, A.M., Russell, D.M. & Benn, C.R. (2010). The nature of proximate damped Lyman α systems. *Monthly Notices of the Royal Astronomical Society*, **406**, 1435–1459.

Ellison, S.L., Prochaska, J.X. & Mendel, J.T. (2011). Metallicities and dust content of proximate damped Lyman α systems in the Sloan Digital Sky Survey. *Monthly Notices of the Royal Astronomical Society*, **412**, 448–468.

Evans, P.A., Willingale, R., Osborne, J.P., O'Brien, P.T., Page, K.L., Markwardt, C.B., Barthelmy, S.D., Beardmore, A.P., Burrows, D.N., Pagani, C., Starling, R.L.C., Gehrels, N. & Romano, P. (2010). The Swift Burst Analyser. I. BAT and XRT spectral and flux evolution of gamma ray bursts. *Astronomy and Astrophysics*, **519**, A102.

Evans, P.A., Goad, M.R., Osborne, J.P. & Beardmore, A.P. (2011). GRB 110715A: enhanced Swift-XRT position. *GRB Coordinates Network*, **1216**.

Fabbian, D., Nissen, P.E., Asplund, M., Pettini, M. & Akerman, C. (2009). The C/O ratio at low metallicity: constraints on early chemical evolution from observations of Galactic halo stars. *Astronomy and Astrophysics*, **500**, 1143–1155.

Fan, X. (2012). Observations of the first light and the epoch of reionization. *Research in Astronomy and Astrophysics*, **12**, 865–890.

Fan, X., Hennawi, J.F., Richards, G.T., Strauss, M.A., Schneider, D.P., Donley, J.L., Young, J.E., Annis, J., Lin, H., Lampeitl, H., Lupton, R.H., Gunn, J.E., Knapp, G.R., Brandt, W.N., Anderson, S.F., Bahcall, N.A., Brinkmann, J., Brunner, R.J., Fukugita, M., Szalay, A.S., Szokoly, G.P. & York, D.G. (2004). A Survey of z¿5.7 Quasars in the Sloan Digital Sky Survey. III. Discovery of Five Additional Quasars. *The Astronomical Journal*, **128**, 515–522.

Fan, X., Strauss, M.A., Becker, R.H., White, R.L., Gunn, J.E., Knapp, G.R., Richards, G.T., Schneider, D.P., Brinkmann, J. & Fukugita, M. (2006). Constraining the Evolution of the Ionizing Background and the Epoch of Reionization with z˜6 Quasars. II. A Sample of 19 Quasars. *The Astronomical Journal*, **132**, 117–136.

Fenimore, E.E., Conner, J.P., Epstein, R.I., Klebesadel, R.W., Laros, J.G., Yoshida, A., Fujii, M., Hayashida, K., Itoh, M., Murakami, T., Nishimura, J., Yamagami, Y., Kondo, I. & Kawai, N. (1988). Interpretations of multiple absorption features in a gamma-ray burst spectrum. *Astrophysical Journal*, **335**, L71–L74.

Fernández, X., van Gorkom, J.H., Hess, K.M., Pisano, D.J., Kreckel, K., Momjian, E., Popping, A., Oosterloo, T., Chomiuk, L., Verheijen, M.A.W., Henning, P.A., Schiminovich, D., Bershady, M.A., Wilcots, E.M. & Scoville, N. (2013). A Pilot for a Very Large Array H I Deep Field. *The Astrophysical Journal Letters*, **770**, L29.

Feroz, F., Hobson, M.P. & Bridges, M. (2009). MULTINEST: an efficient and robust Bayesian inference tool for cosmology and particle physics. *Monthly Notices of the Royal Astronomical Society*, **398**, 1601–1614.

Filgas, R., Krühler, T., Greiner, J., Rau, A., Palazzi, E., Klose, S., Schady, P., Rossi, A., Afonso, P.M.J., Antonelli, L.A., Clemens, C., Covino, S., D'Avanzo, P., Küpcü Yoldaş, A., Nardini, M., Nicuesa Guelbenzu, A., Olivares, F., Updike, E.A.C. & Yoldaş, A. (2011). The two-component jet of GRB 080413B. *Astronomy and Astrophysics*, **526**, A113.

Fishman, G.J. (1981). The NASA/Marshall Space Flight Center program in gamma-ray burst astronomy. *Symposium on Cosmic Gamma-Ray Bursts*, **75**, 125–133.

Fishman, G.J. & Meegan, C.A. (1995). Gamma-Ray Bursts. *Annual Review of Astronomy and Astrophysics*, **33**, 415–458.

Fitzpatrick, E.L. & Massa, D. (2007). An Analysis of the Shapes of Interstellar Extinction Curves. V. The IR-through-UV Curve Morphology. *The Astrophysical Journal*, **663**, 320–341.

Fox, A.J., Ledoux, C., Vreeswijk, P.M., Smette, A. & Jaunsen, A.O. (2008). High-ion absorption in seven GRB host galaxies at z = 2-4. Evidence for both circumburst plasma and outflowing interstellar gas. *Astronomy and Astrophysics*, **491**, 189–207.

Frail, D.A., Kulkarni, S.R., Nicastro, L., Feroci, M. & Taylor, G.B. (1997). The radio afterglow from the γ-ray burst of 8 May 1997. *Nature*, **389**, 261–263.

Frail, D.A., Berger, E., Galama, T.J., Kulkarni, S.R., Moriarty-Schieven, G.H., Pooley, G.G., Sari, R., Shepherd, D.S., Taylor, G.B. & Walter, F. (2000). The Enigmatic Radio Afterglow of GRB 991216. *The Astrophysical Journal*, **538**, L129–L132.

Friis, M., De Cia, A., Krühler, T., Fynbo, J.P.U., Ledoux, C., Vreeswijk, P.M., Watson, D.J., Malesani, D., Gorosabel, J., Starling, R.L.C., Jakobsson, P., Varela, K., Wiersema, K., Drachmann, A.P., Trotter, A., Thöne, C.C., de Ugarte Postigo, A., D'Elia, V., Elliott, J., Maturi, M., Goldoni, P., Greiner, J., Haislip, J.B., Kaper, L., Knust, F., LaCluyze, A., Milvang-Jensen, B., Reichart, D., Schulze, S., Sudilovsky, V., Tanvir, N. & Vergani, S.D. (2015). The warm, the excited, and the molecular gas: GRB 121024A shining through its star-forming galaxy. *Monthly Notices of the Royal Astronomical Society*, **451**, 167–183.

Frontera, F., Amati, L., Lazzati, D., Montanari, E., Orlandini, M., Perna, R., Costa, E., Feroci, M., Guidorzi, C., Kuulkers, E., Masetti, N., Nicastro, L., Palazzi, E., Pian, E. & Piro, L. (2004). A Decreasing Column Density during the Prompt Emission from GRB 000528 Observed with BeppoSAX. *The Astrophysical Journal*, **614**, 301–308.

Fynbo, J.P.U., Holland, S., Andersen, M.I., Thomsen, B., Hjorth, J., Björnsson, G., Jaunsen, A.O., Natarajan, P. & Tanvir, N. (2000). Hubble

Space Telescope Space Telescope Imaging Spectrograph Imaging of the Host Galaxy of GRB 980425/SN 1998BW. *The Astrophysical Journal*, **542**, L89–L93.

Fynbo, J.P.U., Jakobsson, P., Møller, P., Hjorth, J., Thomsen, B., Andersen, M.I., Fruchter, A.S., Gorosabel, J., Holland, S.T., Ledoux, C., Pedersen, H., Rhoads, J., Weidinger, M. & Wijers, R.A.M.J. (2003). On the Lyalpha emission from gamma-ray burst host galaxies: Evidence for low metallicities. *Astronomy and Astrophysics*, **406**, L63–L66.

Fynbo, J.P.U., Starling, R.L.C., Ledoux, C., Wiersema, K., Thöne, C.C., Sollerman, J., Jakobsson, P., Hjorth, J., Watson, D.J., Vreeswijk, P.M., Møller, P., Rol, E., Gorosabel, J., Näränen, J., Wijers, R.A.M.J., Björnsson, G., Castro Cerón, J.M., Curran, P., Hartmann, D.H., Holland, S.T., Jensen, B.L., Levan, A.J., Limousin, M., Kouveliotou, C., Nelemans, G., Pedersen, K., Priddey, R.S. & Tanvir, N.R. (2006). Probing cosmic chemical evolution with gamma-ray bursts: GRB 060206 at z = 4.048. *Astronomy and Astrophysics*, **451**, L47–L50.

Fynbo, J.P.U., Prochaska, J.X., Sommer-Larsen, J., Dessauges-Zavadsky, M. & Møller, P. (2008). Reconciling the Metallicity Distributions of Gamma-Ray Burst, Damped Lyα, and Lyman Break Galaxies at z ˜ 3. *The Astrophysical Journal*, **683**, 321–328.

Fynbo, J.P.U., Jakobsson, P., Prochaska, J.X., Malesani, D., Ledoux, C., de Ugarte Postigo, A., Nardini, M., Vreeswijk, P.M., Wiersema, K., Hjorth, J., Sollerman, J., Chen, H.W., Thöne, C.C., Björnsson, G., Bloom, J.S., Castro-Tirado, A.J., Christensen, L., De Cia, A., Fruchter, A.S., Gorosabel, J., Graham, J.F., Jaunsen, A.O., Jensen, B.L., Kann, D.A., Kouveliotou, C., Levan, A.J., Maund, J., Masetti, N., Milvang-Jensen, B., Palazzi, E., Perley, D.A., Pian, E., Rol, E., Schady, P., Starling, R.L.C., Tanvir, N.R., Watson, D.J., Xu, D., Augusteijn, T., Grundahl, F., Telting, J. & Quirion, P.O. (2009). Low-resolution Spectroscopy of Gamma-ray Burst Optical Afterglows: Biases in the Swift Sample and Characterization of the Absorbers. *The Astrophysical Journal Supplement Series*, **185**, 526–573.

Fynbo, J.P.U., Krühler, T., Leighly, K., Ledoux, C., Vreeswijk, P.M., Schulze, S., Noterdaeme, P., Watson, D.J., Wijers, R.A.M.J., Bolmer, J., Cano, Z., Christensen, L., Covino, S., D'Elia, V., Flores, H., Friis, M., Goldoni, P., Greiner, J., Hammer, F., Hjorth, J., Jakobsson, P., Japelj, J., Kaper, L., Klose, S., Knust, F., Leloudas, G., Levan, A., Malesani, D., Milvang-Jensen, B., Møller, P., Nicuesa Guelbenzu, A., Oates, S.R., Pian, E., Schady, P., Sparre, M., Tagliaferri, G., Tanvir, N., Thöne, C.C., de Ugarte Postigo, A., Vergani, S., Wiersema, K., Xu, D. & Zafar, T. (2014). The mysterious optical afterglow spectrum of GRB 140506A at z = 0.889. *Astronomy and Astrophysics*, **572**, A12.

Galama, T.J., Vreeswijk, P.M., van Paradijs, J., Kouveliotou, C., Augusteijn, T., Böhnhardt, H., Brewer, J.P., Doublier, V., Gonzalez, J.F., Leibundgut, B., Lidman, C., Hainaut, O.R., Patat, F., Heise, J., in't Zand, J., Hurley, K., Groot, P.J., Strom, R.G., Mazzali, P.A., Iwamoto, K., Nomoto, K., Umeda, H., Nakamura, T., Young, T.R., Suzuki, T., Shigeyama, T., Koshut, T.M., Kippen, M., Robinson, C., de Wildt, P., Wijers, R.A.M.J., Tanvir, N., Greiner, J., Pian, E., Palazzi, E., Frontera, F., Masetti, N., Nicastro, L., Feroci, M., Costa, E., Piro, L., Peterson, B.A., Tinney, C., Boyle, B.J., Cannon, R., Stathakis, R., Sadler, E., Begam, M.C. & Ianna, P. (1998). An unusual supernova in the error box of the γ-ray burst of 25 April 1998. *Nature*, **395**, 670–672.

Gallerani, S., Salvaterra, R., Ferrara, A. & Choudhury, T.R. (2008). Testing reionization with gamma-ray burst absorption spectra. *Monthly Notices of the Royal Astronomical Society: Letters*, **388**, L84–L88.

Gehrels, N., Chincarini, G., Giommi, P., Mason, K.O., Nousek, J.A., Wells, A.A., White, N.E., Barthelmy, S.D., Burrows, D.N., Cominsky, L.R., Hurley, K.C., Marshall, F.E., Mészáros, P., Roming, P.W.A., Angelini, L., Barbier, L.M., Belloni, T.M., Campana, S., Caraveo, P.A., Chester, M.M., Citterio, O., Cline, T.L., Cropper, M.S., Cummings, J.R., Dean, A.J., Feigelson, E.D., Fenimore, E.E., Frail, D.A., Fruchter, A.S., Garmire, G.P., Gendreau, K., Ghisellini, G., Greiner, J., Hill, J.E., Hunsberger, S.D., Krimm, H.A., Kulkarni, S.R., Kumar, P., Lebrun, F., Lloyd-Ronning, N.M., Markwardt, C.B., Mattson, B.J., Mushotzky, R.F., Norris, J.P., Osborne, J., Paczynski, B., Palmer, D.M., Park, H.S., Parsons, A.M., Paul, J., Rees, M.J., Reynolds, C.S., Rhoads, J.E., Sasseen, T.P., Schaefer, B.E., Short, A.T., Smale, A.P., Smith, I.A., Stella, L., Tagliaferri, G., Takahashi, T., Tashiro, M., Townsley, L.K., Tueller, J., Turner, M.J.L., Vietri, M., Voges, W., Ward, M.J., Willingale, R., Zerbi, F.M. & Zhang, W.W. (2004). The Swift Gamma-Ray Burst Mission. *The Astrophysical Journal*, **611**, 1005–1020.

Gehrels, N., Sarazin, C.L., O'Brien, P.T., Zhang, B., Barbier, L.M., Barthelmy, S.D., Blustin, A., Burrows, D.N., Cannizzo, J., Cummings, J.R., Goad, M., Holland, S.T., Hurkett, C.P., Kennea, J.A., Levan, A., Markwardt, C.B., Mason, K.O., Mészáros, P., Page, M., Palmer, D.M., Rol, E., Sakamoto, T., Willingale, R., Angelini, L., Beardmore, A.P., Boyd, P.T., Breeveld, A.A., Campana, S., Chester, M.M., Chincarini, G., Cominsky, L.R., Cusumano, G., De Pasquale, M., Fenimore, E.E., Giommi, P., Gronwall, C., Grupe, D., Hill, J.E., Hinshaw, D., Hjorth, J., Hullinger, D., Hurley, K.C., Klose, S., Kobayashi, S., Kouveliotou, C., Krimm, H.A., Mangano, V., Marshall, F.E., McGowan, K., Moretti, A., Mushotzky, R.F., Nakazawa, K., Norris, J.P., Nousek, J.A., Osborne, J.P., Page, K.L., Parsons, A.M., Patel, S., Perri, M., Poole, T., Romano, P., Roming, P.W.A., Rosen, S., Sato, G., Schady, P., Smale, A.P., Sollerman, J., Starling, R., Still, M., Suzuki, M., Tagliaferri, G., Takahashi, T., Tashiro, M., Tueller, J., Wells, A.A., White, N.E. & Wijers, R.A.M.J. (2005). A short γ-ray burst apparently associated with an elliptical galaxy at redshift z = 0.225. *Nature*, **437**, 851–854.

Gendre, B., Stratta, G., Atteia, J.L., Basa, S., Boër, M., Coward, D.M., Cutini, S., D'Elia, V., Howell, E.J., Klotz, A. & Piro, L. (2013). The Ultra-long Gamma-Ray Burst 111209A: The Collapse of a Blue Supergiant? *The Astrophysical Journal*, **766**, 30.

Genet, F. & Granot, J. (2009). Realistic analytic model for the prompt and high-latitude emission in GRBs. *Monthly Notices of the Royal Astronomical Society*, **399**, 1328–1346.

Genet, F., Daigne, F. & Mochkovitch, R. (2007). Can the early X-ray afterglow of gamma-ray bursts be explained by a contribution from the reverse shock? *Monthly Notices of the Royal Astronomical Society*, **381**, 732–740.

Ghirlanda, G., Celotti, A. & Ghisellini, G. (2002). Time resolved spectral analysis of bright gamma ray bursts. *Astronomy and Astrophysics*, **393**, 409–423.

Ghirlanda, G., Ghisellini, G. & Lazzati, D. (2004a). The Collimation-corrected Gamma-Ray Burst Energies Correlate with the Peak Energy of Their νFν Spectrum. *The Astrophysical Journal*, **616**, 331–338.

Ghirlanda, G., Ghisellini, G., Lazzati, D. & Firmani, C. (2004b). Gamma-Ray Bursts: New Rulers to Measure the Universe. *The Astrophysical Journal*, **613**, L13–L16.

Ghirlanda, G., Nava, L., Ghisellini, G. & Firmani, C. (2007). Confirming the γ-ray burst spectral-energy correlations in the era of multiple time breaks. *Astronomy and Astrophysics*, **466**, 127–136.

Ghirlanda, G., Nava, L., Ghisellini, G., Celotti, A. & Firmani, C. (2009). Short versus long gamma-ray bursts: spectra, energetics, and luminosities. *Astronomy and Astrophysics*, **496**, 585–595.

Ghirlanda, G., Nava, L., Ghisellini, G., Celotti, A., Burlon, D., Covino, S. & Melandri, A. (2012). Gamma-ray bursts in the comoving frame. *Monthly Notices of the Royal Astronomical Society*, **420**, 483–494.

Giovanelli, R., Haynes, M.P., Kent, B.R., Perillat, P., Saintonge, A., Brosch, N., Catinella, B., Hoffman, G.L., Stierwalt, S., Spekkens, K., Lerner, M.S., Masters, K.L., Momjian, E., Rosenberg, J.L., Springob, C.M., Boselli, A., Charmandaris, V., Darling, J.K., Davies, J., Garcia Lambas, D., Gavazzi, G., Giovanardi, C., Hardy, E., Hunt, L.K., Iovino, A., Karachentsev, I.D., Karachentseva, V.E., Koopmann, R.A., Marinoni, C., Minchin, R.F., Muller, E., Putman, M., Pantoja, C., Salzer, J.J., Scodeggio, M., Skillman, E., Solanes, J.M., Valotto, C., van Driel, W. & van Zee, L. (2005). The Arecibo Legacy Fast ALFA Survey. I. Science Goals, Survey Design, and Strategy. *The Astronomical Journal*, **130**, 2598–2612.

Glover, S. (2005). The Formation Of The First Stars In The Universe. *Space Science Reviews*, **117**, 445–508.

Gnedin, N.Y. & Kaurov, A.A. (2014). Cosmic Reionization on Computers. II. Reionization History and Its Back-reaction on Early Galaxies. *The Astrophysical Journal*, **793**, 30.

Goldoni, P., Royer, F., François, P., Horrobin, M., Blanc, G., Vernet, J., Modigliani, A. & Larsen, J. (2006). Data reduction software of the X-shooter spectrograph. *Ground-based and Airborne Instrumentation for Astronomy. Edited by McLean*, **6269**, 62692K–62692K–11.

Golenetskii, S., Aptekar, R., Mazets, E., Pal'Shin, V., Frederiks, D., Oleynik, P., Ulanov, M., Svinkin, D. & Cline, T. (2013). Konus-wind observation of GRB 130606A. *GRB Coordinates Network*, **1480**, 1.

Gorosabel, J., Rol, E., Covino, S., Castro-Tirado, A.J., Castro Cerón, J.M., Lazzati, D., Hjorth, J., Malesani, D., Della Valle, M., di Serego Alighieri, S., Fiore, F., Fruchter, A.S., Fynbo, J.P.U., Ghisellini, G., Goldoni, P., Greiner, J., Israel, G.L., Kaper, L., Kawai, N., Klose, S., Kouveliotou, C., Le Floc'h, E., Masetti, N., Mirabel, F., Møller, P., Ortolani, S., Palazzi, E., Pian, E., Rhoads, J., Ricker, G., Saracco, P., Stella, L., Tagliaferri, G., Tanvir, N., van den Heuvel, E., Vietri, M., Vreeswijk, P.M., Wijers, R.A.M.J. & Zerbi, F.M. (2004). GRB 020813: Polarization in the case of a smooth optical decay. *Astronomy and Astrophysics*, **422**, 113–119.

Green, R.F., Schmidt, M. & Liebert, J. (1986). The Palomar-Green catalog of ultraviolet-excess stellar objects. *The Astrophysical Journal Supplement Series*, **61**, 305–352.

Greenstein, J.L. (1963). Red-Shift of the Unusual Radio Source: 3C 48. *Nature*, **197**, 1041–1042.

Greiner, J., Bornemann, W., Clemens, C., Deuter, M., Hasinger, G., Honsberg, M., Huber, H., Huber, S., Krauss, M., Krühler, T., Küpcü Yoldaş, A., Mayer-Hasselwander, H., Mican, B., Primak, N., Schrey, F., Steiner, I., Szokoly, G., Thöne, C.C., Yoldaş, A., Klose, S., Laux, U. & Winkler, J. (2008). GROND—a 7-Channel Imager. *The Publications of the Astronomical Society of the Pacific*, **120**, 405–424.

Guetta, D., Piran, T. & Waxman, E. (2005). The Luminosity and Angular Distributions of Long-Duration Gamma-Ray Bursts. *The Astrophysical Journal*, **619**, 412–419.

Guidorzi, C., Mundell, C.G., Harrison, R., Margutti, R., Sudilovsky, V., Zauderer, B.A., Kobayashi, S., Cucchiara, A., Melandri, A., Pandey, S.B., Berger, E., Bersier, D., D'Elia, V., Gomboc, A., Greiner, J., Japelj, J., Kopač, D., Kumar, B., Malesani, D., Mottram, C.J., O'Brien, P.T., Rau, A., Smith, R.J., Steele, I.A., Tanvir, N.R. & Virgili, F.J. (2014). New constraints on gamma-ray burst jet geometry and relativistic shock physics. *Monthly Notices of the Royal Astronomical Society*, **438**, 752–767.

Guilloteau, S., Delannoy, J., Downes, D., Greve, A., Guélin, M., Lucas, R., Morris, D., Radford, S.J.E., Wink, J., Cernicharo, J., Forveille, T., García-Burillo, S., Neri, R., Blondel, J., Perrigourad, A., Plathner, D. & Torres, M. (1992). The IRAM interferometer on Plateau de Bure. *Astronomy and Astrophysics (ISSN 0004-6361)*, **262**, 624–633.

Guimarães, R., Petitjean, P., de Carvalho, R.R., Djorgovski, S.G., Noterdaeme, P., Castro, S., Poppe, P. C. Da R. & Aghaee, A. (2009). Damped and sub-damped Lyman-α absorbers in z ¿ 4 QSOs. *Astronomy and Astrophysics*, **508**, 133–140.

Gunn, J.E. & Peterson, B.A. (1965). On the Density of Neutral Hydrogen in Intergalactic Space. *The Astrophysical Journal*, **142**, 1633–1641.

Han, X.H., Hammer, F., Liang, Y.C., Flores, H., Rodrigues, M., Hou, J.L. & Wei, J. (2010). The Wolf-Rayet features and mass-metallicity relation of long-duration gamma-ray burst host galaxies. *Astronomy and Astrophysics*, **514**, A24.

Hancock, P.J., Murphy, T. & Schmidt, B.P. (2011). GRB 110715A: ATCA detection of the radio counterpart. *GRB Coordinates Network*, **1217**.

Hartoog, O.E., Malesani, D., Fynbo, J.P.U., Goto, T., Krühler, T., Vreeswijk, P.M., De Cia, A., Xu, D., Møller, P., Covino, S., D'Elia, V., Flores, H., Goldoni, P., Hjorth, J., Jakobsson, P., Krogager, J.K., Kaper, L., Ledoux, C., Levan, A.J., Milvang-Jensen, B., Sollerman, J., Sparre, M., Tagliaferri, G., Tanvir, N.R., de Ugarte Postigo, A., Vergani, S.D., Wiersema, K., Datson, J., Salinas, R., Mikkelsen, K. & Aghanim, N. (2015). VLT/X-Shooter spectroscopy of the afterglow of the Swift GRB 130606A. Chemical abundances and reionisation at z ˜ 6. *Astronomy and Astrophysics*, **580**, A139.

Hazard, C., Mackey, M.B. & Shimmins, A.J. (1963). Investigation of the Radio Source 3C 273 By The Method of Lunar Occultations. *Nature*, **197**, 1037–1039.

Hewett, P.C. & Wild, V. (2010). Improved redshifts for SDSS quasar spectra. *Monthly Notices of the Royal Astronomical Society*, **405**, 2302–2316.

Hjorth, J. & Bloom, J.S. (2012). The Gamma-Ray Burst - Supernova Connection. *Chapter 9 in "Gamma-Ray Bursts"*, 169–190.

Hjorth, J., Sollerman, J., Møller, P., Fynbo, J.P.U., Woosley, S.E., Kouveliotou, C., Tanvir, N.R., Greiner, J., Andersen, M.I., Castro-Tirado, A.J., Castro Cerón, J.M., Fruchter, A.S., Gorosabel, J., Jakobsson, P., Kaper, L., Klose, S., Masetti, N., Pedersen, H., Pedersen, K., Pian, E., Palazzi, E., Rhoads, J.E., Rol, E., van den Heuvel, E.P.J., Vreeswijk, P.M., Watson, D.J. & Wijers, R.A.M.J. (2003). A very energetic supernova associated with the γ-ray burst of 29 March 2003. *Nature*, **423**, 847–850.

Hjorth, J., Watson, D.J., Fynbo, J.P.U., Price, P.A., Jensen, B.L., Jørgensen, U.G., Kubas, D., Gorosabel, J., Jakobsson, P., Sollerman, J., Pedersen, K. & Kouveliotou, C. (2005). The optical afterglow of the short γ-ray burst GRB 050709. *Nature*, **437**, 859–861.

Hjorth, J., Malesani, D., Jakobsson, P., Jaunsen, A.O., Fynbo, J.P.U., Gorosabel, J., Krühler, T., Levan, A.J., Michałowski, M.J., Milvang-Jensen, B., Møller, P., Schulze, S., Tanvir, N.R. & Watson, D.J. (2012). The Optically Unbiased Gamma-Ray Burst Host (TOUGH) Survey. I. Survey Design and Catalogs. *The Astrophysical Journal*, **756**, 187.

Horne, K. (1986). An optimal extraction algorithm for CCD spectroscopy. *The Publications of the Astronomical Society of the Pacific*, **98**, 609–617.

Horváth, I., Hakkila, J. & Bagoly, Z. (2014). Possible structure in the GRB sky distribution at redshift two. *Astronomy and Astrophysics*, **561**, L12.

Hosokawa, T., Omukai, K., Yoshida, N. & Yorke, H.W. (2011). Protostellar Feedback Halts the Growth of the First Stars in the Universe. *Science*, **334**, 1250–1253.

Hou, S.J., Gao, H., Liu, T., Gu, W.M., Lin, D.B., Li, Y.P., Men, Y.P., Wu, X.F., Lei, W.H. & Lu, J.F. (2014). Variability of the giant X-ray bump in GRB 121027A and its possible origin. *Monthly Notices of the Royal Astronomical Society*, **441**, 2375–2379.

Inoue, S., Salvaterra, R., Choudhury, T.R., Ferrara, A., Ciardi, B. & Schneider, R. (2010). Probing intergalactic radiation fields during cosmic reionization through gamma-ray absorption. *Monthly Notices of the Royal Astronomical Society*, **404**, 1938–1943.

Ishida, E.E.O., de Souza, R.S. & Ferrara, A. (2011). Probing cosmic star formation up to z= 9.4 with gamma-ray bursts. *Monthly Notices of the Royal Astronomical Society*, **418**, 500–504.

Iwamoto, K., Mazzali, P.A., Nomoto, K., Umeda, H., Nakamura, T., Patat, F., Danziger, I.J., Young, T.R., Suzuki, T., Shigeyama, T., Augusteijn, T., Doublier, V., Gonzalez, J.F., Boehnhardt, H., Brewer, J.P., Hainaut, O.R., Lidman, C., Leibundgut, B., Cappellaro, E., Turatto, M., Galama, T.J., Vreeswijk, P.M., Kouveliotou, C., van Paradijs, J., Pian, E., Palazzi, E. & Frontera, F. (1998). A hypernova model for the supernova associated with the γ-ray burst of 25 April 1998. *Nature*, **395**, 672–674.

Iye, M., Ota, K., Kashikawa, N., Furusawa, H., Hashimoto, T., Hattori, T., Matsuda, Y., Morokuma, T., Ouchi, M. & Shimasaku, K. (2006). A galaxy at a redshift z = 6.96. *Nature*, **443**, 186–188.

Jakobsson, P., Fynbo, J.P.U., Ledoux, C., Vreeswijk, P.M., Kann, D.A., Hjorth, J., Priddey, R.S., Tanvir, N.R., Reichart, D., Gorosabel, J., Klose, S., Watson, D.J., Sollerman, J., Fruchter, A.S., de Ugarte Postigo, A., Wiersema, K., Björnsson, G., Chapman, R., Thöne, C.C., Pedersen, K. & Jensen, B.L. (2006). H I column densities of z ¿ 2 Swift gamma-ray bursts. *Astronomy and Astrophysics*, **460**, L13–L17.

Japelj, J., Covino, S., Gomboc, A., Vergani, S.D., Goldoni, P., Selsing, J., Cano, Z., D'Elia, V., Flores, H., Fynbo, J.P.U., Hammer, F., Hjorth, J., Jakobsson, P., Kaper, L., Kopač, D., Krühler, T., Melandri, A., Piranomonte, S., Sánchez-Ramírez, R., Tagliaferri, G., Tanvir, N.R., de Ugarte Postigo, A., Watson, D.J. & Wijers, R.A.M.J. (2015). Spectrophotometric analysis of gamma-ray burst afterglow extinction curves with X-Shooter. *Astronomy and Astrophysics*, **579**, A74. 33

Jelínek, M., Prouza, M., Kubánek, P., Hudec, R., Nekola, M., Řídký, J., Grygar, J., Boháčová, M., Castro-Tirado, A.J., Gorosabel, J., Hrabovský, M., Mandát, D., Nosek, D., Nožka, L., Palatka, M., Pandey, S.B., Pech, M., Schovánek, P., Šmída, R., Trávníček, P., de Ugarte Postigo, A. & Vitek, S. (2006). The bright optical flash from GRB 060117. *Astronomy and Astrophysics*, **454**, L119–L122.

Jelínek, M., Gorosabel, J., Castro-Tirado, A.J., Mottola, S., Hellmich, S., Fernández-Muñoz, R. & Muñoz-Martínez, V.F. (2013). GRB 130606A: optical afterglow with BOOTES-2/TELMA and 1.23m CAHA. *GRB Coordinates Network*, **1478**, 1.

Jenkins, E.B. & Ostriker, J.P. (1991). Lyman-alpha depression of the continuum from high-redshift quasars - A new technique applied in search of the Gunn-Peterson effect. *The Astrophysical Journal*, **376**, 33–42.

Jeong, S., Sánchez-Ramírez, R., Gorosabel, J. & Castro-Tirado, A.J. (2014). GRB 140304A: 10.4m GTC refined redshift z = 5.283. *GRB Coordinates Network*, **1593**, 1. 137

Jiang, L., Fan, X., Brandt, W.N., Carilli, C.L., Egami, E., Hines, D.C., Kurk, J.D., Richards, G.T., Shen, Y., Strauss, M.A., Vestergaard, M. & Walter, F. (2010). Dust-free quasars in the early Universe. *Nature*, **464**, 380–383.

Jóhannesson, G., Björnsson, G. & Gudmundsson, E.H. (2006). Energy Injection in Gamma-Ray Burst Afterglow Models. *The Astrophysical Journal*, **647**, 1238–1249.

Kajisawa, M., Ichikawa, T., Tanaka, I., Yamada, T., Akiyama, M., Suzuki, R., Tokoku, C., Katsuno Uchimoto, Y., Konishi, M., Yoshikawa, T., Nishimura, T., Omata, K., Ouchi, M., Iwata, I., Hamana, T. & Onodera, M. (2011). MOIRCS Deep Survey. IX. Deep Near-Infrared Imaging Data and Source Catalog. *Publications of the Astronomical Society of Japan*, **63**, 379–401.

Kaneko, Y., Ramirez-Ruiz, E., Granot, J., Kouveliotou, C., Woosley, S.E., Patel, S.K., Rol, E., in 't Zand, J.J.M., van der Horst, A.J., Wijers, R.A.M.J. & Strom, R. (2007). Prompt and Afterglow Emission Properties of Gamma-Ray Bursts with Spectroscopically Identified Supernovae. *The Astrophysical Journal*, **654**, 385–402.

Kann, D.A., Klose, S. & Zeh, A. (2006). Signatures of Extragalactic Dust in Pre-Swift GRB Afterglows. *The Astrophysical Journal*, **641**, 993–1009.

Kann, D.A., Klose, S., Zhang, B., Malesani, D., Nakar, E., Pozanenko, A., Wilson, A.C., Butler, N.R., Jakobsson, P., Schulze, S., Andreev, M., Antonelli, L.A., Bikmaev, I.F., Biryukov, V., Böttcher, M., Burenin, R.A., Castro Cerón, J.M., Castro-Tirado, A.J., Chincarini, G., Cobb, B.E., Covino, S., D'Avanzo, P., D'Elia, V., Della Valle, M., de Ugarte Postigo, A., Efimov, Y., Ferrero, P., Fugazza, D., Fynbo, J.P.U., Gålfalk, M., Grundahl, F., Gorosabel, J., Gupta, S., Guziy, S., Hafizov, B., Hjorth, J., Holhjem, K., Ibrahimov, M., Im, M., Israel, G.L., Jelínek, M., Jensen, B.L., Karimov, R., Khamitov, I.M., Kiziloğlu, Ü., Klunko, E., Kubánek, P., Kutyrev, A.S., Laursen, P., Levan, A.J., Mannucci, F., Martin, C.M., Mescheryakov, A., Mirabal, N., Norris, J.P., Ovaldsen, J.E., Paraficz, D., Pavlenko, E., Piranomonte, S., Rossi, A., Rumyantsev, V., Salinas, R., Sergeev, A., Sharapov, D., Sollerman, J., Stecklum, B., Stella, L., Tagliaferri, G., Tanvir, N.R., Telting, J., Testa, V., Updike, A.C., Volnova, A., Watson, D.J., Wiersema, K. & Xu, D. (2010). The Afterglows of Swift-era Gamma-ray Bursts. I. Comparing pre-Swift and Swift-era Long/Soft (Type II) GRB Optical Afterglows. *The Astrophysical Journal*, **720**, 1513–1558.

KANN, D.A., KLOSE, S., ZHANG, B., COVINO, S., BUTLER, N.R., MALESANI, D., NAKAR, E., WILSON, A.C., ANTONELLI, L.A., CHINCARINI, G., COBB, B.E., D'AVANZO, P., D'ELIA, V., DELLA VALLE, M., FERRERO, P., FUGAZZA, D., GOROSABEL, J., ISRAEL, G.L., MANNUCCI, F., PIRANOMONTE, S., SCHULZE, S., STELLA, L., TAGLIAFERRI, G. & WIERSEMA, K. (2011). The Afterglows of Swift-era Gamma-Ray Bursts. II. Type I GRB versus Type II GRB Optical Afterglows. *The Astrophysical Journal*, **734**, 96.

KELSON, D.D. (2003). Optimal Techniques in Two-dimensional Spectroscopy: Background Subtraction for the 21st Century. *The Publications of the Astronomical Society of the Pacific*, **115**, 688–699.

KEREŠ, D., VOGELSBERGER, M., SIJACKI, D., SPRINGEL, V. & HERNQUIST, L. (2012). Moving-mesh cosmology: characteristics of galaxies and haloes. *Monthly Notices of the Royal Astronomical Society*, **425**, 2027–2048.

KIRSHNER, R.P. (2002). The extravagant universe : exploding stars, dark energy and the accelerating cosmos. *The extravagant universe : exploding stars*.

KISTLER, M.D., YÜKSEL, H., BEACOM, J.F., HOPKINS, A.M. & WYITHE, J.S.B. (2009). The Star Formation Rate in the Reionization Era as Indicated by Gamma-Ray Bursts. *The Astrophysical Journal Letters*, **705**, L104–L108.

KLEBESADEL, R.W., STRONG, I.B. & OLSON, R.A. (1973). Observations of Gamma-Ray Bursts of Cosmic Origin. *The Astrophysical Journal*, **182**, L85.

KOBAYASHI, S., PIRAN, T. & SARI, R. (1997). Can Internal Shocks Produce the Variability in Gamma-Ray Bursts? *Astrophysical Journal v.490*, **490**, 92–.

KOMATSU, E., SMITH, K.M., DUNKLEY, J., BENNETT, C.L., GOLD, B., HINSHAW, G., JAROSIK, N., LARSON, D., NOLTA, M.R., PAGE, L., SPERGEL, D.N., HALPERN, M., HILL, R.S., KOGUT, A., LIMON, M., MEYER, S.S., ODEGARD, N., TUCKER, G.S., WEILAND, J.L., WOLLACK, E. & WRIGHT, E.L. (2011). Seven-year Wilkinson Microwave Anisotropy Probe (WMAP) Observations: Cosmological Interpretation. *The Astrophysical Journal Supplement Series*, **192**, 18.

KOUVELIOTOU, C., MEEGAN, C.A., FISHMAN, G.J., BHAT, N.P., BRIGGS, M.S., KOSHUT, T.M., PACIESAS, W.S. & PENDLETON, G.N. (1993). Identification of two classes of gamma-ray bursts. *The Astrophysical Journal*, **413**, L101–L104.

Kouveliotou, C., Dieters, S., Strohmayer, T., van Paradijs, J., Fishman, G.J., Meegan, C.A., Hurley, K., Kommers, J., Smith, I., Frail, D. & Murakami, T. (1998). An X-ray pulsar with a superstrong magnetic field in the soft γ-ray repeater SGR1806 - 20. *Nature*, **393**, 235–237.

Kovács, A. (2008). CRUSH: fast and scalable data reduction for imaging arrays. *Millimeter and Submillimeter Detectors and Instrumentation for Astronomy IV. Edited by Duncan*, **7020**, 70201S–70201S–15.

Krühler, T., Küpcü Yoldaş, A., Greiner, J., Clemens, C., McBreen, S., Primak, N., Savaglio, S., Yoldaş, A., Szokoly, G.P. & Klose, S. (2008). The 2175 Å Dust Feature in a Gamma-Ray Burst Afterglow at Redshift 2.45. *The Astrophysical Journal*, **685**, 376–383.

Krühler, T., Ledoux, C., Fynbo, J.P.U., Vreeswijk, P.M., Schmidl, S., Malesani, D., Christensen, L., De Cia, A., Hjorth, J., Jakobsson, P., Kann, D.A., Kaper, L., Vergani, S.D., Afonso, P.M.J., Covino, S., de Ugarte Postigo, A., D'Elia, V., Filgas, R., Goldoni, P., Greiner, J., Hartoog, O.E., Milvang-Jensen, B., Nardini, M., Piranomonte, S., Rossi, A., Sánchez-Ramírez, R., Schady, P., Schulze, S., Sudilovsky, V., Tanvir, N.R., Tagliaferri, G., Watson, D.J., Wiersema, K., Wijers, R.A.M.J. & Xu, D. (2013). Molecular hydrogen in the damped Lyman α system towards GRB 120815A at z = 2.36. *Astronomy and Astrophysics*, **557**, A18. xxii, 35, 36

Krühler, T., Malesani, D., Fynbo, J.P.U., Hartoog, O.E., Hjorth, J., Jakobsson, P., Perley, D.A., Rossi, A., Schady, P., Schulze, S., Tanvir, N.R., Vergani, S.D., Wiersema, K., Afonso, P.M.J., Bolmer, J., Cano, Z., Covino, S., D'Elia, V., de Ugarte Postigo, A., Filgas, R., Friis, M., Graham, J.F., Greiner, J., Goldoni, P., Gomboc, A., Hammer, F., Japelj, J., Kann, D.A., Kaper, L., Klose, S., Levan, A.J., Leloudas, G., Milvang-Jensen, B., Nicuesa Guelbenzu, A., Palazzi, E., Pian, E., Piranomonte, S., Sánchez-Ramírez, R., Savaglio, S., Selsing, J., Tagliaferri, G., Vreeswijk, P.M., Watson, D.J. & Xu, D. (2015). GRB hosts through cosmic time. VLT/X-Shooter emission-line spectroscopy of 96 γ-ray-burst-selected galaxies at 0.1 ¡z ¡ 3.6. *Astronomy and Astrophysics*, **581**, A125. 62

Kulkarni, S.R., Frail, D.A., Wieringa, M.H., Ekers, R.D., Sadler, E.M., Wark, R.M., Higdon, J.L., Phinney, E.S. & Bloom, J.S. (1998). Radio emission from the unusual supernova 1998bw and its association with the γ-ray burst of 25 April 1998. *Nature*, **395**, 663–669.

Lah, P., Chengalur, J.N., Briggs, F.H., Colless, M., de Propris, R., Pracy, M.B., de Blok, W.J.G., Fujita, S.S., Ajiki, M., Shioya, Y., Nagao, T., Murayama, T., Taniguchi, Y., Yagi, M. & Okamura, S. (2007). The H I content of star-forming galaxies at z= 0.24. *Monthly Notices of the Royal Astronomical Society*, **376**, 1357–1366.

Lamb, D.Q. (1995). The Distance Scale to Gamma-Ray Bursts. *The Publications of the Astronomical Society of the Pacific*, **107**, 1152–.

Lamb, D.Q. & Reichart, D.E. (2000). Gamma-Ray Bursts as a Probe of the Very High Redshift Universe. *The Astrophysical Journal*, **536**, 1–18.

Lanzetta, K.M., Wolfe, A.M., Turnshek, D.A., Lu, L., McMahon, R.G. & Hazard, C. (1991). A new spectroscopic survey for damped Ly-alpha absorption lines from high-redshift galaxies. *The Astrophysical Journal Supplement Series*, **77**, 1–57.

Laskar, T., Berger, E., Zauderer, B.A., Margutti, R., Soderberg, A.M., Chakraborti, S., Lunnan, R., Chornock, R., Chandra, P. & Ray, A. (2013a). A Reverse Shock in GRB 130427A. *The Astrophysical Journal*, **776**, 119.

Laskar, T., Zauderer, A. & Berger, E. (2013b). GRB 130606A: EVLA detection. *GRB Coordinates Network*, **1481**, 1.

Lazzati, D. & Perna, R. (2002). Determining the location of gamma-ray bursts through the evolution of their soft X-ray absorption. *Monthly Notices of the Royal Astronomical Society*, **330**, 383–389.

Le Floc'h, E., Duc, P.A., Mirabel, F., Sanders, D.B., Bosch, G., Diaz, R.J., Donzelli, C.J., Rodrigues, I., Courvoisier, T.J.L., Greiner, J., Mereghetti, S., Melnick, J., Maza, J. & Minniti, D. (2003). Are the hosts of gamma-ray bursts sub-luminous and blue galaxies? *Astronomy and Astrophysics*, **400**, 499–510.

Levshakov, S.A. & Kegel, W.H. (1998). The Gunn-Peterson effect and the Lyman alpha forest. *Monthly Notices of the Royal Astronomical Society*, **301**, 323–327.

Li, Z.Y. & Chevalier, R.A. (1999). Radio Supernova SN 1998bw and Its Relation to GRB 980425. *The Astrophysical Journal*, **526**, 716–726.

Liang, E.W., Yi, S.X., Zhang, J., Lü, H.J., Zhang, B.B. & Zhang, B. (2010). Constraining Gamma-ray Burst Initial Lorentz Factor with the Afterglow Onset Feature and Discovery of a Tight Γ0-E γ,iso Correlation. *The Astrophysical Journal*, **725**, 2209–2224.

LILLY, S.J., CAROLLO, C.M., PIPINO, A., RENZINI, A. & PENG, Y. (2013). Gas Regulation of Galaxies: The Evolution of the Cosmic Specific Star Formation Rate, the Metallicity-Mass-Star-formation Rate Relation, and the Stellar Content of Halos. *The Astrophysical Journal*, **772**, 119.

LOPEZ, S. & ELLISON, S.L. (2003). Distinct abundance patterns in multiple damped Ly alpha galaxies: Evidence for truncated star formation? *Astronomy and Astrophysics*, **403**, 573–584.

LÜ, J., ZOU, Y.C., LEI, W.H., ZHANG, B., WU, Q., WANG, D.X., LIANG, E.W. & LÜ, H.J. (2012). Lorentz-factor-Isotropic-luminosity/Energy Correlations of Gamma-Ray Bursts and Their Interpretation. *The Astrophysical Journal*, **751**, 49.

LYNDEN-BELL, D. (1971). Note on N Galaxies and mini-quasars. *Monthly Notices of the Royal Astronomical Society*, **155**, 119.

LYNDS, R. (1971). The Absorption-Line Spectrum of 4c 05.34. *The Astrophysical Journal*, **164**, L73.

MA, Q., MAIO, U., CIARDI, B. & SALVATERRA, R. (2015). PopIII signatures in the spectra of PopII/I GRBs. *Monthly Notices of the Royal Astronomical Society*, **449**, 3006–3014.

MACKEY, J., BROMM, V. & HERNQUIST, L. (2003). Three Epochs of Star Formation in the High-Redshift Universe. *The Astrophysical Journal*, **586**, 1–11.

MAIO, U., SALVATERRA, R., MOSCARDINI, L. & CIARDI, B. (2012). Counts of high-redshift GRBs as probes of primordial non-Gaussianities. *Monthly Notices of the Royal Astronomical Society*, **426**, 2078–2088.

MARTIN, A.M., PAPASTERGIS, E., GIOVANELLI, R., HAYNES, M.P., SPRINGOB, C.M. & STIERWALT, S. (2010). The Arecibo Legacy Fast ALFA Survey. X. The H I Mass Function and Ω(H I) from the 40% ALFALFA Survey. *The Astrophysical Journal*, **723**, 1359–1374.

MAZETS, E.P., GOLENETSKII, S.V., APTEKAR, R.L., GURIAN, I.A. & ILINSKII, V.N. (1981). Cyclotron and annihilation lines in gamma-ray burst. *Nature*, **290**, 378–382.

MCGUIRE, J.T.W., TANVIR, N.R., LEVAN, A.J., TRENTI, M., STANWAY, E.R., SHULL, J.M., WIERSEMA, K., PERLEY, D.A., STARLING, R.L.C., BREMER, M., STOCKE, J.T., HJORTH, J., RHOADS, J.E., LEVESQUE, E.M., ROBERTSON, B., FYNBO, J.P.U., ELLIS, R.S., FRUCHTER, A.S. & PERNA, R. (2015). Detection of three Gamma-Ray Burst host galaxies at $z \sim 6$. *arXiv.org*, arXiv:1512.07808.

McKee, C.F. & Tan, J.C. (2008). The Formation of the First Stars. II. Radiative Feedback Processes and Implications for the Initial Mass Function. *The Astrophysical Journal*, **681**, 771–797.

McQuinn, M., Lidz, A., Zaldarriaga, M., Hernquist, L. & Dutta, S. (2008). Probing the neutral fraction of the IGM with GRBs during the epoch of reionization. *Monthly Notices of the Royal Astronomical Society*, **388**, 1101–1110.

Meegan, C.A., Fishman, G.J., Wilson, R.B., Horack, J.M., Brock, M.N., Paciesas, W.S., Pendleton, G.N. & Kouveliotou, C. (1992). Spatial distribution of gamma-ray bursts observed by BATSE. *Nature*, **355**, 143–145.

Melandri, A., Kobayashi, S., Mundell, C.G., Guidorzi, C., de Ugarte Postigo, A., Pooley, G., Yoshida, M., Bersier, D., Castro-Tirado, A.J., Jelínek, M., Gomboc, A., Gorosabel, J., Kubánek, P., Bremer, M., Winters, J.M., Steele, I.A., de Gregorio Monsalvo, I., Smith, R.J., Garcia-Appadoo, D., Sota, A. & Lundgren, A. (2010). GRB 090313 and the Origin of Optical Peaks in Gamma-ray Burst Light Curves: Implications for Lorentz Factors and Radio Flares. *The Astrophysical Journal*, **723**, 1331–1342.

Mészáros, P. (2002). Theories of Gamma-Ray Bursts. *Annual Review of Astronomy and Astrophysics*, **40**, 137–169.

Mészáros, P. (2006). Gamma-ray bursts. *Reports on Progress in Physics*, **69**, 2259–2321.

Mészáros, P. & Rees, M.J. (1992a). High-entropy fireballs and jets in gamma-ray burst sources. *Monthly Notices of the Royal Astronomical Society (ISSN 0035-8711)*, **257**, 29P–31P.

Mészáros, P. & Rees, M.J. (1992b). Tidal heating and mass loss in neutron star binaries - Implications for gamma-ray burst models. *Astrophysical Journal*, **397**, 570–575.

Mészáros, P. & Rees, M.J. (1993). Relativistic fireballs and their impact on external matter - Models for cosmological gamma-ray bursts. *The Astrophysical Journal*, **405**, 278–284.

Mészáros, P. & Rees, M.J. (1997). Optical and Long-Wavelength Afterglow from Gamma-Ray Bursts. *The Astrophysical Journal*, **476**, 232–237.

Mészáros, P., Asano, K., Murase, K., Fox, D., Gao, H. & Senno, N. (2015). Gamma Ray Bursts in the HAWC Era. *arXiv.org*, arXiv:1506.02707.

Metzger, M.R., Cohen, J.G., Chaffee, F.H. & Blandford, R.D. (1997a). GRB 970508. *Circulars of the International Astronomical Union*, **6676**, 3.

Metzger, M.R., Djorgovski, S.G., Kulkarni, S.R., Steidel, C.C., Adelberger, K.L., Frail, D.A., Costa, E. & Frontera, F. (1997b). Spectral constraints on the redshift of the optical counterpart to the γ-ray burst of 8 May 1997. *Nature*, **387**, 878–880.

Milvang-Jensen, B., Fynbo, J.P.U., Malesani, D., Hjorth, J., Jakobsson, P. & Møller, P. (2012). The Optically Unbiased GRB Host (TOUGH) Survey. IV. Lyα Emitters. *The Astrophysical Journal*, **756**, 25.

Miralda-Escudé, J. (1998). Reionization of the Intergalactic Medium and the Damping Wing of the Gunn-Peterson Trough. *The Astrophysical Journal*, **501**, 15–22.

Miralda-Escudé, J., Haehnelt, M. & Rees, M.J. (2000). Reionization of the Inhomogeneous Universe. *The Astrophysical Journal*, **530**, 1–16.

Modigliani, A., Goldoni, P., Royer, F., Haigron, R., Guglielmi, L., François, P., Horrobin, M., Bristow, P., Vernet, J., Moehler, S., Kerber, F., Ballester, P., Mason, E. & Christensen, L. (2010). The X-shooter pipeline. In D.R. Silva, A.B. Peck & B.T. Soifer, eds., *Proceedings of the SPIE*, 773728–773728–12, European Southern Observatory, Germany, SPIE.

Møller, P., Fynbo, J.P.U., Ledoux, C. & Nilsson, K.K. (2013). Mass-metallicity relation from z = 5 to the present: evidence for a transition in the mode of galaxy growth at z = 2.6 due to the end of sustained primordial gas infall. *Monthly Notices of the Royal Astronomical Society*, **430**, 2680–2687.

Mortlock, D.J., Patel, M., Warren, S.J., Venemans, B.P., McMahon, R.G., Hewett, P.C., Simpson, C., Sharp, R.G., Burningham, B., Dye, S., Ellis, S., Gonzáles-Solares, E.A. & Huélamo, N. (2009). Discovery of a redshift 6.13 quasar in the UKIRT infrared deep sky survey. *Astronomy and Astrophysics*, **505**, 97–104.

Mortlock, D.J., Warren, S.J., Venemans, B.P., Patel, M., Hewett, P.C., McMahon, R.G., Simpson, C., Theuns, T., Gonzáles-Solares, E.A., Adamson, A., Dye, S., Hambly, N.C., Hirst, P., Irwin, M.J., Kuiper, E., Lawrence, A. & Röttgering, H.J.A. (2011). A luminous quasar at a redshift of z = 7.085. *Nature*, **474**, 616–619.

Murakami, T., Fujii, M., Hayashida, K., Itoh, M. & Nishimura, J. (1988). Evidence for cyclotron absorption from spectral features in gamma-ray bursts seen with Ginga. *Nature (ISSN 0028-0836)*, **335**, 234–.

Nagamine, K., Springel, V. & Hernquist, L. (2004a). Abundance of damped Lyman α absorbers in cosmological smoothed particle hydrodynamics simulations. *Monthly Notices of the Royal Astronomical Society*, **348**, 421–434.

Nagamine, K., Springel, V. & Hernquist, L. (2004b). Star formation rate and metallicity of damped Lyman α absorbers in cosmological smoothed particle hydrodynamics simulations. *Monthly Notices of the Royal Astronomical Society*, **348**, 435–450.

Narayan, R., Paczynski, B. & Piran, T. (1992). Gamma-ray bursts as the death throes of massive binary stars. *Astrophysical Journal*, **395**, L83–L86.

Nava, L., Ghirlanda, G., Ghisellini, G. & Celotti, A. (2011a). Fermi/GBM and BATSE gamma-ray bursts: comparison of the spectral properties. *Monthly Notices of the Royal Astronomical Society*, **415**, 3153–3162.

Nava, L., Ghirlanda, G., Ghisellini, G. & Celotti, A. (2011b). Spectral properties of 438 GRBs detected by Fermi/GBM. *Astronomy and Astrophysics*, **530**, A21.

Neeleman, M., Prochaska, J.X., Ribaudo, J., Lehner, N., Howk, J.C., Rafelski, M. & Kanekar, N. (2016). The H I Content of the Universe Over the Past 10 GYRS. *The Astrophysical Journal*, **818**, 113.

Nelson, P. (2011). GRB 110715A optical observations. *GRB Coordinates Network*, **1217**.

Nemiroff, R.J. (1994). A Century of Gamma-Ray Burst Models. *Gamma-Ray Bursts*, **307**, 730–.

Niino, Y. (2011). Revisiting the metallicity of long-duration gamma-ray burst host galaxies: the role of chemical inhomogeneity within galaxies. *Monthly Notices of the Royal Astronomical Society*, **417**, 567–572.

Norris, J.P., Marani, G.F. & Bonnell, J.T. (2000). Connection between Energy-dependent Lags and Peak Luminosity in Gamma-Ray Bursts. *The Astrophysical Journal*, **534**, 248–257.

Noterdaeme, P., Petitjean, P., Ledoux, C. & Srianand, R. (2009). Evolution of the cosmological mass density of neutral gas from Sloan Digital Sky Survey II - Data Release 7. *Astronomy and Astrophysics*, **505**, 1087–1098.

Noterdaeme, P., Petitjean, P., Carithers, W., Pâris, I., Font-Ribera, A., Bailey, S., Aubourg, É., Bizyaev, D., Ebelke, G., Finley, H., Ge, J., Malanushenko, E., Malanushenko, V., Miralda-Escudé, J., Myers, A.D., Oravetz, D., Pan, K., Pieri, M.M., Ross, N.P., Schneider, D.P., Simmons, A. & York, D.G. (2012). Column density distribution and cosmological mass density of neutral gas: Sloan Digital Sky Survey-III Data Release 9. *Astronomy and Astrophysics*, **547**, L1.

Noterdaeme, P., Srianand, R., Rahmani, H., Petitjean, P., Pâris, I., Ledoux, C., Gupta, N. & Lopez, S. (2015). VLT/UVES observations of extremely strong intervening damped Lyman-α systems. Molecular hydrogen and excited carbon, oxygen, and silicon at log N(H i) = 22.4. *Astronomy and Astrophysics*, **577**, A24.

Oates, S.R., Page, M.J., Schady, P., De Pasquale, M., Koch, T.S., Breeveld, A.A., Brown, P.J., Chester, M.M., Holland, S.T., Hoversten, E.A., Kuin, N.P.M., Marshall, F.E., Roming, P.W.A., Still, M., vanden Berk, D.E., Zane, S. & Nousek, J.A. (2009). A statistical study of gamma-ray burst afterglows measured by the Swift Ultraviolet Optical Telescope. *Monthly Notices of the Royal Astronomical Society*, **395**, 490–503.

Oesch, P.A., Brammer, G., van Dokkum, P.G., Illingworth, G.D., Bouwens, R.J., Labbé, I., Franx, M., Momcheva, I., Ashby, M.L.N., Fazio, G.G., González, V., Holden, B., Magee, D., Skelton, R.E., Smit, R., Spitler, L.R., Trenti, M. & Willner, S.P. (2016). A Remarkably Luminous Galaxy at z=11.1 Measured with Hubble Space Telescope Grism Spectroscopy. *The Astrophysical Journal*, **819**, 129.

O'Meara, J.M., Prochaska, J.X., Burles, S.M., Prochter, G., Bernstein, R.A. & Burgess, K.M. (2007). The Keck+Magellan Survey for Lyman Limit Absorption. I. The Frequency Distribution of Super Lyman Limit Systems. *The Astrophysical Journal*, **656**, 666–679.

Paczynski, B. (1995). How Far Away Are Gamma-Ray Bursters? *The Publications of the Astronomical Society of the Pacific*, **107**, 1167–.

Panaitescu, A. & Kumar, P. (2001). Jet Energy and Other Parameters for the Afterglows of GRB 980703, GRB 990123, GRB 990510, and GRB 991216 Determined from Modeling of Multifrequency Data. *The Astrophysical Journal*, **554**, 667–677.

Panaitescu, A. & Vestrand, W.T. (2011). Optical afterglows of gamma-ray bursts: peaks, plateaus and possibilities. *Monthly Notices of the Royal Astronomical Society*, **414**, 3537–3546.

Pe'er, A. & Ryde, F. (2016). Photospheric Emission in Gamma-Ray Bursts. *arXiv.org*, arXiv:1603.05058.

Pei, Y.C. & Fall, S.M. (1995). Cosmic Chemical Evolution. *Astrophysical Journal v.454*, **454**, 69–.

Perley, D.A., Cenko, S.B., Bloom, J.S., Krühler, T., Filippenko, A.V., Fruchter, A., Kalirai, J., Morgan, A.N., Prochaska, J.X. & Silverman, J.M. (2013). A Population of Massive, Luminous Galaxies Hosting Heavily Dust-obscured Gamma-Ray Bursts: Implications for the Use of GRBs as Tracers of Cosmic Star Formation. *The Astrophysical Journal*, **778**, 128.

Perley, D.A., Krühler, T., Schulze, S., de Ugarte Postigo, A., Hjorth, J., Berger, E., Cenko, S.B., Chary, R., Cucchiara, A., Ellis, R., Fong, W., Fynbo, J.P.U., Gorosabel, J., Greiner, J., Jakobsson, P., Kim, S., Laskar, T., Levan, A.J., Michałowski, M.J., Milvang-Jensen, B., Tanvir, N.R., Thöne, C.C. & Wiersema, K. (2016a). The Swift Gamma-Ray Burst Host Galaxy Legacy Survey. I. Sample Selection and Redshift Distribution. *The Astrophysical Journal*, **817**, 7.

Perley, D.A., Niino, Y., Tanvir, N.R., Vergani, S.D. & Fynbo, J.P.U. (2016b). Long-Duration Gamma-Ray Burst Host Galaxies in Emission and Absorption. *Space Science Reviews*, 1–32.

Perley, D.A., Tanvir, N.R., Hjorth, J., Laskar, T., Berger, E., Chary, R., de Ugarte Postigo, A., Fynbo, J.P.U., Krühler, T., Levan, A.J., Michałowski, M.J. & Schulze, S. (2016c). The Swift GRB Host Galaxy Legacy Survey. II. Rest-frame Near-IR Luminosity Distribution and Evidence for a Near-solar Metallicity Threshold. *The Astrophysical Journal*, **817**, 8.

Perna, R. & Lazzati, D. (2002). Time-dependent Photoionization in a Dusty Medium. I. Code Description and General Results. *The Astrophysical Journal*, **580**, 261–277.

Péroux, C., Storrie-Lombardi, L.J., McMahon, R.G., Irwin, M. & Hook, I.M. (2001). Absorption Systems in the Spectra of 66 Z¿˜4 Quasars. *The Astronomical Journal*, **121**, 1799–1820.

Péroux, C., McMahon, R.G., Storrie-Lombardi, L.J. & Irwin, M.J. (2003). The evolution of ΩHI and the epoch of formation of damped Lyman α absorbers. *Monthly Notices of the Royal Astronomical Society*, **346**, 1103–1115.

Péroux, C., Dessauges-Zavadsky, M., D'Odorico, S., Sun Kim, T. & McMahon, R.G. (2005). A homogeneous sample of sub-damped Lyman α systems - III. Total gas mass ΩHI+HeII at z ¿ 2*. *Monthly Notices of the Royal Astronomical Society*, **363**, 479–495.

Péroux, C., Dessauges-Zavadsky, M., D'Odorico, S., Kim, T.S. & McMahon, R.G. (2007). A homogeneous sample of sub-damped Lyman systems - IV. Global metallicity evolution. *Monthly Notices of the Royal Astronomical Society*, **382**, 177–193.

Persson, S.E., Murphy, D.C., Krzeminski, W., Roth, M. & Rieke, M.J. (1998). A New System of Faint Near-Infrared Standard Stars. *The Astronomical Journal*, **116**, 2475–2488.

Petrosian, V., Kitanidis, E. & Kocevski, D. (2015). Cosmological Evolution of Long Gamma-Ray Bursts and the Star Formation Rate. *The Astrophysical Journal*, **806**, 44.

Pettini, M., Smith, L.J., Hunstead, R.W. & King, D.L. (1994). Metal enrichment, dust, and star formation in galaxies at high redshifts. 3: Zn and CR abundances for 17 damped Lyman-alpha systems. *Astrophysical Journal*, **426**, 79–96.

Piranomonte, S., Vergani, S.D., Malesani, D., Fynbo, J.P.U., Wiersema, K. & Kaper, L. (2011). GRB110715A: VLT redshift. *GRB Coordinates Network*, **1216**.

Piro, L., Costa, E., Feroci, M., Cinti, M., Frontera, F., dal Fiume, D., Orlandini, M., Pizzichini, G., Heise, J., Jager, R. & Muller, H. (1996). Gamma-Ray Burst. *Circulars of the International Astronomical Union*, **6467**, 1.

Piro, L., Troja, E., Gendre, B., Ghisellini, G., Ricci, R., Bannister, K., Fiore, F., Kidd, L.A., Piranomonte, S. & Wieringa, M.H. (2014). A Hot Cocoon in the Ultralong GRB 130925A: Hints of a POPIII-like Progenitor in a Low-Density Wind Environment. *The Astrophysical Journal Letters*, **790**, L15.

Planck, C., Ade, P.A.R., Aghanim, N., Armitage-Caplan, C., Arnaud, M., Ashdown, M., Atrio-Barandela, F., Aumont, J., Baccigalupi, C., Banday, A.J., Barreiro, R.B., Bartlett, J.G., Battaner, E., Benabed, K., Benoît, A., Benoit-Lévy, A., Bernard, J.P., Bersanelli, M., Bielewicz, P., Bobin, J., Bock, J.J., Bonaldi, A., Bond, J.R., Borrill, J., Bouchet, F.R., Bridges, M., Bucher, M., Burigana, C., Butler, R.C., Calabrese, E., Cappellini, B., Cardoso, J.F., Catalano, A., Challinor, A., Chamballu, A., Chary, R.R., Chen, X., Chiang, H.C., Chiang, L.Y., Christensen, P.R., Church, S., Clements, D.L., Colombi, S., Colombo, L. P. L., Couchot, F., Coulais, A., Crill, B.P., Curto, A., Cuttaia, F., Danese, L., Davies, R.D., Davis, R.J., de Bernardis, P., de Rosa, A., de Zotti, G., Delabrouille, J., Delouis, J.M., Désert, F.X., Dickinson, C., Diego, J.M., Dolag, K., Dole, H., Donzelli, S., Doré, O., Douspis, M., Dunkley, J., Dupac, X., Efstathiou, G., Elsner, F., Ensslin, T.A., Eriksen, H.K., Finelli, F., Forni, O., Frailis, M., Fraisse, A.A., Franceschi, E., Gaier, T.C., Galeotta, S., Galli, S., Ganga, K., Giard, M., Giardino, G., Giraud-Héraud, Y., Gjerløw, E., González-Nuevo, J., Górski, K.M., Gratton, S., Gregorio, A., Gruppuso, A., Gudmundsson, J.E., Haissinski, J., Hamann, J., Hansen, F.K., Hanson, D., Harrison, D., Henrot-Versillé, S., Hernández-Monteagudo, C., Herranz, D., Hildebrandt, S.R., Hivon, E., Hobson, M., Holmes, W.A., Hornstrup, A., Hou, Z., Hovest, W., Huffenberger, K.M., Jaffe, A.H., Jaffe, T.R., Jewell, J., Jones, W.C., Juvela, M., Keihänen, E., Keskitalo, R., Kisner, T.S., Kneissl, R., Knoche, J., Knox, L., Kunz, M., Kurki-Suonio, H., Lagache, G., Lähteenmäki, A., Lamarre, J.M., Lasenby, A., Lattanzi, M., Laureijs, R.J., Lawrence, C.R., Leach, S., Leahy, J.P., Leonardi, R., León-Tavares, J., Lesgourgues, J., Lewis, A., Liguori, M., Lilje, P.B., Linden-Vørnle, M., López-Caniego, M., Lubin, P.M., Macías-Pérez, J.F., Maffei, B., Maino, D., Mandolesi, N., Maris, M., Marshall, D.J., Martin, P.G., Martínez-González, E., Masi, S., Massardi, M., Matarrese, S., Matthai, F., Mazzotta, P., Meinhold, P.R., Melchiorri, A., Melin, J.B., Mendes, L., Menegoni, E., Mennella, A., Migliaccio, M., Millea, M., Mitra, S., Miville-Deschênes, M.A., Moneti, A., Montier, L., Morgante, G., Mortlock, D., Moss, A., Munshi, D., Murphy, J.A., Naselsky, P., Nati, F., Natoli, P., Netterfield, C.B., Nørgaard-Nielsen, H.U., Noviello, F., Novikov, D., Novikov, I., O'Dwyer, I.J., Osborne, S., Oxborrow, C.A., Paci, F., Pagano, L., Pajot, F., Paladini, R., Paoletti, D., Partridge, B., Pasian, F., Patanchon, G., Pearson, D., Pearson, T.J., Peiris, H.V., Perdereau, O., Perotto, L., Perrotta, F., Pettorino, V., Piacentini, F., Piat, M., Pierpaoli, E., Pietrobon, D., Plaszczynski, S., Platania, P., Pointecouteau, E., Polenta, G., Ponthieu, N., Popa, L., Poutanen, T., Pratt, G.W., Prézeau, G., Prunet, S., Puget, J.L., Rachen, J.P., Reach, W.T., Rebolo, R., Reinecke, M., Remazeilles, M., Renault, C., Ricciardi, S., Riller, T., Ristorcelli, I., Rocha, G., Rosset, C., Roudier, G., Rowan-Robinson, M., Rubiño-Martín, J.A., Rusholme, B., Sandri, M., Santos, D., Savelainen, M., Savini, G., Scott, D., Seiffert, M.D., Shellard, E.P.S., Spencer, L.D., Starck, J.L., Stolyarov, V., Stompor, R., Sudiwala, R., Sunyaev, R., Sureau, F., Sutton, D., Suur-Uski, A.S., Sygnet, J.F., Tauber, J.A., Tavagnacco, D., Terenzi, L., Toffolatti, L., Tomasi, M., Tristram, M., Tucci, M., Tuovinen, J., Türler, M., Umana, G., Valenziano, L., Valiviita, J., Van Tent, B., Vielva, P., Villa, F., Vittorio, N., Wade, L.A., Wandelt, B.D., Wehus, I.K., White, M., White, S.D.M., Wilkinson, A., Yvon, D., Zacchei, A. & Zonca, A. (2014). Planck 2013 results. XVI. Cosmological parameters. *Astronomy and Astrophysics*, **571**, A16.

Postman, M., Coe, D., Benitez, N., Bradley, L., Broadhurst, T., Donahue, M., Ford, H., Graur, O., Graves, G., Jouvel, S., Koekemoer, A., Lemze, D., Medezinski, E., Molino, A., Moustakas, L., Ogaz, S., Riess, A., Rodney, S., Rosati, P., Umetsu, K., Zheng, W., Zitrin, A., Bartelmann, M., Bouwens, R., Czakon, N., Golwala, S., Host, O., Infante, L., Jha, S., Jimenez-Teja, Y., Kelson, D., Lahav, O., Lazkoz, R., Maoz, D., McCully, C., Melchior, P., Meneghetti, M., Merten, J., Moustakas, J., Nonino, M., Patel, B., Regös, E., Sayers, J., Seitz, S. & van der Wel, A. (2012). The Cluster Lensing and Supernova Survey with Hubble: An Overview. *The Astrophysical Journal Supplement Series*, **199**, 25.

Prochaska, J.X. (1999). The Physical Nature of the Lyman-Limit Systems. *The Astrophysical Journal*, **511**, L71–L74.

Prochaska, J.X. (2006). On the Perils of Curve-of-Growth Analysis: Systematic Abundance Underestimates for the Gas in Gamma-Ray Burst Host Galaxies. *The Astrophysical Journal*, **650**, 272–280.

Prochaska, J.X. & Herbert-Fort, S. (2004). The Sloan Digital Sky Survey Damped Lyα Survey: Data Release 1. *The Publications of the Astronomical Society of the Pacific*, **116**, 622–633.

Prochaska, J.X. & Wolfe, A.M. (2009). On the (Non)Evolution of H I Gas in Galaxies Over Cosmic Time. *The Astrophysical Journal*, **696**, 1543–1547.

Prochaska, J.X., Gawiser, E., Wolfe, A.M., Cooke, J. & Gelino, D. (2003). The ESI/Keck II Damped Lyα Abundance Database. *The Astrophysical Journal Supplement Series*, **147**, 227–264.

Prochaska, J.X., Herbert-Fort, S. & Wolfe, A.M. (2005). The SDSS Damped Lyα Survey: Data Release 3. *The Astrophysical Journal*, **635**, 123–142.

Prochaska, J.X., Chen, H.W., Dessauges-Zavadsky, M. & Bloom, J.S. (2007). Probing the Interstellar Medium near Star-forming Regions with Gamma-Ray Burst Afterglow Spectroscopy: Gas, Metals, and Dust. *The Astrophysical Journal*, **666**, 267–280.

Prochaska, J.X., Chen, H.W., Wolfe, A.M., Dessauges-Zavadsky, M. & Bloom, J.S. (2008a). On the Nature of Velocity Fields in High-z Galaxies. *The Astrophysical Journal*, **672**, 59–71.

Prochaska, J.X., Hennawi, J.F. & Herbert-Fort, S. (2008b). The SDSS-DR5 Survey for Proximate Damped Lyα Systems. *The Astrophysical Journal*, **675**, 1002–1013.

Prochaska, J.X., Worseck, G. & O'Meara, J.M. (2009). A Direct Measurement of the Intergalactic Medium Opacity to H I Ionizing Photons. *The Astrophysical Journal Letters*, **705**, L113–L117.

Prochaska, J.X., O'Meara, J.M. & Worseck, G. (2010). A Definitive Survey for Lyman Limit Systems at z ~ 3.5 with the Sloan Digital Sky Survey. *The Astrophysical Journal*, **718**, 392–416.

Quiret, S., Péroux, C., Zafar, T., Kulkarni, V.P., Jenkins, E.D., Milliard, B., Rahmani, H., Popping, A., Sandhya, R.M., Turnshek, D.A. & Monier, E.M. (2016). The ESO UVES Advanced Data Products Quasar Sample - VI. Sub-Damped Lyman-α Metallicity Measurements and the Circum-Galactic Medium. *arXiv.org*, arXiv:1602.02564.

Racusin, J.L., Karpov, S.V., Sokolowski, M., Granot, J., Wu, X.F., Pal'Shin, V., Covino, S., van der Horst, A.J., Oates, S.R., Schady, P., Smith, R.J., Cummings, J., Starling, R.L.C., Piotrowski, L.W., Zhang, B., Evans, P.A., Holland, S.T., Malek, K., Page, M.T., Vetere, L., Margutti, R., Guidorzi, C., Kamble, A.P., Curran, P.A., Beardmore, A.P., Kouveliotou, C., Mankiewicz, L., Melandri, A., O'Brien, P.T., Page, K.L., Piran, T., Tanvir, N.R., Wrochna, G., Aptekar, R.L., Barthelmy, S.D., Bartolini, C., Beskin, G.M., Bondar, S., Bremer, M., Campana, S., Castro-Tirado, A.J., Cucchiara, A., Cwiok, M., D'Avanzo, P., D'Elia, V., Della Valle, M., de Ugarte Postigo, A., Dominik, W., Falcone, A., Fiore, F., Fox, D.B., Frederiks, D.D., Fruchter, A.S., Fugazza, D., Garrett, M.A., Gehrels, N., Golenetskii, S., Gomboc, A., Gorosabel, J., Greco, G., Guarnieri, A., Immler, S., Jelínek, M., Kasprowicz, G., La Parola, V., Levan, A.J., Mangano, V., Mazets, E.P., Molinari, E., Moretti, A., Nawrocki, K., Oleynik, P.P., Osborne, J.P., Pagani, C., Pandey, S.B., Paragi, Z., Perri, M., Piccioni, A., Ramirez-Ruiz, E., Roming, P.W.A., Steele, I.A., Strom, R.G., Testa, V., Tosti, G., Ulanov, M.V., Wiersema, K., Wijers, R.A.M.J., Winters, J.M., Zarnecki, A.F., Zerbi, F., Mészáros, P., Chincarini, G. & Burrows, D.N. (2008). Broadband observations of the naked-eye γ-ray burst GRB080319B. *Nature*, **455**, 183–188.

Rafelski, M., Wolfe, A.M., Prochaska, J.X., Neeleman, M. & Mendez, A.J. (2012). Metallicity Evolution of Damped Lyα Systems Out to z ˜ 5. *The Astrophysical Journal*, **755**, 89.

Rafelski, M., Neeleman, M., Fumagalli, M., Wolfe, A.M. & Prochaska, J.X. (2014). The Rapid Decline in Metallicity of Damped Lyα Systems at z ˜ 5. *The Astrophysical Journal Letters*, **782**, L29.

Ramirez-Ruiz, E., Celotti, A. & Rees, M.J. (2002). Events in the life of a cocoon surrounding a light, collapsar jet. *Monthly Notice of the Royal Astronomical Society*, **337**, 1349–1356.

Rao, S.M., Turnshek, D.A. & Nestor, D.B. (2006). Damped Lyα Systems at z¡1.65: The Expanded Sloan Digital Sky Survey Hubble Space Telescope Sample. *The Astrophysical Journal*, **636**, 610–630.

Rees, M.J. (1998). The Universe at z ¿ 5: When and How did the "Dark Age" End? In *Proceedings of the National Academy of Sciences of the United States of America*, 47–52, Institute of Astronomy, Madingley Road, Cambridge, CB3 OHA, United Kingdom., National Acad Sciences.

Rees, M.J. & Mészáros, P. (1992). Relativistic fireballs - Energy conversion and time-scales. *Monthly Notices of the Royal Astronomical Society (ISSN 0035-8711)*, **258**, 41P–43P.

Rees, M.J. & Mészáros, P. (1994). Unsteady outflow models for cosmological gamma-ray bursts. *The Astrophysical Journal*, **430**, L93–L96.

Rees, M.J. & Mészáros, P. (1998). Refreshed Shocks and Afterglow Longevity in Gamma-Ray Bursts. *The Astrophysical Journal*, **496**, L1–L4.

Resmi, L., Misra, K., Jóhannesson, G., Castro-Tirado, A.J., Gorosabel, J., Bhattacharya, D., Anupama, G.C., Sahu, D.K., Pandey, S.B., Bremer, M. & Sagar, R. (2012). Comprehensive multiwavelength modelling of the afterglow of GRB 050525A. *Monthly Notices of the Royal Astronomical Society*, **427**, 288–297. 109

Rhee, J., Zwaan, M.A., Briggs, F.H., Chengalur, J.N., Lah, P., Oosterloo, T. & van der Hulst, T. (2013). Neutral atomic hydrogen (H I) gas evolution in field galaxies at z ˜ 0.1 and ˜0.2. *Monthly Notices of the Royal Astronomical Society*, **435**, 2693–2706.

Rhoads, J.E. (1997). How to Tell a Jet from a Balloon: A Proposed Test for Beaming in Gamma-Ray Bursts. *The Astrophysical Journal*, **487**, L1–L4.

Rhoads, J.E. (1999). The Dynamics and Light Curves of Beamed Gamma-Ray Burst Afterglows. *The Astrophysical Journal*, **525**, 737–749.

Robertson, B.E. & Ellis, R.S. (2012). Connecting the Gamma Ray Burst Rate and the Cosmic Star Formation History: Implications for Reionization and Galaxy Evolution. *The Astrophysical Journal*, **744**, 95.

Robertson, B.E., Ellis, R.S., Dunlop, J.S., McLure, R.J. & Stark, D.P. (2010). Early star-forming galaxies and the reionization of the Universe. *Nature*, **468**, 49–55.

Robertson, B.E., Furlanetto, S.R., Schneider, E., Charlot, S., Ellis, R.S., Stark, D.P., McLure, R.J., Dunlop, J.S., Koekemoer, A., Schenker, M.A., Ouchi, M., Ono, Y., Curtis-Lake, E., Rogers, A.B., Bowler, R.A.A. & Cirasuolo, M. (2013). New Constraints on Cosmic Reionization from the 2012 Hubble Ultra Deep Field Campaign. *The Astrophysical Journal*, **768**, 71.

Robertson, B.E., Ellis, R.S., Furlanetto, S.R. & Dunlop, J.S. (2015). Cosmic Reionization and Early Star-forming Galaxies: A Joint Analysis of New Constraints from Planck and the Hubble Space Telescope. *The Astrophysical Journal Letters*, **802**, L19.

Roming, P.W.A., Kennedy, T.E., Mason, K.O., Nousek, J.A., Ahr, L., Bingham, R.E., Broos, P.S., Carter, M.J., Hancock, B.K., Huckle, H.E., Hunsberger, S.D., Kawakami, H., Killough, R., Koch, T.S., McLelland, M.K., Smith, K., Smith, P.J., Soto, J.C., Boyd, P.T., Breeveld, A.A., Holland, S.T., Ivanushkina, M., Pryzby, M.S., Still, M.D. & Stock, J. (2005). The Swift Ultra-Violet/Optical Telescope. *Space Science Reviews*, **120**, 95–142.

Rosenberg, J.L. & Schneider, S.E. (2002). The Arecibo Dual-Beam Survey: The H I Mass Function of Galaxies. *The Astrophysical Journal*, **567**, 247–257.

Russell, D.M., Ellison, S.L. & Benn, C.R. (2006). An excess of damped Lyman α galaxies near quasi-stellar objects. *Monthly Notices of the Royal Astronomical Society*, **367**, 412–422.

Ryan, G., van Eerten, H., MacFadyen, A. & Zhang, B.B. (2015). Gamma-Ray Bursts are Observed Off-axis. *The Astrophysical Journal*, **799**, 3.

Rykoff, E.S., Aharonian, F., Akerlof, C.W., Ashley, M.C.B., Barthelmy, S.D., Flewelling, H.A., Gehrels, N., Göğüş, E., Güver, T., Kiziloğlu, Ü., Krimm, H.A., McKay, T.A., Özel, M., Phillips, A., Quimby, R.M., Rowell, G., Rujopakarn, W., Schaefer, B.E., Smith, D.A., Vestrand, W.T., Wheeler, J.C., Wren, J., Yuan, F. & Yost, S.A. (2009). Looking Into the Fireball: ROTSE-III and Swift Observations of Early Gamma-ray Burst Afterglows. *The Astrophysical Journal*, **702**, 489–505.

Salpeter, E.E. (1964). Accretion of Interstellar Matter by Massive Objects. *The Astrophysical Journal*, **140**, 796–800.

Salvaterra, R. (2015). High redshift Gamma-Ray Bursts. *Journal of High Energy Astrophysics*, **7**, 35–43.

Salvaterra, R., Campana, S., Vergani, S.D., Covino, S., D'Avanzo, P., Fugazza, D., Ghirlanda, G., Ghisellini, G., Melandri, A., Nava, L., Sbarufatti, B., Flores, H., Piranomonte, S. & Tagliaferri, G. (2012). A Complete Sample of Bright Swift Long Gamma-Ray Bursts. I. Sample Presentation, Luminosity Function and Evolution. *The Astrophysical Journal*, **749**, 68.

Salvaterra, R., Maio, U., Ciardi, B. & Campisi, M.A. (2013). Simulating high-z gamma-ray burst host galaxies. *Monthly Notices of the Royal Astronomical Society*, **429**, 2718–2726.

Sánchez-Ramírez, R., Ellison, S.L., Prochaska, J.X., Berg, T.A.M., Lopez, S., D'Odorico, V., Becker, G.D., Christensen, L., Cupani, G., Denney, K.D., Pâris, I., Worseck, G. & Gorosabel, J. (2016). The evolution of neutral gas in damped Lyman α systems from the XQ-100 survey. *Monthly Notices of the Royal Astronomical Society*, **456**, 4488–4505. xxvi, 138, 139, 162

Sargent, W.L.W., Young, P.J., Boksenberg, A. & Tytler, D. (1980). The distribution of Lyman-alpha absorption lines in the spectra of six QSOs - Evidence for an intergalactic origin. *The Astrophysical Journal Supplement Series*, **42**, 41–81.

Sari, R. & Piran, T. (1995). Hydrodynamic Timescales and Temporal Structure of Gamma-Ray Bursts. *Astrophysical Journal Letters v.455*, **455**, L143–.

Sari, R. & Piran, T. (1999). Predictions for the Very Early Afterglow and the Optical Flash. *The Astrophysical Journal*, **520**, 641–649.

Sari, R., Piran, T. & Narayan, R. (1998). Spectra and Light Curves of Gamma-Ray Burst Afterglows. *The Astrophysical Journal*, **497**, L17–L20.

Sari, R., Piran, T. & Halpern, J.P. (1999). Jets in Gamma-Ray Bursts. *The Astrophysical Journal*, **519**, L17–L20.

Sault, R.J., Teuben, P.J. & Wright, M.C.H. (1995). A Retrospective View of MIRIAD. In *Astronomical Data Analysis Software and Systems IV*, 433, Australia Telescope National Facility, CSIRO, P.O. Box 76, Epping, N.S.W., 2121, Australia.

Savage, B.D. & Sembach, K.R. (1991). The analysis of apparent optical depth profiles for interstellar absorption lines. *Astrophysical Journal*, **379**, 245–259.

Savage, B.D. & Sembach, K.R. (1996). Interstellar Abundances from Absorption-Line Observations with the Hubble Space Telescope. *Annual Review of Astronomy and Astrophysics*, **34**, 279–330.

Savaglio, S. (2006). GRBs as cosmological probes—cosmic chemical evolution. *New Journal of Physics*, **8**, 195–.

Savaglio, S., Collaboration, K.G. & Le Borgne Collaboration, D. (2006). Stellar Masses and Metallicities of GRB Host Galaxies. *American Astronomical Society Meeting 207*, **207**, 16.18.

Scannapieco, E., Madau, P., Woosley, S., Heger, A. & Ferrara, A. (2005). The Detectability of Pair-Production Supernovae at z ¡˜ 6. *The Astrophysical Journal*, **633**, 1031–1041.

Schady, P., Page, M.J., Oates, S.R., Still, M., De Pasquale, M., Dwelly, T., Kuin, N.P.M., Holland, S.T., Marshall, F.E. & Roming, P.W.A. (2010). Dust and metal column densities in gamma-ray burst host galaxies. *Monthly Notices of the Royal Astronomical Society*, **401**, 2773–2792.

Schady, P., Savaglio, S., Krühler, T., Greiner, J. & Rau, A. (2011). The missing gas problem in GRB host galaxies: evidence for a highly ionised component. *Astronomy and Astrophysics*, **525**, A113.

Schady, P., Dwelly, T., Page, M.J., Krühler, T., Greiner, J., Oates, S.R., De Pasquale, M., Nardini, M., Roming, P.W.A., Rossi, A. & Still, M. (2012). The dust extinction curves of gamma-ray burst host galaxies. *Astronomy and Astrophysics*, **537**, A15.

Schlafly, E.F. & Finkbeiner, D.P. (2011). Measuring Reddening with Sloan Digital Sky Survey Stellar Spectra and Recalibrating SFD. *The Astrophysical Journal*, **737**, 103.

Schlegel, D.J., Finkbeiner, D.P. & Davis, M. (1998). Maps of Dust Infrared Emission for Use in Estimation of Reddening and Cosmic Microwave Background Radiation Foregrounds. *The Astrophysical Journal*, **500**, 525–553.

Schmidt, M. (1963). 3C 273 : A Star-Like Object with Large Red-Shift. *Nature*, **197**, 1040–1040.

Schmidt, M. & Green, R.F. (1983). Quasar evolution derived from the Palomar bright quasar survey and other complete quasar surveys. *Astrophysical Journal*, **269**, 352–374.

Schneider, R., Omukai, K., Inoue, A.K. & Ferrara, A. (2006). Fragmentation of star-forming clouds enriched with the first dust. *Monthly Notices of the Royal Astronomical Society*, **369**, 1437–1444.

Schulze, S., Chapman, R., Hjorth, J., Levan, A.J., Jakobsson, P., Björnsson, G., Perley, D.A., Krühler, T., Gorosabel, J., Tanvir, N.R., de Ugarte Postigo, A., Fynbo, J.P.U., Milvang-Jensen, B., Møller, P. & Watson, D.J. (2015). The Optically Unbiased GRB Host (TOUGH) Survey. VII. The Host Galaxy Luminosity Function: Probing the Relationship between GRBs and Star Formation to Redshift ~ 6. *The Astrophysical Journal*, **808**, 73.

Shahmoradi, A. (2013). Gamma-Ray bursts: Energetics and Prompt Correlations. *arXiv.org*, arXiv:1308.1097.

Shahmoradi, A. & Nemiroff, R.J. (2011). The possible impact of gamma-ray burst detector thresholds on cosmological standard candles. *Monthly Notices of the Royal Astronomical Society*, **411**, 1843–1856.

Sheinis, A.I., Bolte, M., Epps, H.W., Kibrick, R.I., Miller, J.S., Radovan, M.V., Bigelow, B.C. & Sutin, B.M. (2002). ESI, a New Keck Observatory Echellette Spectrograph and Imager. *The Publications of the Astronomical Society of the Pacific*, **114**, 851–865.

Shen, R., Kumar, P. & Robinson, E.L. (2006). No universality for the electron power-law index (p) in gamma-ray bursts and other relativistic sources. *Monthly Notices of the Royal Astronomical Society*, **371**, 1441–1447.

Silva, L., Granato, G.L., Bressan, A. & Danese, L. (1998). Modeling the Effects of Dust on Galactic Spectral Energy Distributions from the Ultraviolet to the Millimeter Band. *The Astrophysical Journal*, **509**, 103–117.

Simcoe, R.A., Sullivan, P.W., Cooksey, K.L., Kao, M.M., Matejek, M.S. & Burgasser, A.J. (2012). Extremely metal-poor gas at a redshift of 7. *Nature*, **492**, 79–82.

Siringo, G., Kreysa, E., Kovács, A., Schuller, F., Weiss, A., Esch, W., Gemünd, H.P., Jethava, N., Lundershausen, G., Colin, A., Güsten, R., Menten, K.M., Beelen, A., Bertoldi, F., Beeman, J.W. & Haller, E.E. (2009). The Large APEX BOlometer CAmera LABOCA. *Astronomy and Astrophysics*, **497**, 945–962.

Skrutskie, M.F., Cutri, R.M., Stiening, R., Weinberg, M.D., Schneider, S., Carpenter, J.M., Beichman, C., Capps, R., Chester, T., Elias, J., Huchra, J., Liebert, J., Lonsdale, C., Monet, D.G., Price, S., Seitzer, P., Jarrett, T., Kirkpatrick, J.D., Gizis, J.E., Howard, E., Evans, T., Fowler, J., Fullmer, L., Hurt, R., Light, R., Kopan, E.L., Marsh, K.A., McCallon, H.L., Tam, R., Van Dyk, S. & Wheelock, S. (2006). The Two Micron All Sky Survey (2MASS). *The Astronomical Journal*, **131**, 1163–1183.

Somerville, R.S. & Davé, R. (2015). Physical Models of Galaxy Formation in a Cosmological Framework. *Annual Review of Astronomy and Astrophysics*, **53**, 51–113.

Sonbas, E., Barthelmy, S.D., Baumgartner, W.H., Beardmore, A.P., Burrows, D.N., D'Elia, V., De Pasquale, M., Evans, P.A., Gehrels, N., Guidorzi, C., Holland, S.T., Kennea, J.A., Krimm, H.A., Kuin, N.P.M., Littlejohns, O.M., Marshall, F.E., O'Brien, P.T., Oates, S.R., Pagani, C., Page, K.L., Romano, P., Rowlinson, A., Sakamoto, T., Siegel, M.H., Stratta, G., Swenson, C.A. & Troja, E. (2011). GRB 110715A: Swift detection of a bright burst with an optical counterpart. *GRB Coordinates Network*, **1215**.

Songaila, A. (2004). The Evolution of the Intergalactic Medium Transmission to Redshift 6. *The Astronomical Journal*, **127**, 2598–2603.

Songaila, A. & Cowie, L.L. (2002). Approaching Reionization: The Evolution of the Ly α Forest from z=4 to z=6. *The Astronomical Journal*, **123**, 2183–2196.

Songaila, A. & Cowie, L.L. (2010). The Evolution of Lyman Limit Absorption Systems to Redshift Six. *The Astrophysical Journal*, **721**, 1448–1466.

Songaila, A., Hu, E.M., Cowie, L.L. & McMahon, R.G. (1999). Limits on the Gunn-Peterson Effect at Z = 5. *The Astrophysical Journal*, **525**, L5–L8.

Stacy, A., Bromm, V. & Loeb, A. (2011). Rotation speed of the first stars. *Monthly Notices of the Royal Astronomical Society*, **413**, 543–553.

Stacy, A., Pawlik, A.H., Bromm, V. & Loeb, A. (2012). Effect of Population III multiplicity on dark star formation. *Monthly Notices of the Royal Astronomical Society*, **421**, 894–907.

Stacy, A., Greif, T.H., Klessen, R.S., Bromm, V. & Loeb, A. (2013). Rotation and internal structure of Population III protostars. *Monthly Notices of the Royal Astronomical Society*, **431**, 1470–1486.

Stamatikos, M. (2009). The Cross-Calibration of Swift-BAT and Fermi-GBM via Correlative Spectral Analysis of GRBs. *arXiv.org*, arXiv:0907.3190.

Stanek, K.Z., Matheson, T., Garnavich, P.M., Martini, P., Berlind, P., Caldwell, N., Challis, P., Brown, W.R., Schild, R., Krisciunas, K., Calkins, M.L., Lee, J.C., Hathi, N., Jansen, R.A., Windhorst, R., Echevarria, L., Eisenstein, D.J., Pindor, B., Olszewski, E.W., Harding, P., Holland, S.T. & Bersier, D. (2003). Spectroscopic Discovery of the Supernova 2003dh Associated with GRB 030329. *The Astrophysical Journal*, **591**, L17–L20.

Starling, R.L.C., Wijers, R.A.M.J., Hughes, M.A., Tanvir, N.R., Vreeswijk, P.M., Rol, E. & Salamanca, I. (2005). Spectroscopy of the γ-ray burst GRB 021004: a structured jet ploughing through a massive stellar wind. *Monthly Notices of the Royal Astronomical Society*, **360**, 305–313.

Starling, R.L.C., Wijers, R.A.M.J., Wiersema, K., Rol, E., Curran, P.A., Kouveliotou, C., van der Horst, A.J. & Heemskerk, M.H.M. (2007). Gamma-Ray Burst Afterglows as Probes of Environment and Blast Wave Physics. I. Absorption by Host-Galaxy Gas and Dust. *The Astrophysical Journal*, **661**, 787–800.

Starling, R.L.C., van der Horst, A.J., Rol, E., Wijers, R.A.M.J., Kouveliotou, C., Wiersema, K., Curran, P.A. & Weltevrede, P. (2008). Gamma-Ray Burst Afterglows as Probes of Environment and Blast Wave Physics. II. The Distribution of p and Structure of the Circumburst Medium. *The Astrophysical Journal*, **672**, 433–442.

Staveley-Smith, L. & Oosterloo, T. (2015). HI Science with the Square Kilometre Array. In *Proceedings of Advancing Astrophysics with the Square Kilometre Array (AASKA14). 9 -13 June*, 167.

Steidel, C.C., Giavalisco, M., Dickinson, M. & Adelberger, K.L. (1996). Spectroscopy of Lyman Break Galaxies in the Hubble Deep Field. *The Astronomical Journal*, **112**, 352.

Stockton, A.N. & Lynds, C.R. (1966). The Remarkable Absorption Spectrum of 3c 191. *The Astrophysical Journal*, **144**, 451.

Storrie-Lombardi, L.J. & Wolfe, A.M. (2000). Surveys for z¿3 Damped Lyα Absorption Systems: The Evolution of Neutral Gas. *The Astrophysical Journal*, **543**, 552–576.

Storrie-Lombardi, L.J., Irwin, M.J. & McMahon, R.G. (1996a). APM z¿˜4 survey: distribution and evolution of high column density HI absorbers. *Monthly Notices of the Royal Astronomical Society*, **282**, 1330–1342.

Storrie-Lombardi, L.J., McMahon, R.G. & Irwin, M.J. (1996b). Evolution of neutral gas at high redshift: implications for the epoch of galaxy formation. *Monthly Notices of the Royal Astronomical Society*, **283**, L79–L83.

Storrie-Lombardi, L.J., McMahon, R.G., Irwin, M.J. & Hazard, C. (1996c). APM Z ¿=4 QSO Survey: Spectra and Intervening Absorption Systems. *The Astrophysical Journal*, **468**, 121.

Strong, I.B. & Klebesadel, R.W. (1976). Cosmic gamma-ray bursts. *Scientific American*, **235**, 66–70.

Tagliaferri, G., Antonelli, L.A., Chincarini, G., Fernandez-Soto, A., Malesani, D., Della Valle, M., D'Avanzo, P., Grazian, A., Testa, V., Campana, S., Covino, S., Fiore, F., Stella, L., Castro-Tirado, A.J., Gorosabel, J., Burrows, D.N., Capalbi, M., Cusumano, G., Conciatore, M.L., D'Elia, V., Filliatre, P., Fugazza, D., Gehrels, N., Goldoni, P., Guetta, D., Guziy, S., Held, E.V., Hurley, K., Israel, G.L., Jelínek, M., Lazzati, D., López-Echarri, A., Melandri, A., Mirabel, F., Moles, M., Moretti, A., Mason, K.O., Nousek, J., Osborne, J., Pellizza, L.J., Perna, R., Piranomonte, S., Piro, L., de Ugarte Postigo, A. & Romano, P. (2005). GRB 050904 at redshift 6.3: observations of the oldest cosmic explosion after the Big Bang. *Astronomy and Astrophysics*, **443**, L1–L5.

Taniguchi, Y., Shioya, Y. & Trump, J.R. (2010). Low-metallicity Star Formation in High-redshift Galaxies at z ˜ 8. *The Astrophysical Journal*, **724**, 1480–1490.

Tanvir, N.R., Levan, A.J., Fruchter, A.S., Fynbo, J.P.U., Hjorth, J., Wiersema, K., Bremer, M., Rhoads, J., Jakobsson, P., O'Brien, P.T., Stanway, E.R., Bersier, D., Natarajan, P., Greiner, J., Watson, D.J., Castro-Tirado, A.J., Wijers, R.A.M.J., Starling, R.L.C., Misra, K., Graham, J.F. & Kouveliotou, C. (2012). Star Formation in the Early Universe: Beyond the Tip of the Iceberg. *The Astrophysical Journal*, **754**, 46.

Thöne, C.C., Kann, D.A., Jóhannesson, G., Selj, J.H., Jaunsen, A.O., Fynbo, J.P.U., Akerlof, C.W., Baliyan, K.S., Bartolini, C., Bikmaev, I.F., Bloom, J.S., Burenin, R.A., Cobb, B.E., Covino, S., Curran, P.A., Dahle, H., Ferrero, A., Foley, S., French, J., Fruchter, A.S., Ganesh, S., Graham, J.F., Greco, G., Guarnieri, A., Hanlon, L., Hjorth, J., Ibrahimov, M., Israel, G.L., Jakobsson, P., Jelínek, M., Jensen, B.L., Jørgensen, U.G., Khamitov, I.M., Koch, T.S., Levan, A.J., Malesani, D., Masetti, N., Meehan, S., Melady, G., Nanni, D., Näränen, J., Pakstiene, E., Pavlinsky, M.N., Perley, D.A., Piccioni, A., Pizzichini, G., Pozanenko, A., Roming, P.W.A., Rujopakarn, W., Rumyantsev, V., Rykoff, E.S., Sharapov, D., Starr, D., Sunyaev, R.A., Swan, H., Tanvir, N.R., Terra, F., de Ugarte Postigo, A., Vreeswijk, P.M., Wilson, A.C., Yost, S.A. & Yuan, F. (2010). Photometry and spectroscopy of GRB 060526: a detailed study of the afterglow and host galaxy of a z = 3.2 gamma-ray burst. *Astronomy and Astrophysics*, **523**, A70.

Thöne, C.C., Goldoni, P., de Ugarte Postigo, A., Campana, S., Vergani, S.D., Krühler, T., Zafar, T., Gorosabel, J., Groot, P., Hammer, F., Nicuesa, A.G., Palazzi, E., Piranomonte, S., Tagliaferri, G., Watson, D.J., Wiersema, K. & Wijers, R.A.M.J. (2013). GRB 100219A with X-shooter - abundances in a galaxy at z =4.7. *Monthly Notices of the Royal Astronomical Society*, **428**, 3590–3606.

Tody, D. (1993). IRAF in the Nineties. *Astronomical Data Analysis Software and Systems II*, **52**, 173.

Toma, K., Sakamoto, T. & Mészáros, P. (2011). Population III Gamma-ray Burst Afterglows: Constraints on Stellar Masses and External Medium Densities. *The Astrophysical Journal*, **731**, 127.

Totani, T., Aoki, K., Hattori, T., Kosugi, G., Niino, Y., Hashimoto, T., Kawai, N., Ohta, K., Sakamoto, T. & Yamada, T. (2014). Probing intergalactic neutral hydrogen by the Lyman alpha red damping wing of gamma-ray burst 130606A afterglow spectrum at z = 5.913. *Publications of the Astronomical Society of Japan*, **66**, 63–63.

Totani, T., Aoki, K., Hattori, T. & Kawai, N. (2016). High-precision analyses of Lyα damping wing of gamma-ray bursts in the reionization era: On the controversial results from GRB 130606A at z = 5.91. *Publications of the Astronomical Society of Japan*, **68**, 15.

Trenti, M., Perna, R. & Jimenez, R. (2015). The Luminosity and Stellar Mass Functions of GRB Host Galaxies: Insight Into the Metallicity Bias. *The Astrophysical Journal*, **802**, 103.

Ukwatta, T.N., Barthelmy, S.D., Gehrels, N., Krimm, H.A., Malesani, D., Marshall, F.E., Maselli, A., Melandri, A., Palmer, D.M. & Stamatikos, M. (2013). GRB 130606A: Swift detection of a burst. *GRB Coordinates Network*, **1478**, 1.

Updike, A.C., Schady, P., Greiner, J., Krühler, T., Kann, D.A., Klose, S. & Rossi, A. (2011). GRB110715A: GROND detection of the Optical/NIR afterglow. *GRB Coordinates Network*, **1216**.

van der Horst, A.J., Paragi, Z., de Bruyn, A.G., Granot, J., Kouveliotou, C., Wiersema, K., Starling, R.L.C., Curran, P.A., Wijers, R.A.M.J., Rowlinson, A., Anderson, G.A., Fender, R.P., Yang, J. & Strom, R.G. (2014). A comprehensive radio view of the extremely bright gamma-ray burst 130427A. *Monthly Notices of the Royal Astronomical Society*, **444**, 3151–3163.

van Dokkum, P.G. (2001). Cosmic-Ray Rejection by Laplacian Edge Detection. *The Publications of the Astronomical Society of the Pacific*, **113**, 1420–1427.

van Eerten, H., van der Horst, A. & MacFadyen, A. (2012). Gamma-Ray Burst Afterglow Broadband Fitting Based Directly on Hydrodynamics Simulations. *The Astrophysical Journal*, **749**, 44.

van Paradijs, J., Groot, P.J., Galama, T.J., Kouveliotou, C., Strom, R.G., Telting, J., Rutten, R.G.M., Fishman, G.J., Meegan, C.A., Pettini, M., Tanvir, N., Bloom, J.S., Pedersen, H., Nørdgaard-Nielsen, H.U., Linden-Vørnle, M., Melnick, J., van der Steene, G., Bremer, M., Naber, R., Heise, J., in't Zand, J., Costa, E., Feroci, M., Piro, L., Frontera, F., Zavattini, G., Nicastro, L., Palazzi, E., Bennett, K., Hanlon, L. & Parmar, A. (1997). Transient optical emission from the error box of the γ-ray burst of 28 February 1997. *Nature*, **386**, 686–689.

Vergani, S.D., Fugazza, D., Gorosabel, J., Puech, M., Salvaterra, R., D'Avanzo, P., Fernández, M., Ghirlanda, G., Palazzi, E., Piranomonte, S., Rodrigues, M., Terrón, V., Thöne, C.C., Antonelli, L.A., Campana, S., Castro-Tirado, A.J., Goldoni, P., Hammer, F., Melandri, A., Sollerman, J., Tagliaferri, G., Wiersema, K. & Wijers, R.A.M.J. (2011). GRB 091127/SN 2009nz and the VLT/X-shooter spectroscopy of its host galaxy: probing the faint end of the mass-metallicity relation. *Astronomy and Astrophysics*, **535**, A127. 38

Vergani, S.D., Salvaterra, R., Japelj, J., Le Floc'h, E., D'Avanzo, P., Fernandez-Soto, A., Krühler, T., Melandri, A., Boissier, S., Covino, S., Puech, M., Greiner, J., Hunt, L.K., Perley, D.A., Petitjean, P., Vinci, T., Hammer, F., Levan, A., Mannucci, F., Campana, S., Flores, H., Gomboc, A. & Tagliaferri, G. (2015). Are long gamma-ray bursts biased tracers of star formation? Clues from the host galaxies of the Swift/BAT6 complete sample of LGRBs . I. Stellar mass at z ¡ 1. *Astronomy and Astrophysics*, **581**, A102.

Vernet, J., Dekker, H., D'Odorico, S., Kjaergaard, P., Hammer, F., Randich, S., Zerbi, F., Groot, P.J., Guinouard, I., Navarro, R., Adolfse, T., Albers, P.W., Amans, J.P., Andersen, J.J., Andersen, M.I., Binetruy, P., Bristow, P., Castillo, R., Chemla, F., Christensen, L., Conconi, P., Conzelmann, R., Dam, J., de Caprio, V., Delabre, B., di Marcantonio, P., Downing, M., Elswijk, E., Finger, G., Fischer, G., François, P., Goldoni, P., Guglielmi, L., Haigron, R., Hanenburg, H., Hendriks, I., Horrobin, M., Horville, D., Jessen, N.C., Kerber, F., Kern, L., Kiekebusch, M., Kleszcz, P., Klougart, J., Kragt, J., Larsen, H.H., Lizon, J.L., Lucuix, C., Mainieri, V., Manuputy, R., Martayan, C., Mason, E., Mazzoleni, R., Michaelsen, N., Modigliani, A., Moehler, S., Møller, P., Norup Sørensen, A., Nørregaard, P., Péroux, C., Patat, F., Pena, E., Pragt, J., Reinero, C., Rigal, F., Riva, M., Roelfsema, R., Royer, F., Sacco, G., Santin, P., Schoenmaker, T., Spano, P., Sweers, E., Ter Horst, R., Tintori, M., Tromp, N., van Dael, P., van der Vliet, H., Venema, L., Vidali, M., Vinther, J., Vola, P., Winters, R., Wistisen, D., Wulterkens, G. & Zacchei, A. (2011). X-shooter, the new wide band intermediate resolution spectrograph at the ESO Very Large Telescope. *Astronomy and Astrophysics*, **536**, A105.

Virgili, F.J., Zhang, B., Nagamine, K. & Choi, J.H. (2011). Gamma-ray burst rate: high-redshift excess and its possible origins. *Monthly Notices of the Royal Astronomical Society*, **417**, 3025–3034.

Virgili, F.J., Mundell, C.G. & Melandri, A. (2013a). GRB 130606A - Liverpool telescope optical afterglow confirmation. *GRB Coordinates Network*, **1478**, 1.

Virgili, F.J., Mundell, C.G., Melandri, A. & Gomboc, A. (2013b). GRB 130606A - Liverpool telescope and Faulkes telescope north optical observations. *GRB Coordinates Network*, **1484**, 1.

Vladilo, G., Centurión, M., Levshakov, S.A., Péroux, C., Khare, P., Kulkarni, V.P. & York, D.G. (2006). Extinction and metal column density of HI regions up to redshift z $\simeq$ 2. *Astronomy and Astrophysics*, **454**, 151–164.

Vlahakis, N., Peng, F. & Königl, A. (2003). Neutron-rich Hydromagnetic Outflows in Gamma-Ray Burst Sources. *The Astrophysical Journal*, **594**, L23–L26.

Vreeswijk, P.M., Møller, P. & Fynbo, J.P.U. (2003). New search strategy for high z intervening absorbers: GRB 021004, a pilot study. *Astronomy and Astrophysics*, **409**, L5–L8.

Vreeswijk, P.M., Ledoux, C., Smette, A., Ellison, S.L., Jaunsen, A.O., Andersen, M.I., Fruchter, A.S., Fynbo, J.P.U., Hjorth, J., Kaufer, A., Møller, P., Petitjean, P., Savaglio, S. & Wijers, R.A.M.J. (2007). Rapid-response mode VLT/UVES spectroscopy of GRB 060418. Conclusive evidence for UV pumping from the time evolution of Fe II and Ni II excited- and metastable-level populations. *Astronomy and Astrophysics*, **468**, 83–96.

WANG, F.Y. (2013). The high-redshift star formation rate derived from gamma-ray bursts: possible origin and cosmic reionization. *Astronomy and Astrophysics*, **556**, A90.

WANG, F.Y. & DAI, Z.G. (2011a). An Evolving Stellar Initial Mass Function and the Gamma-ray Burst Redshift Distribution. *The Astrophysical Journal Letters*, **727**, L34.

WANG, F.Y. & DAI, Z.G. (2011b). Weak gravitational lensing effects on cosmological parameters and dark energy from gamma-ray bursts. *Astronomy and Astrophysics*, **536**, A96.

WANG, F.Y., BROMM, V., GREIF, T.H., STACY, A., DAI, Z.G., LOEB, A. & CHENG, K.S. (2012). Probing Pre-galactic Metal Enrichment with High-redshift Gamma-Ray Bursts. *The Astrophysical Journal*, **760**, 27.

WANG, F.Y., DAI, Z.G. & LIANG, E.W. (2015). Gamma-ray burst cosmology. *New Astronomy Reviews*, **67**, 1–17.

WANG, R., CARILLI, C.L., WAGG, J., BERTOLDI, F., WALTER, F., MENTEN, K.M., OMONT, A., COX, P., STRAUSS, M.A., FAN, X., JIANG, L. & SCHNEIDER, D.P. (2008). Thermal Emission from Warm Dust in the Most Distant Quasars. *The Astrophysical Journal*, **687**, 848–858.

WANG, R., CARILLI, C.L., NERI, R., RIECHERS, D.A., WAGG, J., WALTER, F., BERTOLDI, F., MENTEN, K.M., OMONT, A., COX, P. & FAN, X. (2010). Molecular Gas in z ˜ 6 Quasar Host Galaxies. *The Astrophysical Journal*, **714**, 699–712.

WARREN, S.J., HEWETT, P.C., IRWIN, M.J., MCMAHON, R.G. & BRIDGELAND, M.T. (1987). First observation of a quasar with a redshift of 4. *Nature*, **325**, 131–133.

WAXMAN, E., KULKARNI, S.R. & FRAIL, D.A. (1998). Implications of the Radio Afterglow from the Gamma-Ray Burst of 1997 May 8. *The Astrophysical Journal*, **497**, 288–293.

WEYMANN, R.J., WILLIAMS, R.E., PETERSON, B.M. & TURNSHEK, D.A. (1979). Results of a homogeneous survey of absorption lines in QSOs of small and intermediate emission redshift. *The Astrophysical Journal*, **234**, 33–46.

WIJERS, R.A.M.J. & GALAMA, T.J. (1999). Physical Parameters of GRB 970508 and GRB 971214 from Their Afterglow Synchrotron Emission. *The Astrophysical Journal*, **523**, 177–186.

Williams, R.E., Blacker, B., Dickinson, M., Dixon, W.V.D., Ferguson, H.C., Fruchter, A.S., Giavalisco, M., Gilliland, R.L., Heyer, I., Katsanis, R., Levay, Z., Lucas, R.A., McElroy, D.B., Petro, L., Postman, M., Adorf, H.M. & Hook, R. (1996). The Hubble Deep Field: Observations, Data Reduction, and Galaxy Photometry. *Astronomical Journal v.112*, **112**, 1335–.

Williams, R.E., Baum, S., Bergeron, L.E., Bernstein, N., Blacker, B.S., Boyle, B.J., Brown, T.M., Carollo, C.M., Casertano, S., Covarrubias, R., de Mello, D.F., Dickinson, M.E., Espey, B.R., Ferguson, H.C., Fruchter, A., Gardner, J.P., Gonnella, A., Hayes, J., Hewett, P.C., Heyer, I., Hook, R., Irwin, M., Jones, D., Kaiser, M.E., Levay, Z., Lubenow, A., Lucas, R.A., Mack, J., MacKenty, J.W., Madau, P., Makidon, R.B., Martin, C.L., Mazzuca, L., Mutchler, M., Norris, R.P., Perriello, B., Phillips, M.M., Postman, M., Royle, P., Sahu, K., Savaglio, S., Sherwin, A., Smith, T.E., Stiavelli, M., Suntzeff, N.B., Teplitz, H.I., van der Marel, R.P., Walker, A.R., Weymann, R.J., Wiggs, M.S., Williger, G.M., Wilson, J., Zacharias, N. & Zurek, D.R. (2000). The Hubble Deep Field South: Formulation of the Observing Campaign. *The Astronomical Journal*, **120**, 2735–2746.

Willingale, R., Frederiks, D.D., Pal'shin, V.D., Svinkin, D.S., Lien, A., Cummings, J., Xiong, S., Zhang, B.B., Götz, D., Savchenko, V., Negoro, H., Nakahira, S., Suzuki, K., Wiersema, K., Starling, R.L.C., Castro-Tirado, A.J. & Gorosabel, J. (2014). GRB 130925A: an ultralong gamma ray burst with a dust-echo afterglow, and implications for the origin of the ultralong GRBs. *Monthly Notices of the Royal Astronomical Society*, **444**, 250–267. 178

Willott, C.J., Delorme, P., Reylé, C., Albert, L., Bergeron, J., Crampton, D., Delfosse, X., Forveille, T., Hutchings, J.B., McLure, R.J., Omont, A. & Schade, D. (2010). The Canada-France High-z Quasar Survey: Nine New Quasars and the Luminosity Function at Redshift 6. *The Astronomical Journal*, **139**, 906–918.

Wilson, W.E., Ferris, R.H., Axtens, P., Brown, A., Davis, E., Hampson, G., Leach, M., Roberts, P., Saunders, S., Koribalski, B.S., Caswell, J.L., Lenc, E., Stevens, J., Voronkov, M.A., Wieringa, M.H., Brooks, K., Edwards, P.G., Ekers, R.D., Emonts, B., Hindson, L., Johnston, S., Maddison, S.T., Mahony, E.K., Malu, S.S., Massardi, M., Mao, M.Y., McConnell, D., Norris, R.P., Schnitzeler, D., Subrahmanyan, R., Urquhart, J.S., Thompson, M.A. & Wark, R.M. (2011). The Australia Telescope Compact

Array Broad-band Backend: description and first results. *Monthly Notices of the Royal Astronomical Society*, **416**, 832–856.

Wolf, M.J. & Sheinis, A.I. (2008). Host Galaxies of Luminous Quasars: Structural Properties and the Fundamental Plane. *The Astronomical Journal*, **136**, 1587–1606.

Wolfe, A.M., Turnshek, D.A., Smith, H.E. & Cohen, R.D. (1986). Damped Lyman-alpha absorption by disk galaxies with large redshifts. I - The Lick survey. *The Astrophysical Journal Supplement Series*, **61**, 249–304.

Wolfe, A.M., Lanzetta, K.M., Foltz, C.B. & Chaffee, F.H. (1995). The Large Bright QSO Survey for Damped LY alpha Absorption Systems. *The Astrophysical Journal*, **454**, 698.

Wolfe, A.M., Gawiser, E. & Prochaska, J.X. (2005). Damped Ly α Systems. *Annual Review of Astronomy and Astrophysics*, **43**, 861–918.

Wolfire, M.G., McKee, C.F., Hollenbach, D. & Tielens, A.G.G.M. (2003). Neutral Atomic Phases of the Interstellar Medium in the Galaxy. *The Astrophysical Journal*, **587**, 278–311.

Woosley, S.E. (1993). Gamma-ray bursts from stellar mass accretion disks around black holes. *The Astrophysical Journal*, **405**, 273–277.

Worseck, G. & Prochaska, J.X. (2011). GALEX Far-ultraviolet Color Selection of UV-bright High-redshift Quasars. *The Astrophysical Journal*, **728**, 23.

Worseck, G., Prochaska, J.X., O'Meara, J.M., Becker, G.D., Ellison, S.L., Lopez, S., Meiksin, A., Ménard, B., Murphy, M.T. & Fumagalli, M. (2014). The Giant Gemini GMOS survey of zem ¿ 4.4 quasars - I. Measuring the mean free path across cosmic time. *Monthly Notices of the Royal Astronomical Society*, **445**, 1745–1760.

Wu, S.W., Xu, D., Zhang, F.W. & Wei, D.M. (2012). Gamma-ray bursts: the isotropic-equivalent-energy function and the cosmic formation rate. *Monthly Notices of the Royal Astronomical Society*, **423**, 2627–2632.

Wu, X.B., Wang, F.Y., Fan, X., Yi, W., Zuo, W., Bian, F., Jiang, L., McGreer, I.D., Wang, R., Yang, J., Yang, Q., Thompson, D. & Beletsky, Y. (2015). An ultraluminous quasar with a twelve-billion-solar-mass black hole at redshift 6.30. *Nature*, **518**, 512–515.

Yoldaş, A.K., Krühler, T., Greiner, J., Yoldaş, A., Clemens, C., Szokoly, G., Primak, N. & Klose, S. (2008). First Results of GROND. In *GAMMA-RAY BURSTS 2007: Proceedings of the Santa Fe Conference. AIP Conference Proceedings*, 227–231, Max-Planck-Institut für extraterrestrische Physik, Giessenbachstr. 1 85741 Garching bei München, Germany, AIP.

Yoshida, N., Omukai, K., Hernquist, L. & Abel, T. (2006). Formation of Primordial Stars in a ΛCDM Universe. *The Astrophysical Journal*, **652**, 6–25.

Yu, H., Wang, F.Y., Dai, Z.G. & Cheng, K.S. (2015). An Unexpectedly Low-redshift Excess of Swift Gamma-ray Burst Rate. *The Astrophysical Journal Supplement Series*, **218**, 13.

Zafar, T., Watson, D.J., Fynbo, J.P.U., Malesani, D., Jakobsson, P. & de Ugarte Postigo, A. (2011). The extinction curves of star-forming regions from z = 0.1 to 6.7 using GRB afterglow spectroscopy. *Astronomy and Astrophysics*, **532**, A143.

Zafar, T., Péroux, C., Popping, A., Milliard, B., Deharveng, J.M. & Frank, S. (2013). The ESO UVES advanced data products quasar sample. II. Cosmological evolution of the neutral gas mass density. *Astronomy and Astrophysics*, **556**, A141.

Zel'dovich, Y.B. & Novikov, I.D. (1964). The Radiation of Gravity Waves by Bodies Moving in the Field of a Collapsing Star. *Soviet Physics Doklady*, **9**, 246–.

Zhang, B. (2007). Gamma-Ray Bursts in the Swift Era. *Chinese Journal of Astronomy and Astrophysics*, **7**, 1–50.

Zhang, B. & Yan, H. (2011). The Internal-collision-induced Magnetic Reconnection and Turbulence (ICMART) Model of Gamma-ray Bursts. *The Astrophysical Journal*, **726**, 90.

Zhang, B., Fan, Y.Z., Dyks, J., Kobayashi, S., Mészáros, P., Burrows, D.N., Nousek, J.A. & Gehrels, N. (2006). Physical Processes Shaping Gamma-Ray Burst X-Ray Afterglow Light Curves: Theoretical Implications from the Swift X-Ray Telescope Observations. *The Astrophysical Journal*, **642**, 354–370.

Zhang, B.B., Zhang, B., Murase, K., Connaughton, V. & Briggs, M.S. (2014). How Long does a Burst Burst? *The Astrophysical Journal*, **787**, 66.

Zhang, B.B., van Eerten, H., Burrows, D.N., Ryan, G.S., Evans, P.A., Racusin, J.L., Troja, E. & MacFadyen, A. (2015). An Analysis of Chandra

Deep Follow-up Gamma-Ray Bursts: Implications for Off-axis Jets. *The Astrophysical Journal*, **806**, 15.

Zheng, W., Shen, R.F., Sakamoto, T., Beardmore, A.P., De Pasquale, M., Wu, X.F., Gorosabel, J., Urata, Y., Sugita, S., Zhang, B., Pozanenko, A., Nissinen, M., Sahu, D.K., Im, M., Ukwatta, T.N., Andreev, M., Klunko, E., Volnova, A., Akerlof, C.W., Anto, P., Barthelmy, S.D., Breeveld, A.A., Carsenty, U., Castillo-Carrión, S., Castro-Tirado, A.J., Chester, M.M., Chuang, C.J., Cunniffe, R., de Ugarte Postigo, A., Duffard, R., Flewelling, H., Gehrels, N., Güver, T., Guziy, S., Hentunen, V.P., Huang, K.Y., Jelínek, M., Koch, T.S., Kubánek, P., Kuin, N.P.M., McKay, T.A., Mottola, S., Oates, S.R., O'Brien, P., Ohno, M., Page, M.J., Pandey, S.B., Pérez del Pulgar, C., Rujopakarn, W., Rykoff, E., Salmi, T., Sánchez-Ramírez, R., Schaefer, B.E., Sergeev, A., Sonbas, E., Sota, A., Tello, J.C., Yamaoka, K., Yost, S.A. & Yuan, F. (2012). Panchromatic Observations of the Textbook GRB 110205A: Constraining Physical Mechanisms of Prompt Emission and Afterglow. *The Astrophysical Journal*, **751**, 90. 73

Zitrin, A., Labbé, I., Belli, S., Bouwens, R., Ellis, R.S., Roberts-Borsani, G., Stark, D.P., Oesch, P.A. & Smit, R. (2015). Lymanα Emission from a Luminous $z = 8.68$ Galaxy: Implications for Galaxies as Tracers of Cosmic Reionization. *The Astrophysical Journal Letters*, **810**, L12.

Zucca, E., Bardelli, S., Bolzonella, M., Zamorani, G., Ilbert, O., Pozzetti, L., Mignoli, M., Kovač, K., Lilly, S., Tresse, L., Tasca, L., Cassata, P., Halliday, C., Vergani, D., Caputi, K., Carollo, C.M., Contini, T., Kneib, J.P., Le Fèvre, O., Mainieri, V., Renzini, A., Scodeggio, M., Bongiorno, A., Coppa, G., Cucciati, O., de La Torre, S., de Ravel, L., Franzetti, P., Garilli, B., Iovino, A., Kampczyk, P., Knobel, C., Lamareille, F., Le Borgne, J.F., Le Brun, V., Maier, C., Pellò, R., Peng, Y., Perez-Montero, E., Ricciardelli, E., Silverman, J.D., Tanaka, M., Abbas, U., Bottini, D., Cappi, A., Cimatti, A., Guzzo, L., Koekemoer, A.M., Leauthaud, A., Maccagni, D., Marinoni, C., McCracken, H.J., Memeo, P., Meneux, B., Moresco, M., Oesch, P., Porciani, C., Scaramella, R., Arnouts, S., Aussel, H., Capak, P., Kartaltepe, J., Salvato, M., Sanders, D., Scoville, N., Taniguchi, Y. & Thompson, D. (2009). The zCOSMOS survey: the role of the environment in the evolution of the luminosity function of different galaxy types. *Astronomy and Astrophysics*, **508**, 1217–1234.

Zwaan, M.A., Staveley-Smith, L., Koribalski, B.S., Henning, P.A., Kilborn, V.A., Ryder, S.D., Barnes, D.G., Bhathal, R., Boyce, P.J., de Blok, W.J.G., Disney, M.J., Drinkwater, M.J., Ekers, R.D., Freeman, K.C., Gibson, B.K., Green, A.J., Haynes, R.F., Jerjen, H., Juraszek, S., Kesteven, M.J., Knezek, P.M., Kraan-Korteweg, R.C., Mader, S., Marquarding, M., Meyer, M., Minchin, R.F., Mould, J.R., O'Brien, J., Oosterloo, T., Price, R.M., Putman, M.E., Ryan-Weber, E., Sadler, E.M., Schröder, A., Stewart, I.M., Stootman, F., Warren, B., Waugh, M., Webster, R.L. & Wright, A.E. (2003). The 1000 Brightest HIPASS Galaxies: The H I Mass Function and ΩHI. *The Astronomical Journal*, **125**, 2842–2858.

Zwaan, M.A., van der Hulst, J.M., Briggs, F.H., Verheijen, M.A.W. & Ryan-Weber, E.V. (2005). Reconciling the local galaxy population with damped Lyman α cross-sections and metal abundances. *Monthly Notices of the Royal Astronomical Society*, **364**, 1467–1487.